

NASA/CP-1999-209690/PT2



First NASA/Industry High-Speed Research Configuration Aerodynamics Workshop

Edited by
Richard M. Wood
Langley Research Center, Hampton, Virginia

Proceedings of a workshop held at
Langley Research Center,
Hampton, Virginia
February 27-29, 1996

National Aeronautics and
Space Administration

Langley Research Center
Hampton, Virginia 23681-2199

December 1999

Available from:

NASA Center for Aerospace Information (CASI)
7121 Standard Drive
Hanover, MD 21076-1320
(301) 621-0390

National Technical Information Service (NTIS)
5285 Port Royal Road
Springfield, VA 22161-2171
(703) 605-6000

PREFACE

This publication is a compilation of documents presented at the First NASA/Industry High-Speed Research Configuration Aerodynamics Workshop held on February 27-29, 1996, at NASA Langley Research Center. The purpose of the workshop was to bring together the broad spectrum of aerodynamicists, engineers, and scientists working within the Configuration Aerodynamics element of the HSR Program to collectively evaluate the technology status and to define the needs within Computational Fluid Dynamics (CFD) Analysis Methodology, Aerodynamic Shape Design, Propulsion/Airframe Integration (PAI), Aerodynamic Performance, and Stability and Control (S&C) to support the development of an economically viable High-Speed Civil Transport (HSCT) aircraft. To meet these objectives, papers were presented by representatives from NASA Langley, Ames and Lewis Research Centers, Boeing, McDonnell Douglas, Northrop-Grumman, Lockheed-Martin, Vigyan, Analytical Services, Dynacs, and RIACS.

The workshop was organized in 12 sessions as follows:

- Introduction/Overviews
- Overviews
- PAI I
- PAI II
- Analysis and Design Optimization Methods
- Experimental Methods
- Design Optimization - Applications I
- Design Optimization - Applications II
- Design Optimization - Applications III/Validation
- Reynolds Number Effects
- Stability and Control
- High Lift

Appreciation is expressed to the individuals at NASA Langley, NASA Ames, McDonnell Douglas, and Boeing who developed the structure and content of the workshop; to the session chairs and speakers who contributed to the technical quality; and to the many individuals who contributed to the administration and logistics of the workshop. A list of attendees is included in this document.

Richard M. Wood
NASA Langley Research Center

CONTENTS

Preface	iii
Attendees	xi

Part 1*

Session 1

HSR Aerodynamic Performance Status and Challenges	1
<i>Bill Gilbert, NASA Langley Research Center, Tony Antani, McDonnell Douglas, Doug Ball, Boeing, Rob Calloway, NASA Langley Research Center, Phil Snyder, NASA Ames Research Center</i>	
Configuration Aerodynamics: Past – Present – Future	15
<i>Richard Wood, NASA Langley Research Center; Shreekant Agrawal, MDA; Dan Bencze, NASA Ames Research Center; Bob Kulfan, Doug Wilson, BCA</i>	
Technology Integration Overview.....	41
<i>Peter G. Coen, NASA Langley Research Center</i>	

Session 2

Wind Tunnel Test Technique and Instrumentation Development at NASA Langley Research Center	65
<i>Lawrence E. Putnam, NASA Langley Research Center</i>	
4.3.4 Supersonic Laminar Flow Control, An Overview	81
<i>Bharadvaj, Bala, McDonnell Douglas; Mike Fischer, Ron Joslin, NASA Langley Research Center; Lyn King, NASA Ames Research Center; Pradip Parikh, Boeing Commercial Airplane Group</i>	
High Lift Technology Overview.....	99
<i>Z.T. Applin, NASA Langley Research Center</i>	

Session 3

Experimental Results of the 2.7% Reference H Nacelle Airframe Interference High Speed Civil Transport Model.....	113
<i>Gelsomina Cappuccio, NASA Ames Research Center</i>	
HSCT Propulsion Airframe Integration Studies.....	139
<i>Steve Chaney, The Boeing Company</i>	
HSCT Nacelle Boundary Layer Diverter Study.....	183
<i>Steven S. Ogg, The Boeing Company</i>	

*Part 1 is presented under separate cover.

Analysis of Alternate Inlets and Nacelles for HSCT Configuration	197
P. Sundaram*, Ana Tinetti**, Alan Arslan*, Shreekant Agrawal*, Peter Hartwich*, Jay Jones*, (<i>*McDonnell Douglas Corporation; **Eagle Aeronautics, Inc.</i>)	

Session 4

High Speed Civil Transport (HSCT) Isolated Nacelle Transonic Boattail Drag Study and Results Using Computational Fluid Dynamics (CFD)	223
Anthony C. Midea,* Thomas Austin,** S. Paul Pao,*** James R. DeBonis,* Mori Mani,** (<i>*NASA Lewis Research Center, **McDonnell Douglas Aerospace, ***NASA Langley Research Center</i>)	

Transonic Drag Study for the Installed Ref. H Axisymmetric Nozzle Boattail Configurations	271
Chih Fang Shieh, Jay Jones, Shreekant Agrawal, <i>McDonnell Douglas Aerospace</i>	

Installed Transonic 2D Nozzle Nacelle Boattail Drag Study	291
M. Malone, C. Peavey, <i>Northrop Grumman Corporation</i>	

Afterbody External Aerodynamic and Performance Predictions at High Reynolds Numbers	321
John R. Carlson, <i>NASA Langley Research Center</i>	

Part 2

Session 5

Viscous Analysis of Ref. H Based Wing/Bodies	335
Scott L. Lawrence, <i>NASA Ames Research Center</i>	

CFD Code Validation for HSCT Wing/Body and Wing/Body/Nacelle/Diverter Configurations	355
James O. Hager, Geojoe Kuruvila, Samson H. Cheung, Eric R. Unger, and Shreekant Agrawal, <i>McDonnell Douglas Aerospace</i>	

Overview of HSR Aerodynamic Optimization at Boeing	395
R.S. Conner, <i>The Boeing Company</i>	

Some Recent Enhancements to Aerodynamic Shape Optimization Methods at McDonnell Douglas Aerospace	423
Peter M. Hartwich, Eric R. Unger, Alan E. Arslan, Shreekant Agrawal, <i>McDonnell Douglas Corporation</i>	

Boeing HSR Wing Optimization Using Tranair	445
K.R. Wittenberg, <i>The Boeing Company</i>	

Advances in Design Optimization Using Adjoint Methods	493
James Reuther, <i>RIACS/AAH</i> ; David Saunders, <i>Sterling Software</i>	

Session 6

Aftbody Closure Effects on the Reference H Configuration at Subsonic and Transonic Speeds.....	529
Richard A. Wahls, Lewis R. Owens, Jr., <i>NASA Langley Research Center</i> , W. Kelly Londenberg, <i>ViGYAN, Inc.</i>	
Model Deformation Measurement Technique – NASA Langley HSR Experiences.....	561
A.W. Burner, R.A. Wahls, L.R. Owens, W.K. Goad <i>NASA Langley Research Center</i>	
Boundary Layer Transition in the NTF: HSR Experience and Plans	579
Louis R. Owens, Jr., Richard A. Wahls, <i>NASA Langley Research Center</i> , Marvine P. Hamner, <i>McDonnell Douglas Aerospace</i>	

Session 7

The Application of the NFW Design Philosophy to the HSR Arrow Wing Configuration	597
Steven X.S. Bauer, Steven E. Krist, <i>NASA Langley Research Center</i>	
Analysis and Inverse Design of the HSR Arrow Wing Configuration with Fuselage, Wing, and Flow Through Nacelles.....	641
Steven E. Krist, Steven X.S. Bauer, <i>NASA Langley Research Center</i>	
HSCT Multipoint Aerodynamic Performance Trades from TCA Propulsion and Planform Studies	665
Chester P. Nelson, <i>Boeing Commercial Airplane Group</i>	
CFD Planform Study of the 1400 Series.....	681
G. Kuruvila, J.O. Hager, E.R. Unger, A.E. Arslan, D.B. Bruns, P. Sundaram, G. Martin, S. Agrawal, <i>McDonnell Douglas Aerospace</i>	

Session 8

Investigation of Nonlinear Effects on Reference H Body Area-Ruling and Cambering	705
Thierry Tamigniaux, <i>The Boeing Company</i>	
Fuselage Cross-Sectional Area and Camber Optimization Using Nonlinear Aerodynamic Tools	727
James O. Hager, Shreekant Agrawal, <i>McDonnell Douglas Aerospace</i>	
Wing Design and Suction/Cooling Requirements for an HSCT With Supersonic Laminar Flow Control.....	751
Bala Bharadvaj, Dino Roman, P. Sundaram, Art Powell, K.C. Chang, <i>McDonnell Douglas Aerospace</i> ; Lian Ng, Paul Vijgen, Pradip Parikh, <i>Boeing Commercial Airplane Group</i>	

Projecting and Tracking Advanced Technology Improvements in L/D.....	781
<i>R.M. Kulfan, Boeing Commercial Airplane Group</i>	

Part 3*

Session 9

A Computational/Experimental Study of Two Optimized Supersonic Transport Designs and the Reference H Baseline.....	845
<i>Susan E. Cliff, NASA Ames Research Center; Timothy J. Baker, Princeton University; Raymond M. Hicks, MCAT; James J. Reuther, RIACS</i>	

Update to the Summary of Langley Unitary Test 1649 and Its Implications on Validity of Viscous and Inviscid Analyses.....	969
<i>S. Yaghmaee, K.M. Mejia, Boeing Commercial Airplane Group</i>	

Supersonic Aerodynamic Design Improvements of an Arrow-Wing HSCT Configuration Using Nonlinear Point Design Methods.....	1009
<i>Eric R. Unger, James O. Hager, Shreekant Agrawal, McDonnell Douglas Aerospace</i>	

Experimental Investigation of a Point Design Optimized Arrow-Wing HSCT Configuration	1041
<i>R.P. Narducci, P. Sundaram, S. Agrawal, S. Cheung, A.E. Arslan, G.L. Martin, McDonnell Douglas Aerospace</i>	

Session 10

Initial Results of Reynolds Number Testing at LaRC's NTF Using the 2.2% Reference H Model.....	1073
<i>Marvine Hamner, McDonnell Douglas Aerospace; Lewis R. Owens, Jr., Richard A. Wahls, NASA Langley Research Center</i>	

HSCT Ref-H Transonic Flap Data Base: Wind-Tunnel Test and Comparison with Theory	1109
<i>Paul M. Vijgen, Boeing Commercial Airplane Group</i>	

Assessment of Ref. H HSCT Transonic Flap and Reynolds Number Effects with the OVERFLOW Code.....	1143
<i>Max Kandula, Ross Sheckler, Dynacs Engineering Company, Inc.</i>	

Turbulence Model Comparisons and Reynolds Number Effects Over a High-Speed Aircraft at Transonic Speeds.....	1185
<i>Melissa B. Rivers, Richard A. Wahls, NASA Langley Research Center</i>	

*Part 3 is presented under separate cover.

Session 11

Critical Stability and Control Issues in High-Speed Aerodynamics for the HSCT	1215
Douglas L. Wilson, <i>Boeing Commercial Airplane Group</i> ; Norman H. Princen, <i>McDonnell Douglas Aerospace</i> ; Oran C. Harris, <i>Lockheed Martin Aeronautical Systems Company</i>	
An Experimental Database for Conventional and Alternate Control Concepts on the HSR 1.675% Reference H Model	1233
Naomi McMillin, Jerry Allen, Gary Erickson, Jim Campbell, Mike Mann, <i>NASA Langley Research Center</i> ; Paul Kubiato, David Yingling, <i>McDonnell Douglas Aerospace</i> ; Charlie Mason, <i>Lockheed Martin</i>	
High Reynolds Number Effects on HSCT Stability and Control Characteristics	1253
Michael B. Elzey, <i>The Boeing Company</i> ; Lewis R. Owens, Jr., Richard A. Wahls, <i>NASA Langley Research Center</i> ; Douglas L. Wilson, <i>The Boeing Company</i>	
Simulated Inlet Unstart and Nacelle/Diverter Effects for the Boeing Reference H Configuration	1285
Susan E. Cliff,* Timothy J. Baker,** Scott D. Thomas,** E. Aguayo** (*NASA Ames Research Center, **Princeton University)	

Session 12

Wing Leading-Edge Geometry Effects on High-Lift Performance	1327
David L. Hoyle, Marvine Hamner, <i>McDonnell Douglas Aerospace</i>	
Impact of Alternate Concepts for Wing Planform, Leading Edge Flaps, and Trim Configuration on the High Lift Performance of the Ref H HSCT	1345
G.H. Wyatt, K.D. Visser, <i>Boeing Commercial Airplane Company</i>	
Assessment of CFD Codes for HSCT Ref. H High Lift Aerodynamics	1375
Anthony J. Saladino, Ross D. Sheckler, <i>Dynacs Engineering Co. , Inc.</i>	
Summary of HEAT 1 Aeroacoustics Installation Effects	1407
Brian E. Smith, Paul T. Soderman, Fanny A. Zuniga, <i>NASA Ames Research Center</i>	

ATTENDEES

Abdol-Hamid, Khaled S.....	Analytical Services & Materials, Inc.
Adams, Bill	NASA Langley Research Center
Agrawal, Shreekant.....	McDonnell Douglas Aerospace
Allen, Jerry M.	NASA Langley Research Center
Antani, Tony	McDonnell Douglas Aerospace
Applin, Z.	NASA Langley Research Center
Baker, Timothy J.....	Princeton University
Bard, William.....	Northrop Grumman Corporation
Bauer, Steve	NASA Langley Research Center
Beach, H. Lee.....	NASA Langley Research Center
Bencze, Daniel P.	NASA Ames Research Center
Bharadvaj, Bala.....	McDonnell Douglas Aerospace
Bobbitt, Percy J.	Eagle Aeronautics, Inc.
Burner, A. W.	NASA Langley Research Center
Bushnell, D.....	NASA Langley Research Center
Buttrill, C.	NASA Langley Research Center
Calloway, R. L.	NASA Langley Research Center
Campbell, James F.	NASA Langley Research Center
Campbell, Richard L.	NASA Langley Research Center
Capone, Francis J.	NASA Langley Research Center
Cappuccio, Gelsomina	NASA Ames Research Center
Carlson, John R.	NASA Langley Research Center
Chaney, Steve.....	Boeing
Chu, J.	NASA Langley Research Center
Clark, Roger	McDonnell Douglas Aerospace
Cliff, Susan E.	NASA Ames Research Center
Coen, P.	NASA Langley Research Center
Compton, W.	NASA Langley Research Center
Conner, Roy S.	Boeing Commercial Airplane Group
Covell, P.....	NASA Langley Research Center
DeBonis, Jim.....	NASA Lewis Research Center
Deere, Karen A.	NASA Langley Research Center
Dollyhigh, S.	NASA Langley Research Center
Domack, C.	NASA Langley Research Center

Driver, Cornelius.....	Eagle Aeronautics, Inc.
Dudley, Mike	NASA Ames Research Center
Dwoyer, D.	NASA Langley Research Center
Dwyer, William P.	Northrop Grumman ATDC
Erickson, G.....	NASA Langley Research Center
Flamm, J.....	NASA Langley Research Center
Fox, Mike C.	Vigyan, Inc.
Frink, Neal	NASA Langley Research Center
Gerhardt, Heinz A.	Northrop Grumman Corporation
Ghaffari, Farhad	NASA Langley Research Center
Gibson, Berry T.....	Lockheed Martin Aeronautical Systems
Gilbert, W. P.	NASA Langley Research Center
Glaab, Lou.....	Lockheed Martin
Goldberg, Perry	McDonnell Douglas Aerospace
Goodsell, Aga.....	NASA Ames Research Center
Graber Ed	NASA Lewis Research Center
Green, L.	NASA Langley Research Center
Hager, James	McDonnell Douglas Aerospace
Hahne, David	NASA Langley Research Center
Hamner, Marvine	McDonnell Douglas Aerospace
Harris, Roy V.	NASA Langley Research Center
Hartwich, Peter.....	McDonnell Douglas Aerospace
Hefner, J.	NASA Langley Research Center
Henderson, W.....	NASA Langley Research Center
Hicks, Ray	NASA Ames Research Center/MCAT
Holloway, Paul F.....	NASA Langley Research Center
Hoyle, David	McDonnell Douglas Aerospace
Jameson, A.	Princeton University
Joslin, Ronald D.	NASA Langley Research Center
Kandula, Max	Dynacs Engineering Co.
Kammerly, G.....	NASA Langley Research Center
Kennelly, Jr., Robert A.	NASA Ames Research Center
Keyes, Sandy	NASA Langley Research Center
Krist, Steve	NASA Langley Research Center
Kubiatko, Paul.....	McDonnell Douglas Aerospace
Kulfan, Robert M.	Boeing Commercial Airplane Group

Kuruville, G.....	McDonnell Douglas Aerospace
LaBozzetta, Walt.....	McDonnell Douglas Aerospace
Lawrence, Scott.....	NASA Ames Research Center
Leavitt, Lawrence D.	NASA Langley Research Center
Lessard, Wendy B.	NASA Langley Research Center
Luckring, J.	NASA Langley Research Center
Ludas, Kevin	McDonnell Douglas Aerospace
Malone, Michael B.....	Northrop Grumman
Mason, Charlie	Lockheed Martin
McMillin, S. Naomi	NASA Langley Research Center
Midea, Tony	NASA Lewis Research Center
Naik, Dinesh.....	Vigyan/NASA Langley Research Center
Narducci, Robert	McDonnell Douglas Aerospace
Nelms, Pres	NASA Ames Research Center
Nelson, Chester P.	Boeing Commercial Airplane Group
Owens, L.	NASA Langley Research Center
Ozorowski, L.....	NASA Langley Research Center
Pao, S. Paul	NASA Langley Research Center
Parikh, Paresb.....	TSAB/NASA Langley Research Center
Peavey, Charles C.	Northrop Grumman
Plencner, Bob	NASA Ames Research Center
Pirzadeh, Shahyar.....	Vigyan
Princen, Norm	McDonnell Douglas Aerospace
Putman, Lawrence E.	NASA Langley Research Center
Re, R.....	NASA Langley Research Center
Reuther, James	NASA Ames Research Center/RIACS
Rivers, Melissa B.	NASA Langley Research Center
Saladino, Anthony J.	Dynacs Engineering Co.
Sawyer, W. C.	NASA Langley Research Center
Schuster, Ernie	McDonnell Douglas Aerospace
Shieh, Chih Fang.....	McDonnell Douglas Aerospace
Shields, B.	NASA Langley Research Center
Shin, Jaiwon	NASA Lewis Research Center
Siclaris, Michael J.	Northrop Grumman
Smith, Brian	NASA Ames Research Center
Phillip, T.....	NASA Ames Research Center

South, J.	NASA Langley Research Center
Stephens, D.	NASA Langley Research Center
Sundaram, P.	McDonnell Douglas Aerospace
Thomas, James L.	NASA Langley Research Center
Tinetti, Ana F.	Eagle Aeronautics, Inc.
Tu, Eugene	NASA Ames Research Center
Unger, Eric	McDonnell Douglas Aerospace
Vatsa, V.	NASA Langley Research Center
Veitch, Lisa C.	NASA Langley Research Center
Vijgen, Paul M.	Boeing Commercial Airplane Group
Waggoner, Edgar	NASA Langley Research Center
Wahls, Richard A.	NASA Langley Research Center
Wilhite, A. W.	NASA Langley Research Center
Wilson, Douglas L.	Boeing Commercial Airplane Group
Wing, D.	NASA Langley Research Center
Wood, Richard	NASA Langley Research Center
Wyatt, Greg	BCAG High Lift Aerodynamics
Yaghmaee, S.	Boeing Commercial Airplane Group
Yaros, Steven F.	NASA Langley Research Center
Yetter, J.	NASA Langley Research Center
Zang, T.	NASA Langley Research Center
Zuniga, Fanny A.	NASA Ames Research Center

VISCOUS ANALYSIS OF REF. H BASED WING/BODIES

Scott L. Lawrence
NASA Ames Research Center
Moffett Field, California

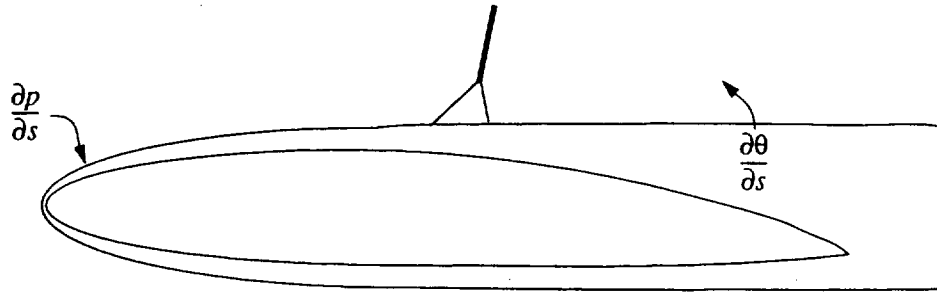
OUTLINE

- INTRODUCTION
- SOLUTION METHOD
- RESULTS
 - FRICTION DRAG STUDY
 - VISCOUS/INVISCID INTERACTION
- SUMMARY

1st NASA/Industry High Speed Research Configuration Aerodynamics Workshop
NASA Langley Research Center
February 27-29, 1996

Computations have been performed on the baseline Reference H wing/body configuration, as well as the Wing 704 configuration, an optimized wing and fuselage combination derived from Ref. H through automated optimization. The parabolized Navier-Stokes solver UPS was employed with viscous terms in two directions in an effort to understand the source and level of potential viscous/inviscid interactions. The paper briefly describes the UPS code and the grids used to obtain the solutions before the discussion of results. Results of these computations indicate that viscous/inviscid interaction can contribute increments to both the pressure- and friction-related drag. Computations were performed for wind tunnel conditions-1.675% scale models at a Reynolds number of 4 million per foot. Turbulent flow results were obtained using the Baldwin-Lomax algebraic turbulence model and were compared with laminar flow results. The laminar flow fields were used to obtain upper bounds on potential interaction effects.

WHY DO VISCOUS ANALYSIS?

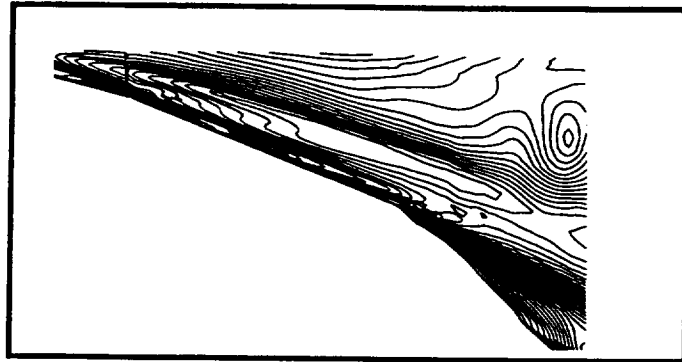


- INCLUDE INFLUENCE OF:
 - PRESSURE GRADIENT ON FRICTION DRAG
 - BOUNDARY LAYER DISPLACEMENT ON WAVE DRAG
 - INTERACTION (NONLINEARITIES)
- FOR THE PURPOSES OF:
 - ESTIMATING LEVEL OF INTERACTION-RELATED DRAG
 - GAINING UNDERSTANDING OF THE MECHANISMS INVOLVED
 - ASSISTING IN MODELING POTENTIALLY IMPORTANT EFFECTS

The boundary layer flow field is influenced by the Euler flow through the imposition of the pressure gradient at the boundary layer edge. In return, the boundary layer provides a displacement effect to the body surface which influences the inviscid flow. In extreme cases, such as a shock/boundary-layer interaction, the inviscid pressure gradient is sufficient to cause separation of the boundary layer which produces large displacement effects significantly affecting the inviscid flow field. Viscous analyses are able to predict these effects, to a large degree, and can be used to better understand the mechanisms of the interactions. This information can then be used to model interaction effects, where important, in Euler-based automated design tools.

WHY RUN THESE CASES?

- SKIN FRICTION DRAG REDUCTION
 - IS IT REAL?
 - WHERE IS IT COMING FROM (LOCATION)?
 - WHERE IS IT COMING FROM (PHYSICS)?
- RECOMPRESSION INTERACTION



- DRAG INCREMENT?
- UNCERTAINTY?

The primary purpose for running the specific cases computed in this study was to verify the wave drag reductions obtained in the Wing 704 design process. The Wing 704 design was obtained through automated design of wing camber and twist, as well as fuselage camber, using Euler analysis techniques in the process. Independent inviscid verification was obtained using the AIRPLANE code, but there was some reason to believe that a significant part of the gain might be lost in a real (viscous) flow, because of a considerable strengthening of the upper wing surface recompression. Thus, the computations were performed in an effort to estimate the level of any wave drag penalty that might be incurred because of viscous/inviscid interaction. Also, the level of sensitivity to turbulence model is of interest because of the lack of extensive validation of Baldwin-Lomax for these types of flows. Finally, owing to observations made by Douglas researchers with respect to the arrow wing, the possibility of skin friction drag reduction on Wing 704 relative to Ref. H was studied in some detail.

UPS CHARACTERISTICS

- PNS (SPACE-MARCHING) SOLVER
 - VIGNERON PRESSURE SPLITTING
- FINITE-VOLUME
- UPWIND
 - 3RD-ORDER FLUX-DIFFERENCE-SPLITTING (ROE)
 - VARIOUS LIMITER AND ENTROPY FIXING OPTIONS
- IMPLICIT
 - CONVENTIONAL LINEARIZATION (BEAM-WARMING) + AF
- TURBULENCE
 - BALDWIN-LOMAX/DEGANI-SCHIFF
 - BALDWIN-BARTH (2-D)
 - SPALART-ALLMARAS

Characteristics of the UPS parabolized Navier-Stokes solver are outlined here. The equations are parabolized using the Vigneron pressure splitting procedure. The equations are discretized in a finite-volume manner with inviscid fluxes evaluated using a Roe-based flux-difference-splitting scheme. Conventional linearization is employed with approximate-factorization to allow efficient space-marching. Finally, turbulence is typically modeled using the algebraic model of Baldwin and Lomax with Degani-Schiff corrections for separated (crossflow) flows. Recently, the one-equation models of Baldwin-Barth and Spalart-Allmaras have been included, but have not been demonstrated in three dimensions.

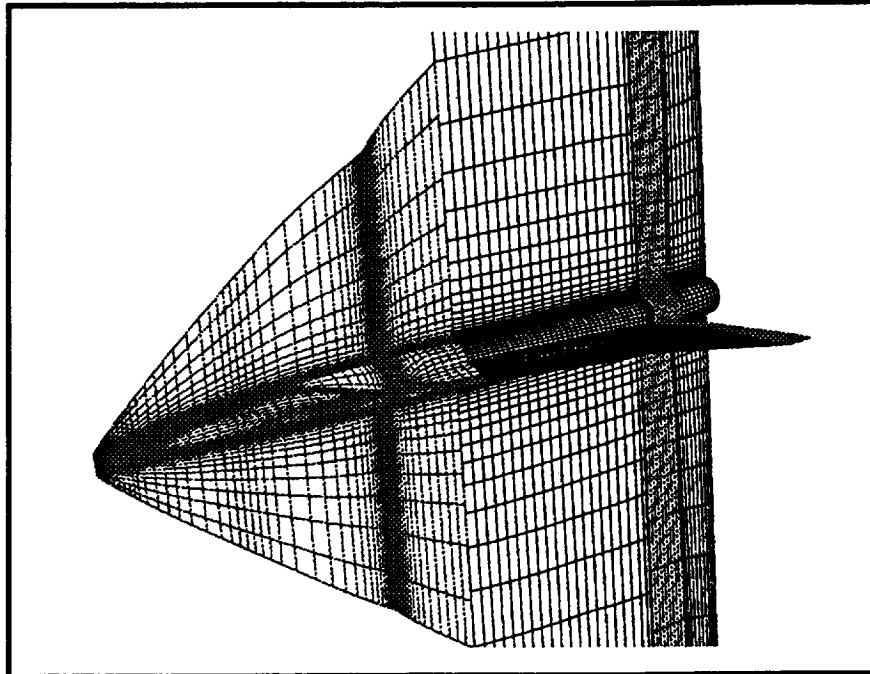
GRID TOPOLOGY

- FOUR AXIAL BLOCKS

- $y^+ = 0.5$

- STATION CUTS (FOR MARCHING)

- $N_{\text{NORMAL}} = 120$



The grid topology used for the case computed in this study is shown above. The space-marching solution procedure requires essentially axial cuts through the body and wing for the entire length of the body. To simplify the grid generation and to reduce computational costs, the body is broken into four sections: the fore, body, trailing edge, and sting sections. For clarity, only every third point are shown in each direction. In each block, 120 points are distributed normal to the body, with the first point located at a y^+ value of approximately 0.5. The fore section uses 73 points in the wraparound direction, the body and trailing edge sections use 160 points, and the sting grid contains 45 points in the wraparound direction. Three bilinear interpolations are required in the solution process.

SKIN FRICTION DRAG

Mach 2.4, Re = 4 million/ft

BODY	α	$C_{Dv}(B-L)$	$C_{Dv}(lam)$	Flat Plate
Ref H	4.4	0.006075	0.001849	0.0063
Ref H	4.6	0.006075	0.001860	0.0063
704	4.3	0.006021	0.001908	0.0063
704	4.5	0.006014	0.001920	0.0063

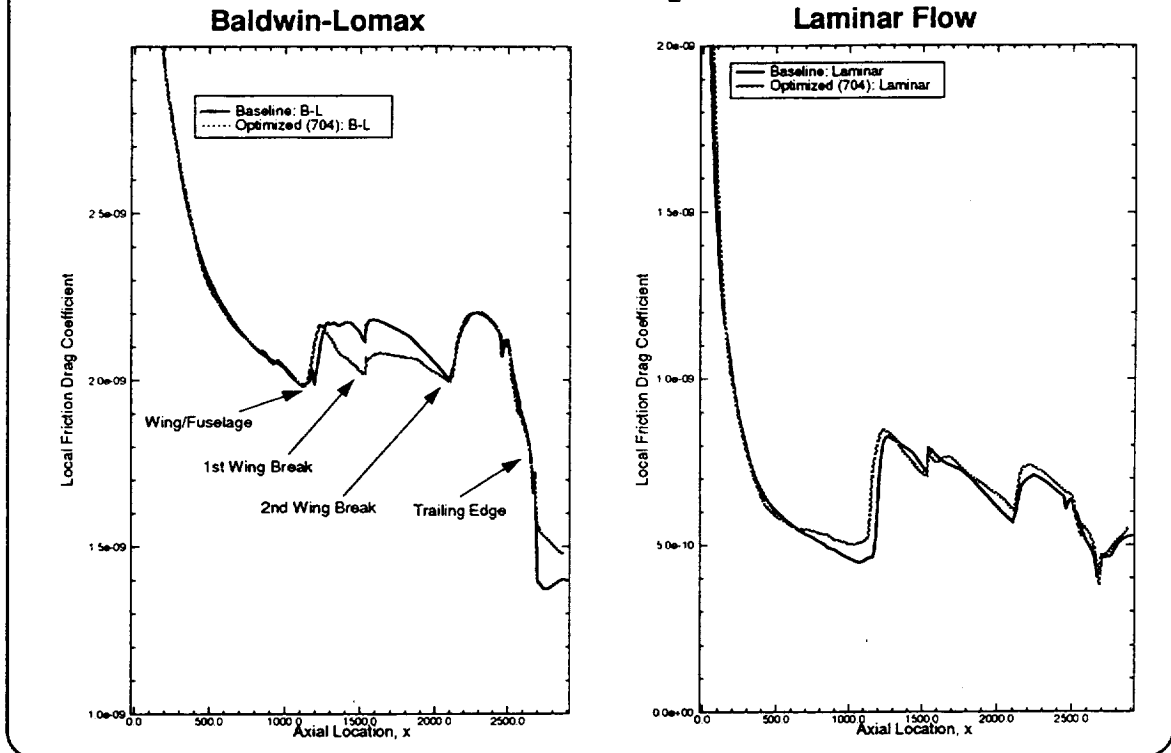
- BALDWIN-LOMAX DRAG REDUCTION
- LAMINAR FLOW DRAG INCREASE

This table shows results of the eight cases in terms of integrated skin friction drag. Also included are results of flat-plate theory for the Ref. H/Wing 704 planform. Pressure gradient information is not included in the flat-plate analysis. Results computed using the Baldwin-Lomax turbulence model underpredict the theoretical value by 2.25 to 2.75 counts (or ~4%). Not surprisingly, the friction drag is relatively insensitive to angle-of-attack.

A modest drag reduction is observed on Wing 704 relative to the baseline Ref. H when the Baldwin-Lomax turbulence model is turned on. However, with the turbulence model turned off, Wing 704 shows an increase in friction drag of the same level as the decrease observed for turbulent flow. The following discussion will attempt to provide some understanding of what is causing this behavior.

FRICTION DRAG DISTRIBUTIONS

$Re = 4 \text{ million/ft}; C_L = 0.123$



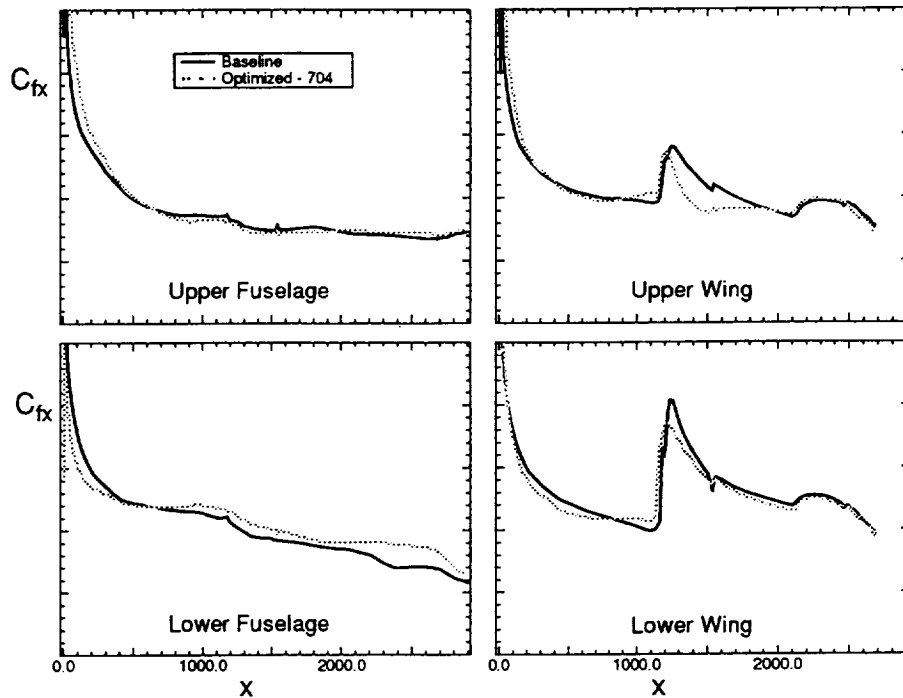
This figure shows axial distributions of circumferentially averaged skin friction coefficient. Thus, to obtain the total friction drag from these distributions, one must weight the local C_f value by the local circumferential arc length prior to integration. Thus, when interpreting these figures, one must keep in mind the vehicle configuration and give appropriate weight to observed differences.

The figure on the left indicates that the majority of the Wing 704 skin friction drag advantage is associated with the subsonic leading edge portion of the wing. A small part of this advantage is given up in the trailing edge and sting regions.

The figure on the right shows the laminar flow results and indicates that, under laminar conditions, the skin friction disadvantage of Wing 704 is distributed over nearly the entire length of the body. Note that Wing 704 included fuselage as well as wing modifications.

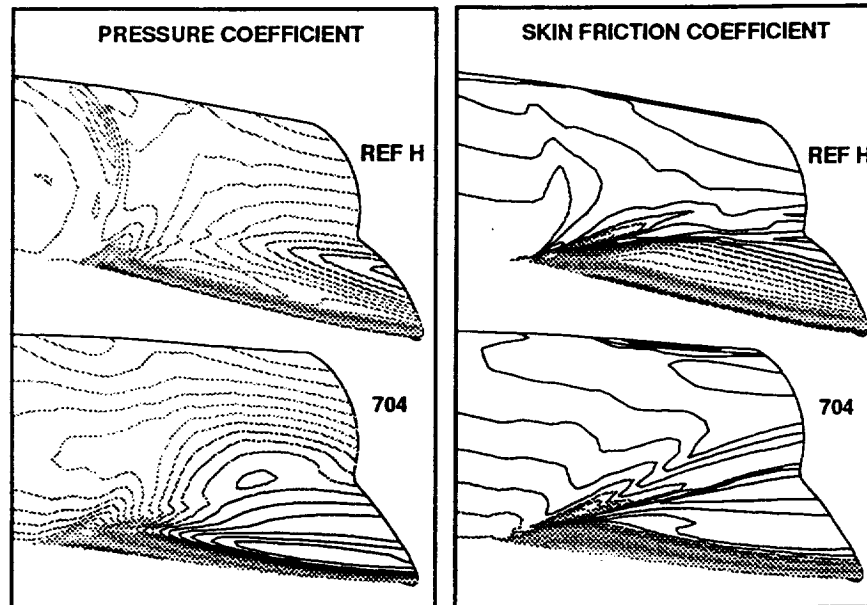
PIECE-WISE FRICTION DRAG DISTRIBUTIONS

$Re = 4$ million/ft; $C_L = 0.123$



In order to further isolate the turbulent friction drag improvements, the configurations are divided circumferentially into sections. The division on the fuselage is somewhat arbitrary and leads to meaningless comparisons since the two surface grids are distributed slightly differently. Downstream of the wing emergence location ($x \sim 1110''$), the circumference is divided at the lower wing/fuselage intersection, the wing leading edge, and the upper wing/fuselage intersection.

The results shown here indicate that the majority of the improvement is obtained on the upper wing surface, especially upstream of the 1st wing sweep break, though the lack of area weighting may be at least partly responsible for the advantage diminishing with downstream distance (see previous paragraph).

UPPER WING SURFACE FLOW FIELD**Baldwin-Lomax Model**

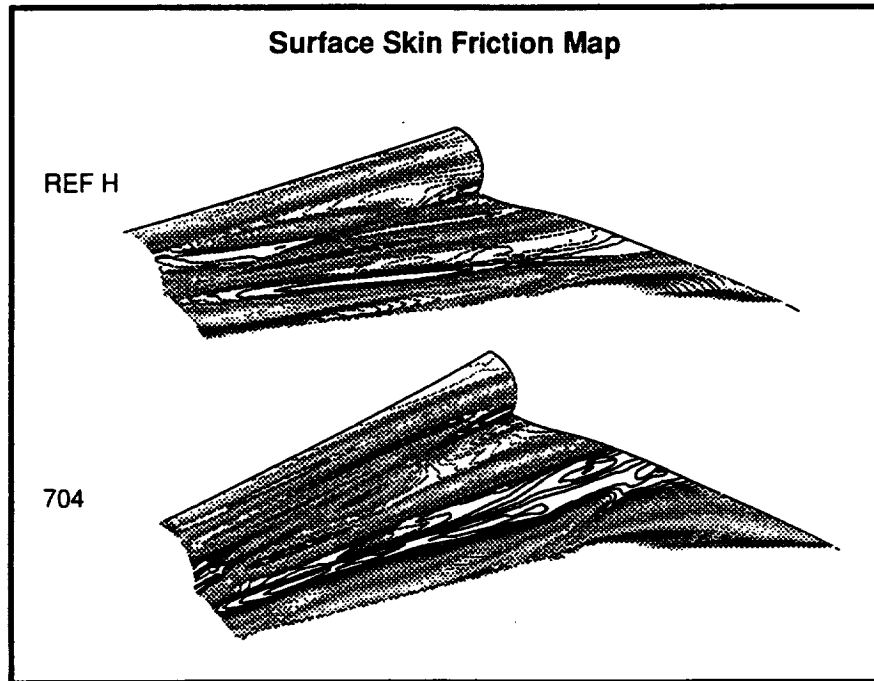
Upper surface pressure and skin friction distributions are shown in this figure as computed for both configurations with the Baldwin-Lomax turbulence model. One observes a difference in character of the pressure distribution between the baseline and the Wing 704 results. The Ref. H configuration shows a somewhat evenly distributed expansion from the leading edge whereas the expansion is concentrated at the leading edge on Wing 704. A similar behavior is observed in the skin friction distributions, with skin friction on Ref. H maintaining somewhat higher values over much of this portion of the upper wing surface.

The most obvious explanation, therefore, for the Wing 704 skin friction advantage is the well known tendency of favorable pressure gradients to produce fuller boundary-layer profiles and higher wall shear and skin friction. The boundary-layer flow on Ref. H experiences a favorable pressure gradient over a greater distance than that on Wing 704, and, as a result, shows elevated skin friction in comparison with Wing 704.

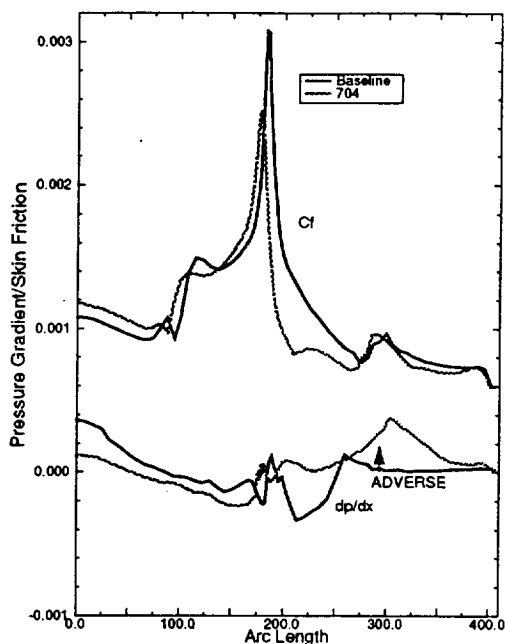
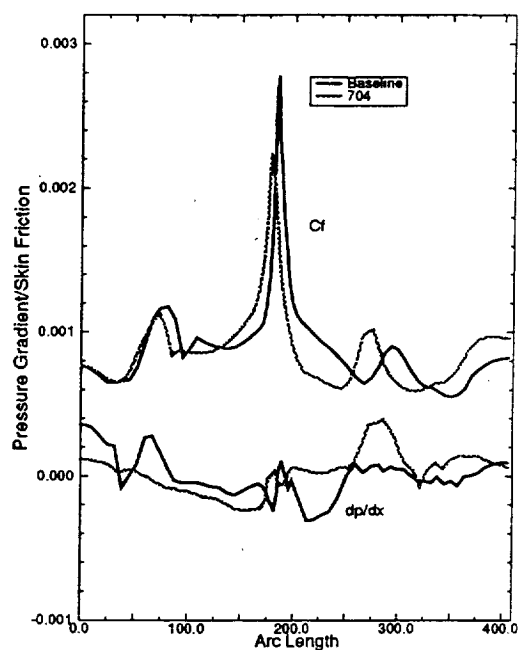
The question remains, however, of why the laminar flow results do not show at least as much of a Wing 704 advantage as do the turbulent results. In fact, although not shown here, the laminar flow results on this section of wing look remarkably similar to those observed above in terms of pressure and skin friction distributions. However, the flow on the body of the wing differs considerably from the turbulent case.

SURFACE FLOW FIELD - LAMINAR

Upper Wing Surface - Downstream of Break



This figure illustrates the complexity of the laminar flow on the upper surface of both the Reference H and the Wing 704 wings. The skin friction maps for both Ref. H and Wing 704 indicate the presence of streaks of relatively high local skin friction values. These streaks are associated with vortical flow features which, like turbulence, transfer high momentum fluid from the outer parts of the boundary layer to the near-wall parts and increase the wall shear. It is believed that the number and strength of these features is greater on the Wing 704 configuration because the Wing 704 pressure distribution contains somewhat more severe lateral gradients.

CORRELATION WITH PRESSURE GRADIENT?Re = 6 million/ft; $C_L = 0.123$; x = 1480" (F-S)**Baldwin-Lomax****Laminar**

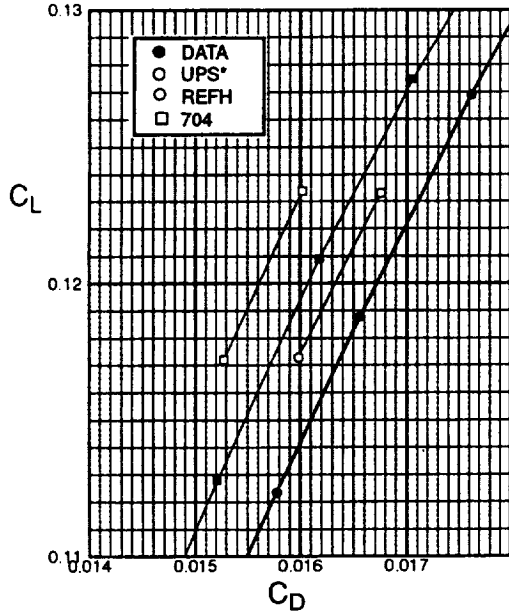
Finally, in an effort to correlate the local skin friction with the local axial pressure gradient, these quantities are plotted together versus circumferential arc length (starting at the lower centerline) in the figure above. In the turbulent case, it is observed that regions where the Ref. H shows more favorable pressure gradient, Wing 704 shows lower local skin friction, and vice versa. Again, the majority of the improvement seems to lie on the outboard section of the upper wing surface. A slightly elevated value for Wing 704 is seen over most of the lower surface.

In the laminar case, the results are complicated by the presence of the various crossflow features, but similar behavior is observed on the outboard section of the upper wing surface.

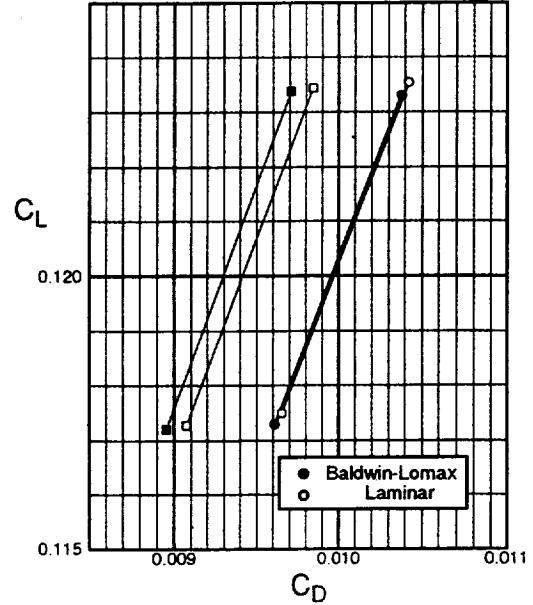
DRAG POLARS

Re = 4 million/ft

Total Drag



Pressure Drag



* - includes 3 cts trip drag

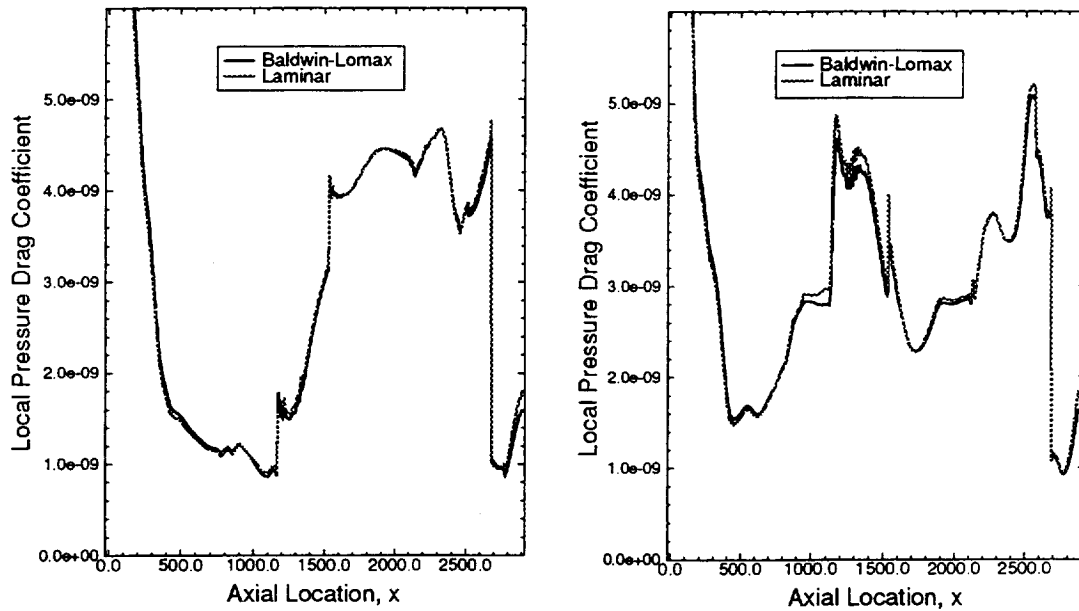
Drag polar results are shown in these figures. On the left, total integrated drag is compared with experimental data from the NASA Langley wind tunnel test. Three counts of drag have been added to the turbulent UPS results to account for predicted trip drag. Nevertheless, the UPS results tend to be approximately four to five counts below the experimental drag data.

On the right, predicted wave drag polars are shown for the turbulent and laminar computations. The effect of laminar flow is to cause a slight wave drag penalty which is more pronounced on the Wing 704 configuration.

PRESSURE DRAG DISTRIBUTIONSRe = 4 million/ft; $C_L = 0.123$

REF H

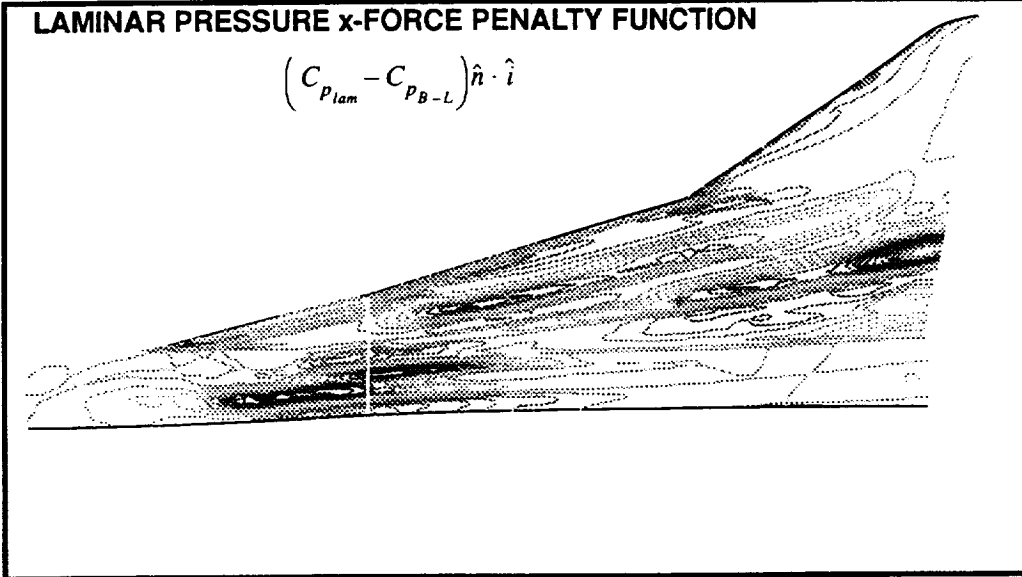
704



Axial distributions of local pressure drag coefficients are plotted here, again in an effort to localize the source of the laminar flow drag increment. While the laminar and turbulent distributions look remarkably similar for the Ref. H body, the results on Wing 704 show slightly higher pressure drag for the laminar case on the fuselage and forward portion of the wing.

UPPER WING SURFACE FLOW FIELDBody 704; $C_L = 0.123$ **LAMINAR PRESSURE x-FORCE PENALTY FUNCTION**

$$(C_{p_{lam}} - C_{p_{B-L}}) \hat{n} \cdot \hat{i}$$



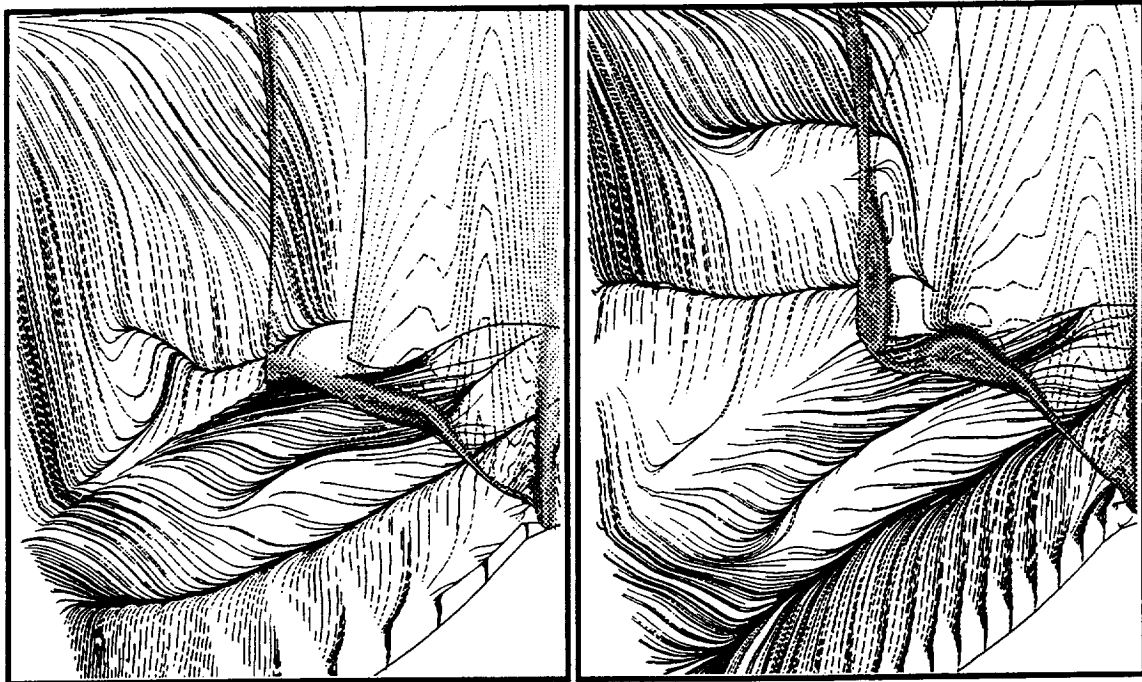
Since the identical grid was used to compute both the laminar and turbulent results, the solutions can be differenced to provide details on how the solutions differ at each point on the wing. Plotted here is the component of the pressure difference in the axial or x direction. Again, streaks of positive value indicate the presence of vortical structures in the laminar solution which displace the pressure gradients from the locations predicted using the Baldwin-Lomax model. The fact that the penalty function is generally positive indicates that the turbulent results are probably similar (at least in the sense of locating pressure gradients) to those of the Euler analysis that produced the Wing 704 geometry.

UPPER WING FLOW COMPARISON - LAMINAR

Surface Oil Flow and Pitot Pressures @ Break

Baseline

704



Surface oil flows and pitot pressures in a crossflow plane located at the second wing break location are shown in this figure for both configurations. The geometries are highly distorted in the vertical direction to easily identify the vortical structures. As shown in an earlier figure, both configurations produce the vortical behavior; however, the Wing 704 exhibits an additional structure on the fuselage, relative to the baseline. In addition, the separation on the wing is significantly stronger, as evidenced by the presence of a more well-defined secondary separation line.

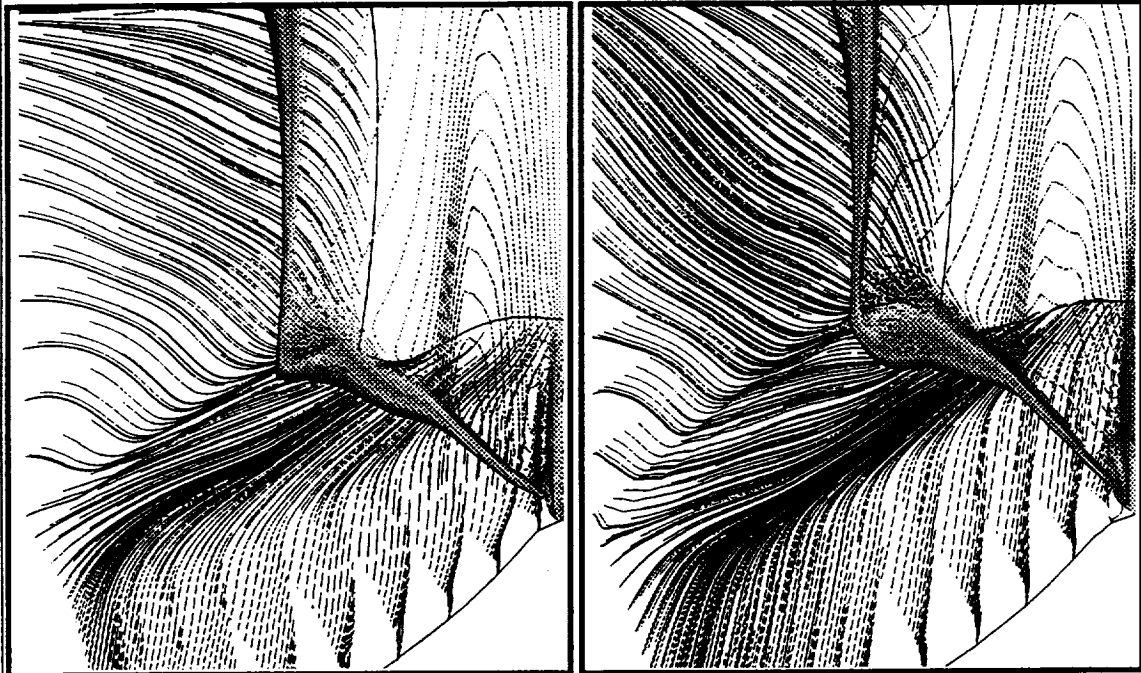
It is clear from the pitot pressure contours in these figures that the vortical features are significantly influencing the inviscid flow field. The upper wing recompression is observed to split into two small compressions near the boundary layer.

UPPER WING FLOW COMPARISON - TURBULENT (B-L)

Surface Oil Flow and Pitot Pressures @ Break

Baseline

704



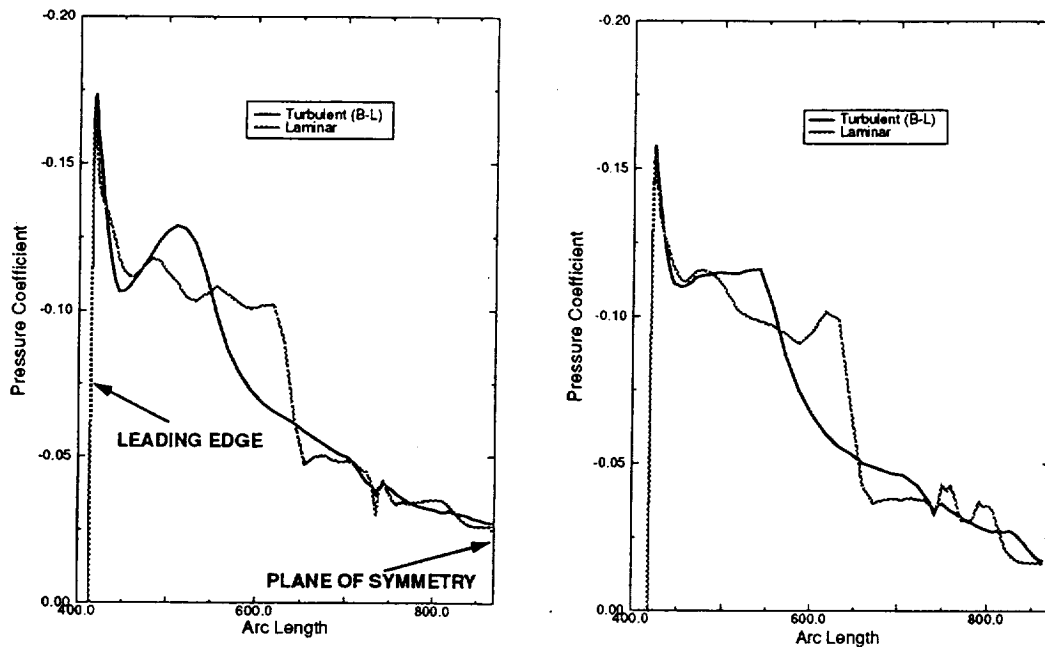
The turbulent flow results shown here are observed to be dramatically different from those of the previous figure. There are no well defined separation lines, though there still clearly exists a single large, diffuse, vortical structure on the upper wing surface on both bodies. There is some diffusion of the inviscid recompression, but not a splitting as was observed in the laminar results.

The Baldwin-Lomax model is known to be inadequate in the treatment of separated flows because of its tendency to use a length scale of turbulence based on the distance from the wall to the separated layer. This is clearly not physical and tends to introduce copious amounts of dissipation into the separation region. The Degani-Schiff correction was introduced to correct this deficiency; however, it often requires careful tuning prompt it to activate at the appropriate locations, and at its best, it is a stop gap approach to treating separated flows. Further analysis is required to determine if Degani-Schiff was acting properly in these cases.

UPPER SURFACE PRESSURE DISTRIBUTIONSRe = 4 million/ft; $C_L = 0.123$; $x = 2160''$ (Break)

Baseline

704



Finally, upper surface pressures are shown at the second wing break in the circumferential direction, starting at the leading edge. These figures provide a more quantitative view of the effects discussed in the preceding paragraphs.

In the turbulent results, the expansion near the leading edge on the baseline configuration is flattened on the optimized body which includes a slightly stronger recompression. Otherwise, the pressure distribution is quite smooth, with the slight exception of a kink at the wing/body intersection.

The laminar pressures, on the other hand, indicate the presence of the wing vortices through the existence of a pre-recompression and oscillations outboard of the main recompression. Evidence of the fuselage vortices is also shown.

SUMMARY OF DRAG INCREMENTS

Re = 4 million/ft; 1.675% Body

$$\Delta C_D = (C_{DREFH} - C_{D704}) @ C_L = 0.12$$

TYPE	Turb. (B-L)	Laminar	Experiment	Interaction ΔC_{Dp} REF H	Interaction ΔC_{Dp} 704
ΔC_{Dv}	0.6	-0.6	N/A	-----	-----
ΔC_{Dp}	6.6	5.6	N/A	0.2	1.2
ΔC_D	7.2	5.0	6.6	-----	-----

Observations

- UPPER BOUND ON INTERACTION $\Delta C_{Dp} = 1$ CT
- INTERACTION EFFECTS TEND TO INCREASE C_{Dv}
- PRESSURE GRADIENT EFFECTS PROBABLY RESPONSIBLE FOR TURBULENT C_{Dv} REDUCTIONS
- BALDWIN-LOMAX PROBABLY SUPPRESSES INTERACTION EFFECTS (TOO MUCH μ_v)

A summary of the findings in terms of integrated drag is shown in this figure. In terms of total drag, UPS overpredicted the improvement in Wing 704 by approximately one half count in the turbulent case. An upper bound on interaction-related pressure drag, as given by the laminar results, is predicted to be approximately one count of drag. In addition, interaction effects are thought generally to increase skin friction drag by acting in a manner analogous to large scale turbulence. Finally, it appears there is some skin friction reduction on the optimized wing associated with a flattening of the pressure distribution near the leading edge; however, much of the advantage gained near the leading edge was given up on the fuselage and sting.

With respect to the turbulent results, it is believed that the Baldwin-Lomax model probably suppresses interaction effects by over-dissipating in regions of crossflow separation. The over-prediction of the drag improvement from Ref. H to Wing 704 provides some support for this belief. A more realistic treatment of separated regions is expected to improve this prediction by slightly reducing predicted gains in both skin friction and wave drag.

FUTURE WORK

- DEBUG SPALART-ALLMARAS FOR 3-D AND APPLY TO THESE CASES
- REYNOLDS NUMBER EFFECTS?
- TCA
- UPS+OVERFLOW FOR W/B/N/D

Future work, then, would begin with making required modifications to the Spalart-Allmaras one-equation model to allow a three-dimensional marching calculation.

Also of interest is the extent to which the effects observed in this study are observed at more flight-like Reynolds numbers.

Finally, similar studies will probably be performed on the TCA configuration using UPS for wing/body configurations and UPS in combination with OVERFLOW for wing/body/nacelle/diverter configurations, where the interaction effects are expected to be significantly more important.

CFD Code Validation for HSCT Wing/Body and Wing/Body/Nacelle/Diverter Configurations

James O. Hager, Geojoe Kuruvila,
Samson H. Cheung, Eric R. Unger, and Shreekant Agrawal
McDonnell Douglas Aerospace
Long Beach, California 90807-5309

The purpose of this study was to evaluate and/or validate CFD predictions of HSCT configurations. This was done in order to recommend analysis codes for HSCT analysis and design. This study can be divided into two parts: supersonic calculations, and transonic calculations.

The supersonic calculations focused on predicting the supersonic cruise performance of wing/body (W/B) and wing/body/nacelle/diverter (W/B/N/D) configurations. The CFD predictions were compared to the 2.7% Ref. H tests in the Ames 9'x7' wind-tunnel. It was demonstrated that both TLNS3D and CFL3D in the Navier-Stokes (N-S) mode (Baldwin-Lomax) can accurately predict the W/B cruise-point drag. CFL3D in the N-S mode (Baldwin-Lomax) can accurately predict the W/B/N/D cruise-point drag. AIRPLANE and CFL3D in the Euler mode did not accurately predict the local flow features.

The transonic calculations focused on predicting Reynolds-number effects and off-design performance for wing/body and wing/body/flaps (W/B/F) configurations. The CFD predictions were compared to the 2.2% Ref. H tests in the Langley NTF wind-tunnel and the 1.675% Ref. H tests in the Langley 16' transonic (16T) wind-tunnel. TLNS3D and CFL3D, using the Baldwin-Lomax turbulence model, predicted the Reynolds-number effect on drag reasonably well. It was also shown that the pressure drag is essentially independent of the Reynolds number for Re_c greater than 30 million for the W/B and W/B/F configurations. CFL3D, with the Baldwin-Lomax or Baldwin-Barth turbulence models, was able to predict the off-design performance reasonably well.

Objective

- Evaluate/validate CFD predictions of HSCT configurations
 - Supersonic: cruise performance
 - Transonic: Reynolds-number and flap effects
- Recommend analysis codes for HSCT design
 - Parametric studies
 - Nonlinear optimization

The main objective of this work is to evaluate and/or validate CFD predictions of HSCT configurations. At supersonic speeds, predicting the cruise-point performance is of prime interest. At transonic speeds, thus far, only the Reynolds-number and flap-effects predictions have been made.

The results of this study will be used to recommend analysis codes for HSCT analysis and design; to be used for parametric studies and nonlinear design optimization.

Outline

- Code description
- Supersonic calculations
 - Ref. H wing/body (W/B) and wing/body/nacelle/diverter (W/B/N/D) configurations
 - Predict cruise performance
- Transonic calculations
 - Ref. H wing/body and wing/body/flaps (W/B/F)
 - Predict Reynolds-number and flap effects

This presentation will begin with a description of the analysis codes that were evaluated.

Then supersonic calculations on the Ref. H wing/body (W/B) and wing/body/nacelle/diverter (W/B/N/D) will be presented. This will be followed by transonic calculations of the Ref. H W/B and wing/body/flaps (W/B/F).

Code Description

- AIRPLANE
 - Unstructured grid
 - Euler with integral boundary layer
 - Central difference, scalar dissipation
 - Runge-Kutta time stepping
- CFL3D
 - Multizone structured grid (patched & chimera)
 - Euler / Navier-Stokes
 - Flux-difference & flux-vector splitting
 - Multigrid, approximately factored implicit
- TLNS3D
 - Multizone structured grid (point-matched)
 - Euler / Navier-Stokes
 - Central diff., scalar & matrix dissipation
 - Multigrid, Runge-Kutta time stepping

All of the codes use a cell-centered, finite-volume based spatial discretization.

AIRPLANE uses unstructured grids, and solves the Euler equations and uses an integral boundary layer scheme to model viscous effects. The convective fluxes are computed using central differences with scalar dissipation. The time integration is performed using a Runge-Kutta scheme.

CFL3D uses multizone structured grids (patched and chimera), and solves the Euler and Navier-Stokes (N-S) equations. The convective fluxes can be computed using flux-difference splitting (used here) or flux-vector splitting. Multigrid and an approximately factored implicit scheme are used for the time integration.

TLNS3D also uses multizone structured grids (point-matched), and solves the Euler and Navier-Stokes equations. Central differences with scalar (used here) and matrix dissipation are used for the convective terms. Multigrid and a Runge-Kutta scheme are used for the time integration.

Supersonic Calculations

- Objective
 - Validate cruise-point performance
- Geometry
 - 2.7% Ref. H W/B and W/B/N/D configurations
- Experimental data
 - Ames 9'x7'
- Flow conditions
 - $M_\infty=2.4$
 - $Re_c=7$ million

The objective of the supersonic calculations is to predict the cruise-point performance.

The 2.7% Ref. H W/B and W/B/N/D configurations were used, and the CFD predictions were compared with the Ames 9'x7' wind-tunnel data. The flow conditions were $M_\infty=2.4$, $Re_c=7$ million.

Wing/Body Calculations

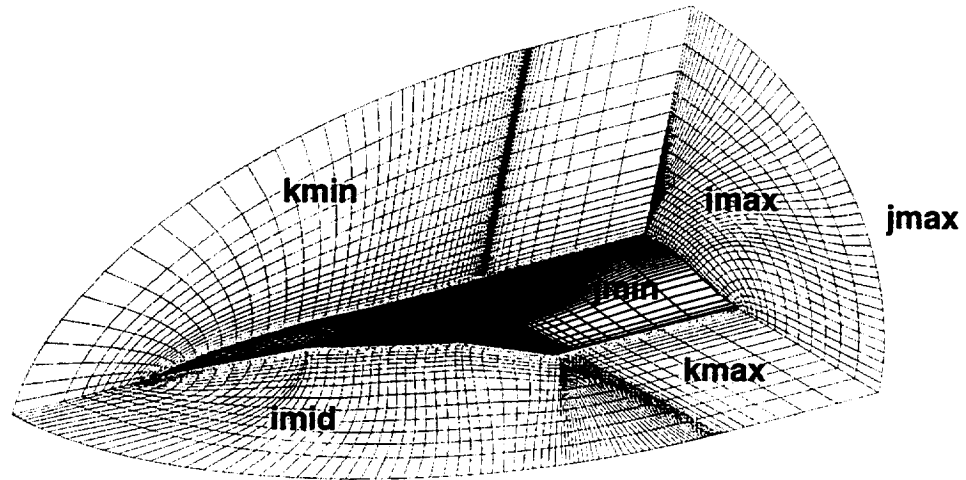
- Experimental data
 - Ames 9'x7', Run 140
- Flow solvers
 - CFL3D: Euler and Navier-Stokes (Baldwin-Lomax)
 - TLNS3D: Euler and Navier-Stokes (Baldwin-Lomax)
- Grid
 - C-O topology
 - Euler: 0.8 million points
 - N-S: 1.1 million points, $y^+=1-2$

The CFD solutions were compared with Run 140 from the Ames 9'x7' test.

Both CFL3D and TLNS3D were used in both the Euler and Navier-Stokes modes. The Baldwin-Lomax turbulence model was used with the Navier-Stokes solutions.

The Euler and Navier-Stokes grids have a C-O topology. The Euler grid has 0.8 million points. The Navier-Stokes grid has 1.1 million grid points, and the y^+ is between one and two.

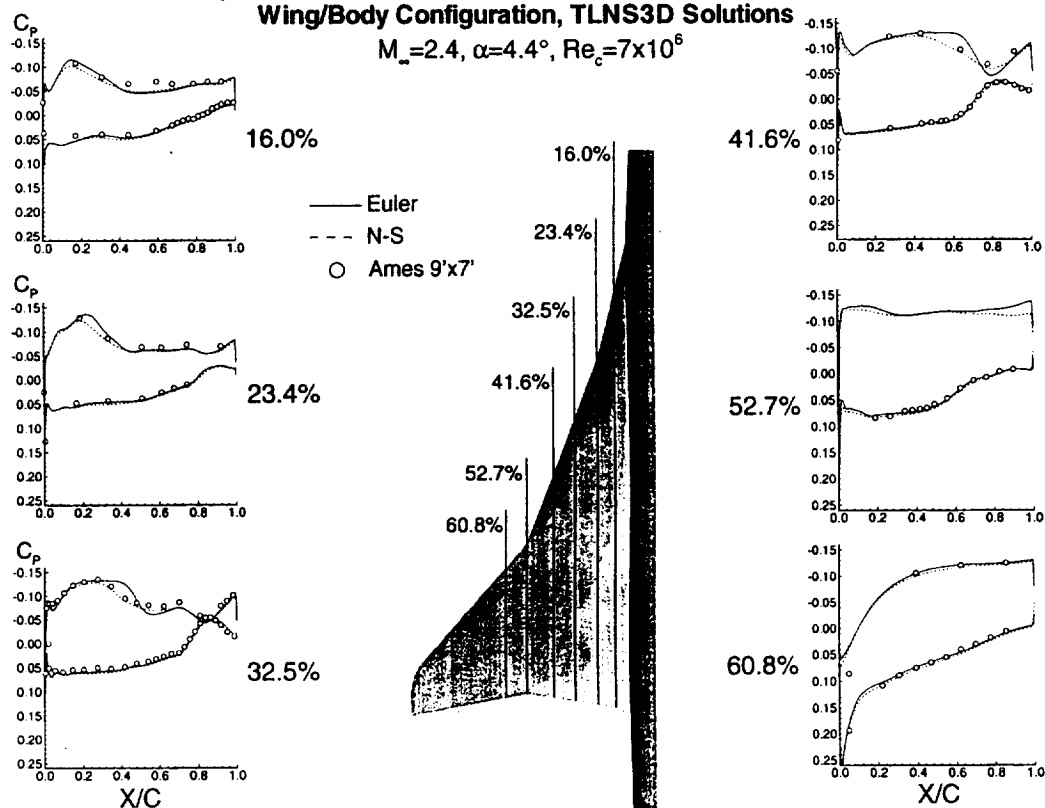
**2.7% Ref. H Wing/Body Euler Grid
C-O Topology, 221x41x91
(Every Other Point Shown)**



This slide shows the C-O grid topology. For clarity, only every-other point in each direction is shown.

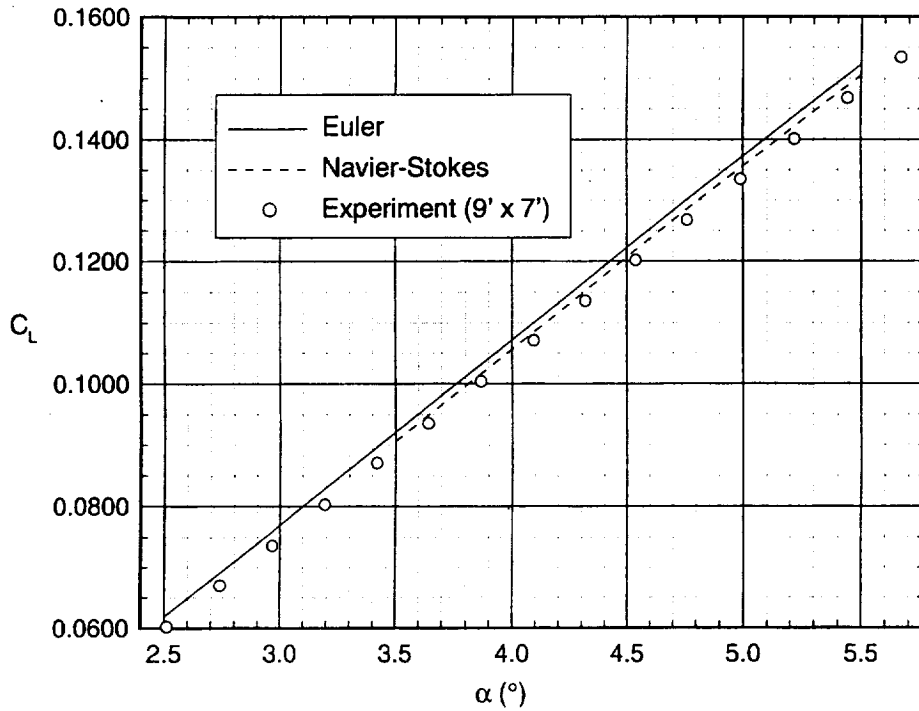
**Comparison of Pressure Distributions for the Baseline Ref. H
Wing/Body Configuration, TLNS3D Solutions**

$M_\infty=2.4, \alpha=4.4^\circ, Re_c=7 \times 10^6$



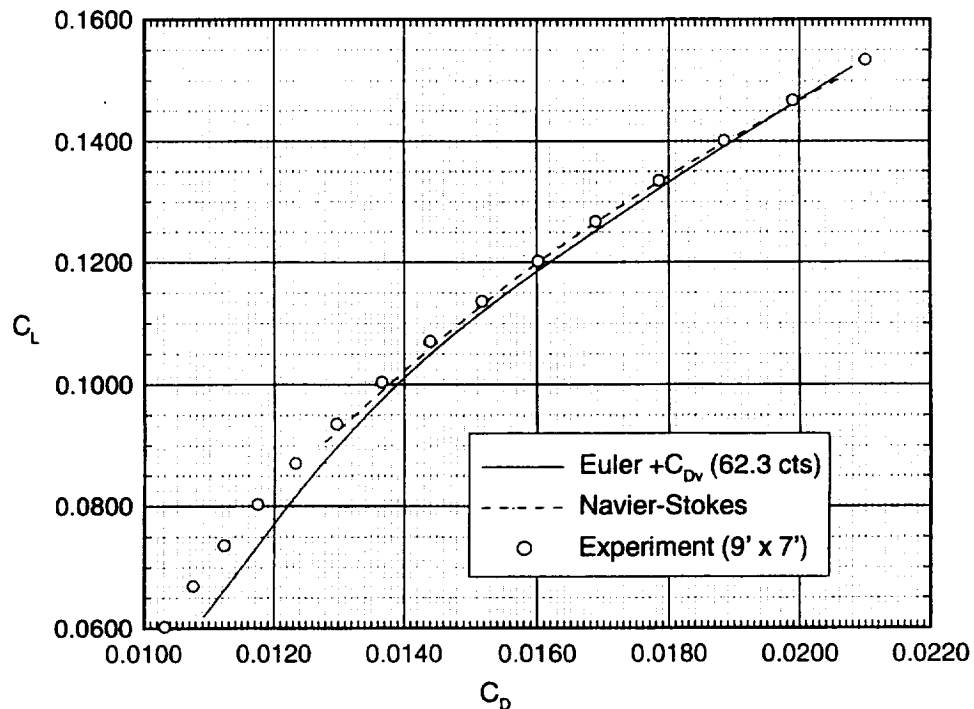
C_p distributions at six span stations, as predicted by TLNS3D in the Euler and N-S modes, are compared at $\alpha=4.4^\circ$ (near the cruise point). The Euler and N-S solutions predict the lower-surface flow well. However, the Euler solution does not predict the compression on the upper surface (see 32.5% and 41.6%) very well, whereas the N-S prediction is much better.

Comparison of TLNS3D and Experimental Results: C_L vs. α
2.7% Ref. H Wing/Body, $M_\infty=2.4$, $Re_c=7 \times 10^6$



The lift curve, as predicted by TLNS3D in the Euler and N-S modes, has a slightly higher slope than the experimental data. The N-S solution slightly over-predicts lift at the cruise point ($C_L=0.12$), and the Euler solution predicts even more lift than the N-S solution.

Comparison of TLNS3D and Experimental Results: C_L vs. C_D
2.7% Ref. H Wing/Body, $M_\infty=2.4$, $Re_c=7 \times 10^6$

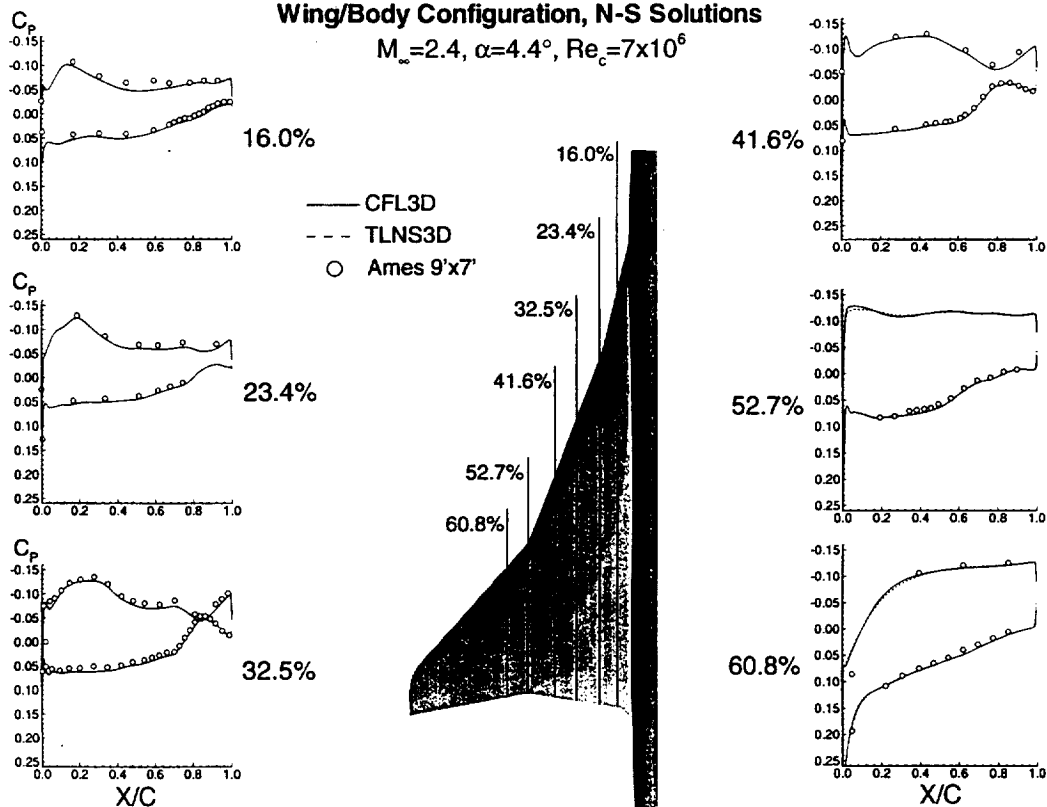


The drag, as predicted by TLNS3D in the Euler mode, is fairly accurate at the cruise point ($C_L=0.12$), however, the shape of the polar is incorrect. (A flat-plate estimate of the skin friction has been added to the Euler pressure drag.) The N-S (Baldwin-Lomax) solution goes through the data at the cruise point, and the polar shape is more accurate.

Note that the experimental data was not corrected to remove trip drag at the time of this study. The trip drag has been estimated to be in the two-to-three count range. Removing this additional drag from the experimental data will shift the data to the left of the N-S predictions.

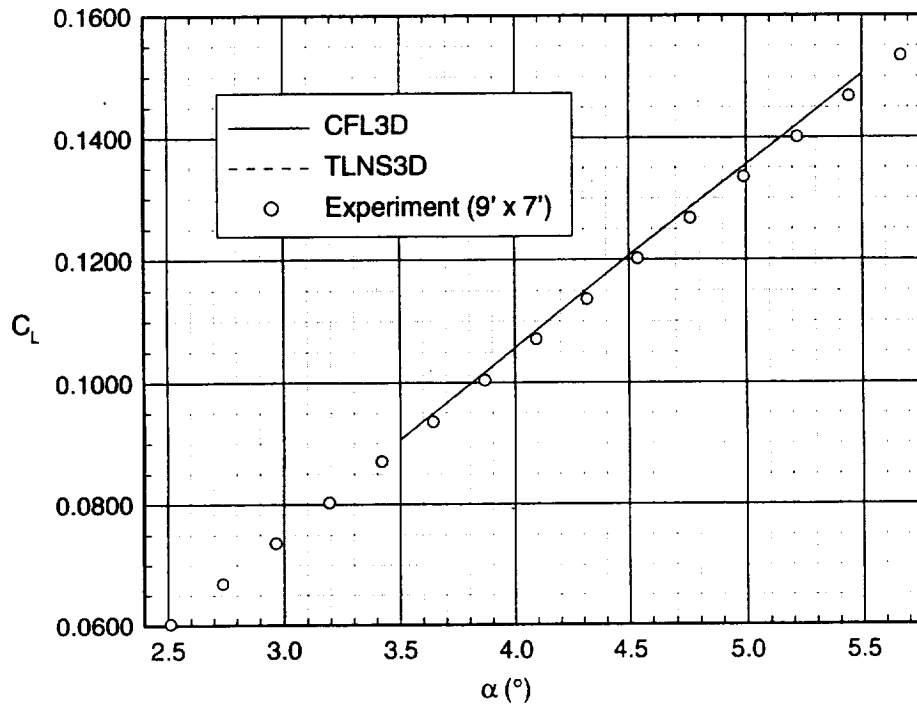
**Comparison of Pressure Distributions for the Baseline Ref. H
Wing/Body Configuration, N-S Solutions**

$M_\infty=2.4, \alpha=4.4^\circ, Re_c=7 \times 10^6$



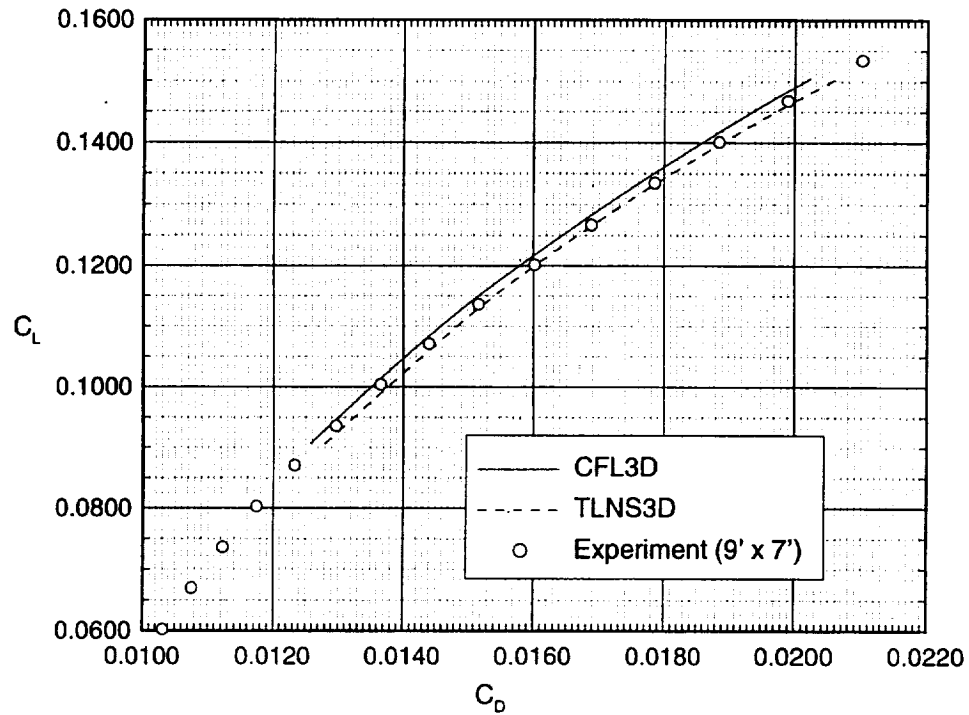
C_p distributions at six span stations, as predicted by CFL3D and TLNS3D in the N-S mode (Baldwin-Lomax), are compared at $\alpha=4.4^\circ$ (near the cruise point). The two solutions predict an almost identical C_p distribution on the inboard section. There is a slight difference beginning at the leading-edge break and extending outboard.

Comparison of N-S CFD and Experimental Results: C_L vs. α
2.7% Ref. H Wing/Body, $M_\infty=2.4$, $Re_c=7 \times 10^6$



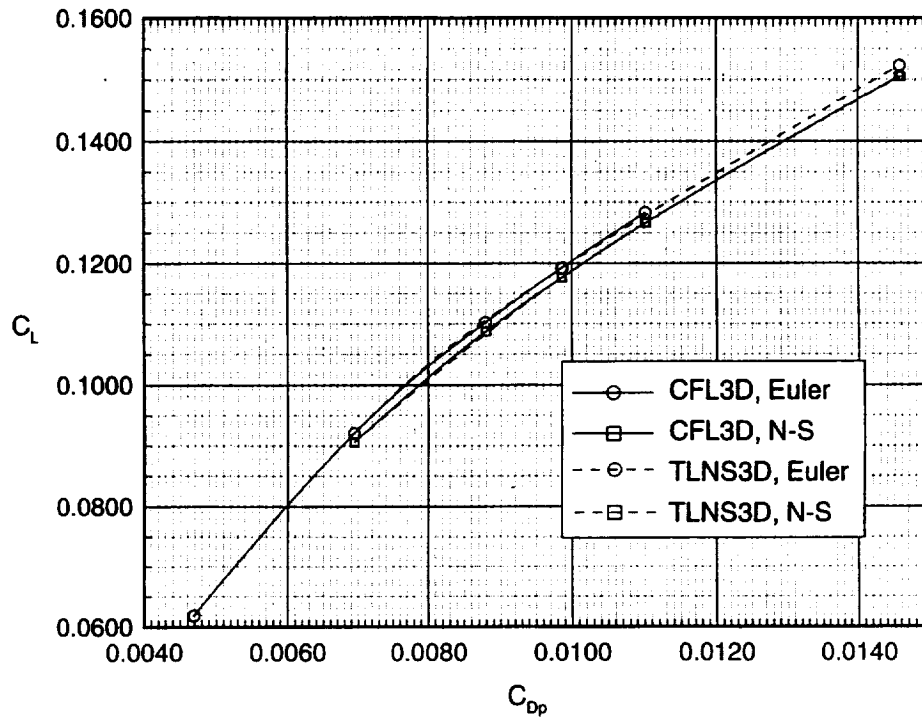
This slide compares the N-S lift predictions from CFL3D and TLNS3D. Both codes predict almost identical lift. However, the slope of the curve is over-predicted and the lift at the cruise angle-of-attack is over-predicted.

Comparison of N-S CFD and Experimental Results: C_L vs. C_D
2.7% Ref. H Wing/Body, $M_\infty=2.4$, $Re_c=7 \times 10^6$



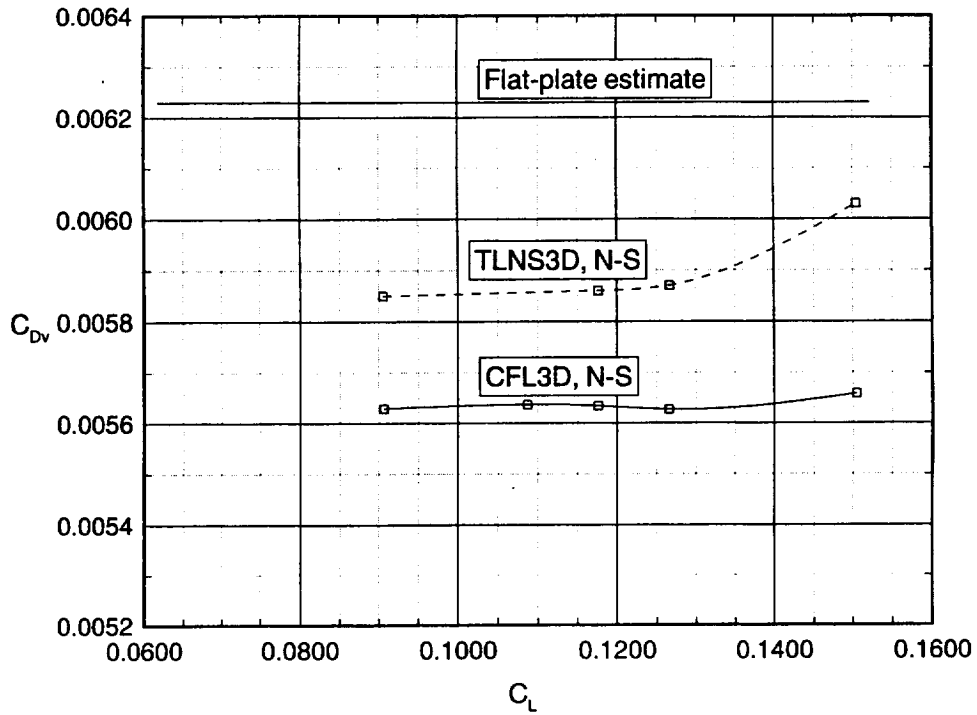
This slide compares the N-S drag predictions from CFL3D and TLNS3D using the Baldwin-Lomax turbulence model. Both codes predict almost the same shape, but CFL3D predicts about two counts less drag than TLNS3D. If the trip drag is removed from the experimental data, CFL3D would predict the cruise drag ($C_L=0.12$) better than TLNS3D.

**Comparison of CFD Predicted Pressure-Drag Polars
2.7% Ref. H Wing/Body, $M_\infty=2.4$, $Re_c=7 \times 10^6$**



The pressure drag predicted by both CFL3D and TLNS3D in both the Euler and N-S (Baldwin-Lomax) modes are compared. The pressure drag for both codes are very similar when the same flow equations are used. The N-S pressure drag is about two counts higher than the Euler pressure drag.

**Comparison of CFD Predicted Viscous Drag
2.7% Ref. H Wing/Body, $M_\infty=2.4$, $Re_c=7 \times 10^6$**



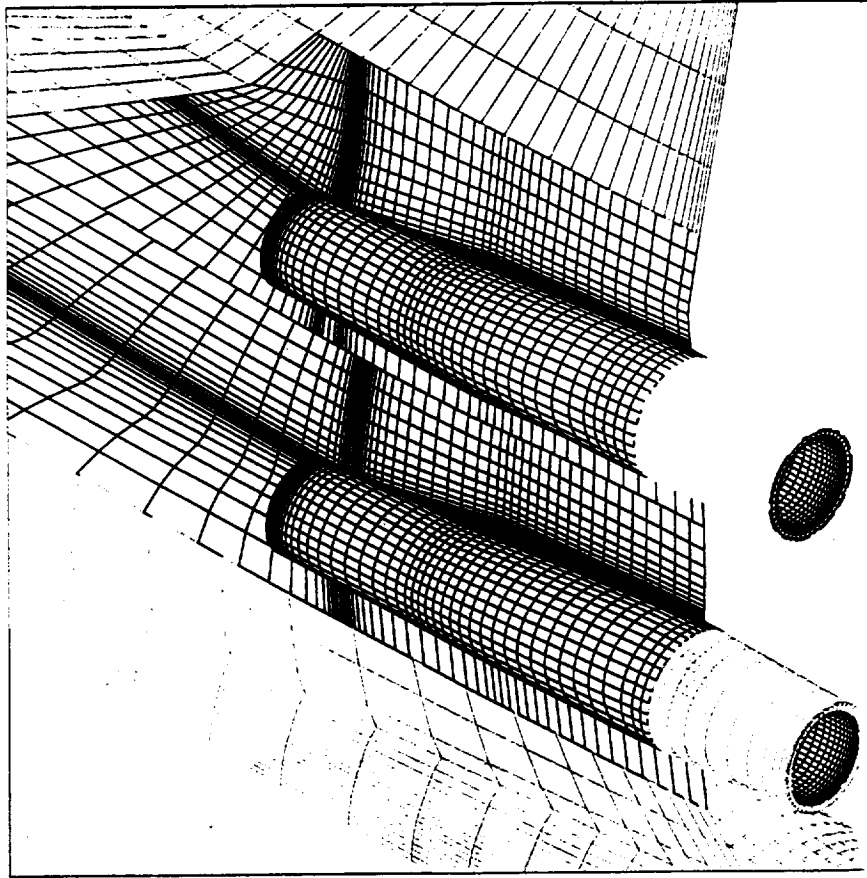
The skin-friction drag predicted by CLF3D and TLNS3D in the N-S modes (Baldwin-Lomax) is compared with a flat-plate estimate. The two-count difference between the CFL3D and TLNS3D total drag is attributable to the difference in the skin-friction drag. Note that the flat-plate estimate is even higher than the N-S predictions.

Wing/Body/Nacelle/Diverter Calculations

- Experimental data
 - Ames 9'x7', Run 155
- Flow solvers
 - AIRPLANE: Euler
 - CFL3D: Euler and Navier-Stokes (Baldwin-Lomax)
- Grid
 - AIRPLANE: 0.5 million nodes
 - CFL3D: 39 zones
 - Euler: 2.6 million points
 - N-S: 4.9 million points, $y^+=1-2$

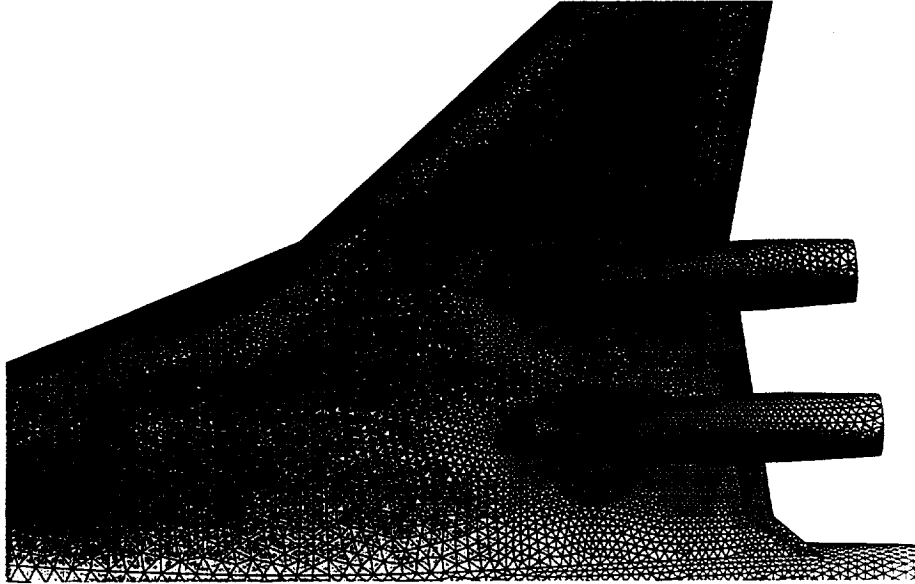
The CFD solutions were compared with Run 155 from the Ames 9'x7' test. AIRPLANE was used in the Euler mode on a grid of 0.5 million nodes. CFL3D was used in both the Euler and N-S (Baldwin-Lomax) modes. The grid was obtained by cutting out the W/B grid in the nacelle/diverter region and generating new blocks to fit the nacelles and diverters. The grids have 39 zones with 2.6 million points for the Euler grid and 4.9 million points for the N-S grid. The spacing at the wall of the N-S grid produces a y^+ of one to two.

Ref. H W/B/N/D Surface Grid with Nacelle Region Details - Lower Surface



The lower-surface view of the multizone structured grid shows the surface grid in the nacelle/diverter region. This grid has 39 zones, 2.6 million points for the Euler grid, and 4.9 million points for the N-S grid.

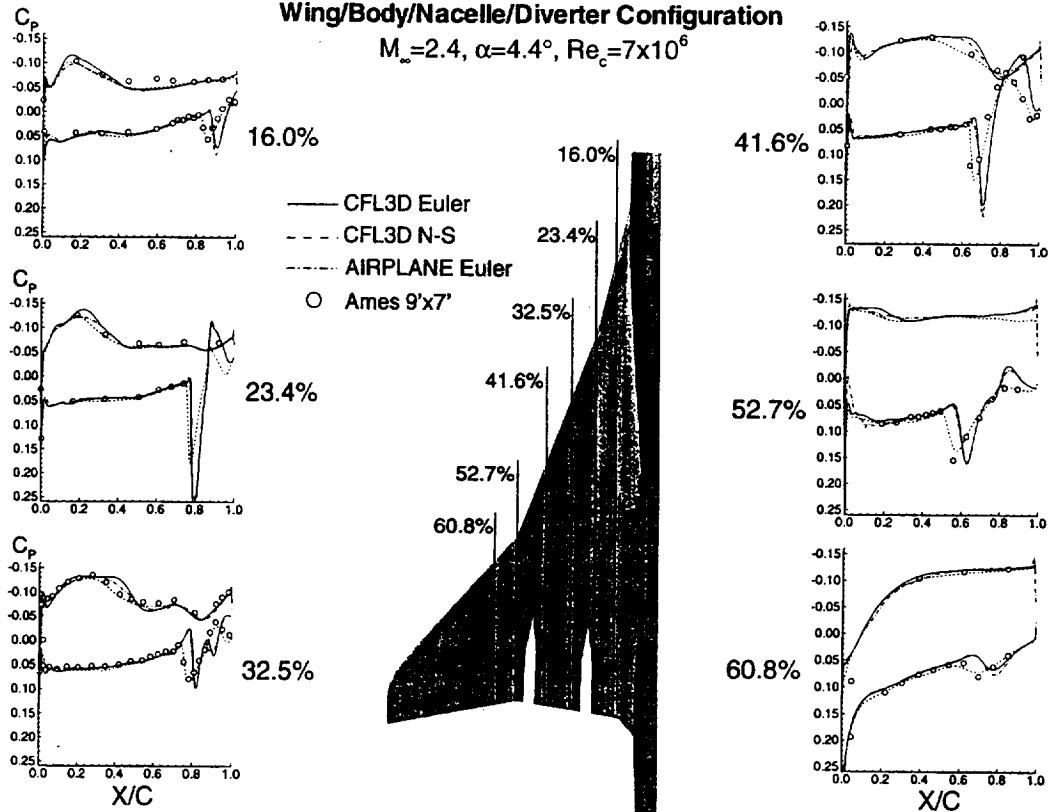
2.7% Ref. H Wing/Body/Nacelle/ Diverter, Unstructured Surface Grid



The lower-surface view of the unstructured grid shows the surface grid in the nacelle/diverter region. This grid, provided by Neal Frink of NASA Langley, has 0.5 million nodes.

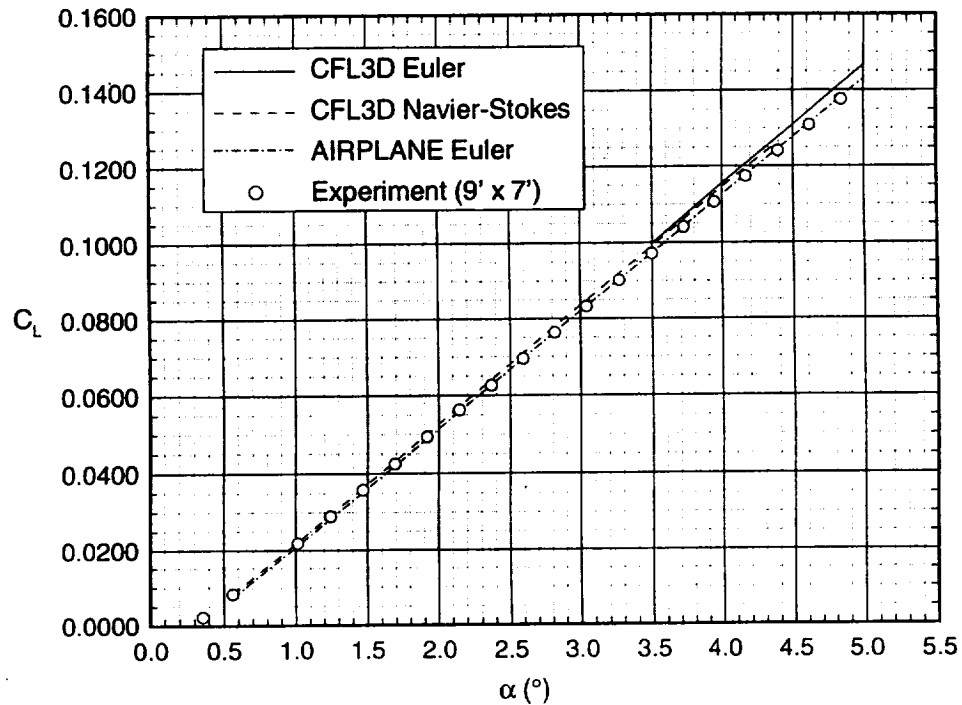
**Comparison of Pressure Distributions for the Baseline Ref. H
Wing/Body/Nacelle/Diverter Configuration**

$M_\infty=2.4, \alpha=4.4^\circ, Re_c=7 \times 10^6$



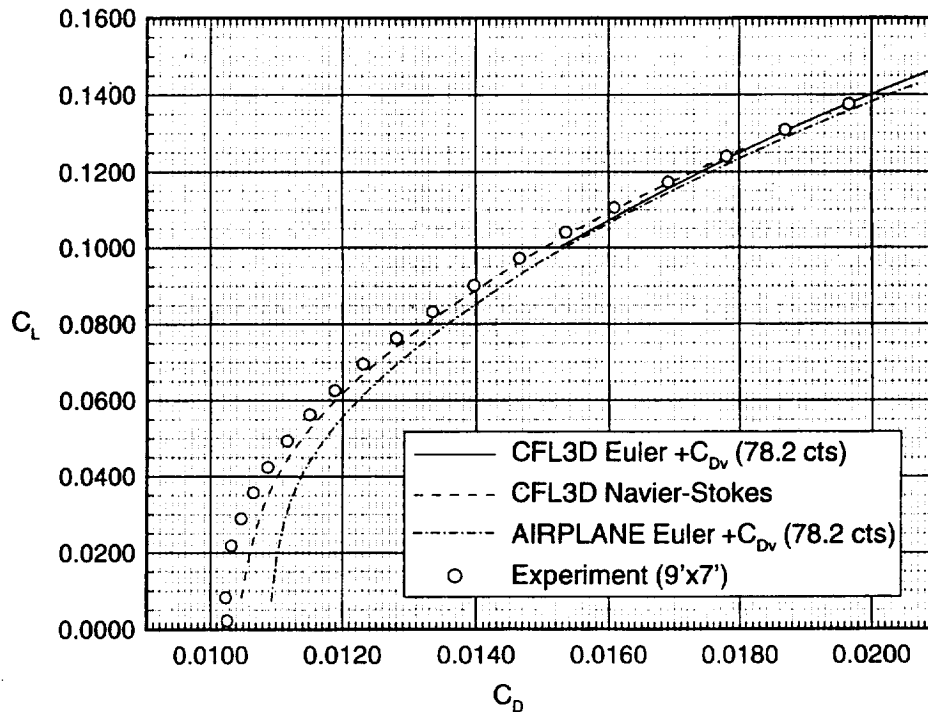
C_p distributions at six span stations, as predicted by CFL3D in the Euler and N-S modes and AIRPLANE in the Euler mode, are compared at $\alpha=4.4^\circ$ (near the cruise point). The AIRPLANE Euler predictions are between the CFL3D Euler and N-S predictions on the upper surface. On the lower surface, the two Euler solutions do not predict the shock strength or position accurately. The N-S solution does a good job at predicting the shock strength and position. The N-S solution is more accurate because the viscous layer on the wing lower surface is thicker (at the tunnel Reynolds number) than the diverter height. This reduces the Mach number of the flow past the diverter therefore reducing the shock strength and increasing the shock angle. The Euler solutions do not model the viscous layer, causing higher-Mach flow to pass by the diverter. This produces an artificially stronger shock at a smaller angle.

**Comparison of CFD and Experimental Results: C_L vs. α
 2.7% Ref. H Wing/Body/Nacelle/Diverter, $M_\infty=2.4$, $Re_c=7 \times 10^6$**



The lift prediction of AIRPLANE in the Euler mode is rather remarkable: it matches the data near the cruise point ($C_L=0.12$). This indicates that accurately predicting the integrated forces does not ensure an accurate local solution. CFL3D in the Euler mode over-predicts lift and the lift-curve slope. CFL3D in the N-S mode (Baldwin-Lomax) does a fair job of predicting the lift and lift-curve slope.

Comparison of CFD and Experimental Results: C_L vs. C_D
2.7% Ref. H Wing/Body/Nacelle/Diverter, $M_\infty=2.4$, $Re_c=7 \times 10^6$



The drag predictions of AIRPLANE are not as good as the lift predictions. Near the cruise point ($C_L=0.12$), AIRPLANE over-predicts the drag by two counts, and near C_{Dmin} , AIRPLANE over-predicts the drag by about seven counts. CFL3D in the Euler mode does a fair job of predicting the cruise drag, but the shape of the polar is incorrect. CFL3D in the N-S mode (Baldwin-Lomax) does a good job of predicting drag (within half a count) at the cruise point, and does a fair job of predicting C_{Dmin} .

Recall however, that trip drag has not been removed from the data. The estimated two-to-three count reduction would push the data further to the left.

Summary of Supersonic Results

- Drag predictions are good near the cruise condition
 - W/B: within 2 counts, 0.5 counts with TLNS3D N-S
 - W/B/N/D: within 4 counts, 0.5 counts with CFL3D N-S
- Baldwin-Lomax turbulence model acceptable

Drag can be predicted fairly accurately at $M_\infty=2.4$ using the codes evaluated. At the cruise point, W/B drag can be predicted within 0.5 counts with TLNS3D in the N-S mode (Baldwin-Lomax), and W/B/N/D drag can be predicted within 0.5 counts with CFL3D in the N-S mode (Baldwin-Lomax).

The Baldwin-Lomax turbulence model appears to be acceptable for HSCT configurations at the supersonic cruise point.

Transonic Analysis Objectives

- Validate Reynolds number effects prediction
- Validate off-design prediction

The objectives of the transonic calculations are: (1) validate the Reynolds-number effects predictions and, (2) validate the off-design performance prediction of wing/body and wing/body/flaps (W/B/F) configurations. The CFD solutions obtained using CFL3D and TLNS3D are compared to the 2.2% Ref. H high Reynolds number data obtained from the Langley NTF wind tunnel and the 1.675% Ref. H low Reynolds number data obtained from the Langley 16' transonic (16T) wind tunnel.

Transonic Calculations

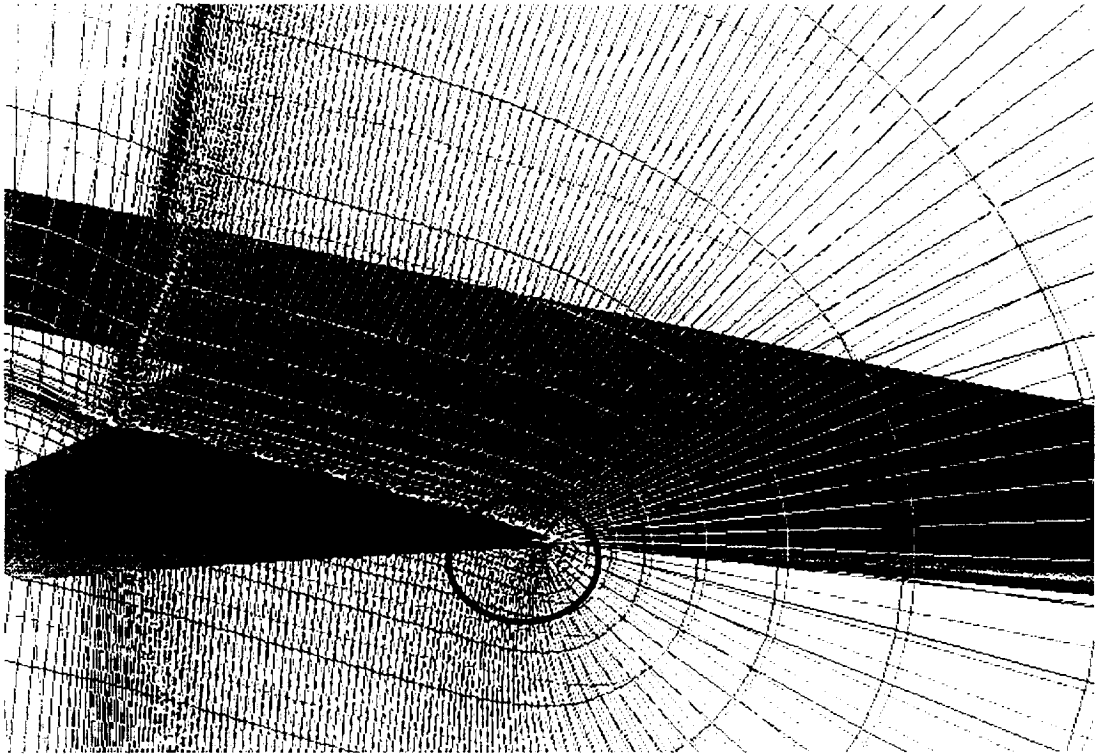
Ref. H, $M_\infty = 0.9$

	NTF (2.2%)		16T (1.675%)	
$Re_c \times 10^{-6}$	Wing/Body	Wing/Body/Flaps (0°/10°/3°)	Wing/Body	Wing/Body/Flaps (0°/10°/3°)
4			CFL3D	CFL3D
10	TLNS3D	CFL3D		
30	TLNS3D	CFL3D		
80	TLNS3D	CFL3D		

Shown here is a matrix of the CFD solutions obtained and the corresponding wind-tunnel data they were compared with.

Grid Topology for Ref. H Wing/Body/Flaps

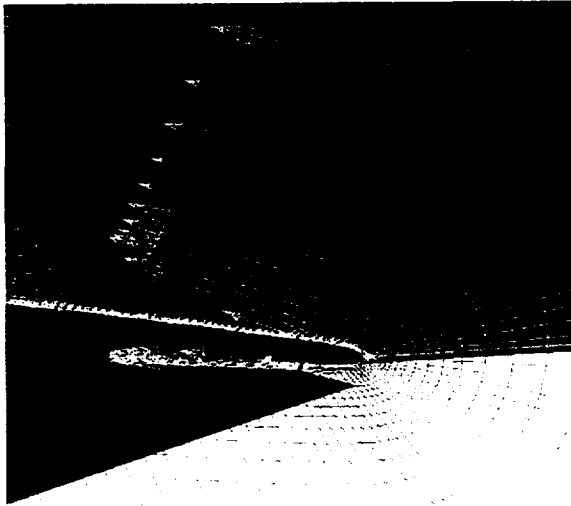
Three Computational Zones: 241 x (57, 37, 17) x 65



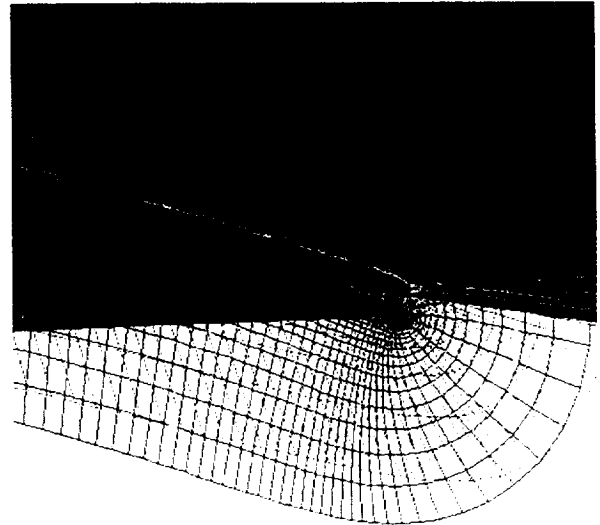
Shown here is part of the grid used in the wing/body/flaps CFD analysis. A C-O topology 3-zone patched grid was used. A grid of dimensions 241x57x65 was used for the inboard-wing/fuselage zone. The outboard wing zone (with leading-edge flaps) had 241x37x65 grid points and the tip zone had 241x17x65 grid points.

Zone Interface and Flow Solution

**Velocity Vectors
at the Flap Leading Edge**



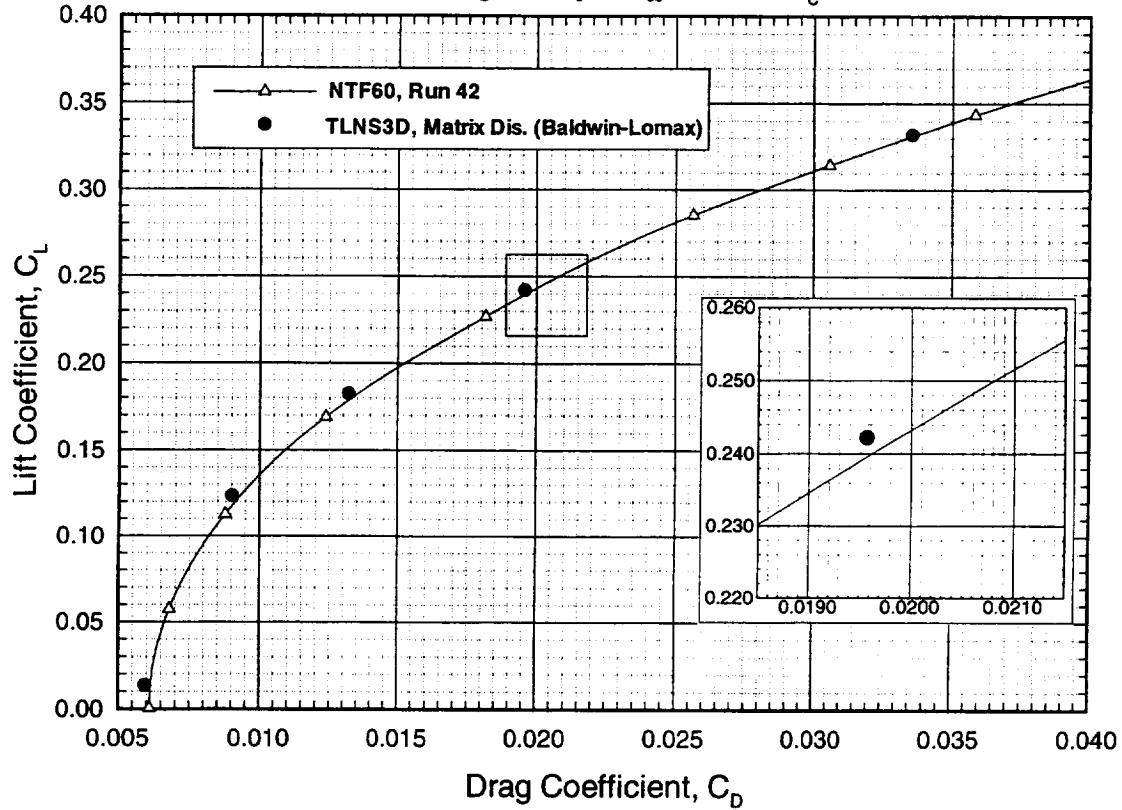
Patched Grid



The figure on the right shows the interface between the inboard and outboard zones. The two grids shown lie on the same physical plane. A virtual zone technique was used to impose the boundary conditions at this zone interface. Shown on the left are a subset of the velocity vectors on the outboard wing near the flap leading edge. It is clear from these vectors that the no-slip region of the flap "rubbing-surface" is well modeled.

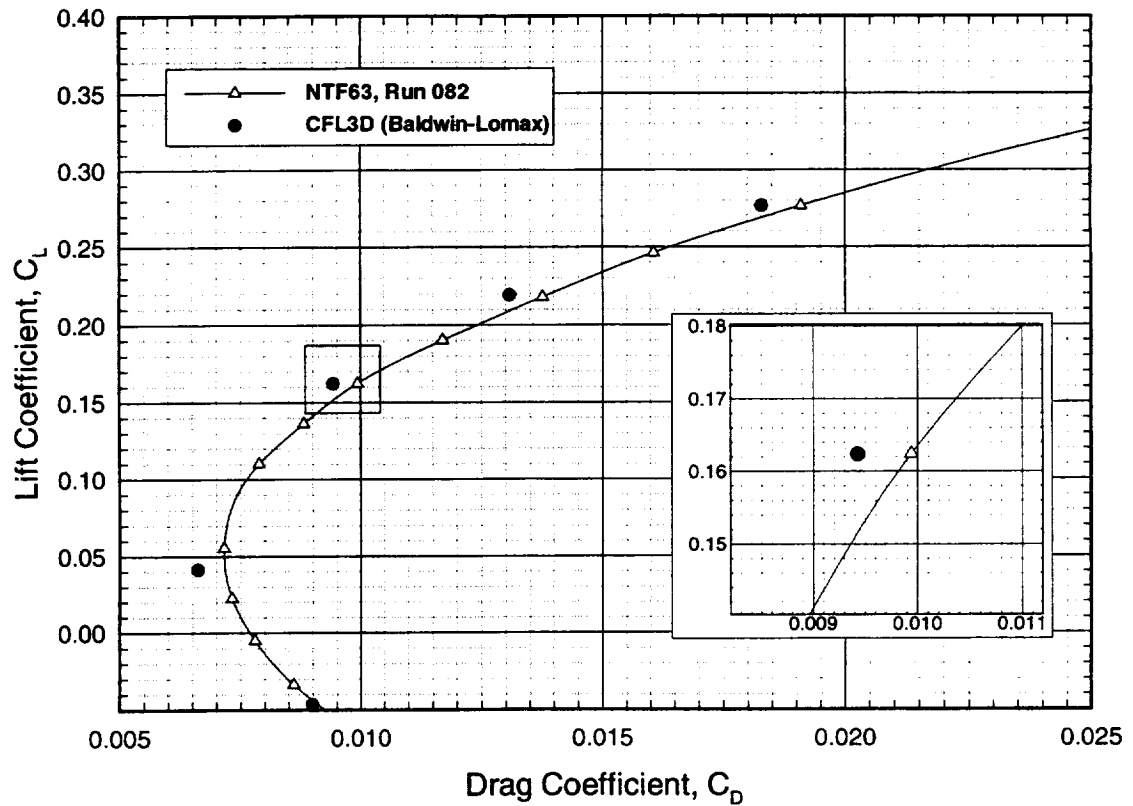
Drag Polars from Navier-Stokes Analysis and Experiment

2.2% Ref. H Wing/Body, $M_\infty=0.9$, $Re_c=80 \times 10^6$



For the wing/body configuration, the drag polars from experiment and TLNS3D Navier-Stokes (Baldwin-Lomax) calculations for $Re_c=80 \times 10^6$ at $M_\infty=0.9$ agree well. The predicted drag is within about 3 counts of the experiment.

Drag Polars from Navier-Stokes Analysis and Experiment
 2.2% Ref. H Wing/Body/Flaps ($0^\circ/10^\circ/3^\circ$), $M_\infty=0.9$, $Re_c=80 \times 10^6$

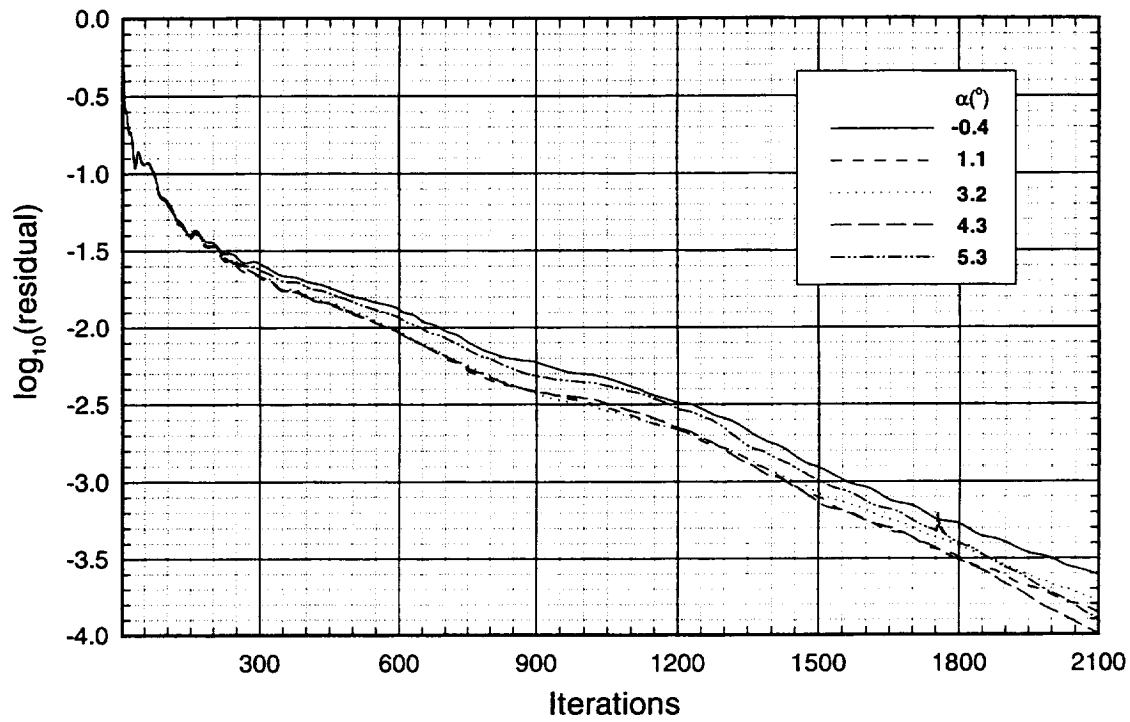


For the wing/body/flaps configuration, the agreement between the experiment and CFL3D Navier-Stokes (Baldwin-Lomax) calculations for $Re_c=80 \times 10^6$ at $M_\infty=0.9$ is satisfactory. The maximum discrepancy between the experimental and CFD results is about 5-6 counts.

Residual Histories for 2.2% Ref. H Wing/Body/Flaps Analysis

CFL3D, Baldwin-Lomax, 3 Zones: 241x(57,37,17)x65

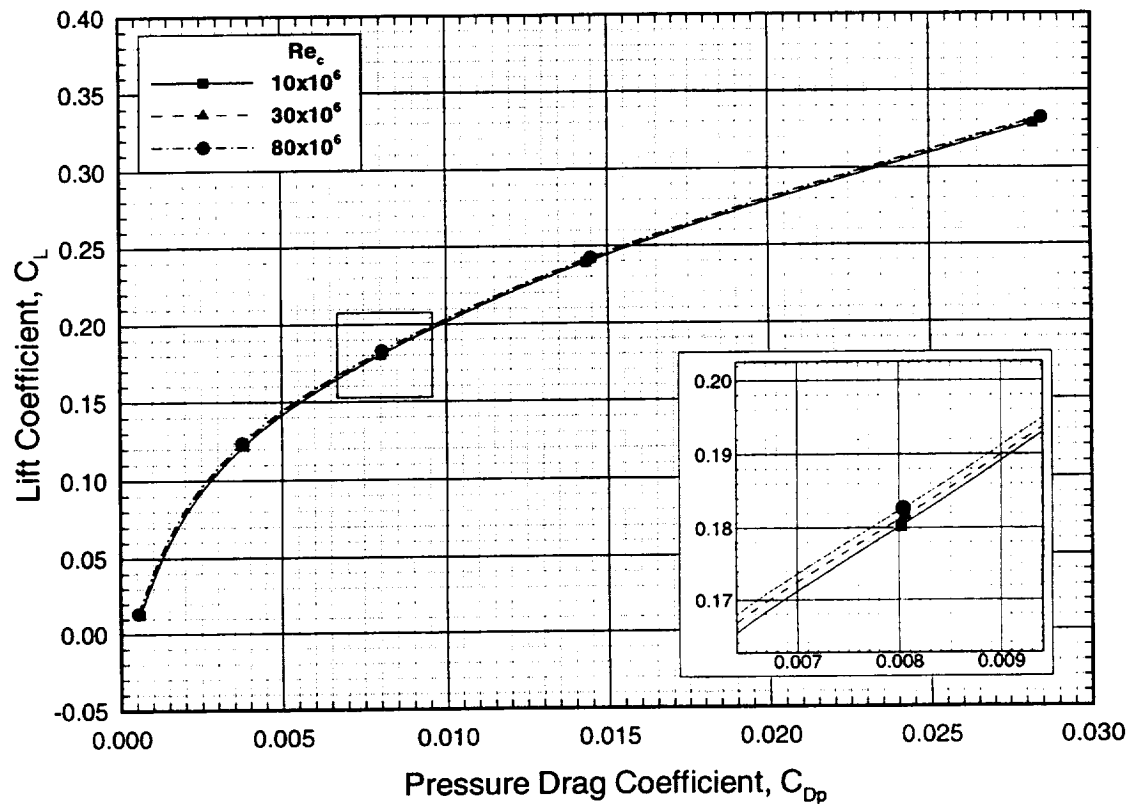
(0°/10°/3°), $M_\infty=0.9$, $Re_c=80 \times 10^6$



For the wing/body and the wing/body/flaps calculations, the residuals were reduced by more than three orders of magnitude for each of the Reynolds numbers and angle-of-attack. A typical residual history for these calculations is shown in the chart above. For the high Reynolds number (30 and 80 million) calculations, each of these cases took about 12 hours (2100 iterations) on the NAS Cray C-90. The lower Reynolds number cases took about 8 hours on the C-90. The three zone grid had a total of 1.7 million grid points.

Pressure Drag Polars from TLNS3D Navier-Stokes Analysis

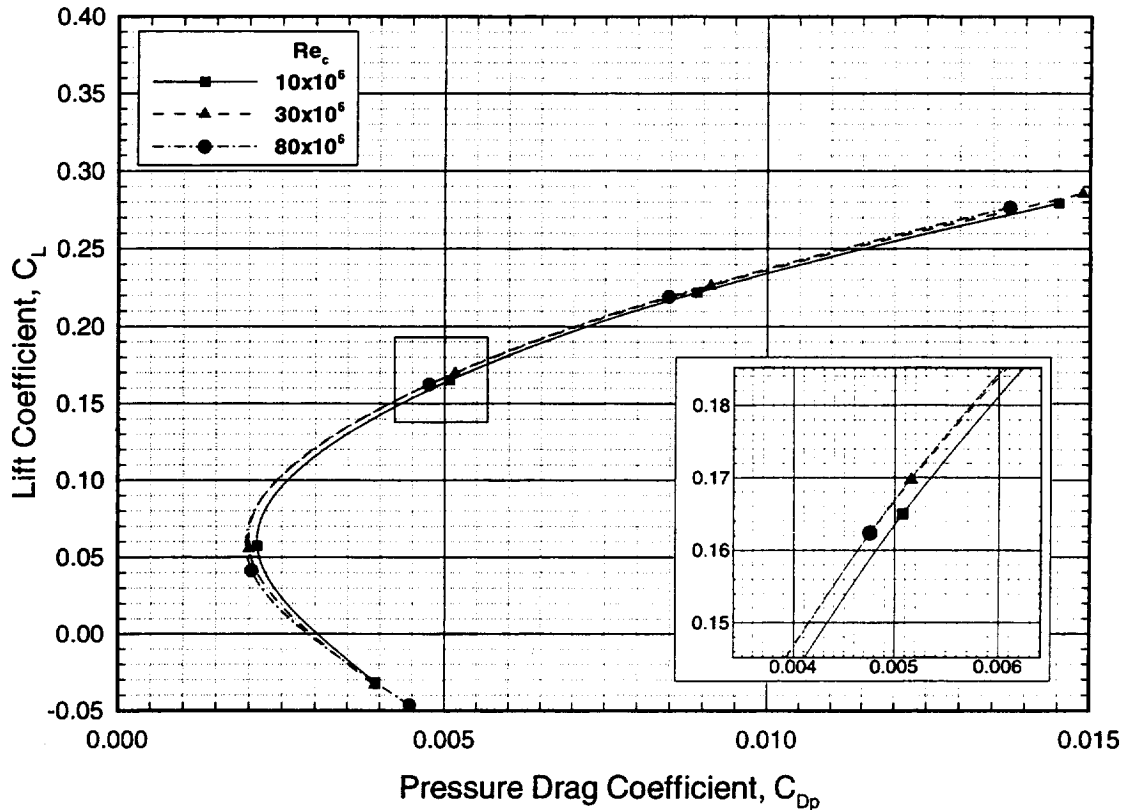
2.2% Ref. H Wing/Body, $M_\infty=0.9$, Baldwin-Lomax, Matrix Dis.



The pressure drag obtained for the wing/body configuration, using TLNS3D (Baldwin-Lomax), for Reynolds numbers (Re_c) of 10, 30 and 80 million is essentially independent of the Reynolds number. There is about 1.5 counts difference in pressure drag between each successive Reynolds-number solution obtained.

Pressure Drag Polars from CFL3D Navier-Stokes Analysis

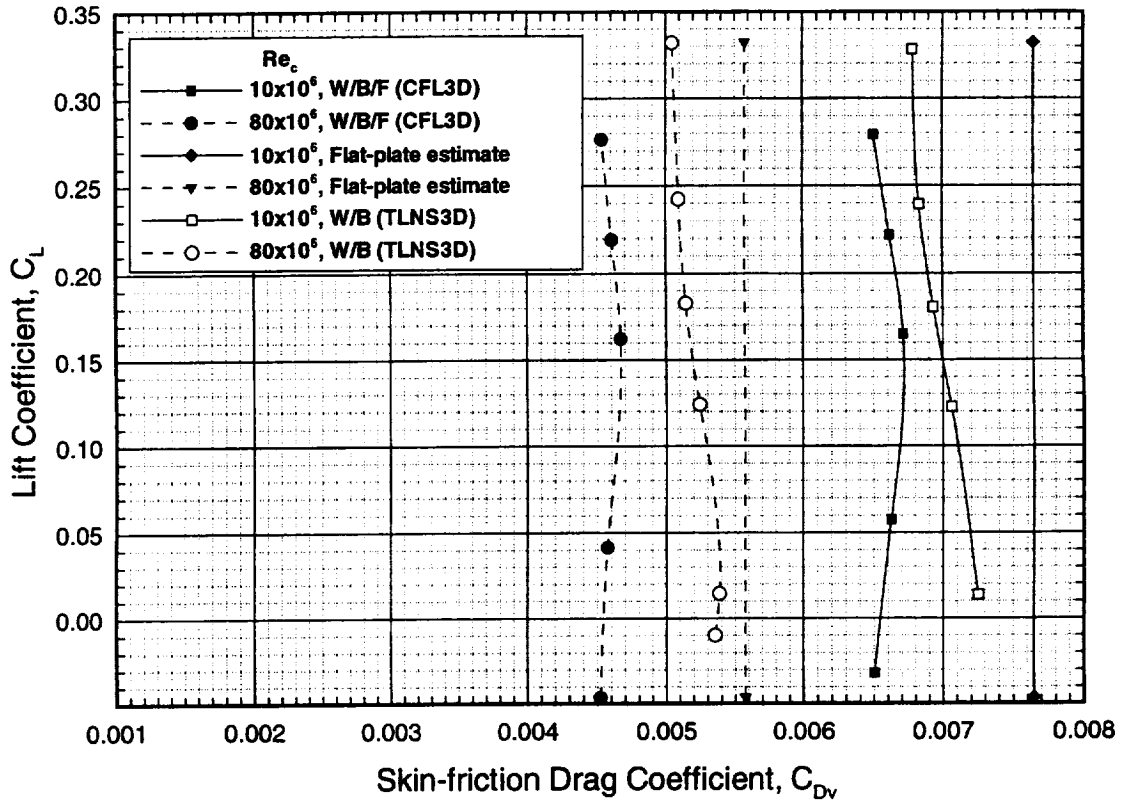
2.2% Ref. H Wing/Body/Flaps ($0^\circ/10^\circ/3^\circ$), $M_\infty=0.9$, Baldwin-Lomax



The pressure drag obtained for the wing/body/flaps configuration, using CFL3D, is essentially independent of the Reynolds number for Reynolds numbers higher than 30 million. Near the transonic cruise condition, there is about a 2 count difference in pressure drag between solutions at Reynolds numbers of 10 and 30 million.

Skin-friction Drag from CFD Analysis and Flat-plate Estimate

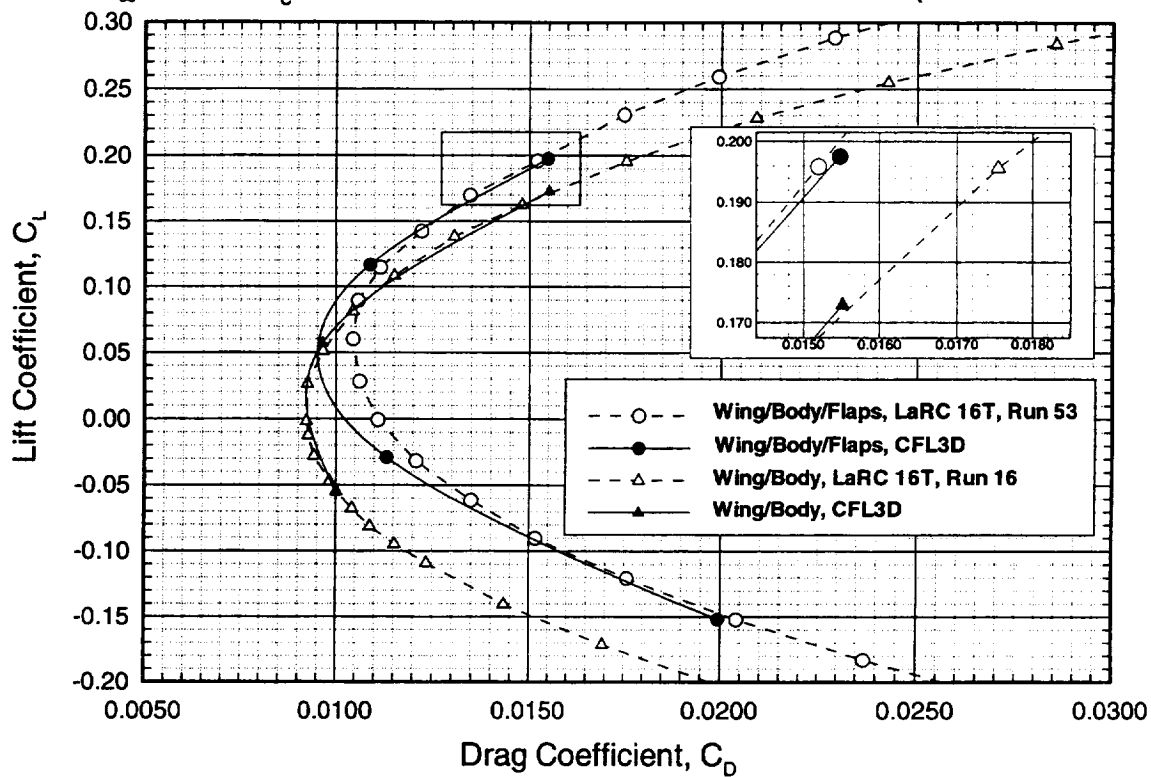
2.2% Ref. H, Wing/Body/Flaps and Wing/Body, $M_\infty=0.9$, Baldwin-Lomax



The skin-friction drag obtained from CFD analysis for Reynolds numbers of 10, 30 (not shown) and 80 million is essentially constant across a wide range of C_L for each Reynolds number. However, the skin-friction drag obtained using the equivalent flat-plate method is off by about 2-5 counts for the wing/body configuration and by about 10 counts for the wing/body/flaps configuration. The equivalent flat-plate skin-friction is insensitive to different flap settings. Therefore the equivalent flat-plate skin-friction drag for the wing/body and wing/body/flaps configurations were identical. All these calculations assume fully turbulent flow. The experiments were conducted without any transition trips and the flow was not fully turbulent, especially for the lower Reynolds number (10 and 30 million) cases. Also, for reasons that are not clear at this time, CFL3D gives a lower skin-friction drag than TLNS3D, when Baldwin-Lomax turbulence model is used. Further investigation is required to understand these discrepancies.

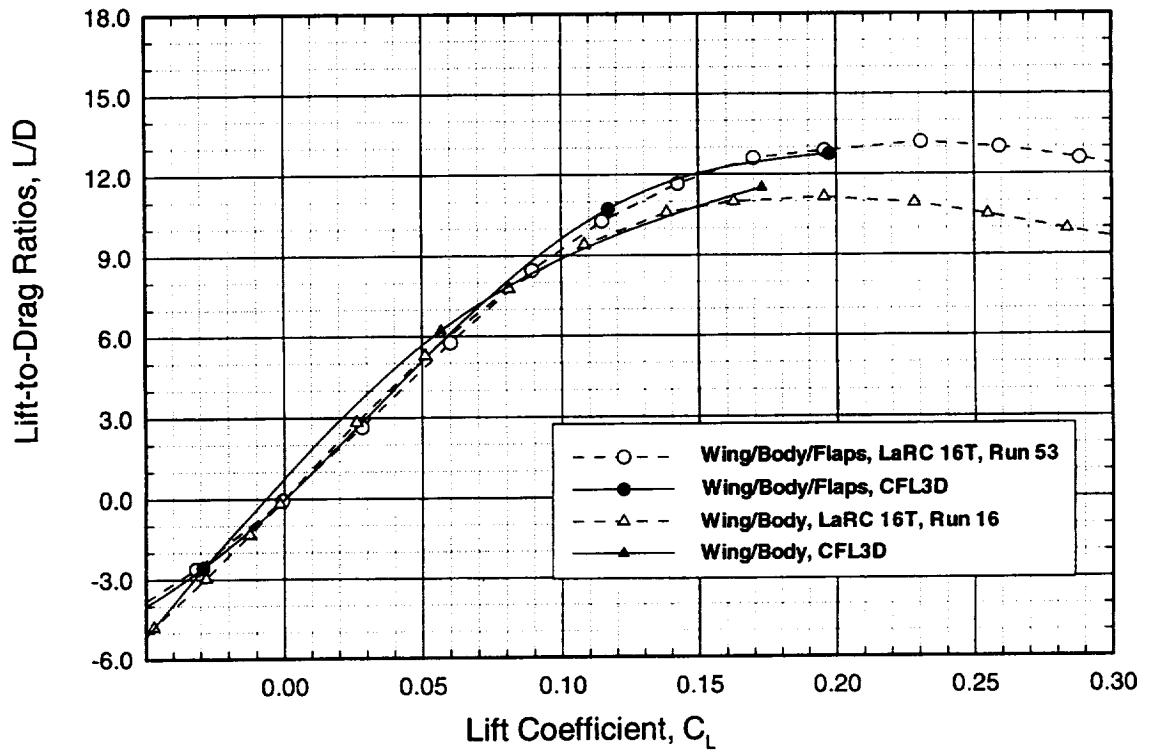
Drag Polars from CFD Analysis and Experiment

1.675% Ref. H Wing/Body/Flaps ($0^\circ/10^\circ/3^\circ$) and Wing/Body
 $M_\infty=0.9$, $Re_c=4 \times 10^6$, 16T Data vs. Navier-Stokes (Baldwin-Barth)



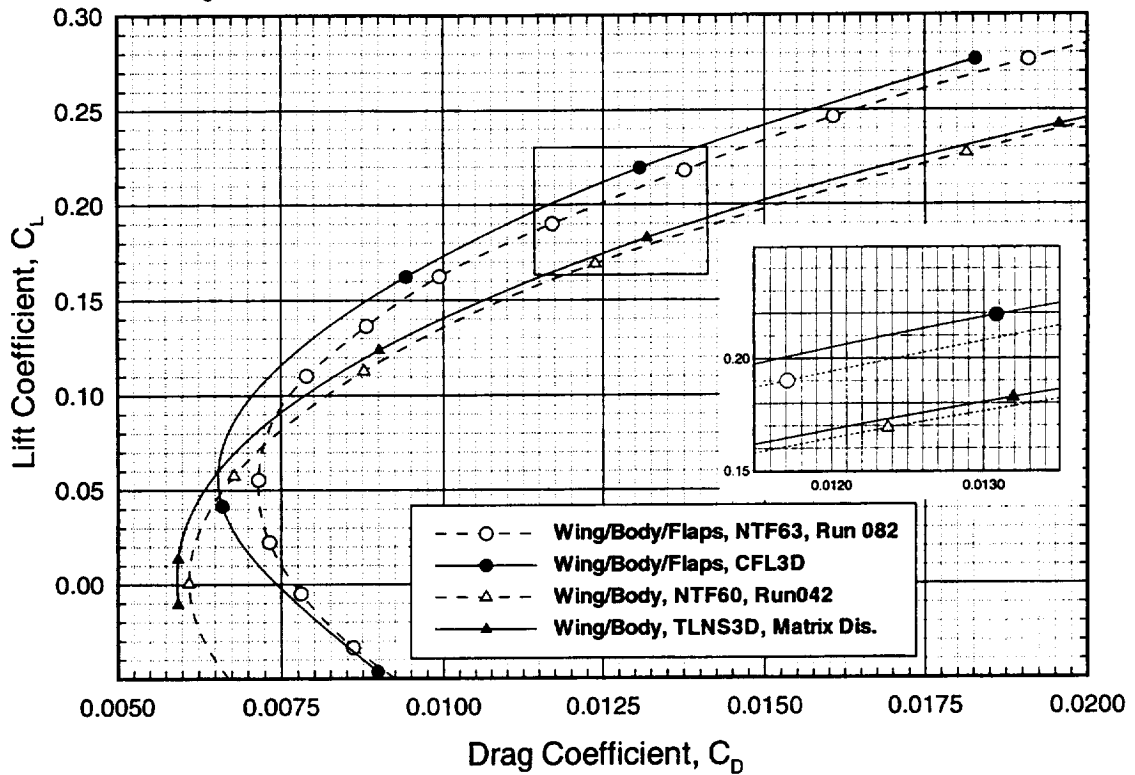
This chart shows the change in drag due to the use of flaps for $Re_c=4 \times 10^6$. At $C_L=0.2$, the drag is reduced by about 22 counts due to the use of flaps. The agreement between the experiment and the computed data is good (within 2 counts) near the transonic cruise point.

Lift-to-Drag Ratios from CFD Analysis and Experiment
 1.675% Ref. H Wing/Body/Flaps ($0^\circ/10^\circ/3^\circ$) and Wing/Body
 $M_\infty=0.9$, $Re_c=4 \times 10^6$, 16T Data vs. Navier-Stokes (Baldwin-Barth)



This chart shows the L/D improvement that is obtained by the use of flaps. L/D is increased by about 2 units at $C_L=0.20$. The agreement between computed and experimental data is satisfactory.

Drag Polars from CFD Analysis and Experiment
 2.2% Ref. H Wing/Body/Flaps ($0^\circ/10^\circ/3^\circ$) and Wing/Body
 $M_\infty=0.9$, $Re_c=80 \times 10^6$, NTF Data vs. Navier-Stokes (Baldwin-Lomax)

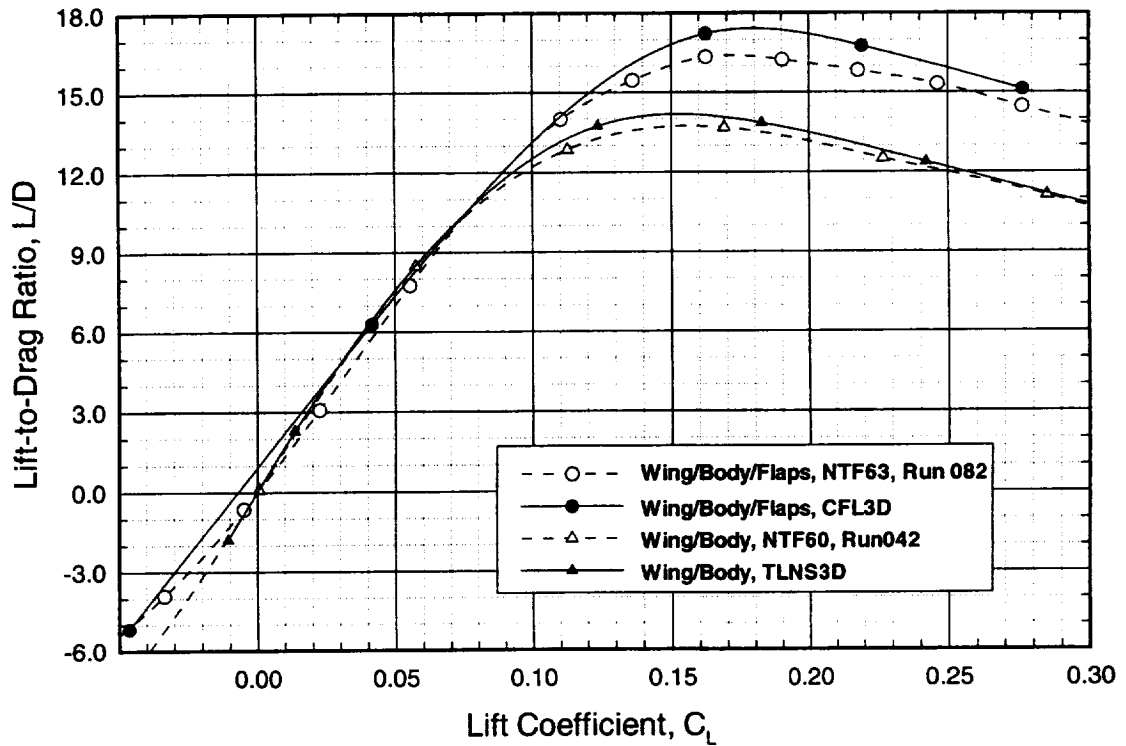


This chart shows the change in drag due to the use of flaps for $Re_c=80 \times 10^6$. At $C_L=0.2$, the drag is reduced by about 25 counts due to the use of flaps. The agreement between the experiment and the computed data is good for the wing/body configuration. However, for the wing/body/flaps configuration, the discrepancy is greater.

Lift-to-Drag Ratios from CFD Analysis and Experiment

2.2% Ref. H Wing/Body/Flaps (0°/10°/3°) and Wing/Body

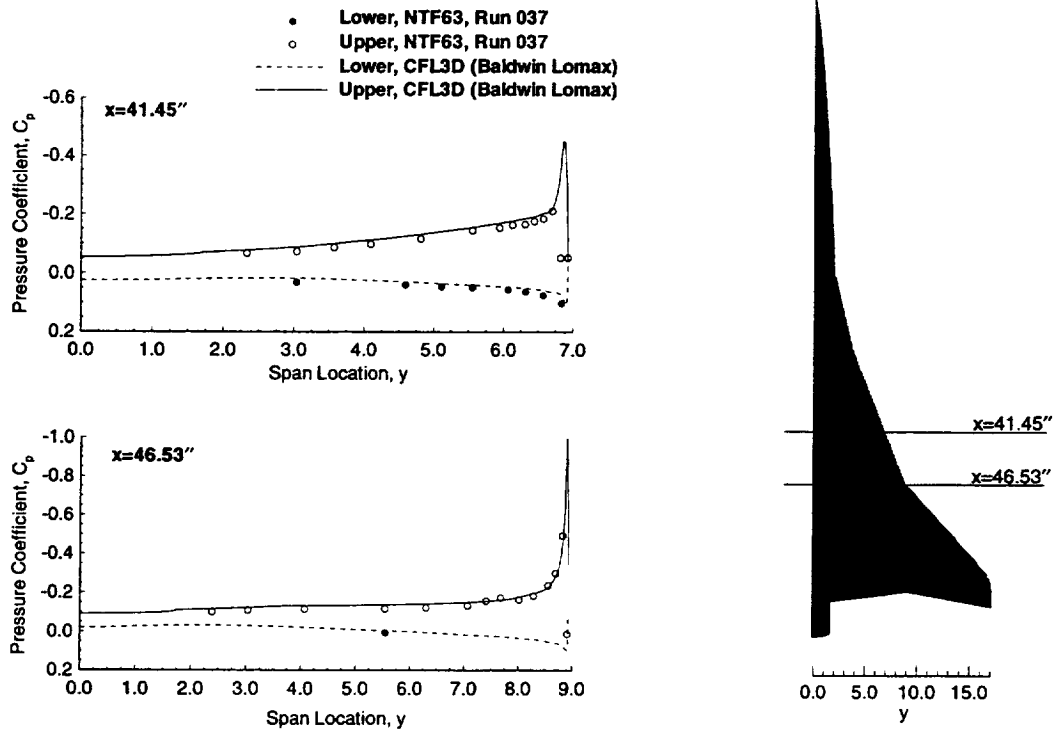
$M_\infty=0.9$, $Re_c=80 \times 10^6$, NTF Data vs. Navier-Stokes (Baldwin-Lomax)



This chart shows the L/D improvement that is obtained by the use of flaps. The experimental data shows an L/D increase of about 3 at $C_L=0.2$. The CFD data on the other hand shows an L/D increase of about 4. This discrepancy is mostly due to the difference in L/D between CFD and experiment for the wing/body/flaps geometry.

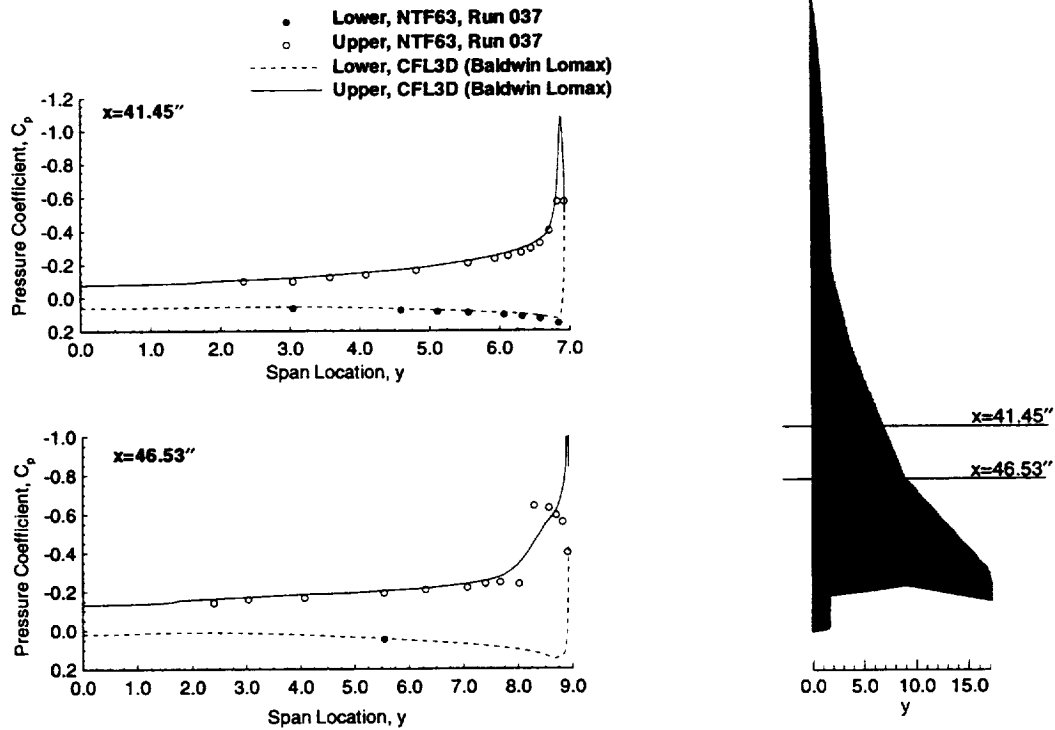
Pressure Distributions from Navier-Stokes Analysis and Experiment

2.2% Ref. H Wing/Body/Flaps ($0^\circ/10^\circ/3^\circ$), $M_\infty = 0.9$, $\alpha = 3.2^\circ$, $Re_c = 80 \times 10^6$



This chart shows pressure distribution comparisons at fuselage stations $x=41.45''$ and $x=46.53''$. The computed pressures agree well with the experimental data.

Pressure Distributions from Navier-Stokes Analysis and Experiment 2.2% Ref. H Wing/Body/Flaps ($0^\circ/10^\circ/3^\circ$), $M_\infty = 0.9$, $\alpha = 5.3^\circ$, $Re_c = 80 \times 10^6$



This chart shows pressure distribution comparisons at fuselage stations $x=41.45"$ and $x=46.53"$. At $x=41.45"$ the computed pressures agree very well with the experimental data. At $x=46.53"$, the agreement is poor near the wing leading edge.

Summary of Transonic Results ($M_\infty=0.9$)

- Drag predictions reasonably good
 - Within 6 counts for wing/body/flaps
- Turbulence model
 - Baldwin-Lomax and Baldwin-Barth acceptable
- Pressure drag essentially independent of Re for $Re_c > 30$ million for wing/body and wing/body/flaps configurations
- Skin-friction drag from CFD and flat-plate estimate significantly different

The off-design ($M_\infty=0.9$) drag predictions for wing/body and wing/body/flaps configurations, using CFD is reasonably good. The Baldwin-Lomax and Baldwin-Barth turbulence models are acceptable. Pressure drag is essentially independent of Reynolds number for Reynolds numbers (Re_c) higher than 30 million for wing/body and wing/body/flaps configurations. Skin-friction drag from CFD and flat-plate estimate are significantly different. Also, CFL3D predicts a lower skin-friction drag than TLNS3D, when the Baldwin-Lomax turbulence model is used. Further investigation is required to understand these discrepancies.

Overview of HSR Aerodynamic Optimization at Boeing

R. S. Conner
The Boeing Company
Seattle, Washington 98124-2207

This presentation provides an overview of the Boeing HSR-AT work on point design, nonlinear aerodynamic optimization of the baseline HSR configuration, Reference H. The efforts can be described as a building block approach, designed to develop the capability for and to evaluate the potential improvement of individual components. These pieces are then combined into increasingly larger problems, moving toward the ultimate goal of simultaneous optimization of the complete configuration. In addition to treating individual components, individual classes of variables are also investigated in isolation. The building block approach is further guided by a goal to evaluate potential differences between the linear Preliminary Design (PD) methods and nonlinear optimization, thereby providing feedback to improve the PD process.

The tool used, TRANAIR, is briefly described with an emphasis on those characteristics which are at the heart of the optimization and/or impact the process of application. This is then followed by a general description of the overall process of application and an introduction to the generic optimization problem that is solved.

This work is a continuation of last year's HSR optimization efforts. The emphasis for this year has been in areas which were either neglected before or revealed by the previous work to be in need of improvement. The first is the incorporation of all relevant and reasonably possible program constraints. This was a major extension of the method. Another area is improvement of the accounting for unfavorable viscous effects. The other major areas are an improvement to the inherent smoothness of the resulting optimizations and an improvement of the resolution of the tool by reducing the aerodynamic variability.

This overview concludes with some engineering analysis of calculations of previous optimizations. Comparisons of full potential and Euler solutions are shown along with examples of suggested physical mechanisms associated with drag reduction.

The details of the specific applications and the results of that work are described in the two companion presentations: "Boeing HSR Wing Optimization using TRANAIR" by Robyn Wittenberg and "Investigation of Nonlinear Effects on Ref. H Body Area-Ruling and Cambering" by Thierry Tamigniaux.



Outline

- Objectives
- Approaches
- Building Blocks
- Project Constraints
- Viscous Effects
- Inherent Smoothness
- Aerodynamic Variability
- Analysis of Optimizations

This presentation provides an overview of the configuration aerodynamic optimization applications that were performed under Aerodynamic Integrations Studies, W.B.S. 4.3.1.5. This work is based on the implementation of capability done under CFD Methodology Adaptation, W.B.S. 4.3.1.1.

An outline of subjects is show here. These items, except for the last, are common to the specific work on body and wing optimization that is covered by the two companion presentations in this workshop, referenced in the abstract. Additional information on the specific tool and process being used can be found in the Midterm Report, presented August 15, 1995 at NASA ARC.

After reviewing the objectives and approaches used, the individual approaches will be discussed in greater detail. The manner in which the complete capability is constructed from individual building blocks is covered. The relationships between certain steps and the Preliminary Design (PD) process are then described. A complete list of project constraints used is presented next, followed by a discussion of the elements of viscous effects treatment used in the inviscid tool. Approaches are concluded by covering the efforts to improve the smoothness of the optimized geometries and to reduce the aerodynamic variability between cases.

The final section presents data taken from analysis of the previous optimization work on the baseline configuration Reference H. Comparison of inviscid results from TRANAIR and STUFF continues to illustrate excellent correlation between the full potential and Euler solutions for the cruise condition of Reference H and its optimizations. Geometric analysis of this same data suggests insights into the physical mechanisms of the optimizations.



Objectives

- **Develop and apply the capability to produce realistically constrained, point designed, nonlinear aerodynamically optimized configurations**
- **Investigate nonlinear effects on Preliminary Design methods**
- **Add and exercise Inlet Flow Quality as a constraint**

The primary objective of the work this year was to apply the capability to produce nonlinear, point-designed, optimized wings and bodies that meet the realistic constraints of the project airplane. This is a major extension in the application of the tool. The wing and body optimizations occur in the presence of aerodynamically consistent nacelle/diverter installations. In the course of building up this capability, and as a second objective, the nonlinear implications for the simplified geometric representations of the PD linear designs were investigated. The final objective was to add inlet flow quality as a constraint.



Approaches

- **Use TRANAIR**
- **Build up Capabilities in Steps**
- **Limit Design Space with Project Constraints**
- **Improve Accounting for Viscous Effects**
- **Reduce Post-Optimization Smoothing Requirements**
- **Reduce Aerodynamic Variability between Cases**
- **Evaluate Effects of Inlet Flow Quality Constraints**

There are several, somewhat interrelated approaches used to accomplish the objectives. They are listed here and each is discussed in more detail later. To begin with, the optimization tool used is TRANAIR. A review of important characteristics of the method highlight its appropriateness for this class of problems.

As indicated earlier, capabilities are built up a step at a time. This approach is used for several reasons. First, it is the straightforward way to assess the success of any given part. Optimization is too complex and unpredictable to proceed without an understanding of the previous result. Another result of a building block approach is a quantitative measure of individual components, the increments. By further basing the steps on the simplified geometries used in the PD process, nonlinear effects, if present, can be exposed and understood, if not exploited.

The next approach is to limit the design space available to the optimizer by implementing a thorough set of project-based, geometric constraints. This permits the emphasis to be placed on solutions which feature inherently acceptable geometry. Constraints which are activated and the corresponding sensitivities will still illuminate potentially attractive solutions which may violate the initial constraints. Possible areas of beneficial compromise are in this way not ignored.

Once the design space is limited by the project constraints, the emphasis shifts to improving the inviscid flow constraints used to avoid viscous degradation, if necessary. Results presented in a following section suggest that the need for flow constraints is reduced by the geometric constraints. Results of the previous optimizations have been used to guide this work on viscous effects.

There are clear advantages to constraining the optimizations to inherently smooth geometries. Both from the standpoint of project acceptability and the flowtime for processing to useful lofts, limiting the results to smooth geometries is desirable. This approach is used.

Many of the increments of interest are relatively small. To increase confidence in the computational results, steps were taken to reduce the aerodynamic variability between cases. These steps are discussed.

Finally, two measures of inlet flow quality were implemented and exercised. The effects of these additional constraints will be used in the upcoming inlet operability trade studies.



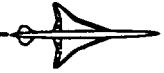
TRANAIR Analysis

- Full Potential -> Conservation of Mass
- Outer Nonlinear Solver : Newton's Method
- Inner Linear Solver
 - GMRES Driver
 - Sparse Solver
- Sequenced, Solution-Adaptive, Cartesian Grid
- Grid-Independent Surface Model
- Currently, No Direct Viscous Modeling in Use

Several important characteristics of the TRANAIR analysis code are outlined here. First, it is based on a conservative formulation of the full potential equation. Theoretically, that is the most computationally-efficient nonlinear flow technology. It also appears to adequately model the inviscid flow physics relevant to an HSCT-type configuration at supersonic cruise conditions. Many comparisons with various Euler codes and wind tunnel data support this observation. One is included in this presentation. In the absence of strong, viscous effects, incremental and absolute inviscid pressure forces are accurately predicated for this class of problems.

As indicated, the nonlinear solver is a Newton's method. It is based on a linear inner solver which in turn is driven by GMRES working on a sparse solver. The grid is a non-surface-fitting, self-similar cartesian type. The solution is produced on a sequence of hierarchically-refined grids where refinement is driven by the solution. The surface model of the object(s) of interest is created independently of the cartesian field grid. As such, the method is flexible and capable of extreme and faithful geometric detail.

The viscous layer modeling available in TRANAIR is not currently used in either analysis or optimization.



TRANAIR Optimization

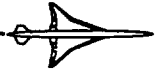
- **Optimizer Imbedded Within Flow Code**
 - **NPSOL**
- **Movements and Constraints via User-Supplied Subroutines**
- **Geometric Perturbations via Surface Transpiration**
- **Optimization on Multiple Grid**
 - **Sensitivity Matrix Passed to Next Grid**
 - **Grids Adaptive to Optimized Solution**

There are several other characteristics of the TRANAIR optimization code that are shown here. In general, these tend to distinguish TRANAIR from most optimization methods. To begin, the optimization routine is actually embedded within the flow solver. NPSOL is the current optimizer and can be replaced if and when better technology becomes available.

All geometric movement driven by the variables, all geometric constraints placed on these movements, and any flow constraint not available directly in TRANAIR are implemented in user-supplied subroutines. In this way, TRANAIR is set up to solve the general optimization problem involving variables, constraints and an objective function. As a result of this structure, application-specific implementations, such as HSR, occur outside of the TRANAIR code.

Objective function sensitivities are based on the difference of two flow solutions. The geometric movements due to the variables are modeled by surface transpirations from the input geometry. These are, as a result, simple linear solutions and are very efficient.

Optimization makes use of the grid-sequencing in TRANAIR. Full optimizations can be requested on any and all grids. In practice, only the final few grids are used. Additional efficiency is realized by passing the optimization sensitivity matrix from one grid to the next, giving the next grid's optimization useful information. Finally, the solution-adaptive grid is based on the optimized solution. As such, features due to optimization are properly gridded.



Nominal TRANAIR Optimization Cycle

- 0) (Analysis Run)
- 1) Optimization Run -> Prediction
- 2) Update Surface Model
- 3) Analysis Run of Updated Surface Model
- 4) If Analysis 3) = Prediction 1) -> Done
- 5) Otherwise, Repeat From 1) Using Updated Surface Model

The nominal TRANAIR optimization process is outlined here. Assuming that a baseline solution exists, the process begins with an optimization run. Within the optimization, flow solutions for the perturbed variables are calculated as linearizations about the baseline. Finite differences taken between these solutions and the baseline constitute the gradient information. The result of the optimization is a prediction. It is a prediction of what the nonlinear flow solution will be about the predicted optimal geometry, and is based on the transpiration-based linearization of the flow. The accuracy of this prediction is a relatively simple function of the accuracy of the transpiration modeling within the optimization.

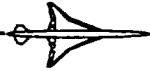
The next step is to update the surface model with the predicted geometry and analyze it. This result is then checked against the prediction. In general, the optimization is considered complete when the analysis verifies the prediction to within some small tolerance. If the analysis does not agree with the prediction, then the steps are repeated using the updated surface model. In our experience thus far, starting from the baseline, two optimization runs have been required for a wing optimization. This double pass through the optimization code appears to be the price paid for the approximations made within the optimization and the relatively large movements needed for the wing. The body optimizations, on the other hand, are adequately treated by a single cycle. More information is provided in the companion presentations.



Preliminary Design Configurations

- **Uncambered Wing/Body, Midwing**
 - **Body Area Optimization**
 - **Wing Thickness Optimization**
- **Uncambered Wing/Body, Low Wing**
 - **Body Area Optimization**
- **Uncambered Wing/Body/Nacelles, Low Wing**
 - **Body Area Optimization**

The simple geometry used in PD and two of the steps toward the real configuration that are addressed in the capability building blocks are shown here. That part of drag due to volume is calculated on the uncambered, nonlifting wing/body configuration. Body area ruling also is done on this configuration. The effects of placing the wing in a more realistic position and of including the nacelles in the body area ruling are illuminated by the other two configurations shown here. Results are discussed in the following section.



Building Blocks

- **Body Area**
 - **Axisymmetric**
 - **Nonaxisymmetric**
- **Body Camber**
- **Body Area & Camber**
- **Wing Thickness**
 - **Uncambered**
 - **Cambered**
- **Wing Twist & Camber**
- **Wing Thickness, Twist & Camber**
- **All Together**
- **Flow Constraints**

The steps of capability buildup are straightforward and shown in order here. The body and wing are optimized independently in the beginning. Each in turn, is built up in steps from simple to complex geometries and optimizations. Specifically, the body started with area optimization of an uncambered, axisymmetric body with an uncambered wing placed on the body axis. Starting area distributions of the body and wing are those of the baseline, Reference H. The wing was then moved down to a Reference H-type location on this same body. To this model was added freeflying nacelles. The axisymmetric body area was varied in an axisymmetric fashion, by simple radius changes. These cases were all run at zero angle of attack and nominally zero lift.

Body area optimization then moved to nonaxisymmetric shapes starting from Reference H, including installed nacelles and diverters, and performed at the design condition, $CL=0.12$. Body camber was optimized separately, also starting from Reference H at the lifting condition. After all these cases, a combined body area and camber optimization was done.

In a similar way, the wing optimization started from the same uncambered, nonlifting wing/body configuration and only thickness was optimized. Thickness was then optimized on the Reference H configuration at the design condition. This was followed by twist and camber optimization of Reference H. The last two were then combined into a thickness, twist and camber optimization.

This is the state of the buildup at this time. The next step is to combine all this into a simultaneous optimization of body and wing, area and camber. This result then will establish the baseline for specific flow constraints to control viscous effects.

The results of all these optimizations are discussed in the two sections which follow.



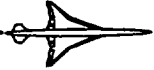
Project Constraints

- **Articulated Cabin Floor**
- **Internal Body Cross Section Envelope**
 - **Cockpit**
 - **Passenger Lobe (Upper Lobe).**
 - **Cargo Lobe (Lower Lobe).**
- **Subsonic Leading Edge Radius**
- **Upper Surface Streamwise Curvature**
- **Trailing Edge Closure Angle**

The set of project constraints used for this year's work is listed on this and the next two charts. This list represents all the project constraints that appear to be relevant to wing/body optimization, based on discussions with the Technology Integration group. Some are self explanatory from the chart and some need further description. Also, the purpose behind some constraints may not be obvious and is included here.

To accommodate the geometric variation of the Reference H body, camber in particular, there are kinks or breakpoints in the baseline floor definition. Work on optimized body camber indicates that additional kinks will be needed to achieve the desired body camber distribution. The kink angles between floor segments are variables in the body camber problems being solved. This is referred here as an articulated floor. The internal body cross section envelope is referenced to the floor location so that it also can move. Limits are placed on the kink angles to prevent unacceptable slope changes. This year's work used a maximum of two degrees. These constraints are described in more detail in the next section.

The minimum radius on the subsonic leading edge is constrained for off design conditions. The only curvature constraint currently imposed for structural or manufacturing reasons is streamwise on the upper surface of the wing. A concave section is not allowed.



Project Constraints (continued)

- Main Cabin Floor Angle of Attack
- Main Landing Gear Bay Thickness
- Front Spar/Cabin Floor Separation
- Spar Thickness'
 - Leading Edge
 - Front
 - Rear
- Overwing Emergency Exit Doors Clearance

The angle of attack, relative to the main cabin floor, is bounded to insure that the inflight attitude is acceptable to the flight crew and passengers. The specific limit value imposed is five degrees.

The separation distance between the front spar and the cabin floor is constrained to a minimum value so that adequate space is left for systems such as environmental control.



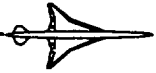
Project Constraints (continued)

- Wing Twist Axis
- Lift Coefficient
- Inlet Flow Quality
- (• Pitching Moment Coefficient)

The project groups are not currently specifying the location of the wing twist axis but experience suggests that it will eventually become an issue.

The values to use for inlet flow quality constraints have not been determined yet. It is possible that this constraint will be used for generating trade study data rather than constraining any specific wing design.

Pitching moment was not constrained in any optimization produced this year. It is trivial to invoke when the time comes. At present, the overall configuration optimization including wing design, trim drag and cg control has yet to determine the appropriate pitching moment to constrain the truncated wing/body/nacelle/diverter configuration to. When the value is known, it will be used.



Viscous Effects

- **Incorporate 2nd Order Upwinding into Optimization Process**
- **Assess Needs after imposing Project & Smoothness Constraints**
- **Develop Candidate Flow Criterion**
- **Evaluate Effects of Maximum Mach Number Limit**
- **Add Surface Curvature Constraints**
 - **Chordwise: Lower Surface Leading Edge**

The first effort to improve the control of viscous effects during optimization was to incorporate 2nd order upwinding into the process. This was based on the theory that better resolution of shocks in the flow would allow the optimization to avoid the accompanying adverse pressure gradients, even though the reason would be related to wave drag, not shock/viscous layer interactions. Navier-Stokes analysis of such a change to the process used to produce wing/body 27S demonstrated a drag improvement of one count.

The next element of the viscous effects plan was to impose the set of project constraints before evaluating the need for additional constraints. This year's work is just shy of this point, although as will be shown in the section on wing optimization, additional control for viscous effects may not be required, at least for Reference H.

This did not preclude work on a candidate viscous criterion, however. Study of analysis of and the wind tunnel results for Reference H, 27S and 704 lead to the selection of lateral cross-flow magnitude as a promising viscous flow criterion. This is discussed in more detail in a separate section later.

As shown previously in the Final Review Report for W.B.S. 4.3.1.1, the effect of the maximum Mach number limit on optimization was also investigated. Lateral cross-flow has a positive correlation with maximum Mach number, which provides another, but indirect, control of this criterion.

The final aspect of this year's efforts on viscous accounting was to add streamwise curvature constraints to the lower surface on the forward quarter or so of the inboard wing. Inviscid optimization was thinning the wing on both sides of the leading edge spar which produced viscously undesirable oscillations in the pressure distributions.



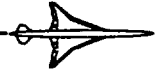
Inherent Smoothness

- **Localized Bump Functions**
- **Nacelle/Diverter Treatment**
 - **Smooth Spanwise Variations**
- **Thickness**
- **Surface Curvature Constraints**
 - **Spanwise: Upper & Lower Surfaces**

There are four parts of this year's efforts to improve the inherent smoothness of the optimized geometry. The bump functions used to perturb geometry have been upgraded to a variety which are strongly localized. Next a great deal of effort was invested in the treatment of the wing in the vicinity of the nacelle/diverters. The result is a smooth variation of geometric changes across the propulsion installations. Although, not the reason for adding it to the optimization, thickness also appears to improve smoothness to the extent that it decouples the upper and lower surfaces of the wing. The flows above and below the wing are, in general, not compatible with camber variations only.

The final aspect of efforts to address inherent smoothness is a straightforward application of spanwise curvature constraints. For an optimization of both thickness and camber, curvature constraints must be applied to both the upper and lower surfaces. Currently, this is treated as a constant for a given surface. The ability to make curvature limits a function of location exists and will be exercised as circumstances permit and/or require it.

There appears to be limits to how inherently smooth an optimization result can be given the limit of discrete variables. As a result, smoothness must be addressed on both sides of the optimization. Going in, efforts are made to constrain the optimization in the direction of smoothness, knowing that it will be incomplete at best. The overall process then must provide for a post-optimization smoothing step to produce the final result. It appears that this should be recognized as an integral part of the process, and perhaps, should be receiving more emphasis on this program.

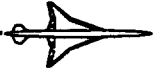


Aerodynamic Variability

- **Single Family of Grids for All Project Cases**
 - ~ Same Pressure Drag as STUFF Euler
- **Aerodynamically Consistent Nacelle/Diverter Installations**
 - **Diverter Heights Maintained at Diverter Leading Edge and Wing Trailing Edge**

Aerodynamic variability was explicitly addressed in the two ways shown here. First, a family of grid specifications was developed and used for all the program optimizations and analyses. The word specification is used since the tool, TRANAIR, uses solution-adaptive grid. The control of the grid is accomplished through a set of guidelines or specifications. Currently the family consists of a wing/body version, a wing/body/nacelle/diverter version and a minor extension of the latter for inlet flow quality work. Extensions to include additional components such as the empennage will be developed as required. One of the encouraging results of this work was that this grid specification produces pressure drag that is in excellent agreement with STUFF Euler solutions.

The other technique to reduce variability is the nacelle/diverter region treatment previously discussed. The details of that work which are important here deal with the diverter and its interface with the wing lower surface. During optimization, the input height of the diverter leading edge and the height of the diverter at the wing trailing edge are maintained. Although the wing is allowed to camber and change thickness across the diverters, the overall installation appears to remain relatively stable by constraining the two locations indicated. This appears to be required to produce a clean aerodynamic increment for wing optimization. This is not a claim that the baseline propulsion installation is optimal but rather a recognition that changes to the installation should not be bookkept as a part of the wing optimization increment. Wing optimization is the goal of this year's work. Nacelle/diverter installation optimization will be addressed as a separate building block next year.



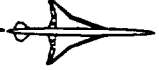
Analysis of Optimizations

- **Consistent Forces & Moments**
 - No apparent advantage of Euler over full potential
- **Aero-Geometric Analysis of Optimizations**
 - Reference H vs 704 vs 27S

This final portion presents more detailed analysis of TRANAIR wing/body solutions for Reference H and its two previous optimizations, 27S and 704. The first part shows force and moment comparisons between TRANAIR and STUFF Euler. This is followed by a more detailed examination of the local geometry and surface solutions of the three configurations.

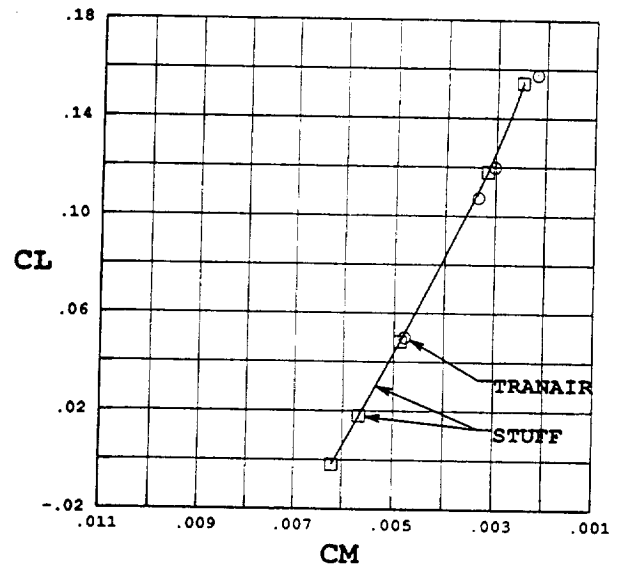
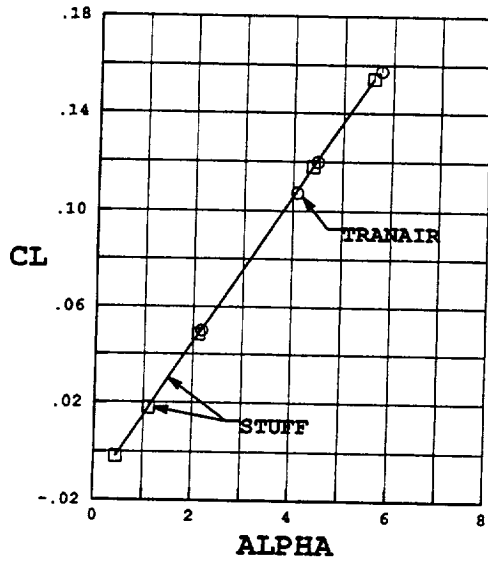
Year's of examination have consistently demonstrated TRANAIR's capacity to calculate the flow about HSCT-type configurations in the neighborhood of the supersonic cruise condition. This is one reason it was chosen as the optimization tool. The code does, however, change with time as improvements are incorporated. Because of this, occasional validation checks are warranted. Results of analysis of Reference H, 27S and 704, done in support of this year's wing tunnel test, are presented here. Lift, drag and pitching moments, in coefficient form, from TRANAIR and STUFF Euler for wing/body are compared. As before, correlation is excellent.

Spanwise variations in local properties illustrate interesting differences between the directions taken by the two optimizations of Reference H. This data is further analyzed in terms of local geometry and surface pressures. Possible drag reduction mechanisms are suggested by the data.



Reference H Wing/Body Lift & Moment

Full Potential (TRANAIR) vs Euler (STUFF)



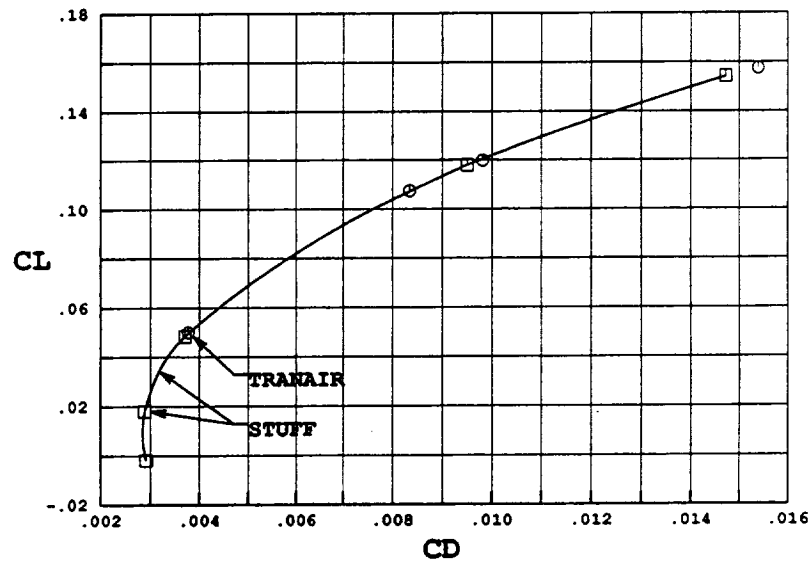
These plots show the lift and pitching moment values calculated by the two codes for Reference H. As with all the plots in this set, these are the forces and moments on the wind tunnel wing/body geometry. The body is truncated at 2904.597, full scale. Moments are taken about the 0.5 MAC location. The STUFF results are plotted as square symbols with a curve fit through the individual points. The corresponding TRANAIR results are plotted as circles only.

The correlation of lift and pitching moment for Reference H is excellent.

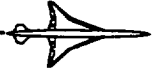


Reference H Wing/Body Drag

Full Potential (TRANAIR) vs Euler (STUFF)

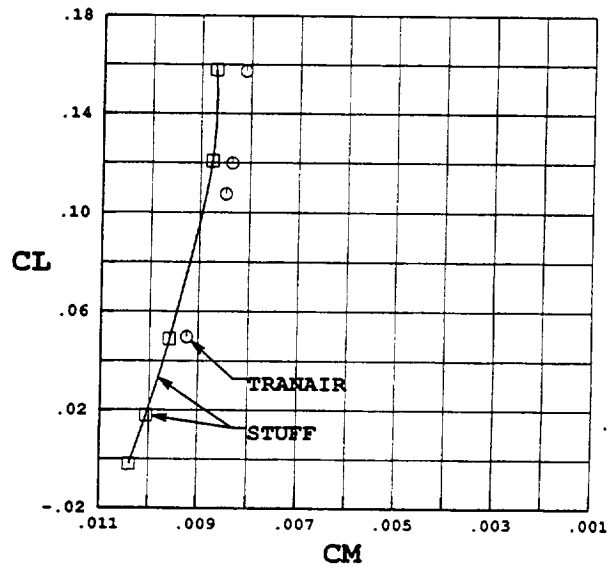
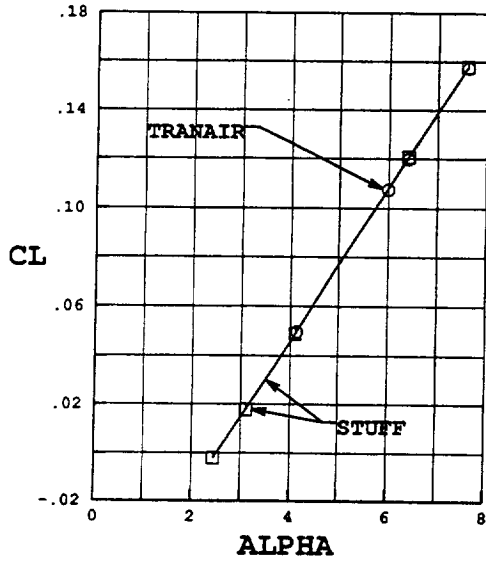


The respective drag polar results for Reference H are shown here. As with lift and pitching moment, the agreement between TRANAIR and STUFF is excellent.

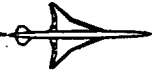


27S Wing/Body Lift & Moment

Full Potential (TRANAIR) vs Euler (STUFF)

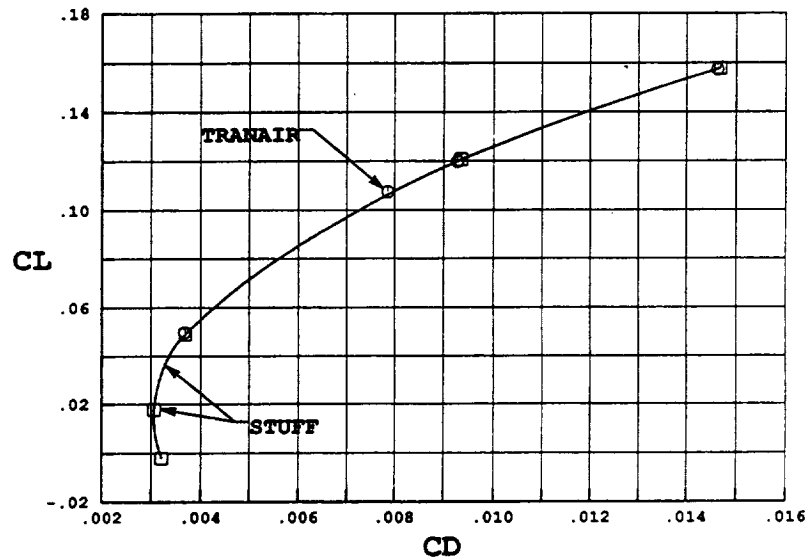


The corresponding lift and pitching moment data for 27S are shown here. The two lift curves are indistinguishable while there is a small offset apparent in the pitching moments. The behavior of the two pitching moments with lift are very similar.



27S Wing/Body Drag

Full Potential (TRANAIR) vs Euler (STUFF)

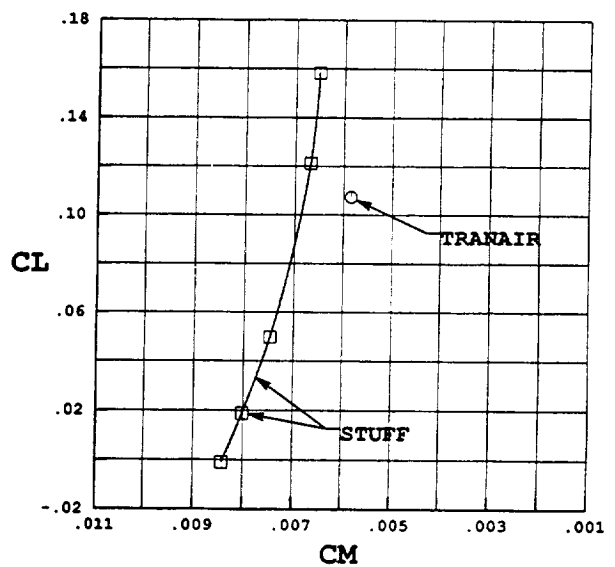
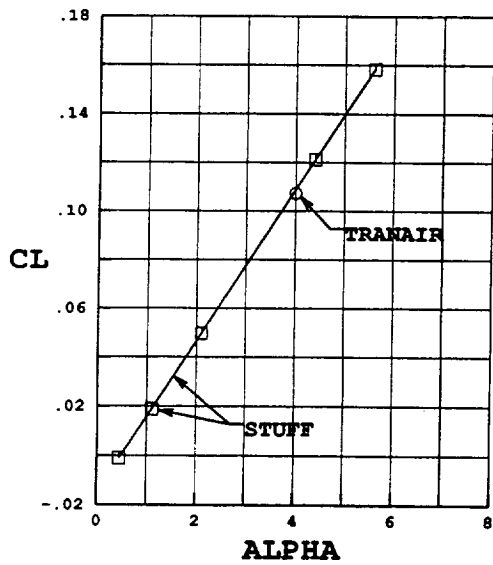


The comparison of drag polars for 27S is shown here. As with Reference H, the correlation is excellent. The small difference shown for the arrowed point may be due to the curve fit. At the two higher points where the conditions are well matched, the two codes are predicting the same drag.



704 Wing/Body Lift & Moment

Full Potential (TRANAIR) vs Euler (STUFF)

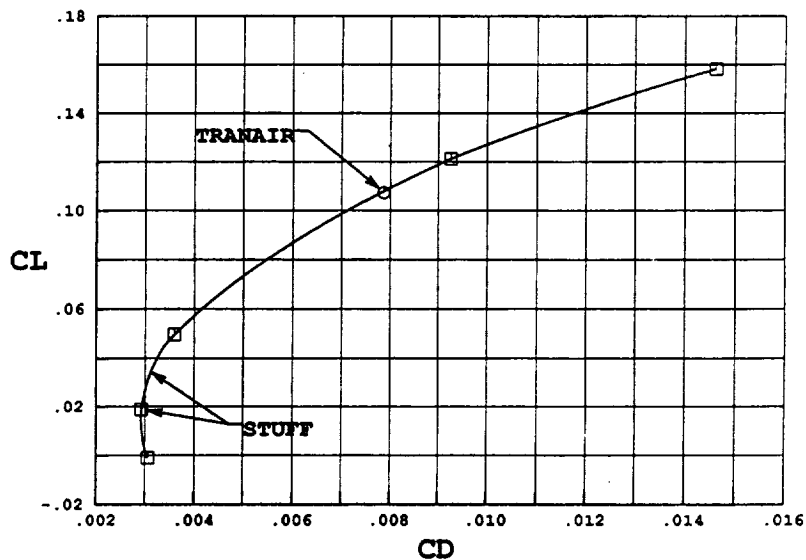


Only one point was calculated for 704 in TRANAIR and the comparison of lift and pitching moment are shown here. The lift is ever so lower than the STUFF data and the pitching moment is low, as was the case with 27S.

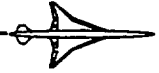


704 Wing/Body Drag

Full Potential (TRANAIR) vs Euler (STUFF)

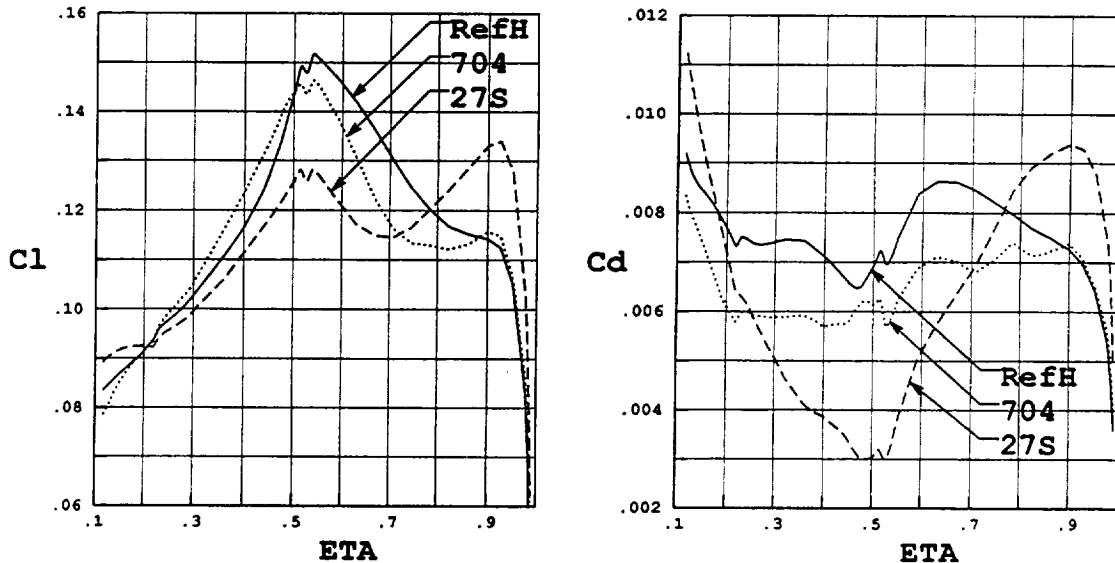


The drag comparison is also similar to 27S, the agreement is very good. In summary, the differences between the forces and moments calculated by full potential and Euler are very small if any, and indicate no obvious reason to favor one or the other for the cruise conditions of this family of HSCT configurations.



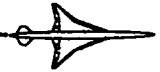
Spanwise Variation of Sectional Properties

TRANAIR Wing/Body Analysis at Cruise Alpha

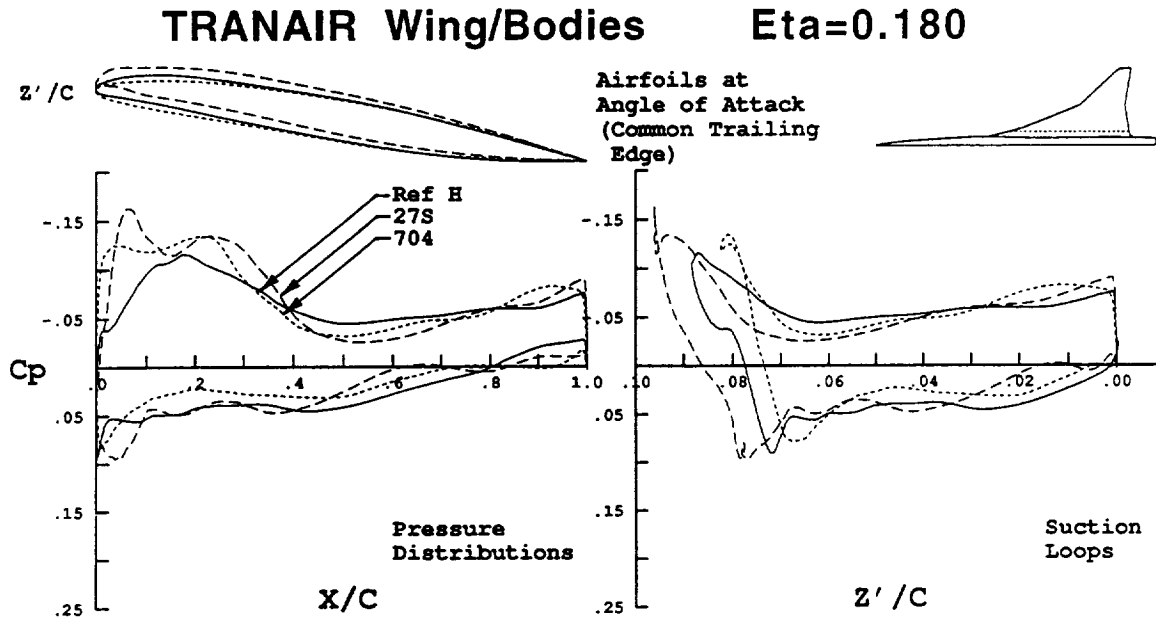


The spanwise variation of sectional lift and drag for the three configurations are shown here. The baseline, Reference H is the solid curve, 27S is the long dash and 704 is the dotted curve. They indicate that 27S and 704 took distinctly different approaches to the optimization of Reference H. In terms of lift, 27S increased the side-of-body lift and reduced the spanload on the rest of the subsonic leading edge portion of the wing. Configuration 704 did exactly the opposite. They both chose to reduce the lift on the inboard portion of the outboard wing but 27S actually increased the loading further out.

The sectional drag plot shows more of the differences in the two optimizations. Interestingly, 27S shows the same relative trend in drag as it does in lift. The 704 result, however, shows a reduction in drag at all locations except for the obvious wing tip area. On the outboard part of the inboard wing, this implies that 704 was able to increase lift and decrease drag simultaneously. It appears that 27S reduced the drag faster than the lift was reduced. Both optimizations found this portion of the wing wanting. The 27S result appears to be more complex in that it chose to accept increased drag in some areas in exchange for substantially lower drag in others. The differences in the two optimizations are consistent with the fact that 704 was done in pieces while 27S was simultaneous.



Sectional Geometry and Surface Pressures



Turning to the local geometry and surface pressures of this data, an inboard wing section is shown here. The format, repeated for three more stations, includes airfoil geometries at angle of attack and with common trailing edges. To the left of the geometries is an airplane planform with the section shown as a dotted line. The airfoils are expanded in the vertical direction to show features and are plotted in nondimensional coordinates corresponding to the chord of the pressure distribution, shown below, and the vertical coordinate that results from the rotation for angle of attack, Z'/C . The plot on the right is the surface pressure resolved in the airplane drag axis and is referred to as a suction loop. Drag is the integral of this pressure distribution.

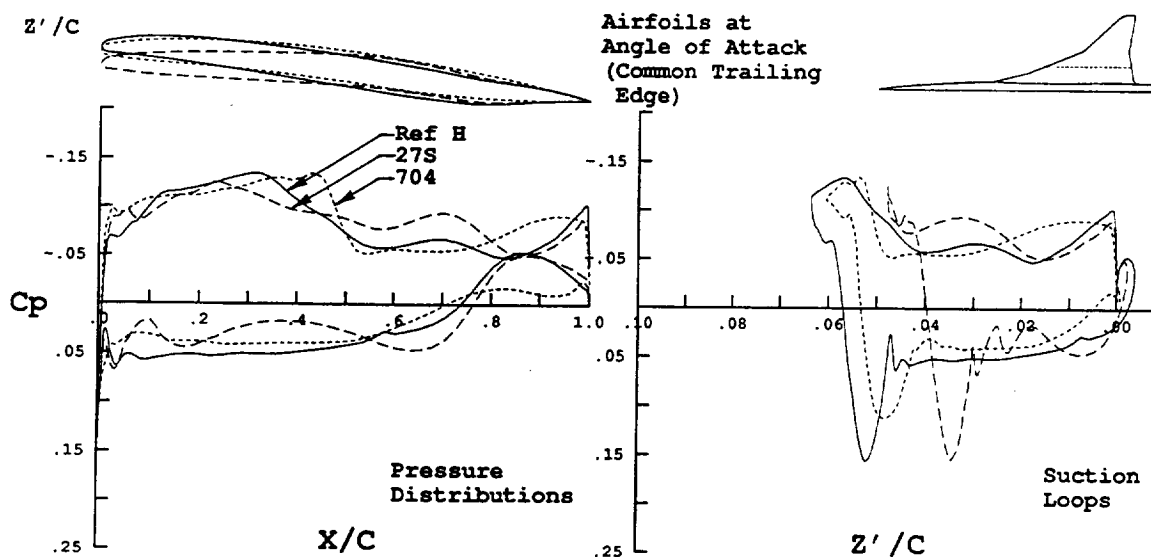
The main body of the suction loops are actually drag loops. This is a visual demonstration of the linear theory result that says all lift is drag. Near the leading edges of the two optimized geometries, there are instances of true suction loops. These are what the nonlinear optimizers are capable of doing to the baseline linear design.

Another observation from this data is the apparent positive correlation of drag with local angle of attack. This is just another example of the general aerodynamic observation that camber is a more efficient means of generating lift than angle of attack.



Sectional Geometry and Surface Pressures

TRANAIR Wing/Bodies Eta=0.321

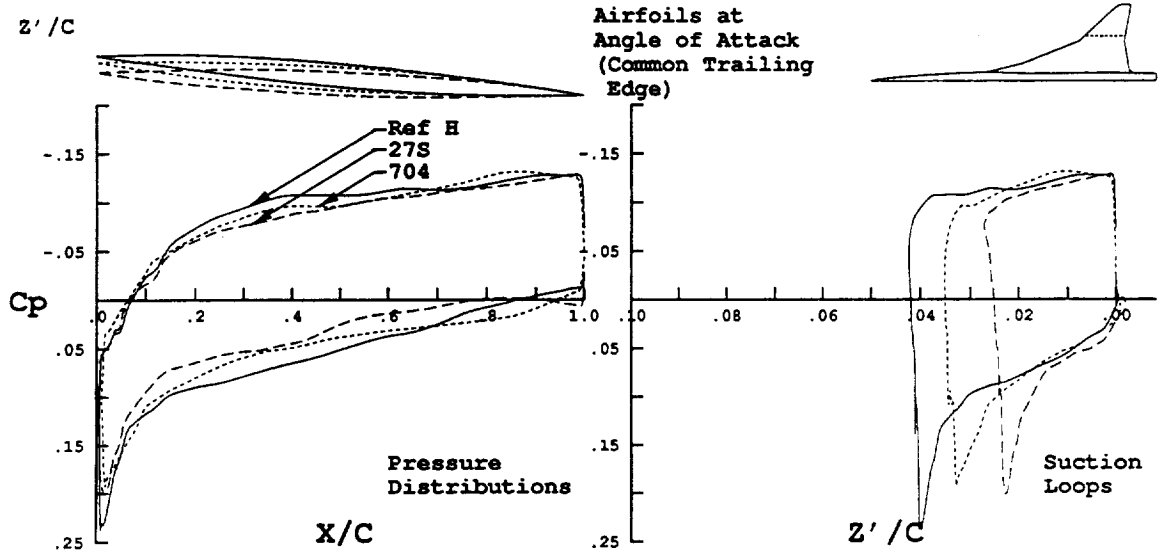


This next section shows an outboard location on the inboard wing. Now the 27S section has the lowest local angle of attack and the smallest integrated drag. It also features the only suction loop, although the 704 section is also clearly better than the baseline. Both the optimizations have lowered the leading edge portion of the section relative to Reference H to accomplish this.



Sectional Geometry and Surface Pressures

TRANAIR Wing/Bodies $\text{Eta}=0.591$

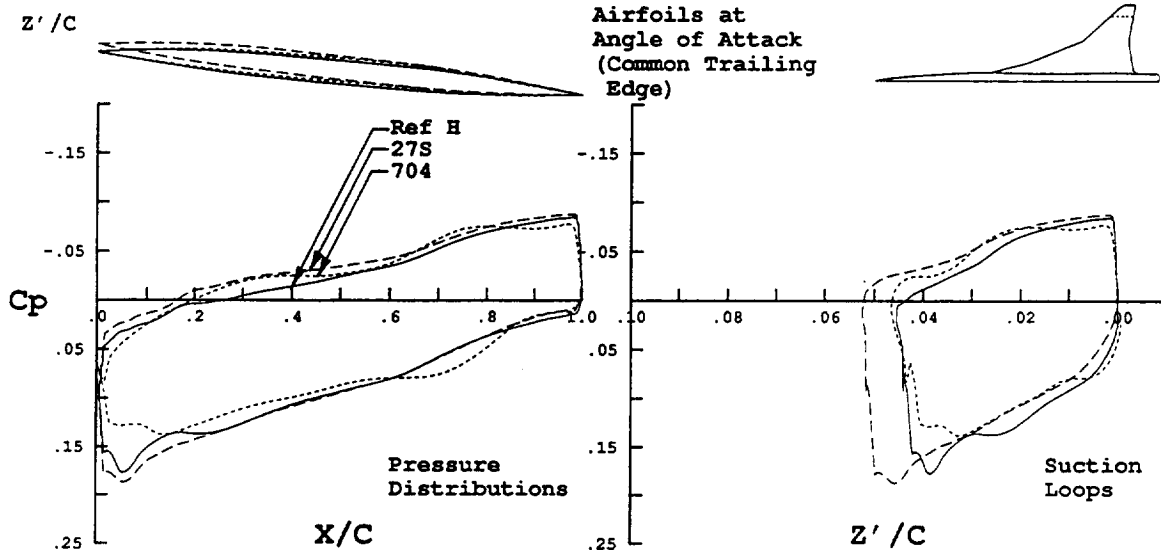


The next section, now on the outboard wing, seems to illustrate the common assumption that the supersonic leading edge portion of the wing has less potential for drag reduction. What is apparent though is that local angle of attack is still powerful. Both the optimizations chose to reduce the lift and, therefore, the drag on this portion of the wing.



Sectional Geometry and Surface Pressures

TRANAIR Wing/Bodies $\text{Eta}=0.848$



Looking nearer the tip of the outboard wing, the result previous shown in the spanwise data is apparent. The highest local lift and drag are produced by 27S.

Some Recent Enhancements to Aerodynamic Shape Optimization Methods at McDonnell Douglas Aerospace

Peter M. Hartwich, Eric R. Unger, Alan E. Arslan, and Shreekanth Agrawal
McDonnell Douglas Corporation
Long Beach, CA 90807

A High-Speed Civil Transport (HSCT) aircraft has to simultaneously satisfy a multitude of often conflicting constraints and to meet rather stringent aerodynamic performance requirements across a wide speed range extending from high-lift, over transonic to supersonic cruise conditions. Extensive use of nonlinear optimization techniques is presently considered the most promising way of satisfying all of these requirements. The technical activities highlighted in this paper are aimed at enhancing the nonlinear aerodynamic design optimization capabilities at McDonnell Douglas. The topics discussed pertain to three areas: alternate sensitivity analysis methods for use with gradient-based optimization methods, a grid perturbation scheme for the rapid adjustment of computational multiblock patched grids over complex configuration during aerodynamic optimization processes, and an alternate approach toward the parametrization of 3-D geometries for use in aerodynamic shape optimization. The methods employed in each area are outlined, and some illustrative results are included to highlight accomplishments as well as future challenges.

Nonlinear Point Design Optimization Methods

- **Objective**

- **Expand the capabilities in aerodynamic design optimization in three areas:**
 - **Alternate gradient evaluation**
 - **Grid perturbation for the direct optimization of wing/body/nacelle/diverter configurations**
 - **Alternate representation of 3-D geometries**

The efforts addressed in this paper pertain to three major technical activities. First, alternate gradient evaluation methods are assessed to determine whether they provide any advantages in the areas of accuracy, efficiency, robustness, and/or user-friendliness compared to the presently employed finite-difference methods when applied to typical optimization tasks at McDonnell Douglas.

The second effort is directed at improving the results from a nonlinear point optimization of wing/body/nacelle/diverter (W/B/N/D) HSCT-type configuration by directly modeling the flow over diverters and nacelles rather than accounting for their presence in an incremental fashion. This requires a rapid grid regeneration capability to adjust the computational grids to the changes in the complex surface geometries during the optimization process. A grid perturbation is expected to deliver this rapid grid modification capability for use with advanced multizone Euler/Navier-Stokes methods.

Finally, a wing optimization involving twist, camber, and thickness distribution as design variables requires an efficient and accurate parametrization of 3-D geometries. The suitability of globally defined orthonormal functions for this purpose was investigated. In principle, global functions avoid the major drawbacks of the presently prevalent local shape functions, namely, the need of being judiciously chosen and placed to be effective, and the tendency to produce nonsmooth surfaces. (Nonsmooth surfaces may trigger premature transition from laminar to turbulent flow, and they may pose difficulties for the airframe manufacture.)

Alternate Gradient Evaluation

- **Present practice**
 - one-sided finite differences
- **Alternate techniques**
 - ADIFOR
 - ADOS

The current optimization methods at McDonnell Douglas are all gradient based. Suitable search directions are computed from finite-differences where the change in a response variable is divided by the perturbation in a specified design variable. This finite-difference approach requires a flow-field solution for each change in each design variable, which makes this approach very costly. Also, the change in a design variable has to be carefully chosen to produce meaningful sensitivities.

In the hope to overcome these handicaps, at least partially, alternate sensitivity evaluation methods are assessed. Specifically, an ADIFOR (Automatic Differentiation using FORTRAN) version of a design code at McDonnell Douglas, and two quasi-analytic techniques as contained in the ADOS (Aerodynamic Design Optimization methodology using Sensitivity analysis) code have been considered.

ADIFOR

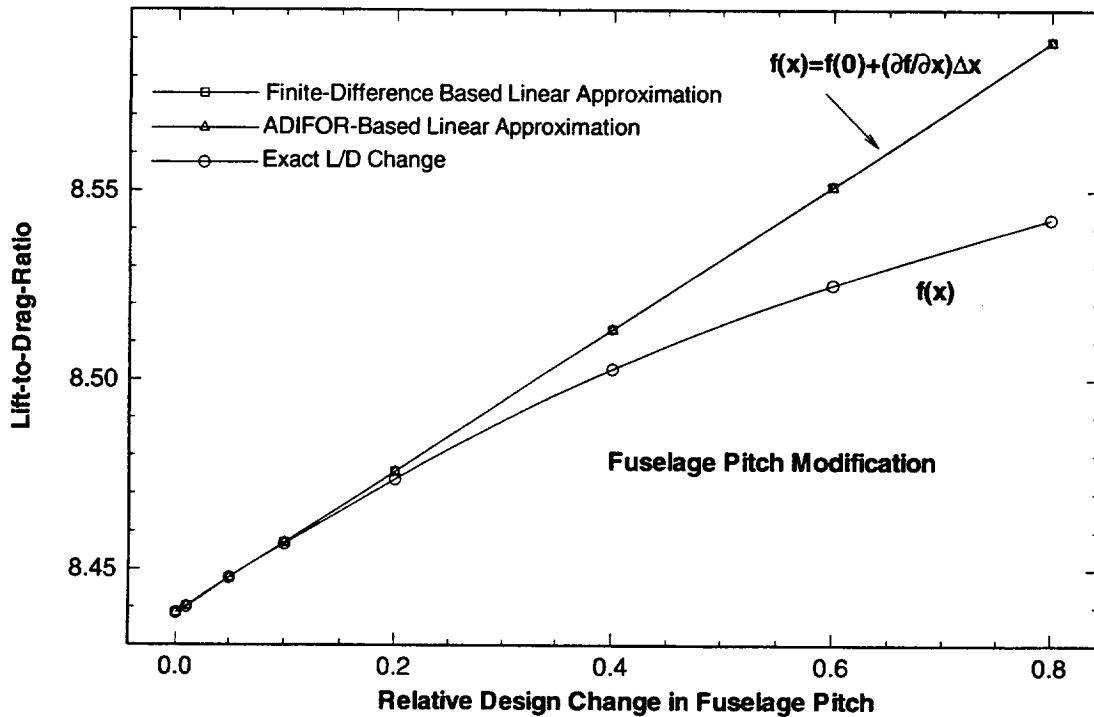
- **FLO67 processed with precompiler & FORTRAN**
- **Memory requirements limit number of design variables (about 3 GW for 90 design variables)**
- **Non-vectorized version of processed code 3-4 times more expensive than finite differences; revectorization underway**
- **The benefits lie in accuracy combined with user-friendliness**

ADIFOR is a FORTRAN-based precompiler which augments a flow solver's source code (here: FLO67) to automatically differentiate user-specified dependent variables with respect to user-specified independent variables. The final code is then processed through the compiler to simultaneously produce analysis as well as sensitivity information.

Major difficulties encountered with the ADIFOR-based design method were its considerably increased run-time memory requirements (which dictates use of a smaller than usual number of design variables), and its reduced computational efficiency when run on a Cray C-90 supercomputer. This computer requires specific coding for maximum efficiency. Portions of such specific coding in FLO67 got destroyed by the ADIFOR application and need to be restored.

While the evaluation of ADIFOR-processed version of the FLO67-based optimization code has been hampered by these difficulties, this effort is still being carried on because of the prospect of combining accuracy with user-independence of the sensitivity information. This is illustrated in the following figure.

Finite-Difference and ADIFOR Derivative Accuracy for a Fuselage Nose Deflection (Rigid Body Rotation)



This figure shows the variation of the lift-to-drag (L/D) ratio with fuselage pitch (or fuselage incidence). The nonlinear curve gives the actual variation of L/D with fuselage pitch as computed with FLO67 in an analysis mode. The two straight-line curves give linear approximations to this actual L/D variation with fuselage pitch. The linear approximations are computed from finite differences and with an ADIFOR version of the design code, respectively. Both approaches produce linear curves that are tangential to the actual L/D variation with fuselage pitch which attests to their accuracy. However, the ADIFOR produced these accurate results in a hands-off fashion whereas the finite-difference result were computed with an experienced person-in-the-loop.

ADOS

- **Quasi-analytical sensitivities**
 - direct approach
 - adjoint approach
- **Design with flow constraints**
- **Flexibility**
- **User-friendliness**
- **Extension to truly 3-D optimization**
 - 3-D surfaces
 - generalization of grid perturbation
- **Test case**
 - M2.4-7A Opt5
 - 90 design variables (9 strips of 13 Bezier-Bernstein control points)
 - executables require 500-700 MWs run time memory

ADOS contains a suite of optimization methods, among them two quasi-analytical sensitivity evaluation methods: a direct method and an adjoint method. The direct method is faster than the adjoint approach if the number of constraints is larger than the number of design variables. If the number of design variables is larger than the number of constraints, the opposite is true.

Both methods allow design optimization with direct flow constraints and without skilled user intervention. Also, by being formulated at the discrete rather than at the continuous level, they are applicable to wide variety of design problems. This is contrary to, for instance, an adjoint method based on control theory which needs to be reformulated for each change of boundary conditions.

The ADOS methodologies were coded very much with proof-of-concept-only studies in mind. Thus, certain limitations had to be removed prior to use in aerodynamic design optimization tasks typically encountered at McDonnell Douglas.

Once a general 3-D surface representation and a truly 3-D (single) grid perturbation method were implemented into ADOS, a further design optimization of the McDonnell Douglas HSCT arrow wing design (M2.4-7A Opt5) with 90 design variables was attempted. This attempt was aborted because the computer memory requirements made this effort impractical. Since the memory requirements are driven primarily by the grid size and to a much lesser degree by the number of design variables, several attempts were made to reduce the size of the executable by splitting it into subdomains using the SADD (Sensitivity Analysis Domain Decomposition) scheme. After several fruitless attempts it was decided to halt this effort since a more radical modification of ADOS involving the implementation of an incremental iterative procedure exceeded time and funding limits.

Multi-Block Grid Perturbation Scheme for Aerodynamic Optimization of Wing/Body/Nacelle/Diverter Configurations

- **Grid block boundaries are transparent to grid perturbation method**
 - each grid point is slaved to closest master node on a solid surface
 - memory management uses indirect addressing
- **Predictor step: displacement of master point is applied to its slave points, scaled by a Gauss-distribution**
 - scaling preserves integrity of grid in presence of multiple surfaces
- **Corrector step: coordinates of each field point are replaced with weighted average of the coordinates of its immediate neighbors using inverse distances as weights**

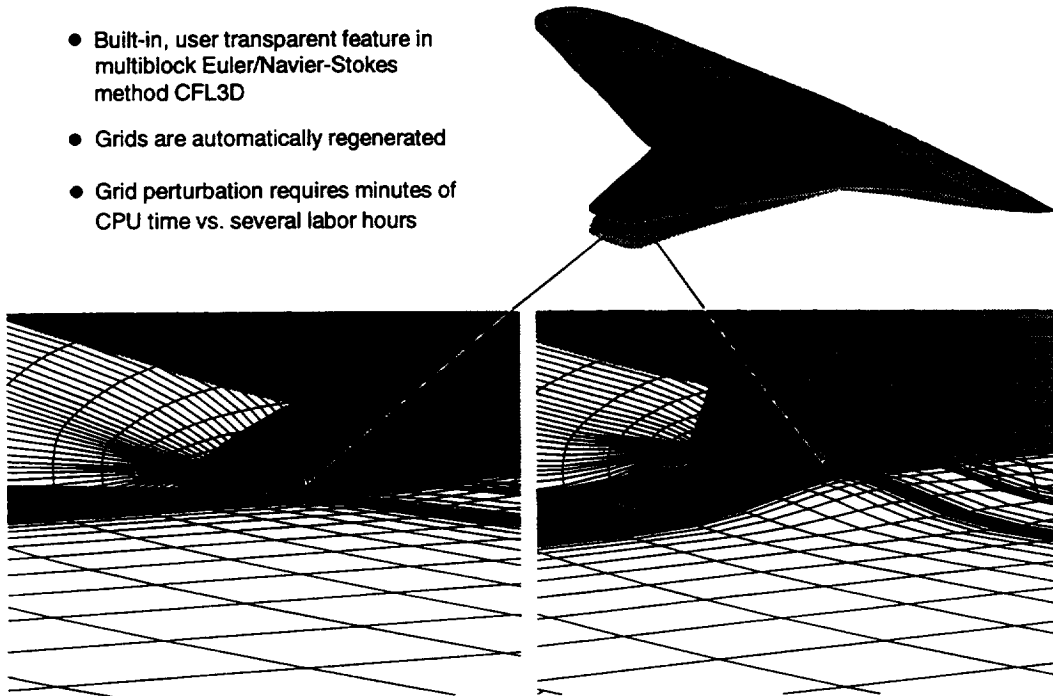
Key in the development of a grid perturbation technique for use in a multiblock patched grid environment is to make the grid block boundaries transparent. Thus, changes in a body surface patch in one block are allowed to be communicated into other grid blocks. This is achieved by (i) basing the relationship between a master (or surface) node and its slave nodes solely on minimum distance, and by (ii) storing the grid information in one-dimensional arrays. The one-dimensional data structure permits a grid point to be identified by a single (address) number. Thus, a slave is associated with its master point by storing the slave's address into the master's address.

After a change in the surface geometry, the displacement of the master points is, scaled with a decay function, applied to their respective slave nodes. The decay function is essentially a Gaussian distribution with the ratio of the distance between slave and master to the magnitude of the displacement vector as the exponential argument. The decay function ensures the integrity of the grid in the presence of multiple deforming surfaces.

The final position of each slave node is computed from a weighted average of the positions of the nodes in its immediate neighborhood. The weights are the inverse distances between a subject slave node and its neighbors. This step eliminates degenerate cells which occur when grid lines cross during the predictor step.

Grid Perturbation Scheme for Aerodynamic Optimization & Aeroelastic Analyses

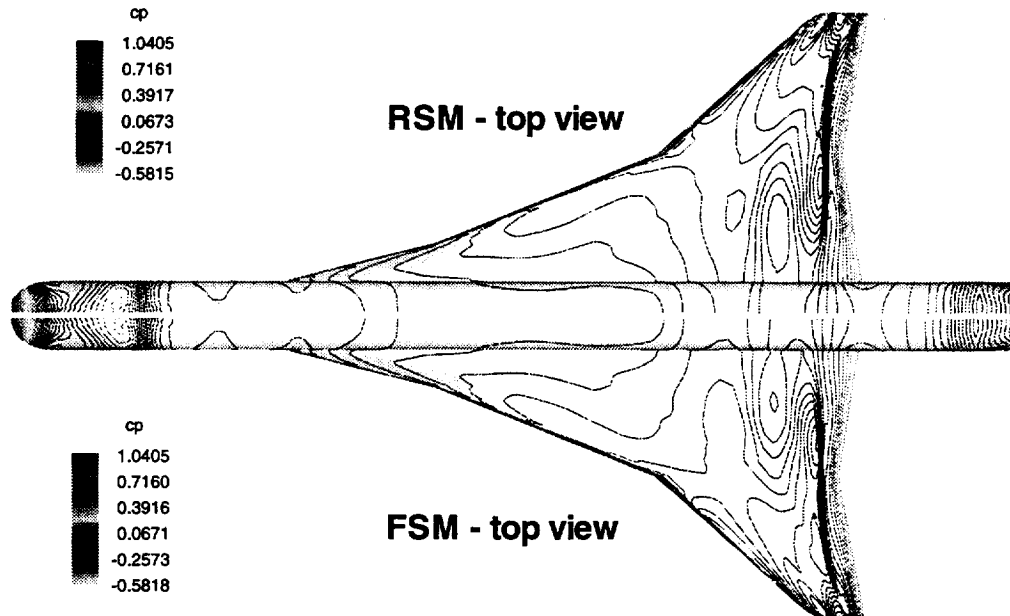
- Built-in, user transparent feature in multiblock Euler/Navier-Stokes method CFL3D
- Grids are automatically regenerated
- Grid perturbation requires minutes of CPU time vs. several labor hours



This composite figure shows a nominal Ref. H wing in its baseline shape and aeroelastically deformed under a steady aerodynamic load. The details in the lower half of the figure demonstrate the effectiveness of the grid perturbation scheme in adjusting the computational grid, which originally conformed to the undeformed wing, to the deflected wing shape.

As indicated in the legend, the grid perturbation scheme is designed for use with the Euler/Navier-Stokes solver CFL3D. This flow solver was chosen because CFL3D was the most versatile among competing flow solvers, at least at the time a flow solver had to be picked. Also, CFL3D had already been demonstrated in aeroelastic applications. This aeroelastic modeling capability will be leveraged in future activities involving aeroelastic optimization of HSCT configurations.

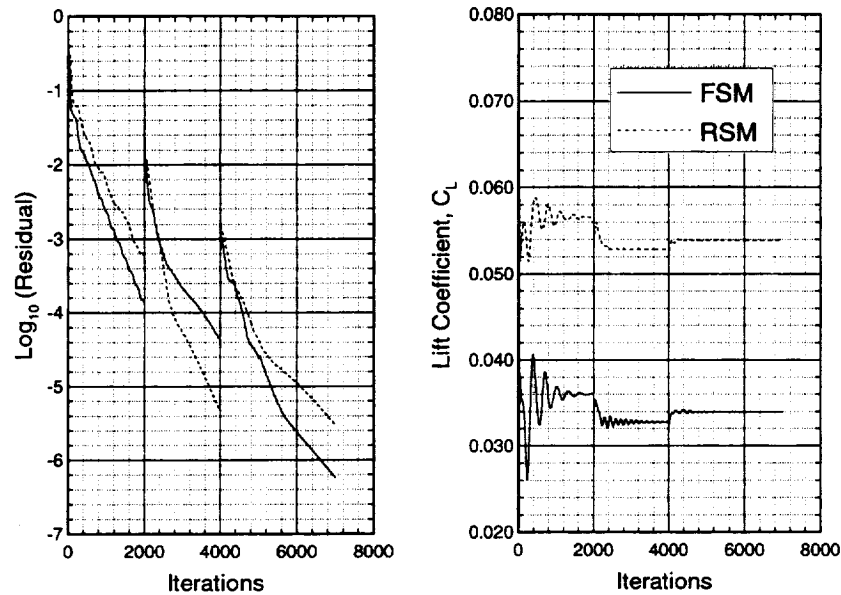
Wing Pressure Distribution for Rigid and Flexible Semispan Model
CFL3D, Euler, $M_\infty=0.95$, $\alpha=2.00$ deg., $\gamma=1.133$, 65x241x49 C-O grid



This composite figure shows top views of surface pressure distributions over a semispan model with a nominal Ref. H wing, at a moderate angle-of-attack. Both pressure distributions pertain to inviscid transonic freon flows as computed with the Euler/Navier-Stokes solver CFL3D. The upper detail shows the solution as computed on a baseline C-O-type grid over the semispan model free of aeroelastic effects. The solution in the lower figure part was computed on a perturbed C-O-type grid that conformed to the semispan model with the wing shape deflected under the static aerodynamic loads. The grids used in these calculations are identical with those illustrated in the preceding figure. These results demonstrate that the grid perturbation scheme produces usable grids.

Convergence Summaries for Flexible and Rigid Semispan Models

CFL3D, Euler, $M_\infty=0.95$, $\alpha=2.00$ deg., $\gamma=1.133$, $65 \times 241 \times 49$ C-O Grid



This figure summarizes the convergence history of the two Euler solutions as shown in the previous figure. These solutions have been computed using grid sequencing (2000 iterations on a coarse grid with $17 \times 61 \times 13$ points, 2000 iterations on an intermediate grid with $33 \times 121 \times 25$ points, and 3000 cycles on a final grid with $65 \times 241 \times 49$ points). The respective asymptotic values for lift indicate the effect of aeroelasticity on the aerodynamic performance of the semispan model. The L_2 -norm of the residual of the continuity equation has dropped by about four orders of magnitude for both cases on all grid levels. The comparable convergence performances indicate that the grid perturbation scheme has essentially preserved the grid quality of the baseline grid (i.e., orthogonality, grid stretching, clustering, etc.).

Efficiency of Multi-Block Grid Perturbation Scheme

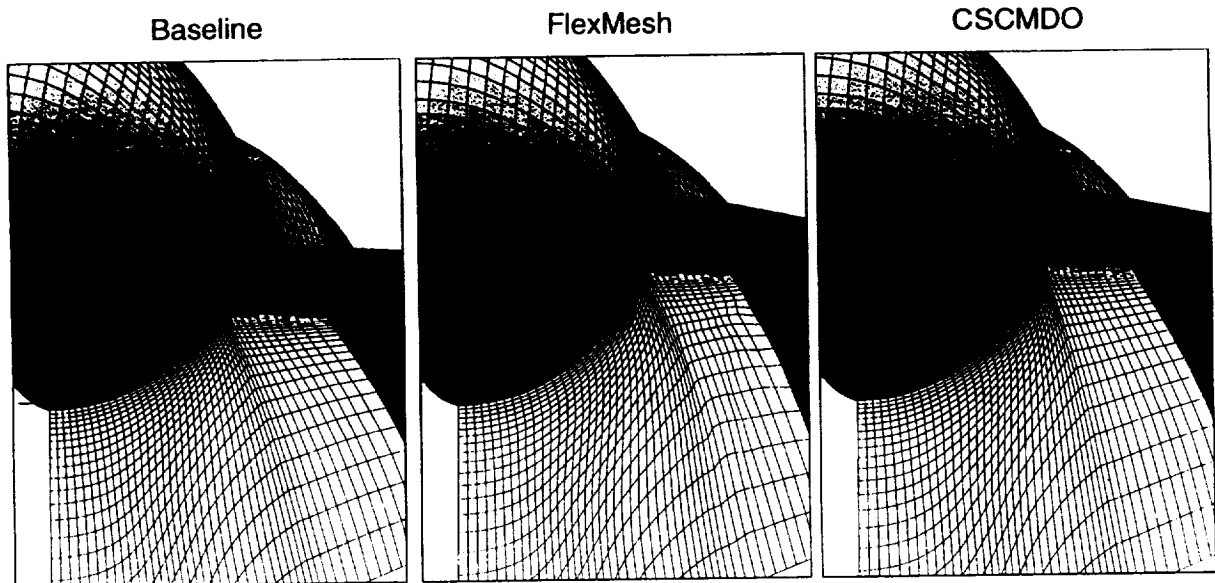
- **Application to RSM with aeroelastically deformed Ref. H type wing**
- **C-O type single-block grid; 65x241x49 grid points**
- **13,794 surface nodes**
- **About 300 secs* to generate connectivity information (i.e., master/slave couplings)**
- **About 3 secs* to perturb entire grid**

*timing for Cray C-90 supercomputer

The computational efficiency of the grid perturbation method is illustrated for the aforementioned application to the semispan configuration with the rigid and the flexible Ref. H-type wing. This single-block C-O-type grid consists of roughly 3/4 of a million grid points. Only about 2 percent of these grid points are solid surface nodes. It takes about 5 mins of computing time on a Cray C-90 computer to generate the master/slave connectivities. The actual perturbation of the grid requires only an insignificant computational expenditure.

Multiblock Grid–Perturbation Demonstration

1404 Wing/Body/Nacelle/Diverter
Wing/Body Junction: Inner JDIM



This figure demonstrates that the grid perturbation scheme also produces acceptable grids over a wing/body/nacelle/diverter HSCT configuration. The close-ups show details of the wing/body juncture for the 1404 HSCT configuration for two different sets of design variables. The configuration in the left detail is termed “Baseline.” The wing/body juncture definitions in the other two details are identical. The design variables are wing twist and plunge, and fuselage angle-of-attack.

Along with portions of the surface grids, this figure also shows a selected body-conforming field grid plane. The grid plane for the “Baseline” geometry was generated with an external grid generator. The field grids in the other two details were generated with the present grid perturbation technique (here called FlexMesh), and with an alternate grid perturbation technique: CSCMDO. The CSCMDO technique, developed at NASA Langley Research Center, produces aesthetically more pleasing grids than FlexMesh.

While the impact of the grid appearance on actual flow-field computations still needs to be explored, FlexMesh offers a faster turnaround than CSCMDO. For the present application to a multiblock grid with 29 patched grid blocks, roughly 2.5 million points, and about 110,000 surface nodes, FlexMesh adjusts the entire grid in a few hours of Cray C-90 computing time, requiring as input only the setting of a few flags. The CSCMDO method is command language driven. While CSCMDO needs only a few minutes of Cray C-90 computing time to adjust the entire grid, it took one of its principal developers about 40 hours labor time to set up the accompanying input deck.

3-D Geometry Representation

Orthonormal functions are

- **global**
 - eliminates the need for judicious placement of shape functions
 - removes one source of “bumpy” designs
- **complete and convergent**
 - guarantees ever improving accuracy with increasing number of modes
- **extendable to truly three-dimensional shapes**

Orthonormal functions are globally defined, thus avoiding the need for the intervention of a skilled user in placing and formulating locally defined shape functions. They also are mathematically complete and convergent. Thus, by definition, they yield an ever-improving approximation to a given target function as their order is increased. Finally, orthonormal functions permit a direct parametrization of 3-D shapes.

Orthonormal Functions

- **Shape function geometry representation**

$$\Phi(\xi) = \sum_{j=0}^n c_j \phi_j(\xi)$$

- **Least square approach**

$$\sum_{j=0}^n c_j \int_{-1}^1 w(\xi) \phi_j(\xi) \phi_k(\xi) d\xi = \int_{-1}^1 w(\xi) f(\xi) \phi_j(\xi) d\xi \quad (k = 1, 2, \dots, n)$$

- **Orthonormalization**

$$c_j = \int_{-1}^1 w(\xi) f(\xi) \phi_j(\xi) dx$$

The task at hand is to approximate a given surface defined by $\Phi(\xi)$ with polynomials $\phi(\xi)$ in a least-square sense. A weight function $w(\xi)$ adds more freedom in devising suitable least-square approximations. The coefficients c_j are called expansion coefficients. Their computation is drastically simplified by an orthogonality condition (which diagonalizes the operator matrix on the left hand side). A subsequent normalization yields the rather simple expression used to calculate the expansion coefficients.

Orthonormal Functions - Cont'd

- **Orthogonalization due to E. Schmidt**

$$\varphi_j(\xi) = \tilde{\varphi}_j(\xi) / \int_{-1}^1 w(\xi) \tilde{\varphi}_j(\xi) \tilde{\varphi}_j(\xi) d\xi$$

where

$$\tilde{\varphi}_j = a_{j0} \varphi_0 + a_{j1} \varphi_1 + \dots + a_{j,j-1} \varphi_{j-1} + \hat{\varphi}_j$$

with

$$a_{jk} = \int_{-1}^1 w(\xi) \varphi_j(\xi) \hat{\varphi}_k(\xi) d\xi \quad \left(\begin{array}{l} j = 0, 1, \dots, n \\ k = 0, 1, \dots, j-1 \end{array} \right)$$

and

$$\tilde{\varphi}_j = x^j, w(x) = (1-x^2)^s$$

Functions $\phi(\xi)$ that satisfy the orthogonality condition are constructed numerically by using the orthogonalization process due to E. Schmidt. The elementary functions are powers of ξ . The weighting function controls the approximation of $\Phi(\xi)$ through the orthonormal functions $\phi(\xi)$. If, for instance, the deviation between function $\Phi(\xi)$ and its approximation $\phi(\xi)$ becomes large at either boundary of the integration domain for, say, $w(\xi)=\text{const}=1$, then the approximation can be improved by formulating $w(\xi)$ such that it itself assumes large values at $\xi=-1$ and $\xi=1$. The definition of $w(\xi)$ given below permitted the assessment of a wide range of orthonormal functions regarding their effectiveness in approximating aerodynamic shapes. A value of $s=-0.5$ for the exponent, which gives Chebyshev-type polynomials, was found to yield the most accurate approximations to airfoils.

Finally, let it be mentioned that two-dimensional orthonormal functions for the direct parametrization of 3-D geometries are constructed by multiplying two one-dimensional orthonormal functions with each other.

Geometric Constraints

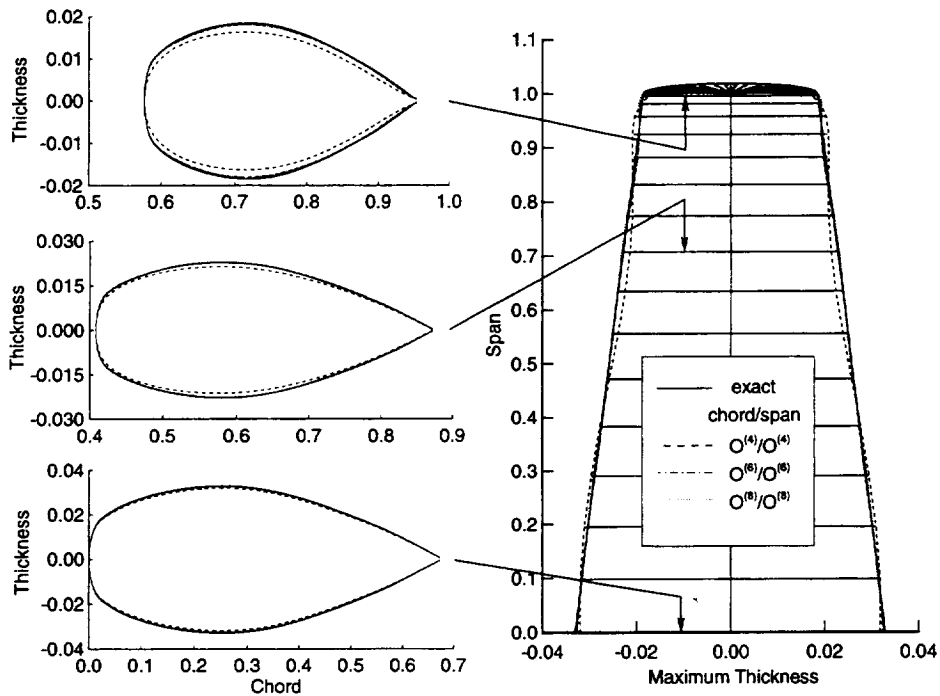
- **Example: Airfoil**
 - of constant cross-sectional area
 - with constant nose radius
 - closed at L.E. & T.E.

$$A \begin{pmatrix} c_0 \\ c_1 \\ c_2 \\ c_3 \\ c_4 \end{pmatrix} = \begin{pmatrix} F_0 - c_5 \int_{-1}^1 \varphi_5 d\xi - c_6 \int_{-1}^1 \varphi_6 d\xi - \dots \\ F_1 - c_5 \varphi_5(-1) + c_6 \varphi_6(-1) - \dots \\ F_2 - c_5 \varphi_5(1) + c_6 \varphi_6(1) - \dots \\ F_3 - c_5 \varphi_5'(-1) + c_6 \varphi_6'(-1) - \dots \\ F_4 - c_5 \varphi_5''(-1) + c_6 \varphi_6''(-1) - \dots \end{pmatrix}$$

When considering global functions for geometry parametrization in the context of aerodynamic shape optimization, an often encountered concern is the handling of geometric constraints. This chart helps to illustrate how such constraints can be handled rather straightforwardly.

The example assumes that during a hypothetical optimization process, cross-sectional area and leading-edge radius of an airfoil are to be maintained along with an enforcement of closure at the leading and trailing edges. This requires to express five shape factors as functions of the remaining shape factors (which are now the design variables) and reference values for the cross-sectional area (F_0), the ordinate at the leading edge (F_1), the ordinate at the trailing edge (F_2), and the nose radius expressed in terms of first and second derivatives at the leading edge (F_3 and F_4).

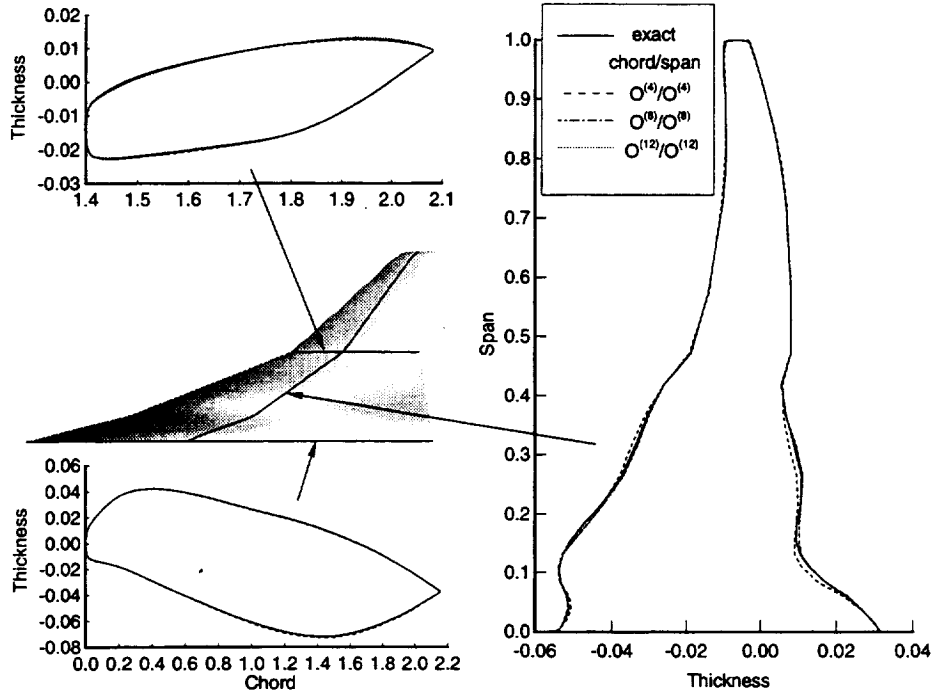
Parametrization of ONERA-M6 Wing with Orthonormal Functions
 - Chebyshev-type Polynomials of Order O^0 -



This figure illustrates the parametrization of the well-known ONERA-M6 wing with two-dimensional orthonormal functions. The exact wing definition is given by the solid lines. There are three levels of approximations using Chebyshev-type polynomials of 4-th, 6-th, and 8-th order in both chord and span directions. The right half of the figure shows the respective performance of the three numerical parametrizations in approximating the spanwise maximum thickness distribution of the ONERA-M6 wing. The details on the left side of the figure compare the exact profile definitions with the three sets of approximations at the root, at the tip, and at an intermediate span station. These comparisons show that 6-th order polynomials (which translates into 36 shape factors for each upper and lower wing surface) give already a quite accurate representation of this wing.

Parametrization of RSM Wing with Orthonormal Functions

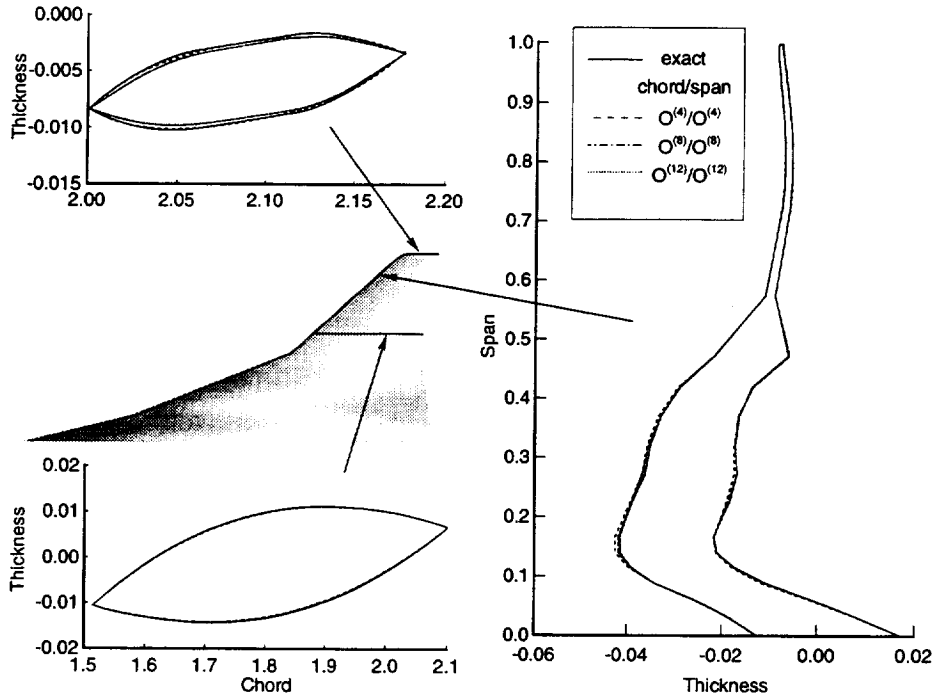
- Chebyshev-type Polynomials of Order O^0 -



This figure illustrates the parametrization of the inboard section of a nominal Ref. H wing as mounted on the so-called Rigid Semispan Model (RSM). This wing is characterized by an inboard section with a blunt leading edge and an outboard wing panel which is essentially defined by circular-arc wing sections. These two wing sections are joined at roughly mid semispan station with a linear transition plug.

This figure shows two chordwise cuts at the root and close to the mid-semispan station along with a spanwise running cut that is located at roughly 40 percent local chord. The solid lines give the loft definition of the wing, and the broken line patterns its approximation with the two-dimensional orthonormal systems. These systems use Chebyshev-type polynomials of 4-th, 8-th, and 12-th order in both span and chord directions. The general impression is that the 8-th order polynomials resolve all salient features of the inboard panel. Thus, upper and lower surfaces of the inner wing portion can be quite accurately modeled with 128 shape factors.

Parametrization of RSM Wing with Orthonormal Functions
 - Chebyshev-type Polynomials of Order O^0 -



Using the same layout as the previous figure, this figure illustrates the parametrization of the outboard section of this nominal Ref. H wing. This figure shows two chordwise cuts at the wing tip and at the station abutting the transition plug. Here, the spanwise running cut is located at roughly 2 percent local chord. Since the definition of the outer wing sections of the outboard wing panel are so simple, even 4-th order polynomials yield a generally quite satisfactory approximation of the lofted geometry. Thus, as few as 32 shape factors render the outboard panel with remarkable accuracy. (The loss in fidelity close to the wing tip will be recouped soon with a better definition of the wing tip.)

Concluding Remarks

- **Alternate Gradient Evaluation**
 - **future work needs to reduce run-time memory requirements and/or improve computational efficiency**
- **Multiblock patched grid perturbation scheme**
 - **functional in CFL3D v4.1**
 - **presently tested in application to a W/B/N/D configuration**
- **Orthonormal functions**
 - **successfully extended to 3-D**
 - **capable of handling geometric constraints**
 - **need to be demonstrated in actual optimization task**

Assessments of alternate gradient evaluation methods, namely ADIFOR and the quasi-analytical sensitivity analysis methods in ADOS, indicated that much progress has still to be made before they will become useful in an industrial environment.

A grid perturbation scheme for multiblock patched grids has been devised and implemented into the Euler/Navier-Stokes solver CFL3D, version 4.1. The method is presently being used to simulate transonic flows over an HSCT-type configuration with an aeroelastically deformed wing. Applications to a W/B/N/D HSCT configuration whose surface has changed due to aerodynamic optimization is underway.

An alternate approach to representing 3-D shapes based on numerically generated orthonormal functions has successfully been formulated and appears to be ready for initial trials in aerodynamic shape optimization

References

- [1] Griewank, A., and Corliss, G.F. (eds.), "Automatic Differentiation of Algorithms: Theory, Implementation, and Application," Society for Industrial and Applied Mathematics, Philadelphia, PA, 1991.
- [2] Bischof, C., Carle, A., Khademi, P., Mauer, A., and Hovland, P., "ADIFOR 2.0 User's Guide," Mathematics and Computer Science Division Technical Memorandum No. 192, Rice University, Houston, TX, August 1995.
- [3] Elshaky, M.E., and Baysal, O., "Design of 3-D Nacelle Near Flat-Plate Wing Using Multiblock Sensitivity Analysis (ADOS)," AIAA Paper 94-0160, Jan. 1994.
- [4] Elshaky, M.E., and Baysal, O., "Discrete Aerodynamic Sensitivity Analysis on Decomposed Computational Domains," Computers & Fluids, Vol. 23, No. 4, 1994, pp. 595-611.
- [5] Vatsa, V.N., Thomas, J.L., and Wedan, B.W., "Navier-Stokes Computations of a Prolate Spheroid at Angle of Attack," Journal of Aircraft, Vol. 26, No. 11, 1989, pp. 986-993.
- [6] Thomas, J.L., Krist, S.L., and Anderson, W.K., "Navier-Stokes Computations of Vortical Flows Over Low Aspect Ratio Wings," AIAA Journal, Vol. 28, No. 2, 1990, pp. 205-212.
- [7] Thomas, J.L., Walters, R.W., Reu, T., Ghaffari, F., Weston, R.P., and Luckring, J.M., "A Patched-Grid Algorithm for Complex Configurations Directed Towards the F/A-18 Aircraft," Journal of Aircraft, Vol. 27, No. 9, 1990, pp. 749-756.
- [8] Hartwich, P.M., and Agrawal, S., "Orthonormal Functions for Airfoil and Wing Parametrization," AIAA Paper 96-2419, June 1996.



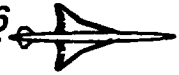
Boeing HSR Wing Optimization Using Tranair

K.R. Wittenberg
The Boeing Company
Seattle, WA 98124-2207

This presentation provides a review of the HSR-AT study of point design, non-linear aerodynamic wing optimization of the baseline HSR configuration, Reference H. Evaluations were made at cruise Mach and C_L . A building block approach was used to develop a robust optimization method using Tranair.

The individual components implemented and tested this year include project, optimization, and flow constraints. Tranair optimization runs consider nearly 30,000 constraints, with over 200 wing variables in a specified grid. The project wing constraints include leading edge, spanwise and chordwise curvatures, thickness at the spars and main landing gear bay, vertical placement relative to the floor, diverter leading and trailing edge heights, and twist axis along a spar. The extensive project constraints improve geometry validity during optimization. The optimization constraints have been implemented for solution convergence and include transpiration, delta Mach, and spanwise curvature. Mach level limits were imposed as the only flow constraint. Much effort was expended to find consistent methods to converge these large optimizations successfully.

As new capability was developed, it was systematically added to previously verified methods. This building block approach allowed determination of thickness only effect, camber and twist effect, and finally thickness with camber and twist.



HSCT Wing Optimization – Outline

Objective

Approach

Constraints

Tranair Optimization Problem & Process

Thickness Optimization

Camber/Twist Optimization

Thickness/Camber/Twist Optimization

Conclusions

HSCT Wing Optimization



HSCT Wing Optimization – Objective

**To develop and apply the capability to produce
realistic, non-linear, point-designed,
optimized wings**

HSCT Wing Optimization

The objective of the effort was to develop and apply the capability to produce realistic, non-linear, point designed, optimized wings. The 1995 objective was to continue the development, adaptation and validation of non-linear CFD methods for HSCT aerodynamics design and analysis.



HSCT Wing Optimization – Approach

Use TRANAIR for Optimization

Validate Implementation of Project Constraints

Build up the Capability in Steps

Reduce Post Optimization Smoothing Requirements

HSCT Wing Optimization – Approach

As discussed earlier in the paper "Overview of HSR Aerodynamic Optimization at Boeing" by R. Conner, the TRANAIR code was chosen as the optimization tool. This selection was made for several reasons. First, TRANAIR has repeatedly demonstrated that the full potential equation contains all the physics, except viscosity, necessary to accurately calculate the flow about the supersonic cruise point of efficient HSCT configurations. Integrated forces, in particular drag, are accurately predicted. Second, the optimization implementation is very efficient. Finally, the ability to handle arbitrary geometry allows accurate and faithful representation of as much of the configuration as desired.

The approach is to limit the design space through implementation of project-oriented geometric constraints. The method permits emphasis on acceptable geometric solutions. By attending to the locations of active constraints, we may still choose to compromise on the constraints for more attractive possible solutions.

We have built up the capability of our optimization in steps or building blocks. This approach was chosen because it is much simpler to assess the success and effect of a single, decoupled step. Considering the complexity of the optimization process, it is too unpredictable to proceed without understanding each successive step. This method allows us to evaluate further how each step contributes to the whole.

There are clear advantages to constraining the optimizer to the smoothest solution that it can find. The improvement in flow time to create a final loft can be dramatic if starting from a relatively smooth optimization product. While some final smoothing will always be required, and since we are limited to a finite number of controlling variables, we can eliminate the larger excursions that are more difficult to smooth.



HSCT Wing Optimization – Project Constraints

Subsonic Leading Edge Radius

Trailing Edge Closure Angle

Upper Surface Chordwise Curvature

Main Landing Gear Bay Thickness

Front Spar / Cabin Floor Separation

Wing Thickness at Spars: Leading Edge, Front, Rear

Wing Twist Axis

Overwing Emergency Exit Door Clearance

Main Cabin Floor Angle of Attack

Lift Coefficient

HSCT Wing Optimization – Project Constraints

The project constraints implemented this year are listed here. These constraints have been verified as working as expected. The reasons for the project constraints are many. The subsonic leading edge is enforced, not for manufacturing, but for off-design concerns. The current streamwise curvature constraint is purely a structural one. The separation of front spar and cabin floor is required for systems clearance.

The list currently represents all the project constraints we are aware of relating to wing and body optimization. As the project matures, the list will undoubtedly grow and/or change.



HSCT Wing Optimization – Other Constraints

Smoothness

Upper/Lower Surface Spanwise Curvature

Aerodynamic Variability

Diverter LE/TE Height

Viscous Effects

Maximum Mach Number

Inboard Upper Surface Cross-Flow

Lower Surface Chordwise Curvature

Inboard Aft of LE

HSCT Wing Optimization – Other Constraints

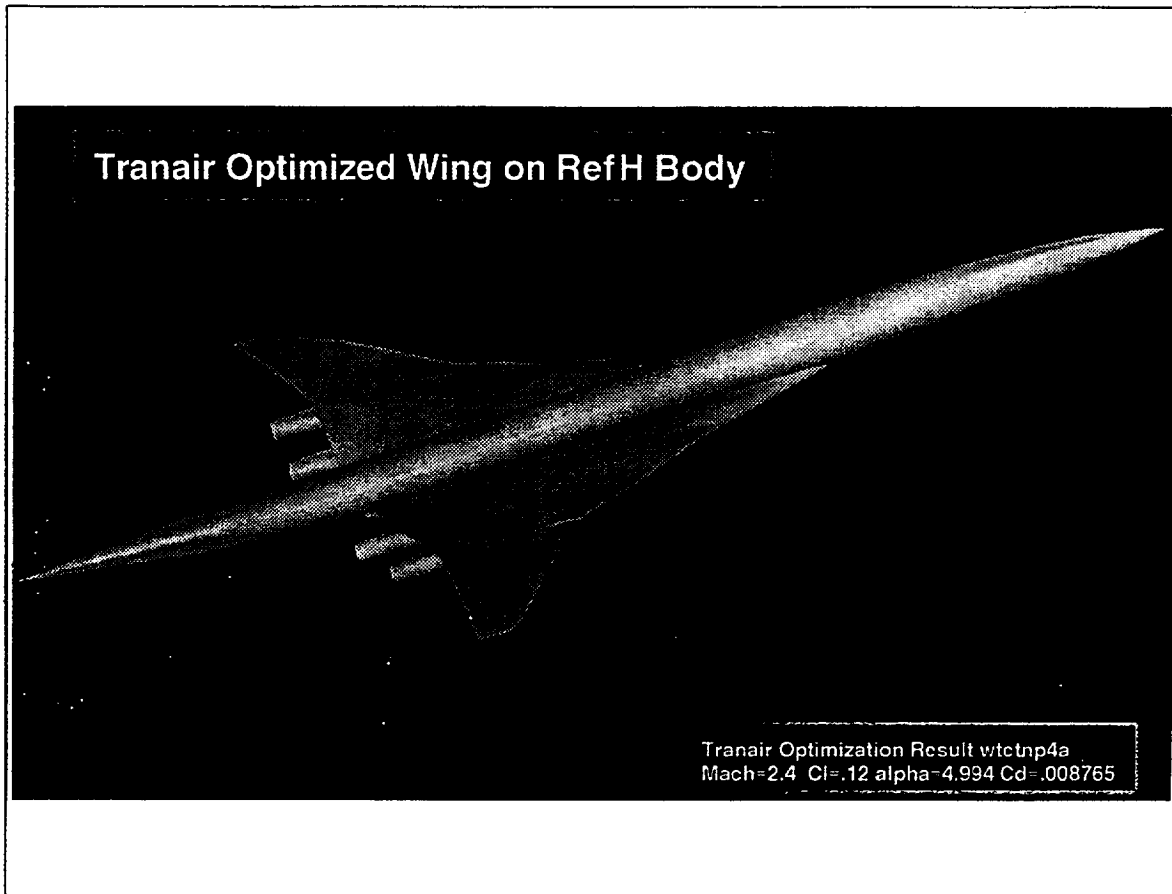
In order to encourage the optimizer to create pleasing shapes and to hold certain areas inviolate, we implemented a series of constraints unrelated to project requirements.

Spanwise curvature constraints were implemented to cause the optimizer to look for solutions with more reasonable contours in the spanwise direction. Allowed to go free, the optimizer opted for wing designs that engineering judgement said was too wavy.

In order to keep within the building block approach discussed earlier, we implemented several constraints requiring the geometry in the nacelle/diverter region to remain relatively fixed. This region will be optimized in the future when the nacelle/diverter increment will be evaluated. This year's work was restricted to wing optimization.

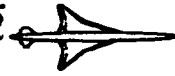
The only flow constraint normally used in optimization is limiting the maximum Mach number. As a supplement to this flow constraint, an additional candidate viscous criterion, cross flow velocity on the upper inboard wing surface, was selected. This criterion is discussed in a later paper, "Summary of Langley Unitary Test 1649 and Its Implications on Validity of Viscous and Inviscid Analyses" by S. Yaghmee and K.M. Meija. With just the incorporation of the full-up project constraints, recent designs meet the cross flow criterion already. Future geometries, such as the TCA, may require the constraint. The Fortran subroutine is coded, verified, and ready for use in subsequent designs.

The only other constraint included this year to address a potential viscous degradation is the addition of streamwise curvature constraints on the lower surface about the leading edge spars. Here thinning was producing viscously undesirable pressure oscillations.



HSCT Shaded Graphics Image

This wing is a result of Thickness/Camber/Twist optimization used 26916 constraints and 211 variables in three design cycles. It was run at Mach=2.4, $Cl=.1197$, with $\alpha \sim 5.0$ degrees. The resultant design showed a 6.35 count drag improvement over the baseline Ref H geometry. The geometry is relatively smooth and showing that improvements in drag are possible with the inclusion of the project constraints.



Tranair Optimization Summary

Wing + Body/Diverter/Nacelle Capability

Wing Thickness + Camber + Twist Optimization

Tranair Full Potential Code for Optimization

Transpiration Boundary Condition

Sensitivity Method

Fixed Lift Constraint

For the wing alone:

Nearly 27000 Linear Constraints

211 Variables

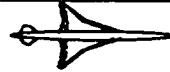
>4000 Surface Curvature Inequality Constraints

Tranair Optimization Summary

TRANAIR is a full potential code for arbitrary geometries. Complex wing/body/diverter/nacelle geometries can be accurately modeled subject to specific boundary conditions. The program's capabilities were previously described in paper "Overview of HSR Aerodynamic Optimization at Boeing" by R. Conner.

TRANAIR uses adaptive grid refinement methodology. This method allows grid to be concentrated in regions where something is happening, and allows the solution to move additional grid to regions where features are appearing. TRANAIR's design capability to formulate and solve constrained aerodynamic problems is also quite general. We were able to tailor the constraints as needed for our airplane using FORTRAN subroutines. In the design mode, TRANAIR relates surface movement to the mass flow boundary conditions on the original surfaces. These transpiration methods were discussed in the referenced paper.

Despite the absence of boundary layer capability at this time, the code has many unique features which lend themselves to the optimization problem. Years of experience, on multiple configurations, have shown that except for viscous effects, TRANAIR's full potential formulation accurately predicts the flow about and forces on HSTC geometries at supersonic cruise.



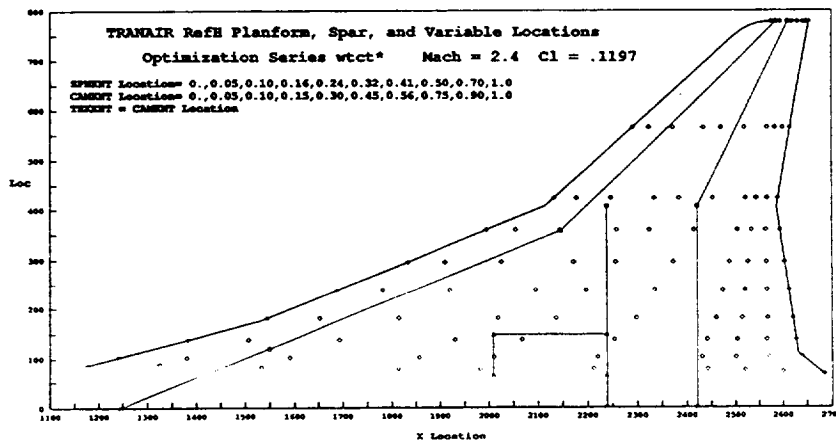
Tranair Optimization Problem Posed

Variables:

- 10 Spanwise Node Belts
- 9 Camber Nodes per Belt
- 10 Thickness Nodes per Belt
- 1 angle-of-attack, α
- 1 Shear per Belt
- 1 Twist per Belt

Objective Function:

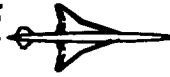
Minimize C_D



Tranair Optimization Problem Posed

The figure shows the final full thickness/camber/twist variable layout on the Ref H planform. The variables are shown as diamonds. The spars are shown (circles with line) as well as the main landing gear bay (triangles with line). A total of 211 variables were used for the thickness/camber/twist study. In the camber/twist cases, 110 variables were used. And in the thickness study 100 variables were used. The variables are layed out in a rectangular grid. In the thickness/camber/twist cases, the camber and thickness variables were located at the same percent chord.

Future plans are to allow the belts to have varying distributions to use the limited number of variables in a more efficient manner.



HSCT Wing Optimization – Capability Steps

Nacelle/Diverter Treatment

Wing Thickness

Uncambered

PD

Cambered

Ref H

Wing Camber & Twist

Ref H

Wing Thickness, Camber & Twist Ref H

No Body Changes from Baseline Ref H Body

Include Flow Constraints

HSCT Wing Optimization – Capability Steps

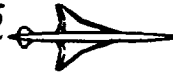
In keeping with the building block method described earlier, we broke the full optimization problem into a logical progression of steps. No body movement other than angle of attack was allowed in any of the study cases, and the Ref H body was used.

First the nacelle/diverter regions were isolated so that each subsequent design would leave the nacelles attached to the wing in the same way. In this manner, we would not have spurious increments due to nacelle/diverter height or placement changes.

Once the nacelle/diverter treatment was verified, the wing thickness capability was evaluated with two models. First, a simple wing/body model with a flat-mid-wing and axisymmetric body was used. This can be thought of as a PD version of Ref H, with the same area and thickness. The second model was the Ref H wing/body/diverter/nacelle. As will be shown later, thickness alone produced a very small drag improvement.

Next the camber and twist changes were simultaneously validated on the Ref H model only. The camber/twist optimization had a small drag benefit. After each part was verified separately, we combined the pieces for the full wing thickness/camber/twist optimization study. Results are shown later.

Work on inlet flow quality constraints was started but remains to be completed.



HSCT Wing Optimization – Process Cycle 1

Use Standard Gridding Strategy

Baseline Analysis

Cycle 1 Optimization

Grids 3:5

1st Order Upwinding

1 Term Transpiration

Reabut Geometry

Analysis of Cycle 1 Reabutted Geometry

Repeat Cycle 1 (as required)

HSCT Wing Optimization – Process

In developing the method for optimizing wings using TRANAIR, several tests were run where the same seed geometry was used but various 'switches' were set in each test case. The result of that investigation was a preferred method of using the code.

This method helped the optimizer toward a successful solution by breaking the solution into parts. The first part, cycle 1, used switches that enabled larger geometry movements, although the solution at that stage was less certain. Once the solution had made the larger steps, finer tuning switches were used, cycle 2, to gain accuracy in the final solution. During each step, convergence was monitored, and if needed, final grids were repeated during a cycle.

Late in the year, due to increasingly larger jobs and a painfully slow NAS C-90 queue, linearized two term transpiration was added. As a result, repeats of cycle 2 might become necessary due to slower convergence toward the optimum.



HSCT Wing Optimization – Process Cycle 2

Cycle 2 Optimization

Grids 4:5, Repeat Grid 5 (one or more times)

2nd Order Upwinding

2 Term Transpiration

Reabut Geometry

Analysis of Cycle 2 Reabutted Geometry

Repeat Cycle 2 (if required by convergence status)

HSCT Wing Optimization – Process

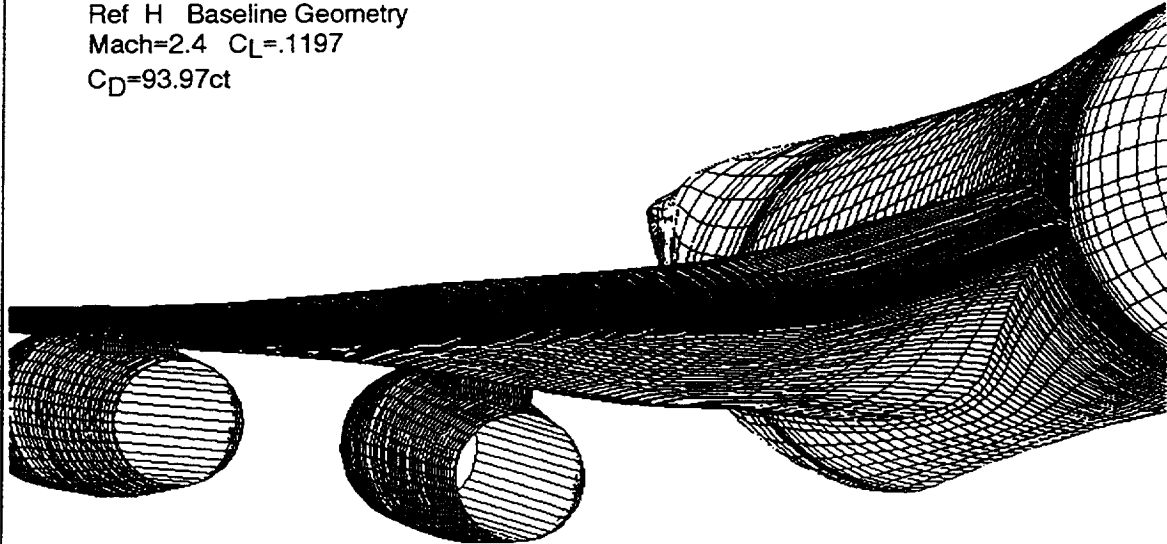


HSCT Baseline Ref H Wing Optimization Geometry

Ref H Baseline Geometry

Mach=2.4 $C_L=.1197$

$C_D=93.97ct$



HSCT Wing Optimization

This image shows a close-up view of the TRANAIR baseline Ref H geometry. As analyzed using the standard wing study adaptive grid strategy, the Ref H showed 93.97 drag counts at Mach=2.4 and $C_L=.1197$, with an angle of attack of 4.14 degrees. The final grid had 534,000 grid boxes and ran in 8000 CPU seconds on the NAS C-90 using 2nd order upwinding.



HSCT Wing Thickness Optimization – 1

No Body Movement

No Camber, Twist, or Shear Movement

**Upper Surface Chordwise
and Spanwise Curvature Constraints**

8153 Linear Constraints

100 Variables

HSCT Wing Thickness Optimization

For this step in the approach, two models were used to verify the optimization. First a simple wing and body model, with flat-mid-wing, axisymmetric body (the same model as used for the first body optimization), was optimized at zero lift. With this model, it was easy to evaluate how well the thickness modes were implemented. Thickness changes were allowed on the wing only, without any camber, twist, or shearing modifications. The upper wing surface curvature was constrained in both chordwise and spanwise directions.

The drag benefit from thickness-only optimization was 0.37 counts predicted from the first cycle. Cycle 2 optimization was not pursued due to the small increment.

Once the thickness model was felt to be working, optimizations were run using the Ref H wing/body/diverter/nacelle model at the cruise condition. Again, only thickness changes were allowed. The drag improvement predicted from the cycle 2 optimization was a mere 0.09 counts from the Ref H baseline at cruise lift.



HSCT Wing Thickness Optimization – 2

Flat Mid-Wing Axi-Body Study, W/B Model

$\alpha=0$. $C_L \sim 0$.

Baseline $C_D=24.10$ ct

Optimized $C_D=23.73$ ct

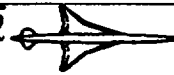
RefH Based Study, WBDN Model

Baseline $C_D=93.97$ ct $\alpha=4.1358$ $C_L=.1197$

Optimized $C_D=93.88$ ct $\alpha=4.0999$ $C_L=.1197$

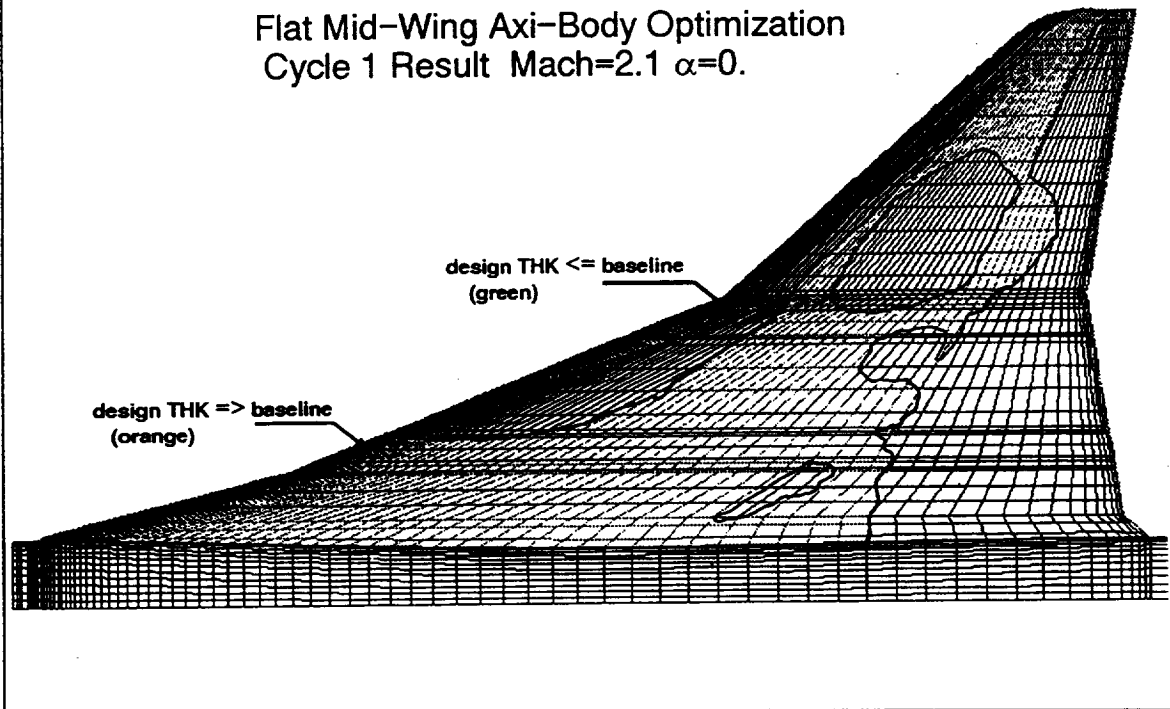
Constrained thickness alone has a small impact on drag.

HSCT Wing Thickness Optimization



HSCT Wing Optimization – Thickness

Flat Mid-Wing Axi-Body Optimization
Cycle 1 Result Mach=2.1 $\alpha=0$.

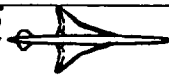


HSCT Flat-Mid-Wing Thickness Optimization

This image shows the green paneling of the input geometry, with the orange areas being the optimization geometry. The orange regions delineate areas where the thickness of the optimization was greater than the baseline wing, and the green areas indicate regions where the thickness was less than or equivalent to the baseline thickness.

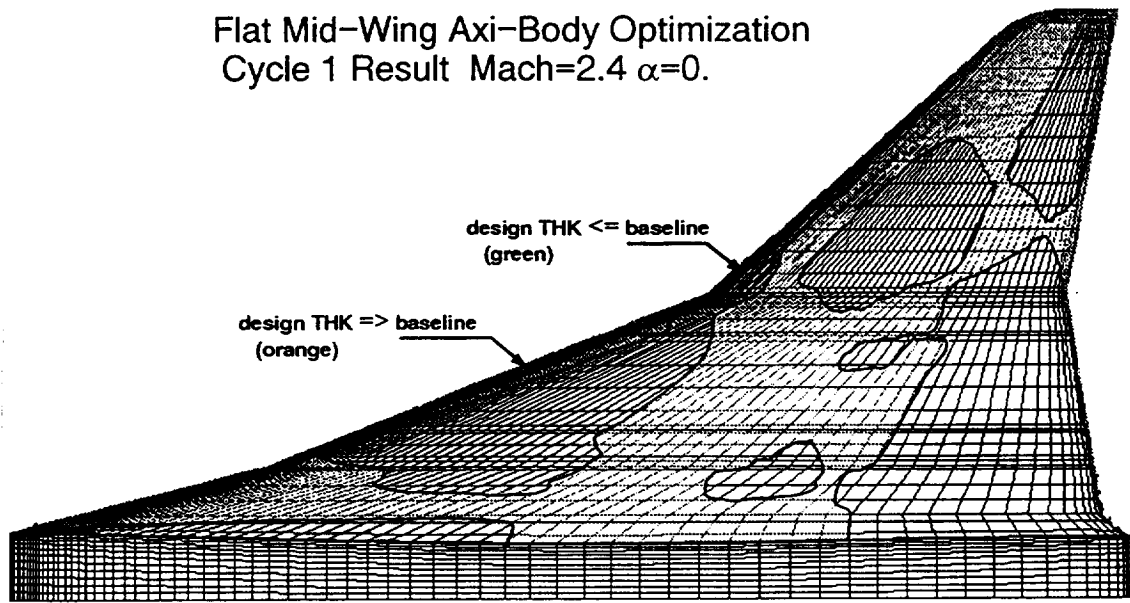
It is easy to see the indications of the leading edge and rear spar locations on the image.

This optimization was run at Mach=2.1, where the baseline linear design area ruling was done.



HSCT Wing Optimization – Thickness

Flat Mid-Wing Axi-Body Optimization
Cycle 1 Result Mach=2.4 $\alpha=0$.



HSCT Flat-Mid-Wing Thickness Optimization

This image shows in green the paneling of the input geometry, with the orange areas being the optimization geometry. The orange regions delineate areas where the thickness of the optimization was greater than the baseline wing, and the green areas indicate regions where the thickness was less than or equivalent to the baseline thickness. The outboard wing appeared to want more thickness at the higher Mach level, and the inboard wing was thinned in more regions.

It is easy to see the indications of the leading edge and rear spar locations on the image. This optimization was run at Mach=2.4, the proposed cruise Mach and $\alpha=0$ degrees.

Representative 2D sections follow for the Mach=2.4 optimization.

BOEING HSR Configuration Aero Final Review FY95

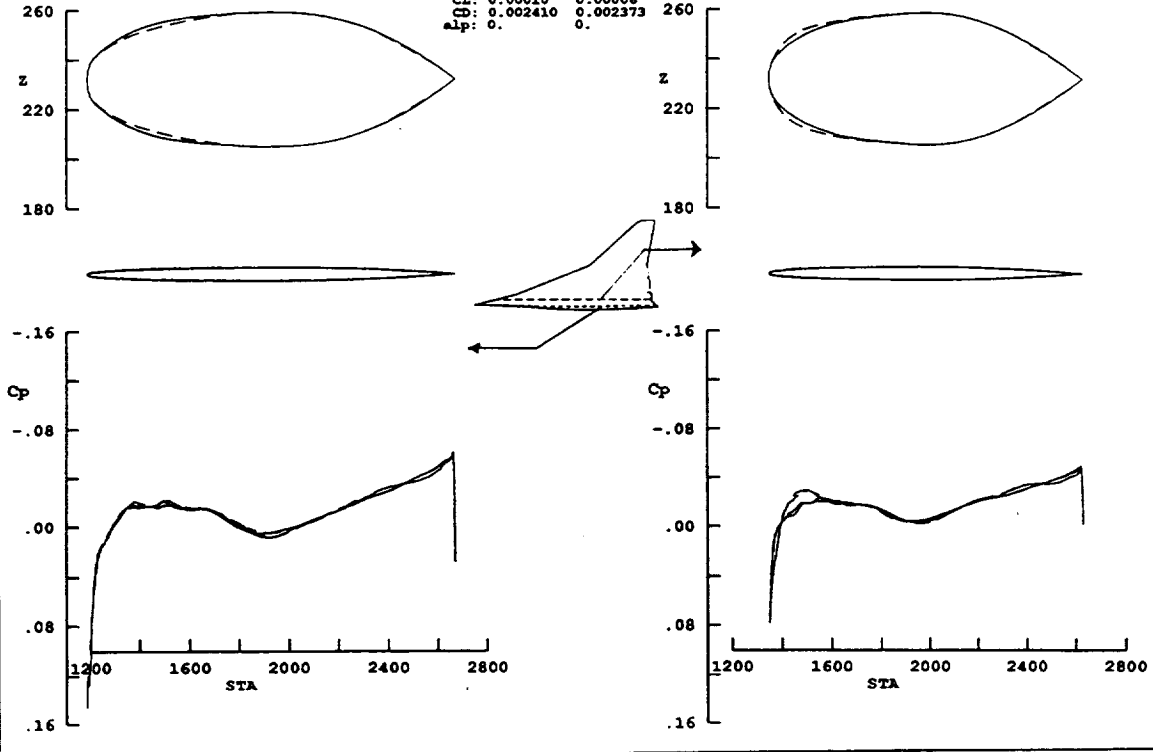


HSCT High Speed Aerodyr

TRANAIR HSCT WING OPTIMIZATION
WB : Flat-Mid-Wing Axi-Body : Mach=2.4
Wing Thickness Optimization

	Baseline	Optimized
CL:	0.00010	0.00006
CD:	0.002410	0.002373
alp:	0.	0.

— Baseline
- - - Optimized



HSCT Flat-Mid-Wing Thickness Optimization

This page and the following two pages show sectional data from the flat-mid-wing axisymmetric-body optimization at Mach=2.4. The plot sets include 10:1 scale in Z and 1:1 scale in X geometry plots, and pressure distributions at six sections. As the plots show, there were very small geometry and pressure changes, resulting in minor drag improvements. The new side-of-body section appears to have moved inboard and eluded the leading edge spar thickness constraint.

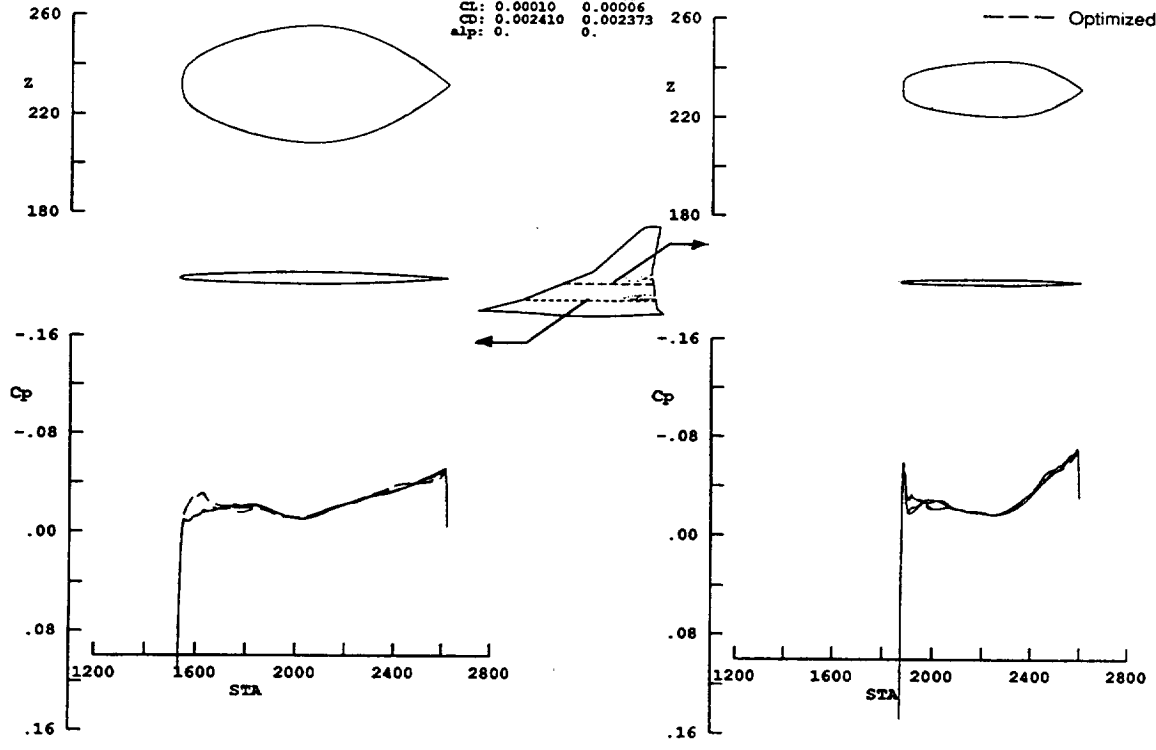
BOEING HSR Configuration Aero Final Review FY95
 HSCT High Speed Aerodynamics



TRANAIR HSCT WING OPTIMIZATION
 WB : Flat-Mid-Wing Axi-Body : Mach=2.4
 Wing Thickness Optimization

	Baseline	Optimized
Cl:	0.00010	0.00006
CD:	0.002410	0.002373
alp:	0.	0.

— Baseline
 - - - Optimized



HSCT Flat-Mid-Wing Thickness Optimization

BOEING HSR Configuration Aero Final Review FY95

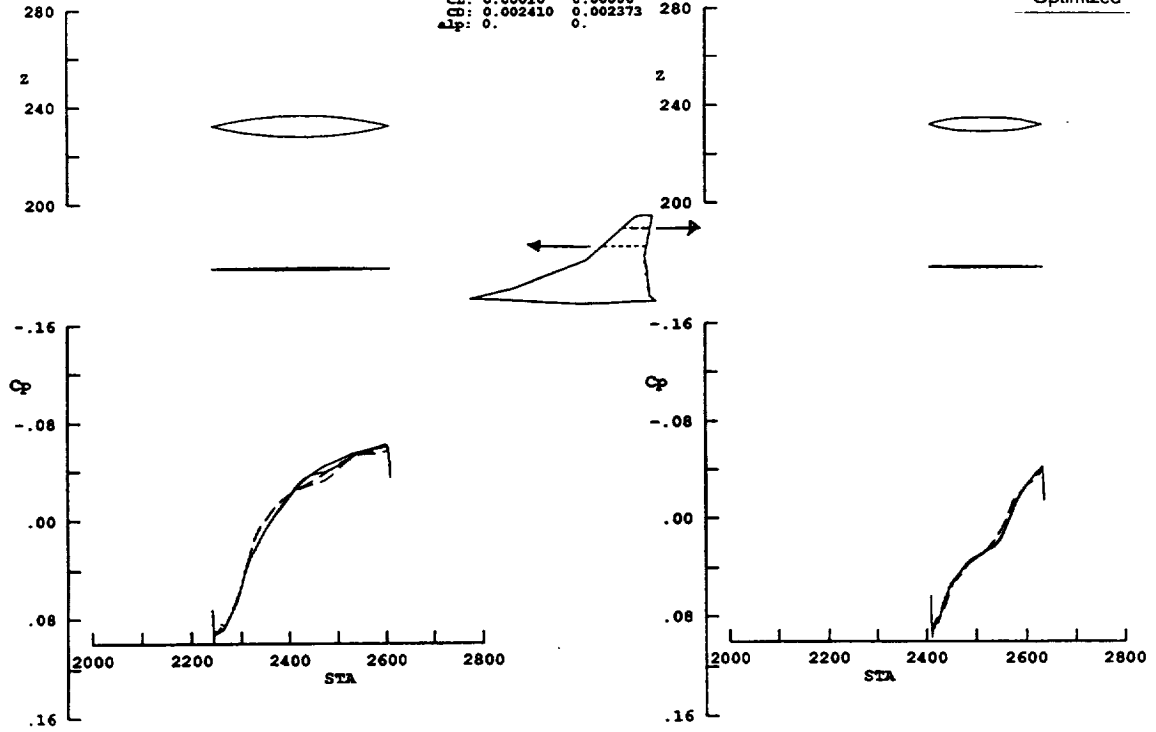


HSCT High Speed Aerodynamics

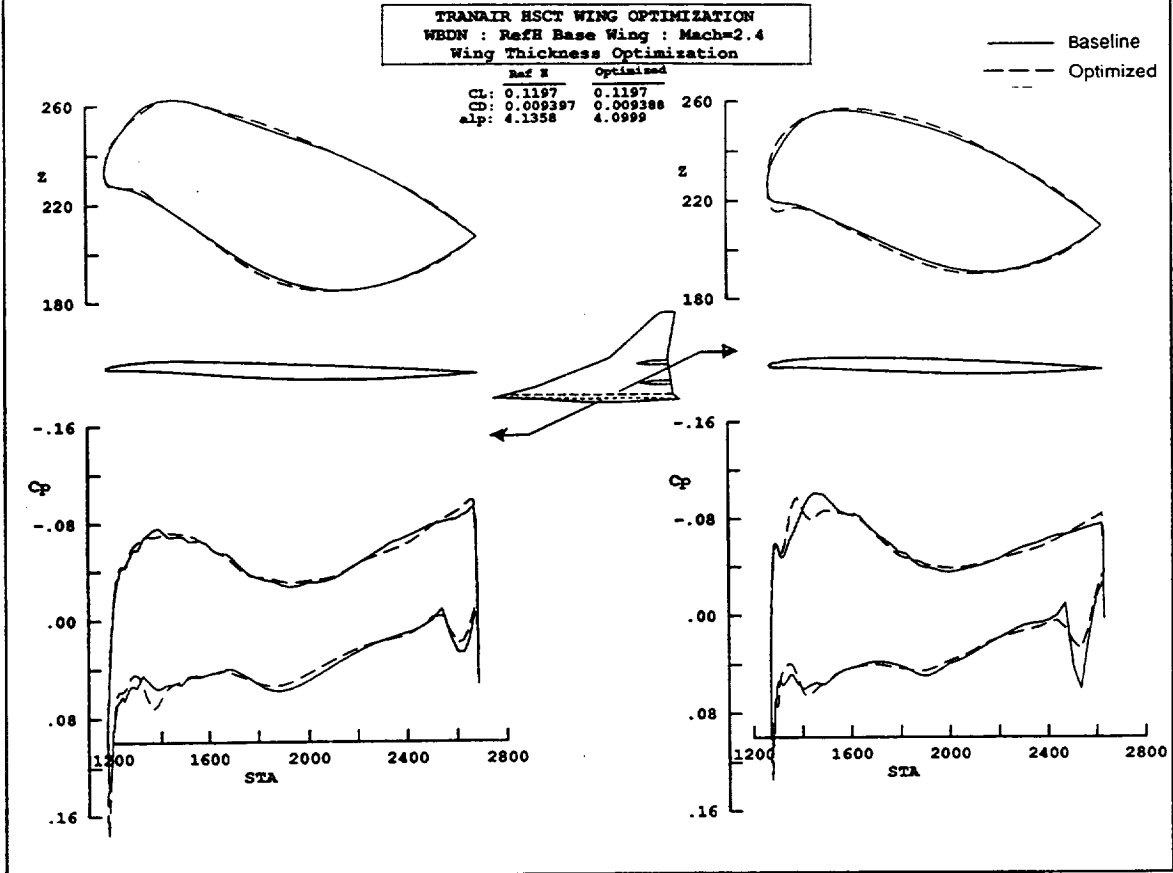
TRANSIR HSCT WING OPTIMIZATION
 WB : Flat-Mid-Wing Axi-Body : Mach=2.4
 Wing Thickness Optimization

	Baseline	Optimized
Cl:	0.00010	0.00006
CD:	0.002410	0.002373
alp:	0.	0.

— Baseline
 - - - Optimized



HSCT Flat-Mid-Wing Thickness Optimization



HSCT Ref H Wing Thickness Optimization

This page and the following two pages show sectional data from the Ref H wing thickness optimization at a cruise condition of Mach=2.4 and $CL=.12$. The plot sets include 10:1 scale in Z and 1:1 scale in X geometry plots, and pressure distributions at six sections. The geometry changes show preservation of spar thickness. Again, the changes to the geometry are relatively small as are the pressure changes. The corresponding drag improvement is smaller than with the flat-mid-wing at 0.09 counts. The diverter shocks appear to have been weakened at some locations. The cycle 2 prediction was not re-analyzed due to the tiny increment.

BOEING HSR Configuration Aero Final Review FY95

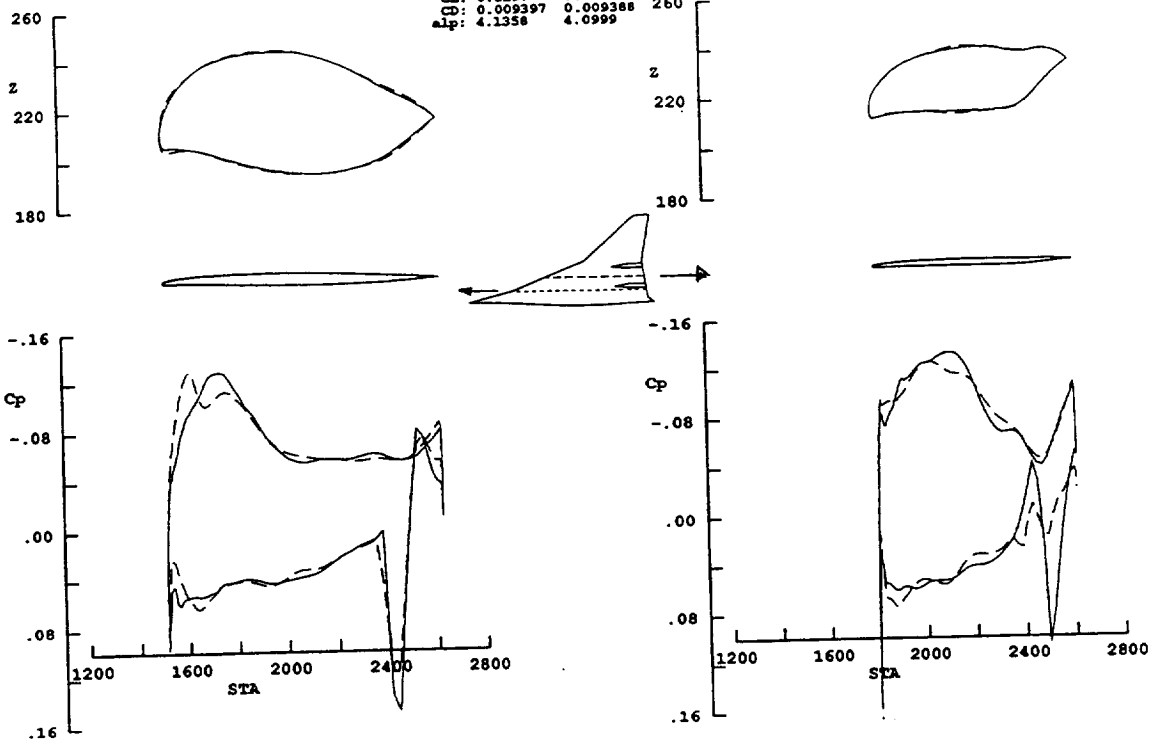
HSCT High Speed Aerodynamics



TRANAIR HSCT WING OPTIMIZATION
 WBDN : RefH Base Wing : Mach=2.4
 Wing Thickness Optimization

	Ref H	Optimized
Cl:	0.1197	0.1197
CD:	0.009397	0.009388
alp:	4.1358	4.0999

— Baseline
 - - - Optimized



HSCT Ref H Wing Thickness Optimization

BOEING HSR Configuration Aero Final Review FY95

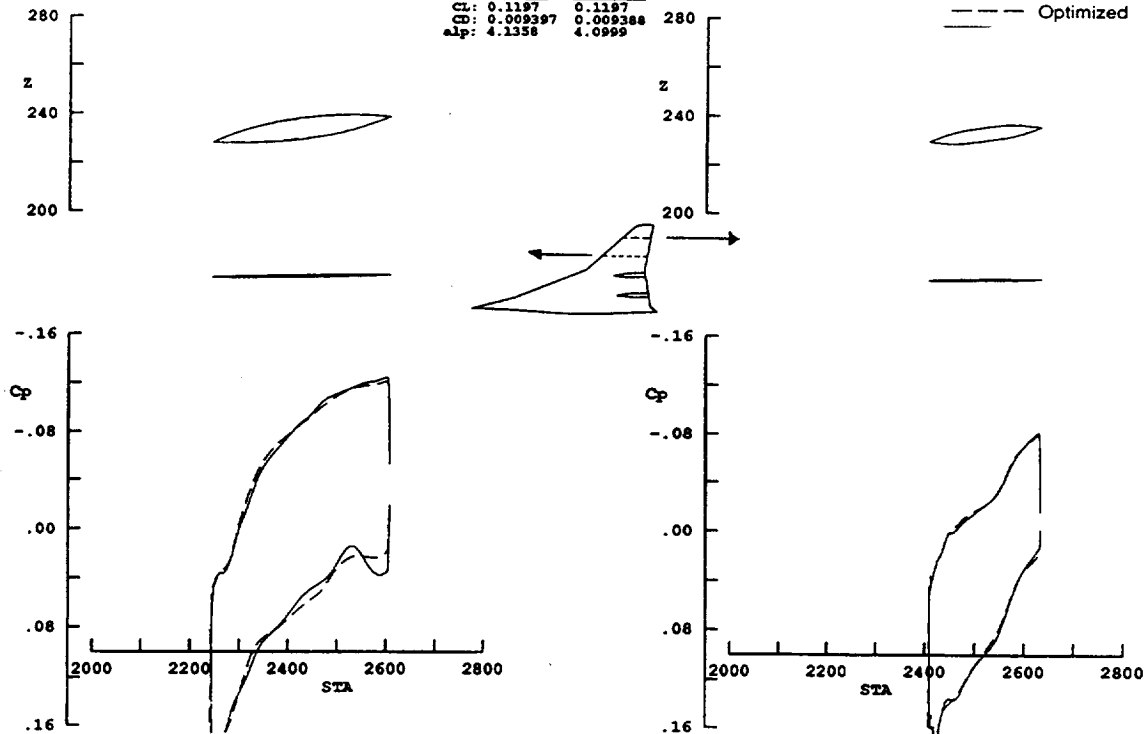
HSCT High Speed Aerodynamics



TRANAIR HSCT WING OPTIMIZATION
 WBDN : RefH Base Wing : Mach=2.4
 Wing Thickness Optimization

	Ref H	Optimized
CL:	0.1197	0.1197
CD:	0.009297	0.009388
alp:	4.1358	4.0999

— Baseline
 - - - Optimized



HSCT Ref H Wing Thickness Optimization



HSCT Wing Camber/Twist Optimization –1

No Body Movement

No Thickness Changes

**Upper Wing Chordwise
and Spanwise Curvature Constraints**

15654 Linear Constraints

110 Variables

HSCT Wing Camber/Twist Optimization

The Ref H geometry was used to verify the camber/twist modes at cruise conditions. No body movement other than angle of attack was allowed. In the absence of wing thickness changes, curvature constraints were imposed only on the upper surface.



HSCT Wing Camber/Twist Optimization -2

RefH Based Study

Baseline $C_D=93.97$ ct $\alpha=4.1358$ $C_L=.1197$

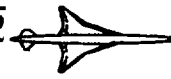
Optimized $C_D=92.65$ ct $\alpha=4.1587$ $C_L=.1197$ cycle 1

Camber/Twist without Thickness has small drag impact.

Cycle 2 was not possible to achieve without adding thickness due to stretching of wing sections.

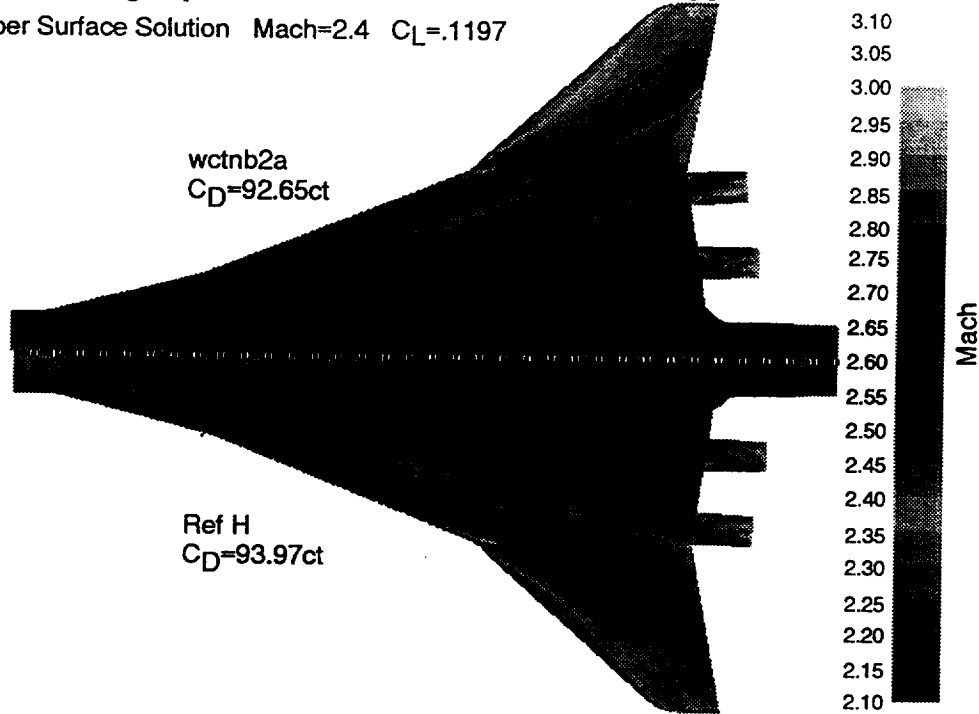
HSCT Wing Camber/Twist Optimization

The analysis of the cycle 1 geometry showed a drag improvement of 1.32 counts for the camber/twist optimization. The planform was preserved in this design. No thickness increase was allowed, even near the leading edge. In attempting cycle 2 optimization, a feasible solution could not be attained. An allowance was made for thinning the spars to help convergence, and while progress was made, after four tries, it was determined that the problem was ill posed. With the stretching to original planform after twisting, the leading edge radius constraint could not be met without adding thickness. Therefore, as a result of our arbitrary definition of thickness and camber, our result showed a "small drag impact." While cycle 1 appeared to have been successful, cycle 2 was finally abandoned in favor of the promising results shown with the full wing thickness/camber/twist optimization.



HSCT Wing Optimization – Camber and Twist

Upper Surface Solution Mach=2.4 $C_L=1.1197$



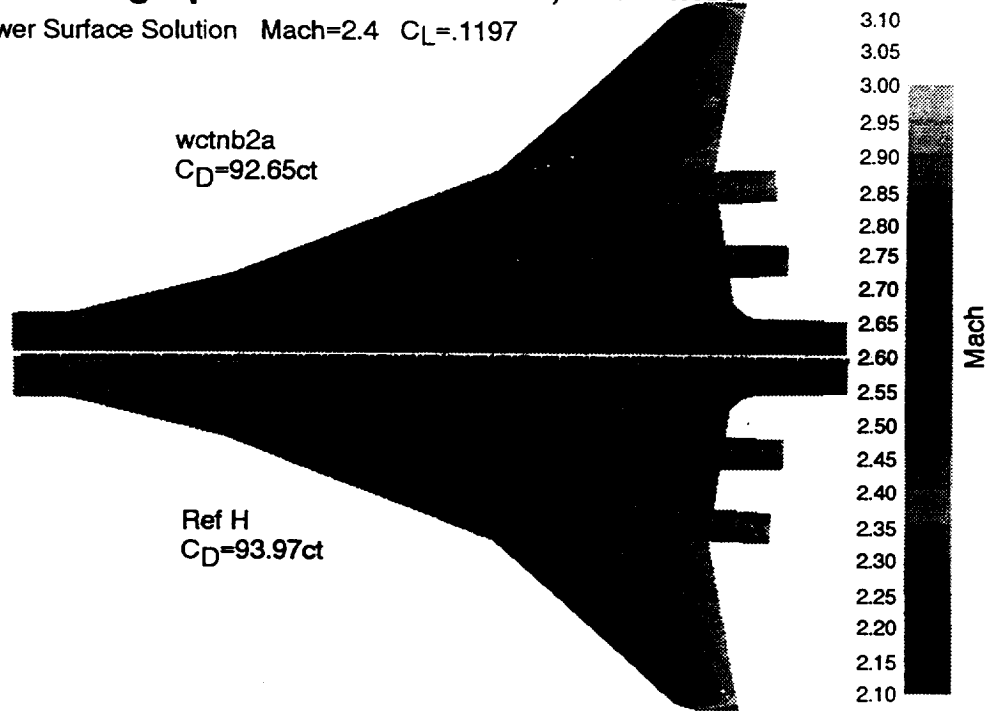
HSCT Wing Camber/Twist Optimization

This page, and the following page, shows the Mach number distribution on the upper and lower wing surfaces, respectively, of the camber and twist optimization versus the Ref H baseline analysis. While there was a reduction in the regions of higher Mach number level, the drag improvement from the cycle 1 optimization was only 1.32 counts.



HSCT Wing Optimization – Camber, and Twist

Lower Surface Solution Mach=2.4 $C_L=.1197$



HSCT Wing Camber/Twist Optimization

This page shows the Mach number distributions on the lower wing surfaces, corresponding to the previous page, of the camber and twist optimization versus the Ref H baseline analysis.

BOEING HSR Configuration Aero Final Review FY95

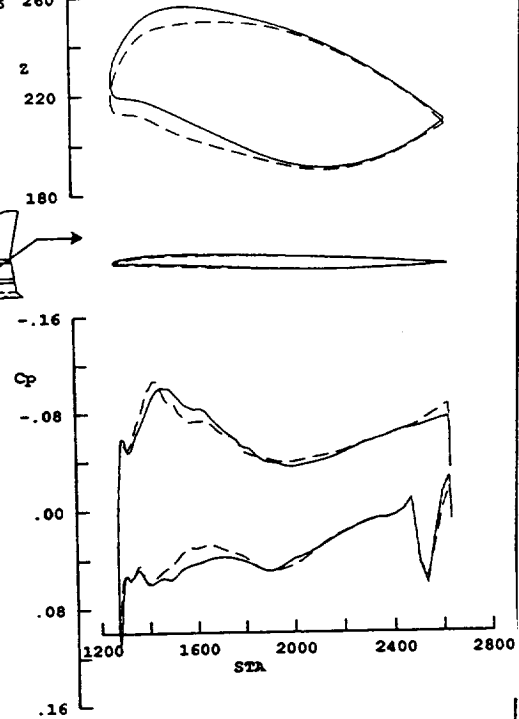
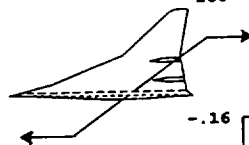
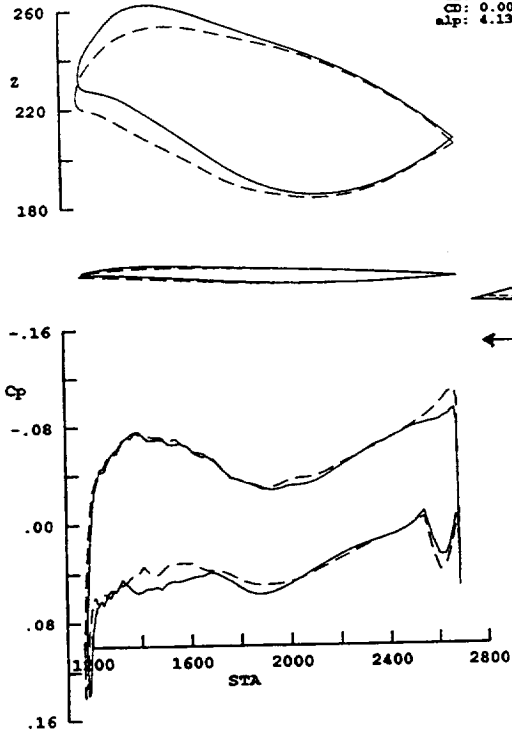
HSCT High Speed Aerodynamics



TRANAIR HSCT WING OPTIMIZATION
 WBDN : RefH Base Wing : Mach=2.4
 Wing Camber/Twist Optimization

Ref #	Optimized
Cl: 0.1197	0.1197
CD: 0.009397	0.009265
slp: 4.1358	4.1587

— Baseline
 - - - Optimized



HSCT Wing Camber/Twist Optimization

This page, and the following two pages, show sectional data from the Ref H camber and twist optimization at Mach=2.4, and $C_L=1.2$. These data are the result of a cycle 1 optimization only. Geometric changes were not dramatic, neither was the drag improvement, which was only 1.32 counts.

BOEING HSR Configuration Aero Final Review FY95

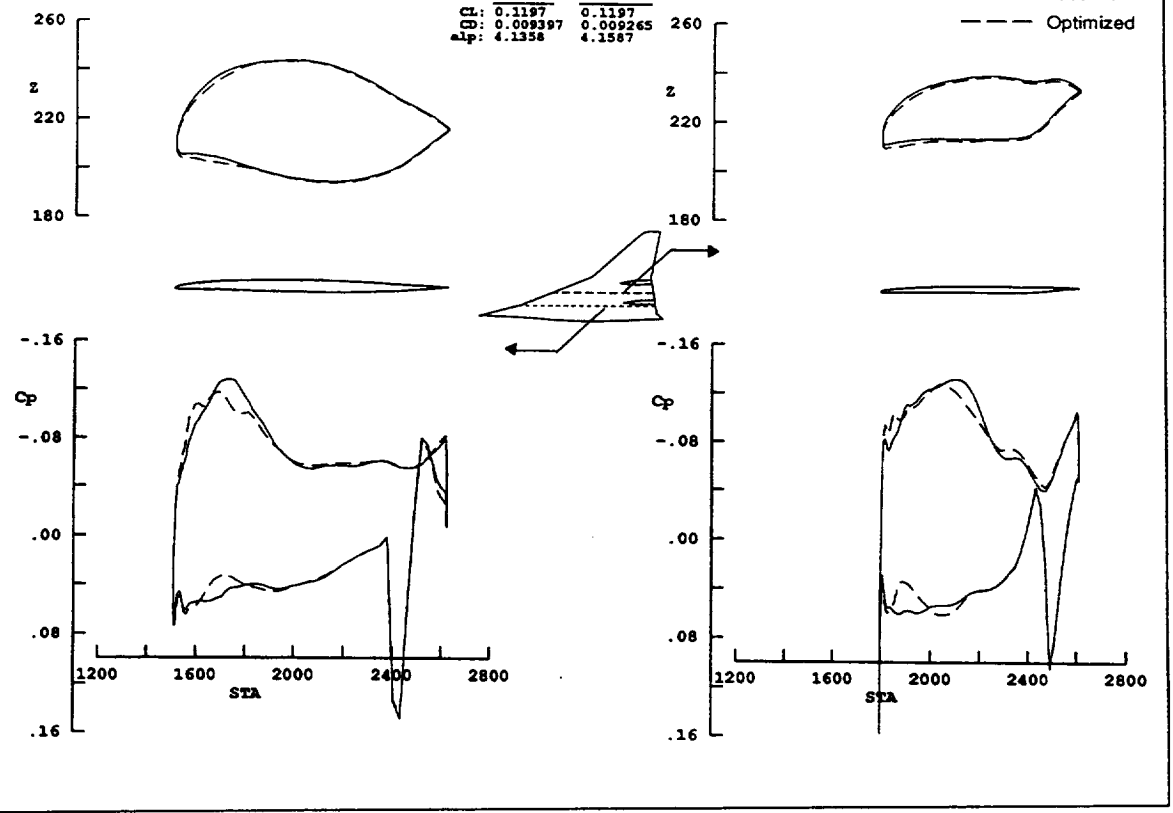
HSCT High Speed Aerodynamics



TRANAIR HSCT WING OPTIMIZATION
 WBDN : RefH Base Wing : Mach=2.4
 Wing Camber/Twist Optimization

	Ref H	Optimized
CL:	0.1197	0.1197
CD:	0.009397	0.009265
alp:	4.1358	4.1587

— Baseline
 - - - Optimized



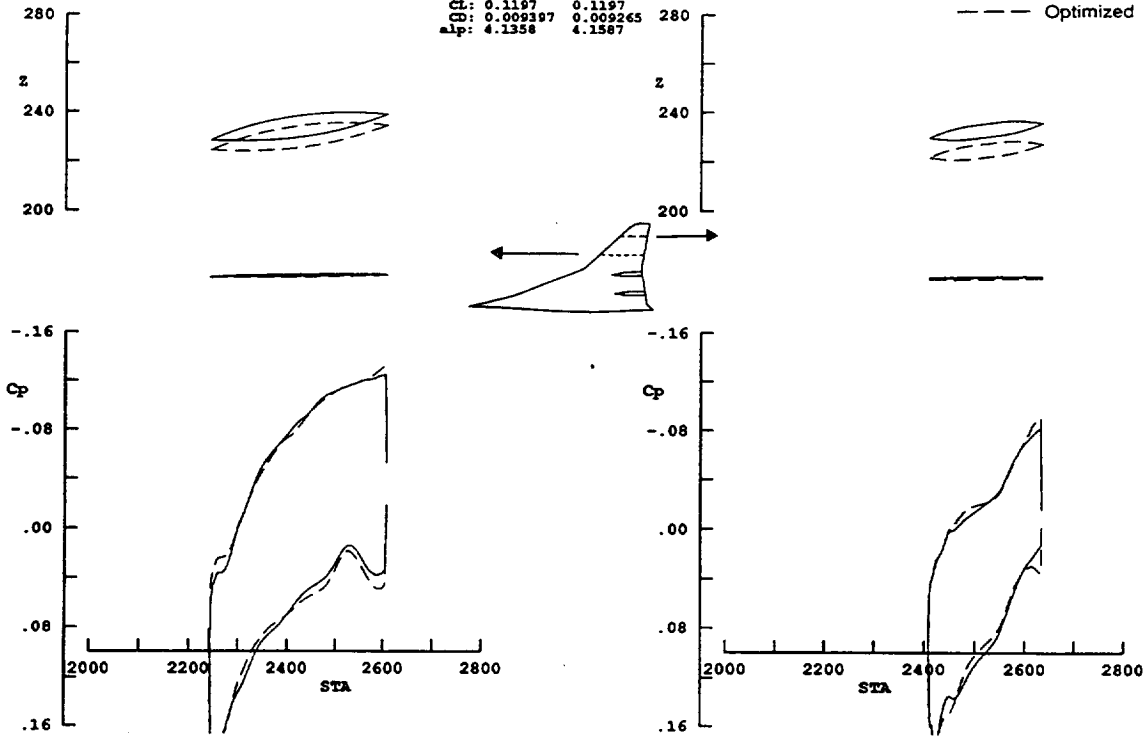
HSCT Wing Camber/Twist Optimization



TRANS AIR HSCT WING OPTIMIZATION
 WBDN : RefH Base Wing : Mach=2.4
 Wing Camber/Twist Optimization

Ref H	Optimized
CL: 0.1197	0.1197
CD: 0.009197	0.009265
alp: 4.1358	4.1587

— Baseline
 - - - Optimized



HSCT Wing Camber/Twist Optimization



**HSCT Wing Optimization
with
Thickness, Camber, and Twist – 1**

No Body Movement

Full Constraint Set

26916 Linear Constraints

211 Variables

HSCT Wing Optimization with Thickness, Camber, and Twist

Once the separate parts were checked out, the full wing optimization with thickness, camber, and twist was done using the Ref H w/b/d/n model. No body movement other than angle of attack was allowed, and a full constraint set was used with 26916 linear constraints and 211 variables. One cycle required two runs to complete due to NAS C-90 job CPU limits. As a result, flow time was typically three to four days.



HSCT Wing Optimization with Thickness, Camber, and Twist – 2

RefH Based Study

Baseline $C_D=93.97$ ct $\alpha=4.1358$ $C_L=.1197$

Optimized $C_D=87.65$ ct $\alpha=4.9936$ $C_L=.1197$ cycle 3

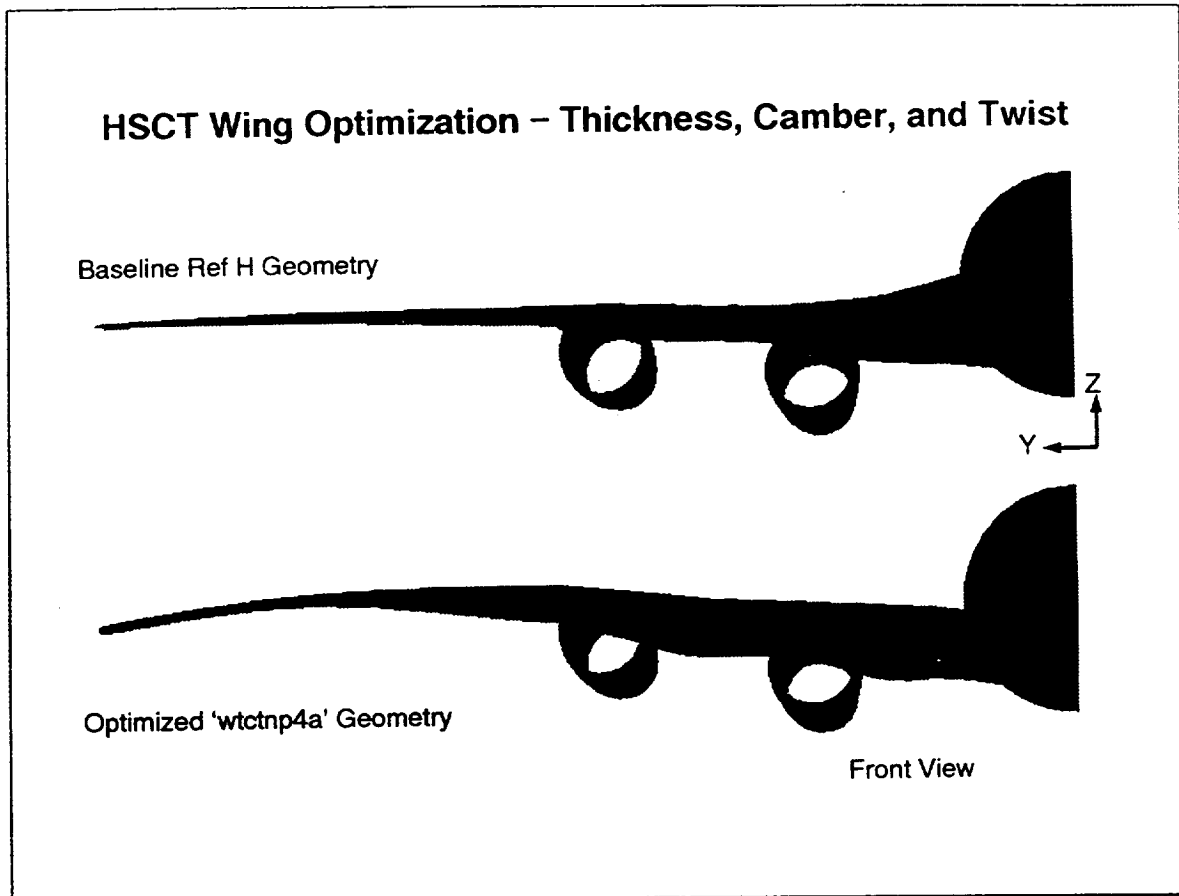
Smoothness of wing was dramatically improved.

**Additional cycles may be needed due to linearized
2 Term Transpiration.**

HSCT Wing Optimization with Thickness, Camber, and Twist

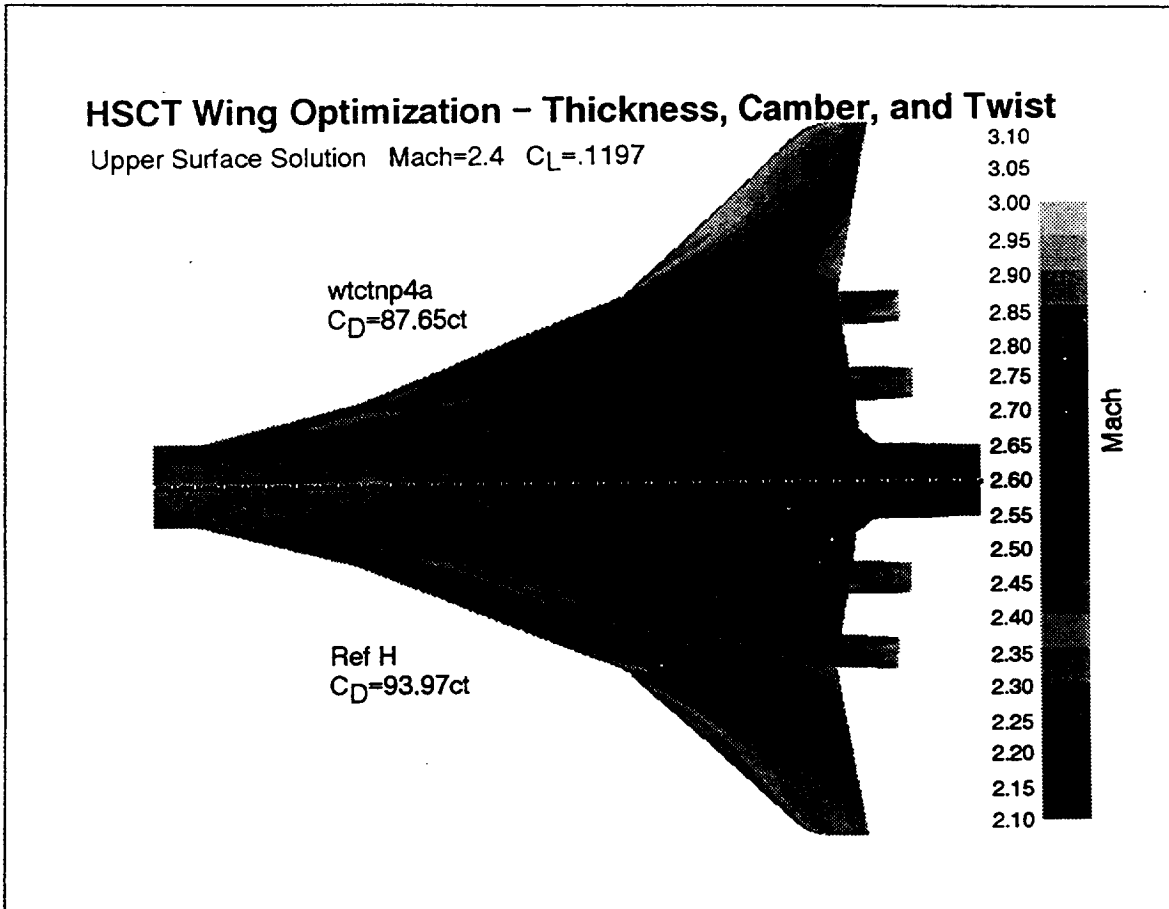
The results were quite promising. A third optimization cycle (repeated cycle 2) was required due to slower convergence using the new linearized 2-Term Transpiration. The final drag benefit was 6.35 counts over the Ref H baseline.

In general, linearized 2 Term Transpiration appears to require additional cycles for convergence of the optimization. The optimizer was "reined in" to take smaller, and more methodical steps with the linearized 2 Term change. The change to a linearized transpiration was required due to the large job size and queue requirements of the NAS C-90.



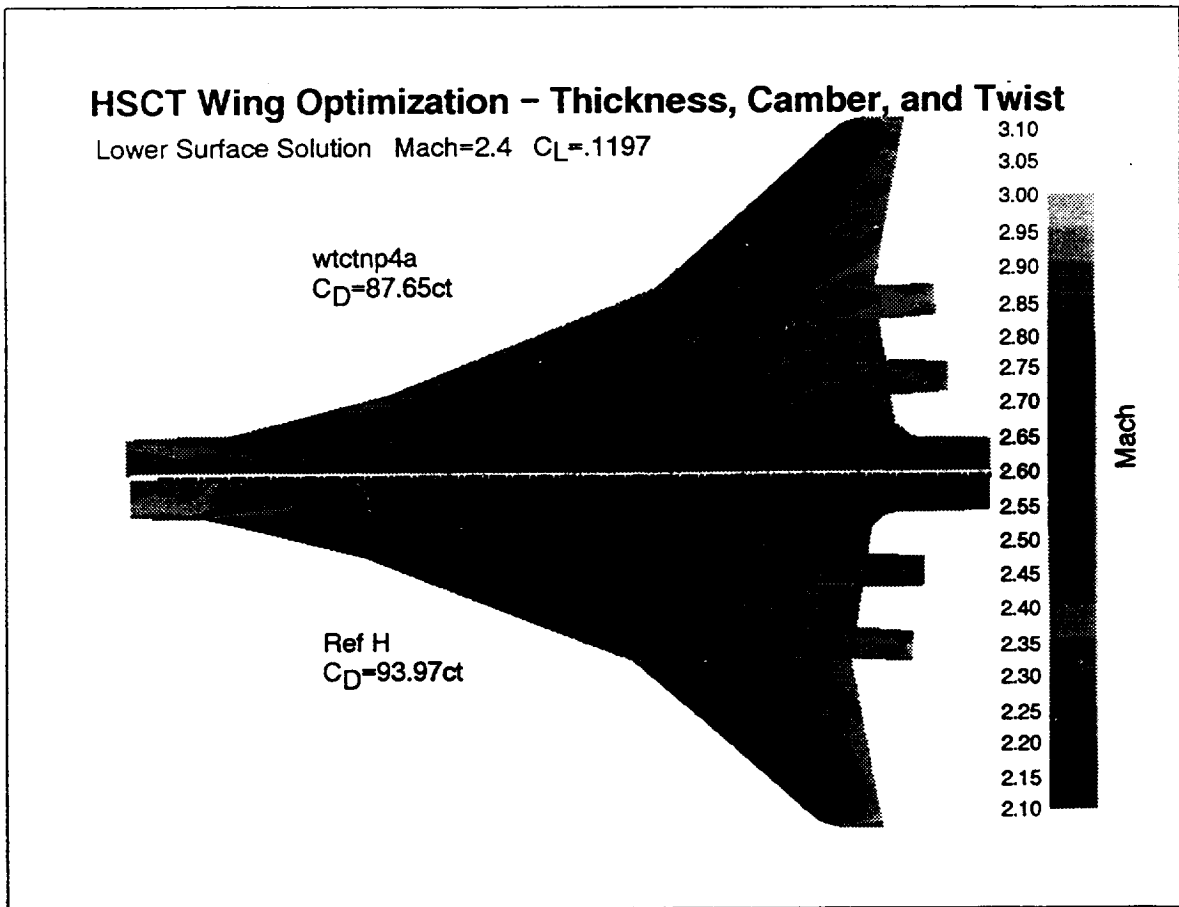
HSCT Wing Optimization – Thickness, Camber, and Twist

This image shows shaded graphics depictions of front views of the baseline Ref H geometry (top) and the final thickness/camber/twist optimization geometry (bottom). The Ref H body is identical, except for the wing/body intersection. It is apparent that the optimization wants to place the wing lower on the body with a negative twist at the side of body relative to Ref H. The overall wing seems to have greater mid span wing camber and has a fairly pronounced gull effect.



HSCT Wing Optimization with Thickness, Camber, and Twist

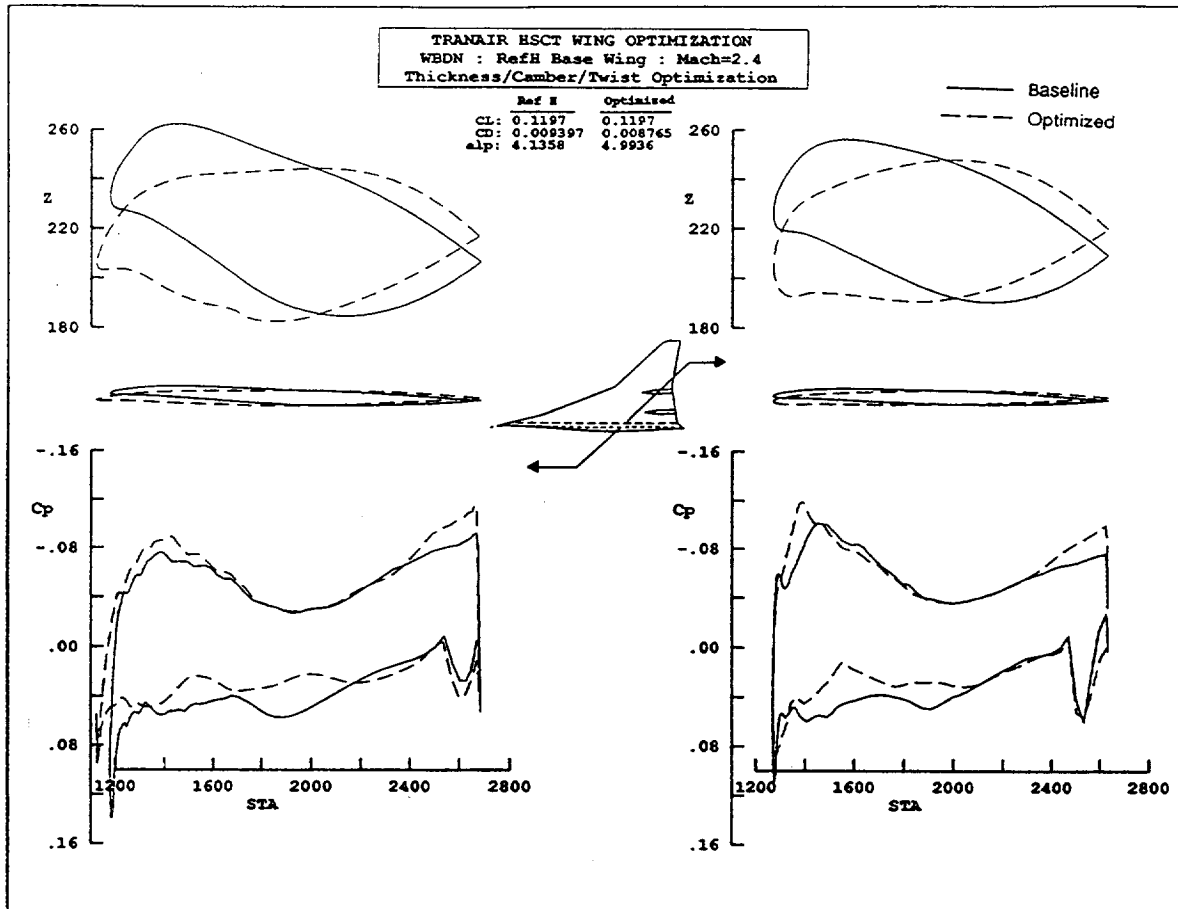
The optimized Mach number distribution on the wing upper surface is shown as the upper figure. The Ref H result is shown on the lower plot. The drag benefit was 6.35 counts from the Ref H wing. The overall upper surface flow is notably slower, with smaller regions of Mach~3.0 flow. The parallel high speed regions near the leading edge of the optimized wing outboard of the inboard break may indicate the need for further smoothing.



HSCT Wing Optimization with Thickness, Camber, and Twist

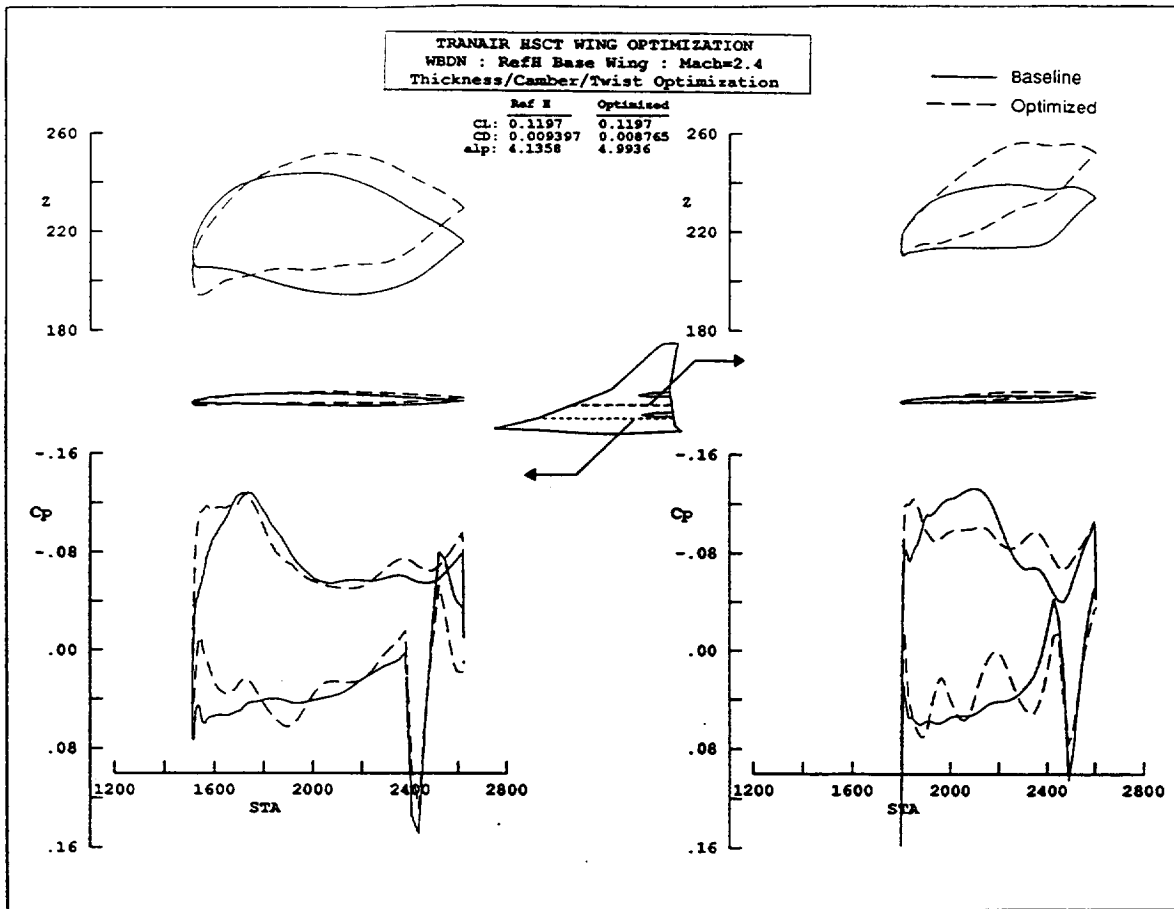
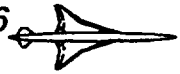
The upper figure shows the optimized wing lower surface TRANAIR solution. The Ref H result is shown on the lower plot. The drag benefit was 6.35 counts from the baseline Ref H wing.

The optimized wing's lower surface Mach number distribution seems generally higher. The nacelle/diverter region's flow seems to have been slowed and smoothed. A hot spot was created mid span at the leading edge.

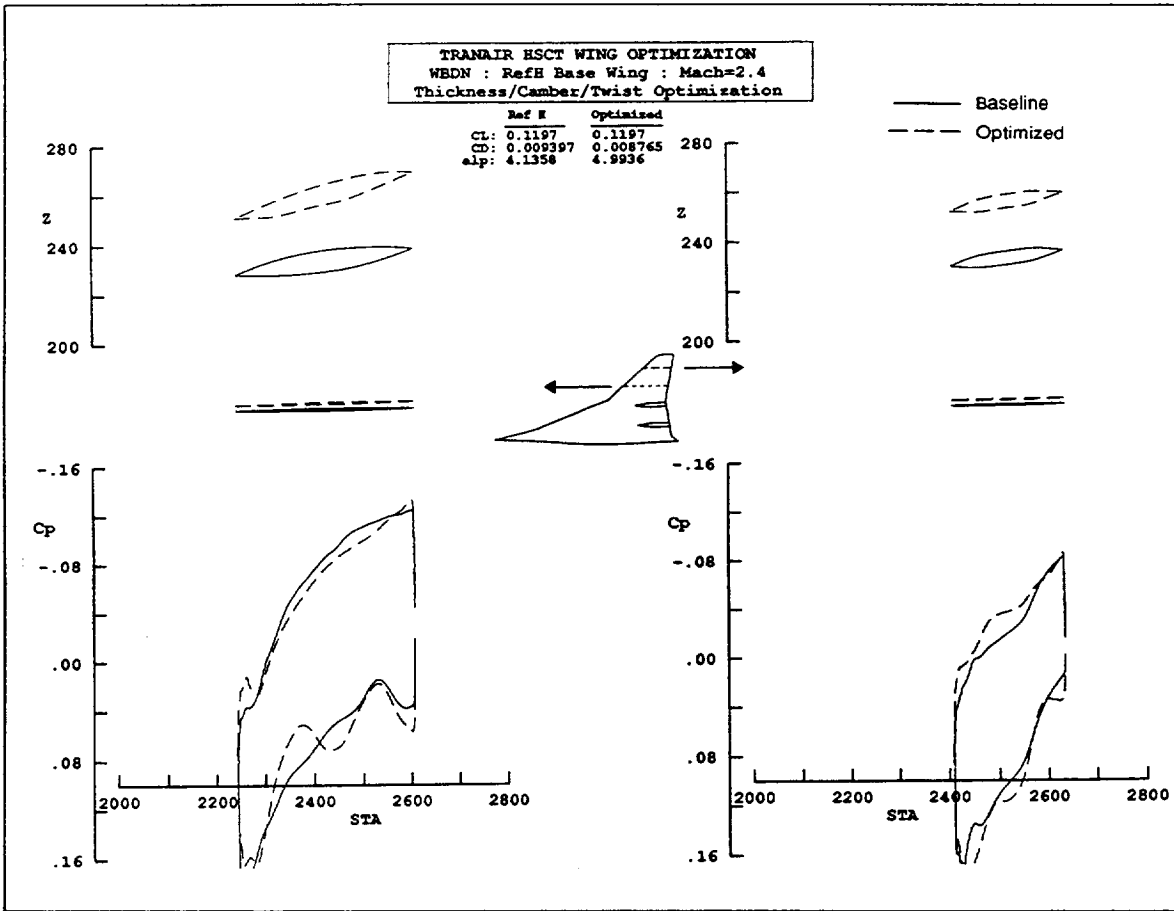


HSCT Wing Optimization with Thickness, Camber, and Twist

This page and the following two pages show sectional data from the final optimization of the Ref H wing with thickness/camber/twist at Mach=2.4, and $C_L=.1197$, the cruise condition. The plot sets include 10:1 scale in Z and 1:1 scale in X geometry, and pressure distribution plots. Dramatic geometry changes were made. The resulting drag benefit was 6.35 counts relative to the Ref H baseline.



HSCT Wing Optimization with Thickness, Camber, and Twist



HSCT Wing Optimization with Thickness, Camber, and Twist



HSCT Wing Optimization

Viscous Verification

Navier–Stokes WB $\Delta C_d = 3.0$ counts

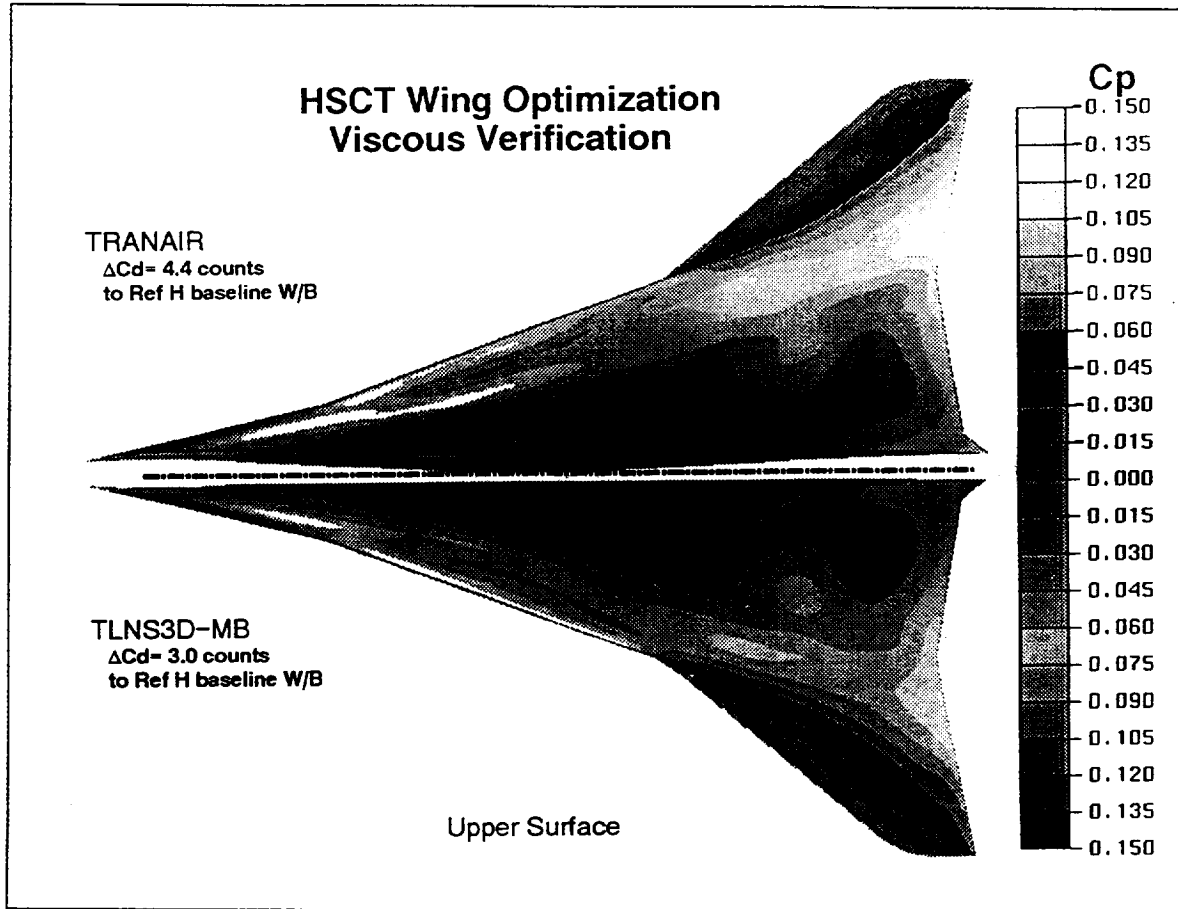
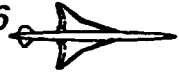
Tranair WB $\Delta C_d = 4.43$ counts

Tranair WBDN $\Delta C_d = 6.35$ counts

HSCT Wing Optimization with Thickness, Camber, and Twist

Viscous Verification using Wing/Body Navier–Stokes

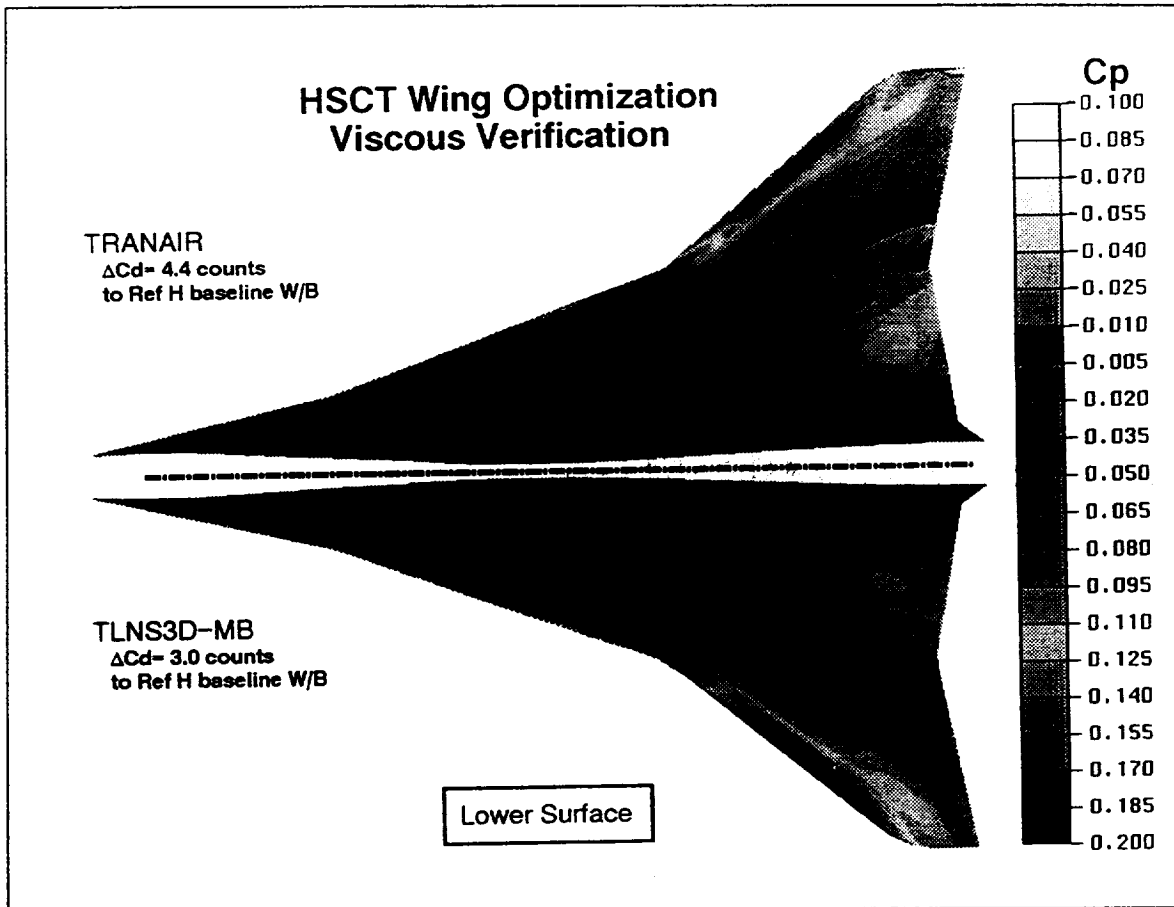
The geometry resulting from the inviscid optimization using Tranair was analyzed using a wing/body version of TLNS–MB. The 1.4 count difference is not unexpected for the visous increment of a design.



HSCT Wing Optimization with Thickness, Camber, and Twist

Viscous Verification using Wing/Body Navier-Stokes

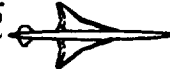
This image shows upper surface Mach distributions for the Tranair optimized wing from the Tranair solution (top) and from the Navier-Stokes result (bottom). It can be seen that the distributions are quite similar.



HSCT Wing Optimization with Thickness, Camber, and Twist

Viscous Verification using Wing/Body Navier-Stokes

This image shows lower surface Mach distributions for the Tranair optimized wing from the Tranair solution (top) and from the Navier-Stokes result (bottom). It can be seen that the distributions are quite similar.



**HSCT Wing Optimization
with
Thickness, Camber, and Twist**

Unexpected First Optimization Result

Wing Allowed to Move Completely Free of Body

Drag Increment -11.59 cts from RefH Baseline

Evaluating Possible Explanations for Result

**Translated Wing Vertically 38" to Re-attach to Body
Drag Increment -7.09 cts from RefH**

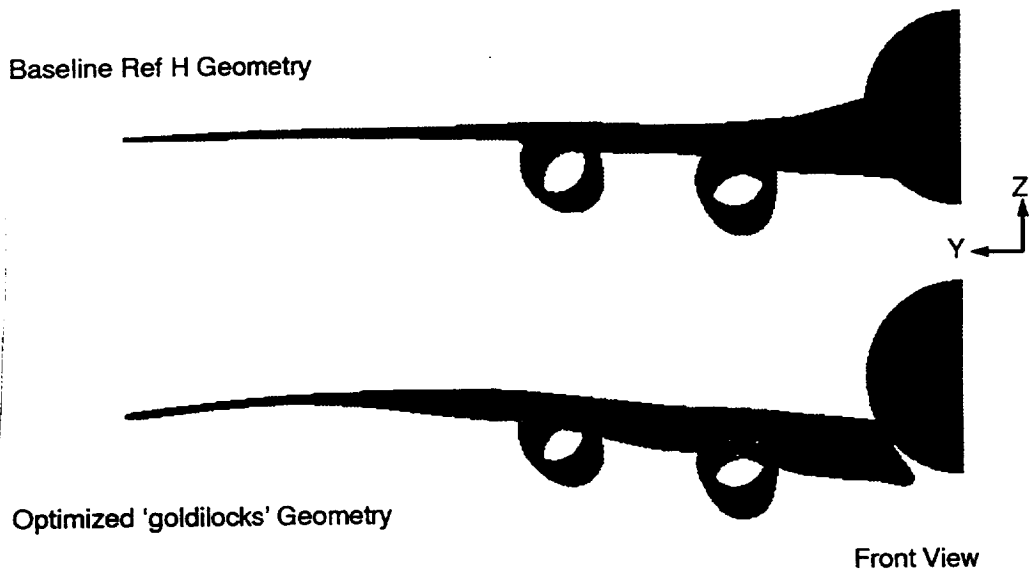
**HSCT Wing Optimization with Thickness, Camber, and Twist
Unexpected First Optimization Result**

The first optimization done using the full wing thickness/camber/twist method resulted in a promising albeit unexpected result. This optimization was the first run with all the project constraints and allowed the wing to move completely free of the body. Since we had anticipated the wing moving upwards, there were constraints available to prevent the wing from rising too far. No constraints existed to prevent the wing from seeking a lower position. This is clearly where the optimizer wanted to place the wing! The resulting geometry was quite smooth and showed a drag improvement of 11.6 counts relative to Ref H. This level may not be quite accurate in as much as the wing was separated from the side-of-body by a significant vertical distance. A great deal of wing (or body) surface would have to be added for an accurate drag level to be given, or for a reabutment to be made. Current evaluations suggest there may be no benefit for placing the wing this low. When the optimizer is permitted smaller increments for each grid's movements, the wing does not tend to drop so significantly.

Since we did not choose to reabut this wing in the 'too low' position at that time, we used judgement to find the 'just right' place on the body. This 'goldilocks' geometry resulted in a -7.0 count drag increment based on analysis after translating the wing vertically 38" to reattach to the Ref H body.



HSCT Wing Optimization – Thickness, Camber, and Twist



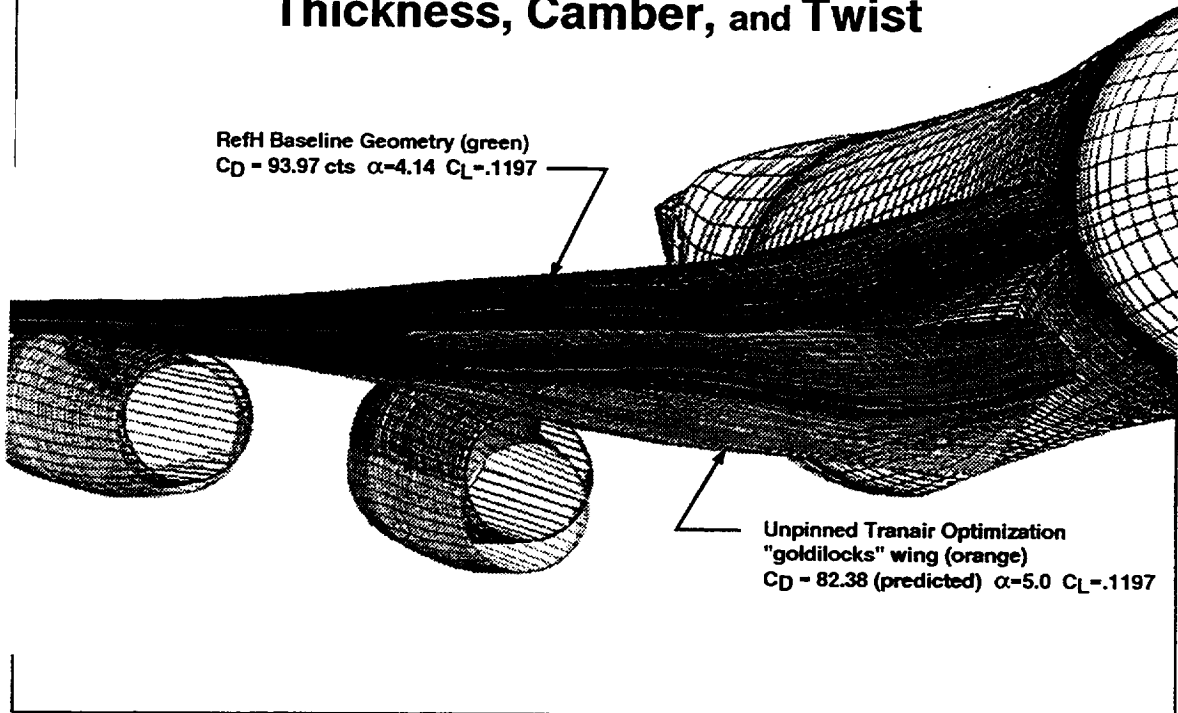
HSCT Wing Optimization with Thickness, Camber, and Twist

This image shows shaded graphics images of front views of the Ref H baseline geometry (top) and the cycle 1 optimization 'goldilocks' wing before the wing was shifted into its 'just right' position.

The pronounced gull wing shape is evident here. Subsequent optimizations, as discussed previously, also generated gull wing shapes, although not as pronounced as this version.



HSCT Wing Optimization Thickness, Camber, and Twist



HSCT Wing Optimization with Thickness, Camber, and Twist

This image shows the Tranair baseline RefH geometry in green. The design prediction geometry is shown in orange. The Ref H body was unchanged and the nacelle/diverters were held in a fixed position relative to the wing.



HSCT Wing Optimization with Thickness, Camber, and Twist

RefH Based Study

Baseline $C_D=93.97$ ct $\alpha=4.1358$ $C_L=.1197$

Optimized $C_D=87.65$ ct $\alpha=4.9936$ $C_L=.1197$ cycle 3

Thinned $C_D=83.69$ ct $\alpha=4.9887$ $C_L=.1197$ cycle 3
Spar thickness allowed to decrease by three inches.

Optimizer dramatically improved drag when allowed more freedom in thickness.

HSCT Wing Optimization with Greater Thickness Allowance

The optimizations were all done with thickness, camber, and twist from the Ref H baseline wing and body with nacelle/diverters. An undetected feature in the code left over from the cycle 2 camber/twist study, allowed the optimizer to remove one inch in spar thickness per cycle, and in the 'thinned' result above, the optimizer did just that! The cycle 3 thinned result showed a drag benefit of 10.3 counts relative to the baseline Ref H geometry. The standard optimization final drag benefit was 6.35 counts over the Ref H baseline with project spar thickness held..



HSCT Wing Optimization – Conclusions

Project Constraints are Effective as Implemented

Smoothness Improved with Project Constraints

**Candidate Viscous Flow Criterion Met with
Project Constraints**

Tranair Inviscid Prediction Verified by Navier–Stokes

HSCT Wing Optimization – Conclusions

The extensive project constraints are effective as implemented. Smoothness has improved with implementation of the project constraints. The candidate viscous flow criterion is met with the use of project constraints.

The comparison of the wing/body optimized configuration between Tranair and Navier–Stokes shows that it is quite possible to do optimizations with an inviscid full potential code that will work quite well viscously.



HSCT Wing Optimization – Follow On Work

Continue Coupled Wing and Body Optimizations

Apply to the TCA Configuration

Add New TCA Project Constraints

Inlet Flow Constraint Study

Viscous Verification of WBDN Design

HSCT Wing Optimization – Follow On Work

The wing optimization effort has evolved into the wing and body optimization effort. In the following year we will continue with the coupled wing and body optimization, as well as evaluating the separate wing and body optimizations.

We are completing the adaptation of the new TCA project constraints to the new TCA configuration. We will apply the methods we have developed using the Ref H to the new TCA once it is available.

Work is proceeding on viscous verification of Tranair results for the wing/body/diverter/nacelle configuration.

Work is also planned on the inlet flow constraint optimization.

ADVANCES IN DESIGN OPTIMIZATION USING ADJOINT METHODS

James Reuther
David Saunders

RIACS/AAH
Sterling Software

February 1996

This presentation outlines the progress made at Ames Research Center in the past 6 months with CFD-based aerodynamic shape optimization software tools, in particular with their adaptation to the High Speed Research program. Given an efficient and robust flow solver, the key to optimization efficiency is the calculation of gradient information cheaply by means of an adjoint solver combined with a fast and reliable grid regeneration capability. The two main topics to be covered are the enhancements made to the single-block adjoint-based wing/body design code SYN87, and the recent development of the multiblock adjoint-based code SYN87-MB, which is also parallelized.

While these programs (particularly SYN87) have been adapted considerably at Ames for HSR purposes, the initial development has been for general purpose aerodynamic optimization by Professor Antony Jameson (Princeton) and James Reuther (RIACS). Implementation of the multiblock code has also been contributed to significantly by other collaborators at Princeton and Brigham Young Universities.

Even though the single-block SYN87 is limited to the Euler-based design of wings or wing/bodies, its ability to provide rapid results by virtue of its built-in grid generation means it should remain a work-horse even as the more general multiblock code becomes established. Thus further enhancements are still warranted. Moreover, SYN87's pseudo-nacelle option (a highly HSR-specific adaptation) provides a means of approximating the effects of under-wing nacelle/diverters. Valid for supersonic applications only, this option imposes delta Cps from external nacelles-on/nacelles-off calculations, which may need updating more than once as the overall design proceeds. The versatility and applicability of SYN87 to problems outside the HSR program are demonstrated by its application to the wing design of a transonic business jet. For this problem, the effects of an aft-mounted nacelle were simulated by means of a large fuselage bump, determined by a preliminary optimization with appropriate target wing pressures, then frozen during the wing design. Thus the single-block code is not as limited as the grid topology suggests, but there certainly remains room for improvement.

The multiblock design code needs an initial point-to-point-matching multiblock grid prepared ahead of time, and is thus inherently more labor-intensive to use. But it significantly expands the complexity of the configurations which can be handled accurately.

SYN87-MB has been implemented with parallelization in mind from the start. The parallelism is at the medium-grain level provided naturally by the grid blocks or groups of blocks. Furthermore, it is portable to any system supporting MPI (standardized Message Passing Interface). Actually, specifying a single processor at the user level allows the same code to run on systems without MPI.

Both SYN87 and SYN87-MB provide for optimization with either finite difference gradients or adjoint-based gradients, for a range of likely objective functions with no application-specific programming required. In the following discussion, the advantages of the adjoint approach will be summarized, the theory will be outlined, and gradient comparisons will be shown. Details of the efficient grid perturbation schemes will also be presented, and desirable enhancements for the two codes will be indicated.

Outline

- **Rationale for Adjoint Methods Instead of Finite Difference Methods**
 - Computational Efficiency
 - More Aerodynamic Constraints and/or Objective Functions
 - Sensitivities to Any Desired Change
 - Comparison of the Two Approaches
 - Symbolic Development of the Adjoint Approach
- **Single Block Adjoint Based Method (SYN87)**
 - Current Capabilities
 - Adjoint vs. Finite Difference Gradient Comparisons
 - Planned Improvements
- **Multiblock Adjoint Based Method (SYN87-MB)**
 - Current Capabilities, and One Gradient Comparison
 - Planned Improvements

Rationale for Adjoint Methods Instead of Finite Difference Methods

For design by optimization using gradient methods in the presence of expensive objective functions, the traditional limitation has been on the number n of design variables because of the high cost of computing the gradient vector of first derivatives or design sensitivities. As is by now well documented, ideas from control theory offer a way of side-stepping the impasse associated with conventional finite difference gradient approximations.

For a given objective or cost function, application of the chain rule of calculus expresses the variation of the cost function with respect to variations in each of the quantities involved in its calculation, be they (in the case of CFD) flow field quantities or computational grid coordinates. Applying the chain rule to the cost function and to the governing differential equations such as the Euler equations, introducing a Lagrange multiplier (field) applied to the (still-zero) expansion of the flow equations as constraints, and rearranging shows that solution of a second set of PDEs (the adjoint system) can eliminate the difficult flow-field variation term in the cost function variation. This variation, and hence the partial derivative of the cost function, can then be calculated very cheaply for any number of grid perturbations—that is, for any number of design variables applied to the aerodynamic shape and thence to the grid.

The cost of a gradient vector is thus reduced to little more than one flow solution and one adjoint solution. Given that the adjoint system is related to the flow system and may be solved by similar techniques, the cost of a gradient is thus reduced to the equivalent of 2 flow solutions. In contrast, the finite difference method requires $n+1$ flow solutions. Moreover, those $n+1$ solutions must be highly converged because the differencing of nearby function values loses the first few significant digits. Error analysis for the adjoint approach shows that the error in the sensitivities obtained is comparable to the error in the cost function. Thus not only are just 2 solutions required per gradient—those solutions need not be as thoroughly converged as the traditional approach demands.

In principle, the adjoint approach could provide full second derivative (Hessian) information for about the same cost ($n+2$ flow solutions) as the finite difference approach requires for first derivatives alone. Finite difference Hessians require $n^2/2$ flow solutions which are normally prohibitive. For the present, removing the traditional limit on the number of design variables is so computationally attractive that any attempt to go beyond first derivative methods makes little sense. Quasi-Newton rather than full Newton methods serve adequately for hundreds of variables; and limited-memory variations of the quasi-Newton methods, which avoid storing even some approximate Hessian or its factors in favor of retaining the last few low-rank updates only in vector form, appear to be the direction in which adjoint-based optimization is likely to move as the number of design variables grows. Of course, no more variables should be used than is strictly necessary even if the gradients are cheap, and good choice of design variables is a topic unto itself (more on which below).

Rationale for Adjoint Instead of Finite Difference Methods

- **Reduce Computational Costs**

- Gradient Evaluations

- * Finite Difference Method: $n + 1$ Flow Calculations

- * Adjoint Method: 2 Flow Calculations

- Full Hessian Information

- * Finite Difference Method: $\approx \frac{n^2}{2}$ Flow Calculations

- * Adjoint Method: $n + 2$ Flow Calculations

The above equivalent flow solution counts applied to a single objective function with no aerodynamic constraints, or to composite objectives (linearly combined) at the same flight condition. They also apply to cases where lift is constrained by means of an inner iteration on Alpha. But in general, the gradient cost increases by one adjoint solution for each additional objective or aerodynamic constraint, because these affect the right-hand side of the adjoint system. (Purely geometric constraints do not require further adjoint solutions.) Thus for a second flight condition, the flow solution must be recomputed along with an adjoint solution for each objective or aerodynamic constraint.

In comparison, the finite difference gradient picture is no worse for additional objectives or aerodynamic constraints at the same flight condition, but for multi-point design is even more bleak, requiring another $n+1$ flow solutions for each additional flight condition. Thus the adjoint strategy is especially desirable for multi-point design.

Presently, SYN87 and SYN87-MB are strictly single-point design codes, with one (or more) of the available objective functions switched on at run time, and no aerodynamic constraints other than the fixed-lift options. Geometric constraints are limited to implicit equality constraints such as on wing thickness, because the optimization package still in use (QNMDIF) is an unconstrained one. But switching to a constrained optimization package is becoming a leading priority for SYN87 now that its grid generation and adjoint technology have been thoroughly adapted for IISR applications.

- **Increase Number of Objective Functions and Aero. Constraints**
 - Gradient Cost for Each Additional Objective or Aero. Constraint
 - * At Same Flight Conditions
 - Finite Difference: 0 Flow Solutions
 - Adjoint: 1 Flow Solution
 - * At Different Flight Conditions
 - Finite Difference: $n + 1$ Flow Solutions per Condition
 - Adjoint: 2 Flow Solutions per Condition
- **Provide Sensitivity Derivatives for any Desired Change Without Additional Calculations**

This slide and the next summarize the finite difference and adjoint approaches, and are self-explanatory. Most of the research community is intimately familiar with the methodology behind the finite difference approach. The adjoint approach differs only in its alternative (and much more efficient) way of providing gradient information to the optimization module. Both capabilities are retained in order that the adjoint-based gradients may be checked for accuracy. There may be occasions when reverting to finite differences can overcome a difficulty encountered by the optimization, so this is always an option, but as the gradient comparisons to be shown later suggest, such an option is unlikely to be needed.

The Finite Difference Gradient Approach

- 1. Generate a Mesh for the Domain**
- 2. Solve the Flow Equations in the Domain**
- 3. Determine the Gradient**
 - Perturb One Design Variable
 - Recalculate Mesh
 - Recalculate Flow Solution
 - Form Finite Difference Gradient Element
 - Repeat for All Design Variables
- 4. Use Gradient Information to Calculate a Search Direction; Determine a Step Length (QNMDIF)**
- 5. Return to (1)**

The Adjoint Variable Gradient Approach

- 1. Generate a Mesh for the Domain**
- 2. Solve the Flow Equations in the Domain**
- 3. Determine the Gradient**
 - Solve the Adjoint Equations in the Domain (\approx One Flow Solution)
 - Determine Analytic Grid Sensitivities from Mesh Perturbation Scheme
 - Calculate Sensitivities to All Design Variables
- 4. Use Gradient Information to Calculate a Search Direction; Determine a Step Length (QNMDIF)**
- 5. Return to (1)**

The next two slides show the basic analysis behind the adjoint approach as outlined under the Rationale section above. The following references provide a more complete treatment and cover the actual application to the governing Euler equations:

- 1) J. Reuther and A. Jameson. Aerodynamic shape optimization of wing and wing-body configurations using control theory. *ALAA paper 95-0123*, Reno, January, 1995.
- 2) J. Reuther and A. Jameson. Supersonic wing and wing-body shape optimization using an adjoint formulation. *Technical report, The Forum on CFD for Design and Optimization (IMECE 95)*, San Francisco, November 1995.

Symbolic Development of Adjoint Approach

Let I be the cost (or objective) function

$$I = I(w, \mathcal{F})$$

where

w = flowfield variables

\mathcal{F} = grid variables

The first variation of the cost function is

$$\delta I = \frac{\partial I^T}{\partial w} \delta w + \frac{\partial I^T}{\partial \mathcal{F}} \delta \mathcal{F}$$

The flowfield equation and its first variation are

$$R(w, \mathcal{F}) = 0$$

$$\delta R = 0 = \left[\frac{\partial R}{\partial w} \right] \delta w + \left[\frac{\partial R}{\partial \mathcal{F}} \right] \delta \mathcal{F}$$

Introducing a **Lagrange Multiplier**, ψ , and using the **flowfield equation** as a **constraint**

$$\begin{aligned}\delta I &= \frac{\partial I^T}{\partial w} \delta w + \frac{\partial I^T}{\partial \mathcal{F}} \delta \mathcal{F} - \psi^T \left\{ \left[\frac{\partial R}{\partial w} \right] \delta w + \left[\frac{\partial R}{\partial \mathcal{F}} \right] \delta \mathcal{F} \right\} \\ &= \left\{ \frac{\partial I^T}{\partial w} - \psi^T \left[\frac{\partial R}{\partial w} \right] \right\} \delta w + \left\{ \frac{\partial I^T}{\partial \mathcal{F}} - \psi^T \left[\frac{\partial R}{\partial \mathcal{F}} \right] \right\} \delta \mathcal{F}\end{aligned}$$

By choosing ψ such that it satisfies the **adjoint equation**

$$\left[\frac{\partial R}{\partial w} \right]^T \psi = \frac{\partial I}{\partial w},$$

we have

$$\delta I = \left\{ \frac{\partial I^T}{\partial \mathcal{F}} - \psi^T \left[\frac{\partial R}{\partial \mathcal{F}} \right] \right\} \delta \mathcal{F}$$

This reduces the **gradient** calculation for an arbitrarily large number of design variables to

One Flow Solution
+ **One Adjoint Solution**

Single Block Adjoint Based Method (SYN87)

The capabilities of the current production version of the inviscid design code SYN87 are now described in further detail. The grid generation is given particular emphasis because it has not been documented before. The flow solver and adjoint technology is well explained in other references, so only highlights and performance details are described here.

Euler Solution (FLO87)

Each flow solution is calculated by a subroutine form of the FLO87 Euler solver by Antony Jameson as modified by James Reuther for wing/body applications rather than wing-alone. FLO87 computes cell-centered Euler solutions using a multistage Runge-Kutta-like time-stepping scheme. Its mature combination of multigridging, residual averaging, enthalpy damping, and 2nd and 4th order blended artificial dissipation provide the rapid, reliable convergence needed for design applications. Some tuning of the suggested convergence parameters may be required for each new configuration or grid dimensions, but the following performance is typical:

For the 5 orders of convergence recommended for use with the adjoint solver, FLO87 takes 180 multigrid cycles (4-level W cycles) and 600 CRAY C90 CPU seconds from a free-stream start (at Mach 2.4 on a 193 x 49 x 41 grid). Line search solutions from a nearby solution normally require significantly less time. (SYN87 updates the stored flow solution whenever the objective function decreases, even during a line search.)

For the 6 orders of convergence recommended for finite difference gradients, FLO87 takes about 250 multigrid cycles in 833 C90 CPU seconds from scratch, or 30-100 cycles in 100-300 seconds for the finite difference perturbation solutions.

Adjoint Solution (ADJ87)

SYN87's adjoint method is based on the continuous sensitivity approach (applied to the underlying PDE) as opposed to the discrete sensitivity approach (applied to the discretized governing equations). As a result, the ADJ87 subroutine can employ the same cell-centered multistage Runge-Kutta-like time-stepping algorithm already perfected for FLO87, including the 2nd and 4th order artificial dissipation and the multigridging and residual-averaging convergence acceleration schemes. Several variations of the co-state flux formulations have been tried, with only minor differences apparent in the resulting gradients. Each multigrid cycle presently takes a little longer than a flow cycle, but experience shows that only 2 orders of convergence are needed in the adjoint solution, combined with 5 orders for the flow solution, in order to produce accurate gradients (to be illustrated below).

For the above Mach 2.4 case, ADJ87 typically takes just 25 cycles and 90 CPU seconds to achieve 2 orders of convergence. Then each gradient element takes just 0.14 CPU seconds not counting the grid regeneration (more on which momentarily).

Single Block Adjoint Based Method (SYN87)

Current Capabilities

- **Euler Flow Solver: FLO87**
 - Inviscid Analysis and Design
 - Cell Centered Finite Volume with Multigridging, etc.
- **Adjoint Solver: ADJ87**
 - Cheap Gradient Information
 - Cell Centered Finite Volume with Multigridging, etc.

Initial Grid Generation (GRID87)

SYN87's present automated C-H grid generation for wing and wing/body configurations has its origins in Lockheed's WBGRID software, but it has largely been rewritten to improve the grid quality, which is marginal at best in the wing/body case because of the single block topology. The main difficulty of negative cell volumes near the body nose has been overcome by introducing an artificial boundary surface forward of the wing leading edge. Along with a second artificial boundary at the plane of the wing tip section, this makes for a 4-block grid even though the flow solver treats it as a single block. An optional C-II/C-O topology has also been implemented to resolve the wing tip better, but this needs some anticipated improvements in the elliptic smoothing to be usable.

Subroutine GRID87 now comprises 35 lower level routines. The first provides an option to calculate the wing/body intersection, which assumes a section is input at the center line. After all wing sections are regularized to the desired grid density, this center section is replaced by the computed intersection, which is found one point at a time using a line/surface intersection algorithm involving 1D and 2D parametric local splines and their derivatives in a 3-variable safeguarded Newton iteration. For "reasonable" geometries, this intersection calculation works well. But extremely low- or high-mounted wings can lead to ill-conditioning for any method. A more robust (if slower) fall-back method is desirable for the difficult cases (not yet incorporated).

SYN87 may also read a wing/body intersection which is fixed thereafter. A third option is its "planar" mode, where a 2D section is lofted at a specified span station near the body, and the grid effectively fills the gap with a fillet, but rather crudely.

The wing surface grid employs a composite sinusoid + quadratic distribution chordwise (parametric spline interpolation along the arcs) and linear lofting spanwise at span stations which may be bunched towards the root or the tip or both. Cranks in the leading edge are now captured automatically by smoothly-varying adjustments of the nominal spanwise distribution.

Some input control over the outer boundary distribution at the center line is provided, although this remains fairly arbitrary. The rest of the outer boundary may be swept to follow the wing and thus alleviate stretching problems which otherwise arise forward of the outer wing. The default sweep of the far grid boundaries is that at the tip leading edge.

The wake sheet boundary of the C mesh is arranged to leave the trailing edge smoothly by bisecting the associated angle, whether the trailing edge is sharp or blunt.

The body surface grid generation begins with a crown/keel line grid derived from the streamwise wake distribution aft of the trailing edge and by one-sided stretching along the arc forward of the trailing edge. Two options are provided for the body grid proper. The more recent parametric scheme works with unnormalized body surface arc-lengths to overcome difficulties near the singular nose point. These arc-lengths are equilibrated in the streamwise direction to avoid a ragged boundary at $v = v_{max}$ corresponding to the last body station, and they are recentered about 0. in the circumferential direction to moderate the stretching of u at the nose. Boundary (u,v) distributions are then established (an awkward 2D inverse problem along the wing/body intersection), then transfinite interpolation (TFI) and 2D elliptic smoothing are applied in four regions, followed by parametric bicubic interpolation at the resulting interior (u,v) points. Some redistribution along the resulting radial lines then provides precise control of the arc-length spacing at the wing root and at the crown line. This involves one-sided stretching, but reverts to two-sided stretching if the increment at the center line is too big.

The original (and since refined) body grid method uses nonparametric techniques, starting with an initial dense 2D mesh in the center plane filled as four regions by TFI and 2D elliptic smoothing. This is projected onto the body surface bilinearly, then the final grid is obtained by redistributing along the arcs between the wing root and the crown/keel as for the parametric method.

The volume grid is initialized and smoothed in four regions as indicated above. Forcing the streamwise distributions forward of the wing leading edge on an artificial boundary surface to match the relative distribution on the body between the root leading edge and the nose was the key to avoiding bad cells near the nose. Once the boundaries of the 4 sub-blocks have been established, the algebraic initialization of interior points is essentially 2D by K planes, followed by 2D elliptic smoothing of each plane.

Three-dimensional elliptic smoothing is then applied to the four sub-blocks—a vital capability in the presence of a body. Considerable effort has been expended on generalizing these 2D and 3D smoothing utilities. They can now impose Thomas-Middlecoff spacing control at any or all of the boundaries, meaning no radial redistribution is required. [Efforts to add Sorenson-type orthogonality control have also been successful in the 2D case, but the 3D analogue still does not give the desired results, so neither the 2D smoother nor the 3D smoother provides orthogonality control in SYN87 at this stage. Even so, the precise spacing control at all boundaries provided by the present versions is valuable. They are fully vectorized apart from the tridiagonal line relaxation solutions.]

A full 193 x 49 x 41 grid takes about 48 seconds of C90 CPU time, including about 32 seconds for 75 iterations of the 3D smoothing (done as 4 sub-blocks).

Grid Perturbation (WARP3D)

Even with its adjoint-based gradient capability, SYN87 still needs to do a grid calculation for every gradient element because this portion of the technique remains in finite difference form. A cheap perturbation method of regenerating the grid is clearly needed to take full advantage of the adjoint approach. If the wing/body intersection changes, as it may well do, simply perturbing the initial grid along lines off the surfaces may not be viable. Thus a generalized scheme is required which allows for any or all of the grid faces to move. Such a utility has been implemented as subroutine WARP3D. Given perturbed block face grids (or sub-block face grids), WARP3D determines corresponding perturbed interior grid points efficiently.

WARP3D is best understood by considering its 2D analogue, WARP2D. Here, a 2-stage algorithm solves the problem—one stage to deal with possible corner point motion, and a second stage to adjust for any further edge motion. Consider perturbing a rectangular grid. If any of the corners has moved and the desired edges remain straight lines, then the first stage alone achieves the desired result because the moved edges are the final edges. Conversely, if the corners remain fixed and only the edges have moved (no longer straight lines), the second stage does all the work. In general, with both corner and (dissimilar) edge motion, each stage does part of the work.

Stage 1 effectively perturbs all points (including edge points) based only on the motion of the 4 corner points. In practice, the edge points are treated first. Stage 1 initially establishes intermediate edge perturbations from the corner perturbations by the obvious 1D method of imposing the same relative locations between the new corners as between the original corners. Corresponding interior point perturbations are then derived from the perturbations of the two pairs of opposite edge points defined by the relevant indices. Since both directions affect these interior perturbations, the contributions from each index direction must be combined as a weighted average.

Stage 2 first determines edge point perturbations from the intermediate edges to the desired edges, then updates each interior point based on the motions of the relevant end points in each index direction. The contributions from each direction can be simply added: they are now independent because the corners haven't moved.

Analogously, WARP3D performs a 3-stage algorithm to handle motion of corners, edges, and faces. That is, the interior point perturbations for stage 1 account for any corner point motion; for stage 2 they account for any additional edge point motion; and for stage 3 they account for any additional face point motion. Again, perturbations determined from each index direction need to be combined as weighted averages except in the final stage where they are independent.

Our initial implementation of WARP3D blurred stages 1 and 2 by (mistakenly) interpreting the quasi-3D version of WARP2D applied to each block face to achieve the correct final edges as the 3D analog of WARP2D's stage 1 which achieves the correct final corners. Testing failed to reveal any flaws, and SYN87's original application in single-block form involved no corner point motion, so 2 stages sufficed. It was only when the grid perturbation was applied to 4 sub-blocks (for proper consistency with the initial 4-block full grid generation) that the need for 3 stages became apparent. The quality of a perturbed grid is now indistinguishable from that of the original grid, even for substantial perturbations.

Rather than making three passes through the interior volume points, WARP3D stores the face perturbations for each stage then accumulates corresponding interior perturbations in a single pass through the volume. Fully vectorized, WARP3D applied to the 4 sub-blocks of a 193 x 49 x 41 grid takes just 0.15 CPU seconds on a CRAY C90 to perturb interior grid points given new faces.

WARPQ3D is also applied where possible, namely to 5 of the numerous sub-block face boundaries, such as the K planes at the tip and the beyond-tip boundary, and the off-body part of the center-line plane. This helps significantly because these boundary grids otherwise require 2D elliptic smoothing (approximately 1.5 CPU seconds worth).

The bulk of the time required for SYN87's grid regeneration is now spent on the wing/body intersection calculation followed by the wing and body surface grid generation, with little hope for improvement. Typical regridding CPU times are 3.0 seconds for a gradient element evaluation (single design variable perturbation), and 3.25 seconds for a line search evaluation (all design variables perturbed, with greater impact on the starting guesses for each point of the wing/body intersection calculation).

All told, a typical adjoint gradient element with 38 non-zero design variables takes about 3.2 CPU seconds.

- **Grid Generation: WBGRID (Rewritten)**

- Fully Automatic Initial Grid Generation
- Single-Block C-H topology
- Wing or Wing/Body Configurations
- Internal Wing/Body Intersection Calculation
- Elliptic Smoothing Using Thomas-Middlecoff Spacing Control

- **Grid Perturbation: WARP3D**

- 3-Stage Algebraic Scheme
 1. Perturb Interior Points Proportional to Corner Point Motion
 2. Perturb Interior Points Proportional to Edge Motion
 3. Perturb Interior Points Proportional to Face Motion
- Each Internal Point is Dependent on the Motion of the 8 Corner Points and 6 Face Points
- Storing the Face Perturbations for the 3 Stages Allows a Single Pass Through the Volume Points
- Very Robust and Efficient (Fully Vectorized)
- Quasi-3D Perturbation of Some Boundary Faces Saves Further Time

Ghost Nacelle Effects (Supersonic Applications Only)

The most obvious drawback of the basic SYN87 wing/body design procedure is its single-block structured grid, for which the Euler solutions (particularly for body wave drag) are only marginally trustworthy. At best, it may be expected just to predict increments in aerodynamic performance. At worst, an inability to incorporate additional components such as nacelles can make wing/body-alone design optimizations worthless.

The importance of including the nacelles and diverters as part of the HSCT design problem was appreciated from the start. Thus SYN87 (like its precursors OPT3D and OPT67) provides an option to simulate their effects using the nacelles-off and nacelles-on flow fields from a more capable solver such as AIRPLANE (as originally suggested by Bob Kulfan at Boeing). These are termed Pseudo or Ghost Nacelle effects. In SYN87, they have been incorporated into the adjoint method for the first time.

The pseudo-nacelle option consists of two distinct parts. The first part uses the surface delta Cps (interpolated from the input AIRPLANE results to the SYN87 grid) to estimate the changes caused by the nacelle/diverters in the forces on the wing and the body (Nacelle on Wing effects). The second part estimates the changes in the forces that might occur on the nacelles as the local flow field in which they reside changes as a function of design changes (Wing on Nacelle or delta buoyancy effects).

Consider for example the case where C_D is the cost function to be minimized. For the nacelle simulation, SYN87 evaluates the objective function as the sum of three components. C_D -wing-body refers to the drag that is actually calculated on the wing-body configuration which results strictly from the flow analysis (i.e., the portion without the nacelle effects). C_D -nacelle-on-wing refers to the contribution to drag developed by the nacelle on wing effects (i.e., by correcting the wing lower surface Cps with delta Cps derived from another solver's results before performing the force integration). This is equivalent to performing two force integrations (one for the uncorrected Cps, and one for just the delta Cps) and then summing them after the fact. The third term, C_D -wing-on-nacelle, refers to the integrated delta forces on the ghost nacelle geometry. In order to understand how the adjoint method develops the gradient for this problem, each of these terms must be examined in turn.

Since the first term does not involve the pseudo nacelles in any way, how it is treated in adjoint mode is independent of the presence of pseudo nacelles. The integrated C_D on a configuration without pseudo nacelles is dependent on the flow field variables at the surface and the mesh metrics at the surface. Thus if we want to know the gradient of this drag with respect to changes in a design variable, we must know the gradient of the values of these two vector quantities with respect to the same change in the design variable, as shown by the chain rule of calculus. The gradient of the flow field variables with respect to the design variable is determined by specifying an adjoint boundary condition, solving the adjoint system, and performing a volume integral involving products of the adjoint variable over the entire domain. The derivatives of the surface mesh metric terms can be obtained from a simple surface integral that is a product of these changes in the metrics. No adjoint variable is necessary. Although this, so far, is simply a repeat of what has been presented in the existing references on the use of adjoint methods, it is discussed here to emphasize the point that the variation involving flow field quantities requires an adjoint boundary condition and solution, while variations of the mesh terms require only surface integrals with these variations explicitly calculated.

- **Nacelle Effects**

- Wing on Nacelle Effects (Lower Surface ΔC_p s)
- Nacelle on Wing Effects (Nacelle Buoyancy Correction)

- **Optimization Algorithm: Unconstrained Quasi-Newton (QNMDIF)**

- QNMDIF2 Variant Adapted to Expensive Iterative Functions

- **Objective Functions**

- Target Wing Pressure Distribution
- Drag at Fixed Alpha
- Drag at Fixed Lift
- L/D at Fixed Alpha

The second term in the cost function summation, C_D -nacelle-on-wing, is defined as an integral over the geometry surface of constant pre-calculated values of delta C_p . Thus the gradient of this term contains no variation of the flow field quantities and hence there is no contribution to an adjoint boundary condition. The only gradient term that results from this term is a surface integral arising from changes in the metrics.

The last term, C_D -wing-on-nacelle, is unfortunately not so simple. It is represented by a surface integral over the ghost nacelles and diverters which involves both changes in the location of these entities (i.e., mesh metrics) and changes in the flow field variables acting on them. This implies that the gradient of this term not only will have a contribution from a surface integral over the nacelle/diverters (mesh metric variation term) but will also have a forcing function that affects the adjoint solution. Now, since the actual position of the ghost nacelles is out in the volume domain of the adjoint system, the contribution to the adjoint forcing function occurs not at the surface as a boundary condition but out in the domain as a source term. It is noteworthy that this HSR-specific adaptation of the adjoint method is the first time that a non-boundary term has been incorporated into the technology by our group. It represents a fundamental advance in the science.

Further details of the pseudo-nacelle implementation were documented for the HSR work-shop talk presented in August, 1995, and will not be repeated here. It suffices to say that the option (for finite-difference mode only in OPT67) has been translated to SYN87's cell-centered finite volume scheme, and that the adjoint solver (which was significantly affected as just explained) has been upgraded accordingly. Its adjoint-based gradients agree with finite difference results quite well as will be shown below.

The initial set-up for the ghost nacelle option can be saved for reuse. It consists of bilinear and trilinear interpolation pointers and blanking information to account for the portions of the lower wing surface covered by the diverters. In the case of the Ref-H geometry, the set-up takes about 360 CPU seconds to generate. Updating the buoyancy corrections for each line-search solution takes about 0.5 CPU seconds, but basically after setting it up the nacelle simulation has negligible further cost.

Optimization Algorithm: Unconstrained Quasi-Newton (QNMDIF2)

Since judicious choice of design variables can impose equality constraints implicitly (e.g., on wing section thickness), an unconstrained optimization package has served well so far. QNMDIF2 has been adapted moderately from QNMDIF to handle expensive iteratively-calculated functions better by trapping function failure and allowing retries where appropriate (such as by reducing the variable perturbation if a finite difference gradient element calculation does not converge). QNMDIF2 is also fully argument driven (no local storage vectors of length n). Note that the availability of adjoint-based gradients is transparent to QNMDIF2 with one exception: QNMDIF's automatic switching from forward to central differencing under certain conditions makes no sense if the gradients are derived from adjoint-based variations. This is therefore handled appropriately in QNMDIF2. Excessive output associated with large numbers of variables has also been suppressed.

A familiar objection to some QNMDIF results in this context is to its "UNSUCCESSFUL LINE SEARCH" message even when a (slightly) lower objective function has indeed been found. Convergence testing in the line search (let alone the overall minimization) is necessarily a balance between working too hard for negligible gain and not working hard enough for crucial improvements. Plotting of typical objective function evaluations from SYN87 in the presence of the above message will almost certainly verify that progress has indeed essentially bottomed out. Nevertheless, as a compromise, QNMDIF2 has had its minimum step-length adjusted from $h^{(2/3)}$ to simply h , where h is the (maximum) finite differencing interval.

As touched on above, in view of the inequality constraints anticipated for the next round of HSCT design optimization, switching to a constrained optimization package is becoming a leading priority for SYN87. Two concerns will be the issue of portability, and making of the above kind of application-specific changes to what is sure to be a much more elaborate package.

Objective Functions (SYN87)

SYN87 provides a choice of likely objective functions which are activated by entering non-zero multipliers in the standard input. The initial non-HSR objective functions provided with SYN87 are matching of target wing pressures at grid points and (more properly, to avoid grid density effects) pressures integrated over the wing area. The target and calculated pressure distributions are parameterized for the least-squares comparison, meaning the wrap-around wing surfaces are transformed to normalized (u,v) -space on $[0,1] \times [0,1]$. A full, structured target distribution is thus expected, but portions of it may be suppressed via the input i and k range (indices referring to the current surface mesh). With each new flow solution, the target distribution is bilinearly interpolated to the current wing surface cell centers in order to perform the objective function evaluation. A typical case requires 0.32 C90 seconds for the first set of interpolations, and 0.2 seconds after that thanks to the better starting guesses.

It was recently realized that the parameterization of pressure distributions must be done in real space (as opposed to reading an already-normalized target distribution). To put it another way: if a surface pressure solution is saved in normalized form then read back for use as a target distribution, there is no way for wing thickness, sweep, and taper information to appear in that target distribution, particularly if the comparison is weighted by area as it should be. Thus SYN87 now expects target pressure distribution inputs to include denormalization quantities which are applied before the arc-length-based parameterization is performed.

Other objective function options developed in conjunction with the HSR program include C_D at fixed Alpha, C_D at fixed C_L , and L/D at fixed Alpha (i.e., minimization of C_D/C_L). Pressure coefficients less than a specified limit may also be penalized as part of any objective, and penalty functions may also be activated in conjunction with a target C_L or a target C_M .

Minimizing drag at fixed lift requires an inner iteration on angle of attack, which is adjusted every 10 or so multigrid cycles. The adjustment in and of itself tends not to slow the convergence rate significantly. Rather, somewhat greater convergence should be specified to be sure of achieving the specified C_L , since no explicit test is made for terminating once the C_L is within some small tolerance. Experience shows that one extra order of magnitude (6 and 7 for adjoint and finite difference modes respectively) easily achieve the target C_L to more digits than is typically acceptable for any objective function. For instance, 6 orders with a target $C_L = 0.11$ produced $C_L = 0.10999996$ in one example. Thus in finite difference mode, fixing the lift costs about half as much again as fixing Alpha (using 7 orders rather than the normal 6 orders).

The adjoint situation is different because some additional sensitivities must be estimated with respect to Alpha. SYN87 actually perturbs the target C_L by -0.005 and performs an additional flow solution prior to the normal flow solution. Combined with the extra order of convergence recommended (6 rather than 5) this represents roughly a doubling of computational cost (including the associated adjoint solution) unless, as is optional, the necessary derivatives are estimated only once at the beginning of the run or (also an option) read as input.

The supersonic fixed-lift case in adjoint mode remains the least satisfying in terms of gradient accuracy as will be shown below.

SYN87 Design Variables (Wing)

SYN87 provides for table-driven specification of the design variables. The present version (in subroutine PERTURB) has been properly vectorized. As an example, the Ref-H figure of 0.03 C90 seconds for 38 nonzero sine bumps spread over about half of 26 defining stations gives some idea of the (minimal) cost of perturbing the geometry prior to grid generation.

Planform-related choices include sweep, span, dihedral, taper ratio, and twist. Wing section perturbing variables include the Hicks-Henne "sine bump" functions in standard, reflected, and symmetric forms, and leading and trailing edge droops (either smoothly varying or as slats or flaps). The Wagner functions (well-suited to airfoils) have recently been installed as well. The thickness distribution may be preserved by applying these y perturbations to both surfaces, thus varying camber only. Otherwise, the thickness may be allowed to vary (without explicit control at this stage) by perturbing just one surface.

The spanwise extent of the section perturbations may be constant over the specified geometry station range ("width" exponent = 0., as appropriate for slats and flaps), but typically they are tapered off to 0. at one side of "center" or the other side or on both sides. The decay may be linear or nonlinear, with some overlap of the different variable influences possible. The "best" way to perform spanwise perturbations (and avoid introducing waviness) with what are essentially 1-dimensional shape functions remains an open question. True 2D shape functions (not necessarily B-spline surfaces with their known difficulties) should be investigated.

SYN87 Design Variables (Body)

Body camber and span perturbing variables are provided by SYN87 much as for the wing (excluding the Wagner functions). The camber changes shear the body sections, while the span perturbations stretch them without disturbing the crown/keel line. Area-preserving shape functions have also been incorporated but not properly exercised yet.

SYN87 PostScript Plots

A small collection of PostScript utilities allows straightforward programming of standard pressure plots as routine outputs from SYN87 runs. The most recent of these provides true cross-stream cuts of body and wing surface results at specified stations. All plots now include page numbering for more efficient previewing via Ghostview on a workstation. Any target pressures are overlaid, and initial surface pressures may optionally be displayed with results from each design step. A carpet plot of the wing (grid) sections and the surface pressures is also generated (the most recent design iteration only).

- **Design Variables (Wing)**

- Planform: Twist, Taper Ratio, Sweep, Span, Dihedral
- Sections: Flaps, Slats, Hicks-Henne Camber, Hicks-Henne Thickness or Scaled Thickness, Wagner Functions

- **Design Variables (Body)**

- Hicks-Henne Camber
- Hicks-Henne Area

- **Computer Platforms**

- CRAY C90
- CRAY J90
- IBM SP2 (coarse grain parallel?)

Miscellaneous SYN87 Enhancements

Apart from the (general purpose) QNMDIF2 optimization package and the reasonably general-purpose PostScript utilities, SYN87 now makes use of a substantial collection of general-purpose numerical utilities—more than 30 such routines, in fact, plus a handful of ancillary functions. Examples are the efficient 1D, 2D, and 3D searching utilities and local [bi]cubic spline utilities, various 1D grid distribution utilities, 2- and quasi-3D TFI routines, a reverse-communication zero-finder and quadrature utility, and the generalized WARP3D package. Thoroughly documented and tested, these library-type routines contribute significantly to the improved quality and maintainability of the SYN87 software.

Speaking of maintainability, one awkward enhancement deserves mention: the OPT67 and early SYN87 nightmare of mixed coordinate conventions has been eliminated! SYN87 now has a consistent $x/y/z-i/j/k$ convention throughout, namely the right-handed system of FLO87, with x increasing downstream, y “up”, and z increasing along the (left) wing span from the centerline.

Finally, a restart option for the flow field and adjoint solutions has been incorporated.

SYN87 Computer Platforms and Distribution

While some versions of OPT67 and SYN87 have been experimented with on the IBM SP2, any past coarse-grain parallelization (at the finite difference gradient level) will need to be redone for the current version, which has seen action only on the DEC AXP development system and the CRAY C90 and J90.

In view of the proprietary nature of the multigrid flow and adjoint solvers, SYN87 distribution presently takes the form of source and object code for everything but those solvers (object modules only), and executable files. Users may make changes to the grid generation or other portions of the supplied source code, or alternatively request changes through the Ames developers.

Gradient Comparisons: Adjoint vs. Finite Difference

- Target Pressure, No Nacelle Effects
- Drag at Fixed Alpha, No Nacelle Effects
- Drag at Fixed Lift, No Nacelle Effects
- L/D at Fixed Alpha, No Nacelle Effects
- L/D at Fixed Alpha with Nacelle Effects

SYN87 Gradient Comparisons (Adjoint vs. Finite Differences)

Figures 1 through 7 summarize the results of extensive testing of SYN87's adjoint-based gradients for the various objective functions at transonic and supersonic speeds. In all cases, the wing sections are being perturbed by two distinct groups of standard Hicks-Henne sine bumps with width parameters (exponents) of 3 for every bump. In most cases, both surfaces of the sections are perturbed in unison (camber-only changes). The spanwise influence decays linearly either side of the two peak sections, with some overlap in the middle. For instance, the relevant span station inputs in the Ref-II case for each of the two groups of variables were 1, 6, 10 and 6, 10 and 16.

The ordering of the design variables for each group gradually moves the centering of the sine bumps from near the leading edge to near the trailing edge. Connecting the plotted gradient elements for design variables in one group or the other makes sense, since the variables are related. But the two groups are not connected (related)—hence the two sets of curves on each plot.

For all of the test cases, 38 variables (two sets of 19) were used in adjoint mode, while only 20 (two sets of 10) were used in finite difference mode because the calculations were so much more expensive—basically every other one was omitted.

Numerous combinations of orders of convergence and forward differencing interval were exercised along with the option to estimate optimal differencing intervals provided by the CENDIF2 adjunct to QNMDIF2 (basically Robert Kennelly's CENDIF package). In the later examples, the extremely expensive central differencing was omitted with justifiable reason for faith in the forward difference results which were shown to be insensitive to a range of differencing intervals. (Extensive testing in the 2D case has also been carried out with SYN42 and SYN82 supporting this conclusion.)

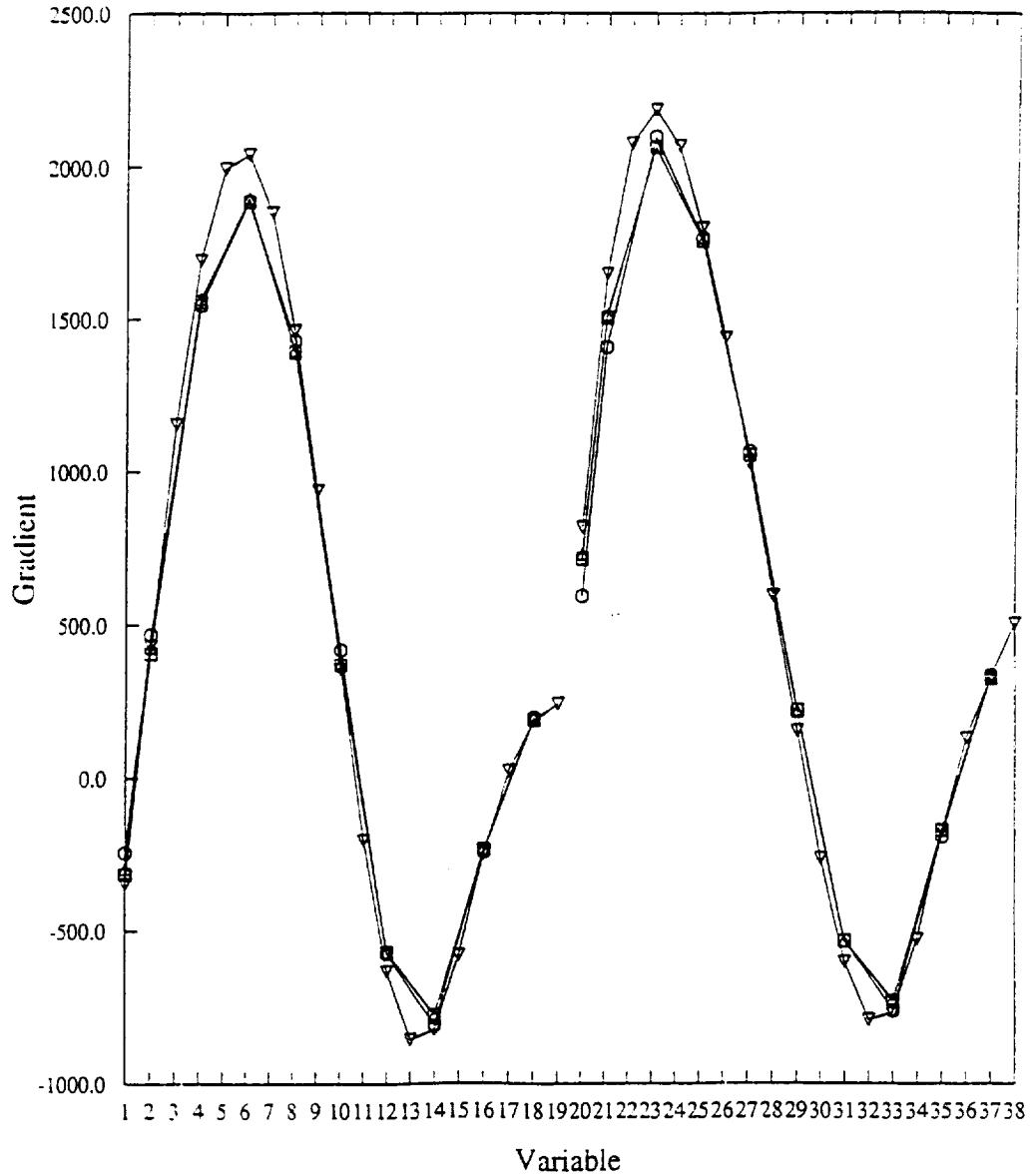
The comparisons illustrated here are certain to be better than any previously shown for earlier versions of SYN87 because a systematic error affecting all adjoint gradient calculations was uncovered during this shake-out of the overhauled code.

As indicated above, experience shows that (good) adjoint gradients normally need 5 orders and 2 orders of convergence in the flow and adjoint solver respectively, while forward differencing needs 6 orders in the flow convergence. If lift is being fixed, the flow solutions may need an extra order of convergence (6 and 7, respectively) for safety, in the absence of a separate test for matching the target C_L to within some tolerance. Of course, useful progress is likely in the early stages of a design iteration with looser convergence criteria, but this study was all about gradient accuracy, and for the most part, as will be seen, the adjoint gradients are indeed accurate.

SYN87 Gradient Comparison

Target Cps objective: Recover wing sections 3, 4 from NACA 0012 upper surfaces

- △— Forward differences (converged 7 orders, $h=0.00025$, 20 variables)
- Central differences (converged 6 orders, $h = 0.00025$ fixed)
- Central differences (converged 6 orders, optimal $h = 0.0000006$ variable)
- ▽— Adjoint method (converged 5 & 2 orders, $h=0.00025$, 38 variables)



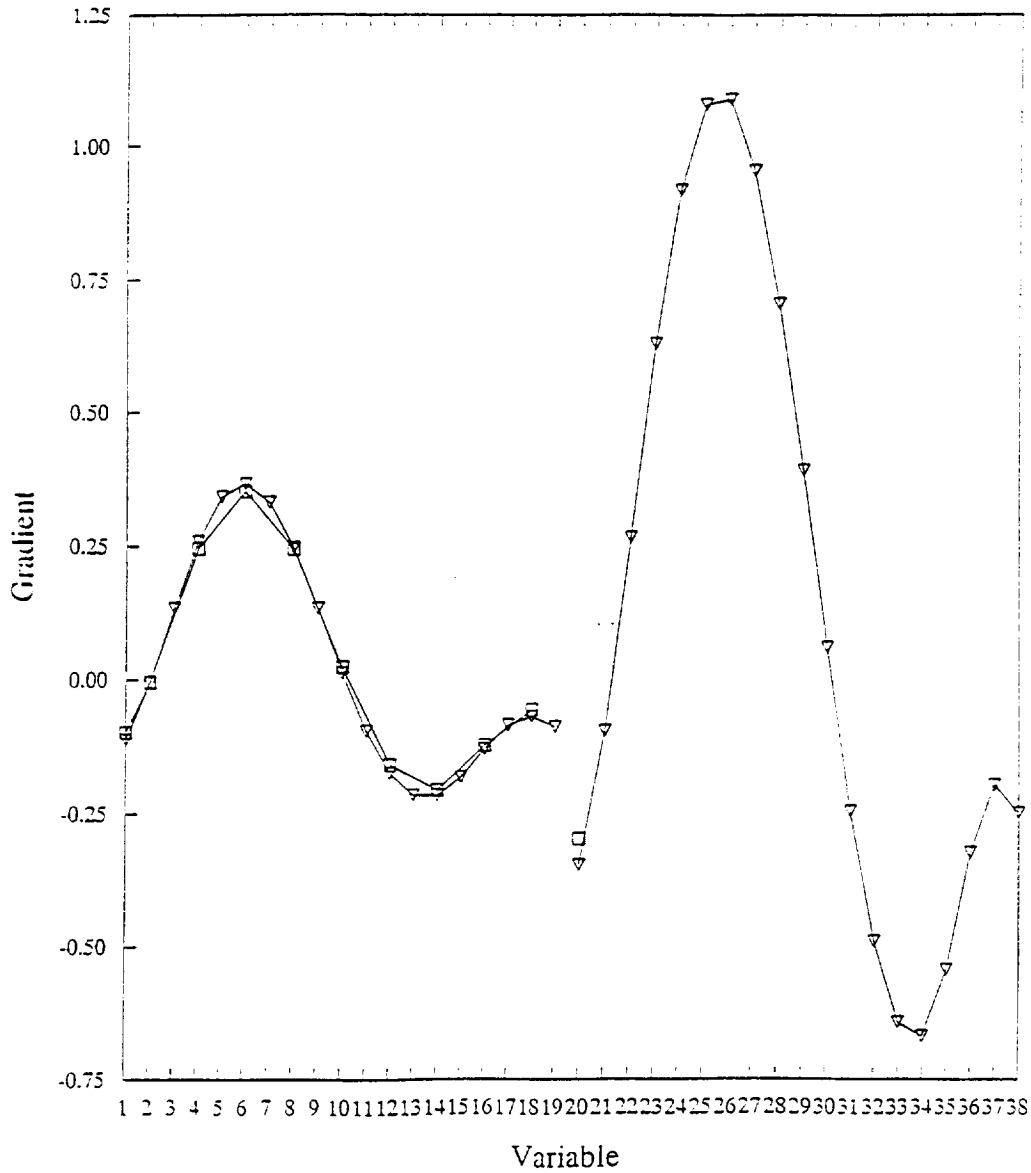
12/31/95

Figure 1

Figure 1 shows the (initial) gradient results with a target pressure objective for a transonic business jet case (Mach 0.75, Alpha = 1.5°). The forward and central difference approximations are virtually indistinguishable, while the adjoint gradients match very closely as well.

SYN87 Gradient Comparison
 CD Objective for fixed $CL = 0.35$

- Central differences (converged 7 orders, $h = 0.00181$ fixed)
- Forward difference (converged 7 orders, $h = 0.00181$)
- ▽— Adjoint method (converged 5 & 2 orders, $h=0.00025$, 38 variables)



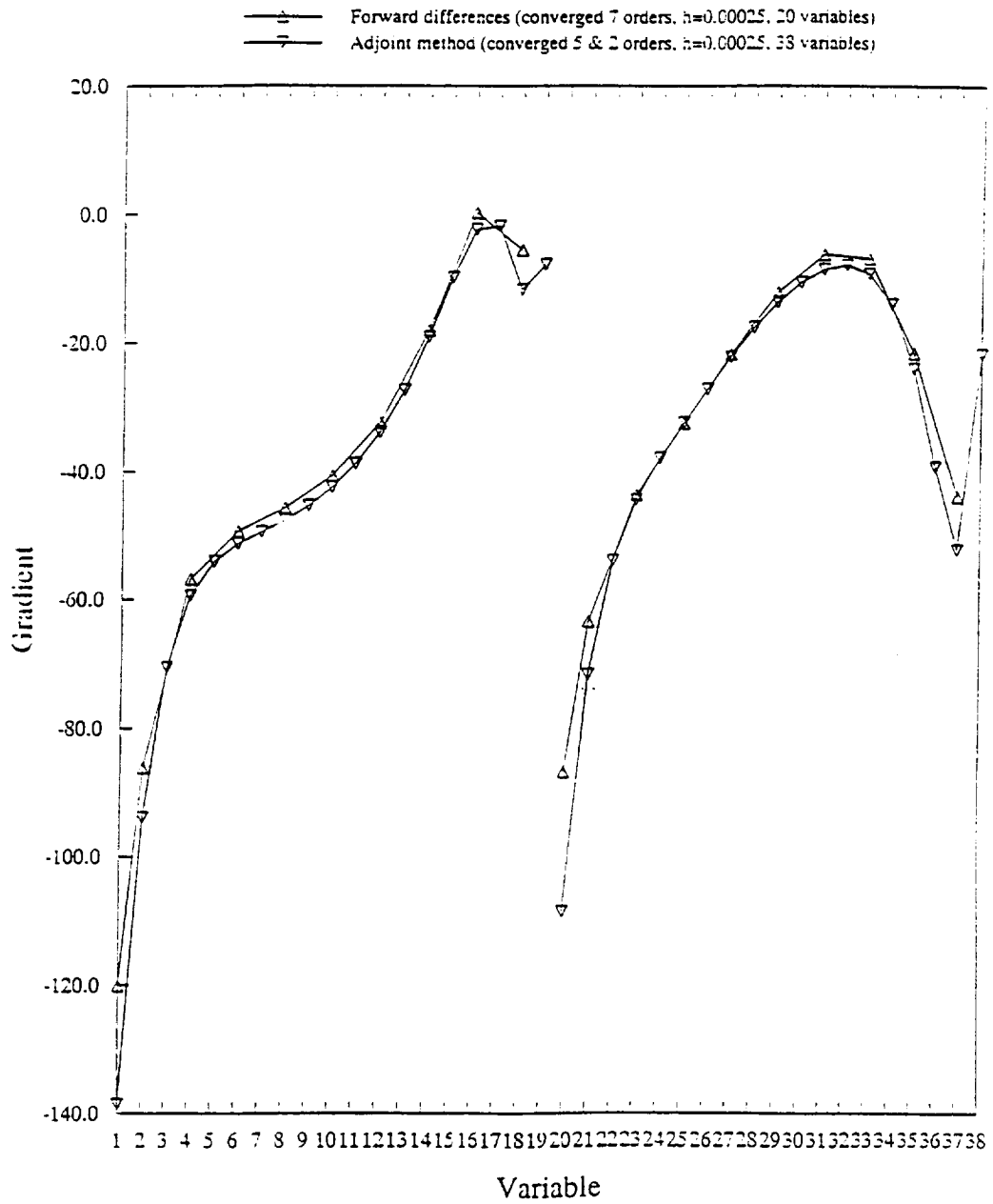
Beech Wing 17 + Body

01/03/96

Figure 2

Figure 2 shows gradients from the start of a transonic (Mach 0.80) drag minimization at a fixed C_L of 0.35. Some of the central difference estimates are missing because the 8-hour CPU time limit was reached—achieving 7 orders of convergence with the inner iteration on Alpha is indeed expensive, and 6 orders would have sufficed. (The last finite difference element shown is a forward difference determined from the interrupted run, which died before the corresponding backward difference had been completed.) Note that the adjoint gradient here (even with 5 orders of convergence) is extremely close to the central difference estimates. The supersonic case is not this good, for reasons not yet understood.

SYN87 Gradient Comparison
 Target Pressure Objective; two sets of camber variables



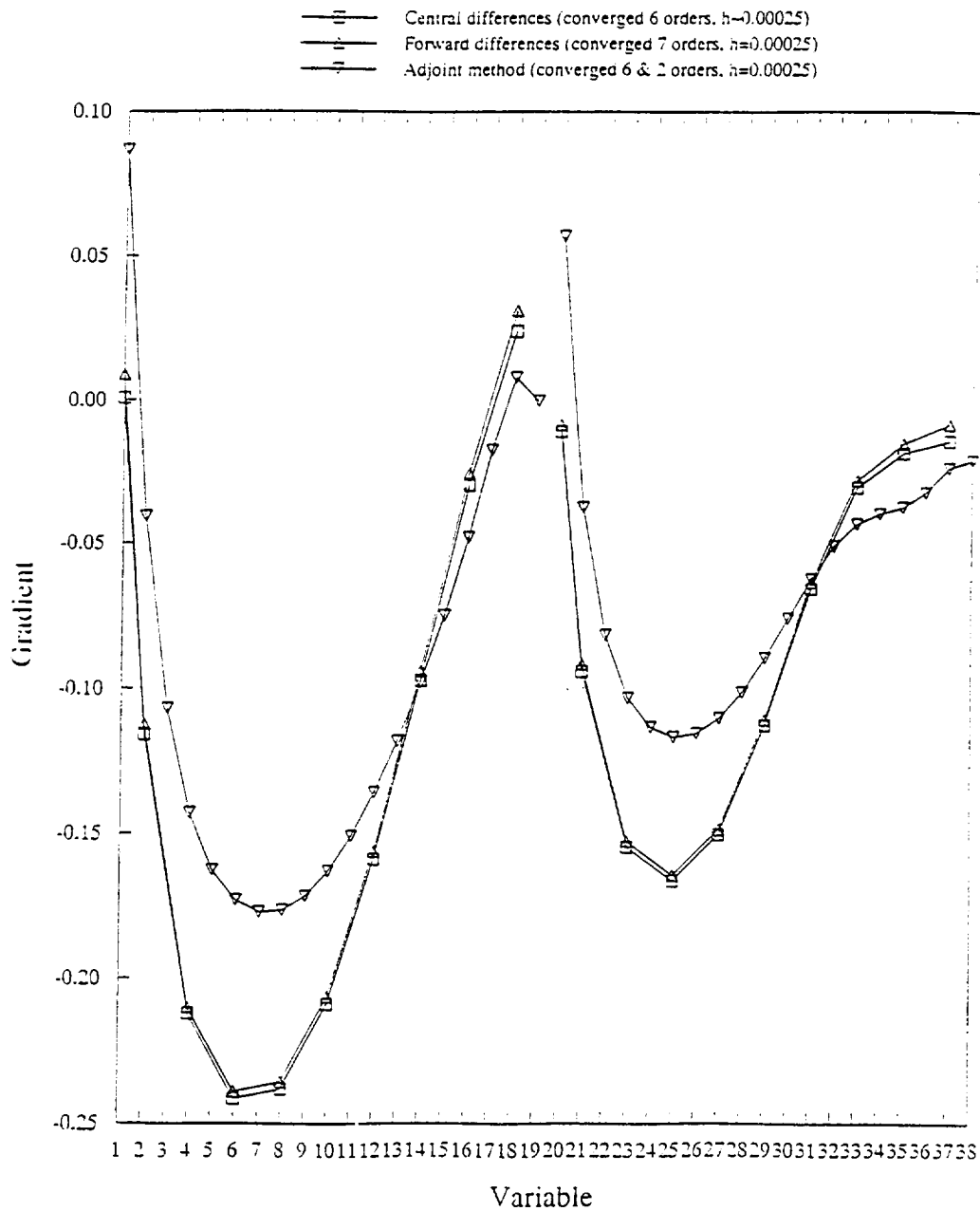
6-section variant of Douglas HSCT

12/28/95

Figure 3

Figure 3 shows a target pressure case again, this time supersonic (Mach 2.4, Alpha = 4.5°, for a slightly simplified variant of a Douglas HSCT design). Apart from some apparent over-prediction near the leading edge, the adjoint agreement is again good.

SYN87 Gradient Comparison
 CD Objective for fixed CL = 0.11; two sets of variables modifying camber



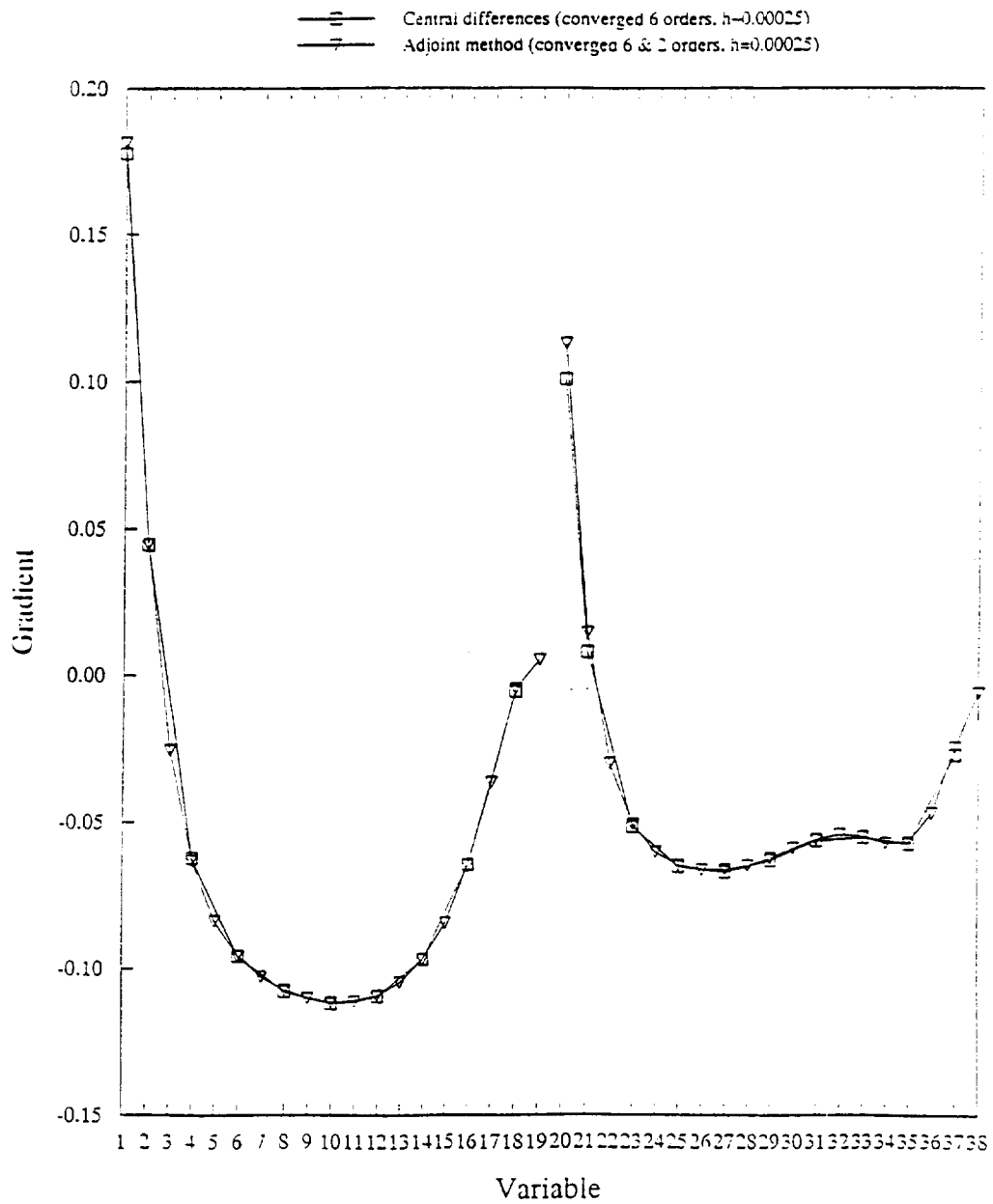
6-section variant of Douglas HSCT

Figure 4

01/04/96

Figure 4 shows the same supersonic case but with drag being minimized at fixed lift ($C_L = 0.11$). Here the forward and central differences agree so well that there clearly seems to be some problem with the adjoint gradients (unlike the transonic situation). This is the least satisfactory comparison, although the adjoint gradient still has the proper character and would be usable. We still hope to pursue and eliminate this discrepancy.

SYN87 Gradient Comparison
 CD Objective for fixed Alpha = 2 deg.; two sets of variables modifying camber



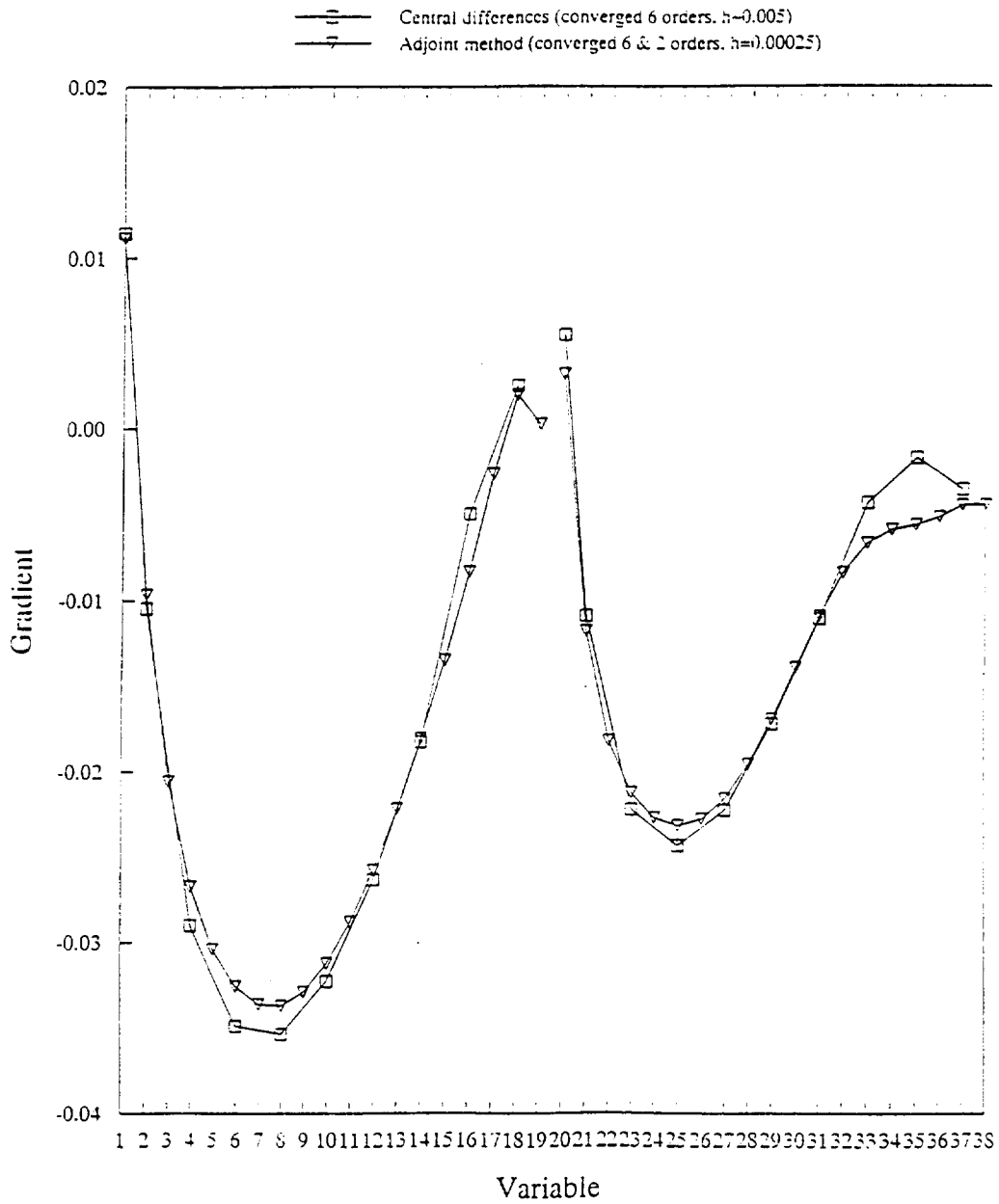
6-section variant of Douglas HSCT

Figure 5

01.05.96

Figure 5 shows the same supersonic case but with Alpha rather than C_L fixed. The agreement could hardly be better.

SYN87 Gradient Comparison
D/L Objective for fixed Alpha = 2 deg.; two sets of variables modifying camber



6-section variant of Douglas HSCT

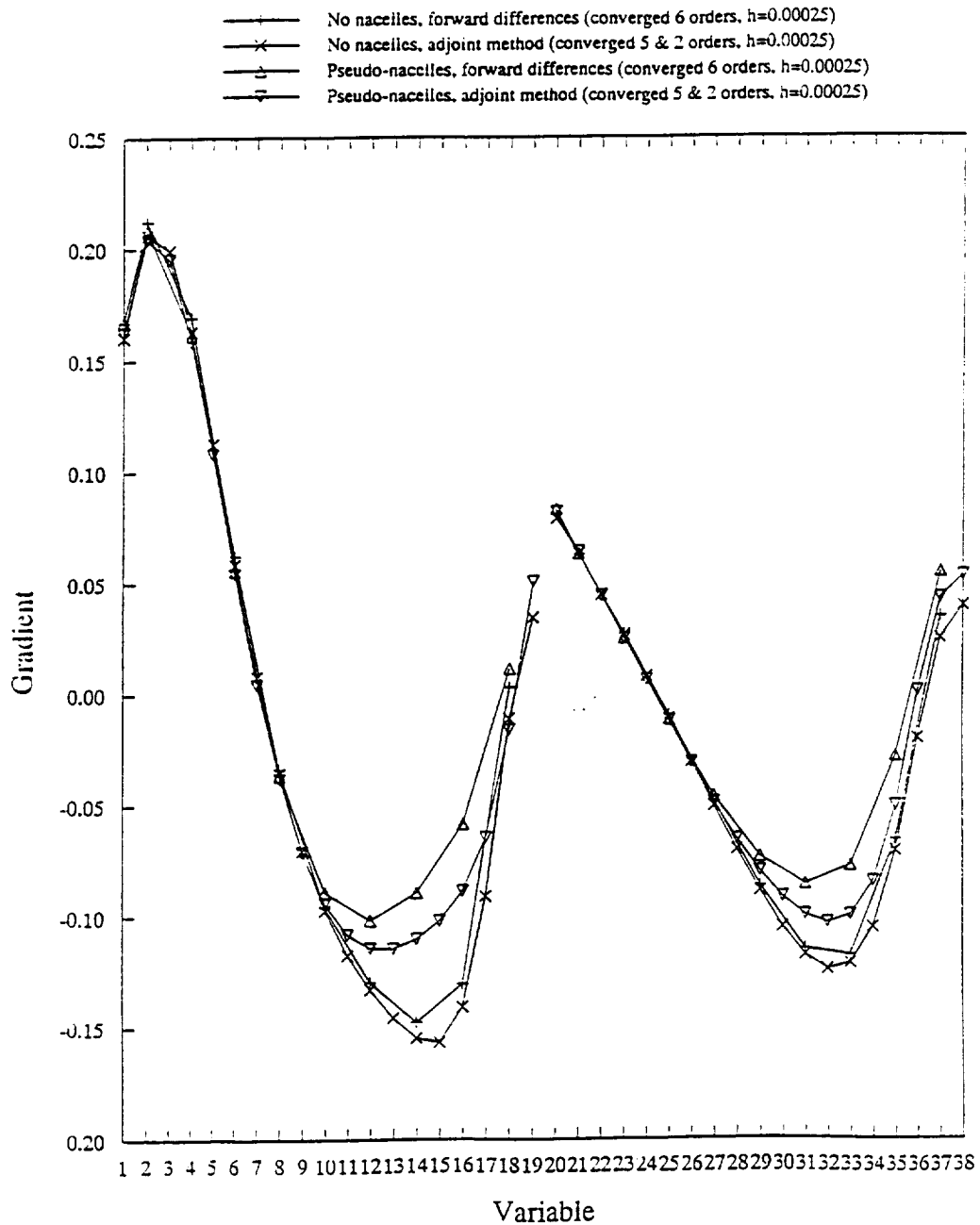
Figure 6

01.06/96

Figure 6 again shows the supersonic case but with L/D being maximized at fixed Alpha = 2°. Minor discrepancies are apparent.

SYN87 Gradient Comparison

L/D Objective for fixed Alpha = 4.5 deg.; two sets of variables modifying camber



Ref-H HSCT, Mach = 2.4

02/20/96

Figure 7

Figure 7 shows L/D results for the Ref-H configuration at Mach 2.4, Alpha 4.5°, with and without pseudo-nacelles. Note first that the presence of the ghost nacelles does make a difference (also apparent in plots of the adjoint solution). Secondly, the agreement for the nacelles-off case is good (overall better than for the Douglas geometry). And thirdly, the agreement with nacelle effects is reasonable (and certainly usable) but not as good as for the clean wing. The reasons are a matter for further study.

SYN87 Planned Improvements

A number of desirable enhancements have been touched on above. A summary follows.

Grid Generation Improvements

Perturbed grids are now reliable and efficient but still dependent upon the quality of the initial grid. The leading requirement here is for orthogonality control in the elliptic smoothing. Sorenson-type orthogonality control has in fact been added to the Thomas-Middlecoff spacing control versions of TTM2D and TTM3D named ELLIP2D and ELLIP3D. The 2D utility works well, but so far ELLIP3D does not give the desired results. It must be close, and should be pursued. This is especially important for the adjoint method, because gradient accuracy is loosely coupled to grid quality. Improved grids will provide better comparisons with finite difference gradients from the same grids.

Once ELLIP3D is working, the already-in-place C-H/C-O topology option should be usable. Grid lines are distributed on a tip cap (either rounded off or squared) for better resolution of the wing tip.

The option to calculate the wing/body intersection for each design iteration allows the wing root region to be perturbed. The present scheme amounts to a surface/line intersection algorithm, using parametric local cubic and bicubic splines (4-point methods in each dimension) and their derivatives in a safeguarded Newton iteration. With occasional resorting to retries using different starting guesses for t , u , and v , this scheme normally works well and is quite efficient. Non-smooth body surfaces, however, will cause difficulties for this gradient-based method. Clearly, mid-mounted wings are preferable. The more high- or low-mounted the wing, the more likely some of the iterations are prone to failure for a couple of reasons: ill-conditioning (nearly-parallel surfaces), and alternative solutions beyond the centerline. Clearly, some more robust wing/body intersection scheme is desirable which does not need surface derivatives.

Grid Perturbation Improvements

The recent change in WARP3D from a 2-stage to a 3-stage algorithm should be fully satisfactory for foreseeable single-block topology SYN87 applications. But some other kinds of boundary perturbations can be constructed which are expected to give trouble with the multiblock version or for other applications altogether. One enhancement planned this year will allow for the projection of all perturbations with respect to the original local cell face normals as opposed to simply using the reference coordinate system.

Planned Improvements

● **Grid Generation**

- Sorenson Orthogonality Added to Thomas-Middlecoff Spacing During Elliptic Smoothing (2-D Done; 3-D Almost Done)
- Single-Block C-H + C-O Tip (Done But Needs Orthogonality)
- More Robust Wing/Body Intersection Calculation

● **Grid Perturbation**

- More General Perturbation Scheme Involving Cell Surface Normals

● **Optimization Algorithm**

- Add NPSOL Constrained Quasi-Newton/Augmented Lagrangian Method
- Add Geometric Constraint Routines (No Adjoint or Flow Solver Modifications are Necessary)

Optimization Algorithm Changes

A nonlinear programming (constrained optimization) package is increasingly desirable in place of the unconstrained QNMDIF scheme. As long as the constraints are geometric, they will not require any SYN87 changes to obtain adjoint-based gradients of the objective. Some table-driven input scheme for such likely constraints needs to be developed comparable to the present means of specifying the type and locality of the design variables. The well-proven NPSOL package is the most obvious candidate. NASA Ames has access to NPSOL but may not distribute the source code. Industry users would need to acquire the software and a licence from Stanford University unless being provided with executable SYN87 code (no object module for NPSOL) is considered acceptable.

If aerodynamic constraints (such as on pitching moment) are to be treated by SYN87, more adjoint solver development is needed because the boundary conditions and source terms are affected. For the near-term HSCT applications, no such development is anticipated.

In this context, the low-memory quasi-Newton algorithms (initially unconstrained) offer attractive advantages, especially in conjunction with large numbers of variables (but for other reasons as well to do with line search accuracy, or lack of it). But the need for more variables than QNMDIF2 can already adequately handle is not immediate, so pursuing inequality constraint capability will take precedence.

Efforts will also be made to develop a more closely coupled design algorithm that does not depend upon either highly converged gradients or accurate line searches to achieve practical descent directions. The idea is for the flow solution, the adjoint solution, and the design algorithm all to be converged simultaneously in a "one-shot" design iteration.

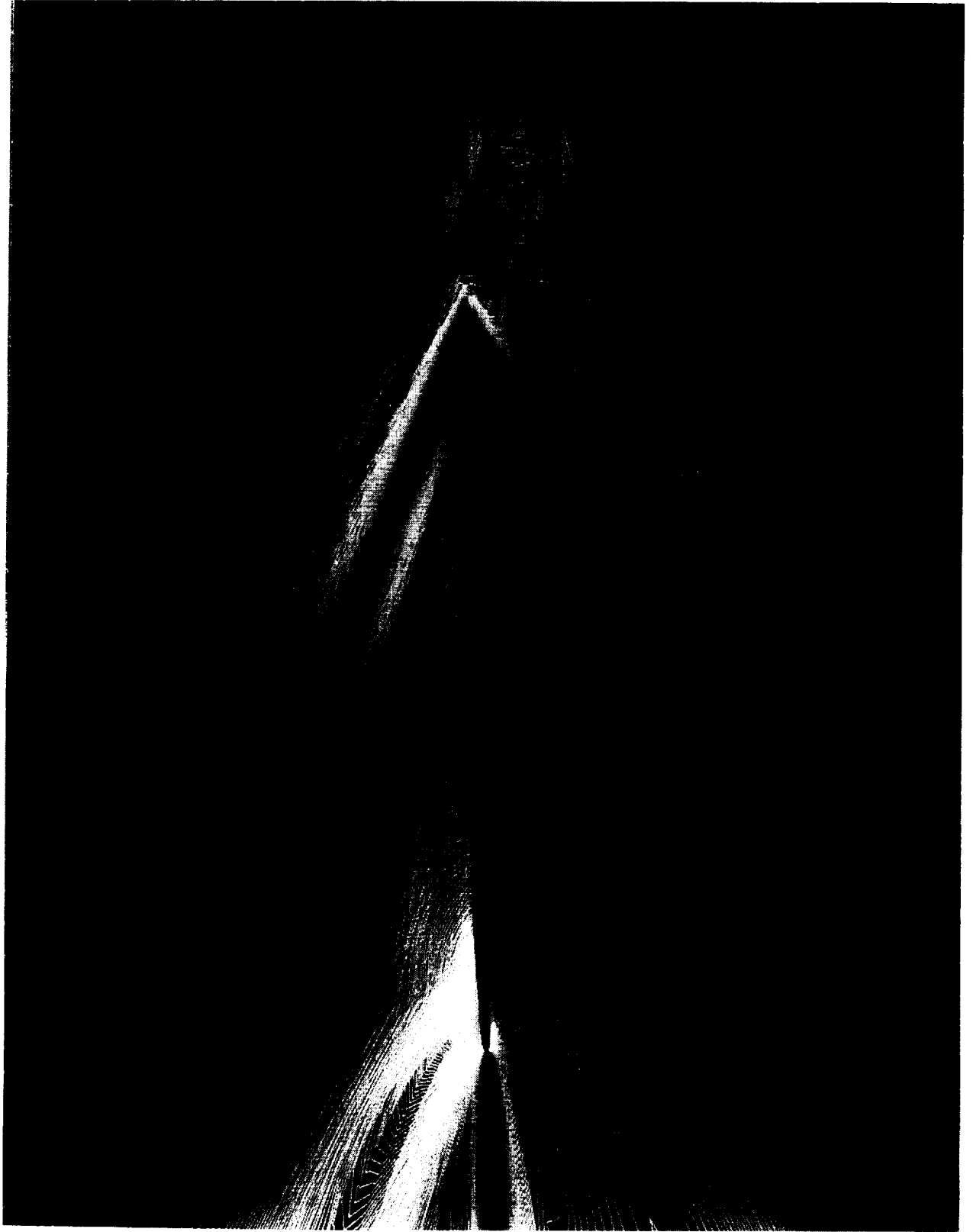
Additional SYN87 Design Variables

The Wagner functions have only recently been installed in SYN87 (along with flaps and slats), so some comparisons with the well-proven Hicks-Henne shape functions should be made soon. They may well permit working with fewer variables, which is always preferable. Some undesirable trailing edge ripples are known to be a possibility, though less so for airfoil perturbations than for least squares airfoil fitting applications.

The 2D experience at Ames with B-spline control points as design variables has been less than reassuring: they are much more inclined (than sine bumps) to admit oscillatory designs along the way, even if they can ultimately match known solutions more closely. Nevertheless, there remains the attraction of compatibility with CAD representations. Considerable work has been done on earlier projects in terms of determining accurate airfoil representations with moderate numbers of control points (via optimization of the knots as well as of the control point coordinates), along with utilities to manipulate such airfoil-type curves. Thus B-spline curves for SYN87 wing sections should be investigated at some stage, followed by B-spline surfaces.

I ploid





SYN87 Multi-Point Design

While it is clear what to do in order to optimize with respect to (say) two flight conditions at the same time, no such option has yet been incorporated in SYN87. Providing loops over the number of design points in all the right places would be straightforward and not too time-consuming, but the memory and CPU requirements would approximately double in the case of two design points. The adjoint gradients situation can fortunately be handled (in series) without complication.

Additional SYN87 Computer Platforms

As indicated above, the current SYN87 has yet to be ported to a parallel system. Given the encouraging progress with the adjoint-based gradients, it would appear to be a backward step to revert to the most obvious form of parallelization (doing the gradient elements in parallel by finite differences). Unless as many processors as design variables are available, the adjoint method still wins at this most coarse-grain level. Some room exists for parallelizing the line search, but for large numbers of variables the finite gradient calculations would still dominate. This leaves only some hope of achieving finer-grained parallelism within the flow and adjoint solvers than presently exists (judging by experiments with autotasking on the C90). Such autotasking studies may be pursued at Ames in the coming months.

Given that parallel computing must ultimately become the only road to ever-increasing computation speeds, there is no question that applications such as SYN87 need to be adapted in that direction. The advent of MPI (Message Passing Interface, which appears to be overtaking PVM as a supported, standardized environment) on both IBM and Cray systems is an encouraging development. The learning process can be started, and the code can remain portable.

- Add More Adjoint Boundary Condition and Source Terms to Treat Other Aerodynamic Objective Functions and Constraints (**Not Needed for HSR in Near Term but Allows Eventual Multi-Point Design**)
- **Design Variables**
 - Wagner Functions Need Exercising
 - Add B-Spline Curve Control Points
- **Computer Platforms**
 - Redo Earlier Port to the IBM SP2
 - IBM Version Should Also Run Under MPI on CRAY

Multiblock Adjoint Based Method (SYN87-MB)

Current Capabilities

SYN87-MB is currently a working multiblock adjoint-based design code which has been demonstrated most recently on a 72-block wing/body/nacelle transonic business jet application as described in report *AIAA 96-0094* presented at the January Reno conference. Designed from the start for parallel computation at the block level, and for full flexibility in terms of the configurations handled, this code is dramatically more complex than SYN87 (even though all of the latter's grid generation no longer applies).

Widespread (and intricate) use of pointers abounds throughout the higher levels to handle the multiple blocks and the multiple versions of each block necessitated by the multigrid convergence acceleration techniques, which have been carried over from FLO87 along with all of its other refined technology. Each multigrid level is applied across all blocks before moving to the next level. By virtue of a two-layer halo of cells around each block, the computed solutions are seamless at the block boundaries. The only effective difference from the single block solution is in the residual smoothing, which is confined to being done within each block only, and this slight difference has no visible effect on the solution convergence rate.

Initially, SYN87-MB required several times the memory of SYN87, but that situation has now been improved significantly. In fact the preprocessing stage under MPI brings the active memory requirements down to roughly the SYN87 level. Clearly much development lies ahead at this early stage, but a major step forward has been made in terms of refining full aircraft configurations efficiently using adjoint-based design by optimization.

The present multiblock code is in considerably better shape than the early SYN87 was at a comparable stage. Nevertheless, it is likely to remain in the hands of its developers (only) for the next couple of months before a production version can be released. The first application of SYN87-MB to supersonic transports is also expected during the next few months, in parallel with the single-block approach.

Further SYN87-MB Details

Much of the discussion for SYN87 above applies also to SYN87-MB, and will not be repeated. The following confines itself to the multiblock-specific issues.

Multiblock Adjoint Based Method (SYN87-MB)

Current Capabilities

- **Euler Flow Solver: FLO87-MB**
 - Inviscid Analysis and Design
 - Multiblock Cell Centered Finite Volume with Multigriding
- **Adjoint Solver: ADJ87-MB :**
 - Cheap Gradient Information
 - Multiblock Cell Centered Finite Volume with Multigriding
- **Grid Generation**
 - Previously Prepared Initial Multiblock Mesh
 - Any Point to Point Match Topology
 - Very Complex Geometries (Nacelle and Diverters Included)

Multiblock Flow Solver (FLO87-MB)

As mentioned above, the multiblock version of SYN87 uses a double-halo strategy which ensures that the complete convective and diffusive stencils used in the numerical scheme are fully supported even at block boundaries through halo updates that occur at every Runge-Kutta-like time stage. It is these halo updates which dominate the message passing in the parallelization of the method. In essence, each block determines its neighboring blocks and (when more than one processor has been specified) passes block boundary information into the halo of each neighbor whether it is assigned to another processor or not.

The cell identifiers for these local and halo elements are calculated in a preprocessor that can handle arbitrary point-to-point matched multiblock topologies and outputs the resultant pointer lists that are processor-specific. The preprocessor also determines the exact size of all the various arrays that are to be used in either single- or multiprocessor mode and creates an include file to be used for recompiling SYN87-MB. Since most of the workspace is stacked in a few very large 1-dimensional arrays in the upper levels of the program and accessed by pointers at the lower levels, the include file is only necessary at the top level, with all subsequent partitioning accomplished through argument lists. This necessitates only a very quick recompile of the top-level routines followed by a relink to create a new executable of the proper size. The alternative of switching to C++ and avoiding even this small amount of recompilation is under consideration.

Multiblock Adjoint Solver (ADJ87-MB)

The multiblock adjoint solver is identical to the multiblock flow solver in its use of the same data structures and pointer lists. The only difference is that the boundary and convective flux routines have been replaced with the adjoint equivalents.

Multiblock Grid Generation

Preparing the initial multiblock grid for SYN87-MB will remain a major hurdle in the absence of much more automated packages than the likes of GRIDGEN (not to detract from the latter's powerful capabilities). This phase seems to be inherently labor-intensive. The present code requires point-to-point matching at the block boundaries but is otherwise fully general. Note that SYN87-MB effectively perturbs grid faces rather than the usual separate underlying geometry definition.

Multiblock Grid Perturbation

The original 2-stage WARP3D algorithm was translated as WARPMB for SYN87-MB and so far has appeared adequate. It still treats just one block at a time, relying on information from the higher level about neighboring blocks to determine any implicit edge perturbations and implicit face perturbations before applying the single-block algorithm.

- **Grid Perturbation: WARP3D-MB**

- Generalized Algebraic Scheme Applied Block By Block Following Explicit Block Face Perturbations
 1. Perturb Edges Implicitly Affected by Corner Motion
 2. Perturb Faces Implicitly Affected by Edge Motion
 3. Apply WARP3D 3-Stage Procedure to Interior Points
- Each Internal Point is Dependent on the Motion of the 8 Corner Points and 6 Face Points
- Very Robust and Efficient

- **Optimization Algorithm: Unconstrained Quasi-Newton (QNMDIF)**

- **Objective Functions**

- Target Pressure Distribution
- Drag at Fixed Lift

Optimization Algorithm

SYN87-MB presently uses not QNMDIF2 but rather the (less polished, but equivalent) version of QNMDIF from the early SYN87. The switch will be made some time before the first IISR production version is released.

Multiblock Design Variables

Application of perturbations to arbitrary block faces has required another layer of complexity over SYN87's scheme. Given shape functions may need to span block boundaries, and given faces may be perturbed in either or both of the relevant index directions. For instance, a design variable may impose a Hicks-Henne shape function in one direction and linear lofting in the other, or it could just as easily be specified to apply Hicks-Henne shape functions in both directions. Also, the directions of the perturbations can be specified so that either camber or thickness is preserved if opposing faces are treated appropriately.

Given that computational surface grids rather than geometry data are to be perturbed (implying many more than the traditional number of shape function evaluations), some new efficiency was called for. This has been implemented in the form of normalized shape function evaluations done once and stored at the start of a run. Subsequent perturbations simply apply the appropriate multiples of these stored evaluations; repeated trigonometric calculations are thus avoided.

Presently, the Hicks-Henne shape functions are supported (in any index direction), along with polynomial-type power functions. More design variables need to be incorporated in the near future.

Multiblock Computer Platforms

At present, the IBM SP2 version of SYN87-MB may be run on a Cray under UNICOS by specifying a single processor at run time—the code distinguishes this case efficiently and avoids unnecessary MPI calls. MPI is not yet available at Ames but is anticipated in the near future. It will then be possible to use multiple Cray processors without resorting to autotasking, which has proved unsatisfactory in the single-block SYN87 case. SYN87-MB scales remarkably well on the IBM SP2 as shown in Figure 8.

- **Design Variables**

- Hicks-Henne Functions in Any Direction
- Polynomials in Any Direction
- Multiple Faces Modified By Same Variable

- **Computer Platforms**

- CRAY C90
- IBM SP2 (Medium Grain—Domain Decomposition Along Block Boundaries)

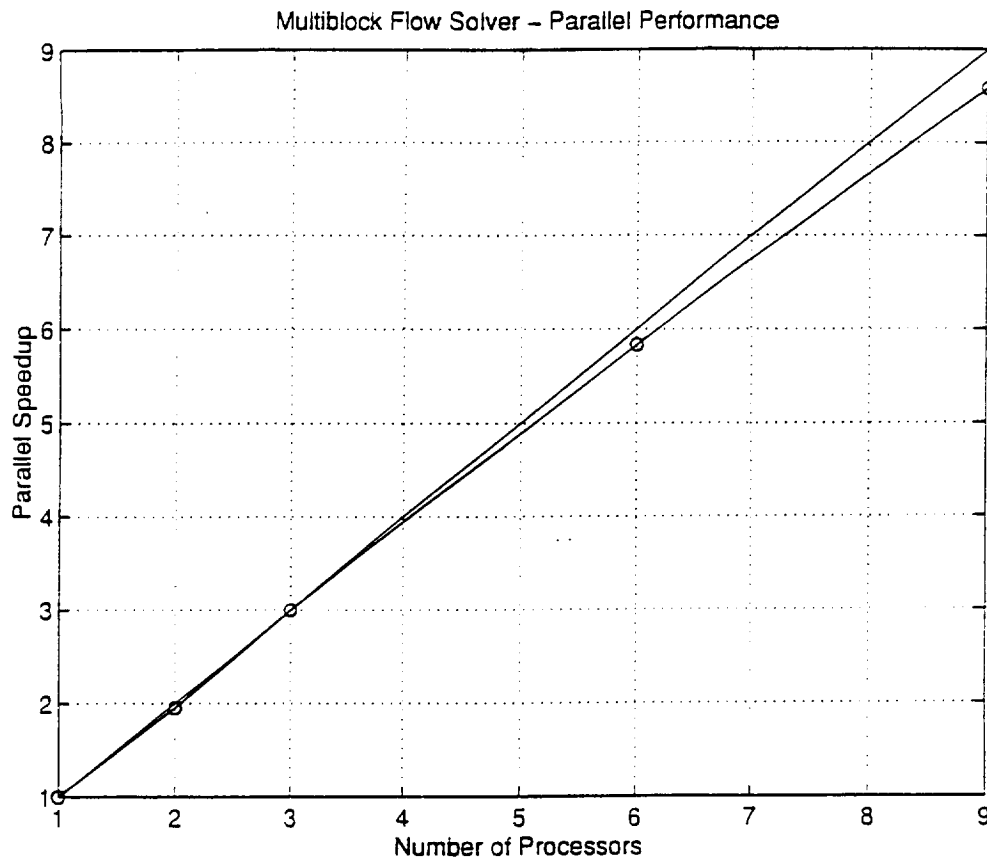


Figure 8

Multiblock Gradient Comparison

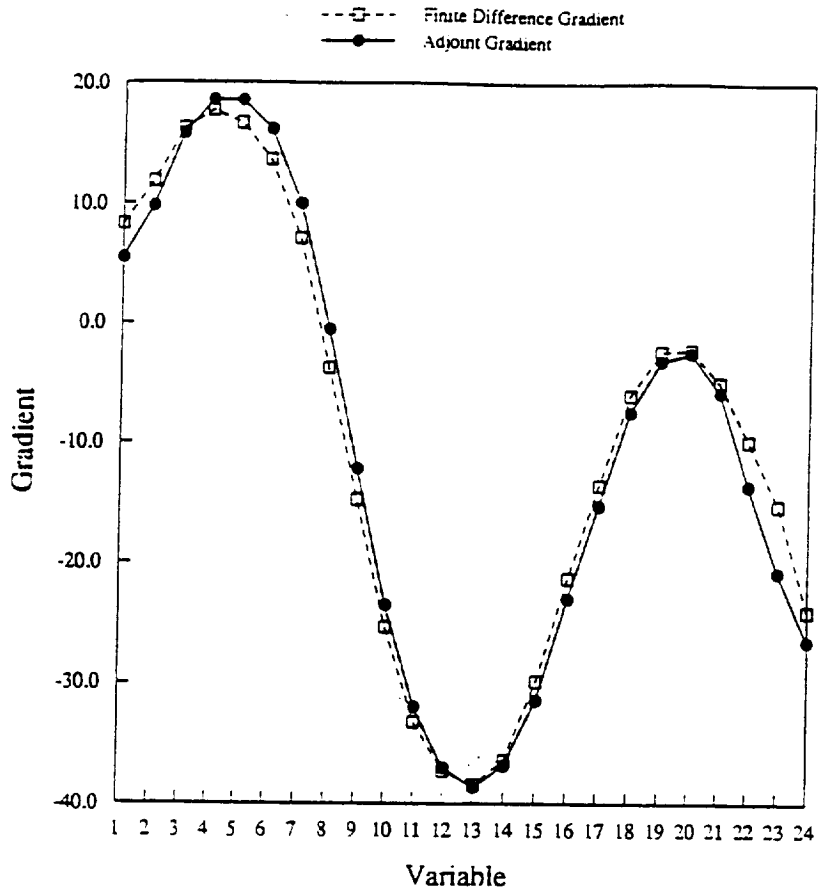
While SYN87-MB has been applied successfully in adjoint mode to minimization of drag, only target pressure gradient comparisons have been made at this stage. Figure 9 shows the kind of agreement obtained for the 72-block transonic business jet case—very good considering the infancy of the code and the fact that the flow solver was converged just 4.5 orders in both finite difference and adjoint modes, with 2.0 orders for the adjoint solver. These 24 Hicks-Henne sine bumps were centered at the 0.44 span station and lofted linearly spanwise. This case actually employed 250 design variables, for which the adjoint gradient took just 37 minutes of C90 single-processor CPU time. The comparable finite difference gradient would have taken at least 17 CPU hours.

Multiblock Planned Improvements

The problem of perturbing intersecting block faces (such as at wing/body junctions) has yet to be addressed. Implementing it in a truly general fashion promises to be a significant challenge. In fact a more general means of tracking perturbed blocks and their impact on neighboring blocks is initially required, since currently the user is forced to determine this by hand. The development of such a general procedure is under way and it should be available in the near future.

The grid perturbation scheme (for interior points) is also known in this context of arbitrary boundaries to need an additional level of complexity involving perturbation components normal to the local cell faces as opposed to simply the global coordinate system as is the case now for both the single- and multiblock implementations.

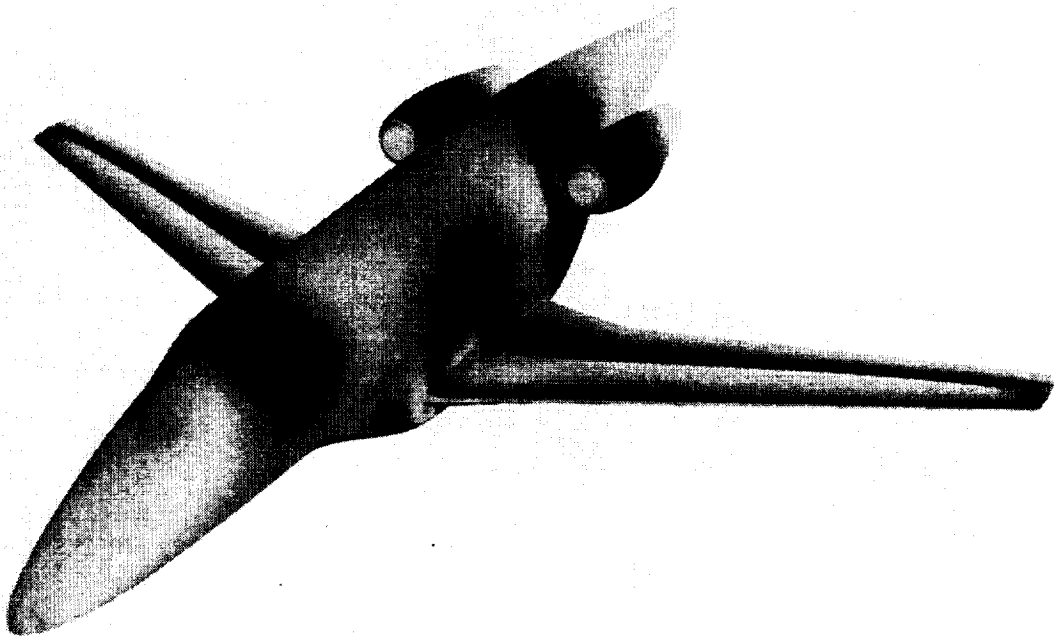
Design variable enhancement possibilities include the Wagner functions and B-spline surfaces.



Comparison of Gradients for 24 Discrete Design Variables
 Adjoint vs. Finite Differences
 Design Variables Span the Upper Surface at a Span Station of 0.44
 Beginning at the Leading Edge and Ending at The Trailing Edge

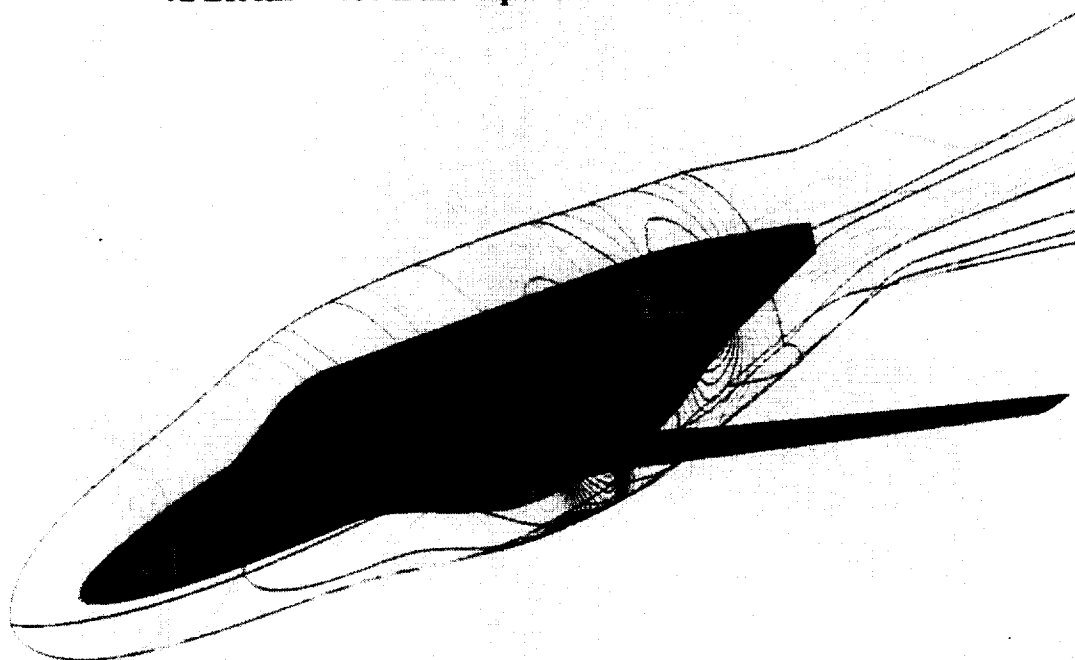
Figure 9

SYN87-MB Solution on a typical business jet
72 Blocks - 750 k mesh points - Mach=0.80 - CL=0.30



RLACS/Reuther

SYN87-MB Solution on a typical business jet
72 Blocks - 750 k mesh points - Mach=0.80 - CL=0.30



LEAP3D Results

Planned Improvements

- **Grid Perturbation**

- Perturbation Along Original Normals Scheme
- Internal Surface/Surface Intersection Calculation
- Automated Perturbed Block Identification

- **Optimization Algorithm**

- Add NPSOL Constrained Quasi-Newton/Augmented Lagrangian Method
- Add Geometric Constraint Routines (**No Adjoint or Flow Solver Modifications are Necessary**)
- Add More Adjoint Boundary Condition and Source Terms to Treat Other Aerodynamic Objective Functions and Constraints (**Not Needed for HSR in Near Term but Supports Extension to Multi-Point Problems**)

- **Design Variables**

- Add Wagner Functions
- Add B-Spline Surface Control Points

- **Computer Platforms**

- MPI on CRAY Instead of Autotasking

AFTBODY CLOSURE EFFECTS ON THE REFERENCE H CONFIGURATION AT SUBSONIC AND TRANSONIC SPEEDS

Richard A. Wahls, NASA LaRC
Lewis R. Owens, Jr., NASA LaRC
W. Kelly Londenberg, Vigyan, Inc.

February 28, 1996

Experience with afterbody closure effects and accompanying test techniques issues on a High Speed Civil Transport (HSCT)-class configuration is described. An experimental data base has been developed which includes force, moment, and surface pressure data for the High Speed Research (HSR) Reference H configuration with a closed afterbody at subsonic and transonic speeds, and with a cylindrical afterbody at transonic and supersonic speeds. A supporting computational study has been performed using the USM3D unstructured Euler solver for the purposes of computational fluid dynamics (CFD) method assessment and model support system interference assessment with a focus on lower blade mount effects on longitudinal data at transonic speeds.

Test technique issues related to a lower blade sting mount strategy are described based on experience in the National Transonic Facility (NTF). The assessment and application of the USM3D code to the afterbody/sting interference problem is discussed. Finally, status and plans to address critical test technique issues and for continuation of the computational study are presented.

Experimental Studies

- Models
 - 1.675% with cylindrical aftbody on straight sting mount
 - 2.2% with closed aftbody on lower blade sting
- Focus on blade mount test technique to date
- Critical Test Technique
 - Cavity seal at blade mount entry point
 - tough design problem in cryo environment
 - previous subsonic transport experience
 - lateral/directional requirements magnify the problem
 - transonic conditions more problematic than $M = 0.3$

Two high-speed models of the HSR Reference H configuration were identified to be part of this study. The first is a 1.675% scale model, sometimes referred to as the modular or controls model, has been tested at transonic speeds in the NASA Langley 16' TT and at supersonic speeds in the NASA Langley UPWT; tests of this model included configurations with a cylindrical aftbody mounted on a straight sting. The second model is the 2.2% scale model, sometimes referred to as the NTF model, which has been tested at low subsonic ($M=0.3$) and transonic conditions over a large R_n range in the NTF at NASA Langley; tests of this model included configurations with a closed aftbody mounted on a lower blade sting. The primary focus to date has been on the 2.2% model and issues relative to the blade mount strategy.

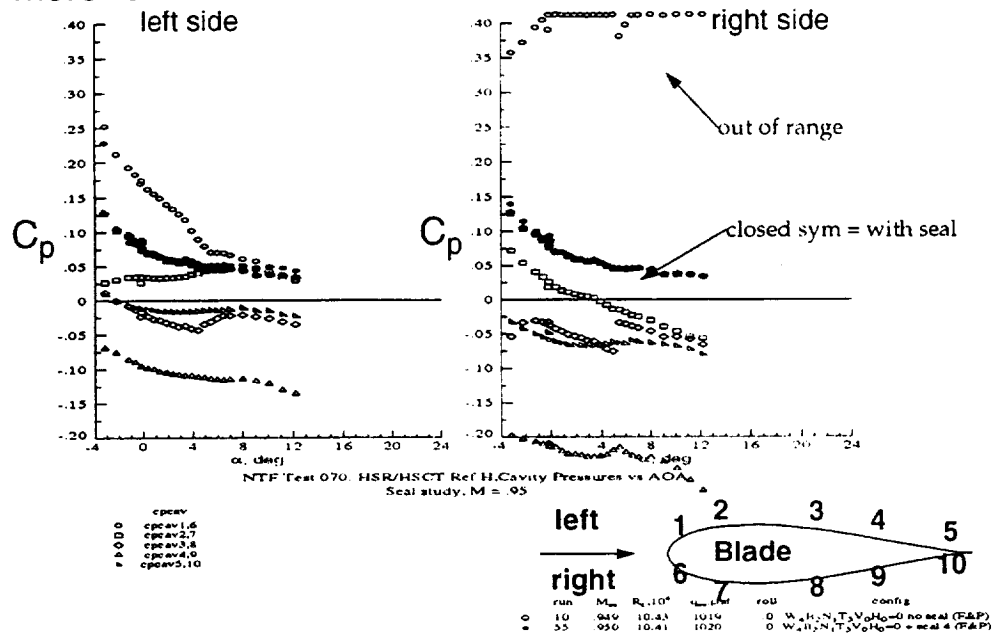
The most critical test technique associated with the blade mount testing in the NTF was the use of a seal, or flow blocker, over the gap between the model and the blade at the blade entry point. Previous seal development applicable to longitudinal, subsonic transport testing served as a starting point; the present problem has proven to be even more difficult due to a larger blade and model-to-blade gap due to the requirements of lateral/directional testing, and to the higher Mach number requirements. The seal was observed to survive significantly better at $M=0.3$ conditions.



This figure shows the 2.2%HSR Reference H model in the NTF test section. The configuration shown includes the closed aftbody and is mounted on the lower blade sting. From the perspective shown in the figure, the location of the blade entry into the model is visible.

Seal Effect on Cavity Pressures

- more realistic to correct data with the seal

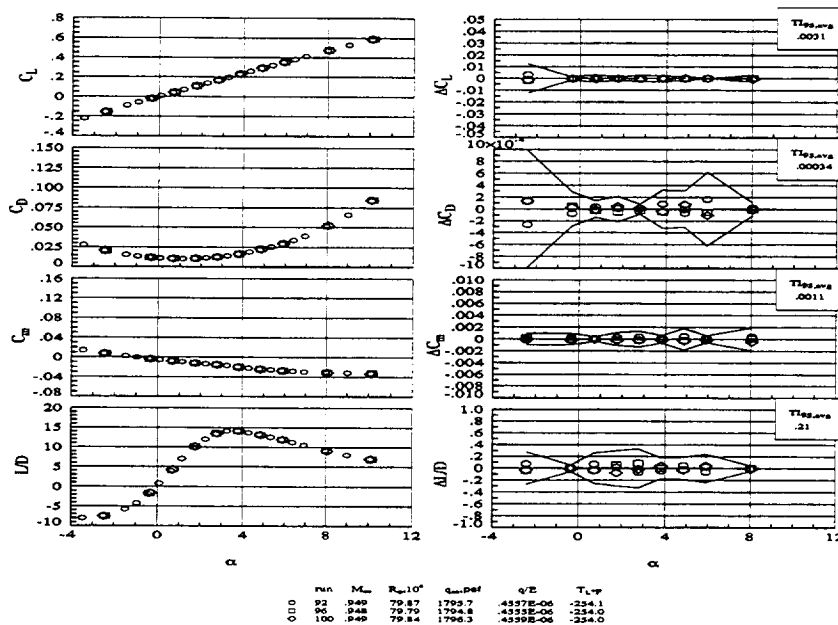


The seal was constructed of Kapton wrapped around a poly-fiber fill material; the thickness of the Kapton and the density of the fill material varied throughout the testing as the design evolved. In addition, a brass shim was eventually used to reduce the gap width.

The seal design requires a trade-off between a perfect flow blocker which bridges the metric break but allows no internal flow, and an open cavity which does not affect the metric break but allows unknown internal flow and resulting forces. The compromise is a seal that minimizes flow into the cavity with minimal fouling effect. The result is a slightly ventilated cavity that has an internal pressure level which may vary with angle of attack while maintaining an internal pressure gradient near zero at any given angle of attack. A correction for the internal pressure is applied over the area of the model/blade interface. The figure shows the different character of the pressures distributed on the blade within the cavity both with and without a seal; it is clear that the sealed cavity is more easily correctable from a pressure perspective. However, some soft fouling was evident.

Representative Within Test Repeatability - NTF070

- good repeatability observed within tests and test to test



Repeatability within each of the two tests using the lower blade mount, and from test to test, was good. The figure shows a representative data set used for within test (NTF070) repeatability. The analysis was performed by fitting each of the 3 polars individually, interpolating to constant angles-of-attack, and generating residuals about the average at each angle. The tolerance interval statistically quantifies the observed scatter of the small sample by defining a range which captures 95% of the data at each local angle (note, the 2 sigma band is roughly half due to the small sample used here). The repeatability during previous tests on the straight sting mount, with a truncated aftbody, were generally better. The most probable degrading factor associated with the blade mount is the current cavity seal design and resulting soft and inconsistent fouling.

Computational Studies

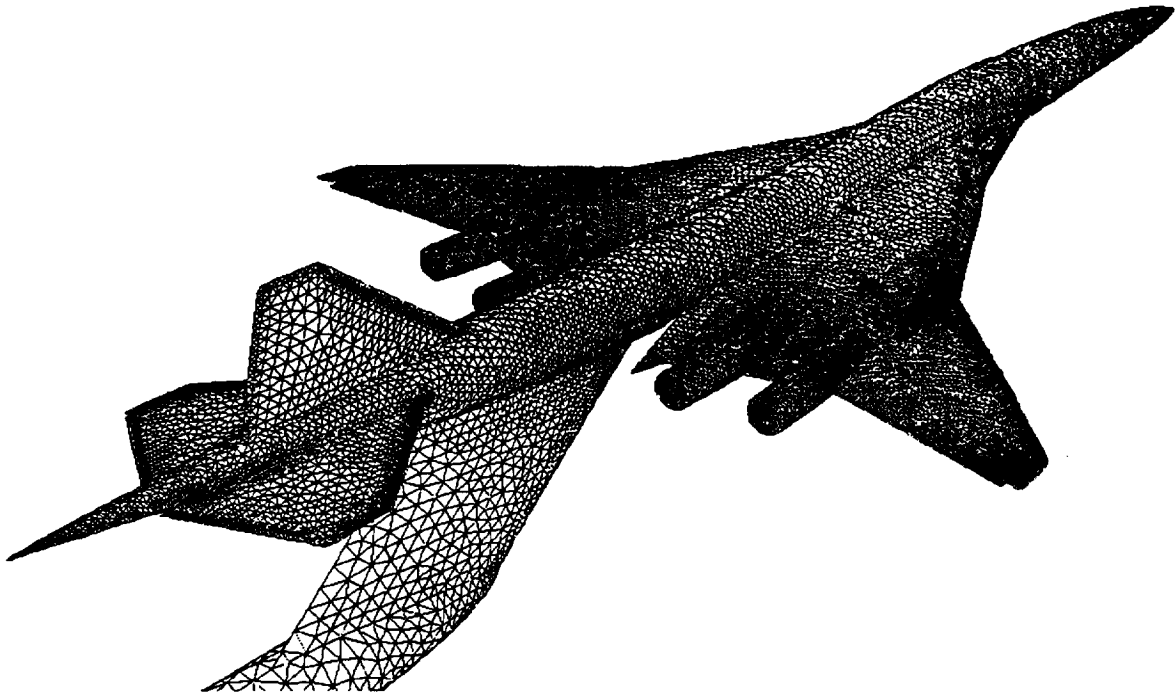
- . Multiple Grids
 - cylindrical aftbody and straight sting
 - closed aftbody and lower blade sting
 - closed aftbody without sting
- . Code Assessment
 - 2.2% model is testbed
 - comparisons of surface pressure and force data
 - wing pressures from truncated aftbody configuration
- . Sting Interference Assessment
 - increments generated by comparison of blade mounted solutions with free-air solutions
 - no viscous, static aeroelastics, or wall effects taken into account

Multiple unstructured grids were generated for use in this study. These grids included full configurations with either cylindrical aftbody and straight sting, closed aftbody and lower blade, or closed aftbody and no support. Flap settings included high-lift (30/20), transonic cruise (10/3 outboard), and supersonic cruise (0/0). The stabilizer settings included 0 and -5 deg. Grid size ranged from approximately 96k points with 505k cells for the no flaps, no sting case to approximately 223k points with 1230k cells for high-lift flaps with the blade sting.

Code assessments were based on comparisons of surface pressure and force data acquired with the 2.2% model; wing pressures were obtained on a truncated aftbody configuration, while all other data was obtained with the closed aftbody and lower blade sting.

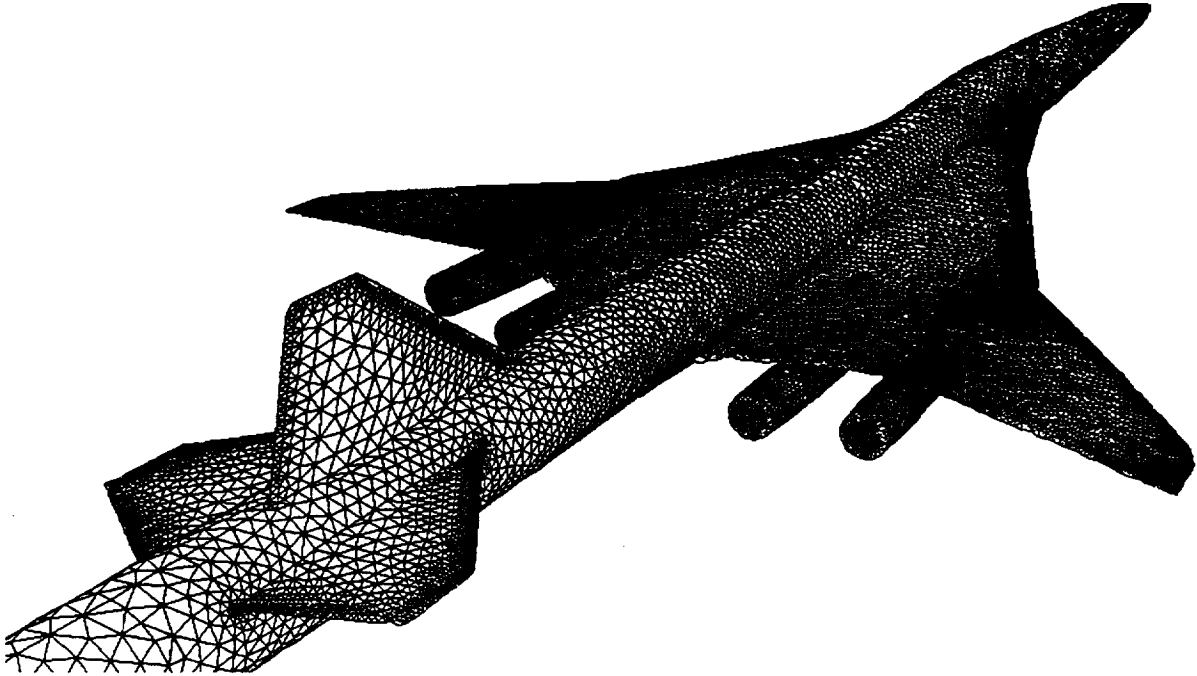
Blade interference effects were determined by comparison of blade mounted and free air solutions; static aeroelastic and wall effects are not taken into account. In addition, viscous effects are not taken into account because the computations are inviscid.

Reference H with Blade Sting Surface Grid



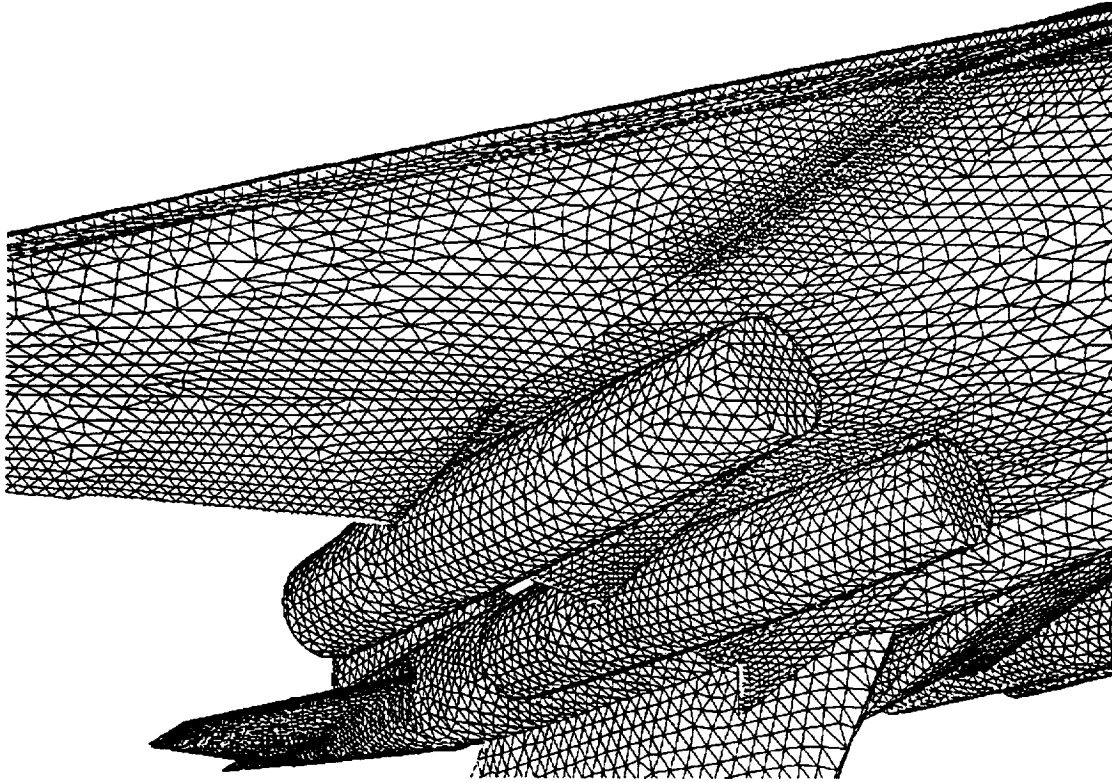
This mirrored image view of the semi-span surface grid for the HSR Reference H configuration with the blade sting was created using the GRIDTOOL and VGRID software. This geometry incorporates a 30° full span leading-edge flap deflection and all trailing-edge flaps deflected 20°.

Circular Sting/Aft-body Surface Grid



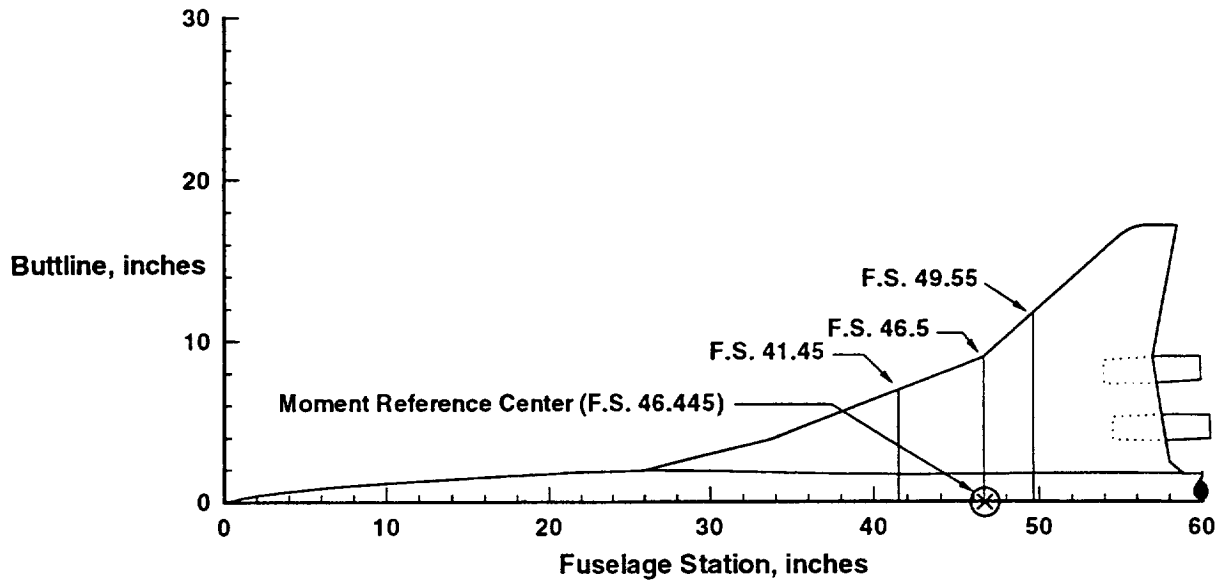
This mirrored image view of the semi-span surface grid for the HSR Reference H configuration with the circular sting/aft-body was created using the GRIDTOOL and VGRID software. This geometry incorporates a 10° outboard leading-edge flap deflection and outboard trailing-edge flaps deflected 3°.

Lower Surface Wing Grid Close-up



This mirrored image close-up view of the semi-span surface grid for the HSR Reference H configuration with the blade sting was created using the GRIDTOOL and VGRID software. This geometry incorporates a 30° full span leading-edge flap deflection and all trailing-edge flaps deflected 20°. The nacelle internal geometry was not modeled. However, flow through boundary conditions were set at the inlet and nozzle faces.

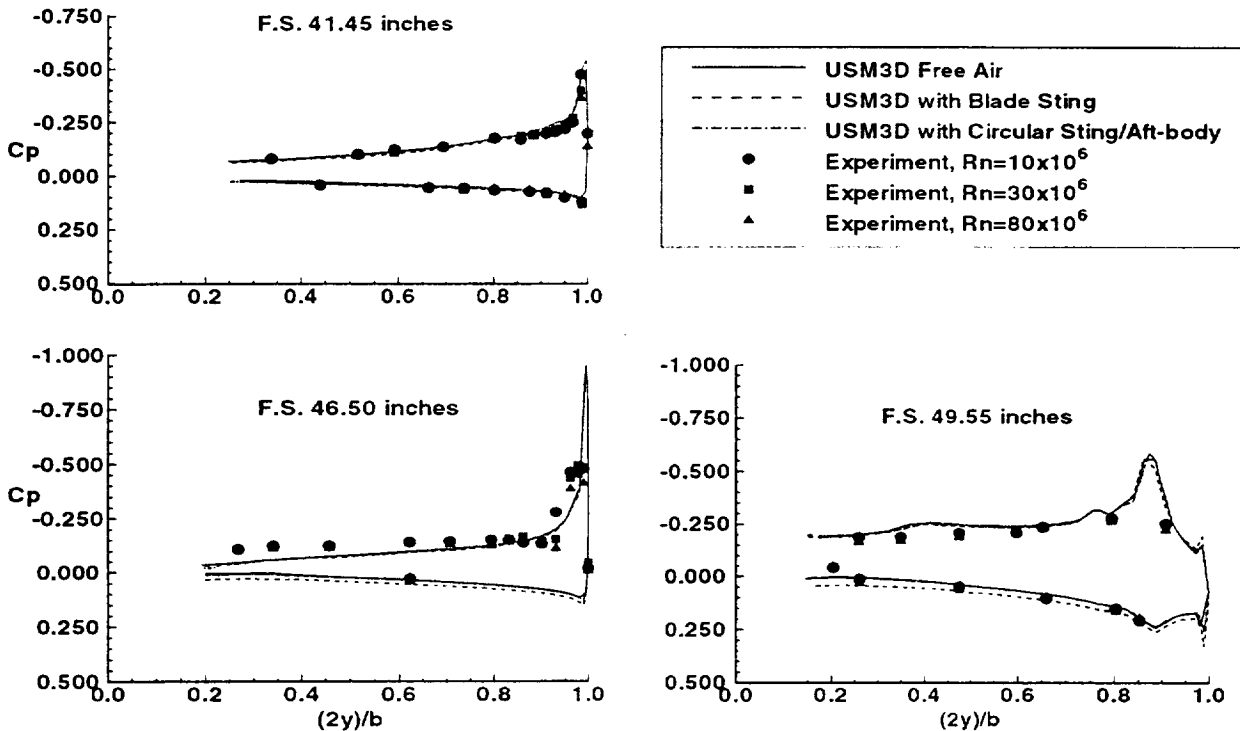
HSR Reference H Planform View



Experimental wing pressures were obtained at the three fuselage stations indicated. The dimensions shown are in model scale coordinates (2.2% full scale). The location of the model moment reference center is also indicated.

Pressure Coefficient Comparisons

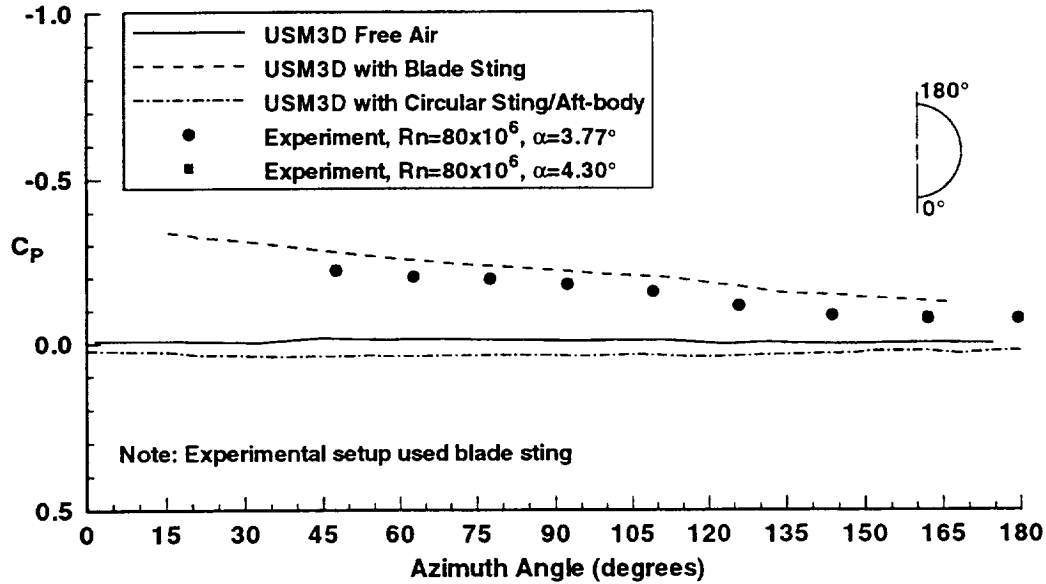
$\delta_{HT}=0^\circ, \delta_{LE}=0^\circ/10^\circ, \delta_{TE}=0^\circ/3^\circ, \alpha=4^\circ, M=0.95$



Comparisons with unpublished experimental data (obtained in the NTF) shows that the theory predicts the experimental data fairly well. The experimental pressures were only measured for a 2.2% scale truncated fuselage geometry. Higher suction pressures around the leading-edge are predicted by the theory than is apparent in the experimental data, but this is typical of an Euler solver. Notice that the results for the three geometries analyzed show very similar predictions for the upper surface pressures while the analysis of the blade sting shows some effect on the lower surface pressures. These results are typical of those obtained throughout the angle-of-attack range analyzed.

Fuselage Pressure Coefficient Comparisons, F.S. 65.306

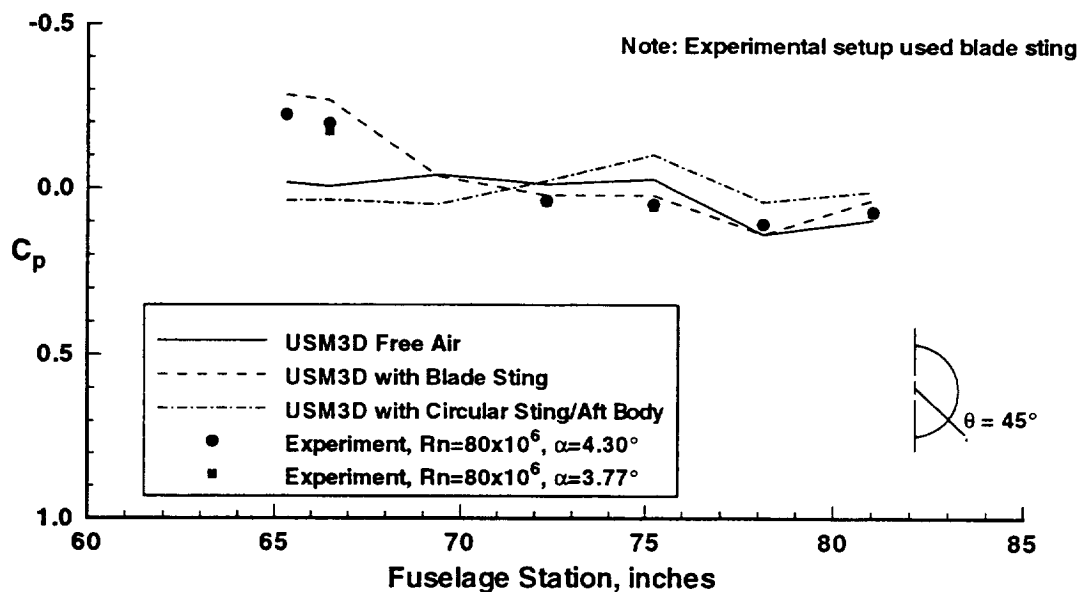
$\delta_{HT}=0^\circ$, $\delta_{LE}=0^\circ/10^\circ$, $\delta_{TE}=0^\circ/3^\circ$, $\alpha=4^\circ$, $M=0.95$



Predicted fuselage surface pressure coefficients for the configuration with the blade sting modeled agree well with NTF experimental data. Note that the computational method is predicting the break in the experimental data between azimuth angles of 105° and 150°. Notice also the significant effect of the blade geometry in the predicted surface pressures. It is expected that the blade is also causing a similar effect in the experimental pressures based upon the agreement between the predicted and calculated blade sting geometry fuselage surface pressures. Again, the comparisons are similar throughout the angle-of-attack range analyzed.

Fuselage Pressure Coefficient Comparisons, $\theta = 45^\circ$

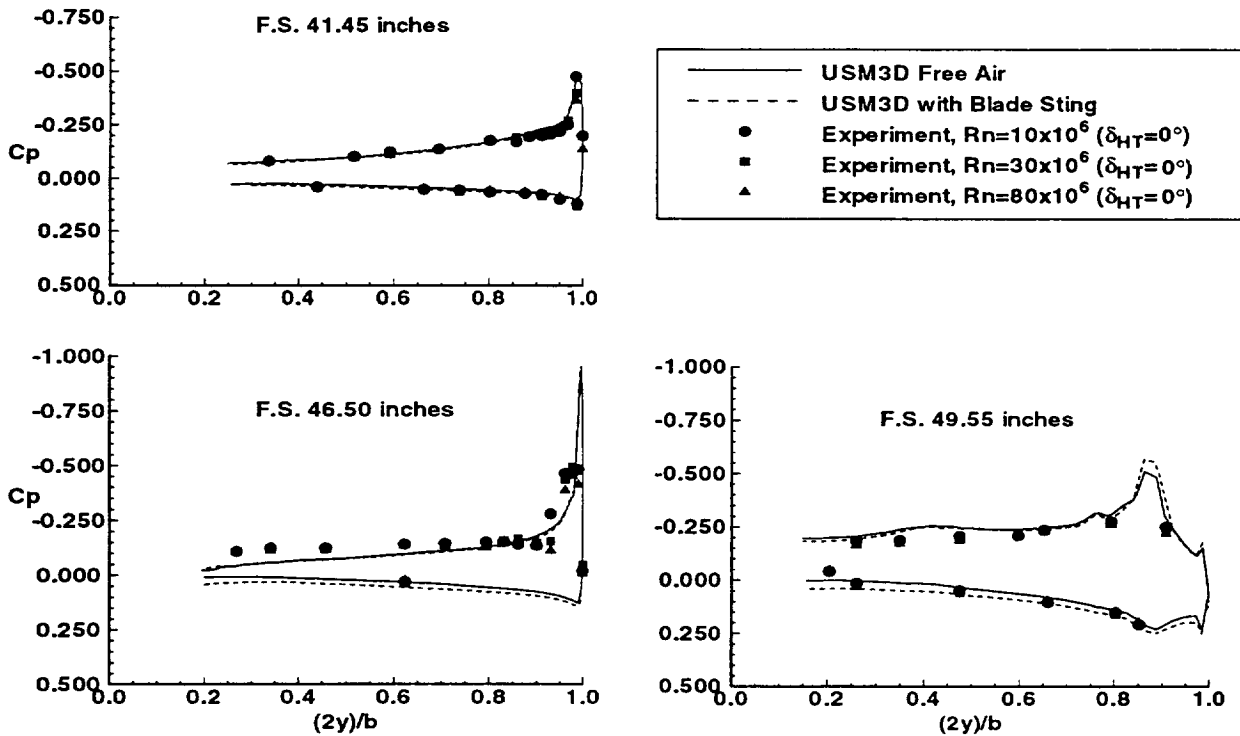
$\delta_{HT}=0^\circ$, $\delta_{LE}=0^\circ/10^\circ$, $\delta_{TE}=0^\circ/3^\circ$, $\alpha=4^\circ$, $M=0.95$



Predicted fuselage pressures coefficients for the blade sting geometry compare well with NTF experimental pressures along a line 45° from the lower plane of symmetry. The effect of the blade sting dissipates by F.S. 78 where the free air and blade sting solutions agree equally as well with the experimental data. There is a significant difference between the circular sting/aft-body and free air results.

Pressure Coefficient Comparisons

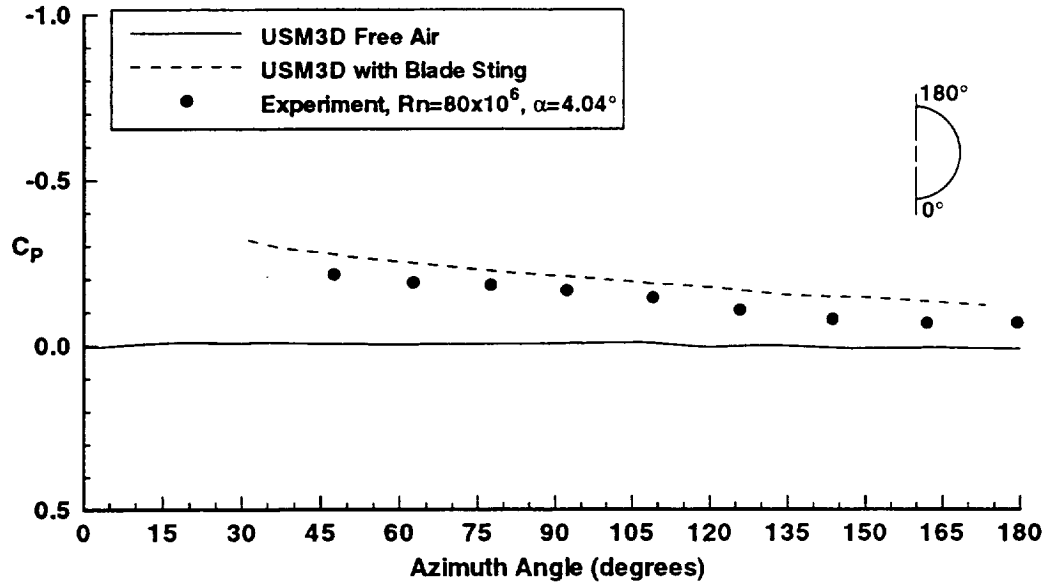
$\delta_{HT} = -5^\circ$, $\delta_{LE} = 0^\circ/10^\circ$, $\delta_{TE} = 0^\circ/3^\circ$, $\alpha = 4^\circ$, $M = 0.95$



Deflection of the horizontal tail is not expected to affect the wing surface pressures so comparisons of predicted pressures for a -5° horizontal tail deflection are made with the experimental data from the truncated fuselage geometry. The Euler predictions again compare well with experiment.

Fuselage Pressure Coefficient Comparisons, F.S. 65.306

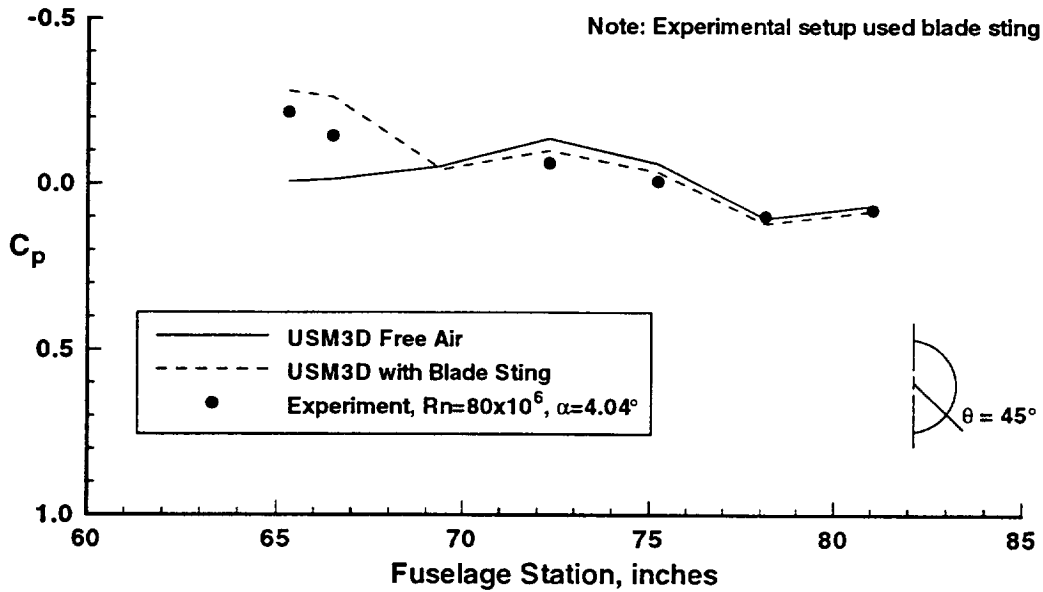
$\delta_{HT}=-5^\circ$, $\delta_{LE}=0^\circ/10^\circ$, $\delta_{TE}=0^\circ/3^\circ$, $\alpha=4^\circ$, $M=0.95$



Predicted fuselage surface pressures compare well with experimental data obtained in the NTF for the reference H model with horizontal tail deflected -5° and with the blade sting.

Fuselage Pressure Coefficient Comparisons, $\theta = 45^\circ$

$\delta_{HT} = -5^\circ$, $\delta_{LE} = 0^\circ/10^\circ$, $\delta_{TE} = 0^\circ/3^\circ$, $\alpha = 4^\circ$, $M = 0.95$

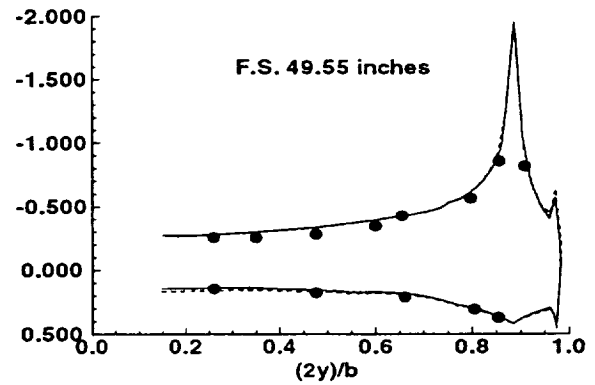
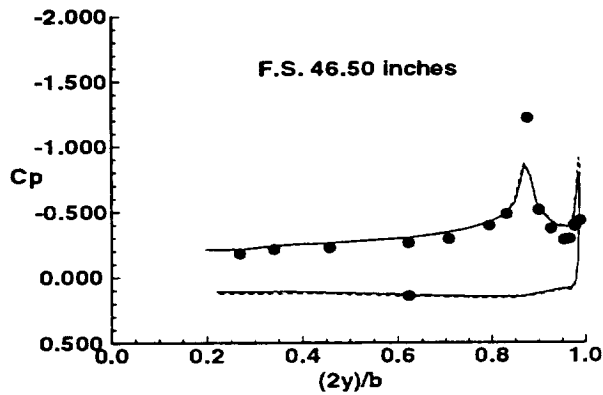
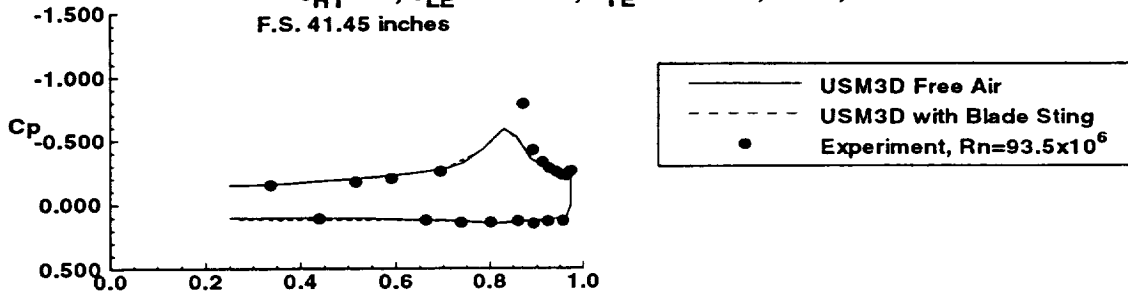


The theoretical method predicts the effect of the deflected horizontal tail on the aft fuselage surface pressures well.

Pressure Coefficient Comparisons

$\delta_{HT}=0^\circ$, $\delta_{LE}=30^\circ/30^\circ$, $\delta_{TE}=20^\circ/20^\circ$, $\alpha=6^\circ$, $M=0.30$

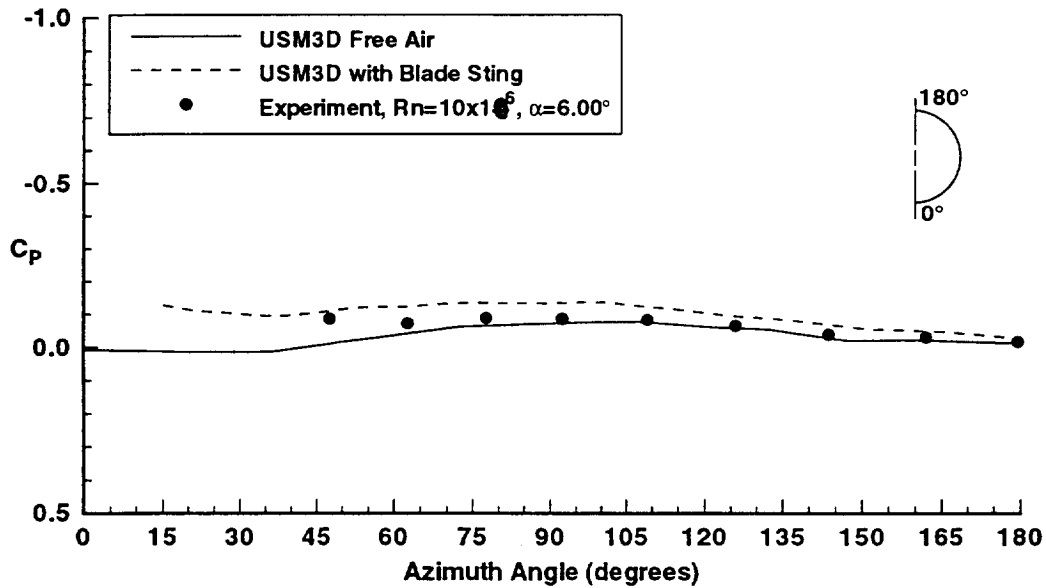
F.S. 41.45 inches



Computed subsonic results at 6° angle-of-attack compare well with experiment. In both the experiment and in the computational model full-span leading-edge flaps are deflected 30° and the all trailing-edge flaps are deflected down 20° and the horizontal tail is undeflected. The theory predicts an over expansion around the leading edge but this is typical of an Euler solver. The presence of the blade sting has very little effect on the computed wing pressure coefficients.

Fuselage Pressure Coefficient Comparisons, F.S. 65.306

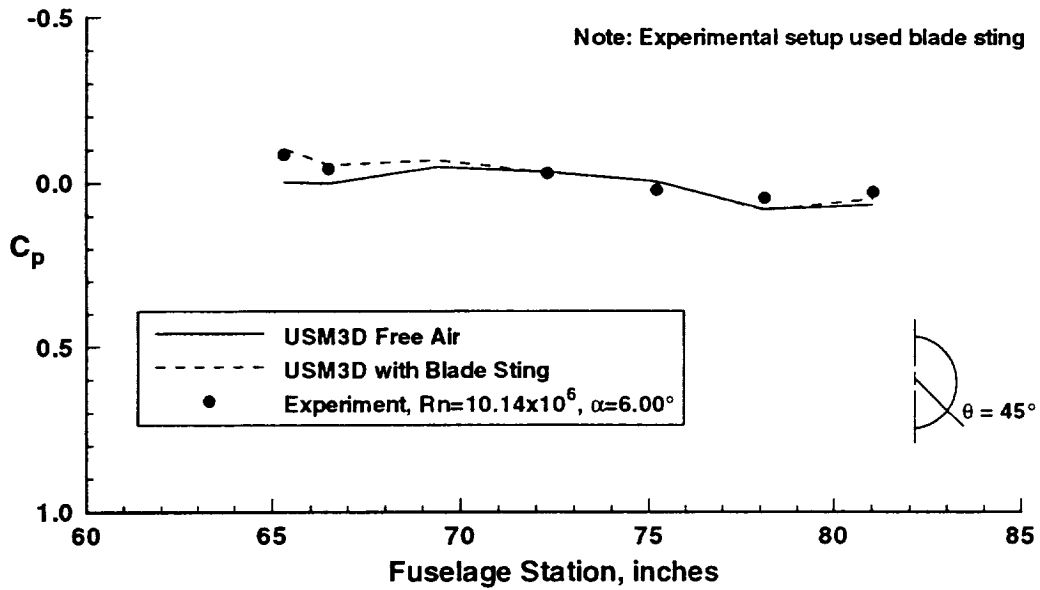
$\delta_{HT}=0^\circ$, $\delta_{LE}=30^\circ/30^\circ$, $\delta_{TE}=20^\circ/20^\circ$, $\alpha=6^\circ$, $M=0.30$



There is good comparison between predicted and experimental fuselage surface pressures with full-span leading-edge flaps deflected 30° and all trailing-edge flaps deflected 20°. However, there is much less of an effect of the blade sting on in the predicted surface pressures than was evident in the transonic solutions.

Fuselage Pressure Coefficient Comparisons, $\theta = 45^\circ$

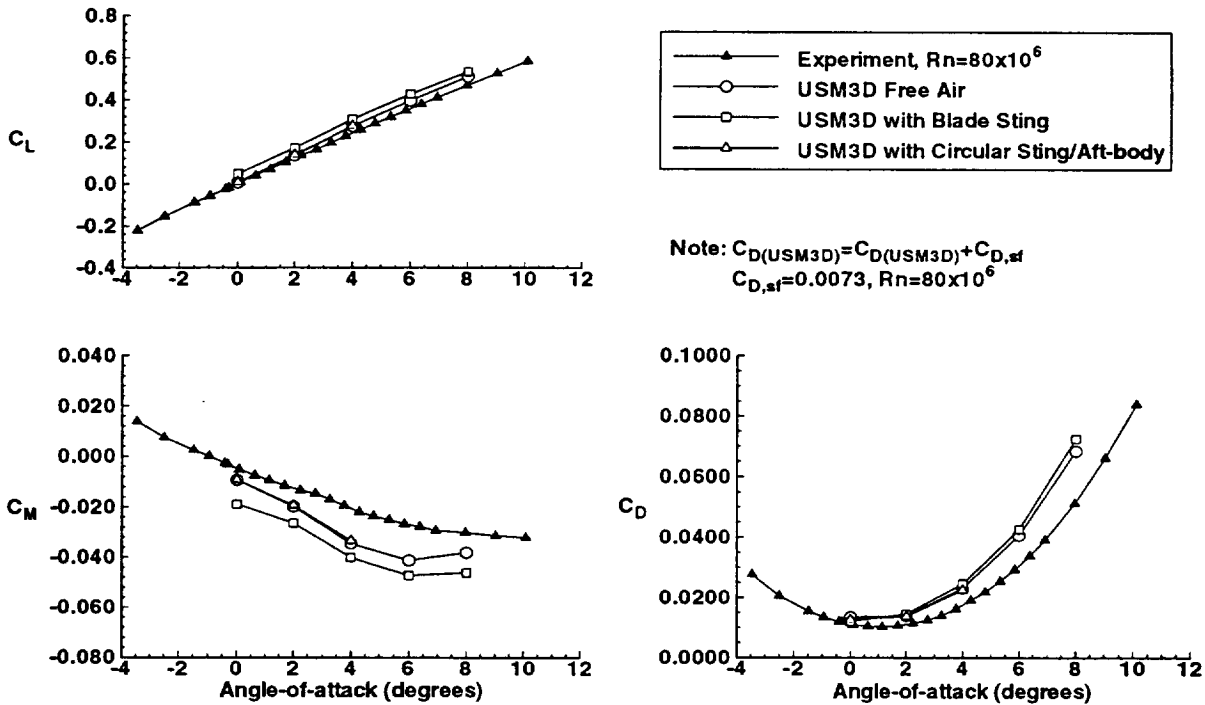
$\delta_{HT}=0^\circ$, $\delta_{LE}=30^\circ/30^\circ$, $\delta_{TE}=20^\circ/20^\circ$, $\alpha=6^\circ$, $M=0.30$



The effect of the sting on aft-body surface pressures is predicted well. Effects of the blade sting dissipate very quickly aft of the blade sting/fuselage intersection.

Force and Moment Comparisons

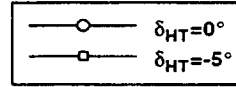
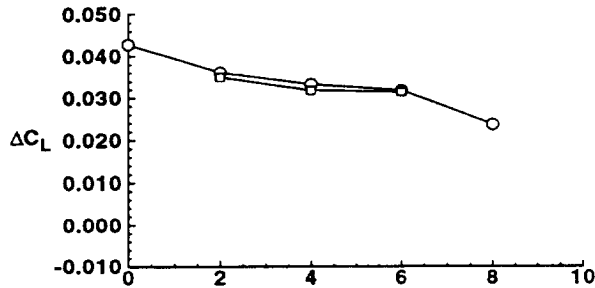
$\delta_{HT}=0^\circ$, $\delta_{LE}=0^\circ/10^\circ$, $\delta_{TE}=0^\circ/3^\circ$, $M=0.95$



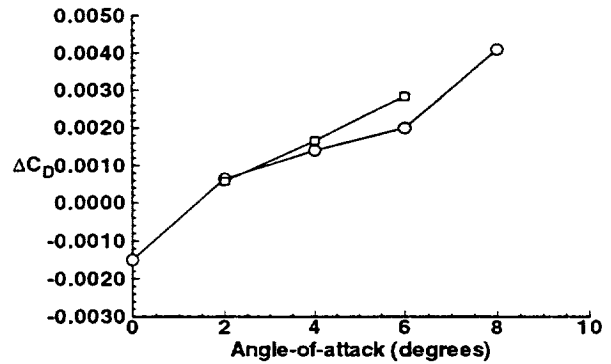
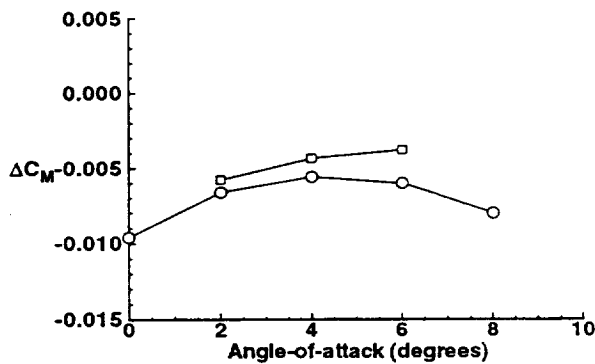
Comparisons of predicted lift, drag and pitching moment with unpublished experimental values are shown here. The experimental data has not been corrected for aeroelastic effects. The Euler method predicts higher lift coefficient levels and more negative pitching moments than observed in the experiment. These differences are consistent with those resulting from small aeroelastic effects. However, the trends of both lift and pitching moment with angle-of-attack are captured in the computed results. An increase in drag is also predicted at each angle-of-attack over the experimental level as would be expected with an over prediction of lift. (Note that the equivalent flat plate skin friction drag coefficient for eighty million Reynolds number has been added to the predicted drag coefficients.) It is also shown that the values predicted for the configuration with the circular sting/aft-body are in good agreement with the free air predictions

Predicted Blade Sting Force and Moment Increments

$\delta_{HT}=0^\circ$, $\delta_{LE}=0^\circ/10^\circ$, $\delta_{TE}=0^\circ/3^\circ$, $M=0.95$
 $(\Delta = \text{Sting results} - \text{Free air results})$



Note: Solution at $\alpha=8^\circ$ obtained using Flux Vector Splitting and First Order Boundary Condition interpolation



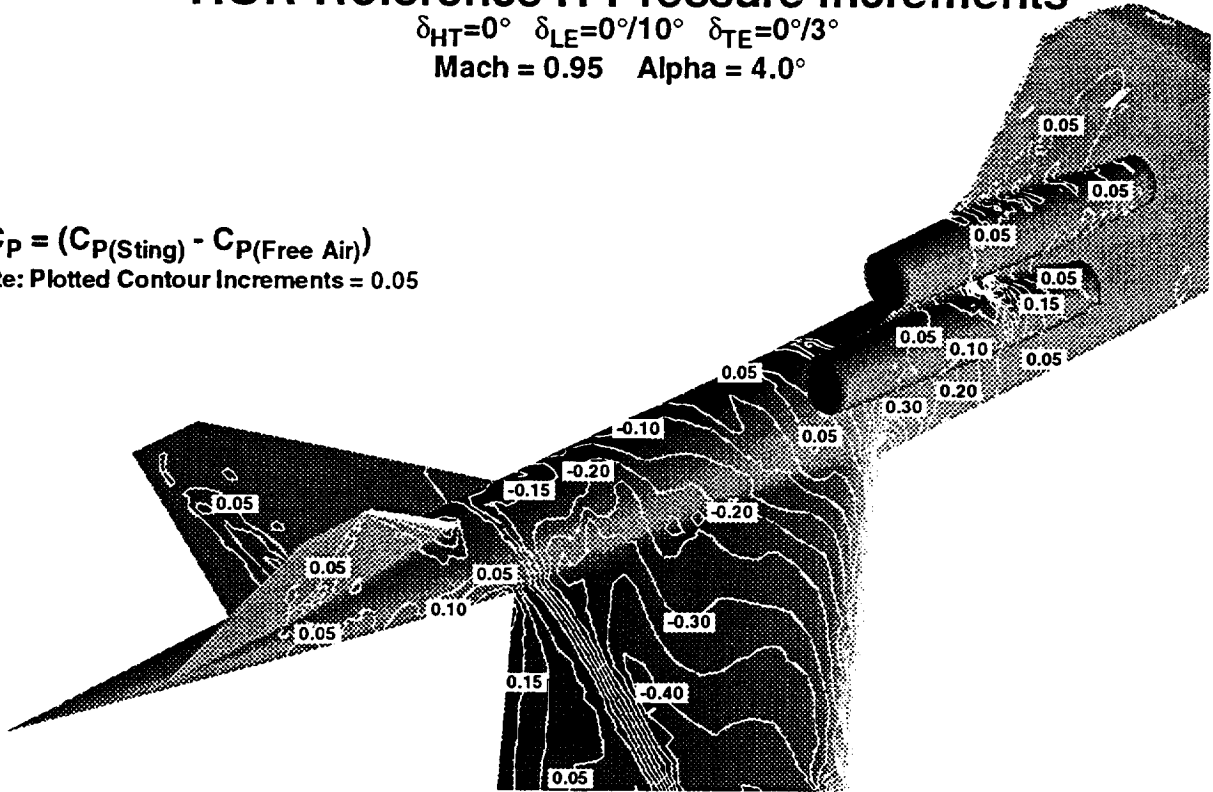
Interference of the sting on the predicted total force and moment coefficients results in an increase in lift over the free air configuration, an increment that decreases with increasing angle-of-attack. The presence of the blade sting also causes an increase in drag at all angles-of-attack except 0° where there is a slight drag decrement. The effect of the sting on predicted drag coefficient is shown to increase with increasing angle-of-attack. A stabilizing pitching moment increment is predicted as a result of sting interference. It should be noted that the data plotted for 8° angle-of-attack were obtained from solutions utilizing flux vector splitting and first order interpolations as opposed to flux difference splitting and higher order interpolation. This would tend to introduce more diffusion into the numerical scheme which could result in the sharp decrease in lift coefficient.

HSR Reference H Pressure Increments

$\delta_{HT}=0^\circ$ $\delta_{LE}=0^\circ/10^\circ$ $\delta_{TE}=0^\circ/3^\circ$
Mach = 0.95 Alpha = 4.0°

$$\Delta C_p = (C_p(\text{Sting}) - C_p(\text{Free Air}))$$

Note: Plotted Contour Increments = 0.05



A more detailed analysis of the pressure coefficient increment, at 0.95 Mach number and $\alpha=4^\circ$, resulting from the blade sting is presented here and in the following two charts. For this analysis, only the outboard wing flaps were deflected -- 10° down along the leading-edge and 3° down along the trailing-edge. The increments were calculated by interpolating the solution for the free air configuration onto the unstructured mesh developed about the configuration with the blade sting modeled. Increments are computed by subtracting the interpolated free air levels from the levels of the configuration with the blade sting. For clarity, contour lines for $\Delta C_p=0$ are not plotted. This pressure coefficient map shows that the sting affects the fuselage lower surface pressures as expected -- a relative compression at the leading-edge of the sting, a relative expansion around the sting and a relative compression at the trailing-edge of the sting. (As shown earlier, the sting has an airfoil cross section.)

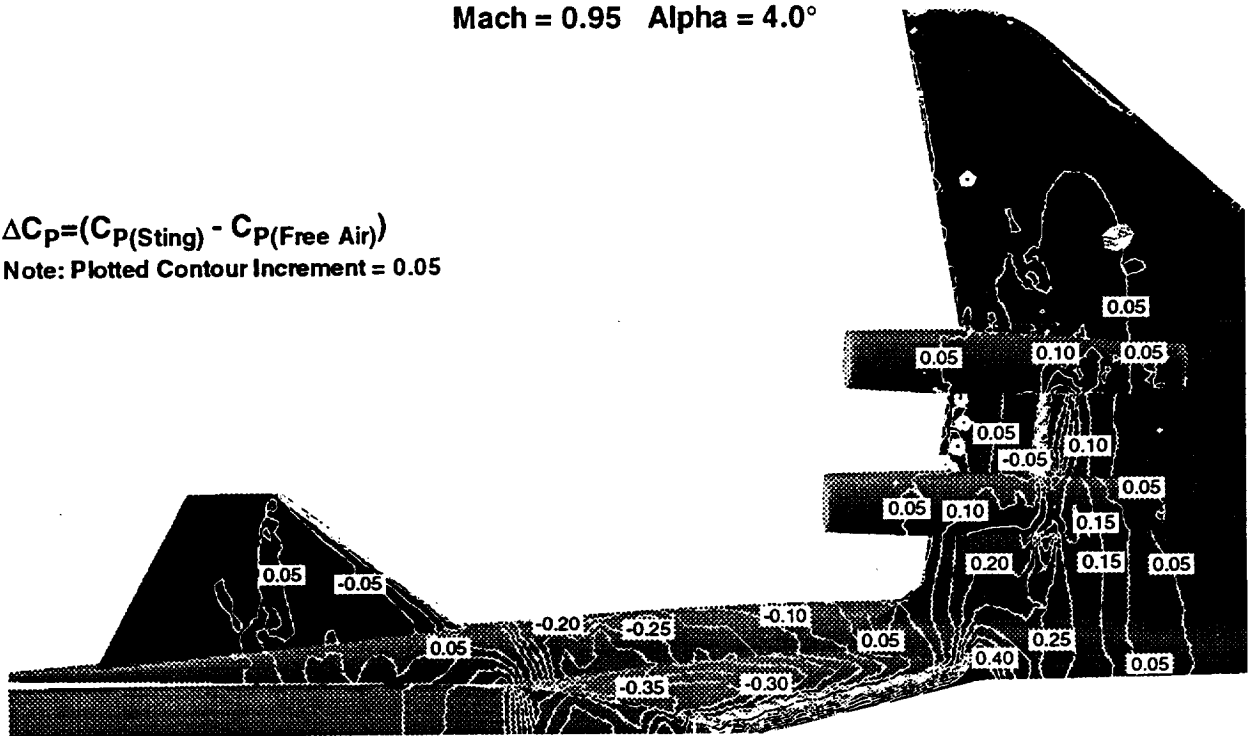
HSR Reference H Pressure Increments

$$\delta_{HT}=0^\circ \quad \delta_{LE}=0^\circ/10^\circ \quad \delta_{TE}=0^\circ/3^\circ$$

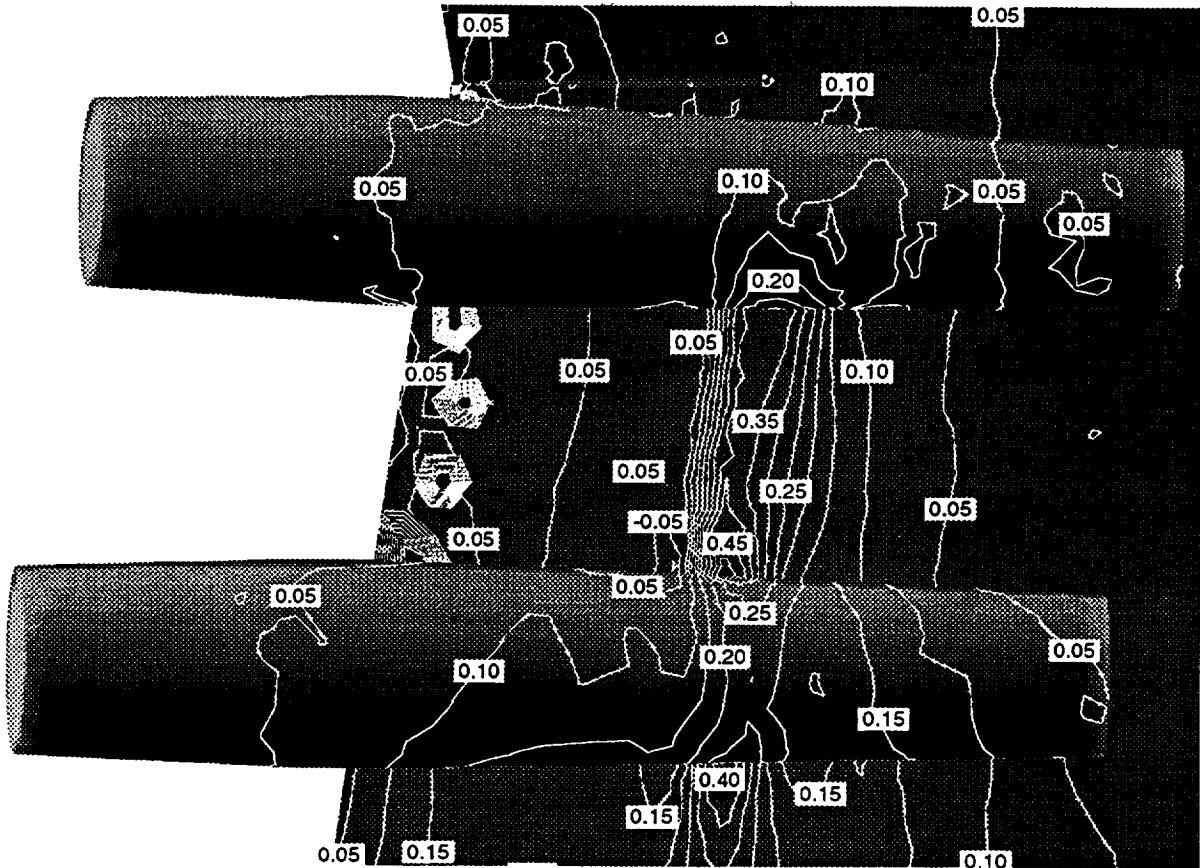
$$\text{Mach} = 0.95 \quad \text{Alpha} = 4.0^\circ$$

$$\Delta C_p = (C_p(\text{Sting}) - C_p(\text{Free Air}))$$

Note: Plotted Contour Increment = 0.05



Lower surface pressure increment contour lines are shown in this figure. Notice the tight clustering of contour lines along the leading-edge of the horizontal tail. An unexpected result of sting interference is the compression that is seen between the nacelles. A detail of this region is presented in the following chart. Note that the pentagonal and hexagonal contour patterns are not real but are due to numeric anomalies in the interpolation algorithm.



This figure, a close-up of the previous chart, shows in detail the region on the lower wing surface between the nacelles. The presence of the blade sting results in a pressure coefficient increase of up 0.45 between the nacelles.

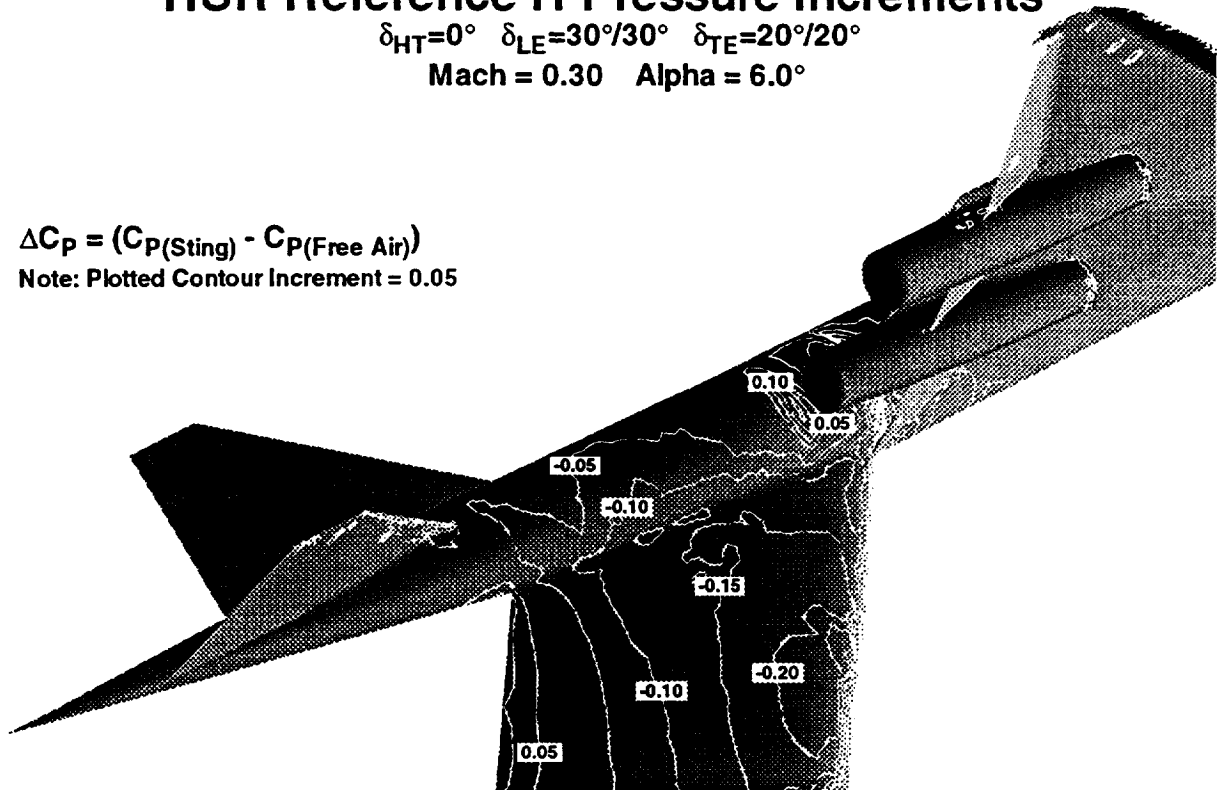
HSR Reference H Pressure Increments

$$\delta_{HT}=0^\circ \quad \delta_{LE}=30^\circ/30^\circ \quad \delta_{TE}=20^\circ/20^\circ$$

$$\text{Mach} = 0.30 \quad \text{Alpha} = 6.0^\circ$$

$$\Delta C_p = (C_p(\text{Sting}) - C_p(\text{Free Air}))$$

Note: Plotted Contour Increment = 0.05



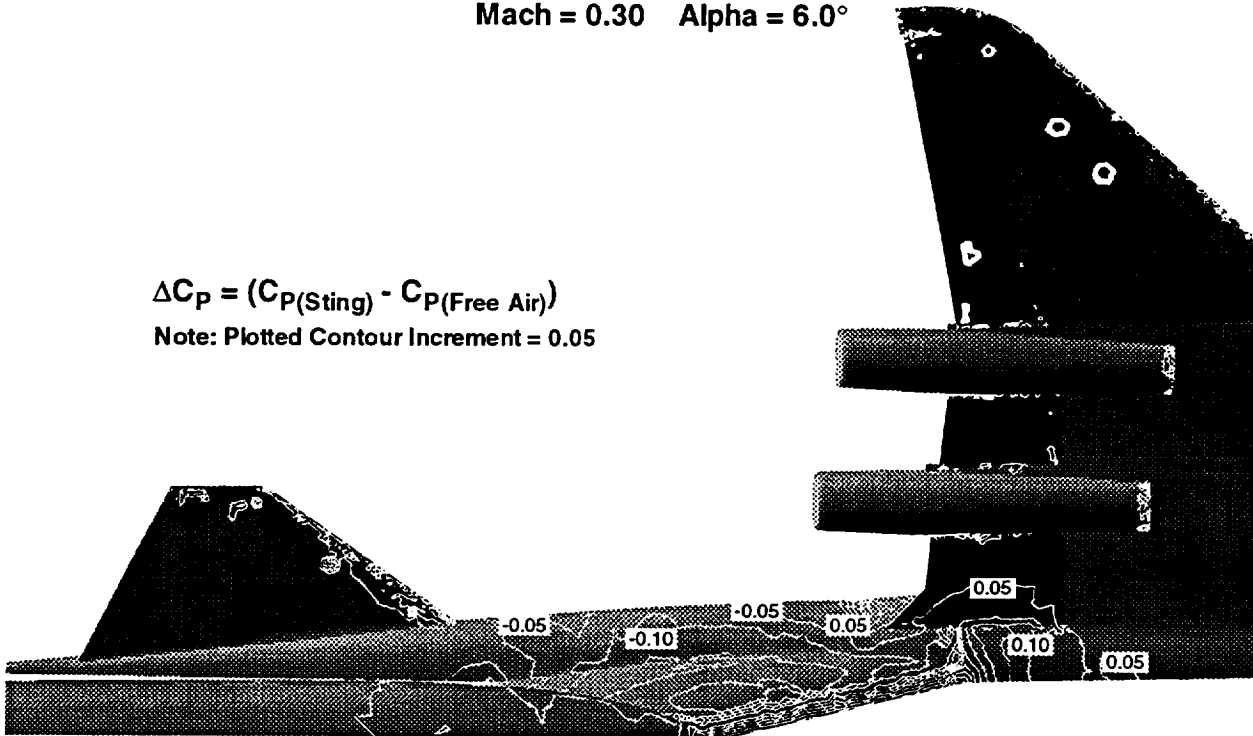
The surface pressure increments for 0.30 Mach number and six degrees angle-of-attack are presented here and in the next three figures. In this analysis the inboard and outboard leading-edge flaps were deflected 30° and the inboard and outboard trailing-edge flaps were deflected 20°. The increments are again calculated as the difference between the sting on results and the sting off results. For clarity, contour lines for $\Delta C_p=0$ are not plotted. Notice the reduced effect of the sting on the aft fuselage at the subsonic conditions as compared to the transonic analysis.

HSR Reference H Pressure Increments

$\delta_{HT}=0^\circ$ $\delta_{LE}=30^\circ/30^\circ$ $\delta_{TE}=20^\circ/20^\circ$
Mach = 0.30 Alpha = 6.0°

$$\Delta C_p = (C_p(\text{Sting}) - C_p(\text{Free Air}))$$

Note: Plotted Contour Increment = 0.05



This figure presents a view of the lower surface pressure increment contour lines. Presence of the sting at this subsonic condition does not cause the compression that was observed between the nacelles at the transonic condition in the previous charts.

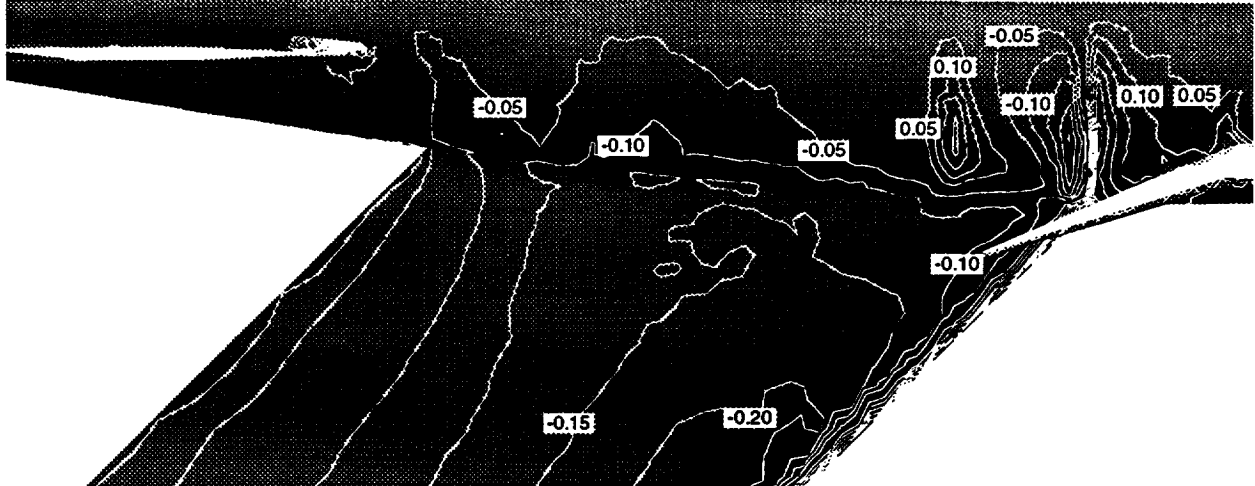
HSR Reference H Pressure Increments

$$\delta_{HT}=0^\circ \quad \delta_{LE}=30^\circ/30^\circ \quad \delta_{TE}=20^\circ/20^\circ$$

$$\text{Mach} = 0.30 \quad \text{Alpha} = 6.0^\circ$$

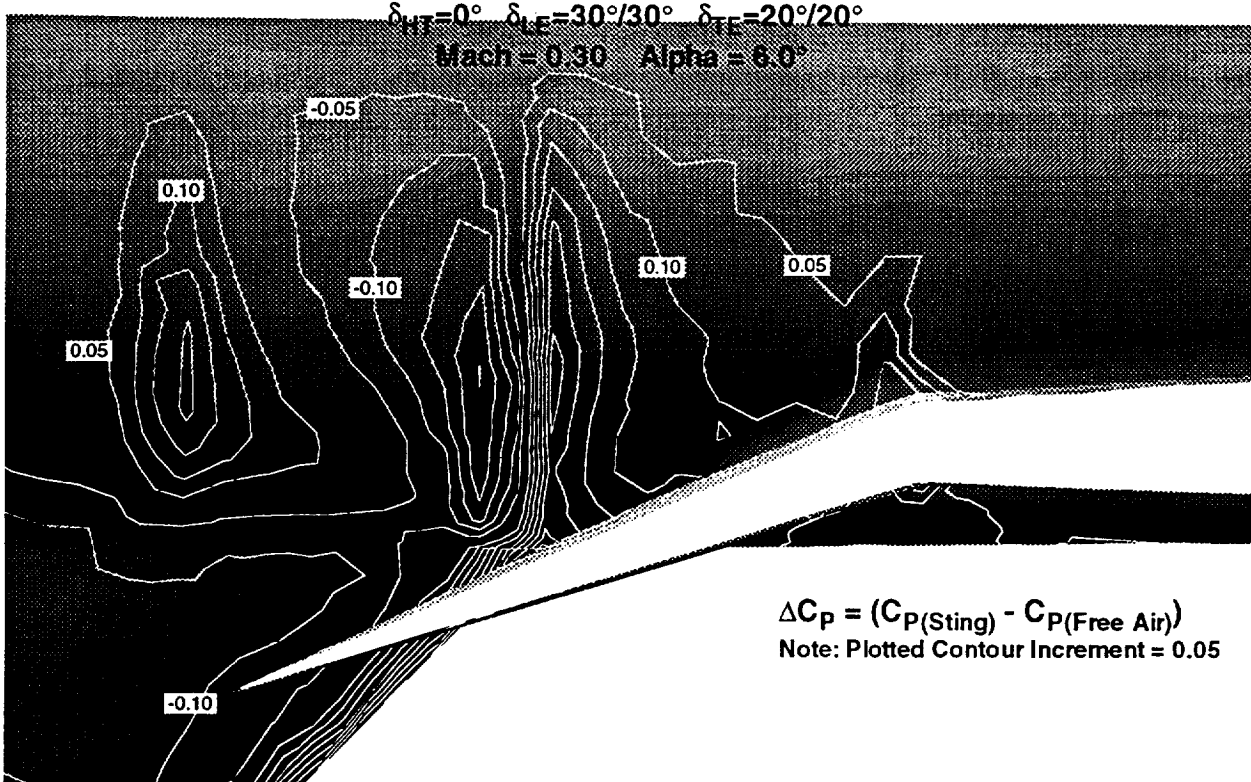
$$\Delta C_p = (C_{p(\text{Sting})} - C_{p(\text{Free Air})})$$

Note: Plotted Contour Increment = 0.05



This side view also shows less of an effect of the sting on the aft fuselage pressures. A relative compression, a relative expansion and another relative compression, all near the leading-edge of the fuselage-sting junction, is evident as a result of sting/trailing-edge flap deflection interference.

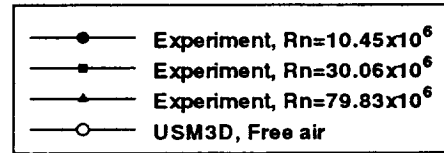
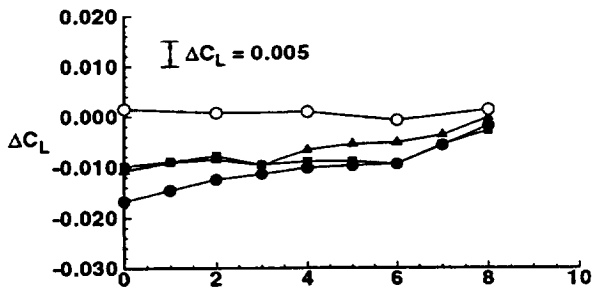
HSR Reference H Pressure Increments



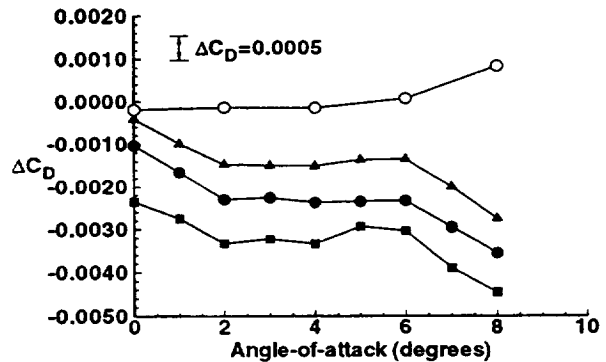
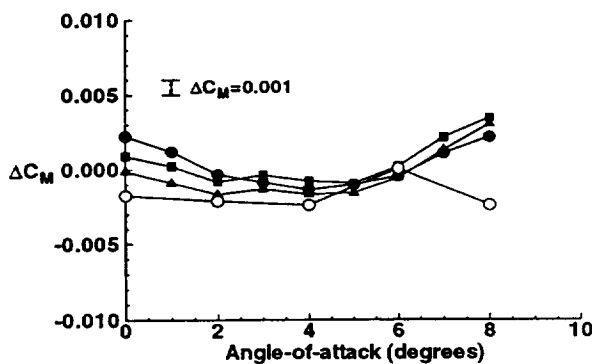
This close-up of the fuselage side shows that the interaction of the sting and trailing-edge flap deflection at results in a pressure coefficient increase of up to 0.30 forward of the fuselage/sting intersection. Just aft of the intersection a pressure coefficient decrease of up to 0.25 occurs. Another localized region of increased pressure coefficient occurs on the fuselage near the flap trailing-edge.

Corrected Empennage Force and Moments Increments

$\delta_{HT}=0^\circ$, $\delta_{LE}=0^\circ/10^\circ$, $\delta_{TE}=0^\circ/3^\circ$, $M=0.95$
 (Δ = Empennage Integrated - Empennage Not Integrated)



Note: Equivalent flat plate skin friction drag subtracted from experimental drag data



The contribution of the afterbody on total force and moment coefficients is shown in this figure. The computational increments were determined by integration of the predicted inviscid pressures of the free air configuration over only the aft fuselage and tail surfaces. Corresponding equivalent flat plate skin friction drag coefficients of 0.0025 for $Rn=10 \times 10^6$, 0.0021 for $Rn=30 \times 10^6$, and 0.0018 for $Rn=80 \times 10^6$ are subtracted from the experimental drag data. The experimental increments were obtained by differencing the force and moments of the complete configuration and a truncated afterbody configuration. The experimental data has been corrected for blade interference utilizing the USM3D predicted increments. An increment showing a level of significant change is shown on each force and moment increment plot. In general, there is good agreement between the Euler results and the corrected experimental data. However, there is some significant differences, the nature of which is not fully understood. The differences are partially due to the lack of viscous effects in the computational method. The uncertainty in the experimentally data as well as variability in the seal around the sting/fuselage intersection are also possible causes of these differences.

Summary

- The critical test technique for blade mounted testing is development of a improved seal
 - increase data quality and productivity
- USM3D performs compares well with experiment
 - differences are typical of Euler methods
 - provides confidence in computed increments
- Computational blade increments are good
 - viscous enhancement needed
- No assessment of blade effects with sideslip to date

Development of an improved seal for the model/blade sting interface is the critical test technique issue. This is necessary to improve both data quality and productivity.

The computational study has shown that the USM3D code can be used to predict the interference effects of a lower mounted blade sting with a high degree of confidence. It has been shown that wing and fuselage pressures, both levels and trends, can be predicted well. Force and moment levels are not predicted as well, but experimental trends are predicted. Based upon this, predicted force and moment increments are assumed to be predicted well. Most differences observed between the code and experiment are typical of Euler methods; an assessment of viscous effects on the closed aftbody and blade sting increments is needed.

To date, blade effects in sideslip have not been quantified.

Plans

- Aftbody/blade seal development has started
 - expect risk reduction test in 0.3m TCT
 - do not expect impact before NTF productivity upgrade
- Continue CFD analysis
 - expand analysis to supersonic conditions
 - include sideslipped conditions
 - viscous effects upon availability in USM3D
- Analysis including cylindrical aftbody/straight sting data acquired in UPWT and 16' TT
- Continue study of experimental sting interference testing strategies

A program to develop an improved seal design has been initiated. The plan is broader than the HSR program; that is, the results are expected to be applicable to all configurations. However, HSR has the most immediate short term need and longitudinal testing of a subsonic transport has been performed with a blade mount. A risk reduction experiment is expected to be performed in the NASA Langley 0.3m TCT. Results of this program are not expected to affect any NTF testing prior to the scheduled facility productivity upgrade which begins in March 1997.

CFD analysis using USM3D will continue. Plans are to analyze more fully supersonic conditions, analyze sideslipped conditions, and incorporate viscous analysis. Additional analysis of the cylindrical aftbody database obtained in UPWT and 16' TT should further clarify testing issues as compared to blade mounted testing. The study addressing sting interference testing strategies will continue.

Model Deformation Measurement Technique - NASA Langley HSR Experiences

A. W. Burner
R. A. Wahls
L. R. Owens
W. K. Goad

NASA Langley Research Center
Hampton, Virginia 23681-0001

Model deformation measurement techniques have been investigated and developed at NASA's Langley Research Center. The current technique is based upon a single video camera photogrammetric determination of two dimensional coordinates of wing targets with a fixed (and known) third dimensional coordinate, namely the spanwise location. Variations of this technique have been used to measure wing twist and bending at a few selected spanwise locations near the wing tip on HSR models at the National Transonic Facility, the Transonic Dynamics Tunnel, and the Unitary Plan Wind Tunnel. Automated measurements have been made at both the Transonic Dynamics Tunnel and at Unitary Plan Wind Tunnel during the past year. Automated measurements were made for the first time at the NTF during the recently completed HSR Reference H Test 78 in early 1996. A major problem in automation for the NTF has been the need for high contrast targets which do not exceed the stringent surface finish requirements. The advantages and limitations (including targeting) of the technique as well as the rationale for selection of this particular technique are discussed. Wing twist examples from the HSR Reference H model are presented to illustrate the run-to-run and test-to-test repeatability of the technique in air mode at the NTF. Examples of wing twist in cryogenic nitrogen mode at the NTF are also presented.

Facilities

- **National Transonic Facility**
- **Transonic Dynamics Tunnel**
- **Unitary Plan Wind Tunnel**
- **16-Foot Transonic Tunnel**

Model Deformation measurements for HSR models have recently been made at three NASA Langley Research Center facilities: the National Transonic Facility (NTF), the Transonic Dynamics Tunnel (TDT), and the Unitary Plan Wind Tunnel (UPWT). Dedicated video measurement systems to determine wing twist and bending are available at the NTF and the TDT. Successful results during HSR test 1651 last year at UPWT with a temporary system led to the decision to procure a dedicated system for that facility as well. In addition, a feasibility study has been initiated to determine the practicality of a similar measurement system at the 16-Foot Transonic Tunnel. The NTF has had a limited capability for model deformation measurements since 1984. Instrumentation development at the NTF led to the current technique. The first automated measurements of wing twist and bending were made at the TDT in 1994 where the application of high contrast targets on the wing made possible the use of image processing techniques to automatically determine the image coordinates of the targets. Data has been taken at the TDT for several tests of a rigid semispan HSR model. The first automated measurements of wing twist made at the NTF occurred in early 1996 during HSR Reference H Test 78. A polished paint technique was used to create high contrast white dot targets on a flat black background which enabled the automated measurements at the NTF.

NTF Instrumentation Concerns

- **120° F \Rightarrow -250° F**
- **9 atm**
- **Limited access and mounting options**
- **Productivity**
- **Expense**
- **Conflicting requirements of optical techniques**

The constraints imposed by operation in a high pressure environment over such a wide range of temperatures have had a significant impact on instrumentation development for the NTF. Even though the facility has been operational since August 1984, instrumentation development, improvement, and optimization continues. All of the currently available optical measurement techniques as well as those under consideration must be able to accommodate the limited access and mounting options at the NTF. The increased importance of productivity and the very high cost of tunnel operation make it very difficult to justify dedicated run time for test technique development or enhancement. Another instrumentation development problem which has recently become more apparent is the competition between various optical techniques for lighting, viewports, and mode of operation. During the recent HSR Test 78, fluorescent mini-tuft and wing twist data were taken together for some runs. This required manual changing of the test section lighting for each point and an additional delay to be introduced into the wing twist measurement system in order to accommodate both measurement systems. As temperature and pressure sensitive paints and other flow visualization techniques are employed at the NTF, the competition between the various techniques will worsen.

Question

Should some small fraction of polars be set aside for test technique development, enhancement, and uncertainty analysis at the NTF?

The setting aside of some small fraction of polars for test technique development, enhancement, and uncertainty analysis should be viewed as an investment in the future. Such an investment will pay off in the long term with increased measurement capability, productivity, and lower cost per useful information.

Model Deformation

- **Wing Twist**
more important
AOA
- **Wing deflection or bending**
less important
harder to verify

In discussions about model deformation measurement requirements among a number of people involved in aerodynamic testing, the determination of the induced wing twist under aerodynamic load appears to be the primary concern, with wing deflection (bending) being of secondary importance. In addition, angle measurements (not deflection) occur naturally at wind tunnels. The resolution of photogrammetric measurements generally is inversely proportional to the field-of-view. Thus it is possible to increase resolution at the expense of limited field-of-view by using longer focal length lenses to zoom in on the outboard portion of the wing near the tip. However, once this is done the fuselage is no longer in the field of view to serve as a reference in order to remove the sting deflection component from the wing deflection. Thus, without fuselage deflection data, deflection measurements at various semispan locations will contain this sting deflection component as well as the wing bending. If wing bending is desired while maintaining the high resolution for wing twist with a limited the field-of-view, then either calculated values for sting deflection must be used or a second camera will be required to view the fuselage in order to measure the sting deflection to subtract from the measured bending on the wing.

Wing Twist Uncertainty Requirements?

AOA of balance	⇒	Wing Twist
0.01°	?	0.05°

The uncertainty requirements for the measurement of wing twist caused by aerodynamic loads are unresolved. It has been suggested that the desired uncertainty for wing twist which corresponds to an uncertainty of 0.01° for the model pitch angle is of the order of 0.05°, not 0.01°. In other words, an uncertainty of the order of 0.05° in wing twist is thought to have about the same magnitude effect on drag measurements as 0.01° uncertainty in model pitch angle. A sensitivity study of the effects of wing twist and bending on CFD solutions will aid in uncertainty analyses and can impact future test technique developments.

Technique

- **Single view photogrammetry**
- **Wind-off polar as reference**
- **Change in local AOA on wing**
- **Easier to automate**

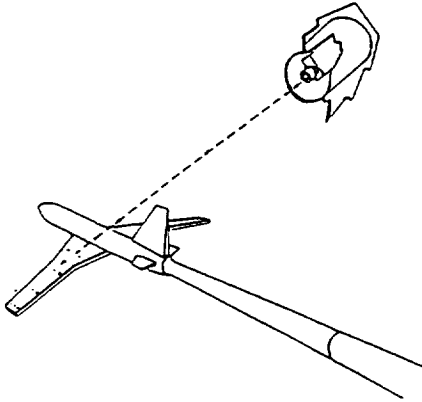
The optical technique used to determine wing twist data is based upon the recording and analysis of digitized video images. A video signal from a standard RS-170 solid state camera with 752 horizontal by 240 vertical pixels per field is routed to a frame grabber controlled by a Pentium 90-MHz PC which records one second or more of digitized video images into the frame grabber memory. Several of the digitized images are then analyzed in order to reduce the effects of dynamic yaw. It currently takes approximately one second per digitized image to automatically determine the image coordinates of three rows of wing targets. The charge-coupled device (CCD) video camera used for wing twist measurements at the NTF has an adjustable field integration time in order to reduce the effects of dynamics on image recording. A 10 to 100 mm focal length remote zoom lens is currently used for imaging. NASA TM 110229, published in Feb. 1996, presents the history of model deformation development at the NTF and describes the non-automated measurement technique used until recently at the NTF. A report on the automation of the technique will be presented at the Ground Testing Conference at New Orleans in June, 1996. Considerations when calibrating zoom lenses for wind tunnel use are discussed in SPIE Proceedings 2598 pp. 19 - 33, Oct. 1995.

Limitations and Problems

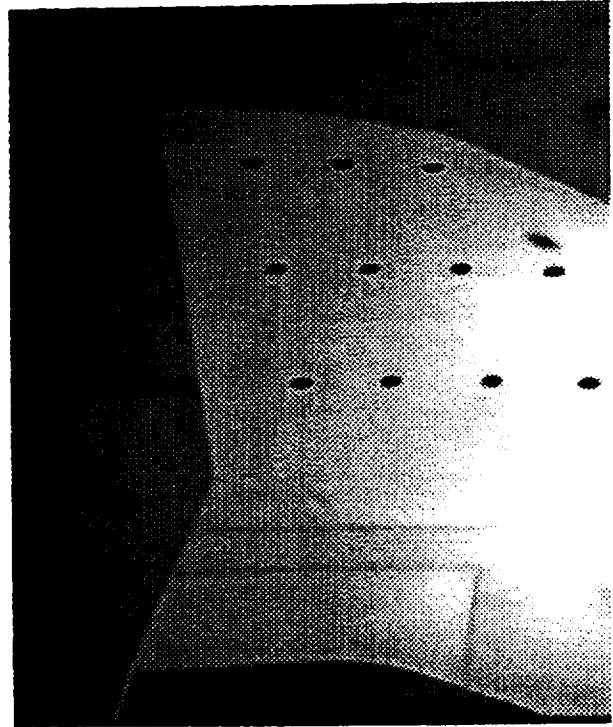
- **One coordinate must be known (spanwise)**
- **NOT 3D measurement**
- **Alpha sweeps only**
- **Wing targets**

Wing twist measurement error can occur due to errors in the camera position and pointing angles used to determine the X and Z coordinates. Pre-test calibration errors can also contribute to wing twist error if, for instance, incorrect lens distortion or frame grabber affinity corrections are used. Also note that errors in wind-off reference angle and wind-on angle will contribute to the error in the wing twist angle although generally the expected error in twist due to the wind-off pitch angle is much smaller than the error due to the wind-on angle. The Y coordinate, assumed to be known for the single camera solution, is constant and well-behaved for ambient wind-off pitch sweeps. This is verified by independent measurements in the test section as well as by the single camera technique, which typically has an rms error of 0.03° or less when compared to the onboard inertial angle sensor under wind-off ambient conditions. However, Y is not constant during wind-on conditions due to model yaw dynamics and wing bending. This variation in Y contributes to the precision error. As long as the image locations are not too far separated, the errors in X and Z will be similar and will tend to partially cancel. Wing bending causes the Y coordinate of wing targets to decrease which also causes a bias error in the computation of X and Z . This error partially cancels since targets at a given semispan location will experience similar Y shifts due to bending.

NTF Camera Location and View



Camera location



Video image

At the NTF the CCD camera is mounted in a protective housing in the test section sidewall. The camera looks over the fuselage at one of the wings of the model. Since perspective causes the images to be foreshortened in the vertical direction, the camera is rotated 90° so that the flow direction is vertical on the image plane in order to more nearly match the number of pixels vertically and horizontally across a target image. The protective housing is equipped with insulation and sheath heaters to maintain camera temperature. The housing is pressure rated to greater than 9 atm. In order to prevent frost, air heated by an inline heater flows to a purge ring with a number of holes to direct the heated air over the inside surface of the one inch thick fused silica window viewport. A purge air vent to atmosphere maintains the camera housing pressure at approximately 1 atm. Retroreflective tape targets have been used at the TDT and UPWT. In the past at the NTF, circular targets were applied to the wing surface with a Sharpie® marking pen. More recently (early 1996), a polished paint technique has been used at the NTF to produce high contrast targets. Initial X and Y coordinates of the targets are determined from pressure tap and other reference locations on the wing. The Z coordinates are estimated from cross-sectional drawings of the wing.

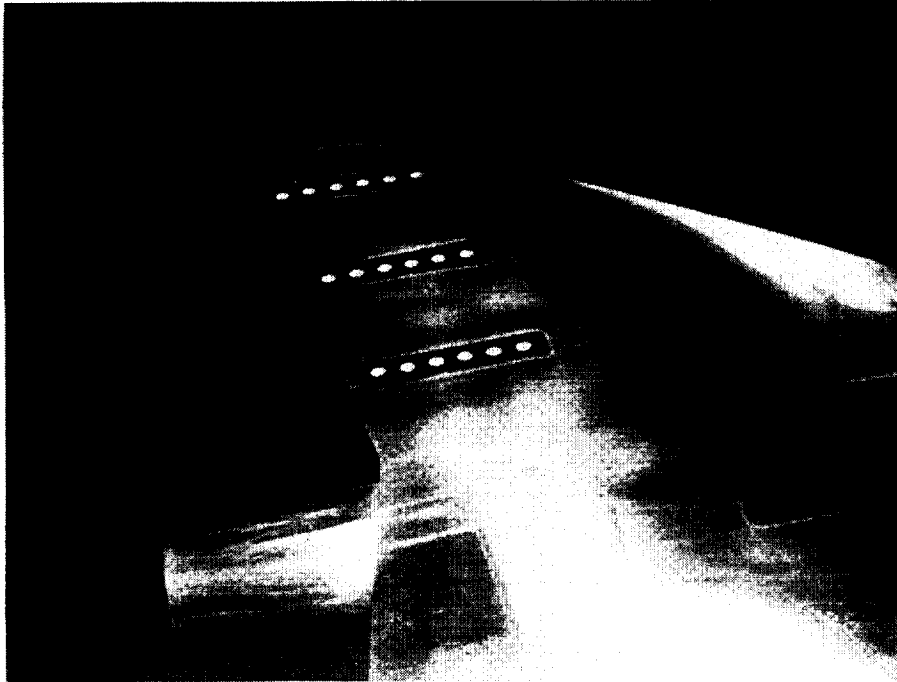
Recommendations

Emphasis be placed on developing high contrast, permanent, nondisturbing, optical targets for new and existing models at NTF

Emphasis be placed on determining the effects of wing target step height and surface roughness on aerodynamic data at the NTF

Innovations are sought to obtain high contrast, durable wing targets which do not exceed the surface finish requirements at the NTF. The surface finish of models at the NTF can approach 10 microinches or better, resulting in a "mirror like" surface. Thus images of the wing surface may also contain additional artifacts produced by reflections of a wall or ceiling. In order to successfully automate the wing twist measurement at the NTF high contrast targets are needed which do not exceed the surface finish requirements or unintentionally trip the flow. These targets should be flat-white solid-filled circles on a flat-black background or the opposite contrast. Sharpie® marking pen black targets are neither high contrast nor durable. In addition, some customers of the facility would prefer not to apply the targets due to uncertainty about the effects of the targets on aerodynamic performance; however, results to date do not indicate a measurable adverse effect. Targets applied by a chemical etching technique would be durable, but of low contrast. Gun bluing could also produce durable targets on at least some of the materials used for models at the NTF, but would still produce low contrast targets and have the additional problem of being a "controlled rusting process". Ideas for a suitable target application method at the NTF are solicited.

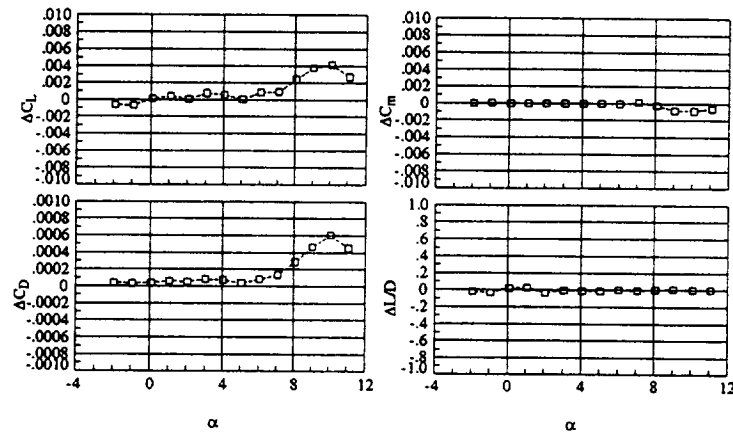
Polished Paint Targets at the NTF



A polished paint technique for applying high contrast targets suitable for cryogenic operation has been developed and was applied on the outboard panel for two configurations of the 2.2% HSR Reference H model recently (Feb. 1996) tested at the NTF (Test 78). The two configurations were the baseline wing with no flap deflection and the transonic wing with 10° and 3° flaps. This development of high contrast targets enabled automated wing twist measurements to be made for the first time at the NTF. Initial results are very encouraging and led to the decision to apply the same type targets on the wing of a subsonic transport model during the NTF test immediately following the HSR test.

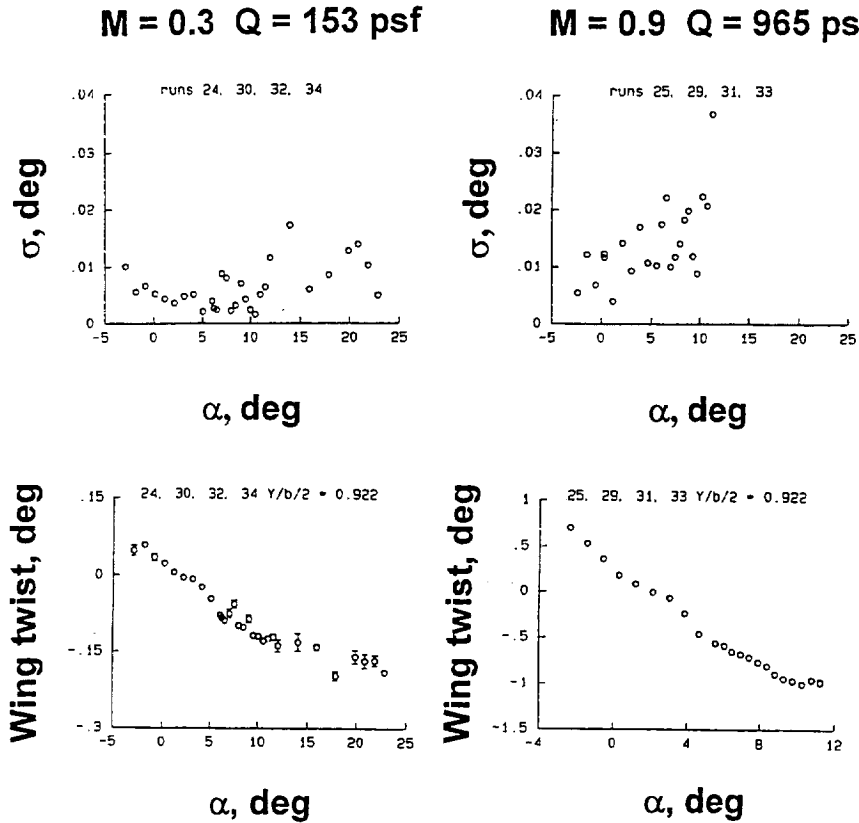
Model Deformation Target Effect

- Preliminary Data from NTF078: Baseline Config.
M = 0.90, Rn = 10.24e6, q = 967 psf
 Δ = targets on - targets off



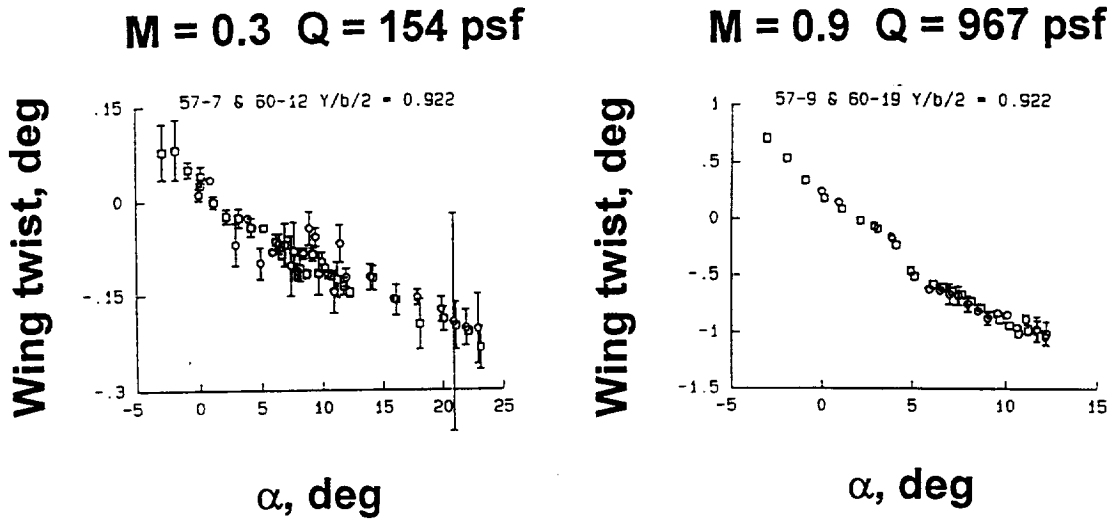
This figure shows the effect of the new high contrast, painted targets on the aerodynamic data. A set of 4 polars, plus 1 inverted polar, was run for both the target on and target off conditions at low Reynolds number in the air mode of operation. The data shown is the difference between curve fits of the data at selected angles-of-attack. Lift and drag coefficient data indicate a negligible effect at low angle-of-attack, but show an increasing effect beyond $\alpha = 8$ deg. Examination of the raw data indicate that the curve fits may have slightly biased the differences (order of one drag count high) at high angles-of-attack. In addition, data repeatability at the higher angles was on the order of ± 2 drag counts. Thus, it is not clear that the differences shown in the figure are significant. The effect on pitching-moment and lift-to-drag ratio is negligible, as was the effect of the lateral/directional coefficients (recall the targets were installed on the left outboard wing panel only). Further work is required to fully quantify the target effect on the aerodynamics data.

Run-to-Run Repeatability at the NTF



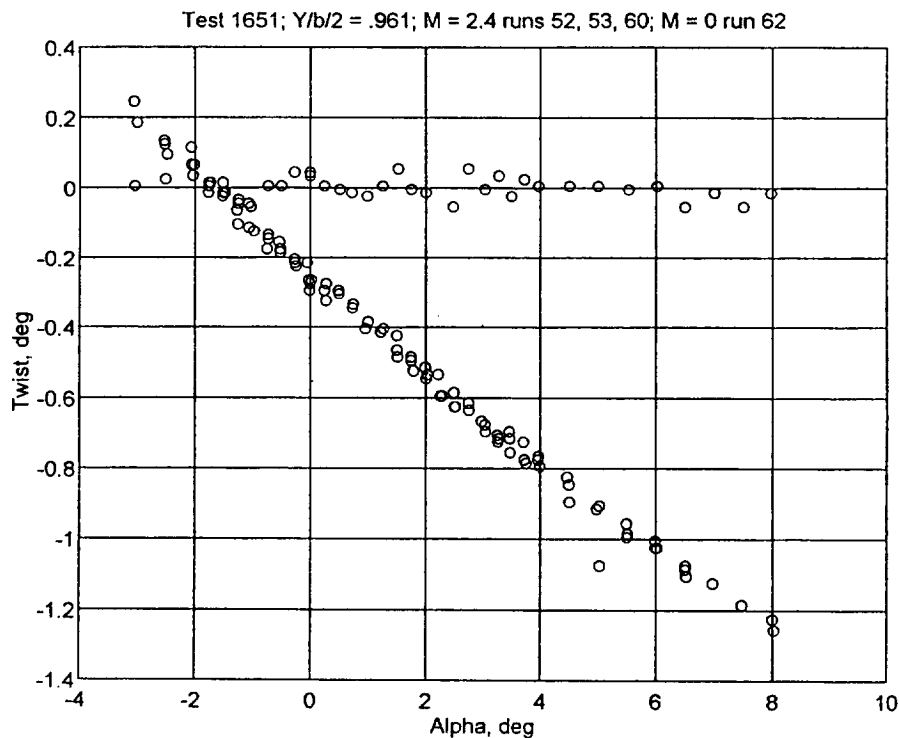
Same day, run-to-run repeatabilities of the video wing twist technique for an HSR model during air runs are presented for Mach number of 0.3 and dynamic pressure of 153 psf on the left and $M = 0.9$ and $Q = 965$ psf on the right for a normalized semispan of 0.922. Data for semispan stations at 0.778 and 0.635 behaved similarly, but with correspondingly less wing twist. The error bars (which are plotted if greater than the symbol size) represent plus and minus one standard deviation of the four repeats at each Alpha. The mean standard deviation in twist angle for repeat points was less than 0.02° in air mode with a worse case standard deviation at the higher Mach number equal to less than 0.04° . Note that any error and variability in the onboard angle of attack for wind-on alpha or wind-off reference alpha will be added to the measured twist value.

Test-to-Test Repeatability at the NTF



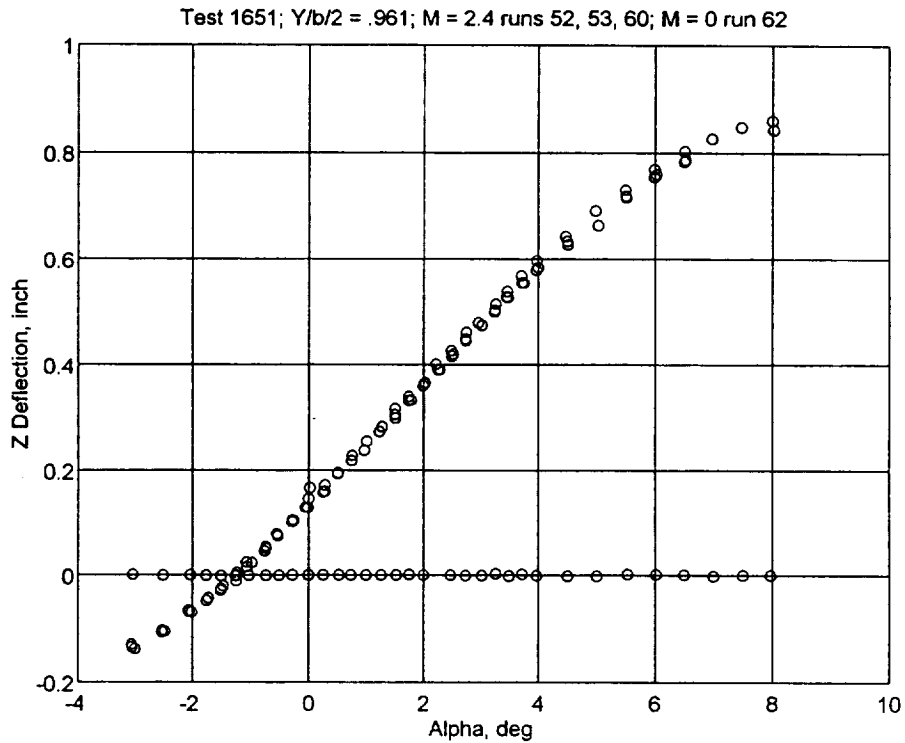
Comparisons of repeat runs from two HSR tests at the NTF (Tests 57 and 60) in air mode separated by over five months are presented above. Data from the two tests are represented by different symbols. The error bars represent plus and minus one standard deviation as computed from the least squares conformal transformation used in the computation of wing twist. Linear interpolation was used to account for differences in model pitch angle setpoint between the tests. For the plot to the left the Mach number was 0.3 and the dynamic pressure was 154 psf. For the plot to the right the Mach number was 0.9 and the dynamic pressure was 967 psf. Note how deviations from linearity repeat from test to test for the 967 psf data. The mean differences between the two tests are less than 0.03° with a worst case disagreement of 0.24° at $\alpha = 24^\circ$. For α 's below 20° , the worst case disagreement is 0.05° .

Unitary Test 1651 Wing Twist



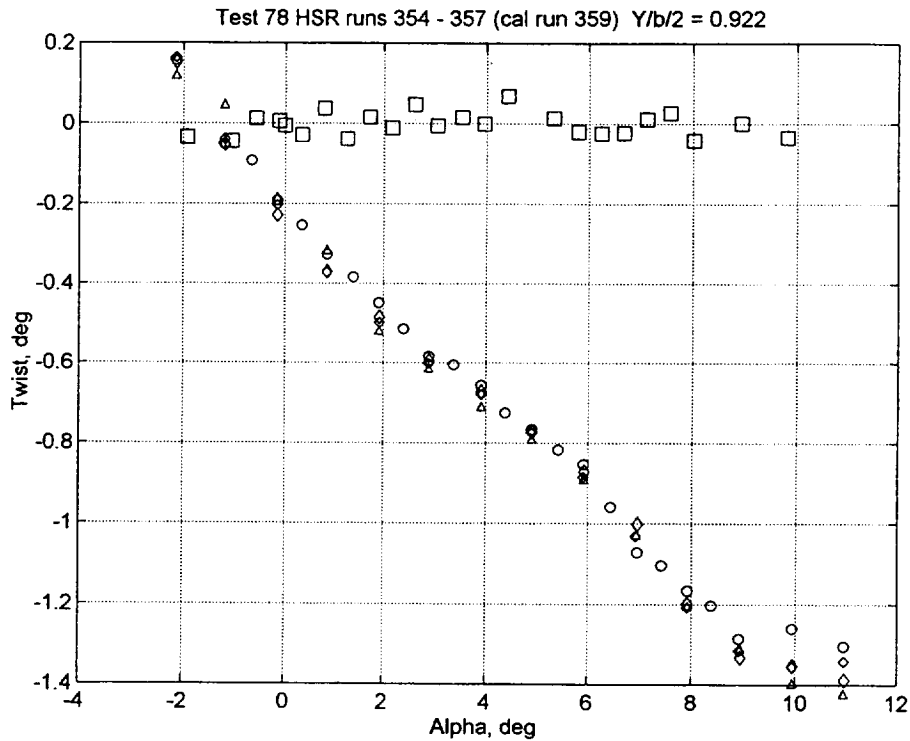
The wing twist data plotted above were recorded at the Langley Unitary Plan Wind Tunnel Test Section #2 during HSR Test 1651 of the 1.675% scale HSR Reference H model. Wing twist and deflection data were recorded for three repeat runs at Mach number equal to 2.4. Data were taken at two semispan stations, $Y/b/2 = 0.845$ and 0.961 . Least squares curve fits to a wind-off run were used to establish an online calibration. Wind-off standard deviations when compared to $Alpha$ were 0.0086° at $Y/b/2 = 0.845$ and 0.031° for $Y/b/2 = 0.961$. There were 7 targets at the 0.845 semispan location which occupied a larger portion of the field-of-view compared to the 4 targets at the 0.961 semispan location. Thus the 0.845 semispan had the better resolution. Worst case disagreement was 0.08° between the three runs, part of which may have been attributable to error in $Alpha$ since $Alpha$ is subtracted in the computation of wing twist. Note that the $Alpha$ for no twist is near -1.7° , in good agreement to the expected value. These successful results at UPWT with a temporary system led to the decision to procure a dedicated system for that facility. The procurement is currently underway.

Unitary Test 1651 Wing Deflection



The deflection of the 0.961 semispan row of targets is given above for HSR Test 1651 at the Unitary Plan Wind Tunnel Test Section #2 at a Mach number of 2.4. Deflection due to sting bending is included in the above plot. Note that for these tests the model shifted longitudinally several inches as the pitch was varied, further complicating the interpretation of deflection in the vertical direction. The Z deflection values above are computed as the difference in the vertical direction between wind-off and wind-on at a normalized chord location $X/C = 0.5$. The wind-off values of deflection were fitted to a 4th order polynomial before subtraction. The standard deviations of the wind-off residuals after the fit were 0.0011 inch for $Y/b/2 = .845$ and 0.0012 inch for $Y/b/2 = 0.961$. Worst case disagreement for the three runs during the Mach 2.4 flow was 0.01 inch.

NTF Test 78



The change in wing twist due to aerodynamic load is presented in the above plot as a function of model angle-of-attack, α for four repeat runs during Test 78 of the transonic configuration of the HSR Reference H model at the NTF. For these runs the Mach number was 0.9, the dynamic pressure was 1005 psf, the total temperature was -184°F , and the total pressure was 20.8 psi. Data is presented at the 0.922 semispan location. Data were also taken at the 0.778 and 0.635 semispan locations. The square symbols represent the wind-off reference polar used to calibrate the angle measurement system at the same tunnel temperature and pressure as for the flow runs. The angle data from four images at each point were averaged to determine the change in wing test

Summary

- **Model Deformation at 3 LaRC Facilities (Feasibility study for 4th)**
- **NTF instrumentation issues**
- **Wing twist and bending**
- **NTF and UPWT data presented**

Model deformation measurements have been made at three NASA Langley Research Center facilities: the National Transonic Facility (NTF), the Transonic Dynamics Tunnel, and the Langley Unitary Plan Wind Tunnel (UPWT). The development of a model deformation system at the NTF has been especially challenging. Some of the instrumentation concerns at the NTF have been presented. The emphasis in the development of a model deformation capability has been on the accurate and repeatable measurement of the change in wing twist due to aerodynamic load in a manner suitable for routine wind tunnel testing. The uncertainty requirements for model deformation, specifically the change in wing twist, remain an open issue. Model deformation examples from the NTF and Langley UPWT have been presented.



Boundary Layer Transition in the NTF:
HSR Experience and Plans

Lewis R. Owens, Jr.,	NASA LaRC
Richard A. Wahls,	NASA LaRC
Marvine P. Hamner,	McDonnell Douglas Aerospace

February 28, 1996

Efforts towards understanding boundary layer transition characteristics on a High Speed Civil Transport (HSCT)-class configuration in the National Transonic Facility (NTF) are ongoing. The majority of the High Speed Research (HSR) data base in the NTF has free transition on the wing, even at low Reynolds numbers (R_n) attainable in conventional facilities. Limited data has been obtained and is described herein showing the effects of a conventional, Braslow method based wing boundary-layer trip on drag. Comparisons are made using force data polars and surface flow visualization at selected angles-of-attack and Mach number. Minimum drag data obtained in this study suggest that boundary layer transition occurred very near the wing leading edge by a chord R_n of 30 million. Sublimating chemicals were used in the air mode of operation only at low R_n and low angles-of-attack with no flap deflections; sublimation results suggest that the forebody and outboard wing panel are the only regions with significant laminar flow. The process and issues related to the sublimating chemical technique as applied in the NTF are discussed. Beyond the existing experience, status of efforts to develop a production transition detection system applicable to both air and cryogenic nitrogen environments is presented.



Outline

- Background
- Experiences in NTF067
 - sublimation procedures
 - sublimation results
 - minimum drag results
- Comparison to equivalent flat plate theory
- Plans
 - temperature sensitive paint (TSP)
- Summary

The outline of the topics covered in this presentation is shown here. First, some background on technical issues associated with NTF testing is discussed followed by a presentation of the transition detection and fixing results obtained in the NTF to date. Next, some analysis results are presented that compare drag data with equivalent flat plate predictions. Finally, plans for further transition detection work is discussed with summary comments to close.



Background

- Test free-transition at flight Reynolds numbers
- HSR testing in NTF
 - Flight Reynolds number not obtained (in general)
 - More intermediate Reynolds numbers added to gain understanding of trends
- Fixed Transition for HSR testing in NTF
 - Forebody grit ring added after yaw dynamics at some low alpha, transonic test conditions
 - Internal grit ring added to nacelles to facilitate an internal flow-through nacelle drag correction
 - No wing, external nacelle, tail trips were added for general HSR testing
 - Different trip sizes and locations required

A basic testing strategy in the NTF includes testing a model at high Rn conditions with free transition. The high Rn test condition typically corresponds to a design flight condition. To anchor this NTF data to a low Rn data base obtained in a conventional wind tunnel, the NTF model is usually tested at a matching low Rn condition with the tripping strategy used in that facility. Also, an aeroelastic increment is usually acquired at a feasible intermediate Rn condition to allow a correction of the test data to a given model shape.

For the HSR testing in the NTF, flight Reynolds numbers are, in general, not reached because of the large reference chord length and model load limits. Having to extrapolate the test data to flight conditions required the addition of more intermediate Rn conditions so that a more intelligent extrapolation could be made.

Complete transition fixing was not incorporated into the early HSR testing for a number of reasons. Some of these included the basic high Rn testing philosophy, potential for a one-third scale flight article, undefined low-speed transition fixing strategy for this type of wing, etc. However, transition was fixed on the forebody in an attempt to alleviate a yaw dynamics problem that occurred at low alpha, transonic test conditions. Nacelle internal trips were used consistently to facilitate an internal nacelle drag correction. Other trips were not added because of the complexity of sizing and locating trips at each of the numerous test conditions.



Sublimation Procedures

- Tunnel Constraints
 - Access to model (approx. 1/2 hour to get to model in the air mode of operation)
 - Time to get to test condition
 - approx. 4-6 hours per test case
- 5 Test Cases were run in about 2 days
 - 1 practice (M=0.9, alpha=4 deg)
 - 3 free transition (M=0.3,0.9 at alpha=4 deg and M=0.3 at alpha=0 deg)
 - 1 conventional wing trip (M=0.9 at alpha=4 deg)

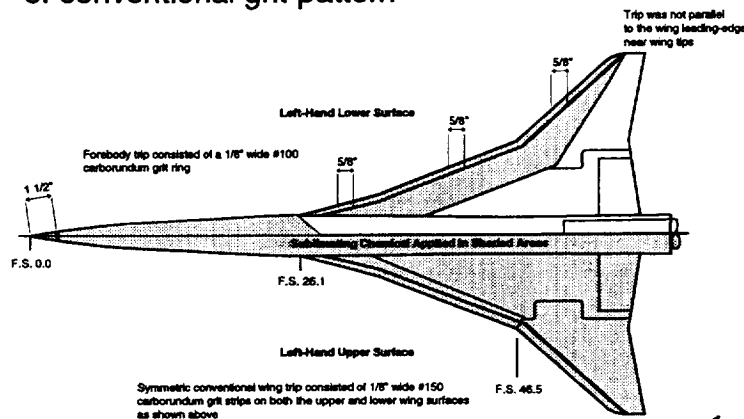
Transition detection using a sublimating chemical was performed during NTF test 67; the sublimating chemical approach was the only workable “global” transition detection option available at the NTF at the time. However, this option is not a very productive one. With the tunnel operating procedures associated with cryogenic operations, the time to access the model is approximately 1/2 hour, even in the air mode of operation. To get to a chord Reynolds number of 10 million requires the pressurization of the tunnel and this can take up to another 1/2 hour for typical high-lift test conditions (M=0.30). Although the sublimation results obtained were very useful for the limited test conditions studied, the productivity of this technique is low.

During NTF067, five different test cases were obtained in about a two day period. However, this cost was considered prudent to give the research community an idea of what the boundary layer states look like for a low aspect-ratio wing model with a surface finish that ranges from approximately 4 to 16 microinches (rms), which is typical for NTF models.



Sublimation Procedures

- sublimation chemical areas of application and details of conventional grit pattern

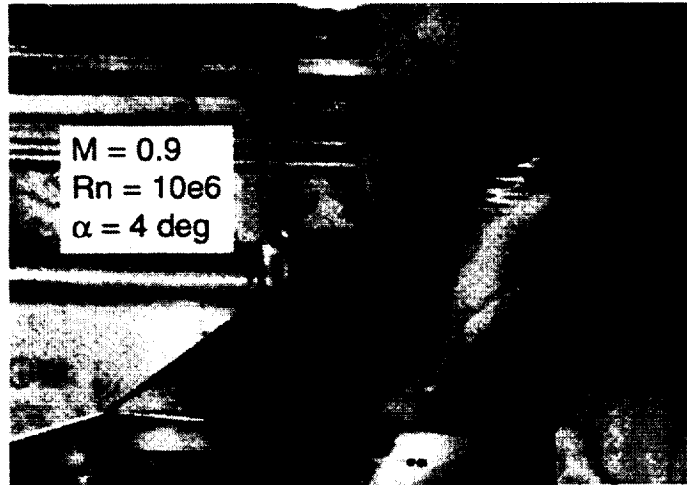


A planform view of the 2.2% HSR Reference H model configuration that was used in this study is shown in the figure. The left-hand lower surface of the model is shown in the top half of the figure and the left-hand upper surface is shown on the bottom half. The model was mounted on a straight support sting for this testing. Only the baseline wing configuration was studied during this transition work. This configuration had undeflected leading- and trailing-edge flaps and was tested without nacelles so that comparisons could be made with force data from NTF060. The shaded areas of the model planform (in the figure) indicate where the sublimating chemical (fluorene) was applied. The left-hand wing was chosen to avoid the right wing upper surface static pressure orifices. The details associated with the sizes and location of the symmetric "conventional" trip strategy that will be referred to in both the sublimation results and the drag data comparisons are also shown on the planform view. The carborundum grit sizes and the locations were selected by using the Braslow method.



Sublimation Results

- laminar run on lower wing surface, free transition



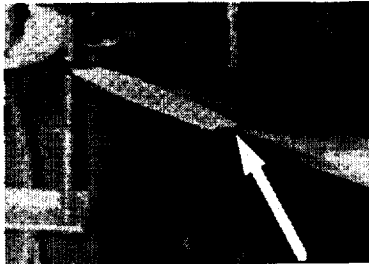
This sublimation result shown here indicates the presence of a laminar boundary-layer region on the lower surface of the outboard wing panel. The onset of transition is signaled by the jagged front (downstream facing) of the growing turbulent wedges. This was the only area of the wing that had any chemical remaining. Similar results were obtained for Mach = 0.3 at the same Rn and angle-of-attack. The resulting chemical pattern is generally confined to the first 10 to 30 percent of the local chord outboard of the leading-edge crank. At the wingtip, the laminar boundary layer run extends to the trailing edge.



Sublimation Results

- laminar run on forebody, free transition

$M = 0.9$
 $Rn = 10e6$
 $\alpha = 4 \text{ deg}$



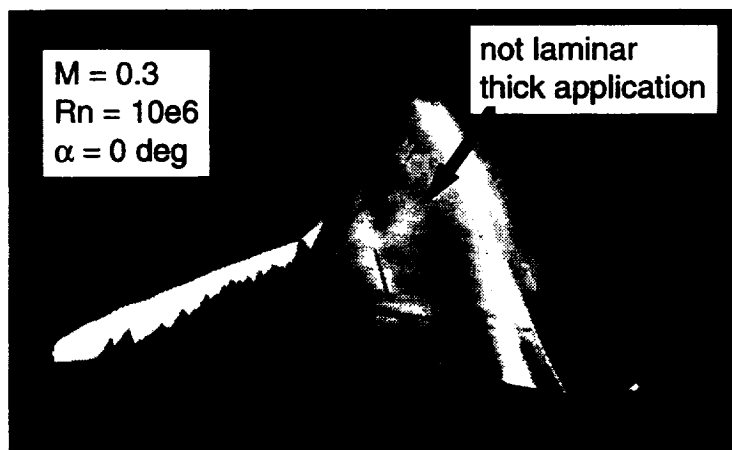
laminar run ends here

This figure shows the laminar boundary layer run on the forebody. The length of this laminar run was approximately 4 to 5 inches. The chemical pattern was continuous around the bottom half of the forebody within the 5 inch length. The top half of the forebody within this same length had no sign of the chemical suggesting that this region had already transitioned. Again, the pattern for Mach = 0.3 at the same Rn and angle-of-attack was very similar to that shown here for Mach = 0.9, except that the laminar run length was longer, 7 to 8 inches, and extended higher on the sides of the forebody.



Sublimation Results

- laminar run on upper wing surface, free transition



When lowering the angle-of-attack to 0 deg, the laminar boundary layer run followed the attachment line onto the upper surface of the outboard wing panel. Also note that the laminar run appeared to move slightly, 1 to 2 inches, inboard of the wing leading-edge crank. The very thin layer of chemical on the inboard wing and the fuselage was considered to be associated with a potentially nonuniform and thick application of the sublimating chemical. This conclusion can be debated because a quantitative measure of the chemical application thickness is not available, and due to the judgment necessary to declare when the sublimation run is complete.



Sublimation Results

- laminar run on forebody, free transition

$M = 0.3$
 $Rn = 10e6$
 $\alpha = 0 \text{ deg}$



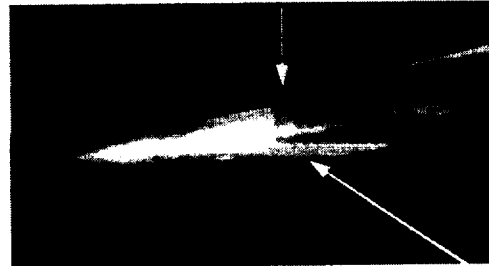
At an angle-of-attack of 0 deg, the laminar run on the forebody was continuous in the crossflow plane from the apex to a length of approximately 5 inches. Beyond this length, laminar flow extended another 2 to 3 inches downstream in certain narrow regions.



Sublimation Results

- laminar run on forebody, fixed transition

$M = 0.9$
 $Rn = 10e6$
 $\alpha = 4 \text{ deg}$



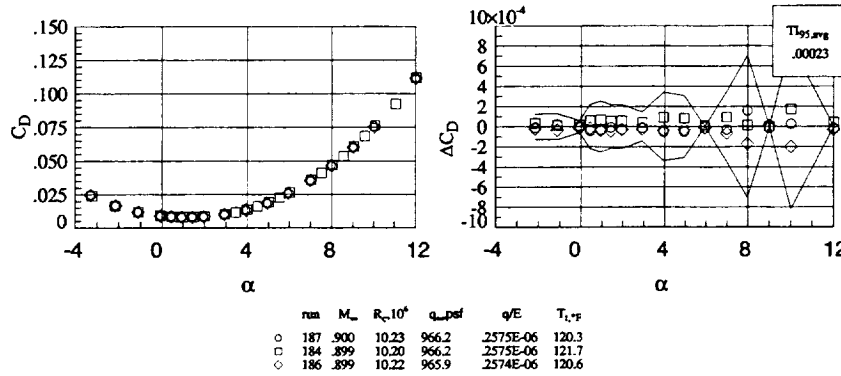
intentional gap in grit ring
laminar flow passes through

A conventional boundary-layer trip consisting of carborundum grit was sized and located based upon the criteria of the Braslow method. The forebody is shown here with a grit ring located 1.5 inches downstream of the apex. The laminar regions present with free transition are now confined upstream of the trip location. As a check, gaps were intentionally left in the trip strips in areas where laminar flow was observed in the free transition case. At these gaps, laminar flow was observed extending through and downstream of the trip strips. One area was found in which the trip did not work. This region was near the wing tips where the transition strip did not remain parallel to the wing leading edge. In this area, the grit was unintentionally undersized because the chordwise distance from the leading edge to the trip decreased and the grit size was not appropriately increased.



Minimum Drag Results

- Repeatability of drag measurements (M=0.9, Rn=10e6, wing trip on)

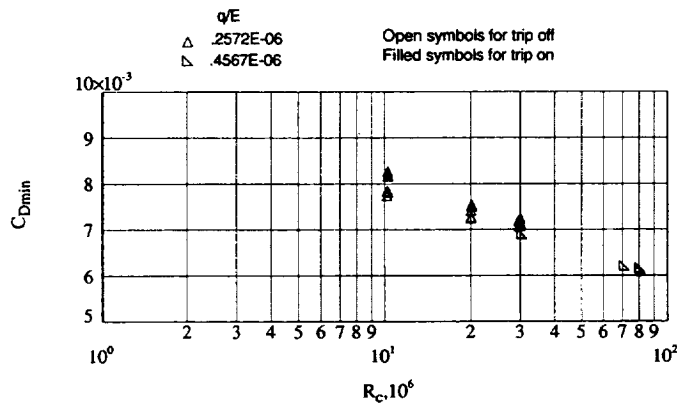


A sample of typical short term repeatability of drag measurements is shown in this figure to provide a measure of what drag difference may be considered significant. The plot on the left is shown to give an overall view of the drag character for the baseline (undeflected flaps) configuration. On the right, the drag residual is plotted; the residuals are referenced to the average drag value obtained from 3 drag polars interpolated to specific angles-of-attack. The symmetric curve that brackets the residual data represents the tolerance interval (95% confidence level) that resulted from a statistical analysis. In this case (based on 3 polars), the 95% tolerance interval is approximately 4-sigma (standard deviations). From this data, a drag level change of more than 2 drag counts is significant in the minimum drag angle-of-attack range.



Minimum Drag Results

- “Conventional” trip on/off comparisons, $M=0.9$
(Trip off data from NTF060)

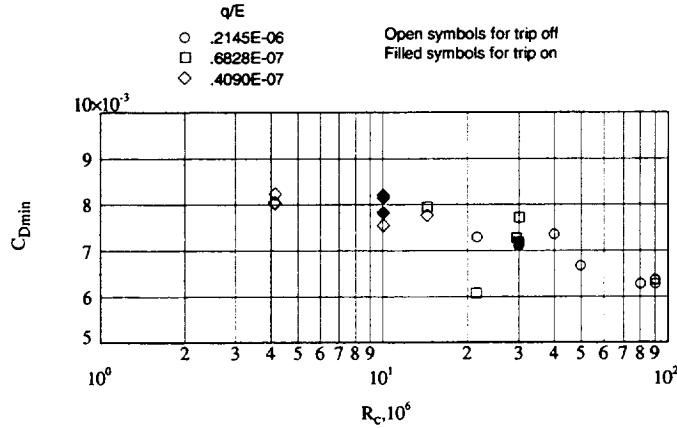


A plot of the minimum drag trend with R_n is shown here for the baseline configuration at a Mach of 0.9. The open symbols represent data obtained over the entire R_n range with free boundary layer transition on the wings. The filled symbols represent data obtained in NTF067 at chord R_n 's of 30 million and below with an appropriately sized and located “conventional” wing trip. Below a R_n of 30 million, the difference between the tripped and free transition data increases as the R_n decreases. Lower drag values for the free transition data is characteristic of flow with laminar boundary layer regions present. The wing trips reduce the extent of these laminar regions for the lower R_n data. The agreement between both the trip on and the trip off data at a R_n of 30 million suggests that the wing boundary layers naturally transition at or near the trip location. If this is the case, then fixing the wing transition is only necessary below this R_n . Note that the lower R_n fixed transition data along with the higher R_n free transition data can be approximated by a 1/7-th power law that is a function of the R_n .



Minimum Drag Results

- “Conventional” trip on/off comparisons, M=0.3
(Trip off data from NTF060)

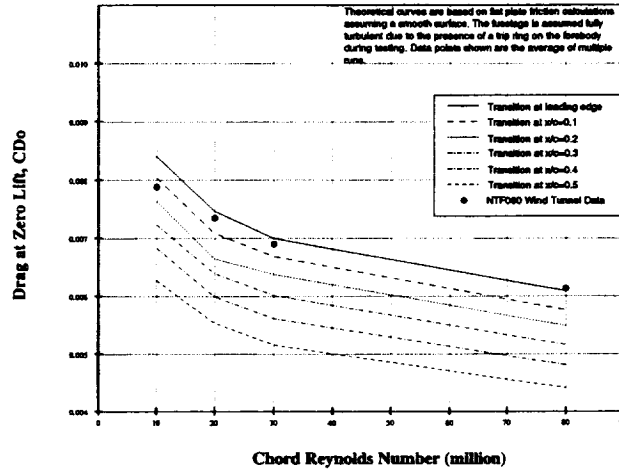


The corresponding minimum drag trend with R_n for Mach=0.3 is shown here. These results do not show the effect of the wing trip as clearly as the Mach=0.9 results. Some of the lack of clarity in these results is attributed, in part, to the lower measurement resolution associated with the lower load levels obtained at Mach=0.3. Note that a tripped data point at a R_n of 4 million would have been useful in the comparison with the free transition data, but the trip was designed for a R_n of 10 million and would not trip the flow at a R_n of 4 million due to undersizing.



Comparison to Equivalent Flat Plate Theory

- M=0.9 data from NTF060

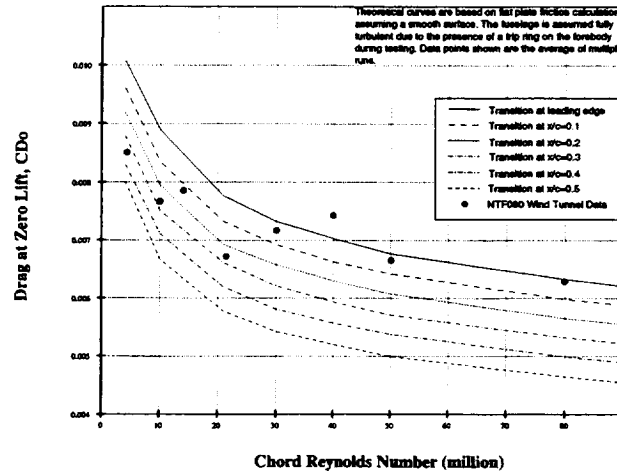


An equivalent flat plate theory model was used to generate zero lift drag trends with R_n for various wing transition locations. The curves shown on this plot represent the predicted drag trends for a fully turbulent wing boundary layer and for wing transition occurring every 10-percent of chord up to 50-percent. Experimental data is plotted with the theoretical curves in an attempt to understand the movement of the wing boundary layer transition location with R_n . For the Mach=0.9 data, this analysis also suggests that the wing boundary layer location occurs very near the wing leading edge by a chord R_n of 30 million.



Comparison to Equivalent Flat Plate Theory

- M=0.3 data from NTF060



A similar comparison of free transition data to equivalent flat plate theory was also made for Mach=0.3. This comparison suggests more variability in the wing boundary layer transition location at the lower Rn's (below 30 million). Note that the data point for a Rn of 40 million indicates that the wing boundary layer transitioned ahead of the wing leading edge. However, a closer examination of this data point indicated that this represented a single run at this test condition. Multiple runs at each test condition are required to offset the lower measurement resolution that is associated with the Mach=0.3 data. Even so, this analysis tends to support the idea that the wing boundary layer transitioned very near the wing leading edge by a chord Rn of 30 million.



Plans

- Develop "global" transition detection system
- Initial attempt will utilize temperature-sensitive-paint (TSP)
- Risk reduction experiment in 0.3-m TCT (March '96)
 - 2-D airfoil: HSNLF(1)-0213
 - first entry will be approx. 2 weeks long
 - evaluate available paints, cameras, data acquisition
- Develop system for use in NTF during next HSR entry (July '96)
- Analyze NTF TSP data for HSR model
 - select appropriate boundary layer trip strategy or strategies

In an attempt to better understand attached flow boundary layer transition on wind tunnel models, the effort to develop a transition detection system applicable to the cryogenic environment in the NTF continues. The most promising candidate system available at this time will use temperature sensitive paint. However, many technical obstacles will need to be overcome before such a system will be practical in general wind tunnel testing. An experiment designed to reduce the risks associated with this type of transition detection system will be performed in the 0.3-m Transonic Cryogenic Tunnel (TCT). From this initial entry in the 0.3-m TCT, the best candidate paints that will work at temperatures ranging from 120 deg F down to -250 deg F will be identified. These paints will need to be robust (no degradation in a cryogenic environment) allowing for the fine surface finishes required for high R_n testing. These paints also need to be sensitive enough to work with a data acquisition system (lights, camera, image processing software) to resolve the small temperature differences that exist between laminar and turbulent boundary layers. After identifying and resolving these technical obstacles, the system will be adapted for use in the NTF. Pending the outcome of the 0.3m TCT work, the goal is to use this system in the NTF during the next HSR model entry. The data supplied by this transition detection system will be very useful in designing an appropriate boundary layer fixing strategy for low R_n testing, which anchors the scaling process to high R_n data.



Summary

- Limited b.l. transition data (flow vis.) obtained on the 2.2% HSR Reference H model in the NTF
 - low alpha for attached flow conditions
 - low chord R_n (air mode tunnel operations)
 - laminar b.l. on forebody and outboard wing panel
 - “conventional” trips sized by Braslow method worked
- Wing trip on/off drag data and equivalent flat plate analysis suggest that natural transition occurred very near the wing leading edge by a chord R_n of 30 million for attached flow
- Efforts ongoing to develop a productive transition detection system using TSP in the NTF

In summary, a limited amount of boundary layer free transition flow visualization data was obtained on the baseline configuration (no flaps, no nacelles) of the 2.2% HSR Reference H model in the NTF. This free transition data were obtained at a low chord R_n for attached flow conditions and suggests the presence of two major laminar boundary layer regions: one on the forebody and the other on the outboard wing panel. Flow visualization data obtained for a “conventional” wing trip suggests that a trip properly sized and located (based on Braslow method) does work, as expected. Analysis of trip on/off drag data as well as comparisons with equivalent flat plate theory suggests that natural laminar transition occurred very near the wing leading edge at chord R_n 's around 30 million for attached flow conditions. Also, plans to develop and use a TSP transition detection system for use on the HSR model in the NTF were shown. Such a system is fundamental to the understanding of the effects of R_n on boundary layer transition in wind tunnel testing strategies. However, results from a TSP system must be studied carefully when the flowfield includes separated flow (ie. leading-edge separations).



THE APPLICATION OF THE NFW DESIGN PHILOSOPHY TO THE HSR ARROW WING CONFIGURATION

Steven X. S. Bauer

Steven E. Krist

NASA Langley Research Center

The Natural Flow Wing design philosophy was developed for improving performance characteristics of highly-swept fighter aircraft at cruise and maneuvering conditions across the Mach number range (from Subsonic through Supersonic). The basic philosophy recognizes the flow characteristics that develop on highly swept wings and contours the surface to take advantage of those flow characteristics (e.g., forward facing surfaces in low pressure regions and aft facing surfaces in higher pressure regions for low drag). Because the wing leading edge and trailing edge have multiple sweep angles and because of shocks generated on nacelles and diverters, a viscous code was required to accurately define the surface pressure distributions on the wing. A method of generating the surface geometry to take advantage of those surface pressures (as well as not violating any structural constraints) was developed and the resulting geometries were analyzed and compared to a baseline configuration.

This paper will include discussions of the basic Natural Flow Wing design philosophy, the application of the philosophy to an HSCT vehicle, and preliminary wind-tunnel assessment of the NFW HSCT vehicle.



OUTLINE

- Description of the Natural Flow Wing (NFW) Design Philosophy
- Application of NFW to the HSR M2.4-7A Arrow Wing Configuration
- Navier-Stokes (OVERFLOW) comparisons of NFW and MDA OPT5 W/B/N/D configurations
- Results from the NFW Arrow Wing Configuration tested in the NASA LaRC Unitary Plan Wind Tunnel
- Conclusions

As outlined above, this paper will begin by describing the Natural Flow Wing design philosophy, describe how the NFW design philosophy was applied to the HSR M2.4-7A Arrow Wing configuration, show Navier-Stokes results (comparing the MDA OPT5 configuration with the NFW designs), discuss the OVERDISC modifications to the NFW designs, give some preliminary results from the NASA LaRC Unitary Plan Wind Tunnel Test (in test section 1, off design Mach number), and conclude with a brief summary of 1995 activities.



NATURAL FLOW WING DESIGN METHODOLOGY/PHILOSOPHY

- **At Subsonic, Transonic, and Supersonic Conditions; the flow over a highly swept wing at lift has the following characteristics:**
 - Upper surface is dominated by a conical flow field:
 - The flow is in a direction normal to the leading edge of the wing (at the leading edge)
 - The flow expands at the leading edge of the wing (i.e., low pressures)
 - The flow recompresses to higher pressures and this recompression region occurs in a location that is conical with the apex of the wing
 - Aft of the recompression, the flow is in the streamwise direction
 - Lower surface is dominated by a "high" pressure field
- **At Supersonic Conditions, the upper and lower surface aerodynamics of a swept wing are independent of one another**
 - Allows for independent design and design philosophy
 - Allows for method application to differ for different flow physics of upper and lower surfaces
- **Natural Flow Wing Design Philosophy**
 - Does not change the Cp distribution on the wing to improve performance
 - Contours the surface to take maximum advantage of the naturally occurring flow field, surface pressure distribution, etc.
- **NFW Description**
 - The NFW design method uses a "near-conical" thickness distribution to match the wing upper surface contour to the conical nature of the flow at all speeds
 - Typical subsonic/transonic wings have thick airfoil sections and blunt leading edges. Typical supersonic wings have thin airfoil sections and sharp leading edges. This method blunts the leading edges and thickens the airfoils inboard to provide increased performance
 - The lower surface is reflexed aft of the maximum thickness location and is much "flatter" than a typical wing designed for the same conditions
- **Advantages**
 - This approach reduces drag at cruise and "off-cruise" conditions without a mechanical change of geometry (flaps or slats)
 - Better flow conditions for engines mounted below wing (due to the lower surface being "flatter")

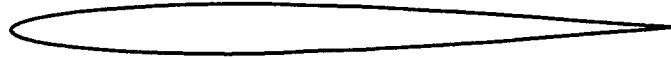
The Natural Flow Wing (NFW) design philosophy was developed by Richard M. Wood and Steven X. S. Bauer (NASA LaRC) between 1986 and 1988 for improved performance of military aircraft (low aspect ratio) at cruise and maneuvering conditions. By compiling a large amount of empirical data, the following characteristics of flow over a highly swept wing at lift and at any Mach number could be observed: (1) on the upper surface, the flow is dominated by a "conical" flowfield (i.e., the flow expands around the leading edge and recompresses to a higher pressure inboard and this recompression occurs on a ray that intersects the apex of the wing) and (2) the pressure on the lower surface is dominated by "high" pressures. Additionally, at supersonic conditions, the upper and lower surface aerodynamics are independent of one another and thus, independent design and design philosophies may be applied to each surface and different methods (Navier-Stokes, Euler) for different flow physics may be applied to each surface.

Perhaps the biggest difference between the NFW design philosophy and other design methods is that the goal of the NFW design philosophy is not to change the pressure distribution on the wing to improve performance, but rather to contour the surface to take maximum advantage of the "naturally" occurring flow field and resulting surface pressure distribution.

The advantages of this method are a continuous definition of the wing from root to tip, flatter lower surface (for more uniform flow characteristics at the inlet face), and less geometric "wiggles" in the streamwise and spanwise directions.



MODIFIED FOUR- AND FIVE-DIGIT AIRFOIL SERIES



- Forward of the Maximum Thickness Location

$$z = a_0\sqrt{x} + a_1x + a_2x^2 + a_3x^3$$

- Aft of the Maximum Thickness Location

$$z = d_0 + d_1(1-x) + d_2(1-x)^2 + d_3(1-x)^3$$

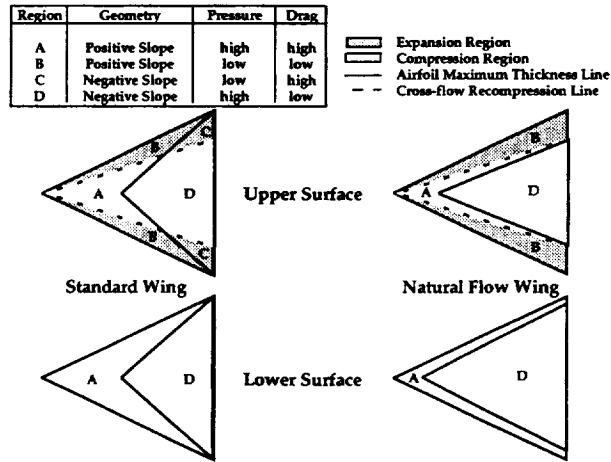
- Leading-Edge Radius

$$\frac{r}{c} = \frac{a_0^2}{2} = 1.1019 \left(\frac{t}{c} \right)^2$$

Shown above is the typical NACA 4- and 5-digit airfoil series definition of $z(x)$ and leading-edge radius.

When the NFW design method was applied to the M2.4-7A Arrow Wing planform, the general airfoil shape shown above was generated for the entire wing. Then modifications were made to each airfoil shape to account for structural box, landing-gear, and other constraints. This airfoil definition, because it is analytic, provides continuous, “smooth” airfoil distribution from the root to the tip. Eventually, the capability to specify any airfoil shape will be incorporated into the wing generation code (biconvex and diamond airfoil definitions already can be used in the existing code).

NATURAL FLOW WING DESIGN



The figure above illustrates the NFW design approach.

The delta wings shown above represent the upper (top) and lower (bottom) surfaces. The standard distribution of maximum thickness location (i.e., constant percent chord location) is shown on the left and represented by the solid black line. The Natural Flow (or “near-conical”) maximum thickness location is shown on the delta wings to the right. Also shown on the figures are the regions of high (white) and low (shaded) pressure. The dashed line on the upper surface indicates approximate recompression location and is conical with the apex of the wing, whereas the maximum thickness line for a standard wing is conical with the wing tip. By observing where these two lines intersect, 4 regions of high and low drag can be identified. Region A has a forward-facing surface and a high pressure, thus a high drag region. Region B has a forward-facing surface and a low pressure, thus a low drag region. Region C has an aft-facing surface and a low pressure, thus a high drag region. And region D has an aft-facing surface and a high pressure, thus a low drag region. Therefore, it would be advantageous to reduce the high drag regions (A and C). The NFW delta wing shown on the right has reduced region A and eliminated region C by sweeping the maximum thickness location aft (near-conical) and moved the maximum thickness location at the root closer to the leading edge. On the lower surface, since the pressures are high everywhere, region A is reduced by moving the maximum thickness location for all the airfoils further forward (toward the l.e.).



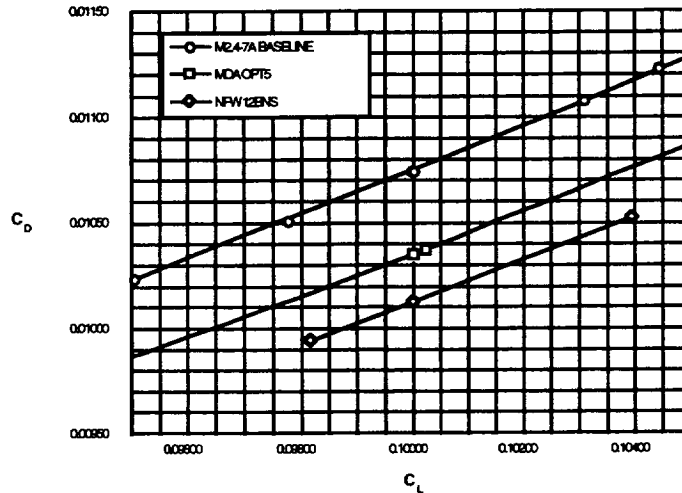
APPROACH

- Apply the Natural Flow Wing (NFW) Design Method [developed by Richard M. Wood and Steven X. S. Bauer (1986 to 1988) for Improved Performance of Military Aircraft at Cruise and Maneuvering Conditions.] to the M2.4-7A Arrow Wing Configuration by redefining the maximum thickness location and the (t/c) , (r/c) , camber, etc. distributions to minimize drag at cruise.
 - Apply NFW and conduct Euler analyses of Wing/Body configurations to minimize drag at cruise.
 - OPT3D (version 1.10, A. Jameson and J. Reuther, NASA ARC w/o implementing the design algorithm, i.e., QNMDF)
 - Grid: (Generated internally WBGRID C-H topology) 151 x 41 x 41
 - Apply NFW and conduct Navier-Stokes analyses of Wing/Body/Nacelle/Diverter configurations to minimize drag at cruise.
 - OVERFLOW (P. Buning, NASA ARC), Baldwin-Barth turbulence model, Central Differencing
 - Grid: 221 x 94 x 65 C-O Wing/Body Grid (17 block 3.1 million grid point chimera grid), PEGSUS (interpolation between overset grids)
 - Apply NFW and Computational Optimization of Wing/Body/Nacelle/Diverter.
 - OVERDISC: Couples OVERFLOW, PEGSUS, and CDISC (the Constrained Direct Iterative Surface Curvature inverse design method, R. Campbell, NASA LaRC) in a script file.
 - CDISC routines were modified (S. Krist, NASA LaRC) to partially ignore target pressure distributions and to use the NFW philosophy by changing the wing lower surface to take advantage of the Nacelle/Diverter shock impinging on the wing.

In order to apply the Natural Flow Wing design philosophy to the M2.4-7A Arrow Wing configuration, an aerodynamic analysis tool (that could quickly generate grids and calculate the forces and surface pressures) had to be chosen. The OPT3D code developed at NASA Ames was chosen and run in analysis mode for the Wing/Body configurations. Numerous geometries were generated for variations in $(t/c)_{\max}$ location and upper and lower (t/c) and (r/c) distributions and the resulting shapes were analyzed and the performance was logged and the best combination was then sent on for Wing/Body/Nacelle/Diverter analysis using the OVERFLOW (Navier-Stokes) code. The final step was to use a modified version of OVERDISC (OVERFLOW coupled with the Constrained Direct Iterative Surface Curvature inverse design method) code. In this phase of the design, the lower surface (and to some extent the upper surface) was modified to take advantage of the pressure field generated by the Nacelles and Diverters.



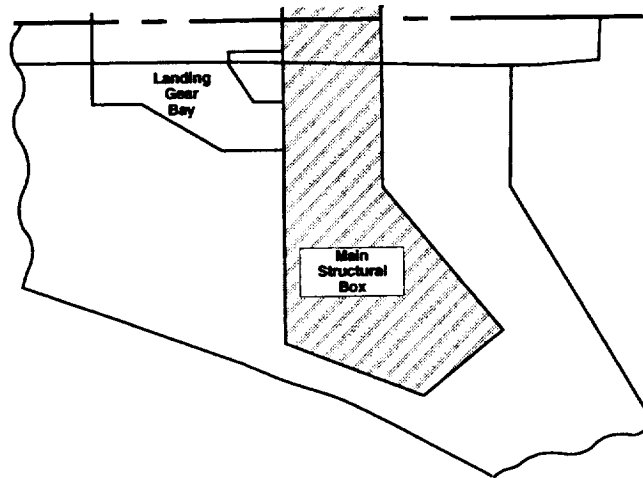
EULER (OPT3D) PREDICTED DRAG CHARACTERISTICS
M2.4-7A ARROW WING W/B CONFIGURATIONS
 $M_\infty = 2.40, C_L = 0.10$



The data above are Euler calculations from the OPT3D code for the Wing/Body configurations at Mach 2.4 and the design C_L (0.10). The 3 configurations shown are the baseline (linear theory), the MDA OPT5, and an interim NFW design. A skin friction drag of 39.6 counts (0.00396) has been added to all of the inviscid results. The baseline data (represented by circles) was found to have the highest drag at about 107.5 counts. The OPT5 configuration had about 103.5 counts of drag and the NFW configuration had about 101.5 counts of drag. By running the OPT3D code in optimization mode (where twist was optimized), the NFW 12BNS T (for twist) was found to have about 99.5 counts of drag at the cruise condition. Thus, a 6 to 8 count reduction in drag over the baseline was found to be achievable. However, since this was early in the design process (about a month and a half after starting the project), not all considerations had been made. The biggest consideration that was neglected were considerations of how the wing structural box would affect the shape and performance of the designs.



HSCT M2.4-7A ARROW WING
MAIN STRUCTURAL BOX BOUNDARIES

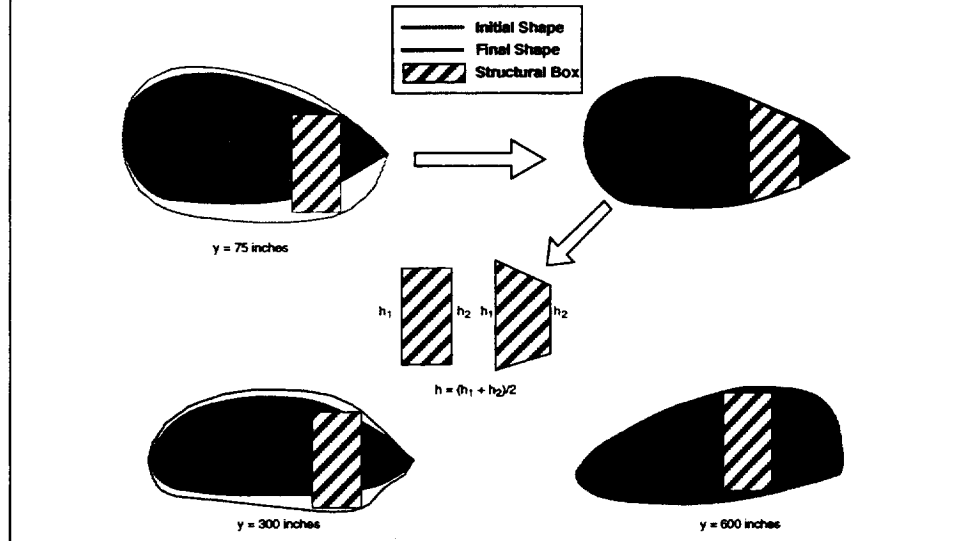


Shown above is a schematic of the location of the main structural box and the landing-gear bay. Because the structural box is placed very far aft on the wing, impact to the design was quite dramatic.

Because of the impact in the design, structures experts at MDA were asked what the critical dimensions of the structural box were and if they could be modified to any extent. The critical dimension was determined to be "h" which is defined as the average of the forward and aft structural box heights. Thus, a wing was generated using this "warped" structural box and is shown on the next figure.

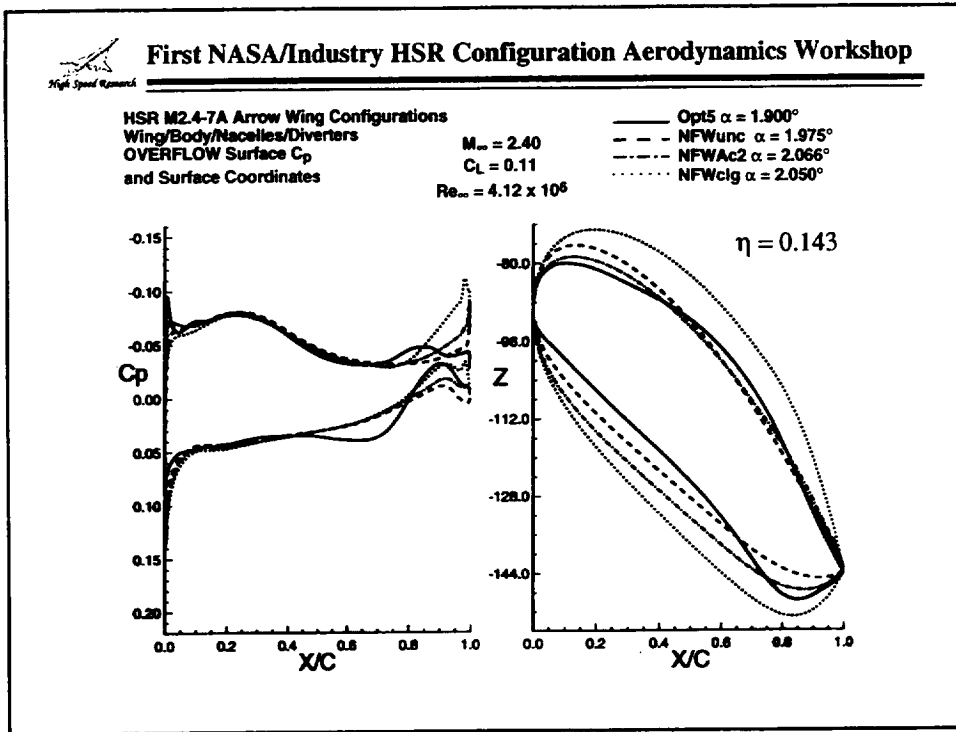


MODIFICATIONS TO THE NFW "AIRFOIL" SHAPE DUE TO STRUCTURAL BOX CONSTRAINTS



In the middle of the figure above, is a schematic of the rectangular structural box and the “warped” structural box used as the design constraint in the NFW generation code. Because all other design efforts were using a “rectangular” structural box, it was decided to design wings with both structural box shapes to determine the impact of changing that shape. The shaded region (in the airfoils above) are the “warped” structural box constrained airfoils and the solid line is the “rectangular” structural box constrained airfoils. The effect of the changes adds volume inboard and a substantial amount of drag.

In the following figures, the “warped” structural box constrained wing will be labeled as nfwunc, the “rectangular” structural box constrained wing will be labeled as nfwc (nfwac or nfwac2), and with the additional landing gear constrained wing will be labeled nfwac1g.



The figure above (and the figures on the next two pages) shows the 4 geometries previously described. On the right are airfoil definitions and on the left are the corresponding pressure distributions at the 14.3% semi-span location on the wing. The results are from OVERFLOW at Mach 2.4, Re 4 million/foot and a lift coefficient of 0.11 (Wing/Body/Nacelle/Diverter).

The airfoil geometries show that all three NFW wings have more volume near the leading edge than the OPT5 geometry and that the NFWac1g geometry has the most volume everywhere.

The pressure contours show less suction at the leading edge for the NFW wings than the OPT5 geometry and in general the NFW pressure contours have more gradual variations in the streamwise direction than the OPT5 geometry (on the lower surface this could provide more uniform flow conditions at the nacelle inlet).

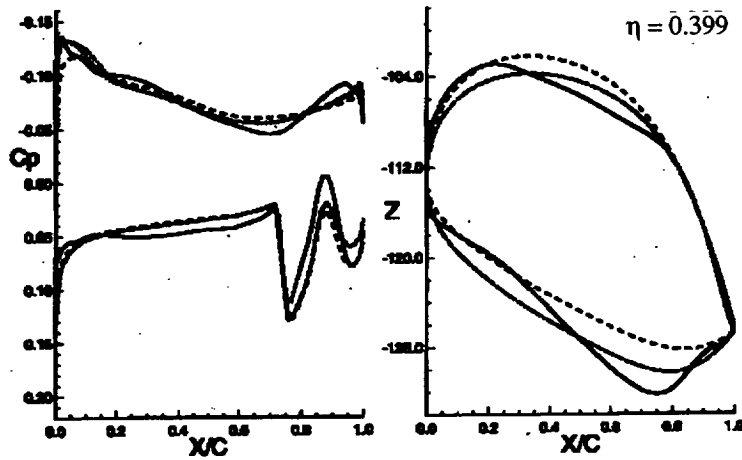


First NASA/Industry HSR Configuration Aerodynamics Workshop

HSR M2.4-7A Arrow Wing Configurations
Wing/Body/Nacelles/Diverters
OVERFLOW Surface C_p
and Surface Coordinates

$M_\infty = 2.40$
 $C_L = 0.11$
 $Re_\infty = 4.12 \times 10^6$

— Opt5 $\alpha = 1.900^\circ$
- - - NFWunc $\alpha = 1.975^\circ$
- · - · NFWAc2 $\alpha = 2.066^\circ$
· · · · NFWclg $\alpha = 2.050^\circ$



The figure above are the airfoil shapes and corresponding surface pressure distributions at the 40% semi-span location. Once again, the NFW configurations have more volume near the leading edge than the OPT5 configuration. Also, the NFWAc2 and NFWAc1g configurations have the same shape from this span station to the tip, because the landing-gear constraint only affects the inboard region of the wing.

The surface pressure distributions again show slightly less expansion on the upper surface leading edge for the NFW wings than OPT5 wing and the recompression is smoother. The lower surface pressure distribution is again very gradual expansion (though nearly constant pressure) to the shock generated from the Nacelle/Diverter.

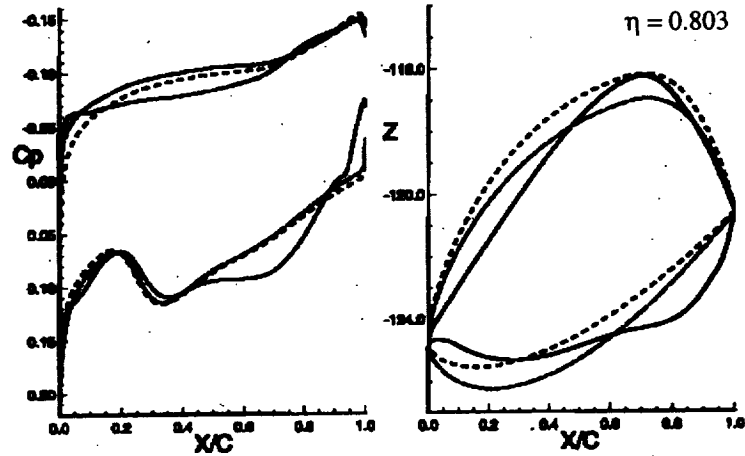


First NASA/Industry HSR Configuration Aerodynamics Workshop

HSR M2.4-7A Arrow Wing Configurations
Wing/Body/Nacelles/Diverter
OVERFLOW Surface C_p
and Surface Coordinates

$M_\infty = 2.40$
 $C_L = 0.11$
 $Re_\infty = 4.12 \times 10^6$

— Opt5 $\alpha = 1.900^\circ$
- - - NFWunc $\alpha = 1.975^\circ$
- · - · NFWac2 $\alpha = 2.066^\circ$
· · · · · NFWcig $\alpha = 2.050^\circ$



This figure shows airfoils and corresponding surface pressure distributions at the 80% semi-span location on the wings.

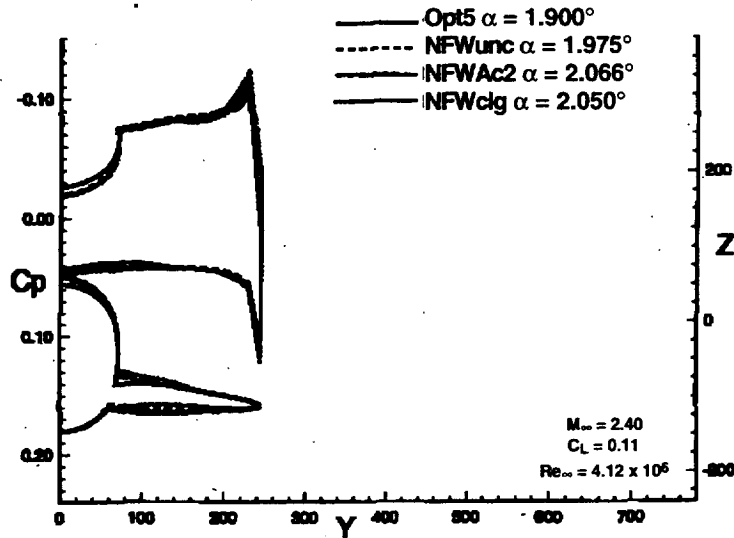
Once again, the NFW wings have more thickness near the leading-edge than the OPT5 configuration and in addition, the NFW wings have very blunt leading-edge radius whereas the OPT5 has a sharp leading edge.

The surface pressure distributions indicate a smoother expansion at the leading edge for the NFW wings than for the OPT5 (as expected due to the differences in the leading-edge shapes). All four wings have expanding flow conditions from the leading to the trailing edge on the upper surface (as expected and as predicted from the Natural Flow Wing assumptions). The lower surface pressure distributions are slightly different on the OPT5 and NFW wings mainly due to the OPT5 taking advantage of the Nacelle/Diverter shock impinging on the surface.



First NASA/Industry HSR Configuration Aerodynamics Workshop

HSR M2.4-7A Arrow Wing Configurations Wing/Body/Nacelles/Diverter OVERFLOW Surface C_p and Surface Coordinates at $X = 1700$ inches



The figure above and the following figure are cross-sectional cuts of the same 4 configurations with corresponding surface pressure coefficient data.

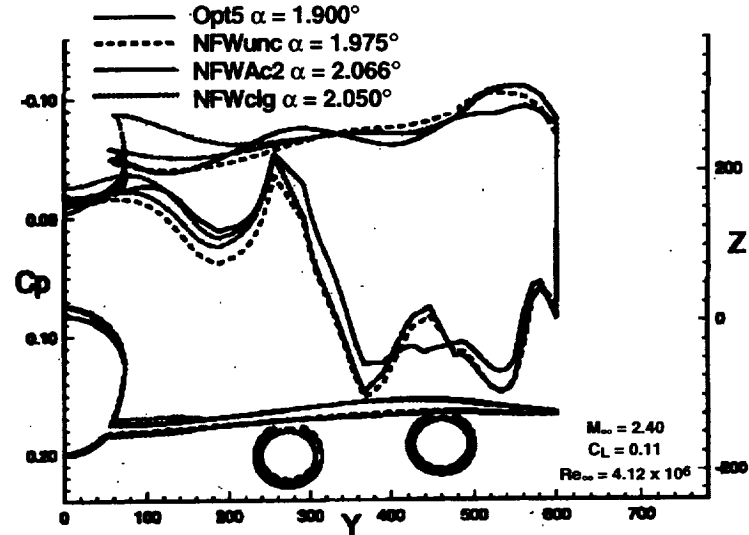
Two main geometrical observations can be made at this station (1700 inches). The fuselage and wings of the NFW configurations, all have more volume than the OPT5 configuration. Additionally, there are fewer geometrical “wiggles” in the spanwise direction for the NFW designs than the OPT5 design. The NFWcig design again has the most volume inboard due to the landing-gear constraint.

The surface pressure distributions for all four wings are very similar with the NFW designs having nearly constant pressure inboard to the leading edge.



First NASA/Industry HSR Configuration Aerodynamics Workshop

HSR M24-7A Arrow Wing Configurations Wing/Body/Nacelles/Diverters OVERFLOW Surface Cp and Surface Coordinates at X = 2700 inches



In this figure (located at $x = 2700$ inches), all four wings have similar cross-sectional shape (the NFWAc1g again has the landing-gear bump inboard). The fuselages of the NFW configurations, all have more volume than the OPT5 configuration.

The surface pressure distributions on the NFW wings upper surfaces have less variation spanwise than the OPT5 wing, however, the lower surface pressure distributions all behave similar with the largest differences occurring between the 2 nacelles.



First NASA/Industry HSR Configuration Aerodynamics Workshop

OVERFLOW AERODYNAMIC COMPARISONS OF THE M2.4-7A ARROW WING CONFIGURATION

Configuration	Mach No.	α (deg)	Reynolds No. (mill/ft)	S/2 (sq. in.)	V/2 (cu. in.)	Δ Volume (%-diff.)	CL	CD
OPT5	2.4	1.900	4	644400	40040000	0.00	0.110598	0.013604
NFW	2.4	2.000	4	644400	40440000	1.00	0.110695	0.013473
NFWAc	2.4	2.050	4	644400	41450000	3.52	0.110528	0.013620
NFWAc1g	2.4	2.050	4	644400	43240000	7.99	0.110667	0.013941

Configuration	Mach No.	α (deg)	Reynolds No. (mill/ft)	S/2 (sq. in.)	V/2 (cu. in.)	Δ Volume (%-diff.)	CL	CD
OPT5	2.4	1.900	4	644400	40040000	0.00	0.110598	0.013604
NFWAc2	2.4	2.066	4	644400	41980000	4.85	0.110604	0.013676
NFWAc4	2.4	2.076	4	644400	41970000	4.82	0.110614	0.013608

The data above reflects the results of the two portions of the viscous design activity. The upper table are OVERFLOW analyses of the Wing/Body/Nacelle/Diverter configurations for the OPT5, NFW (unconstrained), NFWAc (constrained), and NFWAc1g (constrained for wing box and landing gear). The lower table are the results from the application of the OVERDISC method for Nacelle/Diverter integration. The results are at the design Mach number (2.40) and C_L (1.1). At these conditions, the NFW configuration (shown in the upper table) has the lowest predicted drag (about 1.5 counts lower than the OPT5 configuration) and has a 1 percent increase in volume. The constrained configuration, NFWAc, has roughly the same drag as the OPT5 (0.2 counts higher) and has about 3.5 percent increase in volume. The landing-gear constrained configuration, NFWAc1g, has the highest predicted drag (about 3.4 counts higher than OPT5) and has an 8 percent increase in volume.

Because all structural box constraints had to be met, the NFWAc configuration was chosen for the OVERDISC nacelle/diverter optimization (the rectangular structural box was chosen to be consistent with previous designs). In order to compare the Natural Flow Wing Philosophy directly to the OPT5 configuration, the leading and trailing edges were set to those of the OPT5 configuration (to remove any biases introduced by the twist optimization) and thickness distribution was slightly modified. This configuration was designated as the NFWAc2 configuration and was the starting point of the OVERDISC design cycle. The NFWAc4 configuration listed above was the final "optimized" design. The drag was equivalent to the OPT5 configuration, however, an additional 4.8 percent increase in volume was achieved (and deck angle constraints were met, i.e., they were not met in the OPT5 configuration).

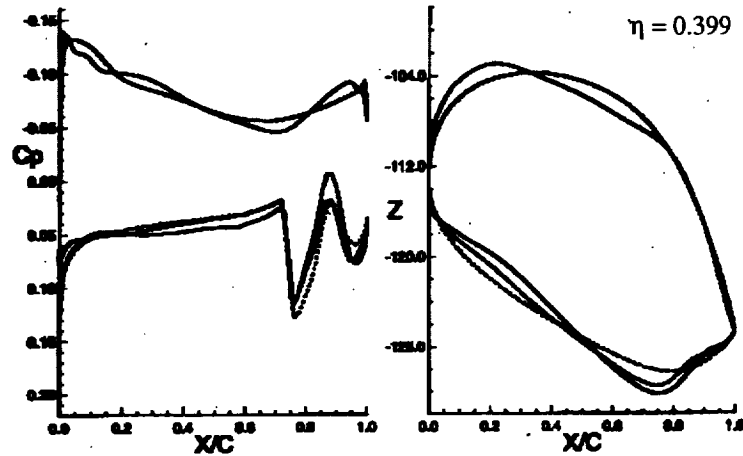


First NASA/Industry HSR Configuration Aerodynamics Workshop

HSR M2.4-7A Arrow Wing Configurations
Wing/Body/Nacelles/Diverter
OVERFLOW Surface C_p
and Surface Coordinates

$M_\infty = 2.40$
 $C_L = 0.11$
 $Re_\infty = 4.12 \times 10^6$

— Opt5 $\alpha = 1.900^\circ$
- - - NFWAc2 $\alpha = 2.066^\circ$
- · - · - NFWAc4 $\alpha = 2.076^\circ$



The figure above (and the figures on the next two pages) shows the 3 geometries listed at the bottom of the previous table and shows the effect of the OVERDISC optimization to the lower surface shape of the NFW designs due to Nacelle/Diverter effects. Once again, on the right are airfoil definitions and on the left are the corresponding pressure distributions at the 40% semi-span location of the wings. The results are from OVERFLOW at Mach 2.4, Re 4 million/foot and a lift coefficient of 0.11 (Wing/Body/Nacelle/Diverter). The data at the 14.3% semi-span location are not shown, because the OVERDISC method did not change that semi-span station (all changes were done outboard of that location).

The airfoil geometries show that OVERDISC did not affect the shape of the upper surface, however the lower surface shape is beginning to look more like the OPT5 design to take advantage of the high pressures generated from the shocks generated on the Nacelle/Diverter.

The pressure contours between the two NFW designs shows very little difference until the shock impingement location on the lower surface. Here the shock strength is weakened and slightly lower drag is achieved locally.

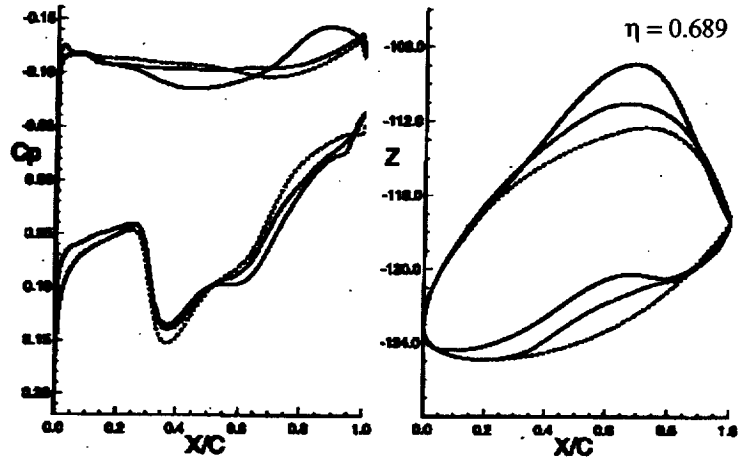


First NASA/Industry HSR Configuration Aerodynamics Workshop

HSR M2.4-7A Arrow Wing Configurations
Wing/Body/Nacelles/Diverters
OVERFLOW Surface C_p
and Surface Coordinates

$M_\infty = 2.40$
 $C_L = 0.11$
 $Re_\infty = 4.12 \times 10^6$

— Opt5 $\alpha = 1.900^\circ$
- - - NFWac2 $\alpha = 2.066^\circ$
- · - · - NFWac4 $\alpha = 2.076^\circ$



At the 70% semi-span station (shown above), the surface pressures look very similar between the two NFW designs, however, the geometries have varied quite a lot and can be seen primarily in the lower surface shape. Again, this recontouring of the lower surface shape provides localized drag reductions.

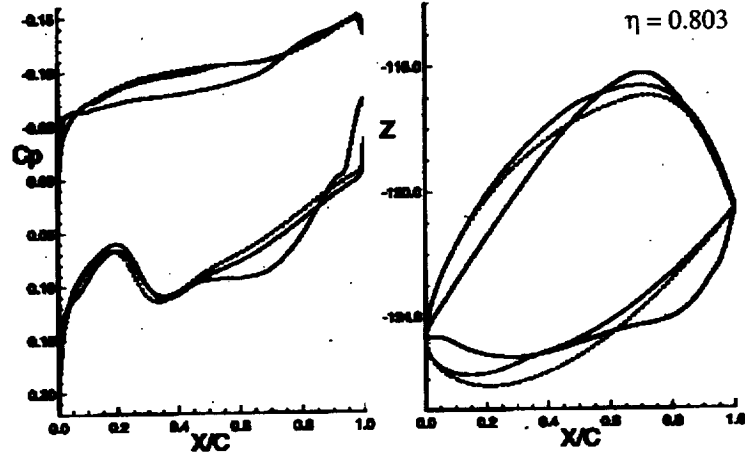


First NASA/Industry HSR Configuration Aerodynamics Workshop

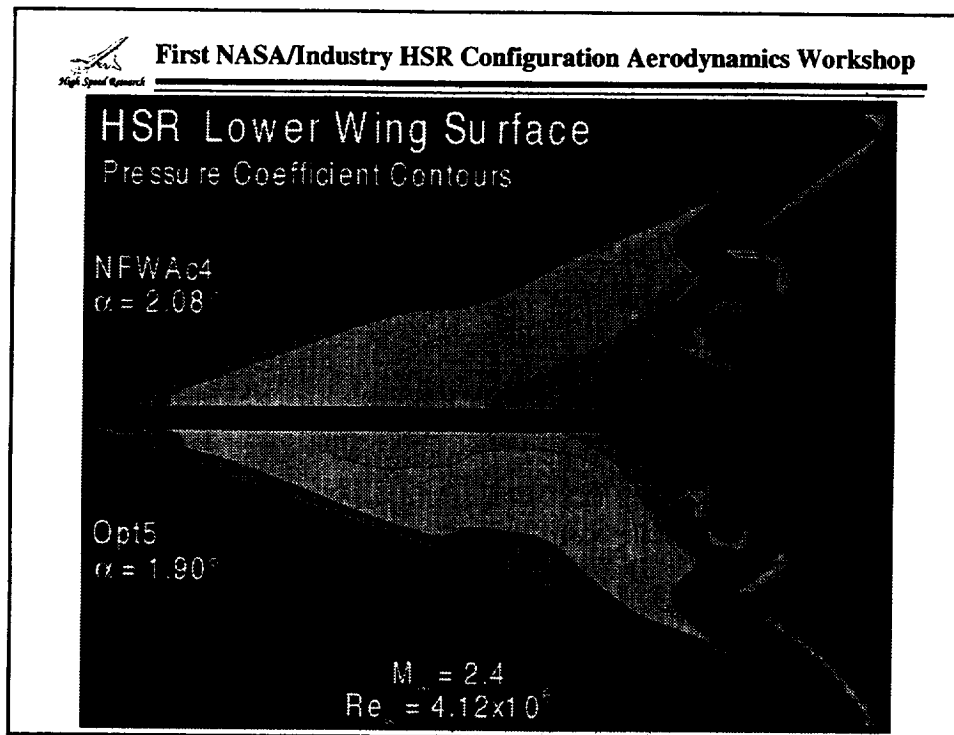
HSR M2.4-7A Arrow Wing Configurations
Wing/Body/Nacelles/Diverters
OVERFLOW Surface C_p
and Surface Coordinates

$M_\infty = 2.40$
 $C_L = 0.11$
 $Re_\infty = 4.12 \times 10^6$

— Opt5 $\alpha = 1.900^\circ$
- - - NFWAc2 $\alpha = 2.066^\circ$
- · - · NFWAc4 $\alpha = 2.076^\circ$

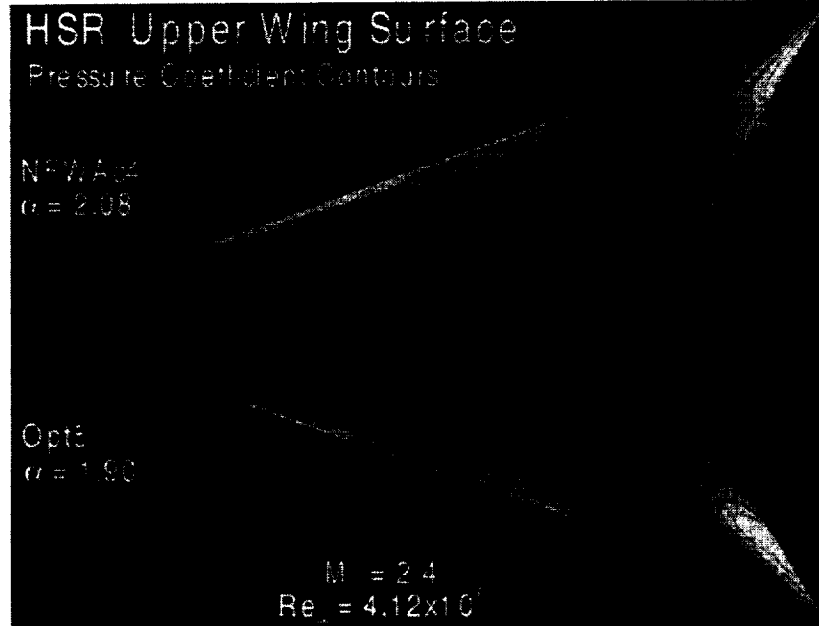


As was the case at the 70% semi-span station (previous page), the surface pressures at 80% semi-span location look very similar between the two NFW designs, and the geometries have varied a little and those differences can be seen primarily in the lower surface shape. Again, this recontouring of the lower surface shape provides localized drag reductions.



Shown above are the lower surface pressure coefficient contours for the NFWAc4 (top) and the OPT5 (bottom) Wing/Body/Nacelle/Diverter configurations as predicted from the OVERFLOW Navier-Stokes code at the design Mach number (2.40) and Lift ($C_L = 0.11$) at tunnel conditions ($Re = 4$ million/foot).

In general, the pressure fields are fairly similar between the two configurations (i.e., high pressure at the leading edge followed by gradually decreasing pressures in the streamwise direction). Both wings have a little too much expansion at the wing-body intersection trailing edge. This is unavoidable due to the location of the wing structural box being located so far aft on the wing. Finally, the NFW wing streamwise pressure distribution varies very little from root to tip (except where the pressures are dominated by the Nacelle/Diverter shocks and flowfields). The OPT5 configuration has slightly larger variations from the root to the tip (i.e., maintaining slightly higher pressures further in the streamwise direction inboard than the NFWAc4 configuration).



Shown above are the upper surface pressure coefficient contours for the NFWAc4 (top) and the OPT5 (bottom) Wing/Body/Nacelle/Diverter configurations as predicted from the OVERFLOW Navier-Stokes code at the design Mach number (2.40) and Lift ($C_L = 0.11$) at tunnel conditions ($Re = 4$ million/foot).

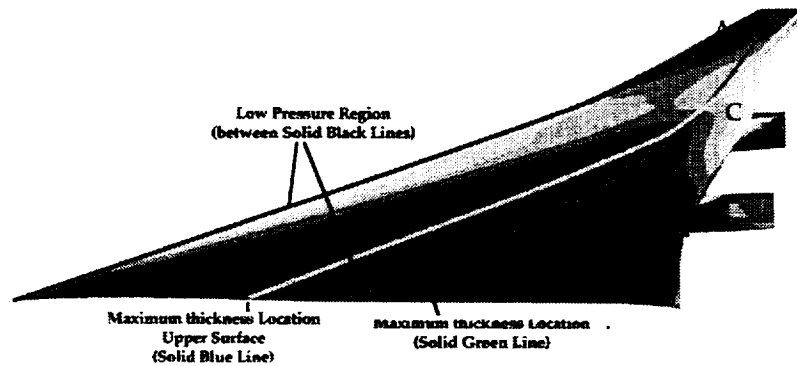
Once again, the character of the flow is very similar between both designs (i.e., expansion near the leading edge followed by a recompression region and then a fairly constant “higher” pressure streamwise with a slight re-expansion near the trailing edge). The NFW pressure distribution varies smoothly from root to tip, whereas the OPT5 pressure distribution varies a little less smoothly.

As an aside, because the NFW pressures don’t “peak” and then abruptly fall off at the leading edge of the wing, but rather reach a minimum pressure and then slowly increase from that level in the streamwise direction, the NFW designs should actually be able to maintain natural laminar flow (NLF) further downstream than most “optimized” designs.



NATURAL FLOW WING DESIGN APPLIED TO THE M2.4-7A PLANFORM

REGION	GEOMETRY	PRESSURE	DRAG
A	Positive Slope	high (compression)	high
B	Positive Slope	low (expansion)	low
C	Negative Slope	low (expansion)	high
D	Negative Slope	high (compression)	low



The figure above is the same upper surface pressure contour plot for the NFWAc4 configuration from the previous figure. The purpose of this figure is to illustrate the effectiveness of matching the upper surface contours to the surface pressures. Two solid “black” lines bound the “low” pressure region on the wing. The first one is located at the leading edge of the wing inboard to the crank and then fairly closely matches the inboard sweep outboard of the crank. The second black line runs roughly parallel with the leading edge of the wing inboard and then near the crank region it turns and comes back inboard to the top of the inboard nacelle. The solid “blue” (or light gray) line indicates the maximum thickness location for the wing upper surface. The solid “green” (or dark gray) line indicates the maximum thickness location for the entire wing (upper and lower surfaces). As in the definition of the NFW design philosophy, regions of high and low drag can be identified by observing where the upper surface maximum thickness line (blue) intersects the low pressure region lines (black). Surface slopes forward of the maximum thickness line are positive (or forward facing) and aft of the maximum thickness line are negative (or aft facing). Thus, region A is a high drag region because high pressures are acting on a forward-facing surface. Region B is a low drag region because low pressures are acting on a forward-facing surface. Region C is a high drag region because low pressures are acting on an aft-facing surface. And region D is a low drag region because high pressures are acting on an aft-facing surface. Region A is fairly small, however, region C is fairly large and the surface contours could be modified to reduce the drag in those regions.



First NASA/Industry HSR Configuration Aerodynamics Workshop

NASA LaRC UNITARY PLAN WIND TUNNEL HSR NFWAc4 M2.4-7A ARROW WING CONFIGURATION

- The NFWAc4 configuration was tested at the following conditions:
 - Mach 1.80, Re 2.0×10^6 /ft (bow shock impinged on sting and perhaps aftbody); Mach 2.00, Re 1.0, 1.5, 2.0, 2.5, 3.0, 3.5, 4.0×10^6 /ft; and Mach 2.16, Re 2.0×10^6 /ft [free transition and forced transition using 0.0107” sand grit]
 - The model was pitched from -3° to 8° angle of attack and yawed from -6° to 6° sideslip angles.
 - Force/Moment and Surface Pressure data were obtained for the Wing/Body and Wing/Body/Nacelle/Diverter Configurations.
 - Uncertainty analysis was run on the Wing/Body configuration at Mach 2.0, Re 4.0×10^6 /ft. The following data show the maximum data variability over the entire angle of attack range:
 - $C_L = \pm 0.0012$
 - $C_D = \pm 0.00008$
 - $C_M = \pm 0.0002$
 - $C_N = \pm 0.001$
 - $C_A = \pm 0.00007$

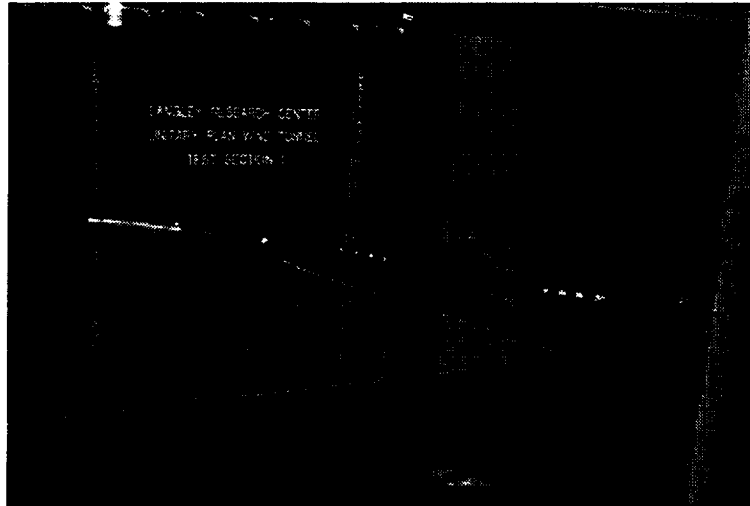
The next section of the paper concerns the NASA LaRC Unitary Plan Wing Tunnel (UPWT) Test Section 1 entry of the NFWAc4 configuration.

As mentioned above, data was taken at three Reynolds numbers with emphasis at the Mach 2 Reynolds number 4 million/foot condition. Angle of attack varied between -3° and 8° and beta varied between -6° to 6° . In addition to the normal data acquisition, repeat runs were made to assess the uncertainty of the force and moment coefficients. Some of these data are shown above for the Mach 2 Reynolds number 4 million/foot condition. The maximum variation in C_D for the entire angle of attack range investigated was ± 0.00008 (± 0.8 counts).



First NASA/Industry HSR Configuration Aerodynamics Workshop

NFWAc4 MODEL INSTALLED IN THE NASA LaRC UPWT T.S.1

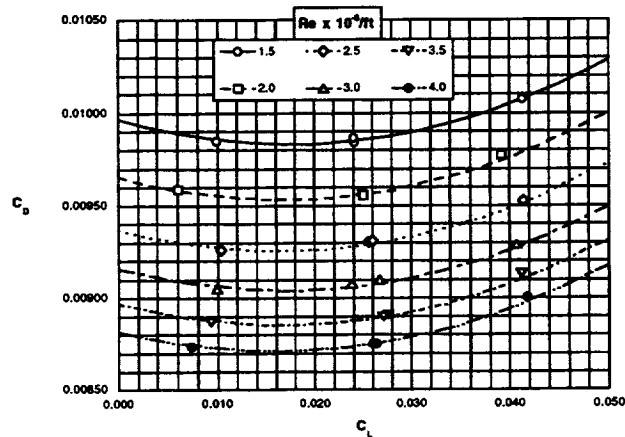


The photograph above shows the model installed in the NASA LaRC UPWT Test Section 1. The model is a truncated 1.675% scale of the M2.4-7A configuration. The overall length is 52.74 inches with a span of 25.7 inches.



VARIATION IN MINIMUM DRAG AT VARIOUS REYNOLDS NUMBERS

DRAG CHARACTERISTICS OF THE NFWA04 CONFIGURATION
NASA LaRC UPWT TS#1 DATA
M = 2.0, k = 0.0107" sand grit

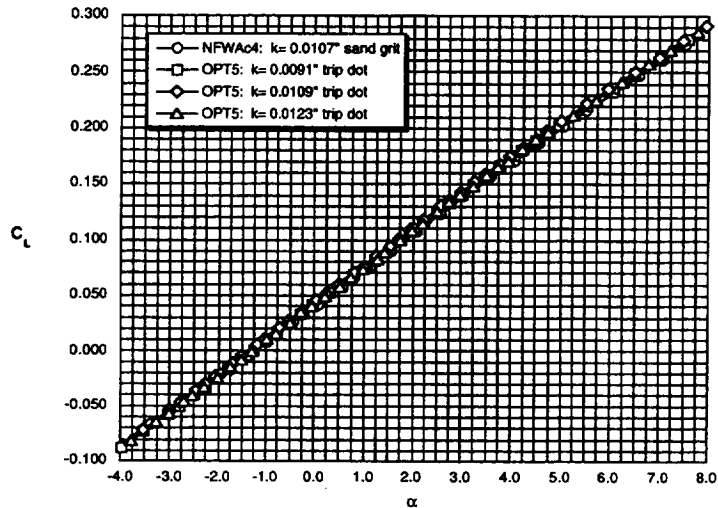


There are many methods of determining whether a transition trip is effective at transitioning the boundary layer to turbulent methods. One quick method employed in most UPWT tests is a Reynolds number sweep at alphas around $C_{D,min}$. If the trips are effective at transitioning the boundary layer to turbulent conditions, the data will show that for a given Mach number and size of grit that the minimum drag will decrease with increasing Reynolds number. The data above shows this very nicely. The Reynolds number was varied by 0.5 million/foot and the increments between the different conditions is slowly varying to smaller and smaller deltas in the $C_{D,min}$ values. If the boundary layer would not have been tripped, the data at one of the lower Reynolds number conditions would have had drag levels equivalent or lower than one of the higher Reynolds number conditions. This method does not provide an absolute value of the drag due to the trip, but it gives a quick determination of the state of the boundary layer and whether the trips are working properly.



First NASA/Industry HSR Configuration Aerodynamics Workshop

LIFT CHARACTERISTICS COMPARISONS MDAM24-7A OPT5 and NFWAc4 W/B Configurations $M_\infty = 2.00$, $Re_\infty = 4$ million/ft

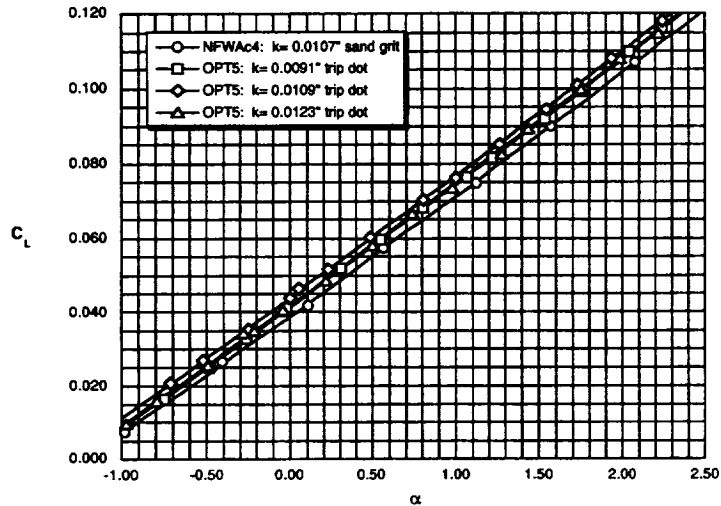


The lift characteristics of the M2.4-7A configurations (OPT5 and NFWAc4) are shown above at Mach 2.0, Reynolds number 4 million per foot. The circles represent the data for the NFW configuration and the others represent three variations in trip dot height on the OPT5 configuration. (The NFW test used sprinkled sand grit of 0.0107" at 0.4 inches back from the leading edge in the streamwise direction. This sand grit size was chosen by sizing the grit for Mach 2.0, Reynolds number 2 million/foot and 0.4 inch from leading edge conditions. The OPT5 test varied the trip dot height and observed whether transition occurred using sublimating chemicals).



First NASA/Industry HSR Configuration Aerodynamics Workshop

LIFT CHARACTERISTICS COMPARISONS
MDA M24-7A OPT5 and NFWAc4 WB Configurations
 $M_\infty = 2.00$, $Re_\infty = 4$ million/ft



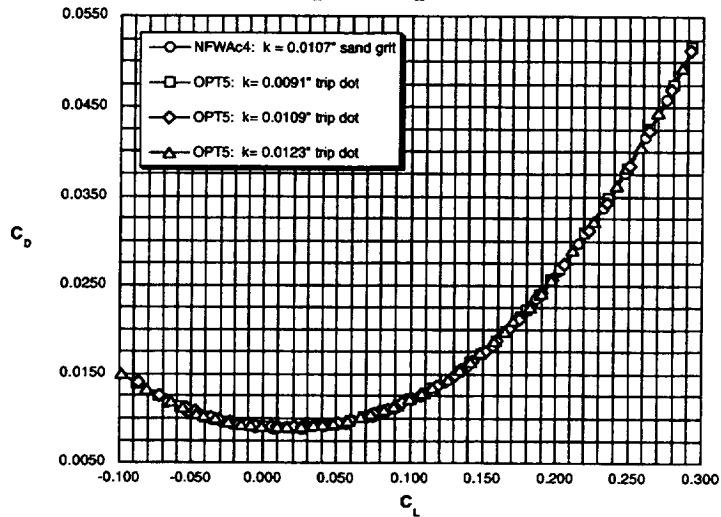
The figure above reduces the scale in angle of attack to make the differences in the lift curves more pronounced. It should be noticed that for the OPT5, the 0.0109" trip dots have an offset lift curve that may be accountable to variations in the tunnel conditions for that specific run and will be disregarded.

The slopes of the two configurations is the same as predicted for configurations with the same platform.



First NASA/Industry HSR Configuration Aerodynamics Workshop

DRAG CHARACTERISTICS COMPARISONS
MDA M24-7A OPT5 and NFWAc4 W/B Configurations
Unitary Plan Wind Tunnel, Test Section #1
 $M_\infty = 2.00$, $Re_\infty = 4$ million/ft

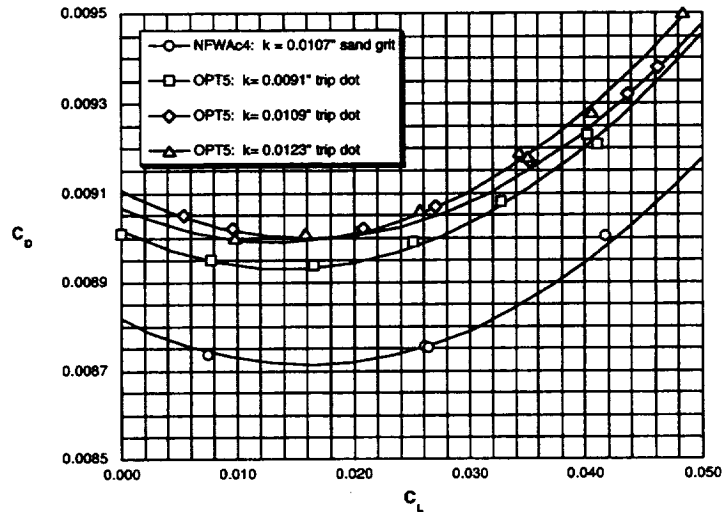


The figure above illustrates the drag characteristics for the 2 Wing/Body configurations again across the entire angle of attack range and for the different trip dot heights. The drag polar shapes are very similar between the two configurations, however, to see differences in the drag between the configurations one must blow up the scale and this is done in the next two figures (one at $C_{D,min}$ and one at the cruise condition $C_L = 0.10$).



First NASA/Industry HSR Configuration Aerodynamics Workshop

DRAG CHARACTERISTICS COMPARISONS
MDA M24-7A OPT5 and NFWA04 W/B Configurations
Unitary Plan Wind Tunnel, Test Section #1
 $M_\infty = 2.00$, $Re_\infty = 4$ million/ft

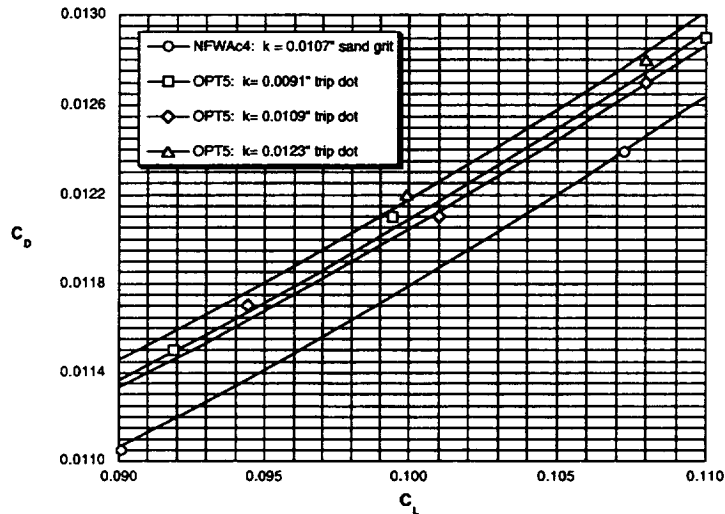


The data above show that the OPT5 W/B configuration was found to have between 2 and 2.5 counts (0.0002 to 0.00025) higher drag than the NFW W/B configuration. The “off-design” characteristics of the NFW design configurations should be slightly better than those for the OPT5 cruise-point designed configuration (recall that the NFW design philosophy was developed for highly swept wings across the Mach number range). This delta in C_D could also occur from small changes from one test to another (that have somehow been uncorrected for, i.e., slight change in placement of the models streamwise or spanwise in the tunnel, etc.).



First NASA/Industry HSR Configuration Aerodynamics Workshop

DRAG CHARACTERISTICS COMPARISONS
MDA M24-7A OPT5 and NFWAc4 WB Configurations
Unitary Plan Wind Tunnel, Test Section #1
 $M_\infty = 2.00$, $Re_\infty = 4$ million/ft



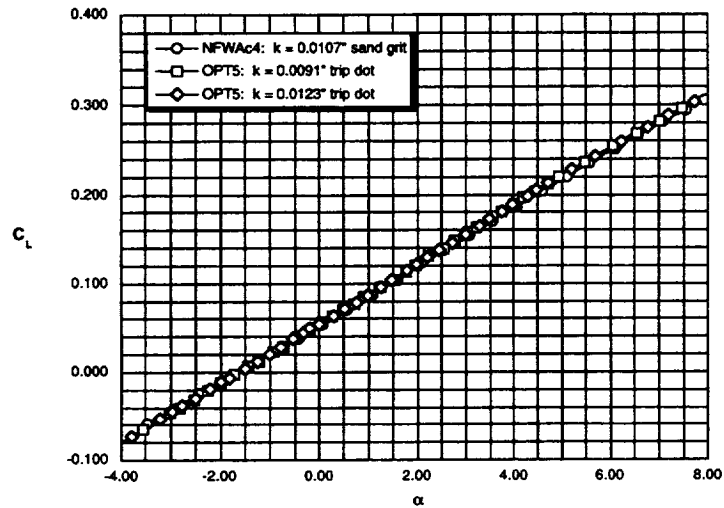
The data above again show about 2.5 to 3.5 counts (0.00025 to 0.00035) lower drag for the NFW W/B configuration than the OPT5 W/B configuration. Since this difference in drag is seen both at minimum drag and at cruise conditions, it appears that a minimum drag delta has occurred between the two models and that future tests will determine if this is physical or a result of testing two models 6 months apart. Another issue comes from the fact that the original test of the OPT5 configuration had a lot of dynamics occurring during the test (model dynamics influences α and C_D accuracy). The NFW test used a slightly shorter sting with the same balance. Most of the model dynamics was removed and much steadier conditions were observed. The effect of this on the data can be quite significant. Each individual data point better matches the averaged data (the scatter in the data can be quite large for a model undergoing dynamic oscillations, however, this is all washed out once it is averaged over a given amount of time). In addition, the test on the OPT5 condition also reported unsteady flow at Mach 2.0 which was not the case for the NFW test.

Aside from offset in drag, the characteristic shape of the drag polars are similar between the two configurations.



First NASA/Industry HSR Configuration Aerodynamics Workshop

LIFT CHARACTERISTICS COMPARISONS MDA M24-7A OPT5 and NFWAc4 W/BND Configurations $M_\infty = 2.00$, $Re_\infty = 4$ million/ft



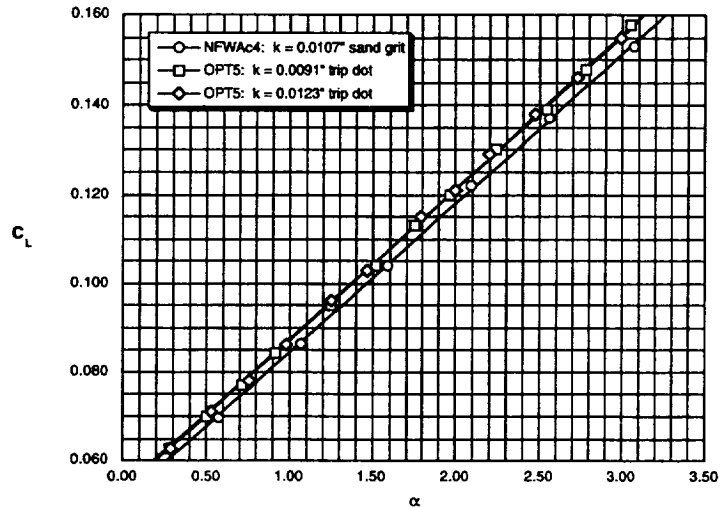
The full lift curve is shown above for the NFW and OPT5 W/B/N/D configurations. Again the NFWAc4 configuration had a 0.0107" sand grit and the OPT5 configuration had two trip dot heights that bracketed the sand grit height.

The lift curves were once again found to be quite similar.



First NASA/Industry HSR Configuration Aerodynamics Workshop

LIFT CHARACTERISTICS COMPARISONS
MDA M24-7A OPT5 and NFWAc4 W/BND Configurations
 $M_\infty = 2.00$, $Re_\infty = 4$ million/ft



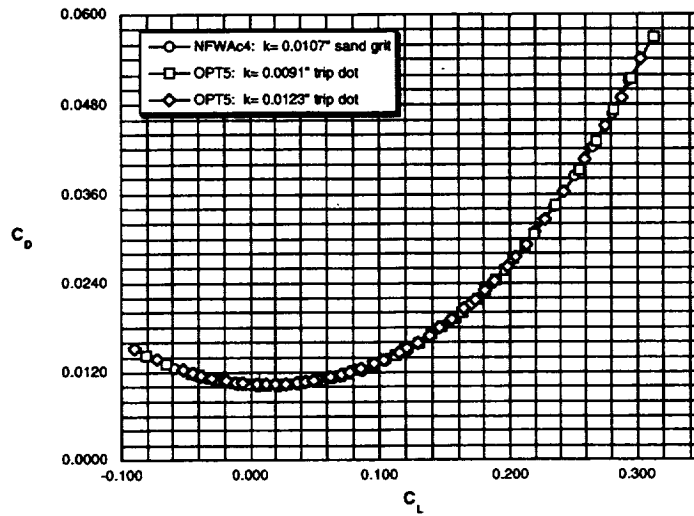
In the data shown above, the NFW configuration was found to have the same lift-curve slope but offset by around 2 tenths of a degree. This was predicted in the CFD analysis and the design condition was found to be around 0.2° higher than that for the OPT5 configuration.

The repeatability of the OPT5 for the two variations in trip dot height is also very good.



First NASA/Industry HSR Configuration Aerodynamics Workshop

DRAG CHARACTERISTICS COMPARISONS
MDA M24-7A OPT5 and NFWAc4 W/BND Configurations
Unitary Plan Wind Tunnel, Test Section #1
 $M_\infty = 2.00$, $Re_\infty = 4 \text{ million/ft}$

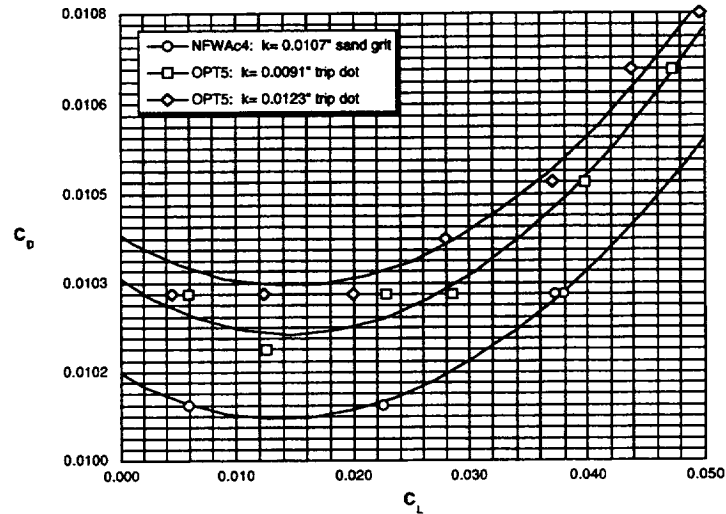


The corresponding drag characteristic plot for the two Wing/Body/Nacelle/ Diverter configurations is shown in the data above.



First NASA/Industry HSR Configuration Aerodynamics Workshop

DRAG CHARACTERISTICS COMPARISONS
MDA M2.4-7A OPT5 and NFWAc4 W/B/N/D Configurations
Unitary Plan Wind Tunnel, Test Section #1
 $M_\infty = 2.00$, $Re_\infty = 4$ million/ft



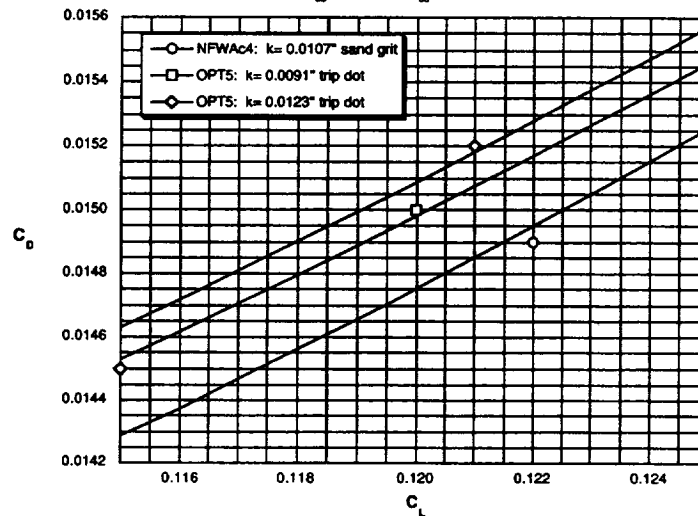
At the minimum drag condition, the OPT5 W/B/N/D configurations once again exhibited about 2 to 3 counts (0.0002 to 0.0003) higher drag than the NFW W/B/N/D configuration.

It should be pointed out that the scatter in the data for the OPT5 configuration is quite large and can be attributed to the dynamic character of the model in the tunnel.



First NASA/Industry HSR Configuration Aerodynamics Workshop

DRAG CHARACTERISTICS COMPARISONS
MDA M24-7A OPT5 and NFWAc4 W/BND Configurations
Unitary Plan Wind Tunnel, Test Section #1
 $M_\infty = 2.00$, $Re_\infty = 4$ million/ft



At the Mach 2 cruise C_L (0.12), the OPT5 W/B/N/D configurations once again exhibited about 2.5 to 3 counts (0.00025 to 0.0003) higher drag than the NFW W/B/N/D configuration.

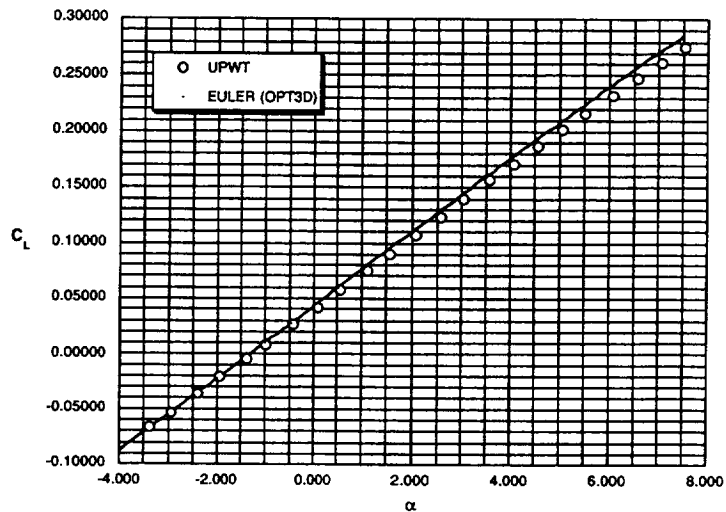
Because the CFD analyses did not predict 2 counts of drag reduction for the NFW over the OPT5 (about half a count, 0.00005, was predicted). Efforts to resolve this discrepancy are ongoing. It is the opinion of this researcher that a detailed grid study on the blunt leading edge of the outboard panel of the NFW configuration will account for some of the differences, however, most if not all of the discrepancies may be the cause of slight variations in the test setup between the two entries that have not been accounted for.

The next series of data will compare wind tunnel data to predicted Euler and Navier-Stokes data for the NFWAc4 configuration.



First NASA/Industry HSR Configuration Aerodynamics Workshop

LIFT CHARACTERISTICS COMPARISONS OF EPD AND CFD
MDAM24-7A NFWAc4 CONFIGURATION
 $M_\infty = 2.00$, $Re_\infty = 4 \text{ million ft}$



Shown above are the predicted (Euler) and wind-tunnel lift characteristics for the NFWAc4 Wing/Body configuration. As has been found repeatedly, the predicted levels of lift are always higher than those found experimentally. This effect can be attributed to the aeroelastic effects that occur and worsen at higher angles of attack (more bending and twisting of the wing at the higher loading conditions). However, in general, the data agrees very well.



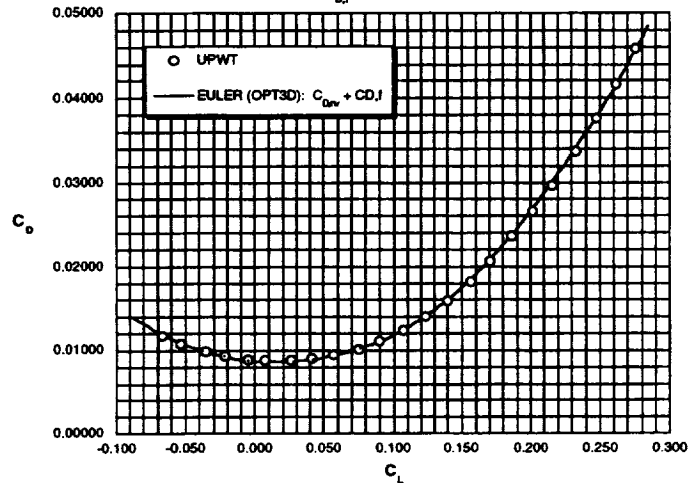
First NASA/Industry HSR Configuration Aerodynamics Workshop

DRAG CHARACTERISTICS COMPARISONS OF EFD AND CFD

MDA M24-7A NFWAc4 CONFIGURATION

$M_\infty = 2.00$, $Re_\infty = 4$ million/ft

$C_{D,f} = 0.0062$



Shown above are the predicted (Euler) and wind-tunnel drag coefficient values for the NFWAc4 Wing/Body configuration. The Euler data has been corrected by calculating a delta drag value between experiment and CFD at the minimum drag condition. This delta in drag was found to be 62 counts ($\Delta C_{D,f} = 0.0062$, skin friction and trip drag). The data fell within ± 0.25 counts of drag (± 0.000025) across the entire polar (except for 2 points at C_L values of 0.20 and 0.22 where the data was approximately a count off). This close comparison in both lift and drag characteristics between the predicted and experimental results provide a high confidence level in the use of the OPT3D (Euler) code for analysis purposes.

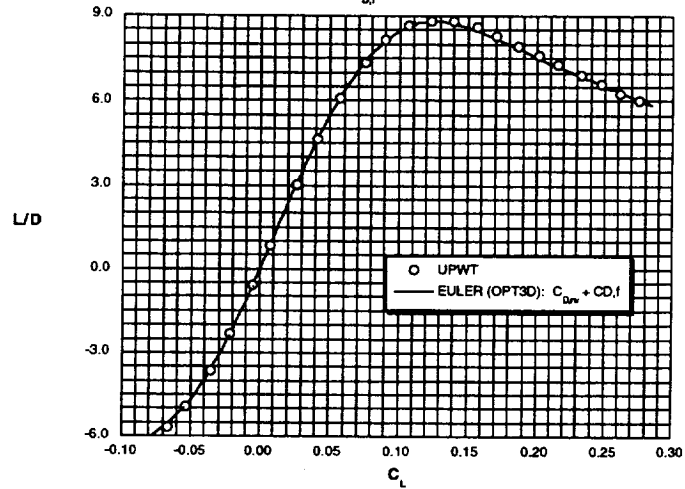


First NASA/Industry HSR Configuration Aerodynamics Workshop

PERFORMANCE CHARACTERISTICS COMPARISONS OF EFD AND CFD MDA M24-7A NFWAc4 CONFIGURATION

$M_\infty = 2.00$, $Re_\infty = 4 \text{ million ft}$

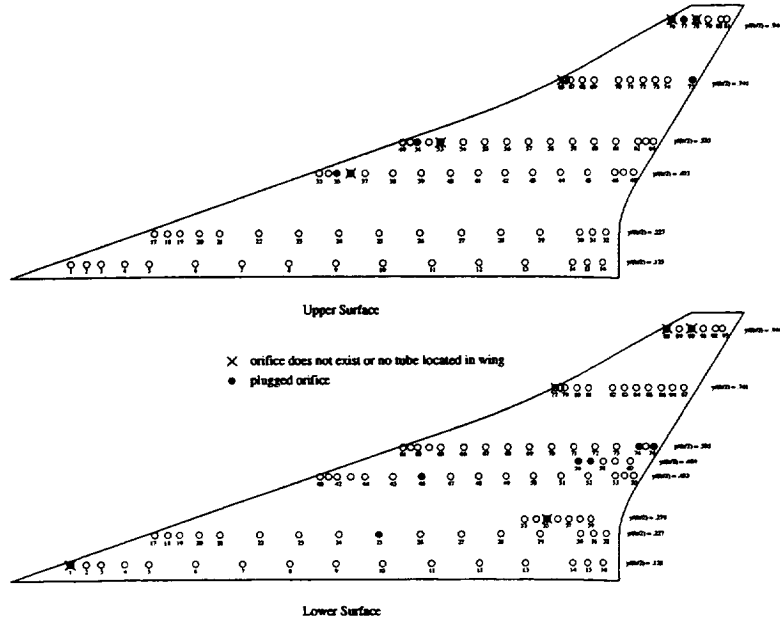
$C_{D,0} = 0.0062$



Shown above are the predicted (Euler) and wind-tunnel performance characteristics of the NFWAc4 Wing/Body configuration. Again, very good agreement is seen between the predicted and experimental results.



NASA Langley Research Center
Unitary Plan Wind Tunnel
Test 1828 - HSR NFW M2.4-7A Arrow Wing
Upper and Lower Wing Pressure Locations

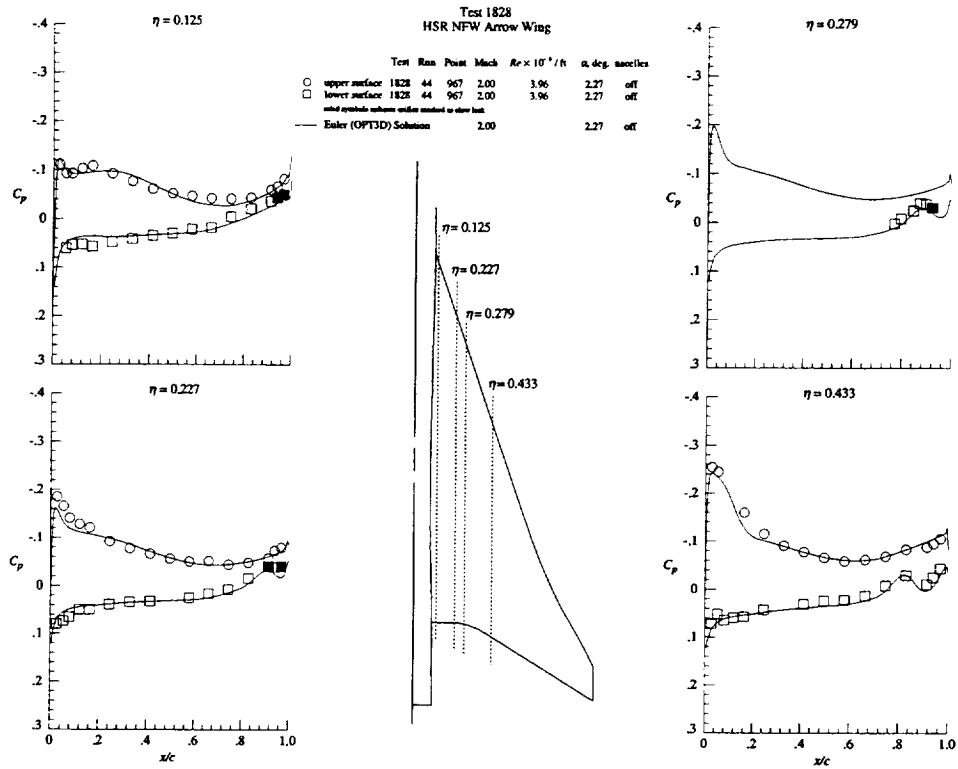


The figure above shows the surface pressure orifice locations on the NFWAc4 wind tunnel model. Plugged models are indicated by solid circles. Tubes that could not be manufactured into the model are indicated by an "X".

The next four figures will compare computational surface pressure coefficient distributions with wind tunnel results at Mach 2.0 and Reynolds number of 4 million/foot at a lift coefficient of 0.12.



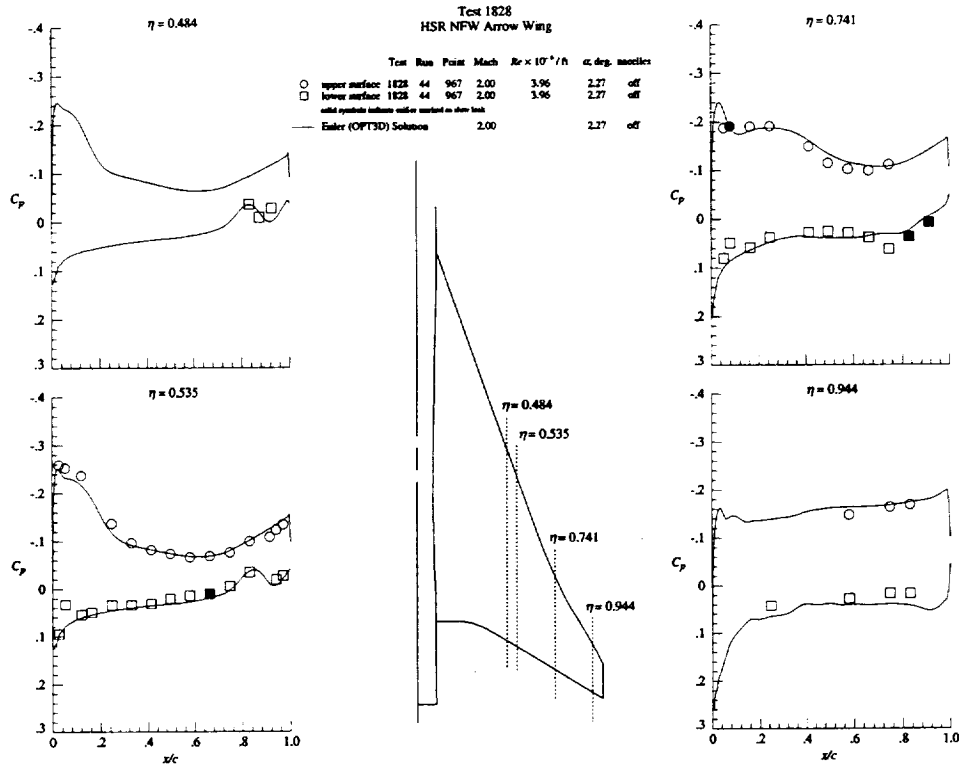
First NASA/Industry HSR Configuration Aerodynamics Workshop



The pressure distributions shown above compare the Euler (OPT3D) Wing/Body results to the wind tunnel data for the inboard 4 pressure tap locations on the wing. In general, the predicted pressures match the character of the flow very well and do a very good job at predicting the actual C



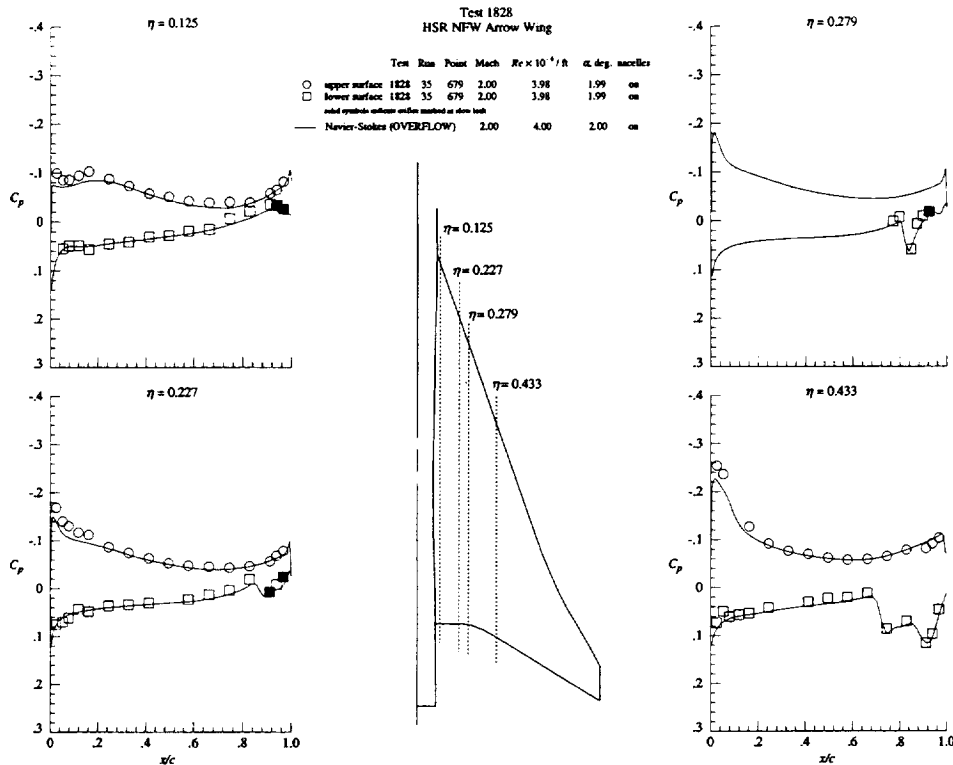
First NASA/Industry HSR Configuration Aerodynamics Workshop



The pressure distributions shown above compare the Euler (OPT3D) Wing/Body results to the wind tunnel data for the outboard 4 pressure tap locations on the wing. In general, the predicted pressures match the character of the flow very well. However, due to aeroelastic effects, the loading at the outboard panels is predicted to be slightly higher than was found experimentally. This corresponds with what was found from the force data shown earlier.



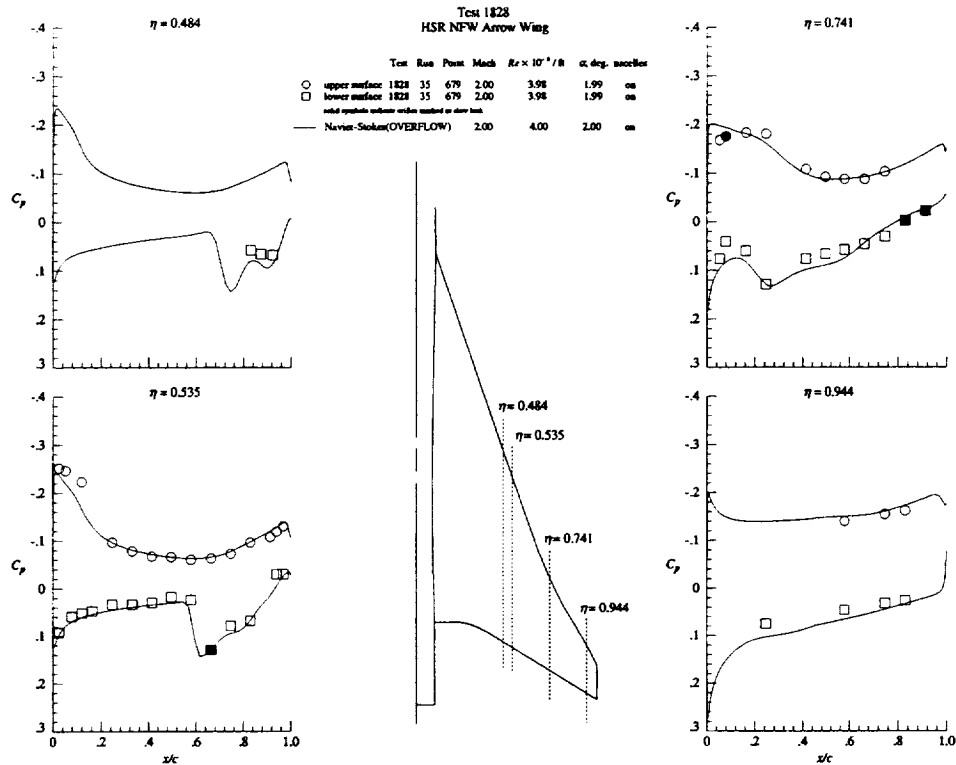
First NASA/Industry HSR Configuration Aerodynamics Workshop



The pressure distributions shown above compare the Navier-Stokes (OVERFLOW) Wing/Body/Nacelle/Diverter results to the wind tunnel data for the inboard 4 pressure tap locations on the wing. Again, the predicted pressures match the character of the flow very well and do a very good job at predicting the actual C_p values. Note, the code does an excellent job at predicting the character of the flow and the actual values of C_p in the Nacelle/Diverter regions of the wing.



First NASA/Industry HSR Configuration Aerodynamics Workshop



The pressure distributions shown above compare the Navier-Stokes (OVERFLOW) Wing/Body/Nacelle/Diverter results to the wind tunnel data for the outboard 4 pressure tap locations on the wing. Again, the predicted pressures match the character of the flow very well and do a very good job at predicting the actual C_p values. Note, the code does an excellent job at predicting the character of the flow and the actual values of C_p in the Nacelle/Diverter regions of the wing. Once again, the predicted loading is substantially higher than that found in the wind tunnel and can be related to aeroelastic bending and twisting of the wing (which tends to unload the outboard panel of the wing).



CONCLUSIONS

- The Natural Flow Wing design methodology was successfully applied to the HSR M2.4-7A Arrow Wing configuration.
 - The resulting geometry with the same total vehicle volume had large reductions in drag, however, due to 'structural box' constraints; a configuration with less drag reduction but with more volume was chosen for fabrication.
- OVERDISC (OVERFLOW/CDISC & NFW)
 - Gross modifications to the wing/body geometry were quickly and efficiently incorporated into the wing/body/nacelle/diverter volume grid. Full Navier-Stokes solutions were then obtained and the performance was compared to the MDA OPT5 configuration as a baseline datum. Modified routines in the CDISC environment allowed the surfaces to be reshaped due to the effects of the nacelle/diverter in the flowfield (i.e., the shock impingement on the lower surface of the wing).
- Wind Tunnel Results
 - The results from the NASA LaRC Unitary Plan Wind Tunnel test compare very well with those predicted using either an Euler method (OPT3D) for Wing/Body calculations or Navier-Stokes (OVERFLOW) for Wing/Body/Nacelle/Diverter Solutions.
 - Because the NFW design philosophy was developed for configurations with highly swept wings for all Mach numbers, the NFW M2.4-7A should and did exhibit improved drag characteristics over a cruise-point-design configuration.

As the conclusions state above, a Natural Flow Wing designed configuration can have large performance gains over a linear theory design. If structural box constraints can be "modified", even larger benefits can be achieved.

The preliminary experimental results show that the NFW designed configuration can have as much improvement over a linear theory design as a computationally optimized configuration. A knowledge based design applied early in the configuration design process, followed by a computational optimization procedure, should be able to more rapidly reach a more globally optimized configuration.

The CFD tools chosen for this effort had excellent agreement with the results found in the experimental test both force values and surface pressure values. Variations were evident due to aeroelastics and in the future those effects will be routinely measured in the wind tunnel and predicted in the CFD methods.

First NASA/Industry HSR Configuration Aerodynamics Workshop

Analysis and Inverse Design of the
HSR Arrow Wing Configuration with
Fuselage, Wing, and Flow Through Nacelles

Steven E. Krist
Steven X. S. Bauer
NASA Langley Research Center



Analysis and Inverse Design of the HSR Arrow Wing Configuration with Fuselage, Wing, and Flow Through Nacelles

The design process for developing the natural flow wing design on the HSR arrow wing configuration utilized several design tools and analysis methods. Initial fuselage/wing designs were generated with inviscid analysis and optimization methods in conjunction with the natural flow wing design philosophy. A number of designs were generated, satisfying different system constraints. The initial design process and details on the different natural flow wing designs are provided in the paper "Application of the Natural Flow Wing Design Philosophy to the HSR Arrow Wing Configuration" by S.X.S. Bauer and S.E. Krist, contained in these proceedings.

Of the three natural flow wing designs developed, the NFWAc2 configuration is the design which satisfies the constraints utilized by McDonnell Douglas Aerospace (MDA) in developing a series of optimized configurations; a wind tunnel model of the MDA designed OPT5 configuration was constructed and tested.

The present paper is concerned with the viscous analysis and inverse design of the arrow wing configurations, including the effects of the installed diverters/nacelles. Analyses were conducted with OVERFLOW, a Navier–Stokes flow solver for overset grids. Inverse designs were conducted with OVERDISC, which couples OVERFLOW with the CDISC inverse design method.

An initial system of overset grids was generated for the OPT5 configuration with installed diverters/nacelles. An automated regriding process was then developed to use the OPT5 component grids to create grids for the natural flow wing designs. The inverse design process was initiated using the NFWAc2 configuration as a starting point, eventually culminating in the NFWAc4 design for which a wind tunnel model was constructed. Due to the time constraints on the design effort, initial analyses and designs were conducted with a fairly coarse grid; subsequent analyses have been conducted on a refined system of grids. Comparisons of the computational results to experiment are provided at the end of this paper.

OVERFLOW Analysis of Opt5

MDA 1.35 million grid point fuselage/wing grid generated for flow conditions of $M=2.4$, $Re=2.0 \times 10^6$

GRIDGEN was to generate Nacelle/Diverter component surface and volume grids, HYPGEN was used to generate volume grids for some of the surface grids

17 block 3.1 million grid point chimera grid

OVERFLOW Analyses:

Baldwin–Barth turbulence model

Central Differencing

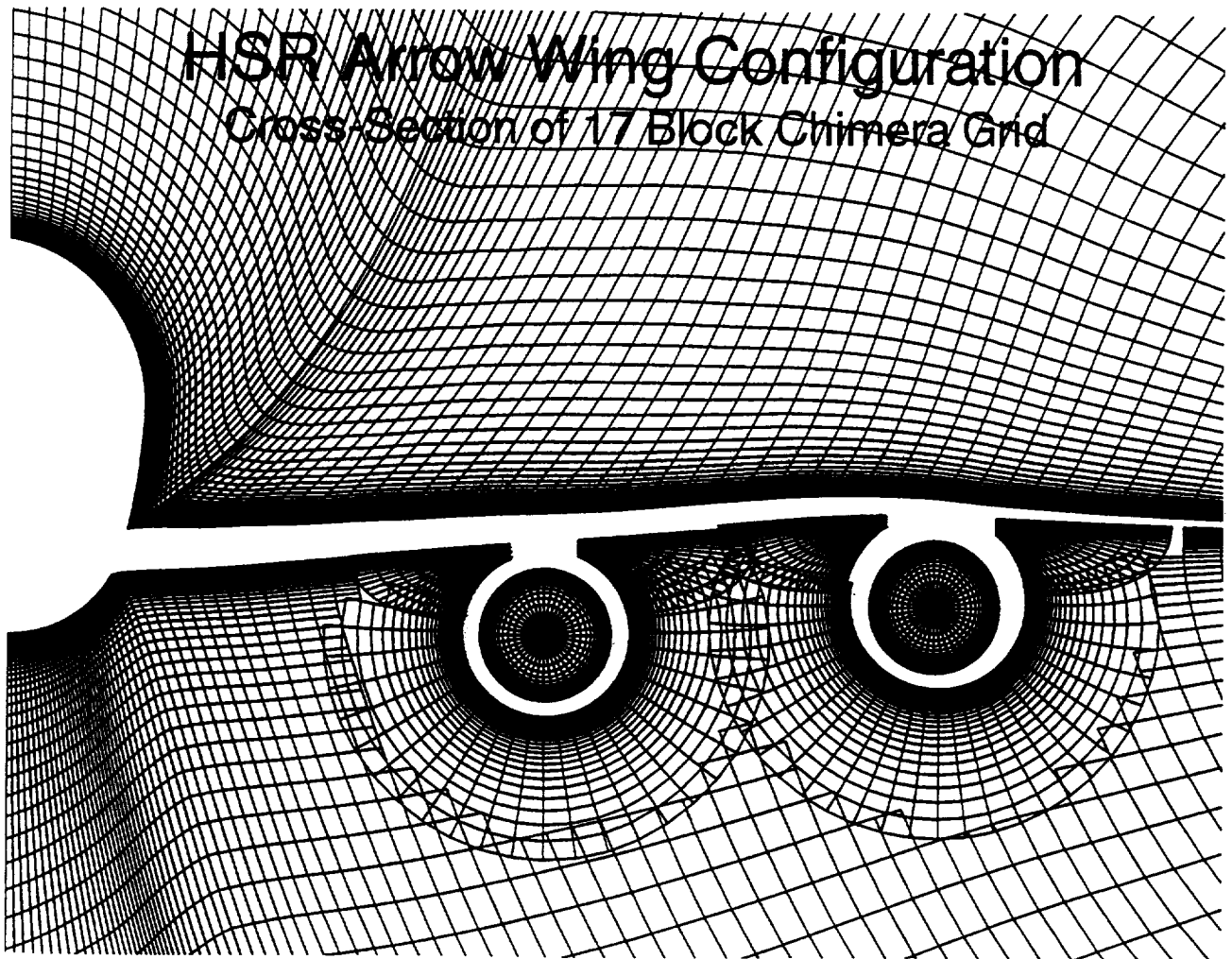
$Re=2.0 \times 10^6$ $M=2.4$

OVERFLOW Analysis of OPT5

Viscous analyses for redesigns on the HSR arrow wing planform were begun with the MDA fuselage/wing grid generated for the OPT5 configuration. This 1.35 million grid point single block grid was generated for flow conditions of $M=2.4$, $Re=2.0 \times 10^6$. All initial analyses and inverse design runs were conducted at these conditions.

Component surface and volume grids for the inboard and outboard diverter/nacelle configurations were generated with GRIDGEN. Volume grids were generated for the diverter grids which have three faces lying on a solid surface (the wing, diverter, and external nacelle). Surface grids were generated for the shelf and external nacelle; HYPGEN was used to generate volume grids from the surface grids. The resulting chimera grid for the full configuration embodies 17 blocks consisting of a total of 3.1 million grid points.

Analyses were run with OVERFLOW, using central–differencing and the Baldwin–Barth turbulence model.



Cross-Section of 17 Block Chimera Grid

This cross-section on the wing body grid is taken at roughly 60% chord, with cross-sections of component grids taken at sections as close to the wing grid cross-section as possible. Gaps appear to occur between the grids, however, this is solely due to the difficulty in finding a single station where cross-sections from the various component grids line up.

The components of each diverter/nacelle configuration shown here are an external nacelle grid, nacelle core grid, and two diverter grids, inboard and outboard, with surfaces lying on the wing, diverter, and nacelle. In addition, each diverter/nacelle configuration contains a shelf grid and two wedge grids which run side by side with the shelf until the shelf becomes flush with the nacelle surface.

Analyses for the NFW Configurations

Start with Surface Grid from TEAM

Generate a surface grid topologically identical to the OPT5 surface grid, then project the OPT5 volume grid onto the new surface grid

Run 1700 line script file to add component grids

- maintain a constant length at the diverter leading edge
- translate all blocks with a nacelle surface accordingly
- restretch wing surfaces onto new wing definition
- all translations and projections are in the vertical direction

Run PEGSUS, OVERFLOW, FOMOCO

Inverse designs were started with the NFWAc2 configuration

Analyses for the NFW Configurations

Navier–Stokes analyses were generated for each of the natural flow wing designs. This process started with the single block surface grids for the redesigned fuselage/wing configurations obtained from the TEAM code. The initial surface grids were then used to generate new surface grids topologically identical to the OPT5 surface grid. Volume grids were generated by projecting the OPT5 volume grid onto the new surface grids, restretching the grid from the surface to the far boundary.

Grids for the installed configuration were generated through use of a script file to translate and project the diverter/nacelle component grids from the OPT5 configuration onto the new fuselage/wing surface definition. Within the script, all grids associated with each nacelle are translated to maintain a constant distance between the wing and nacelle at the diverter leading edge. Then all grids containing a surface which lies on the wing surface are restretched, projecting the appropriate surface onto the new wing surface. The shelf surface is redefined by projecting the shelf grid line which lies on the trailing edge of the wing onto the trailing edge of the new wing and linearly stretching all grid lines running from the wing trailing edge to the intersection of the shelf with the nacelle surface.

With the new component grids defined, PEGSUS is rerun to compute the interpolations for the new set of overset grids, OVERFLOW is run to get a new solution, and FOMOCO is run to compute the configuration force and moments.

The natural flow wing redesigns on the arrow wing planform were analyzed at the design point ($M=2.4$, $Cl=0.11$). From these analyses the NFWAc2 configuration was found to have the best performance. All inverse designs were started from the NFWAc2 configuration.

OVERDISC

OVERDISC couples OVERFLOW, PEGSUS, and the Constrained Direct Iterative Surface Curvature (CDISC) inverse design method in a script file

- OVERFLOW: Navier–Stokes flow solver for overset grids
- CDISC: stand alone inverse design code with flow and geometry constraints (CFL3D, TLNS3D, OVERFLOW)
- Regridding Script: run TRANBLK for nacelle translations, PROGRD, GRIDED, etc., to preserve grid continuity after a design change
- PEGSUS: compute interpolations for new grid system
- FOMOCO: force and moment integration

OVERDISC

OVERDISC is composed of a number of script files and codes which couple OVERFLOW, a Navier–Stokes flow solver for overset grids, PEGSUS, which computes the appropriate interpolations between overset grids, and CDISC, the Constrained Direct Iterative Surface Curvature inverse design method. Implementations of the scripts are sufficiently general to allow for the design iterations to proceed with minimal input from the user. CDISC has been demonstrated for a number of flow solvers, including CFL3D, TLNS3D, and OVERFLOW.

Upon obtaining an analysis from OVERFLOW, the script runs the CDISC inverse design method to obtain new surface definitions for all surfaces of the configuration which are to be redesigned. The output from CDISC includes new volume grids for all grid blocks containing a surface which has been redesigned. Upon completion of CDISC, all grid blocks containing a surface which overlaps a modified surface must be repaired to maintain consistency between blocks. In addition, constraints between components, such as the distance between the nacelle lip and the wing surface, must be enforced. The grid repair process is implemented through a script file, running a sequence of regridding tools, which outputs all the component grids for the new configuration.

After generating the new system of component grids, PEGSUS is rerun to compute the interpolations between the grids, then the main script loops to the call to OVERFLOW, generating an updated solution file. Upon completion of the design iterations, OVERFLOW is run to a user specified level of convergence and forces and moments of the new configuration are computed using FOMOCO, which was designed specifically for integrating the forces and moments on complex configurations which utilize overset surface grids.

OVERDISC Design Runs

Generate a target file:

- Target pressure distribution
- Constraints on local and integrated flow quantities
- Geometry constraints
- CDISC modified to include surface movement constraints

Design constraints:

- Constraint on wing thickness from 50% to 78% chord
- Diverter leading edge lengths fixed at OPT5 values
- wing leading edge held fixed
- wing trailing edge allowed to float

Design decisions based on the volume weighted Lift to Drag ratio:

$$L/D_V = L/D^* (V / V_{ref})$$

OVERDISC Design Runs

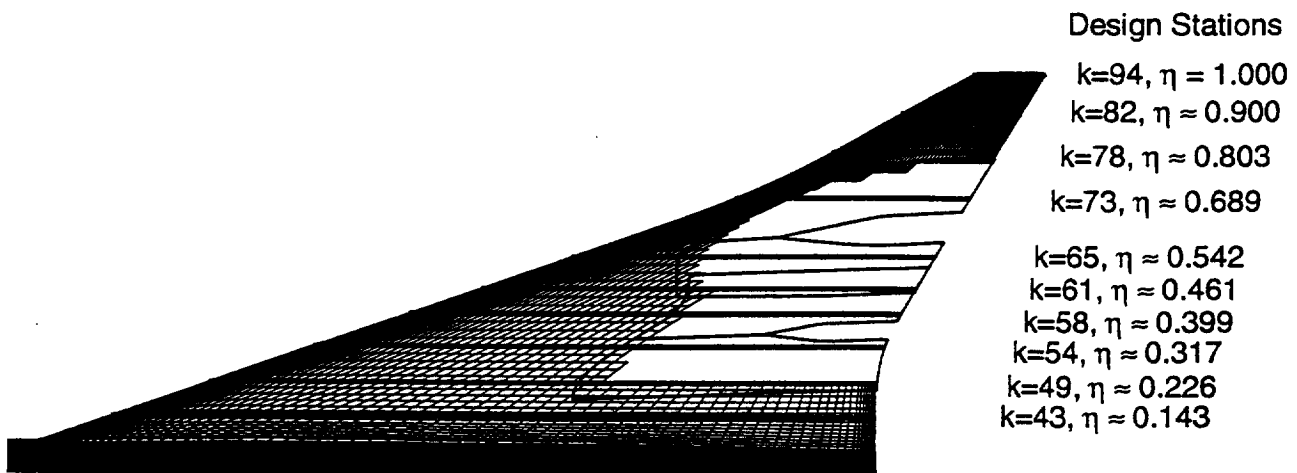
CDISC is based on the premise that along a streamline of the flow, changes in surface curvature can be related to changes in the pressure distribution. Hence, the difference between a pressure distribution obtained from analysis and a user specified desired pressure distribution can be used to compute a modification to the initial configuration shape which, after a number of iterations, produces the desired pressure distribution. In CDISC, the desired pressure distribution can either be input as a data file or created by using "flow constraints" to modify the initial pressure distribution obtained from analysis. In addition, "geometry constraints" may be invoked to restrict geometry changes in a manner which is appropriate for meeting manufacturing or system constraints. Since the inverse design method is inherently two-dimensional in nature, three-dimensional designs are implemented by specifying a number of "target stations" at which the design method is to be applied; changes at the design stations are linearly interpolated between stations. Specifications for the design options, the locations of design stations, and constraints on both the characteristics of the pressure distribution and the geometry are input to the code in a "target file".

Contrary to the methodology for inverse designs, the natural flow wing design philosophy is based on the recognition that the flow over highly swept wings is dominated by a conical pressure field; the camber and thickness of the wing is then modified to take advantage of the characteristics of that flow. On the lower wing surface, the flow is dominated by the shocks emanating from the diverter and nacelle leading edges, the positions of which remain relatively unchanged with changes in wing camber and thickness. In order to take advantage of the flow characteristics on the lower wing surface, additional geometry constraints were added to CDISC which allow the user to directly specify changes in the wing surface. The actual design process utilized to generate the final design (NFWAc4) made use of both the standard CDISC flow constraints and the additional surface movement constraints.

The starting point for the inverse design process was to utilize the NFWAc2 configuration. Constraints enforced on the design were to keep the wing thickness greater than or equal to that of the NFWAc2 wing from 50% to 80% chord, and to keep the distance between the wing surface and nacelle surface constant at the diverter leading edge. In addition, the wing leading edge was held fixed; the trailing edge was allowed to float.

Design decisions were based on a volume weighted lift to drag ratio, with V denoting the volume of the new configuration and V_{ref} denoting the volume of the NFWAc2 configuration.

NFWAc4 Design Stations



NFWAc4 Design Stations

In redesigning the NFWAc2 configuration, the fuselage was held fixed and the wing was redesigned from 14.3% span out to the wing tip. The implementation of CDISC on a wing involves specifying design stations along streamwise grid lines of the computational grid. Although the computational grid lines do not necessarily line up with streamlines of the flow, particularly in regions with a strong cross-flow component, the method has still been found to be effective in obtaining the specified pressure distribution.

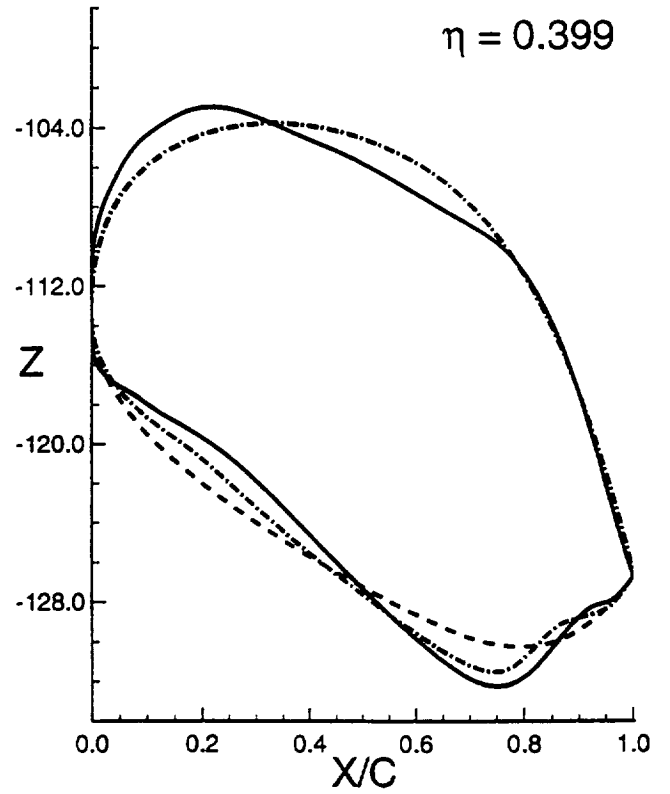
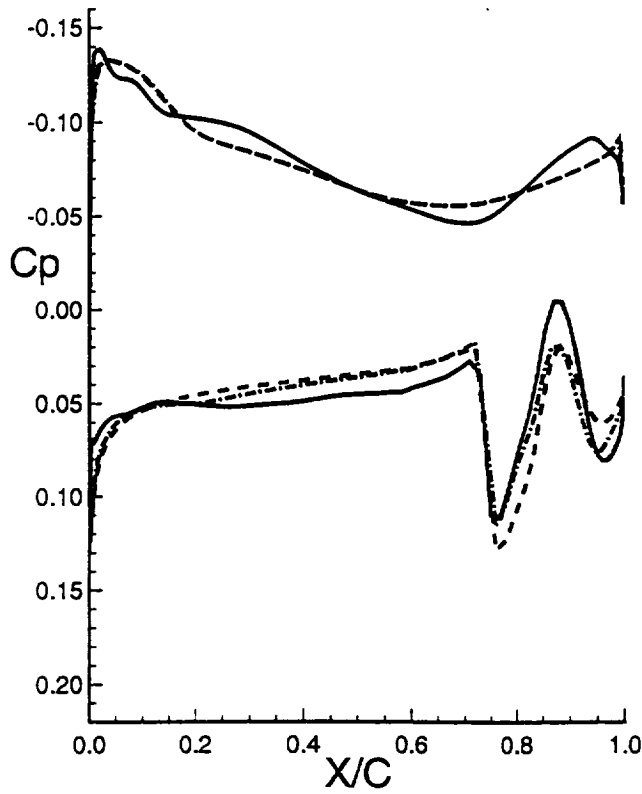
Ten target stations were employed in redesigning the NFWAc2 configuration, with the inboard most station at 14.3% span held fixed and the outboard most station at the wing tip; changes at the wing tip were aliased to changes at the ninth target station. Three design stations are located inboard of the inboard diverter, 3 stations are located between the two diverters, and four stations are located outboard of the outboard diverter.

The figure represents the wing surface grid on the lower surface, with sections of the grid blanked out where the diverter grids cut holes in the wing grid. OVERDISC is set up to design through these regions of the wing by interpolating the solutions from the diverter grids onto those sections of the wing grid which are cut out. In order to limit spanwise waviness in the final design, the CDISC constraint to perform spanwise smoothing on the design increments was invoked at each design cycle.

HSR Configurations with Diverters/Nacelles
 Analysis Cp's & Surface Coordinate

$M_\infty = 2.40$
 $C_L = 0.11$
 $Re_\infty = 4.12 \times 10^6$

— OPT5 $\alpha = 1.900^\circ$
 - - - NFWAc2 $\alpha = 2.066^\circ$
 - · - · NFWAc4 $\alpha = 2.076^\circ$



Analysis Cp's and Surface Coordinate – 39.9% Span

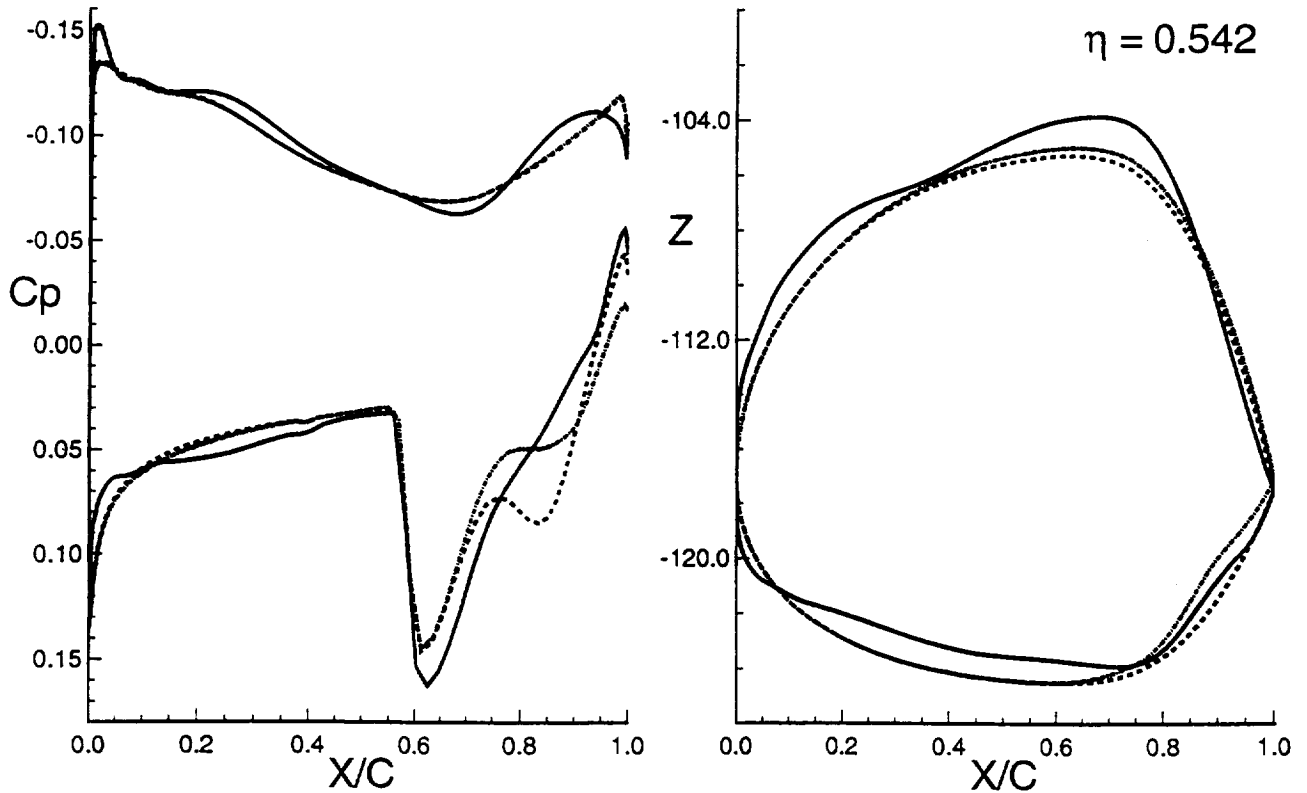
The figure shows the pressure coefficient versus X/C on the left and the surface shape versus X/C on the right (with 120X magnification of the vertical axis) for the OPT5, NFWAc2, and NFWAc4 configurations at 39.9% span; NFWAc4 is the final configuration obtained from the inverse design process. The 39.9% span station is located just outboard of the inboard nacelle. The final shape of NFWAc4 at this station was obtained through the use of a combination of flow and geometry constraints, using the pressure distribution and shape of the OPT5 configuration as a guide in choosing how to modify NFWAc2.

From 5% to 60% chord, a specified target pressure distribution was chosen to drive the pressure distribution of NFWAc2 towards that of OPT5. Due to the strong shock beginning at roughly 70% chord, any attempt to specify a target pressure distribution through this region invariably causes huge changes in geometry with only modest changes in the pressure distribution at the shock; likewise attempts to specify a target pressure distribution in the recovery region behind the shock met with limited success since it is difficult to know a priori exactly what a realistic desirable pressure distribution would look like. Instead, these regions of the section were modified by using geometry constraints on the surface shape to generate features similar to those for OPT5, namely, the minimum point on the lower surface was lowered and moved upstream to occur near the shock and a reflex was added to the shock recovery region. The extents of the modifications were determined through a parameter study. Note that the modifications were implemented in a manner which avoided violation of the minimum thickness constraint from 50% to 80% chord. Consequently, the upper surface of NFWAc4 is identical to that of NFWAc2 at this station.

HSR Configurations with Diverters/Nacelles
Analysis Cp's & Surface Coordinate

$M_\infty = 2.40$
 $C_L = 0.11$
 $Re_\infty = 4.12 \times 10^6$

— OPT5 $\alpha = 1.900^\circ$
- - - NFWAc2 $\alpha = 2.066^\circ$
- · - · NFWAc4 $\alpha = 2.076^\circ$



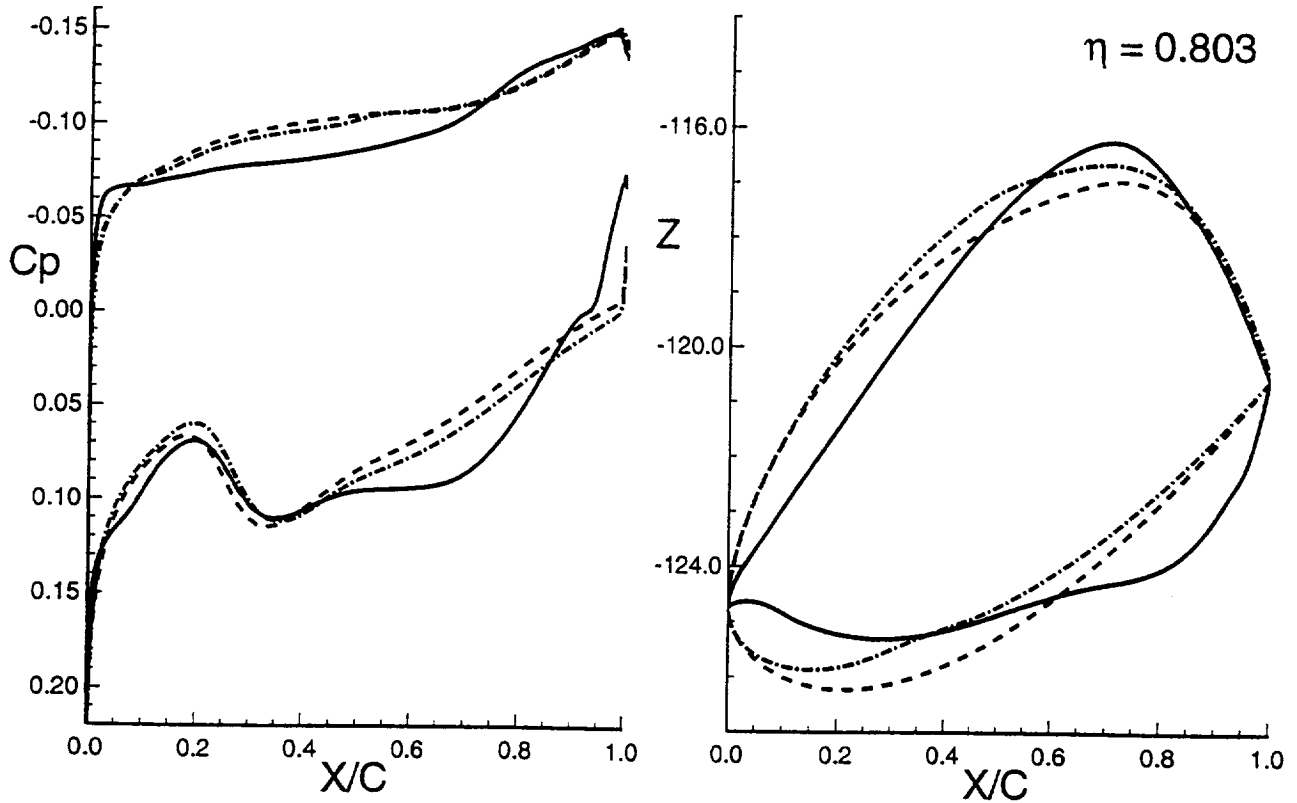
Analysis Cp's and Surface Coordinate – 54.2% Span

The figure shows the pressure coefficient versus X/C on the left and the surface shape versus X/C on the right for the OPT5, NFWAc2, and NFWAc4 configurations at 54.2% span, which is just inboard of the outboard nacelle. The design strategy at this station was much the same as that at 39.9% span, but in this case the changes on the lower surface cause a violation of the minimum thickness constraint from 50% to 80% chord unless the upper surface is adjusted as well. Satisfaction of the constraint was automatically obtained through use of the CDISC constraints to modify the upper surface.

HSR Configurations with Diverters/Nacelles
 Analysis Cp's & Surface Coordinate

$M_\infty = 2.40$
 $C_L = 0.11$
 $Re_\infty = 4.12 \times 10^6$

— OPT5 $\alpha = 1.900^\circ$
 - - - NFWAc2 $\alpha = 2.066^\circ$
 - · - · NFWAc4 $\alpha = 2.076^\circ$



Analysis Cp's and Surface Coordinate – 80.3% Span

The figure shows the pressure coefficient versus X/C on the left and the surface shape versus X/C on the right for the OPT5, NFWAc2, and NFWAc4 configurations at 80.3% span, which is well outboard of the outboard nacelle. Whereas OPT5 has a sharp leading edge at this station, the natural flow wing designs have a blunt leading edge, with the leading edge of NFWAc4 being less blunt than that of NFWAc2.

OVERFLOW Performance Predictions

$$M = 2.4$$

$$Re = 4.0 \times 10^6$$

Grid	α	CL	CD	ΔCd
OPT5	1.90	.1106	.01360	—
NFWAc2	2.07	.1106	.01367	.00007
NFWAc4	2.08	.1106	.01360	.00000

OVERFLOW Performance Predictions

Initial OVERFLOW analyses of OPT5 and NFWAc2 and the OVERDISC design of NFWAc4 were conducted at a Mach number of 2.4 and a Reynolds Number of 2 million. However, other design efforts on the arrow wing planform were conducted at a Reynolds Number of 4 million. Therefore, analyses for the three configurations were rerun at a Reynolds number of 4 million, but on the grids which were created for the flow conditions occurring at a Reynolds number of 2 million. Hence, values of y^+ on the various component grids are on the order of 10, rather than the order of 1 values commonly maintained for simulations with the Baldwin-Barth turbulence model.

Predicted performance levels of the three configurations with installed diverters /nacelles are provided in the table. The results suggest that the performance of OPT5 is roughly seven tenths of a count better than NFWAc2. The somewhat labor intensive inverse design process for a viscous flow solver succeeded in improving the performance level of the natural flow wing design to the level of OPT5 while maintaining the same wing volume as NFWAc2. Of course the performance numbers listed here must be viewed with some degree of caution, since the resolution of the chimera grids is known to be inadequate for the design flow conditions.

Grid Resolution Study

$$M=2.4$$

$$Re = 4.0 \times 10^6$$

Fuselage/Wing Grid Wall–Normal Resolution

- $Y^+ < 1.2$
- Uniform spacing over first 2 (or 3?) cells
 - 2.15 drag counts for 2 uniform cells at $M=2.4$
 - 2.16 drag counts for 3 uniform cells
- Number of grid points
 - 0.7 drag counts using 89 rather than 65 grid points

Component Grid Resolution Study – Inboard nacelle

- Wall–Normal resolution completed
- Streamwise resolution Initiated

Generated a 5.1 million grid point 17 block chimera grid

Grid Resolution Study

Due to time constraints in developing the natural flow wing design, grid resolution studies for the arrow wing configuration were deferred until after the design deadline. Studies were performed first for the fuselage/wing grid, then for the fuselage/wing with the inboard nacelle installed, at flow conditions of $M=2.4$, $Re=4.0 \times 10^6$, and $\alpha = 2.0$ degrees.

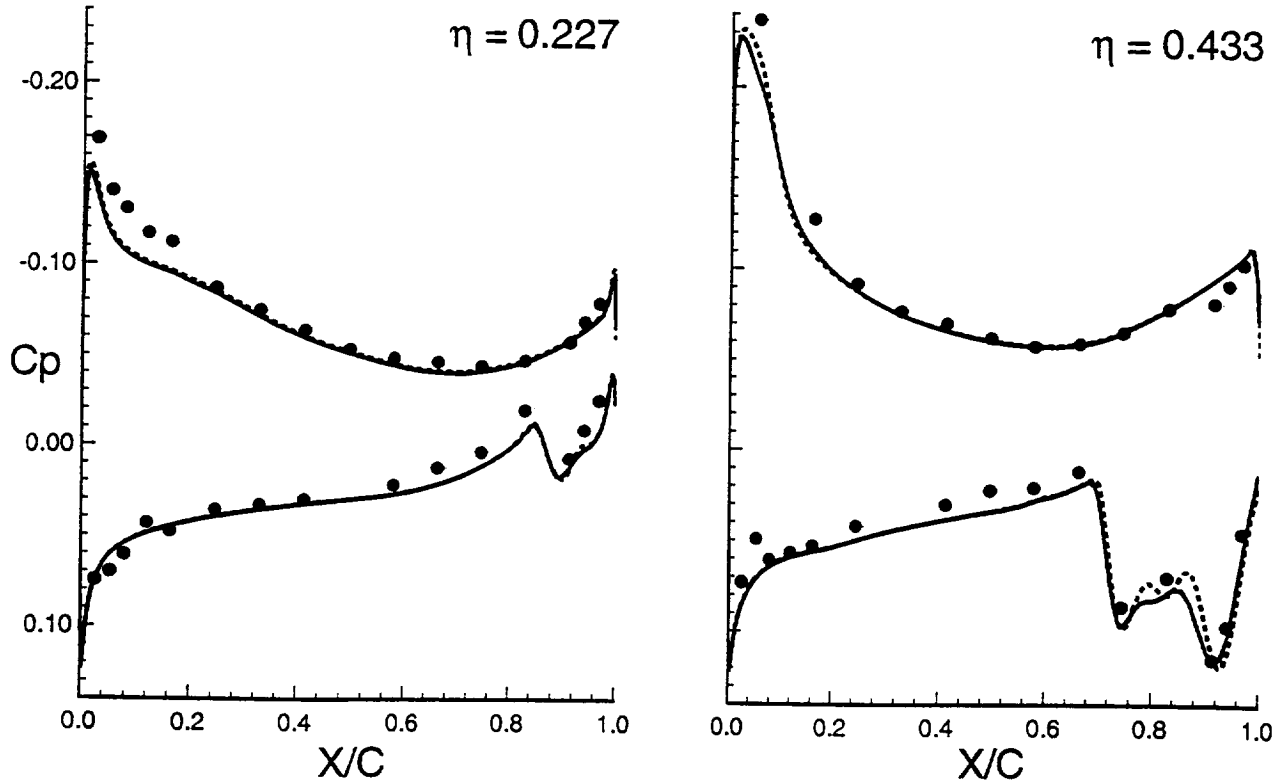
On the fuselage/wing grid, the first correction was to decrease the wall-normal spacing at the wall to provide an appropriate value of y^+ for the Baldwin-Barth turbulence model. The second correction involved generating grids for which the wall-normal spacing was held constant over the first two or three grid cells; the need for this correction was demonstrated by Boeing at the mid-term review, where it was shown that OVERFLOW computations of the skin friction are incorrect when standard grid stretching is applied at the wall. The results for the NFWAc4 fuselage/wing grid show a 2.15 count difference in skin friction when the grid is created with 2 uniform grid cells in the wall-normal direction rather than with standard stretching. The difference between using 3 uniform grid cells rather than 2 is negligible, being on the order of 1/100 of a drag count. Finally, the number of grid points in the wall normal direction was increased from 65 to 73, then 81 and 89. The results showed a difference of 7/10 of a drag count between the use of 89 rather than 65 grid points; the difference between using 81 and 89 grid points is on the order of 15/100 of a drag count.

The grid resolution study on the diverter/nacelle component grids was conducted on the installed inboard nacelle alone. The component grids were generated to provide y^+ values less than 1.2, wall-normal grids were generated with 2 uniform grid cells at the wall, and the number of grid points in the wall normal direction was varied. A streamwise grid resolution study was also initiated, adding grid points to the component grids and refining the grids near the diverter and nacelle leading edges and at the regions of maximum thickness.

Based on the grid resolution study for the inboard diverter/nacelle, a new system of grids was generated for the full configuration, consisting of 5.1 million grid points in 17 blocks.

● experiment
 — OVERFLOW Coarse Grid
 - - - OVERFLOW Fine Grid

Pressure Coefficient - Experiment vs. CFD
 NFWAc4 Fuselage/Wing/Diverters/Nacelles
 $M = 2.00$ $\alpha = 2.00^\circ$ $Re = 4.12 \times 10^6$



Pressure Coefficient – Experiment vs. CFD at 22.7% and 43.3% span

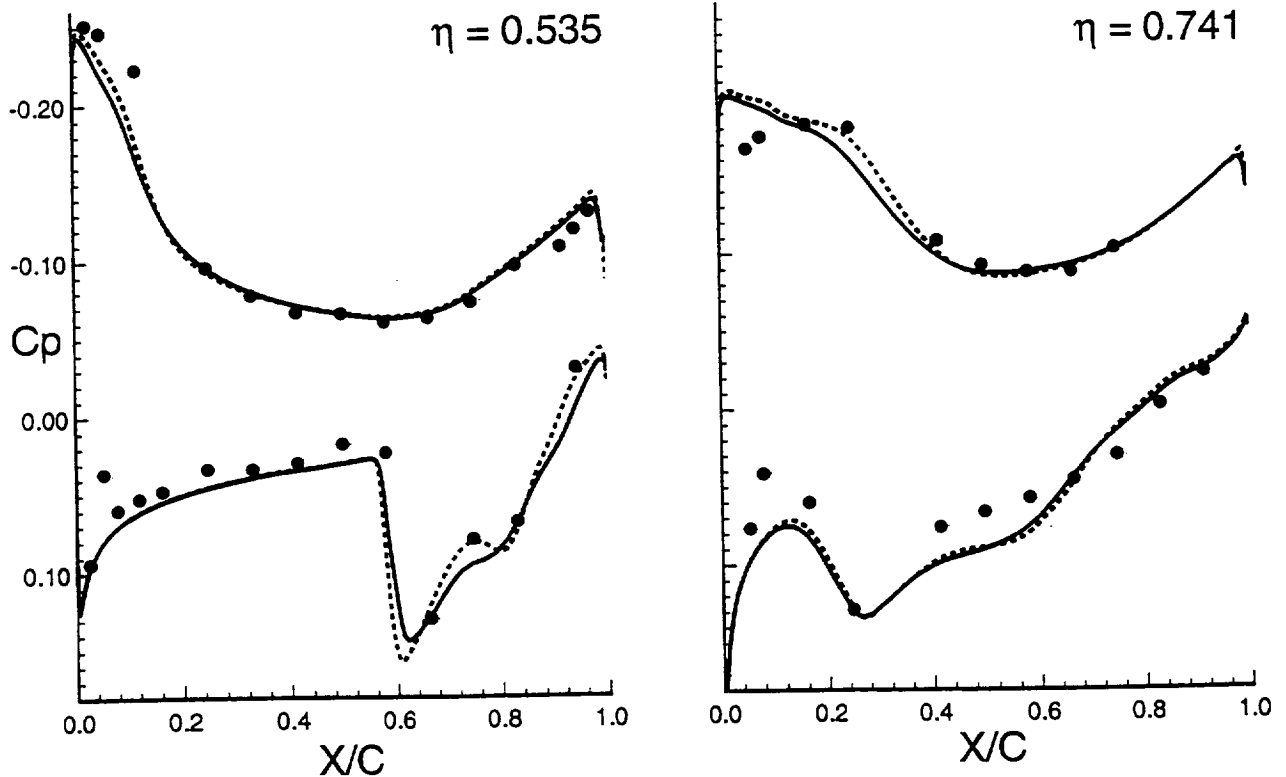
At the time this presentation was put together, experimental data for the NFWAc4 configuration was only available at off-design conditions; the model is scheduled for entry in test section 2 of the NASA Langley Unitary Plan Wind Tunnel on March 11, at which time experimental data at the design point will be obtained.

Shown in the figure are plots of the pressure coefficient versus X/C for the NFWAc4 configuration with installed diverter nacelles at $M=2.0$, $Re=4 \times 10^6$, and $\alpha=2.0$ degrees. The 22.7% span station is inboard of the inboard diverter, while the 43.3% span station is roughly midway between the two diverters. Experimental results were obtained from test section 1 of the Unitary Plan Wing Tunnel (UPWT). CFD results are shown for both the 3.1 million grid point 17 block chimera grid utilized in the initial analyses and design (Coarse Grid) and for the 5.1 million grid point refined grid (Fine Grid).

Comparison of the results indicate that the refined grid is modestly more effective at picking up the acceleration of the flow over the leading edge and does a better job of representing the character of the flow in the shock recovery region, particularly at 43.3% span. However, there are still significant differences between the experimental and CFD results over the first 20% of the chord on the upper wing surface.

● experiment
 — OVERFLOW Coarse Grid
 - - - OVERFLOW Fine Grid

Pressure Coefficient - Experiment vs. CFD
 NFWAc4 Fuselage/Wing/Diverters/Nacelles
 $M = 2.00$ $\alpha = 2.00^\circ$ $Re = 4.12 \times 10^6$

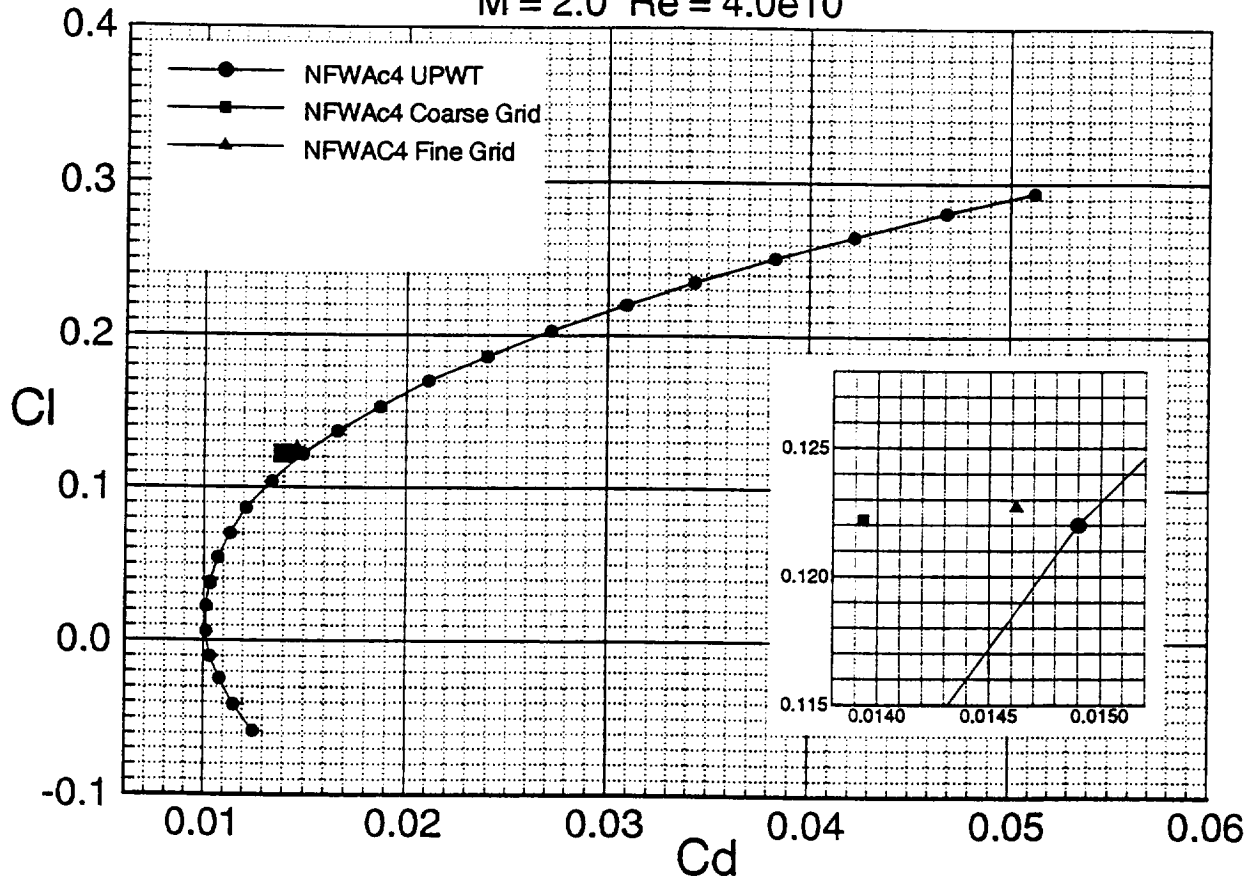


Pressure Coefficient - Experiment vs. CFD at 53.3% and 74.1% span

Shown in the figure are plots of the pressure coefficient versus X/C for the NFWAc4 configuration with installed diverter nacelles at $M=2.0$, $Re=4 \times 10^6$, and $\alpha=2.0$ degrees. The 53.3% span station is just inboard of the outboard diverter, while the 74.1% span station is well outboard of the outboard diverter.

Once again, the refined grid is modestly more effective at picking up the acceleration of the flow over the leading edge and does a better job of representing the character of the flow in the shock recovery region at 53.5% span. At 74.1% span, however, the CFD results do not represent the character of the flow over the first 20% of the chord on either the upper or lower surface. In fact, the entire shock recovery region is significantly different from the experimental results.

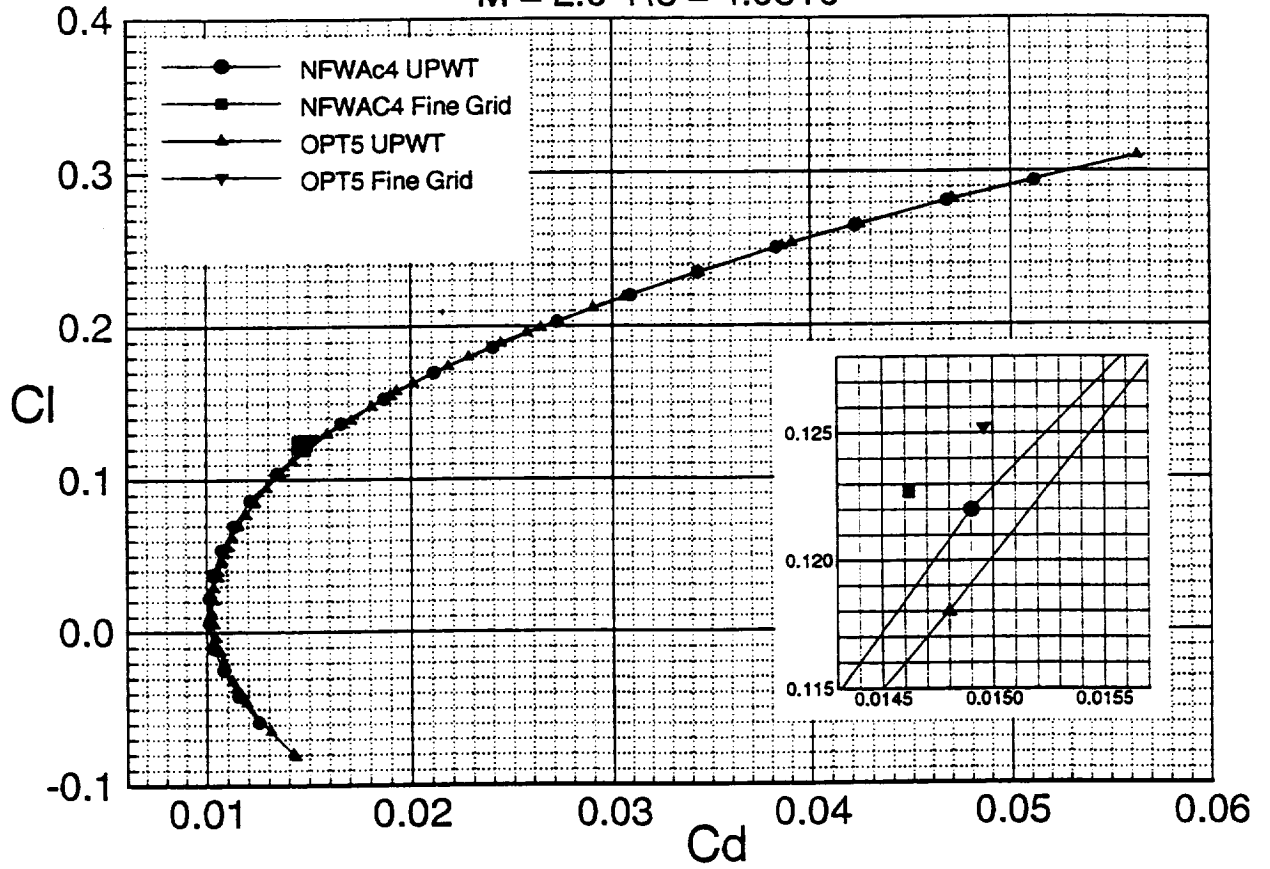
HSR Arrow-Wing Drag Characteristics NFWAc4 CFD vs. Experiment $M = 2.0 \quad Re = 4.0e10^6$



HSR Arrow-Wing Drag Characteristics – NFWAc4

Shown in the figure is a plot of the C_l vs C_d polar for NFWAc4 at $M=2.0$, $Re=4 \times 10^6$, along with CFD results at $\alpha=2.0$ degrees. CFD results are shown for the initial 3.1 million grid point grid (Coarse Grid), and the 5.1 million grid point refined grid (Fine Grid). The results indicate a significant improvement between the correlation of the CFD with experiment by using the fine grid, with the predicted drag from CFD roughly 4 drag counts lower than the experimental values. It should be noted that the comparisons presented in this paper do not account for trip drag in the experiment, which has been estimated to be on the order of 1.5 counts.

HSR Arrow-Wing Drag Characteristics
 NFWAc4 vs. OPT5 - CFD vs. Experiment
 $M = 2.0$ $Re = 4.0e10^6$



HSR Arrow Wing Drag Characteristics – NFWAc4 vs. OPT5

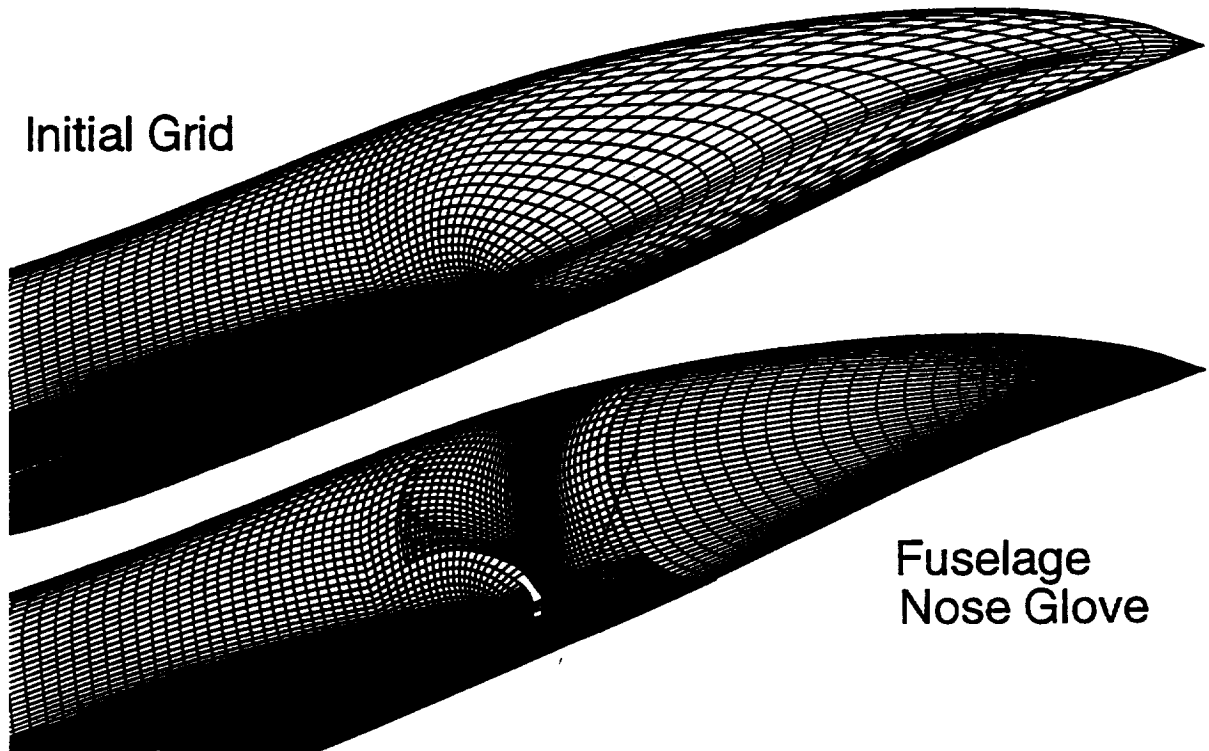
Shown in the figure is a plot of the C_l vs C_d polar for the NFWAc4 and OPT5 configurations at $M=2.0$, $Re=4 \times 10^8$, along with CFD results at $\alpha=2.0$ degrees for NFWAc4 and $\alpha=1.9$ degrees for OPT5 on the refined grid. Experimental results indicate that performance of the NFWAc4 design is between one and two drag counts better than that of OPT5 over a range of angles of attack. The CFD predictions at a C_l around 0.125 suggest that the NFWAc4 performance is less than half a count better than that of OPT5. The difference between CFD and experiment is on the order of 4 drag counts for NFWAc4 and 5 drag counts for OPT5.

The discrepancy between the CFD and experimental incremental drag levels is somewhat disturbing, since one needs to get the increments correct in order to validate the analysis and design processes. Possible sources for these discrepancies have been identified in both the wind tunnel tests and CFD simulations.

The most significant difference in the wind tunnel tests is that the OPT5 model was mounted on a longer sting than the NFWAc4 model. Because of the longer sting, oscillations in the OPT5 test were more severe, increasing the uncertainty in the angle of attack and force/moment measurements. This discrepancy will be corrected in the UPWT entry scheduled for March 11, where models of the baseline arrow wing configuration, OPT5, and NFWAc4 will all be tested using the same sting/balance combination.

While the OPT5 and NFWAc4 CFD simulations were conducted with topologically identical grids, serious deficiencies in the simulations have been identified. The most easily corrected deficiency is in the coarseness with which the fuselage forebody is discretized with the single block fuselage/wing grid. Since the forebodies for OPT5 and NFWAc4 are significantly different, substantial differences in the drag increments can be expected by gridding the forebody with a separate overset grid. Other discrepancies occur due to the topology of the component grids constructed for the diverters/nacelles. It is apparent from the solutions that the extents of the component grids are insufficient for capturing the shock interactions between the diverters or the shock outboard of the outboard diverter.

HSR Arrow-Wing Configuration Fuselage Nose Glove



Fuselage Nose Glove

In order to correct inaccuracies in the computations on the fuselage nose, refined overset grids for the nose were constructed for the NFWAc4 configuration. Three blocks were used rather than a single block because FOMOCO, the force and moment integration code for overset grids, was incapable of picking up the correct interpolations when a single block nose glove was used.

Simulations on the single block fuselage/wing grid and the 4 block fuselage/wing grid with a nose glove for the NFWAc4 configuration at $M=2.4$, $Re=4 \times 10^6$, and $\alpha=2.0$ degrees, indicate a 1.5 drag count difference. The generation of a nose glove for the OPT5 configuration is ongoing.

Phase 2 Activities

Close Out Arrow Wing Study

- Create Fuselage nose glove for OPT5
- Run polars for the baseline, OPT5, and NFWAc4; evaluate CFD prediction of the experimental drag increments

Chimera Grid For TCA-6

- Collaboration with other overset grid users essential
- Use double fringe points in PEGSUS

Automatic Regeneration of Overset Grids For TCA Redesigns

- Fuselage/Wing shape changes
- Nacelle: Translation (Vertical Only)
Pitch
Toe Angle
Clock

Phase 2 Activities

Close Out Arrow Wing Studies: Investigations of the arrow wing are continuing, with wind tunnel tests on the baseline, OPT5, and NFWAc4 configurations running through April. The CFD effort will be continued until closure is reached on obtaining incremental drag levels between the three configurations at a number of points on the drag polar which encompasses the design point.

Chimera Grid For TCA-6: While a chimera grid will be generated for the TCA-6 configuration, it is envisioned that this will be a collaborative effort. It is further recommended that the chimera grids be generated using double fringe points at the boundaries, as numerous studies have indicated significant increases in accuracy are obtained when double fringe points are used rather than single fringe points; virtually all of the chimera grids generated in phase 1 of the HSR program utilized single fringe points.

Automatic Regeneration of Overset Grids For TCA Redesigns: In order to use Navier-Stokes analyses to evaluate optimized redesigns of the TCA configuration within a reasonable time frame, it is essential to have an automatic regridding capability. The method used in the present study of reprojecting and restretching the component grids for different designs on the arrow wing planform is directly applicable to TCA redesigns, but needs to be made more general in order to handle diverter and nacelle modifications.

Phase 2 Activities (cont.)

Natural Flow Wing Design

Nacelle/Diverter Design

- Meeting Inlet Flow Constraints
- Diverter Redesign
- External Nacelle Reshaping

Phase 2 Activities (cont.)

Natural Flow Wing Design: It is anticipated that a number of natural flow wing designs will be created for the TCA configuration. In addition to starting the design from the baseline configuration, it is anticipated that optimized designs from other organizations in the HSR program will be used as a starting point for application of the natural flow wing design philosophy.

Nacelle/Diverter Design: A major emphasis in redesigning the nacelles and diverters will be to determine the effectiveness of modifications to the nacelle orientation in meeting inlet flow constraints. The effectiveness of OVERDISC in redesigning the nacelle and diverter shapes for drag reduction will be evaluated.

HSCT Multi-point Aerodynamic Performance Trades From TCA Propulsion and Planform Studies

**Chester P. Nelson
HSCT Aerodynamics
Boeing Commercial Airplane Group
Seattle, Washington**

**First NASA / Industry High Speed Research
Aerodynamics Workshop, February 27-29, 1996
NASA Langley Research Center, Hampton, VA**

HSCT Multi-point Aerodynamic Performance Trades From TCA Propulsion and Planform Studies

Chester P. Nelson*

Boeing Commercial Airplane Group
P.O. Box 3707, MS 6H-FK
Seattle, WA 98124--2207

Abstract:

The Aerodynamics discipline is progressing toward achieving HSCT technology requirements using a "staged" approach. In the initial stage, both High Lift and "Config. Aero" (CA) were primarily focused on validating CFD analysis tools against wind tunnel data from HSCT configurations that were previously designed and optimized using linearized potential flow methods. During the second stage, CA has been intensively involved in developing CFD-based direct non-linear optimization methods. Thus far, these new tools have been applied only at the supersonic cruise L/Dmax point of the "Ref.H" and "M2.4-7A" configurations. Future steps will include the development of multi-point non-linear aerodynamic optimization capability and the increased use of CFD-based data in Technology Integration/ "MDO" processes.

In anticipation of these developments, this paper reviews the results of the propulsion and airframe integration trades leading up to the selection of the Technology Concept Airplane (TCA), from the perspective of potential multi-point optimization benefits and challenges. The data from these studies provides some insight into the trade-offs between HSCT supersonic point design L/D, and performance in the transonic and high lift regimes, along with related structural weight considerations.

*Lead Engineer, Boeing HSCT
High Speed Aerodynamics
Configuration Development Group

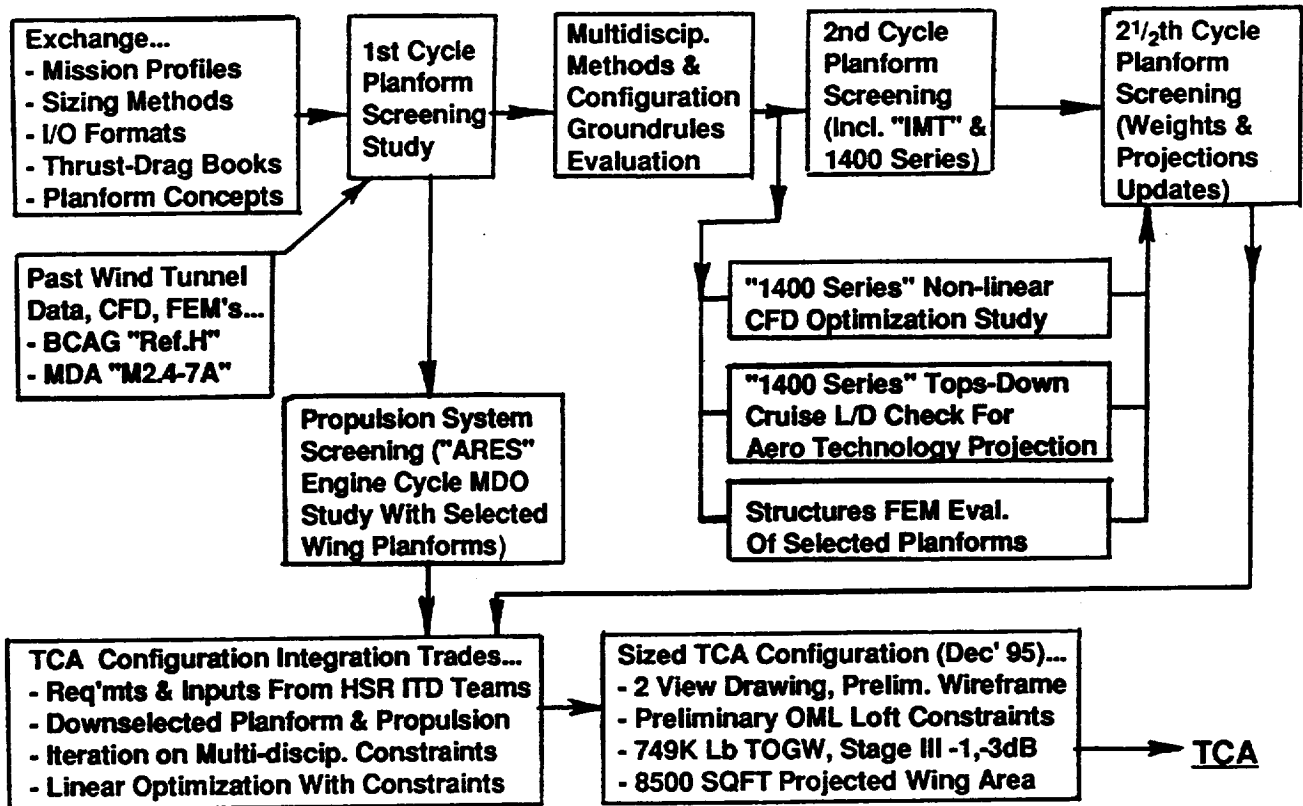
HSCT Multi-point Aerodynamic Performance Trades

- o Configuration development and screening trades leading to definition of the TCA**
- o Relative impact of transonic and high lift aerodynamics vs. supersonic cruise**
- o Multi-point optimization in the configuration development process**
- o Observations and conclusions**

Introduction:

The configuration development and screening trade studies which led up to the selection of the HSR "Technology Concept Airplane" (TCA) provide insight into relative aerodynamic performance trades across the Mach number range of the HSCT. Some opportunities and challenges for future multi-point aerodynamic optimization will be discussed in light of selected results from these studies.

'94/ '95 Configuration Development And Screening



In the 1994-95 time-frame, a major focus of the NASA High Speed Research Program (HSR) has been the selection of features for a NASA-industry consensus HSCT design to serve as a single, up-to-date reference configuration for technology development. This reference configuration, the TCA, has been determined based on the results of a series of HSR Technology Integration (TI) contract studies, and supplemented by information from NASA and industry IR&D design trades. A schematic representation of this process is shown by the flowchart above.

As shown, results of the initial semi-parametric planform screenings conducted independently at MDA and BCAG were used to generate an "Industry Methods Test" configuration (IMT) for analysis methods comparisons, and an equivalently configured set of alternate planforms, the 1400 series. A subset of these geometries were used in side studies including structural FEMs and CFD. A subset of the original planforms was also used in a "multidisciplinary optimization" (MDO) type screening of candidate mixed-flow turbofan engine cycles using the Boeing ARES multi-dimensional sizing code.

Primary requirements of the TCA were to provide a realistically integrated design which would;

- 1) include representative HSCT configuration features for technology development, and
- 2) be capable of meeting established economic viability parameters when reasonable technology projections were applied in each discipline.

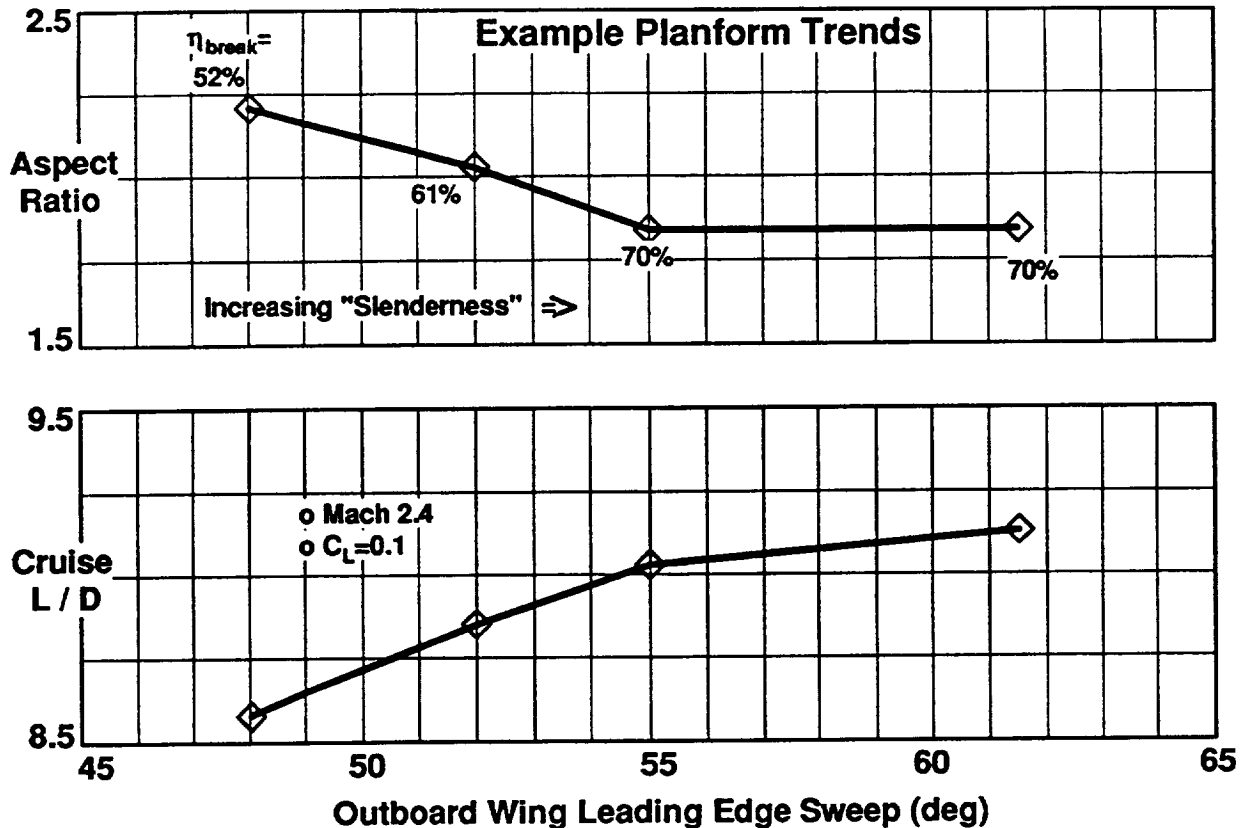
The aerodynamic features, general arrangement, size, detailed design constraints, and integrated mission performance of the down-selected TCA satisfied these objectives, given the technology projections of the HSR "ITD" technology teams as of December, 1995.

- o Technology Concept Airplane Definition...
 - Concensus HSCT for technology development reference
 - Multi-disciplinary geometry constraints for aero optimization
 - HSCT viability goals satisfied with TCA projected performance

- o Results and experience from systematic geometry variations...
 - Several dozen representative high speed configurations
 - Multi-disciplinary iterations on aero lift constraints
 - Wing aspect ratio, planform break, and sweep
 - Design C_L , wing twist, and incidence
 - Wing thickness vs. span (box depth and fuel volume)
 - Body area rule and landing gear fairings
 - Nacelle longitudinal positioning and shape
 - Integrated performance across mission /speed regimes

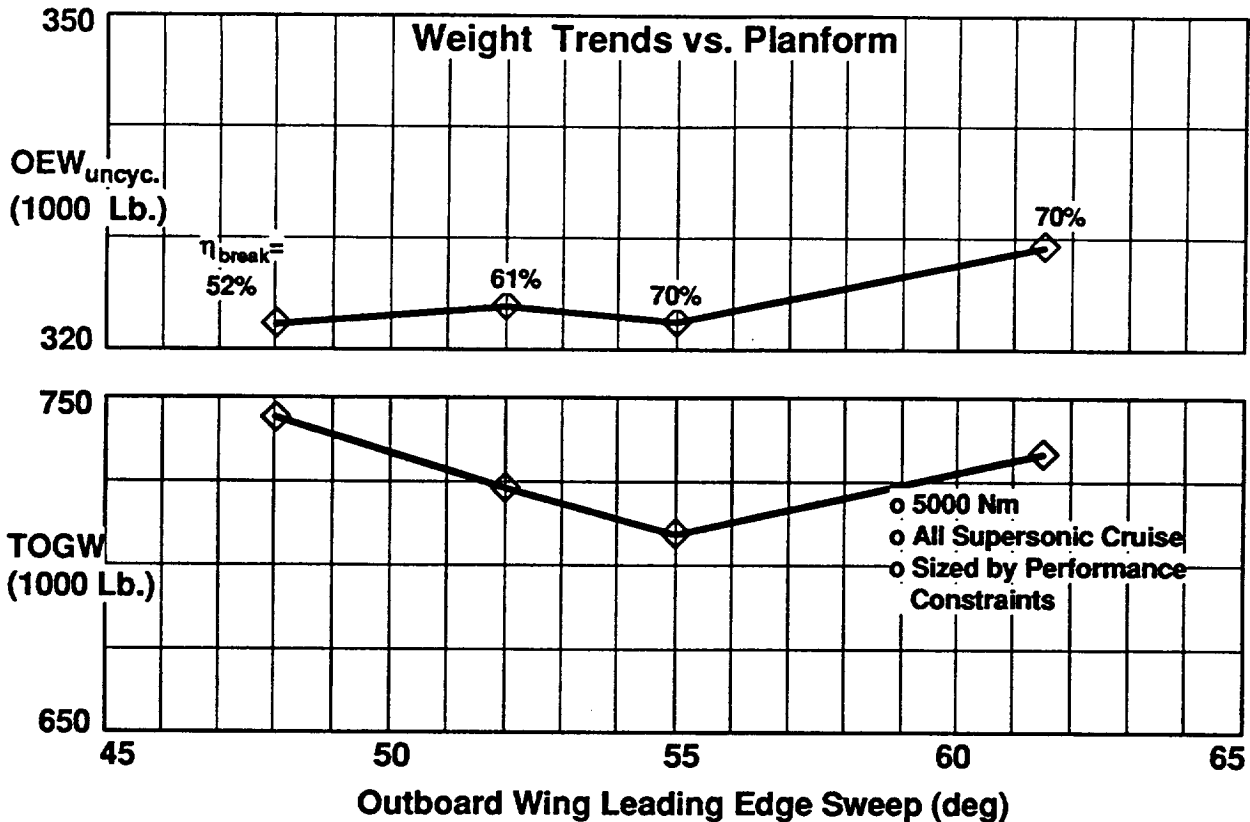
In addition to a viable TCA configuration, the development work and concept screening trades provided added integration experience and performance assessments of interest to the High Speed Aerodynamics discipline. The aerodynamic geometry variations covered in these studies included examples of wing-body camber and twist sensitivities, body area rule constraint impacts, wing thickness and planform options, and engine nacelle shape and location sensitivities. As these variations were not simply aerodynamic shape parametrics, but part of systematic design integration changes, they resulted in realistic examples including multidisciplinary limitations. In most cases, the impact of the aerodynamic variations were assessed across the Mach number range, and many were "rolled-up" into total mission performance and airplane sizing.

Several example geometry variations have been selected to illustrate the impact of supersonic cruise geometry changes on aerodynamic performance in other speed regimes, and on the net mission performance of the airplane. The degree of interaction of these changes with structural weight, structural arrangement constraints, payloads, etc. are also an indication of how effective CA may be in independently "optimizing" the external lines to improve the configuration through drag reductions alone.

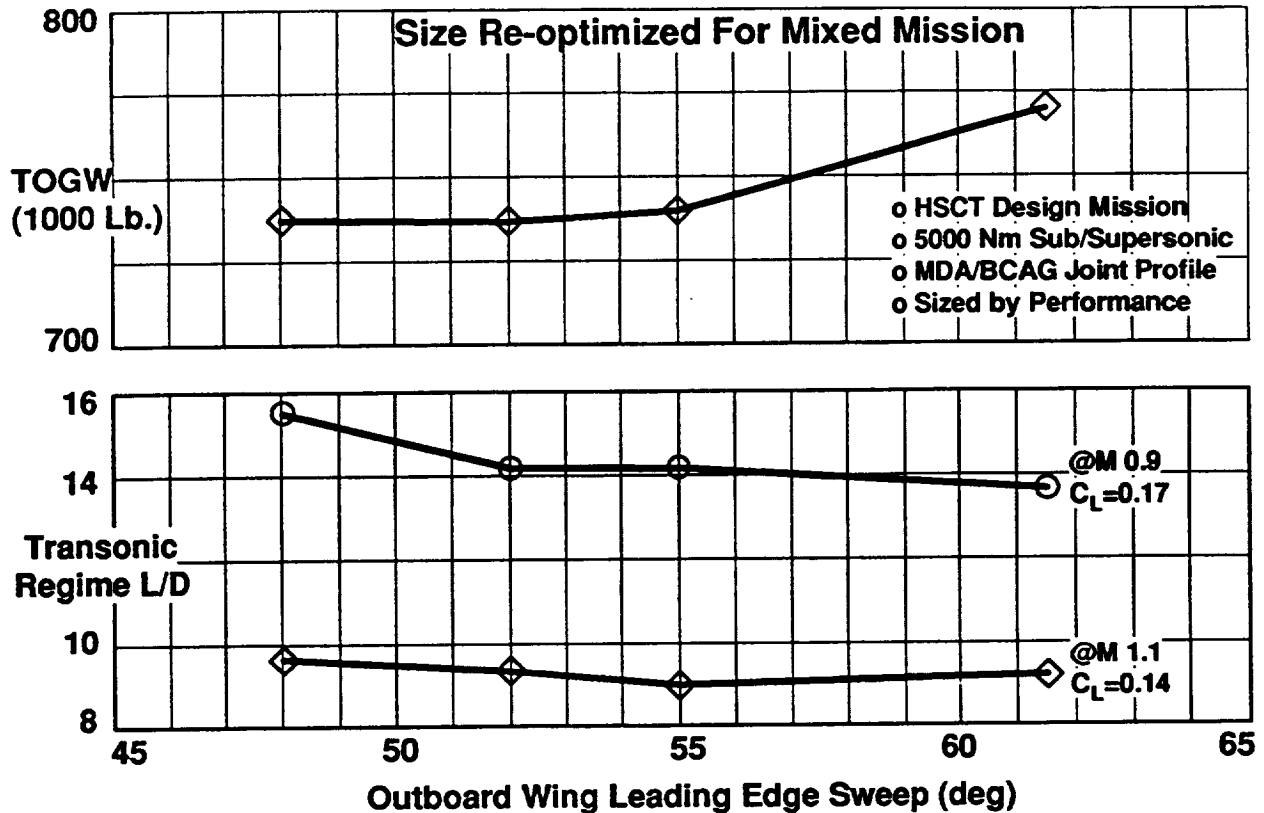


A large portion of the TCA downselect effort involved wing planform related trades. Wing planform selection has a major role in determining the engine-airframe matching, the airplane structural layout, and the entire general arrangement of the airplane. Due to the strong interactions with other disciplines it is impossible for Configuration Aerodynamics (CA) to independently select an optimum planform. Nearly two dozen candidate planforms were subjected to multidisciplinary evaluations at BCAG and MDA. Most of these were integrated into full configurations with specific structural arrangements, leading and trailing edge surfaces, landing gear bay and cabin volumes, and specific engine installations. The interaction of the disciplines caused unique integration problems for many of the planforms. For this reason it was necessary to keep the designers "in the loop" while configuring the study airplanes. Although this process helped capture inherent discontinuities in the realistic HSCT design space, it resulted in a family of configurations that are not pure "parametric" variations in any characteristic. Caution must be used in interpolating results between specific planforms. (The "lumpiness" of the resulting design space, especially when the planform matrix was combined with multiple engine types, is an indication of the difficulty in performing semi-automated "rules based" MDO's.)

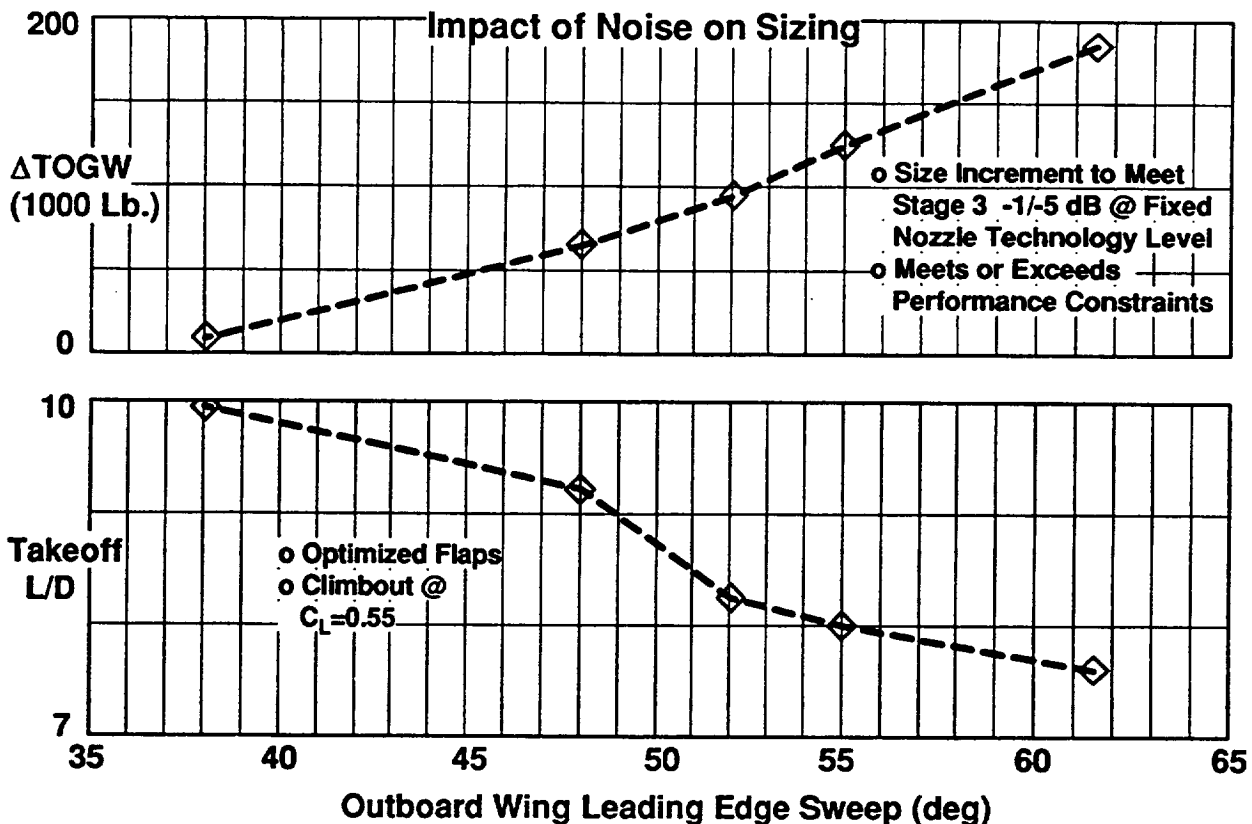
Given this background, it is possible to look at selected planform study results to understand basic HSCT configuration trends. The figure above shows a slice through the matrix of candidate planforms covering a family of outboard wing sweeps and leading edge break locations. This slice provides a variation in wing span at a relatively constant wing area (i.e. different aspect ratios). The net geometric effect is a line of increasing overall wing-body slenderness which correlates very well with increasing supersonic cruise point lift-to-drag ratio (L/D). This correlation is of course due to the fact that at Mach 2.4 the contribution of vortex drag due to spanwise loading is far overpowered by the supersonic wave drag which depends on streamwise slenderness. This set of planforms is therefore a good representation of the "mainstream" HSCT configurations of interest with similar levels of structural and stability risks.



Each of the planforms in this design space have different structural arrangement details to accommodate the variations in outboard wing size and sweep, but the bodies, tails, nacelle locations, landing gear, and wing box depth versus span are all configured to similar groundrules. With care in selection of the wing box geometry it is possible to minimize the impact of the increased structural span and planform break "kick loads" on wing weight as the aerodynamic slenderness is increased. The uncycled operational empty weight of these configurations was therefore kept relatively constant. When a "thumbprint" engine-airframe sizing code was used to optimize the wing loading and engine size for each of these airplanes for a 5000 nautical mile mission with an all supersonic cruise segment, the increase in supersonic L/D versus slenderness translates into more efficient takeoff weights. For the lowest aspect ratio, most highly swept planform this advantage was not enough to offset the resultant structural and takeoff gross weight increases. This represents an economic viability penalty as the sized TOGW is a good indicator of airplane production and operating costs.



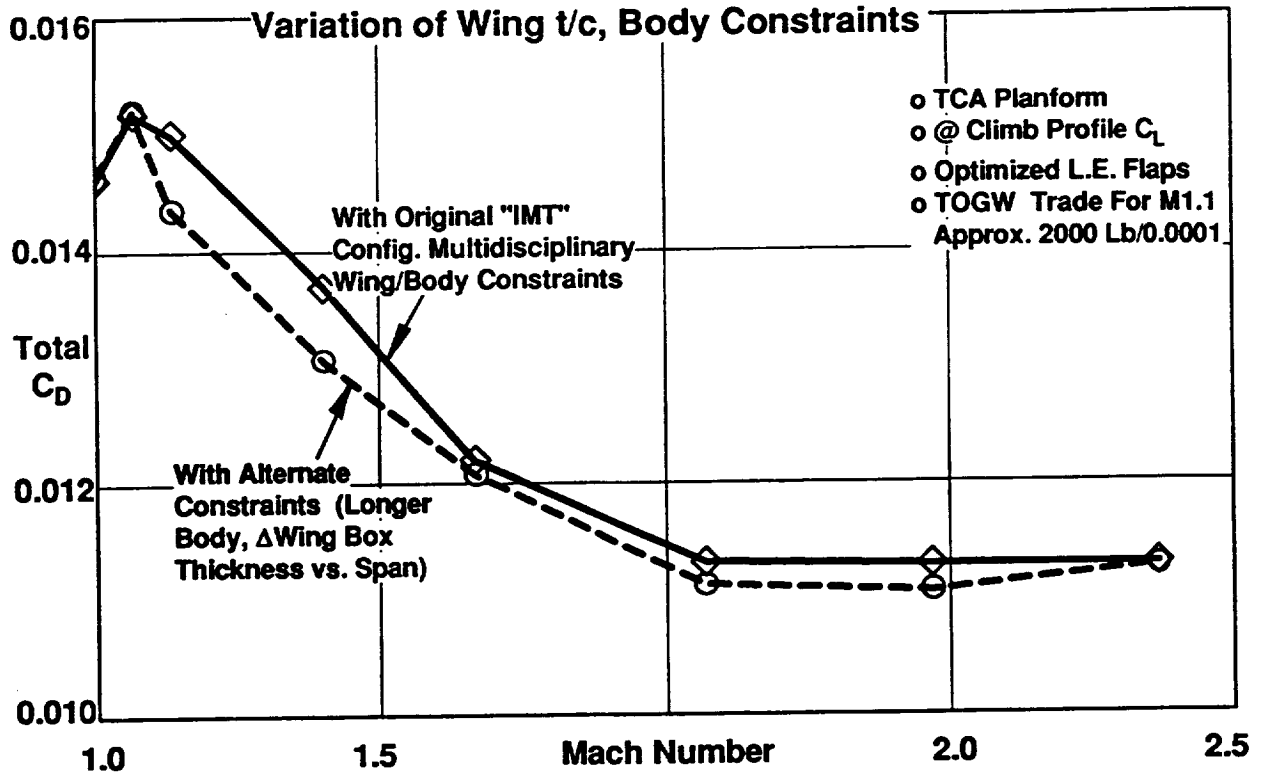
The HSCT is not envisioned to be a totally trans-oceanic airplane like the Concorde. The typical HSCT route structure will include many subsonic legs over potentially boom-sensitive land and coastal areas. MDA and BCAG have agreed to size all HSCT study configurations using a more typical mission profile with a 750 nautical mile subsonic leg following the Mach 2.4 cruise segment. When the previously shown planforms are re-sized to this mixed subsonic / supersonic mission requirement the advantages of increased slenderness for supersonic L/D are quickly overpowered by the loss in transonic efficiency. The net result is that the sized TOGW remains relatively flat for most planforms but increases significantly for the most arrow-wing like planforms which combine maximum sweep and low aspect ratio. Moving farther to the left along the curve (i.e. to even higher aspect ratios, and more inboard leading edge breaks) eventually increases the empty weight and supersonic L/D penalty to the point where the net sized TOGW once again increases. There is some theoretical and non-linear optimization experience to indicate that wings with farther inboard leading edge breaks show decreasing potential for taking advantage of non-linear aerodynamic optimization technology. The drag levels for the planforms shown include an appropriate high speed aerodynamic technology projection which includes this effect based on "tops-down" L/D potential analysis charts. The planform finally selected for the TCA is near the right hand end of the TOGW "bucket" to allow CA the greatest opportunity for full development of the CFD-based non-linear optimization technology.



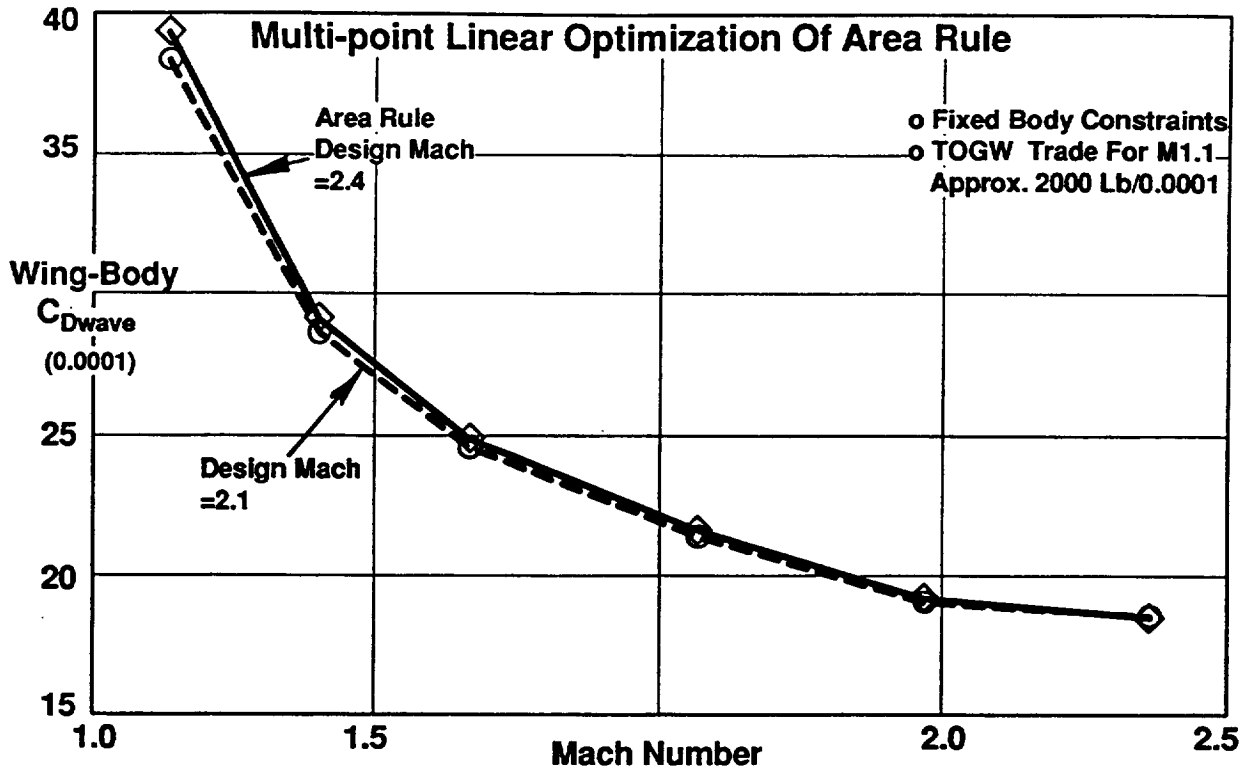
The trend of higher sized takeoff gross weight with increasing overall aerodynamic slenderness becomes even more pronounced when sizing constraints for takeoff noise are included. This is directly related to the loss of aerodynamic efficiency for the takeoff high lift regime as aspect ratio is decreased.

When the achievable nozzle technology level and optimum engine match are better known through future HSR trades and testing, the eventual noise goal of Stage 3 minus 5dB at cutback can be better addressed. With fixed TCA engine type and noise technology projections, the figure above shows the ability of planform changes alone to reach the -5dB goal. Re-sizing the mixed mission airplane incurs a TOGW penalty that climbs steadily as aspect ratio is decreased. The planform family in the figure has been extended left to include a potential higher aspect ratio, 38 degree outboard sweep design which shows good noise robustness but has increased aeroelastic risk.

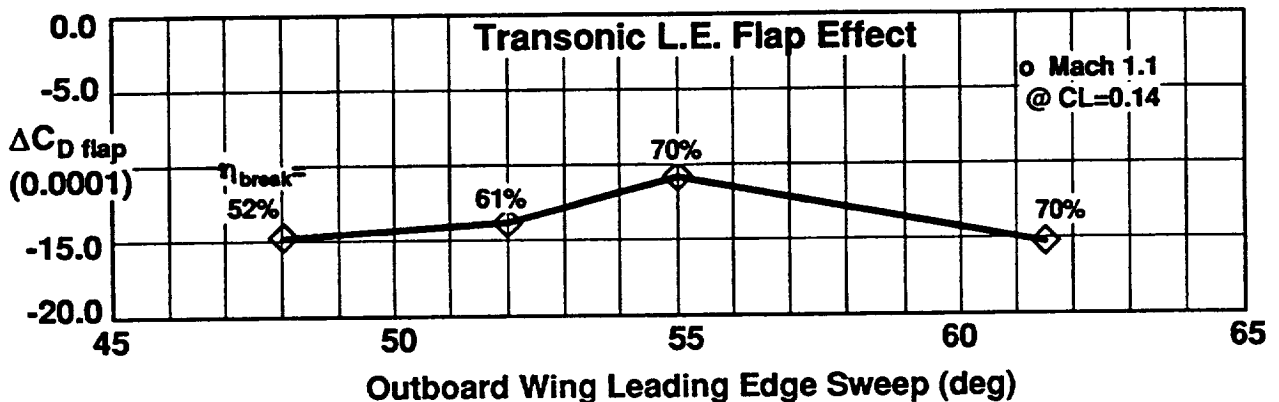
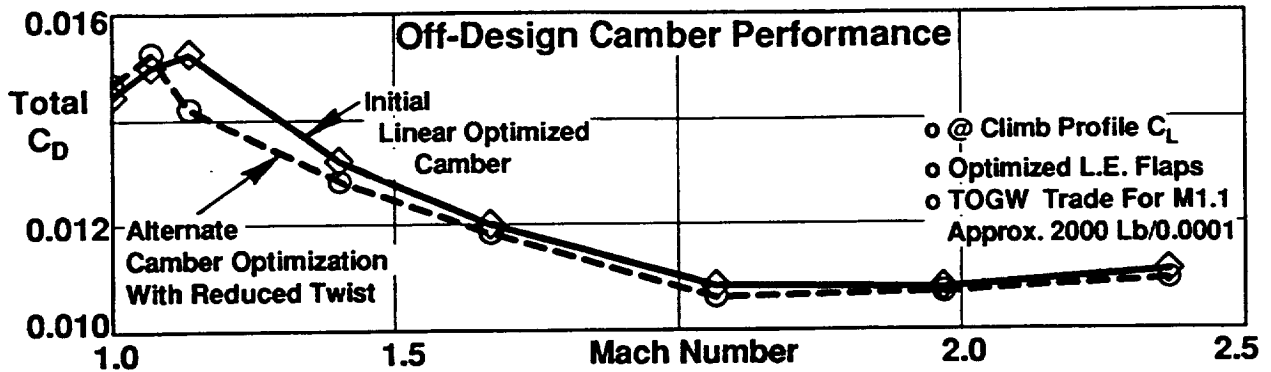
For the given levels of engine and nozzle technology projection, the planform chosen for the TCA was capable of simultaneously meeting the basic HSCT viability goals of 750,000 Lb takeoff weight with Stage 3 minus 1dB noise at sideline, and -3dB at cutback. The TCA planform selection was therefore based on the best performance sized airplane and not on "noise robustness".



The multidisciplinary interactions involved in general arrangement changes make it impossible for CA to independently evaluate or optimize wing planforms in all but an academic or generic sense. The same is true of altering those regions of the wing and body geometry which have a strong impact on internal payload volume distribution or primary structure. In fact, the increased wing box thickness and larger body diameter which are desired to minimize structural weight and maximize structural stiffness are totally opposite the aerodynamic requirements. This is similar to the way that wing span benefits aerodynamics at the expense of weight on subsonic transports. It is for this reason that multicycle designer-in-the-loop trades were required to establish reasonable interdisciplinary compromises for all of the wing and body shape constraints to be honored by the final aerodynamic loft lines. In this iteration process, intermediate geometries were cycled through linear drag analyses, weights, payloads, fuel volume and often overall sizing evaluations. As shown above, the compromised design constraints selected for their favorable impact on net TOGW also tended to be those which resulted in some improvement to off-design aerodynamic performance. While this result illustrates the difficulty of optimizing the high speed configuration, it also points to the potential value of a multi-point aerodynamic optimization process that accounts for interdisciplinary penalties .

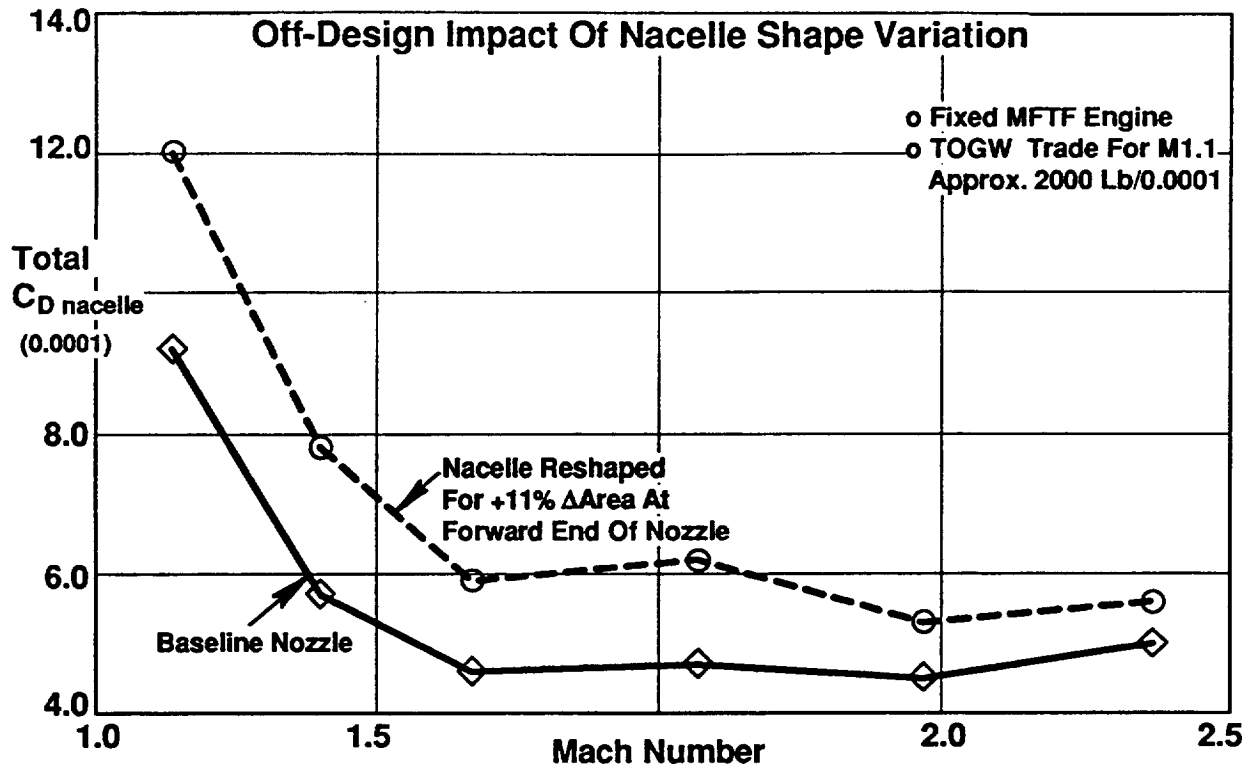


After the interdisciplinary compromised constraints were established for the fuselage of the TCA, the defining sections for the aerodynamic loft were defined using traditional linearized aerodynamic optimization tools. Following standard BCAG supersonic design practices, the body volume was area ruled at several different design Mach numbers, each optimization honoring the fixed wing geometry and "hard" body area constraints at key cross-sections. In effect this allows a basic form of linearized aero multi-point optimization by creating slight variations in body contouring that may improve off-design performance. As shown above, area rulling the body for a design Mach number of 2.1 rather than 2.4 did result in a transonic wave drag improvement with no cruise penalty (resulting in 1800 pounds TOGW reduction). The shape produced by the lower reference Mach number also had an increase of 120 cubic feet of internal volume for payload.



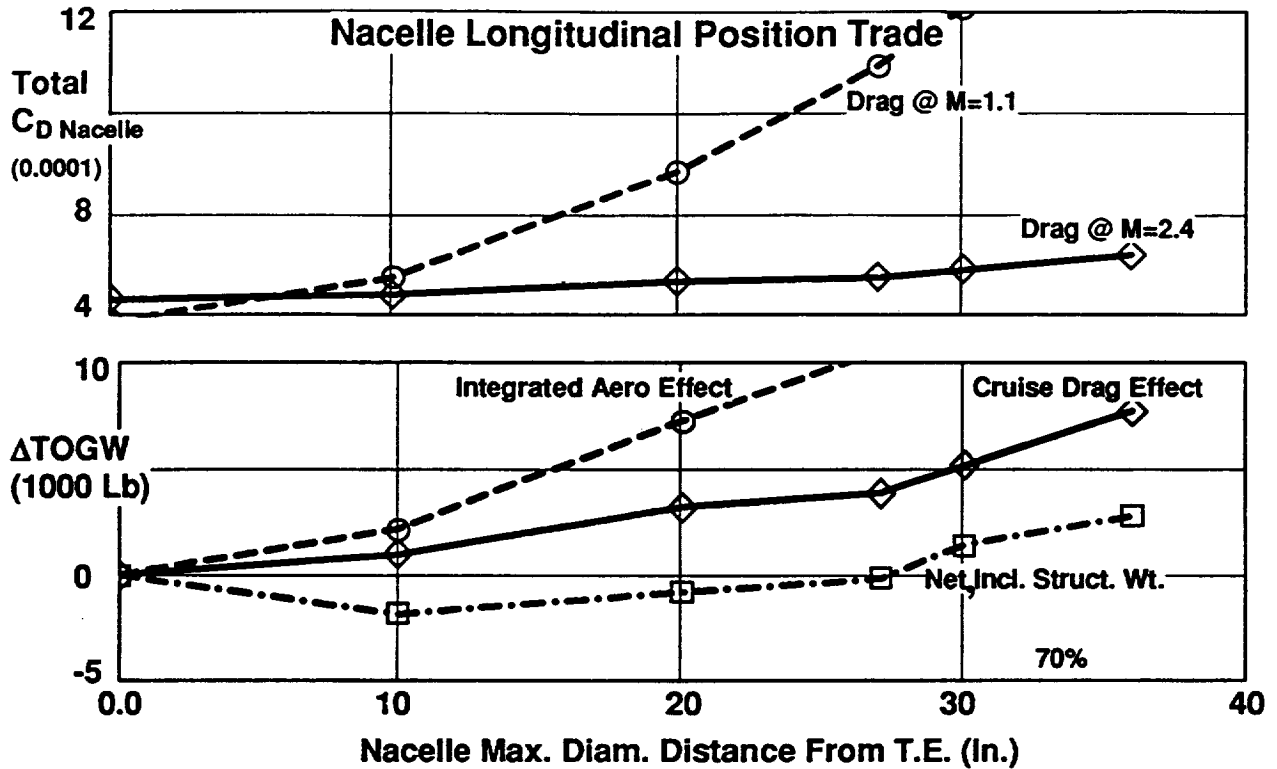
The body area rule showed a net improvement by choosing a reference Mach number for linear aerodynamic optimization that was different from the airplane's actual cruise Mach number. Similarly, experience has shown that linear camber optimization sometimes results in better overall performance by specifying a design C_L that is somewhat lower than the predicted cruise C_L . Linear aerodynamic optimization cambers also vary depending on the optimization method (lift loadings vs. shape functions), and the manner in which the "lumpy" twist distributions produced are smoothed for the final lofting. The above example shows a comparison of two linear optimized cambers that have nearly identical cruise performance levels. The camber surface with reduced twist (e.g. more smoothing, lower $C_{L \text{ design}}$) has noticeably better transonic performance. The flatter twist generally also benefits subsonic cruise (less triangular span load) and high lift (higher C_L at geometry limited takeoff alpha).

The difficulty with performing a multi-point optimization of the high speed camber/twist definition is that the HSCT has adaptive leading edge flaps which will be programmed to minimize the drag due to lift as upwash varies at transonic and subsonic conditions. As shown in the lower figure above, this effect can be considerable and varies from planform to planform. Multi-point optimization of the high speed camber and twist is not valid unless the off design evaluations include optimized flap deflections specific to each Mach and C_L . At some Mach numbers, the flap deflections may be very close to those for hingeline flow separation so the evaluations should be done in a Navier-Stokes code (not inviscid). Even that may not be sufficient as some studies have indicated that the optimized flap performance levels obtained on a rigid wing geometry may not be valid for the aeroelastically deflected wing. At transonic conditions, the pitching moment and trim may also have a significant effect. This would require including the effects of nacelle spillage and bypass interference, aft body downwash, tail lift and drag, thrust effects, and CG management optimization.



Nacelle shape constraints are handled in a manner very similar to the body area rule constraints. Multiple iterations between the propulsion designers and aerodynamics are usually needed to arrive at an interdisciplinary compromise on the desired nacelle shape. Once the internal envelope of structural supports, engine, engine accessories, nozzle dimensions and key inlet points are defined, an aerodynamic loft can be defined which minimizes the total installed nacelle drag. In the example shown above, linearized potential flow aerodynamic assessments of two different sets of nacelle lines are shown to illustrate the relative size of the drag increment at Mach 2.4 versus off design conditions. The fact that there is a difference in drag across the supersonic speed regime indicates the potential for shape tailoring around the hard constraints for multi-point optimization.

Currently, the entire nacelle shape generated by this process using linear aerodynamic tools is held fixed during non-linear CFD optimizations, with only the toe-in, pitch, and roll angles as variables to optimize installed drag or inlet flow distortion. This is based on the goal that all nacelles should be geometrically similar to minimize manufacturing and maintenance costs. If future studies indicate this requirement could be relaxed, a non-linear optimizer may be used to tailor asymmetric nacelle shapes that minimize inlet distortion and drag simultaneously. This would require that the internal structural and equipment envelopes be specified as 3D objects inside the aero loft lines similar to the current body area constraints. A transonic to supersonic drag "weighting factor" based on performance thumbprint TOGW sensitivities could be used to allow CA to do multi-point nacelle drag trades.



Another area where iteration between high speed aerodynamics and other disciplines is required to establish the compromise design constraints is the longitudinal positioning of the nacelles. The lateral positioning is usually not an issue as it is heavily constrained by non-aerodynamic considerations (rotor burst zones, FOD ingestion, inlet unstart, flutter). As the upper figure in the example above shows, the supersonic cruise drag favors placement of the nacelle maximum diameter section (usually near the forward end of the nozzle) directly under the wing trailing edge to maximize favorable aerodynamic interference. The off-design condition at the Mach 1.1 thrust-drag pinch shows an even steeper drag trend. The lower figure shows the impact of the cruise drag term, the total high speed drag contribution, and the net impact on TOGW including the effect of the structural weight required for supporting the nacelle at a given location. The net result favored positioning the nacelle at roughly 10 inches ahead of the trailing edge. In the final aerodynamic loft development this is generally treated as a hard constraint because of the interdisciplinary considerations.

Conclusions:

- o **The TCA is a globally optimized PD configuration**
 - Downselects supported by multidisciplinary trades
 - Evaluations based on total mission performance (TOGW)

- o **TCA aerodynamics**
 - Linearized supersonic optimization for camber & twist, area rule
 - CFD used only as "virtual wind tunnel" to identify problems
 - Interdisciplinary compromises for geometry constraints
 - Off-design performance benefits obtained where possible without impacting cruise L/D

- o **Non-linear multi-point optimization has potential**
 - Big increase in complexity, must address multidisciplinary constraints and concerns (easily underestimated)
 - Concentrate on areas where interdisciplinary coupling is weak or easily defined (nacelle shape tailoring, body area rule, local planform tailoring details, inlet distortion)
 - Rely on TI global performance trades for drag "weighting" functions and approximate TOGW impact

The basic TCA "linear aerodynamic" design is actually quite complex. It is the result of a sort of "MDO" process involving multiple design iterations across the major disciplines. The TCA looks very different from a design optimized for supersonic cruise only. The areas of the geometry that are strongly coupled to interdisciplinary trades are specified in the TCA configuration description by "hard" geometric constraints. These constraints are compromises optimized through "global" system performance trades. These constraints allow CA the maximum flexibility in their configuration sub-optimization of the high speed aerodynamic lines without danger of incurring penalties on other disciplines.

Several of the side trade studies and linear aero optimizations have indicated the importance of transonic and high lift aerodynamics to the total configuration viability. The potential benefits of multi-point aerodynamic optimization can be seen in some of the linear designs. Successful CA non-linear multi-point optimization will depend on being able to properly assess,

- 1) the value of one count of drag at transonic conditions versus one count at Mach 2.4,
- 2) the impact of high speed lines changes on high lift performance and noise
- 3) the secondary impact of off-design changes on structural weight, aerodynamic loads, stability, etc., and
- 4) new high speed lines constraints that might arise from (3).

Evaluation of the sensitivity of drag changes at each Mach number to geometry perturbations will not be sufficient for multi-point optimization. A combination of off-design viscous CFD analysis, FEM based weight trades, and global performance sensitivities (from TI programs such as DOSS) will likely be required to provide the necessary drag "weighting factors", constraints, and figures of merit. Initially, multipoint non-linear optimization may focus on areas where the interdisciplinary coupling is relatively weak, such as body area ruling.

CFD Planform Study of the 1400 Series

G. Kuruvila, J. O. Hager, E. R. Unger, A. E. Arslan,
D. B. Bruns, P. Sundaram, G. Martin, S. Agrawal

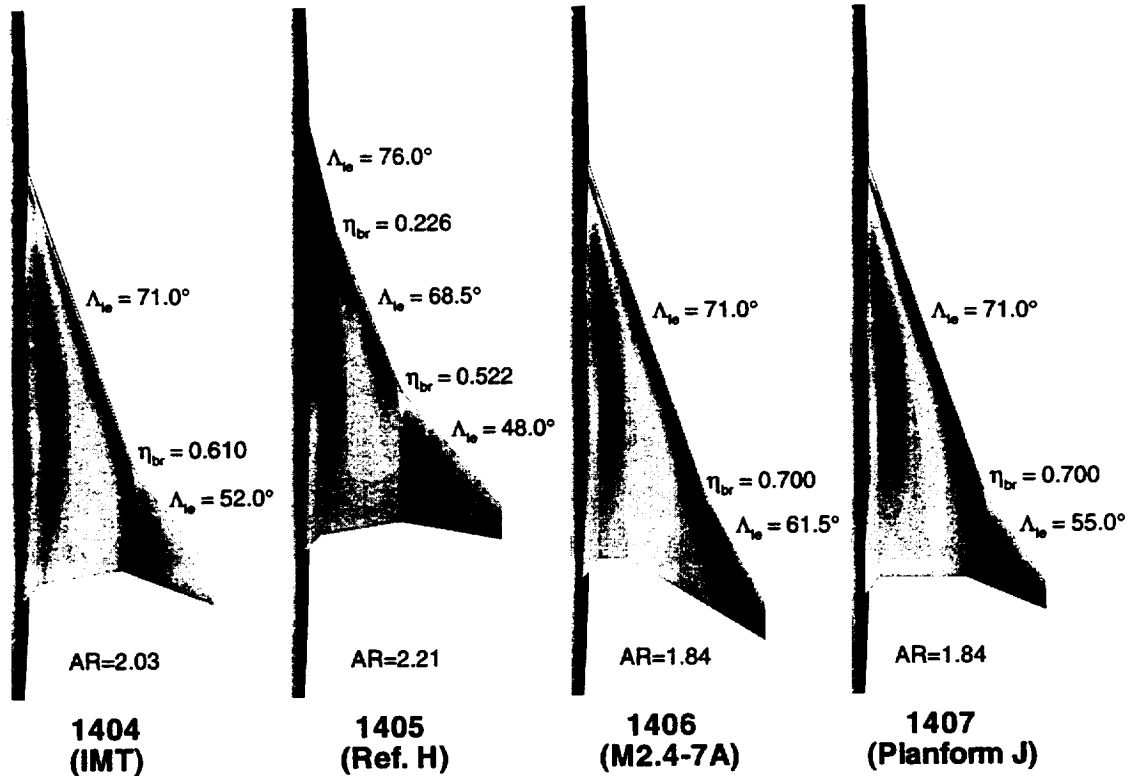
McDonnell Douglas Aerospace
Long Beach, California

The Technology Integration (TI) element of the High Speed Research (HSR) program was tasked with configuring a new Technology Concept baseline aircraft, by the end of 1995, in order to provide, the industry and NASA, a common baseline to serve as the starting point for the next three years of technology development for an HSCT aircraft. The TI team, comprised of personnel from Boeing (BCAG), McDonnell Douglas (MDA), and NASA, selected four distinct planforms: (1) FY94-95 technology baseline, Reference H; (2) MDC HSCT Arrow wing configuration, M2.4-7A; (3) Industry Methodology Test (IMT) airplane; and (4) Planform J, a derivative of M2.4-7A. The team sought inputs from the various disciplines such as Aerodynamics, Structures, Propulsion, etc., in order to select the "best" wing planform for the Technology Concept baseline aircraft. The task of assessing the relative supersonic cruise performance was given to the MDC High Speed Aerodynamics team.

One of the key aspects of aerodynamics is the prediction of supersonic cruise lift-to-drag ratio, L/D . Until a few years ago, only linear theory methods had been used for such predictions. However, nonlinear computational fluid dynamics (CFD) methods have recently demonstrated great success in accurately predicting the nonlinear flow physics associated with supersonic Mach numbers on HSCT configurations. They, coupled with optimization methods, have also been used very successfully in optimizing wing and fuselage designs in order to improve the supersonic cruise L/D of HSCT configurations. Recent wind-tunnel tests of the optimized Reference H and M2.4-7A models have also validated the CFD-based design optimization methods. Therefore, this study was focused on applying the validated nonlinear computational methods in not only the prediction of L/D , but also in further optimization of the wing and fuselage designs for improved supersonic cruise L/D for configurations initially designed using linear theory methods.

Thus, the MDA's CFD study was centered around addressing two questions: (a) How are the potential cruise performance improvements from nonlinear design methods dependent on planform?; and (b) How do the nonlinear design improvements correlate with the linear theory-based projections?. The CFD study involved performing Euler analyses, using CFL3D, of the four baseline configurations and to optimize the four configurations, using MDA version of FLO67/OPT3D, in order to maximize the supersonic cruise L/D ratios. In order to remove any biasing of solutions for different configurations, a common set of groundrules was used in the analysis and optimization of all four planforms.

Planform Views of the Four Wing/Body Configurations



Shown above are the planform views of the four configurations. The important parameters of these planforms are the inboard and outboard leading-edge sweep angles and the outboard break locations. These planforms were lofted by Boeing and they included realistic landing-gear fairing.

CFD Study Approach

- Nonlinear analysis (Euler)
 - Wing/body configurations
 - Wing/body/nacelle/diverter configurations
- Nonlinear optimization (Euler)
 - Wing/body with nacelle effects
 - Maximize L/D at $M_\infty=2.4$, altitude=60,000 ft., $C_L=0.11$

For the CFD study, first Euler analyses of the four baseline wing/body and wing/body/nacelle/diverter configurations were performed using the CFL3D code. Then the wing/body of the four configurations were optimized, with nacelle effects using the Euler-based MDC version of FLO67/OPT3D. The objective of the optimization was to maximize the lift-to-drag (L/D) ratios at $M_\infty = 2.4$ and $C_L = 0.11$ at an altitude of 60,000 ft.

Nonlinear Analysis Guidelines

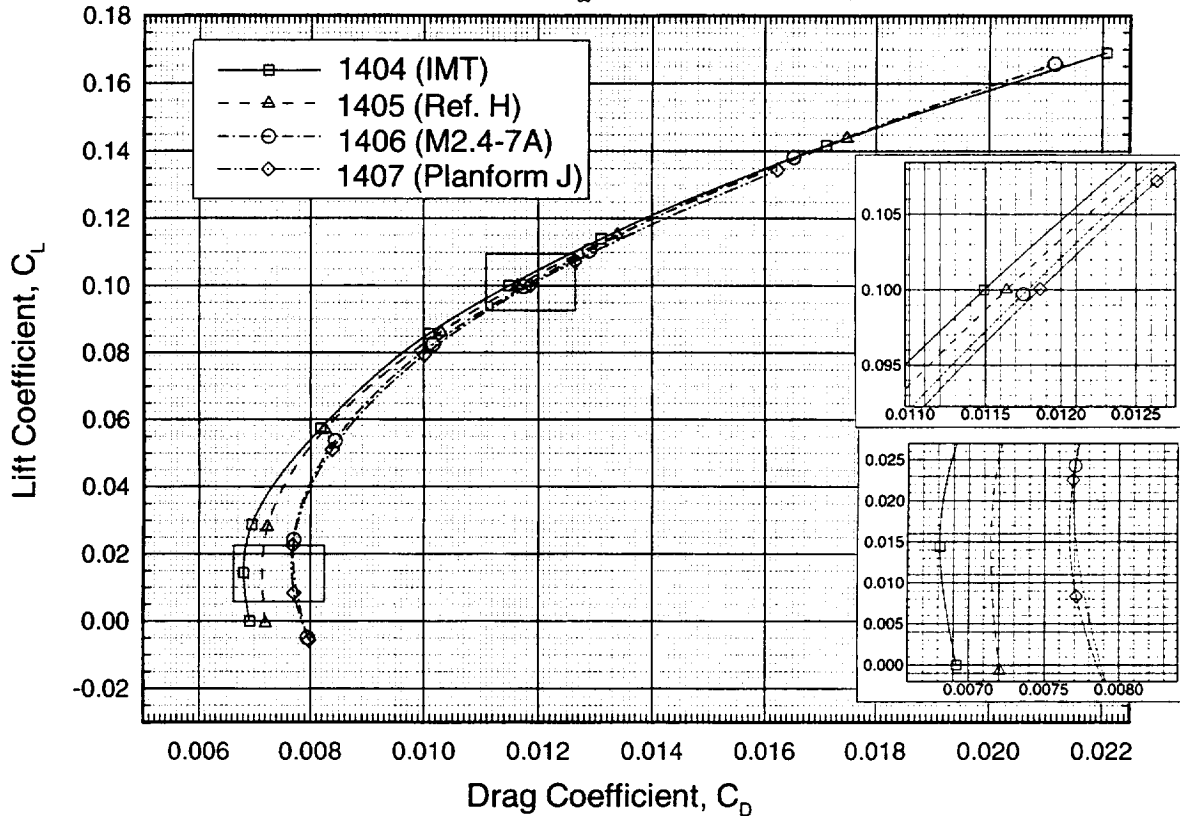
- CFL3D in Euler mode with flux-difference splitting
- C-O topology for wing/body configurations
- Patched multi-block for wing/body/nacelle/diverter configurations
- No. of grid points, grid quality, etc., maintained
- Solution residuals reduced by 3-4 orders of magnitude
- Viscous drag from equivalent flat-plate method
- Nacelles aligned with the flow

For consistency the following set of guidelines were followed when analyzing the four planforms.

- CFL3D in Euler mode with flux difference splitting was used for analysis
- Grid generation was done using COWF2/MACGS
- C-O topology was used for wing/body
- No. of grid points for wing/body was kept the same for each planform
- No. of blocks (28 blocks) for each wing/body/nacelle/diverter configuration was kept the same
- Grid spacing and quality were maintained
- Farfield boundaries were kept the same for each planform
- C_D was converged to 10th of a count for most cases
- Solution residuals were reduced by 3-4 orders of magnitude
- Viscous drag at flight Reynolds number (60,000 ft.) was determined using an MDA method based on equivalent flat plate skin-friction
- Nacelle was aligned with the flow by rotating about the diverter leading-edge nacelle intersection

Drag Polars for the Wing/Body Configurations

CFL3D, Euler, $M_\infty=2.4$, Altitude=60,000 ft.

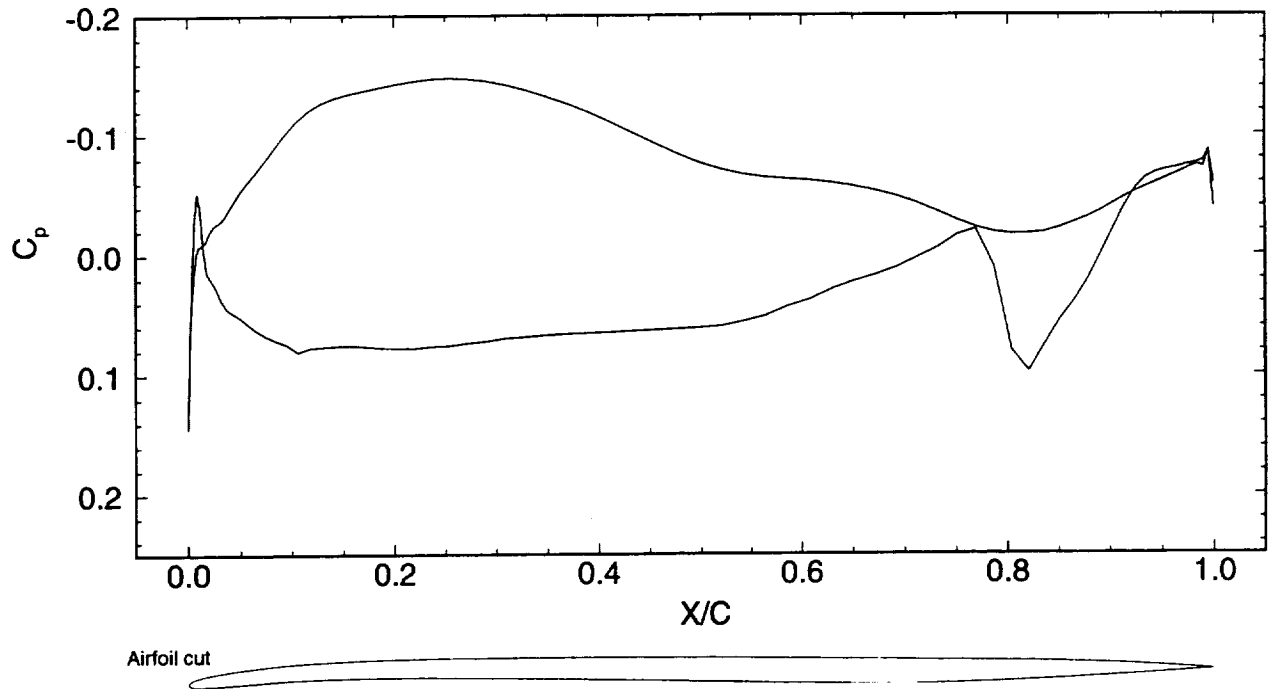


The four baseline (unoptimized) wing/body configurations were analyzed using CFL3D in the Euler mode at $M_\infty = 2.4$. The viscous drag at an altitude of 60,000 ft ($Re/ft = 1.756 \times 10^6$), obtained using an MDA method based on the equivalent flat plate area, are included in these calculations.

The expectation was that at cruise ($C_L = 0.1$), 1406 would have the least drag followed by 1407, 1404 and 1405. However, CFD analysis showed that 1404 had the least drag followed by 1405, 1406 and 1407. This unexpected trend could be due to several reasons. The initial design of the different planforms were not necessarily of the same quality. The initial design of 1404 was better than the others. The pressure distributions on some configurations were not very good. There were volume differences, especially the wing volume, among the planforms. Also, an MDC IRAD study concluded that the landing-gear fairing on each of the planforms produced unexpectedly high drag (about 6-8 counts of additional drag).

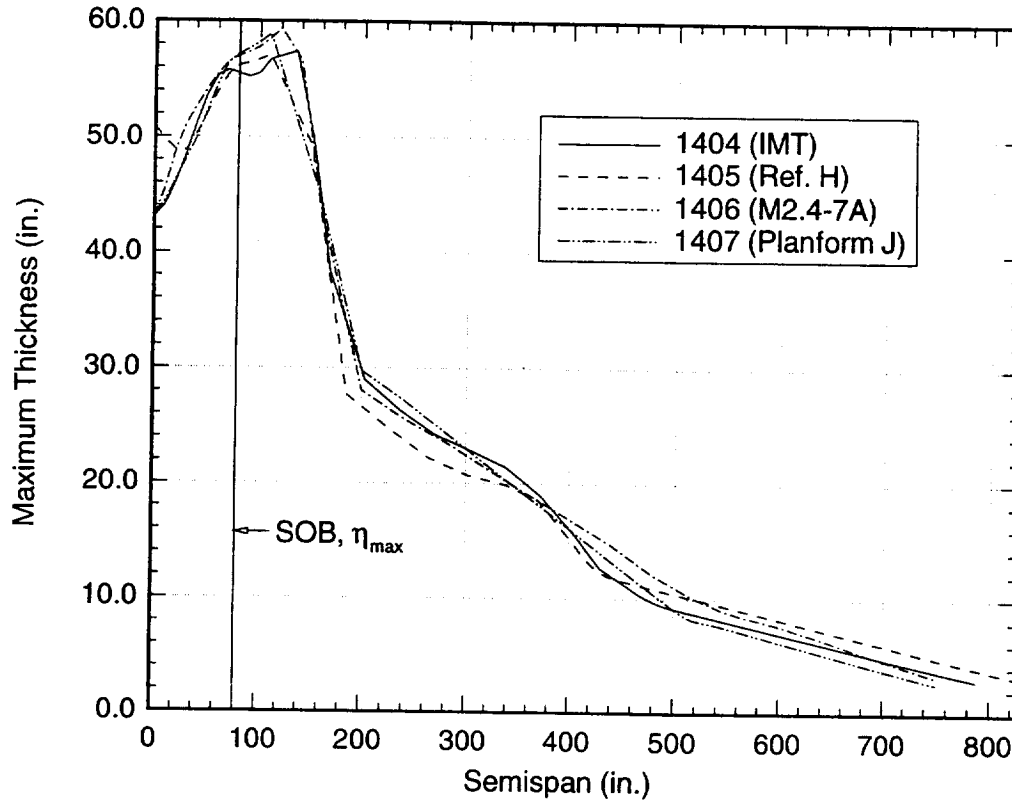
Pressure Distribution and Airfoil Cut at the 40% Semispan Location of the Baseline 1406 Configuration

FLO67 Euler w/ Nacelle Effects, $M_\infty=2.4$, $C_L=0.11$



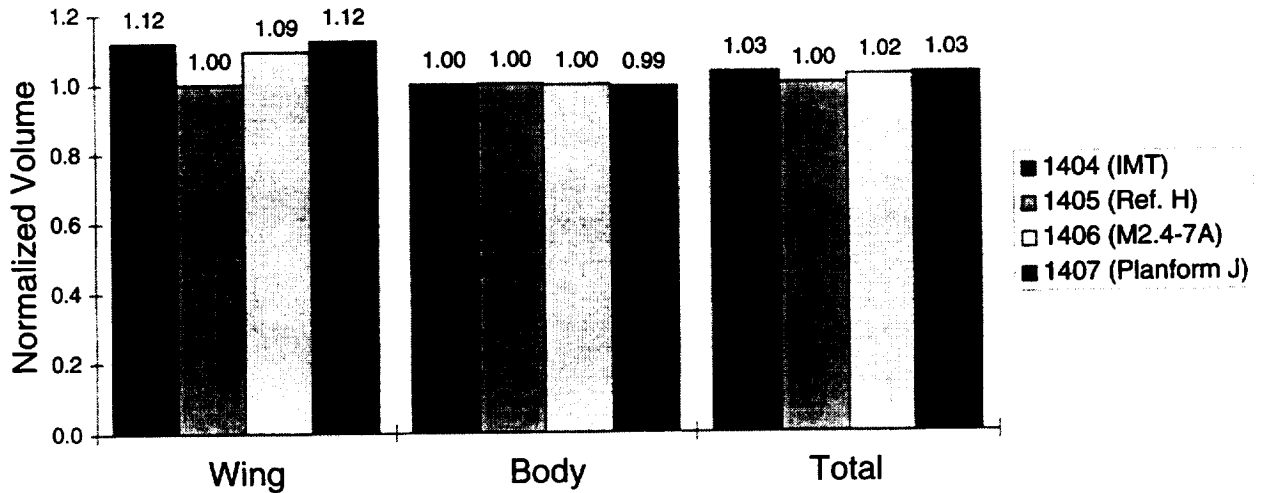
Shown is the pressure distribution of the 1406 baseline (unoptimized) configuration at 40% semispan station. As observed, there is very little or no leading-edge suction. There is also criss-crossing of the pressure near the leading edge, indicating an undesirable flow acceleration and then deceleration around the lower surface of the wing. This behavior was typical of all the planforms except 1404.

Maximum Wing Thickness Variations Along the Span



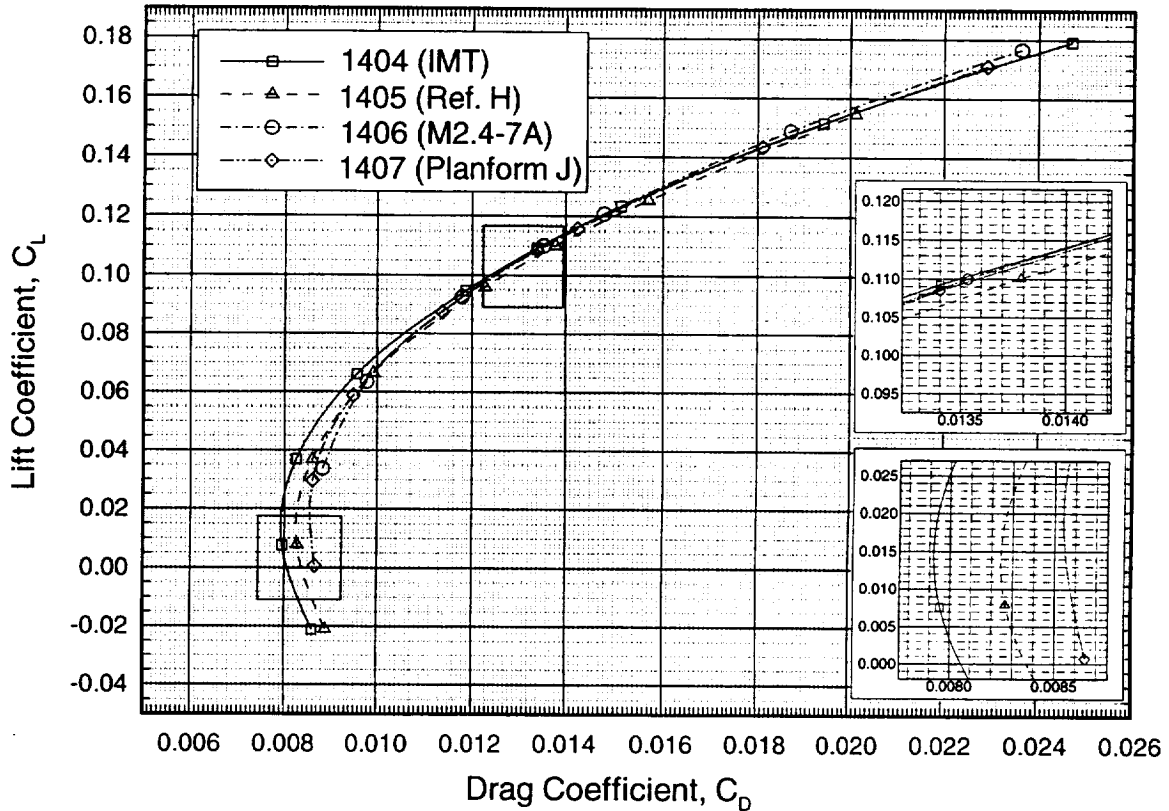
The variation of the maximum wing thickness along the span is shown. The large thickness near the root is due a longer chord length and the landing gear fairing. All the configurations have similar thickness distributions. However, the inboard wing of 1405, outboard of the landing-gear fairing, appears to have a lower maximum thickness than the others.

Volume of the Four Wing/Body Configurations (Normalized with 1405)



The volume ratios for the wing alone, body alone and the wing/body configurations for all four planforms are shown. The volumes have been normalized with respect to the 1405 configuration. The wing volumes of 1404, 1406 and 1407 are larger by about 9 to 12% with respect to 1405. The significantly higher volumes of 1406 and 1407 wings with respect to 1405 may be one of the reasons why the CD_{cruise} and CD_{min} of these configurations are unexpectedly high as shown later. The total volumes of the planforms are larger by about 2 to 3% with respect to 1405.

Drag Polars for the Wing/Body/Nacelle/Diverter Configurations CFL3D, Euler, $M_\infty=2.4$, Altitude=60,000 ft.

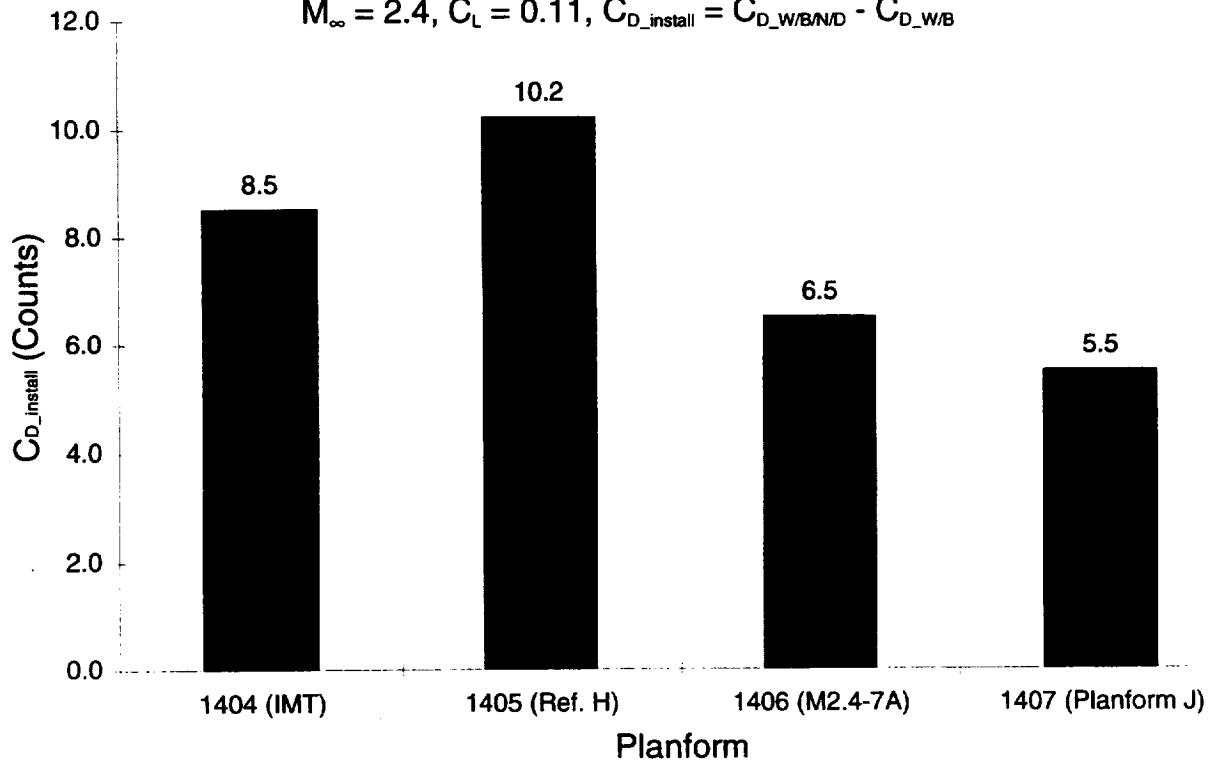


The four baseline (unoptimized) wing/body/nacelle/diverter configurations were analyzed using CFL3D in the Euler mode at $M_\infty = 2.4$. The nacelles were aligned with the local flow, calculated for wing/body at $C_L = 0.1$. The viscous drag at an altitude of 60,000 ft ($Re/ft = 1.756 \times 10^6$), obtained using an MDA method based on the equivalent flat plate area, are included in these calculations. Viscous drag of the nacelle and diverter external surfaces are also included. CFL3D has difficulty converging near C_{Dmin} for the 1406 configuration.

Once again the results obtained were unexpected, i.e., the relative drag of the planforms was different from what was predicted using the linear theory. The reasons could be similar to the ones cited for the wing/body configurations. In addition to that, the nacelle installation drag was different for each planform.

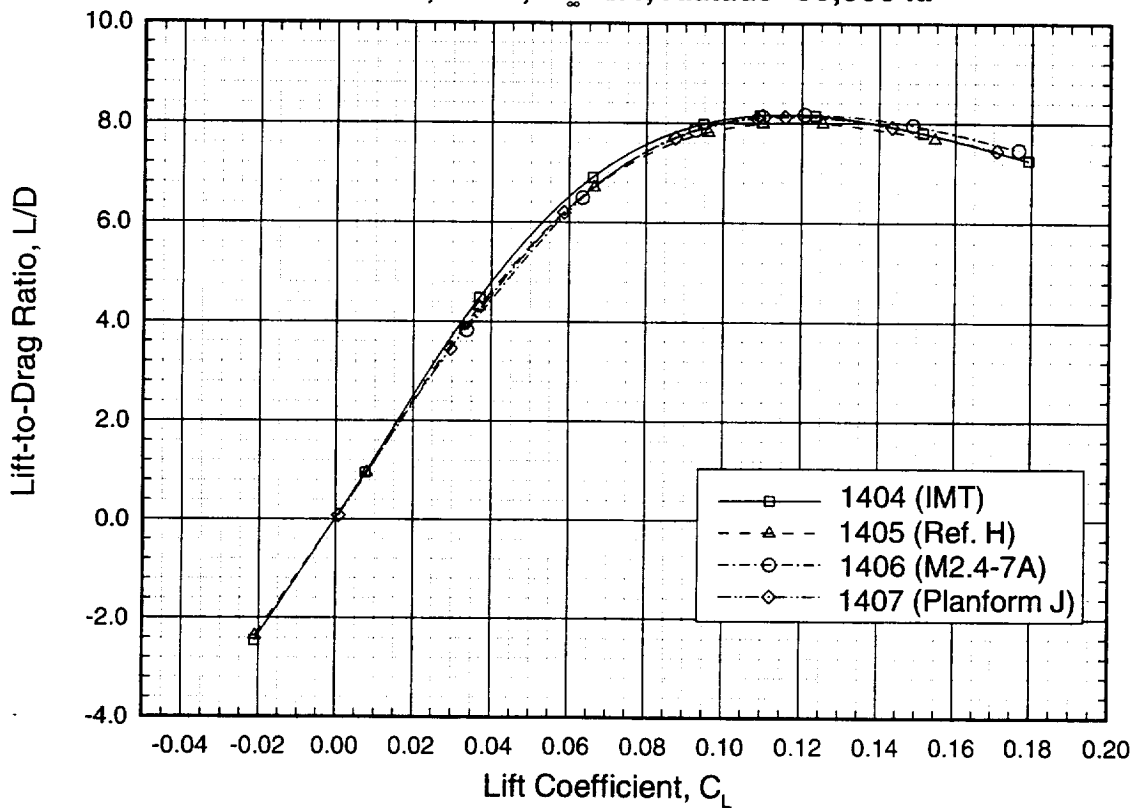
Nacelle Installation Drag for the Four Planforms

$$M_\infty = 2.4, C_L = 0.11, C_{D_install} = C_{D_W/B/N/D} - C_{D_W/B}$$



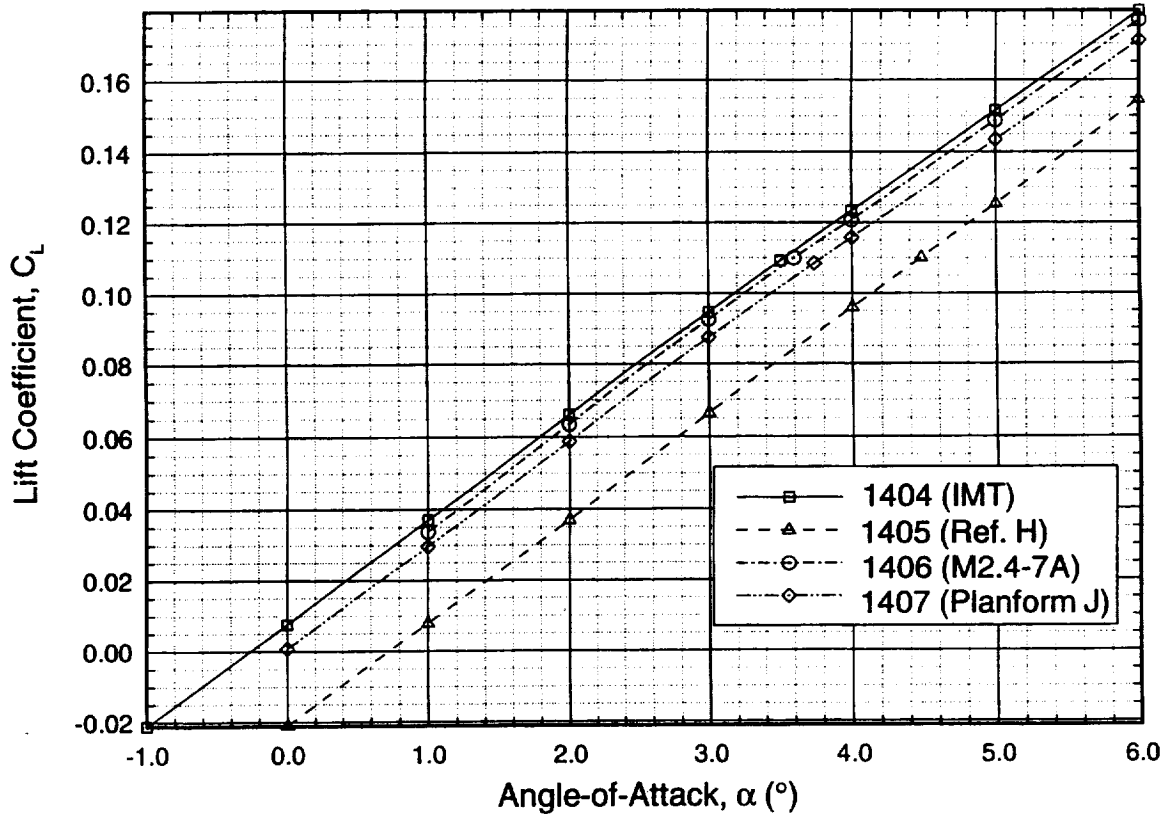
The nacelle installation drag at cruise ($C_L = 0.11$) is shown. The nacelle installation drag is the difference in total drag between the wing/body/nacelle/diverter configuration and the wing/body configuration. The nacelles were not "installed" to give the lowest installation drag for each planform. However, they were aligned with the local flow computed from the wing/body configuration at $C_L = 0.10$.

**Lift-to-Drag Ratios for the
Wing/Body/Nacelle/Diverter Configurations
CFL3D, Euler, $M_\infty=2.4$, Altitude=60,000 ft.**



The ratios of lift-to-drag as a function of the lift coefficient for the baseline wing/body/nacelle/diverter configurations are shown. It is very interesting to note that the maximum L/D for all the planforms is about 8.0 at $C_L = 0.11$. Of course, it is very surprising, but as mentioned earlier, there are numerous reasons for such unexpected results.

Lift Coefficients for the Wing/Body/Nacelle/Diverter Configurations CFL3D, Euler, $M_\infty=2.4$



The lift coefficients as a function of the angle-of-attack for the baseline wing/body/nacelle/diverter configuration are shown. The cruise condition is: $C_L = 0.11$. As for the wing/body, the 1405 planform cruises at about 1° higher angle than the other three. The lift curve slopes for all the planforms are very similar.

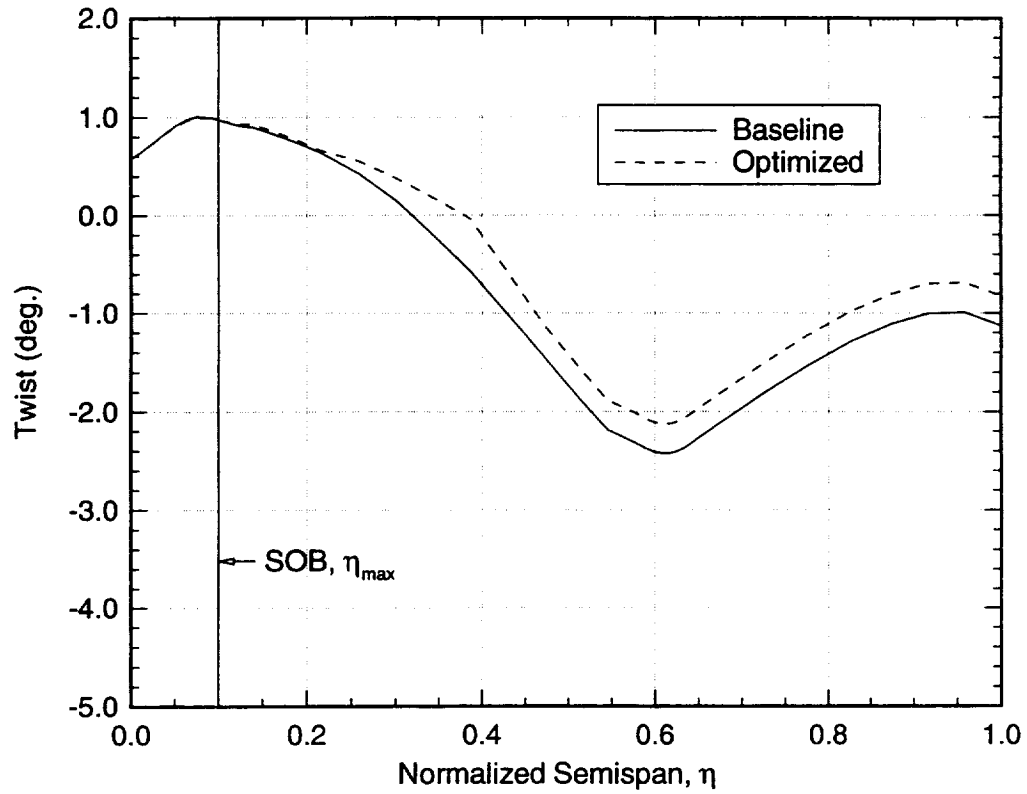
Optimization Guidelines

- Maximize L/D at $M_\infty=2.4$, 60,000 ft., $C_L=0.11$
- Wing/body optimization with nacelle effects
- MDA version of FLO67/OPT3D
- QGRID topology
- Design variables
 - Wing twist and camber
 - Fuselage camber
- Constraints
 - C_L , deck angle, landing-gear fairing
- Viscous drag at flight Re included in C_D

For consistency the following set of guidelines were followed when optimizing the four planforms.

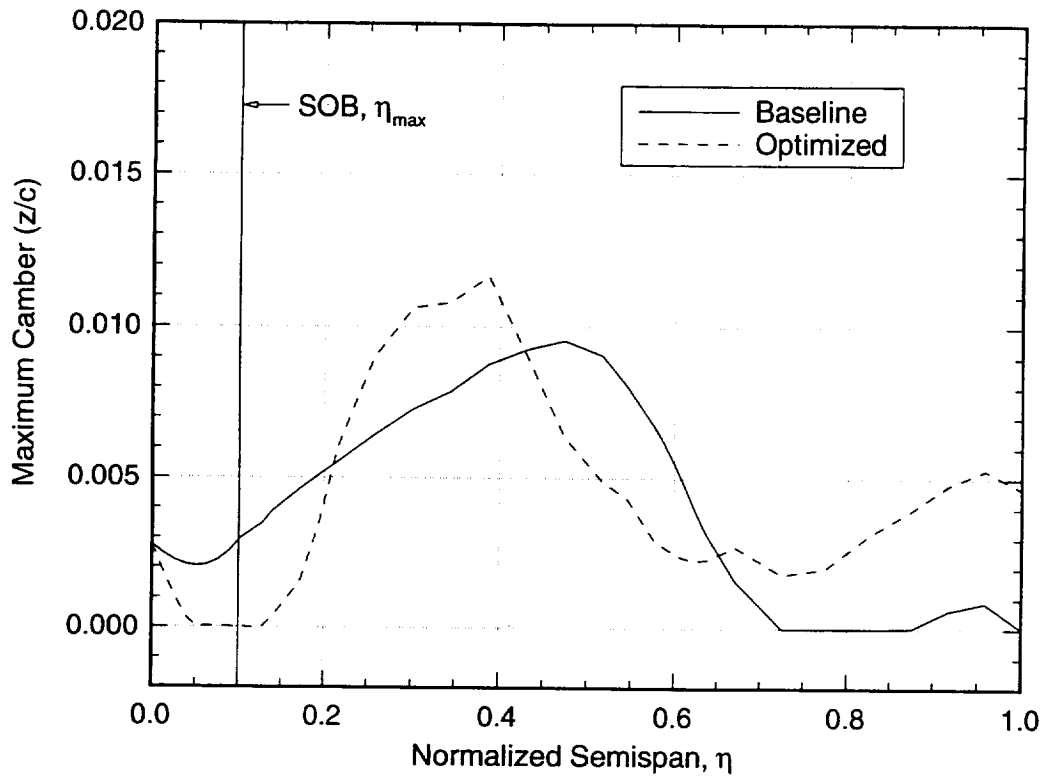
- Optimization was done using the MDC version of FLO67/OPT3D code
- Grid generation was done using QGRID
- The wing/body optimization for each planform that included the nacelle effects was done
- Objective was to maximize L/D at $C_L = 0.11$
- The primary design variables were wing camber and twist and fuselage camber
- Approximately the same number of design variables (80-99) were used
- The constraints were C_L , the deck angle and the landing-gear fairing
- Viscous drag at flight Reynolds number was included in C_D

Wing Twist of the Baseline and Optimized 1404 Configurations



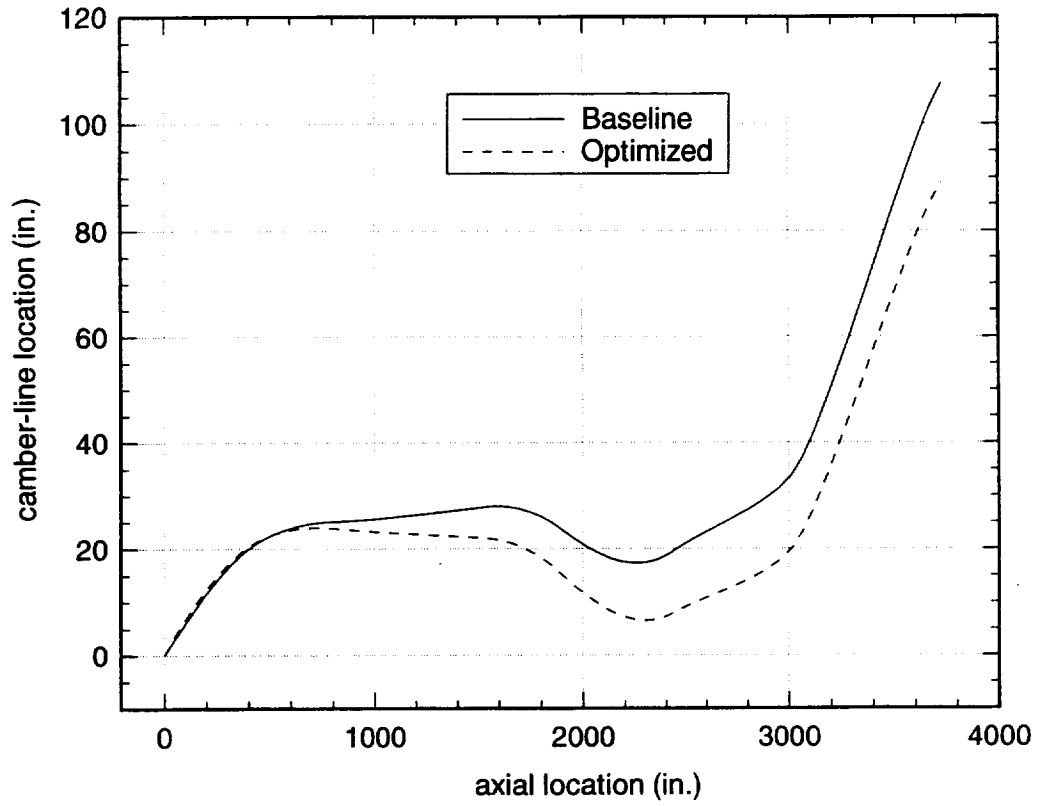
The wing twist of the baseline and the optimized 1404 configurations, respectively, are shown. The twist of the wing is increased. The location of the maximum wing camber is shifted inboard.

Maximum Wing Camber of the Baseline and Optimized 1404 Configurations



The maximum camber of the baseline and the optimized 1404 configurations, respectively, are shown. The maximum camber of the outboard wing is increased.

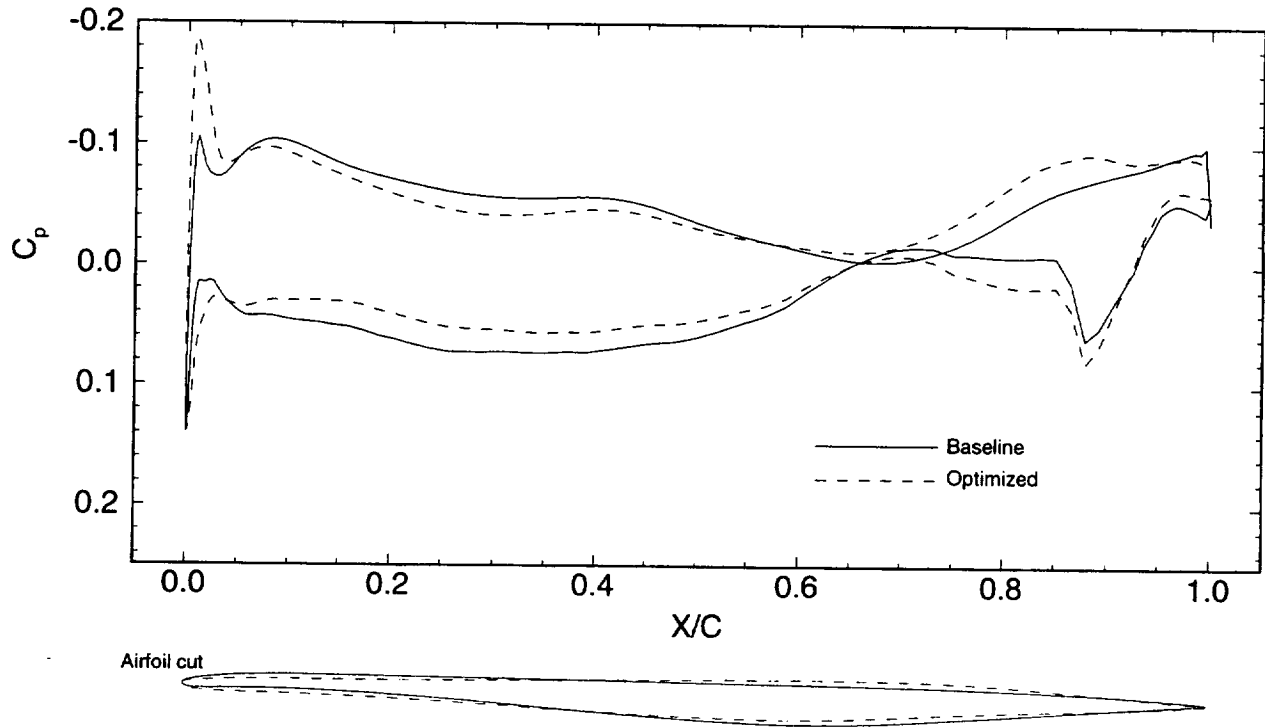
Fuselage Camber of the Baseline and Optimized 1404 Configurations



The camber of the forward fuselage is increased.

Pressure Distributions and Airfoil Cuts at the 15% Semispan Location of the Baseline and Optimized 1404 Configurations

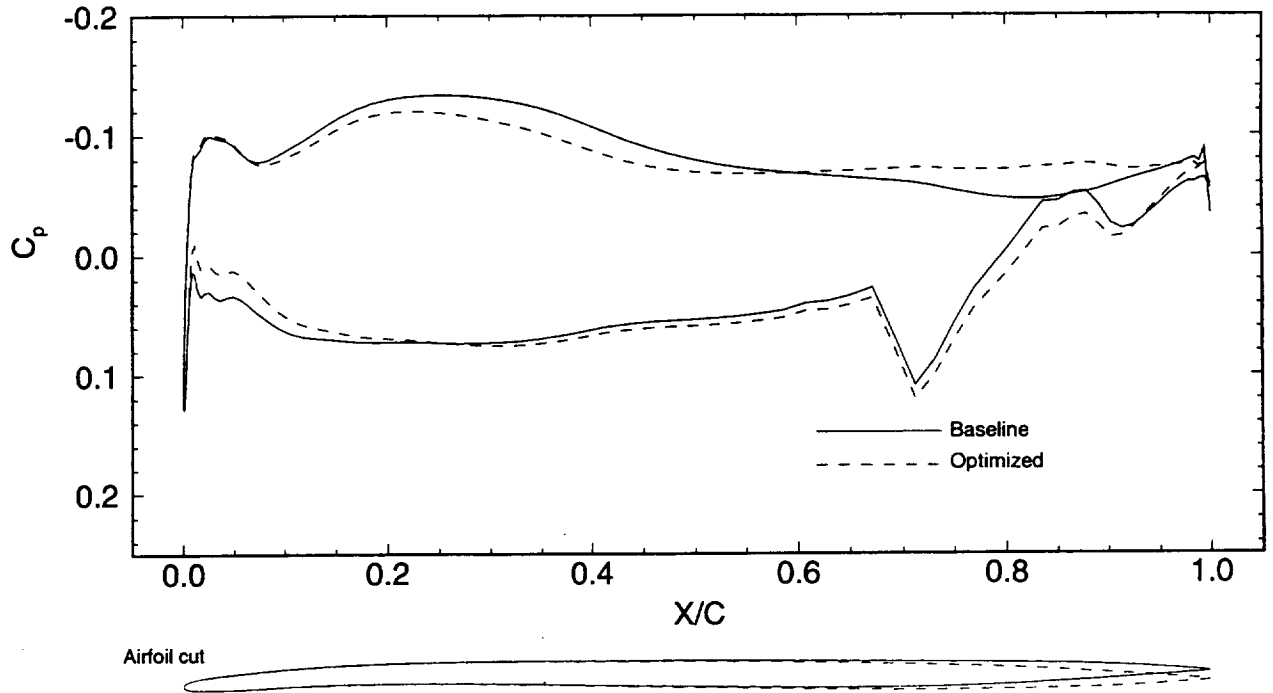
FLO67 Euler w/ Nacelle Effects, $M_\infty=2.4$, $C_L=0.11$



At the 15% semispan station, the leading-edge suction has increased considerably for the optimized configuration. The incidence of the airfoil is unchanged. The maximum camber is decreased. Also, the aft loading is increased.

Pressure Distributions and Airfoil Cuts at the 40% Semispan Location of the Baseline and Optimized 1404 Configurations

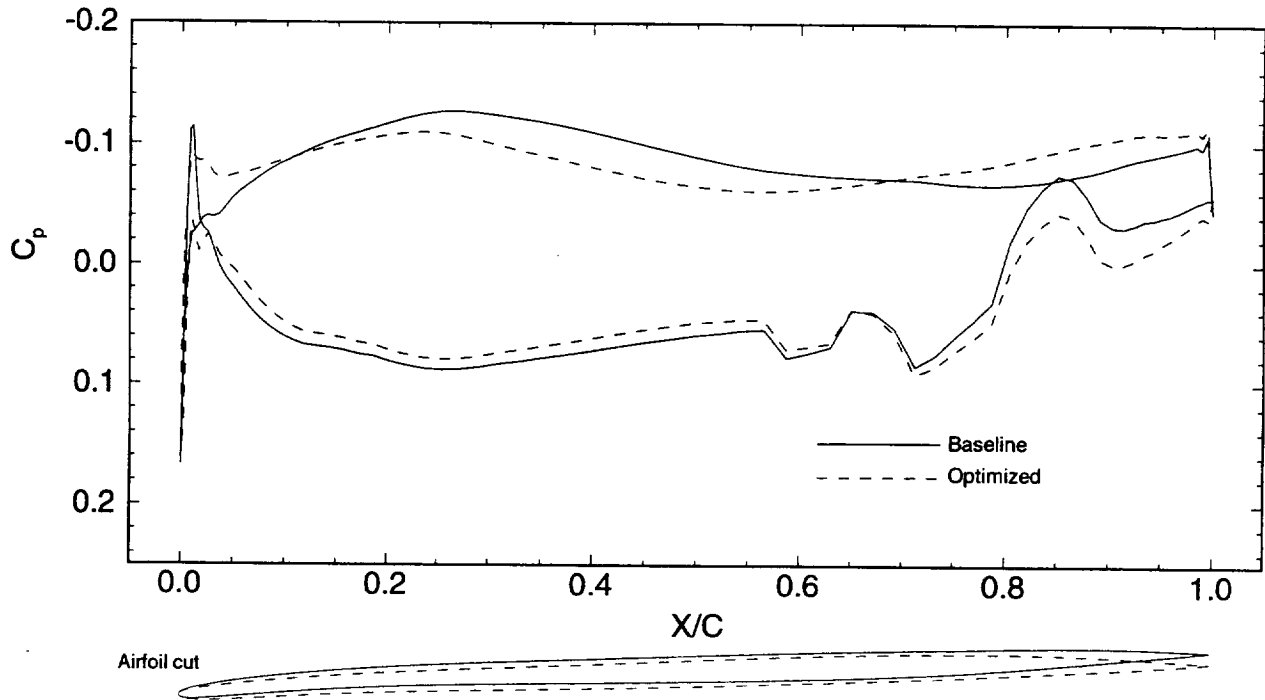
FLO67 Euler w/ Nacelle Effects, $M_\infty=2.4$, $C_L=0.11$



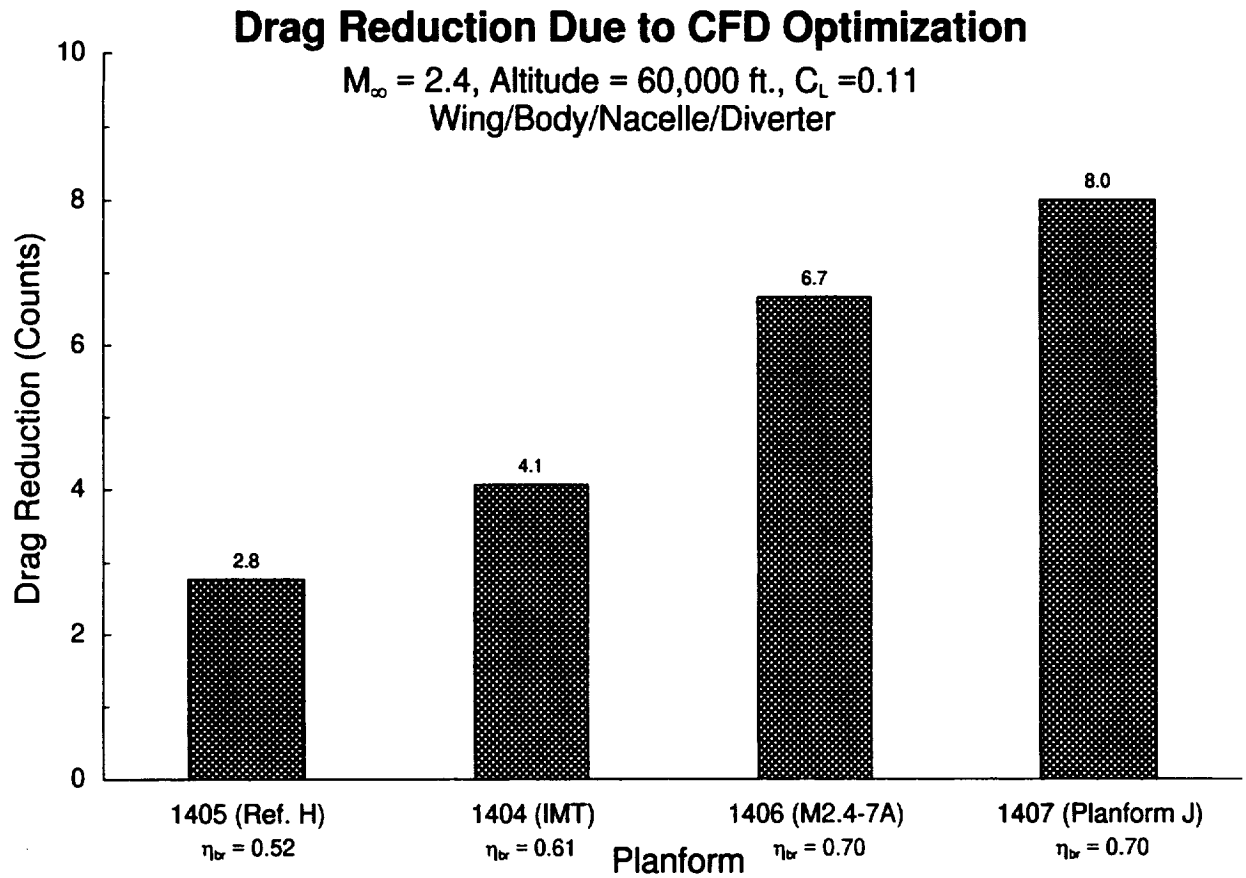
At the 40% semispan station, the aft loading on the airfoil has increased. The twist of the section is increased. The maximum camber is increased. The pressure distribution on the upper surface is flatter. The shock location and the strength near the lower surface trailing-edge is unchanged.

Pressure Distributions and Airfoil Cuts at the 40% Semispan Location of the Baseline and Optimized 1405 Configurations

FLO67 Euler w/ Nacelle Effects, $M_\infty=2.4$, $C_L=0.11$



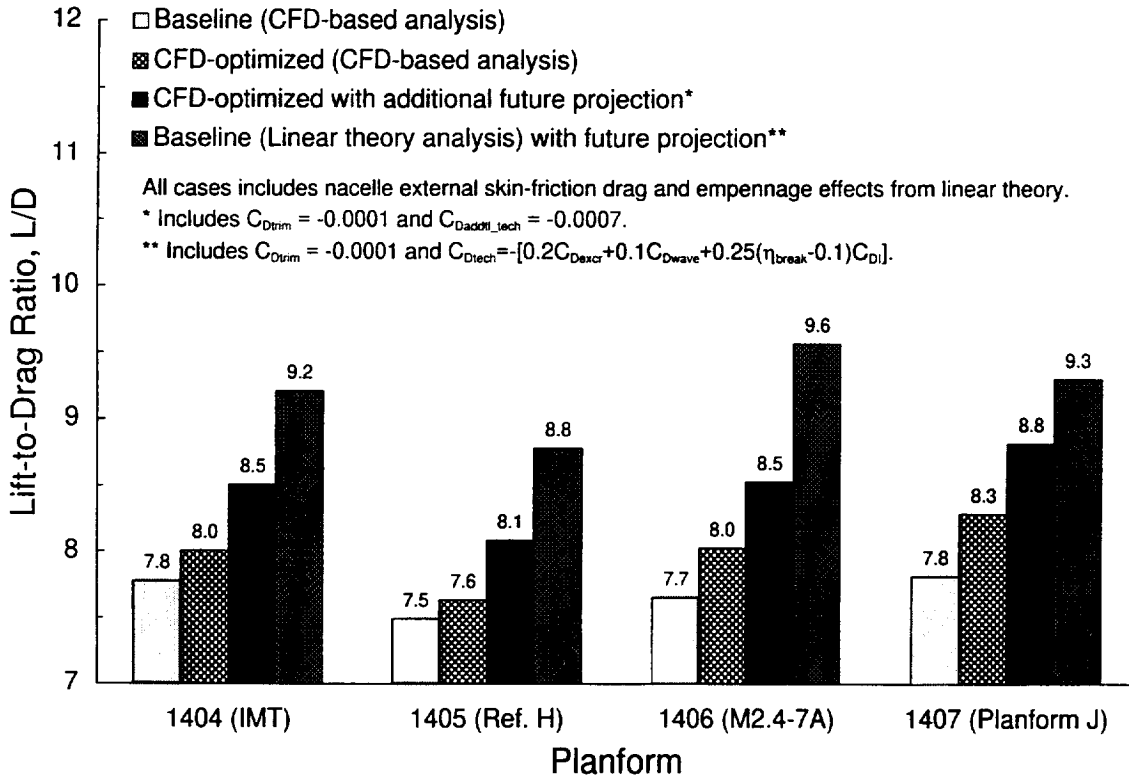
At the 40% semispan station, the leading-edge suction has improved considerably and the criss-crossing of the pressure has been removed. The aft loading of the section is increased. There are two compression waves on the lower surface. The twist of the section is increased. The maximum camber is decreased.



The most drag reduction was achieved for the 1407 planform, while 1405 gained the least. It is an interesting observation that the drag reduction is proportional to the leading-edge break location.

L/D for the Complete Aircraft Configurations

$M_\infty = 2.4$, Altitude = 60,000 ft., $C_L = 0.11$



For the CFD drag build-up the total drag can be written as:

$$\begin{aligned}
 C_{D_{\text{baseline_CFD}}} &= C_{D_p} + C_{D_v} + C_{D_{V/H}} \\
 C_{D_{\text{optimized}}} &= C_{D_{\text{baseline_CFD}}} + C_{D_{\text{opt}}} \\
 C_{D_{\text{future_CFD}}} &= C_{D_{\text{optimized}}} + C_{D_{\text{trim}}} + C_{D_{\text{addtl_tech}}}
 \end{aligned}$$

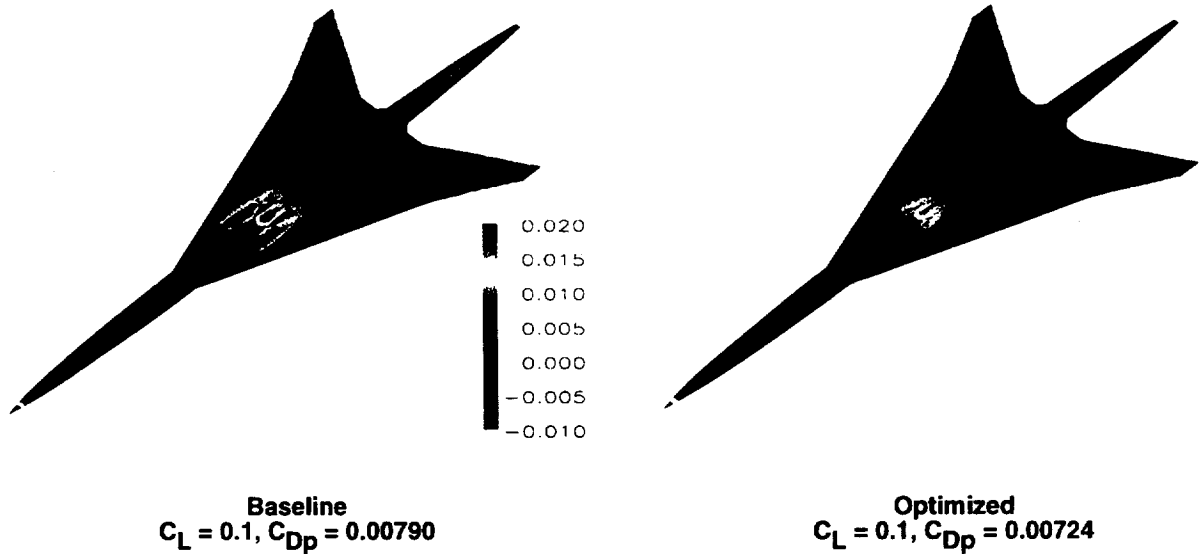
where the pressure drag, C_{D_p} , of the baseline wing/ body/nacelle/diverter (W/B/N/D) configurations were determined using CFL3D in the Euler mode. The viscous drag, C_{D_v} , were computed using an MDA method based on the equivalent flat plate area. The drag due to the vertical and horizontal tails, $C_{D_{V/H}}$, were obtained from the MDA linear theory method. The baseline wing/body configurations with nacelle/diverter pressure effects were optimized, for twist and camber, using FLO67/OPT3D and the reductions in drag, $C_{D_{\text{opt}}}$, were determined. A trim drag benefit, $C_{D_{\text{trim}}}$, of -0.0001 and an additional future technology benefit, $C_{D_{\text{addtl_tech}}}$, of -0.0007 were assumed.

For the linear theory build-up, the total drag can be written as

$$\begin{aligned}
 C_{D_{\text{future_Linear}}} &= C_{D_{\text{baseline_Linear}}} + C_{D_{\text{trim}}} + C_{D_{\text{tech}}} \\
 C_{D_{\text{tech}}} &= - [0.2C_{D_{\text{Dexcr}}} + 0.1C_{D_{\text{Dwave}}} + 0.25(\eta_{\text{break}} - 0.1)C_{D_i}]
 \end{aligned}$$

CFD Optimization of the 1400 Series Planform

Lower Surface Pressure Drag Contours for 1406 Wing/Body Configuration



The L/D projections for all the planforms obtained using CFD are significantly lower than the linear theory projections. In order to understand this difference, an MDC IRAD study was conducted. Conclusions of this study can be summarized as follows.

The landing gear fairing on each of the planforms seems to be the main source of unexpectedly high drag. The flow over this fairing (bump) is very nonlinear which the linear theory method is incapable of modeling accurately. On the other hand, CFD is not handicapped by such limitations. Also, the number of panels that were used to model the configurations using linear theory method, is significantly fewer than the number of grid points used in the CFD method. Therefore, the linear method could be missing many details of the flow field. The total drag predicted by the linear theory is lower than that of CFD by over 8 counts and hence the difference in L/D. Shown in the figure are the contours of the component of pressure that contribute to the drag. The high drag region around the landing-gear fairing is clearly evident.

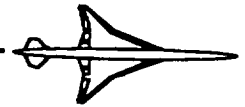
Summary and Conclusions

- Improvement in cruise L/D was achieved for all planforms
- L/D improvement increased as the wing-break location moved outboard
- Supersonic cruise L/D projections obtained using CFD was significantly lower than linear theory projections
- Landing-gear fairing was the major source of unexpectedly high drag predicted using CFD
- Differences in wing volumes and poor initial design are also suspects in the discrepancy of the L/D projections

Improvements in cruise L/D were achieved for all four planforms through the application of the Euler-based FLO67/OPT3D design optimization code. The most drag reduction was achieved for the 1407 planform (8 cts.), followed by 1406 (6.7 cts.), 1404 (4.1 cts.), and 1405 (2.8 cts.). The L/D improvement increased as the wing-break location moved outboard. The improvement for 1404 was determined to lie between that of 1405 and 1406. These results suggest that the cruise performance improvements from the nonlinear design optimization methods are dependent on the wing planform. These also suggest that there is a very strong correlation between the leading-edge break location and the nonlinear design improvement potential.

The landing-gear fairing on each of the planforms produced unexpectedly high drag. The flow over this fairing is very nonlinear which the linear theory method fails to model accurately, hence missing the flow field details. The total drag predicted by the linear theory was lower than that of CFD by about 8-10 counts and hence the difference in L/D.

The differences between the CFD-based and linear-theory based L/D projections were mainly due to the landing-gear fairing. Differences in wing volumes and poor initial design are also suspects in the discrepancy of the L/D projections.



Investigation of Non-Linear Effects on Reference H Body Area-Ruling and Cambering

Thierry Tamigniaux
The Boeing Company
P.O. Box 3707
Seattle, WA 98124

The goal of this task is to develop a tool capable of investigating non-linear effects on point design body area-ruling and cambering of a HSCT wing/body/diverter/nacelle configuration. Upon completion, this tool is scheduled to be merged with its wing equivalent.

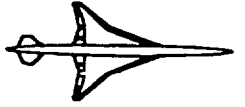
The full potential TRANAIR code was used throughout this investigation. TRANAIR's arbitrary geometry and in-house design optimization capabilities allow shape optimization satisfying complex aerodynamic and geometric constraints.

The baseline configuration (Reference H) was area-ruled with linear methods at a freestream Mach of 2.1. This investigation into the effects of non-linearity was conducted at Mach 2.4.

Optimizations were first conducted at zero lift on an uncambered Reference H configuration. Both mid-wing and low-wing configurations showed no improvement of circular cross-section area distribution over the baseline. Nacelles also had an equally negligible impact on area-ruling of the body.

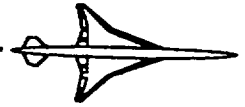
Optimizations were conducted on a cambered Reference H configuration at cruise lift. For that purpose, the optimization routine was extended to include both a minimum interior envelope, a piecewise linear floor definition, and a multi-variable cross-section definition. The optimization showed that cambering of the fore and aft bodies yielded improvements of up to 1 count of drag (see Figure). Area-ruling and camber optimization of the same configuration yielded up to 3 counts of drag improvement.

In conclusion, this investigation showed that if non-linear methods could not improve on a linear design in zero lift (with or without nacelles), constrained optimizations could significantly improve the area-ruling and cambering of a cambered body in lifting conditions.



OUTLINE

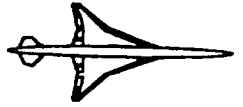
- 1) Objectives of the Study
- 2) Approach
- 3) Linear vs Non-Linear Optimization
- 4) Constrained Optimization
- 5) Conclusions
- 6) Follow On Activities



OBJECTIVES OF THE STUDY

- **Adapt and Validate Non-Linear CFD Methods for HSCT Aerodynamic Design and Analysis.**
- **Include Development of Geometric Shape Functions and Design Constraints.**
- **Apply to Reference H Body Area Distribution and Shape.**

The main FY'95 objective included continued development, adaptation, and validation of non-linear CFD methods for HSCT aerodynamic design and analysis. The specific objectives included continuation of non-linear point design optimization methods adaptation to body area-ruling and cambering of the Reference H HSCT configuration. It also included development of geometric shape functions and design constraints to support the non-linear optimization.



APPROACH

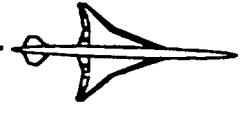
- **Building Block Steps**
 - linear vs non-linear in zero lift
 - camber design in lifting conditions
 - camber & area ruling in lifting conditions
- **Baseline Boeing Reference H Configuration**
- **Design Variables and Constraints**

The goal of improving the Reference H wing/body/diverter/nacelle configuration followed a building block approach. The goal was split into two tasks: a wing optimization task and a body optimization task. Each task included sub-tasks. This report covers the progress made in body optimization in the presence of the wing, but future plans include merging of both optimizations.

A building block approach was followed in the investigation of the body optimization. Three basic sub-tasks were identified. The first task investigated whether improvements can be made on the linear design of the Reference H configuration in non-lifting conditions. A second task determined whether cambering of the body could be improved in lifting conditions. Finally, the third task determined whether camber and cross-section area distribution could be improved in lifting conditions.

The baseline geometry, known as Reference H, was developed using linear methods. A simplified Reference H with a flat wing (uncambered and untwisted) and axisymmetric body was used throughout area-ruling comparisons in non-lifting conditions. The cambered Reference H configuration was used in lifting conditions.

The design problem was specified as an optimization. For a given geometry, geometry change variables (mode shapes), constraints (aerodynamic and geometric), and an objective function needed to be identified. The objective function was defined as the pressure drag (CD) of the entire configuration.



THE TRANAIR CODE

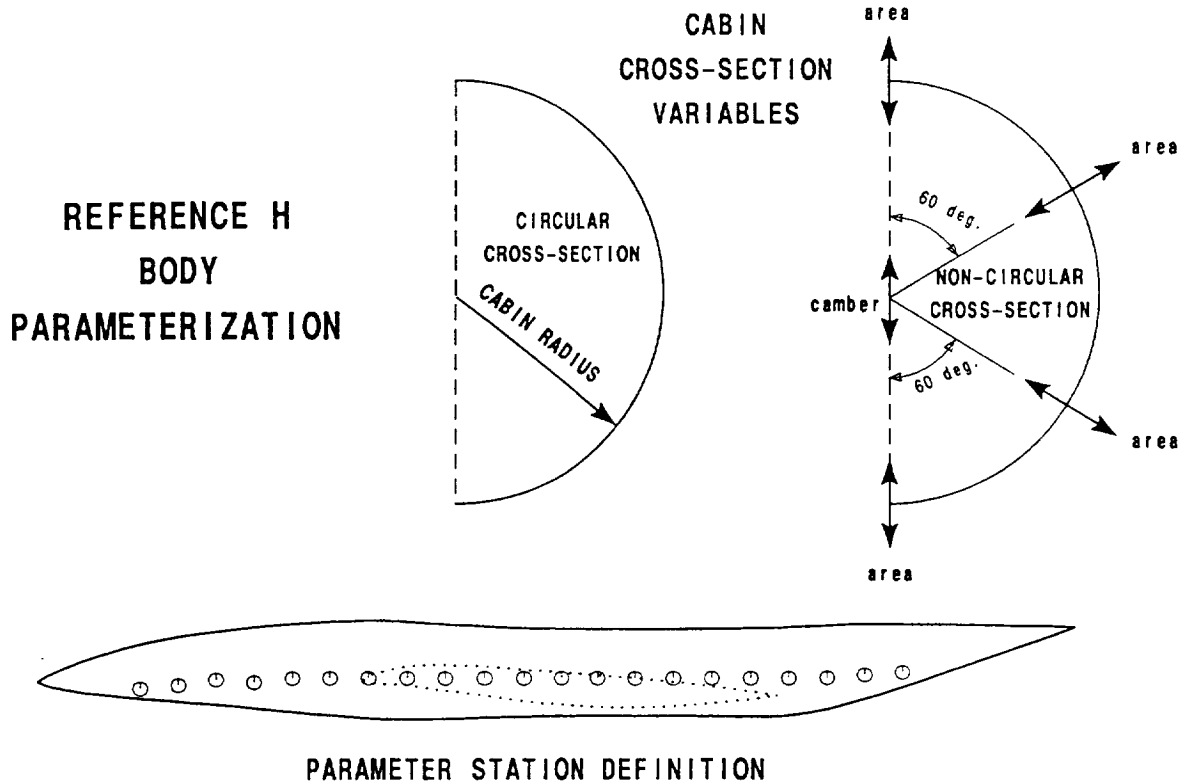
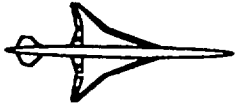
- Full Potential Code
- Arbitrary Wing/Body/Diverter/Nacelle Geometry
- Boundary Conditions Model Impermeable Surfaces, Wakes, Exhausts, ...
- Adaptive Grid Refinement & 2nd Order Upwinding
- Design Uses Two-Term Transpiration Model
- Extensive Design Experience at Boeing

TRANAIR is a full potential code for arbitrary geometries. Complex wing/body/diverter/nacelle geometries can be accurately modelled subject to specific boundary conditions modelling impermeable surfaces, wakes, bases, exhausts, power effects, etc.

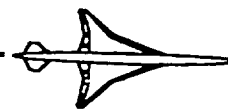
TRANAIR uses an adaptive grid refinement methodology. Throughout this investigation, the code was used with second order upwinding. This model introduces less artificial viscosity than a first order model and generally results in a more accurate solution (sharper peaks, gradients, etc.).

TRANAIR also has a design capability to formulate and solve constrained aerodynamic design problems. Currently the user must define geometry changes (mode shapes) using a FORTRAN subroutine. In the design mode, TRANAIR relates surface movement to mass flow boundary conditions on the original surface (transpirations). Past experiences show that a two term transpiration model gives the best results when optimizing a body in the presence of the wing.

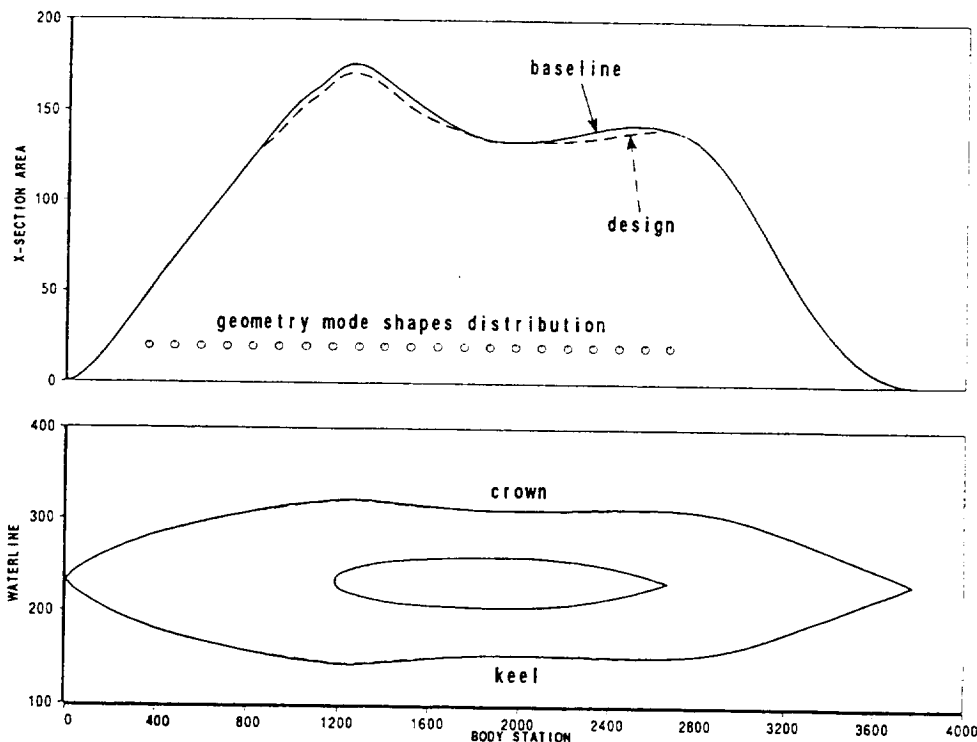
Finally, Boeing engineers have extensive experience in problem solving using the TRANAIR code. Despite the absence of supersonic boundary layer modelling, the code has many unique features that make it suitable for such an optimization problem. As long as there are no vortical flow Euler solutions offer no advantage over full potential solutions.



A multi-variable definition of body cross-sections was necessary to investigation cambering and area distribution effects. The first model simply consisted of a single mode shape defined as the radius of a circular cross-section at equally spaced stations. This model was used to support optimization of the uncambered Reference H configuration (flat wing/mid or low wing/axisymmetric body) in non-lifting conditions. A second model consisted of five mode shapes (one camber and four area variables) at each station. The camber mode shape was located at the center of each cross-section and was allowed to move vertically. The four area mode shapes located on the crown, the keel, and two in-between stations (60 deg. from the keel and 60 deg. from the crown) were allowed to move radially. This new definition allowed a departure from circular cross-section definitions (not available in linear optimizations methods).



Flat Wing/Mid Wing/Axisymmetric Body Optimization @ $M=2.4$ $\alpha=0$.

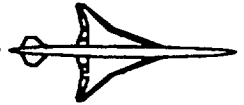


The goal of the investigation is to improve on the existing Reference H body in the presence of the wing using a non-linear method. Recalling that the baseline Reference H configuration was obtained using linear optimization of a flat wing/mid wing/axisymmetric body configuration, the TRANAIR code was used to optimize the body cross-section area distribution.

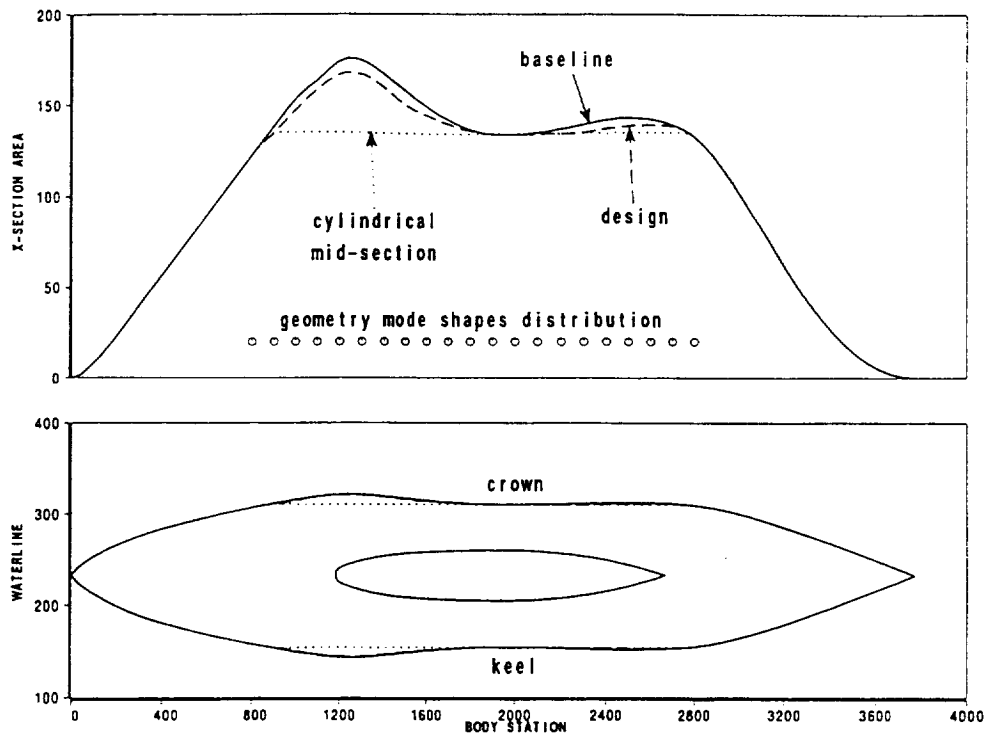
The geometry mode shapes were defined as the radius of circular cross-sections equally spaced between the pilot's eye and the wing trailing edge at the side of the body. Between the end points, a total of 19 mode shapes were used. Mode shapes were limited to a minimum value equal to the radius of the body at the waist. The pressure drag was optimized at a freestream Mach number of 2.4 and zero degree angle of attack.

The figure above shows the result of this optimization. Plotted are the body cross-section area and the body perimeter along the crown and keel lines. Comparisons are made between the baseline Reference H and the designed geometries (solid and dashed lines respectively). After re lofting and reanalyzing of the design configuration (a procedure necessary to eliminate errors due to transpirations), the pressure drag levels were equivalent at roughly 24.10 counts. The geometry showed no significant changes except for a slight lowering of the peaks of the optimized geometry. This result concurs with the fact that the baseline geometry was optimized at a slightly lower freestream Mach number (2.1).

Evaluation of the effect of the number of mode shapes yielded no improvement. An optimization with nine mode shapes yielded a similar result.



Flat Wing/Mid Wing/Axisymmetric Body Optimization @ $M=2.4$ $\alpha=0$.



In light of the results of the first optimization, it was necessary to build confidence in the method. For that reason, it was decided to start with a non-optimized geometry (cylindrical cross-section from STA800 to STA2800). The mode shapes definition, their constraints, and the freestream conditions were identical to that of the first optimization.

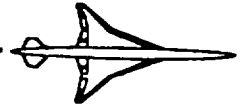
The results of this second optimization are shown in the figure above. The optimized cross-section area distribution adopted a shape very similar to the baseline Reference H design and almost identical to the first optimization (slightly lower peaks). The pressure drag was slightly lower (-0.37 counts) than the baseline Reference H configuration. This was sufficient confirmation that the method indeed worked and that additional building block steps could be taken to better understand non-linear effects.

Our first conclusion was reached: the baseline linear design is a very good first guess for a simplified geometry in non-lifting conditions. It also showed that the TRANAIR optimization method indeed worked although no payoff could be identified.

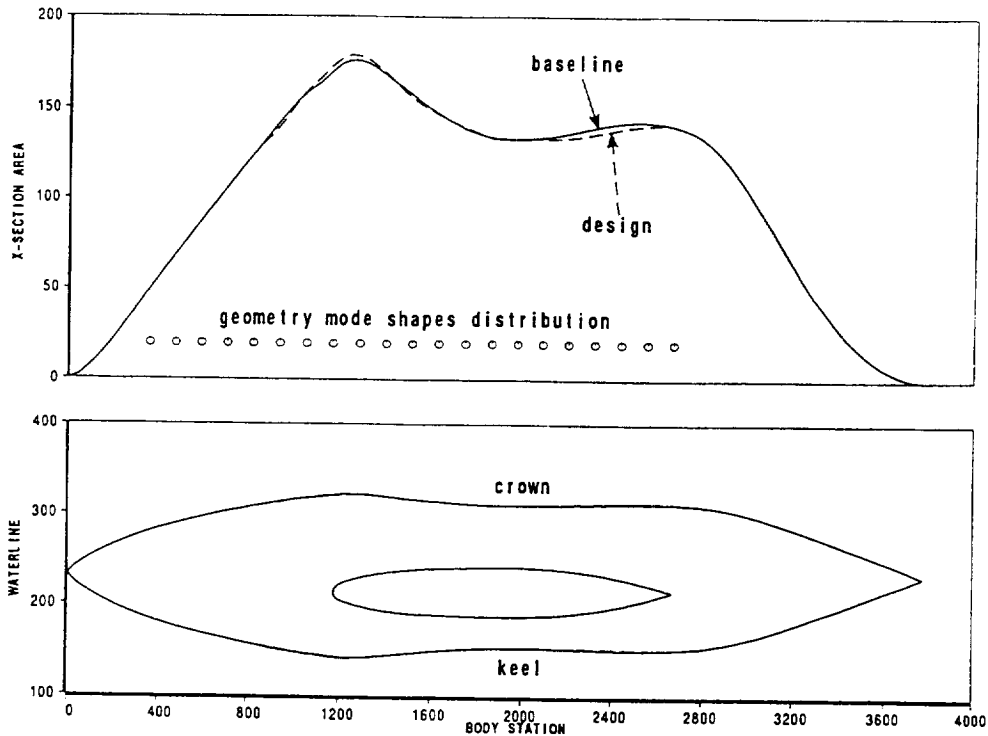
HSR Configuration Aerodynamics Workshop Feb96

BOEING

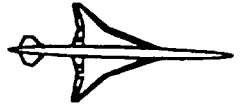
HSCT High Speed Aerodynamics



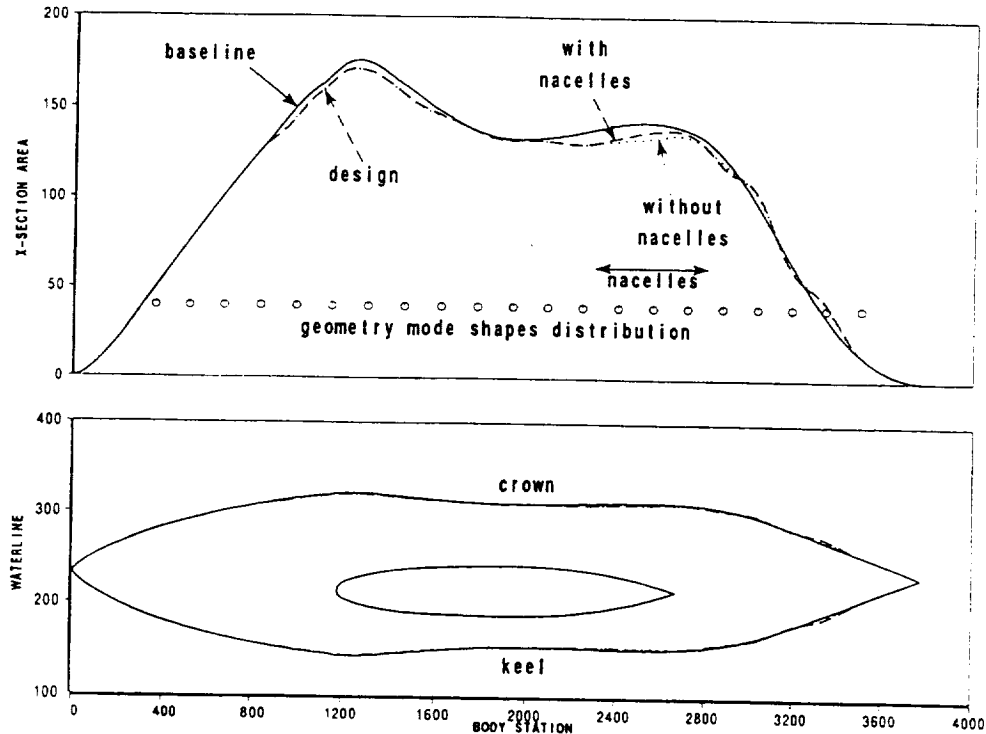
Flat Wing/Low Wing/Axisymmetric Body Optimization @ $M=2.4$ $\alpha=0$.



The same method was also extended to a flat wing in a low position. Vertical positioning of the wing maintained the distance between the apex of the wing and the crown of the body (when compared with the cambered Reference H geometry). The mode shape definitions, their limits, and the freestream conditions remained unchanged. The optimization started with the uncambered Reference H configuration (same as in the first optimization) and yielded, yet another very similar cross-section area distribution as shown in the figure below. While the aft-peak showed a similar behavior to previous designs (slight lowering), the forward peak slightly increased. This effect should be attributed to the positioning of the wing, the impact on pressure drag was insignificant. Finally, the pressure drag was lower by one tenth of a count.



Flat Wing/Low Wing/Axisymmetric Body Optimization with Nacelles @ $M=2.4$ $\alpha=0$.



One last step was taken with the simplified flat wing/low wing/axisymmetric body configuration. It involved determination of nacelle effects on body cross-section area distribution. The freestream Mach number (2.4) and the angle of attack (0 deg.) remained unchanged. The geometry mode shape definition was altered to better capture nacelle effects. Between the end points located at STA355 and STA3500, 19 mode shapes were equally spaced. Each mode shape was defined as the radius of a circular cross-section and constrained at its minimum value at the waist of the body.

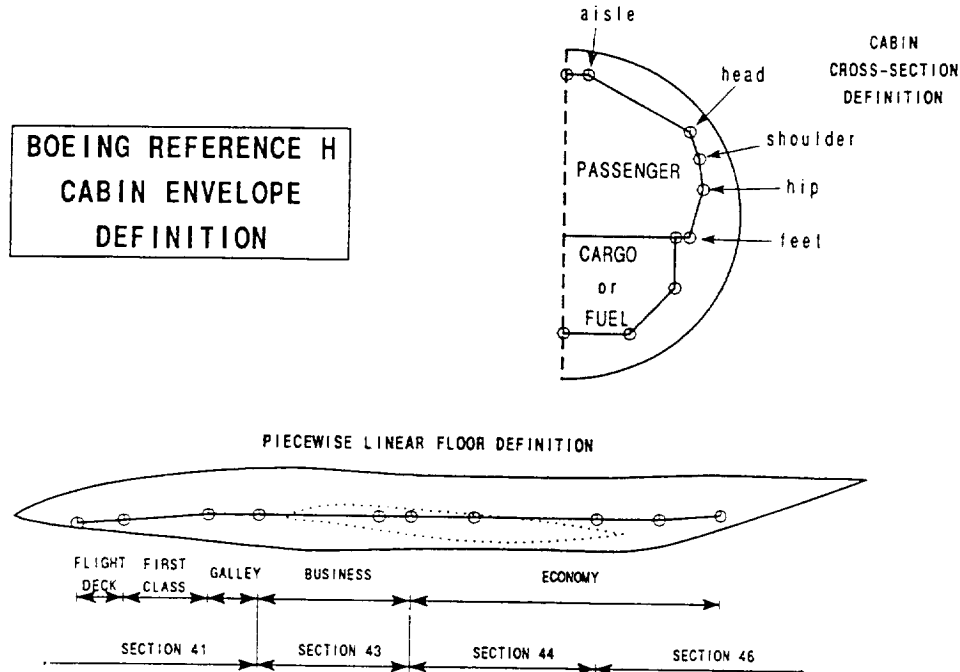
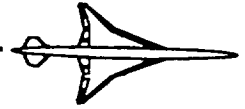
The effect of non-linear optimization with nacelles are shown in the figure above. Changes to the cross-section area distribution are small and the pressure drag of the wing/body configuration (excluding the nacelles) is slightly lower (-0.76 counts) when compared with the uncambered Reference H.

While this new conclusion also points in the same direction as the previous ones (small effects, lowering of the peaks, little drag improvement), one phenomenon nevertheless needs to be looked at. Indeed, the presence of modes shapes in the region aft of the trailing edge of the wing and their interaction with expansion and compression waves originating on the wing and nacelles yield undulations along the aft-body. Although these undulations have very little impact on the overall pressure drag, they nevertheless point at the necessity of improving the aft-body design.

HSR Configuration Aerodynamics Workshop Feb96

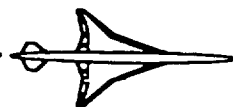
BOEING

HSCT High Speed Aerodynamics

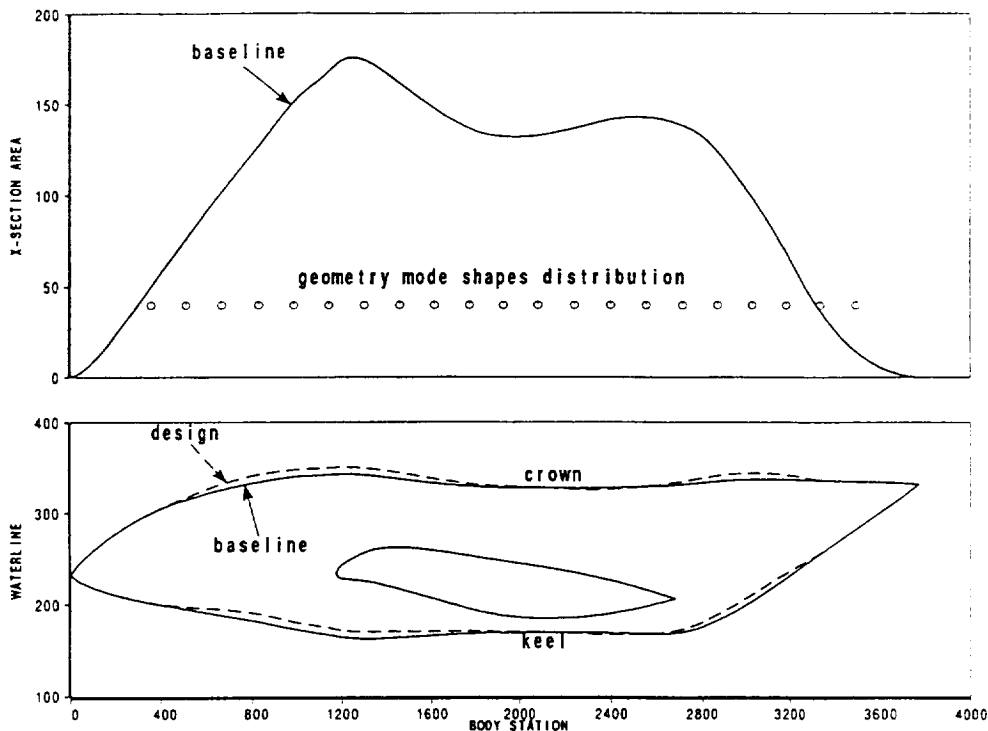


Several improvements were needed before proceeding with the optimization of the cambered Reference H configuration. The multi-variable cross-section parameterization (camber and area variables) was used in conjunction with floor variables. An additional eight variables match elements of the piecewise linear definition of the articulated cabin floor.

A cabin cross-section envelope based on a tri-class arrangement was also generated. The internal polygonal envelope defines hard points for the aisle, head, shoulder, hip, and feet. It also includes a cargo/fuel compartment. All hard points are defined with respect to the floor. Throughout the optimizations, the cabin envelope will constrain the external shape design. Provisions have also been made for a fuselage wall thickness of six inches. The figure above illustrates the envelope definition.



Reference H Body Camber Optimization @ M=2.4 CL=0.12



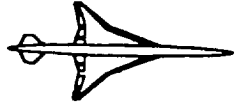
The following plot shows the result of camber optimization on the baseline Reference H configuration. The optimization was run at typical cruise conditions; i.e. freestream Mach number 2.4 and lift coefficient 0.12. On top of the 8 variables specifying the articulated floor, 19 camber mode shapes were equally spaced between the pilot's eye (STA355) and the aft-body (STA3500). Including cabin envelope, cabin floor, surface curvature, and aerodynamics, a total of 7,800 constraints were used in this optimization.

Results show significant recambering of the fore and aft body. The resulting drag benefit is approximately 1.1 counts below the baseline Reference H pressure drag level.

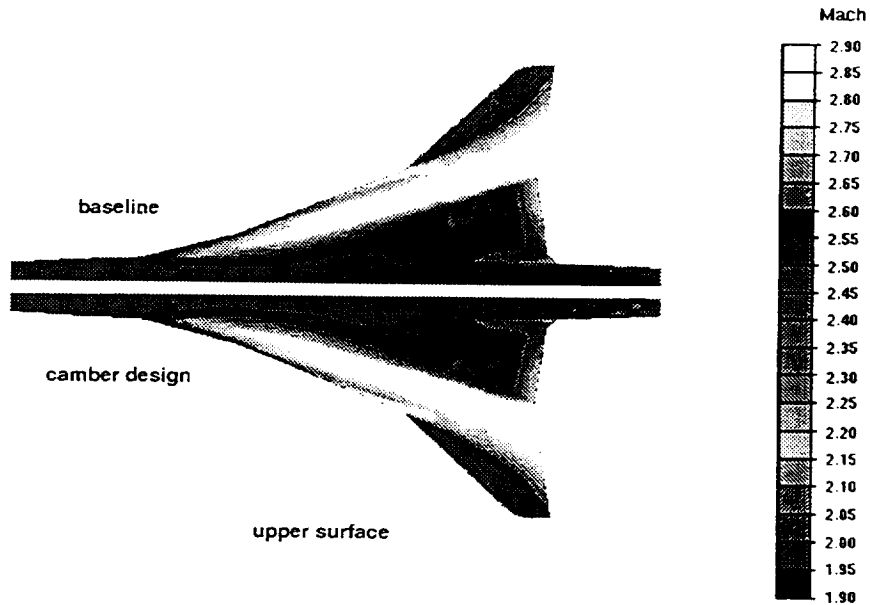
HSR Configuration Aerodynamics Workshop Feb96

BOEING

HSCT High Speed Aerodynamics



Reference H Wing/Body Camber TRANAIR Optimization
Mach=2.4 CL=0.12 dCD=-1.1 counts

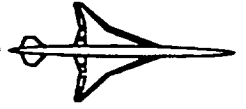


The following two pages show local Mach number plot comparisons between the baseline Reference H configuration and the camber design. Most of the drag benefits identified in the optimization actually originated on the wing, but local Mach number changes are very small.

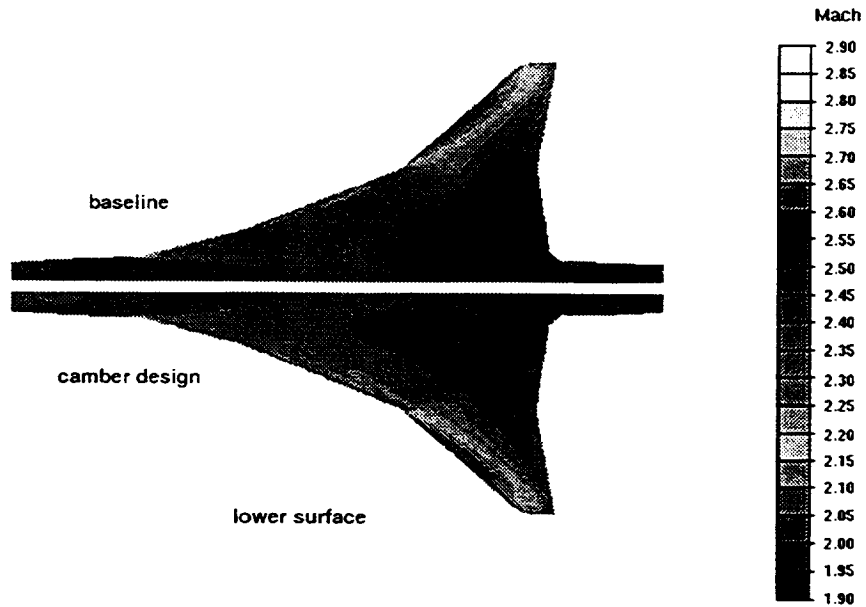
HSR Configuration Aerodynamics Workshop Feb96

BOEING

HSCT High Speed Aerodynamics



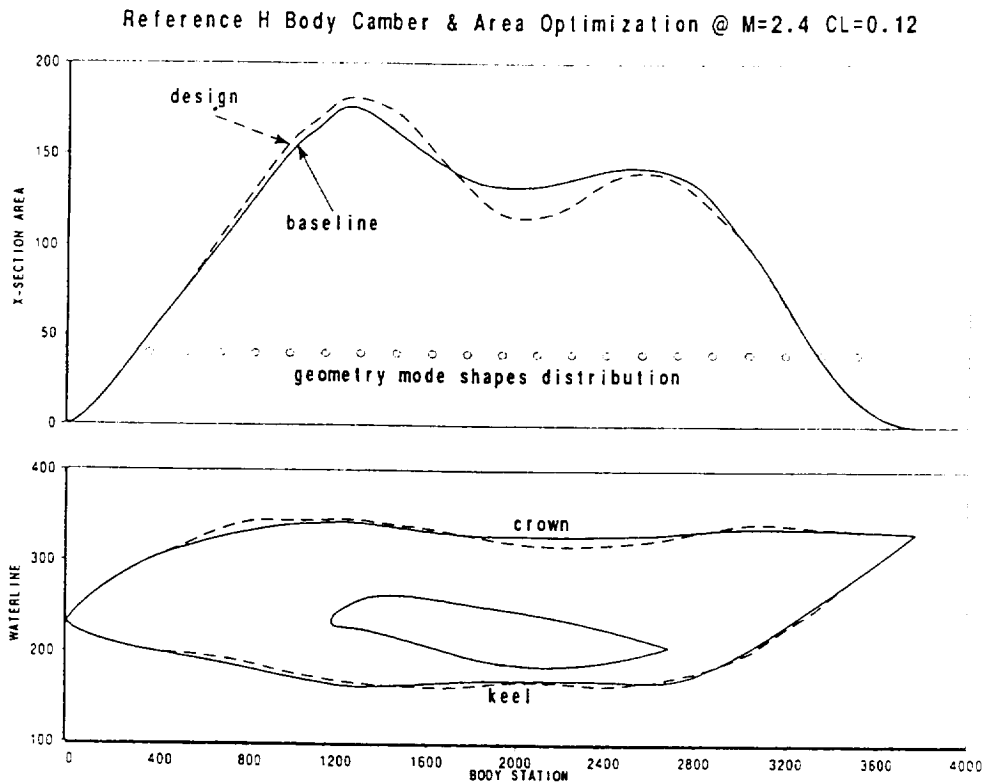
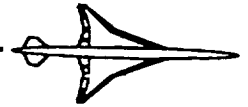
Reference H Wing/Body Camber TRANAIR Optimization
Mach=2.4 CL=0.12 dCD=-1.1 counts



HSR Configuration Aerodynamics Workshop Feb96

BOEING

HSCT High Speed Aerodynamics



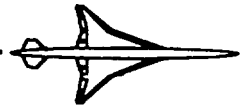
The following plot shows the result of camber and area optimization on the baseline Reference H configuration. The optimization was run at typical cruise conditions; i.e. freestream Mach number 2.4 and lift coefficient 0.12. On top of the 8 variables specifying the articulated floor, 19 camber and 76 area (in groups of 4) mode shapes were equally spaced between the pilot's eye (STA355) and the aft-body (STA3500). Including cabin envelope, cabin floor, surface curvature, and aerodynamics, a total of 11,600 constraints were used in this optimization. The maximum and minimum values of the area variables were arbitrarily chosen (they did not maintain the waist of the body).

Once again, results show significant recambering of the fore and aft body. Changes in cross-section area are quite significant in the aft-body region. The resulting pressure drag benefit is approximately 2.85 counts below the baseline Reference H.

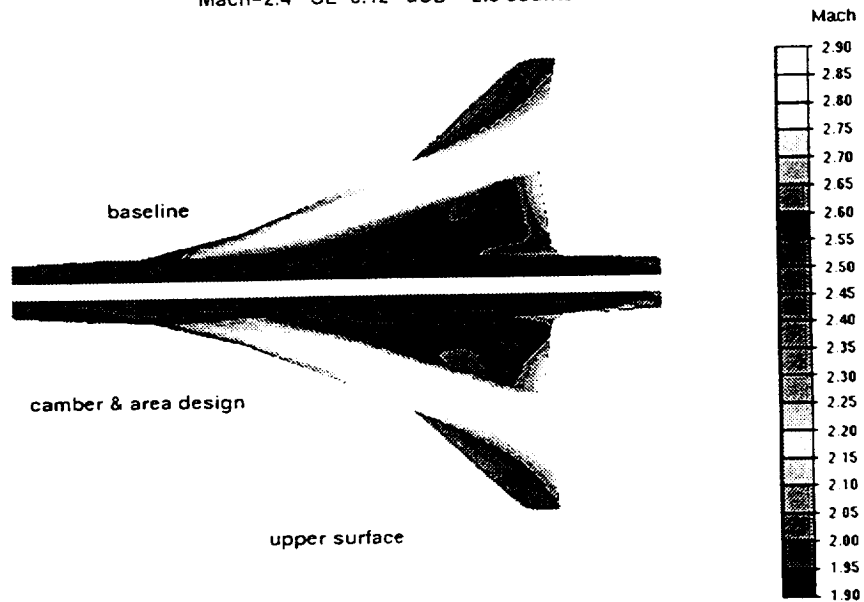
HSR Configuration Aerodynamics Workshop Feb96

BOEING

HSCT High Speed Aerodynamics



Reference H Wing/Body Camber & Area TRANAIR Optimization
Mach=2.4 CL=0.12 dCD=-2.8 counts

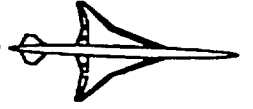


The following two plots show local Mach number plot comparisons between the baseline Reference H configuration and the camber and area design. Most of the drag benefits identified in the optimization actually originated on the wing, but local Mach number changes are very small.

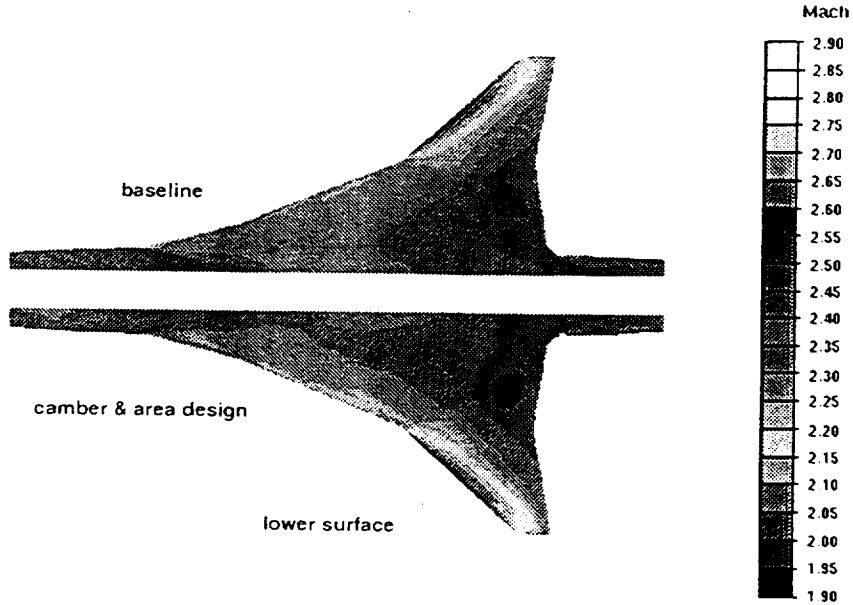
HSR Configuration Aerodynamics Workshop Feb96

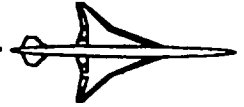
BOEING

HSCT High Speed Aerodynamics

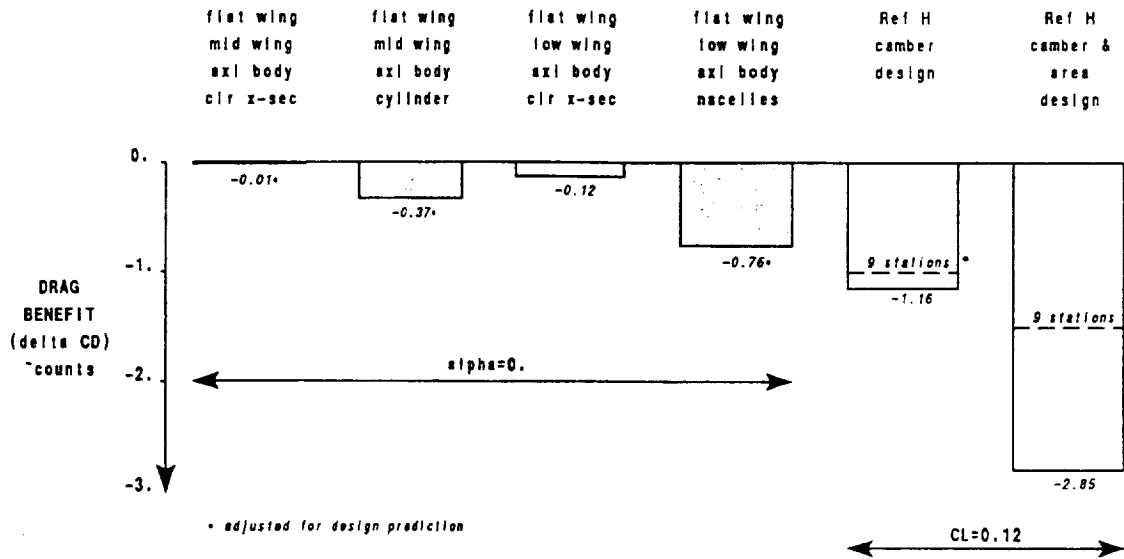


Reference H Wing/Body Camber & Area TRANAIR Optimization
Mach=2.4 CL=0.12 dCD=-2.8 counts





Drag Benefit of Optimized Configurations



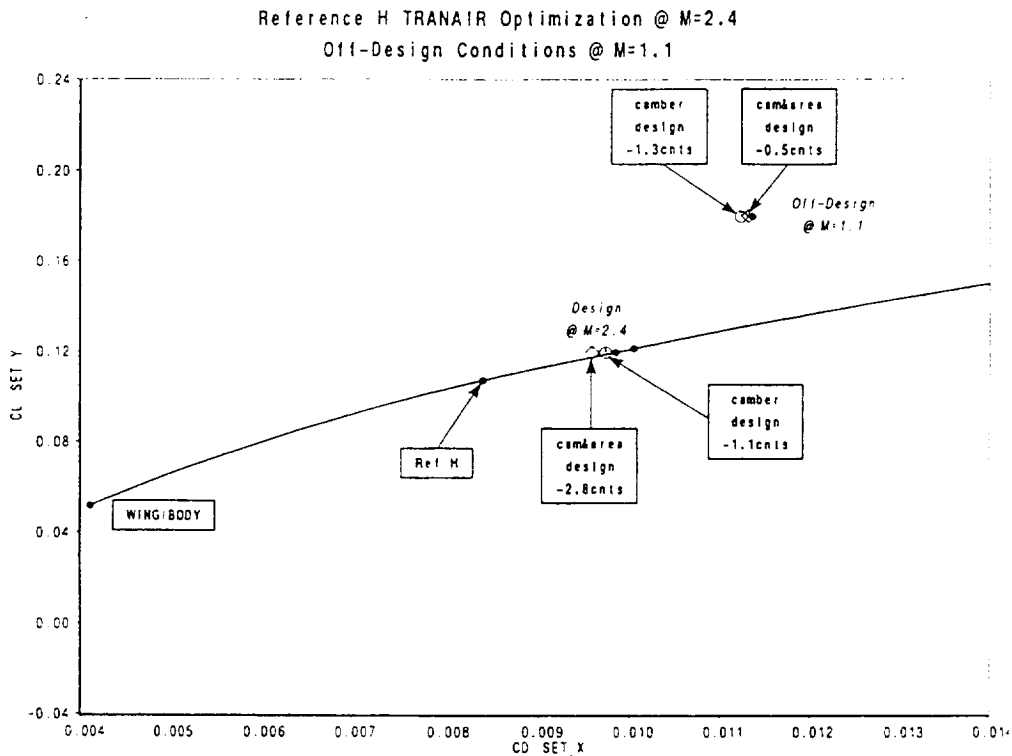
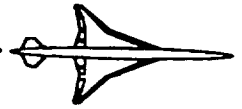
The following plot summarizes the drag benefits of optimized geometries from the basic area-ruling of an uncambered Reference H configuration to the complex constrained camber and area optimization of the cambered Reference H.

Both optimizations of Reference H were also investigated with a smaller number of variables. This was dictated by our concern to run a wing/body optimization with more than 300 variables. The computing resources needed for such an optimization are presently beyond the CPU time limit of 8 hours. It was therefore necessary to investigate the drag benefits of an optimization with half as many stations as previously used. The camber optimization was run with 9 stations (instead of 19) and the camber and area optimization was run with 54 variables (instead of 104). The reduced variable optimizations are indicated by dashed lines. While the camber optimization yielded an almost identical benefit (-1 count of pressure drag), the camber and area optimization yielded a substantially smaller drag benefit (-1.5 counts). This disappointing result highlighted the necessity of choosing an optimum variable station location and reevaluate possible drag benefits.

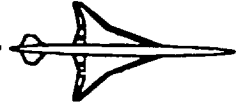
HSR Configuration Aerodynamics Workshop Feb96

BOEING

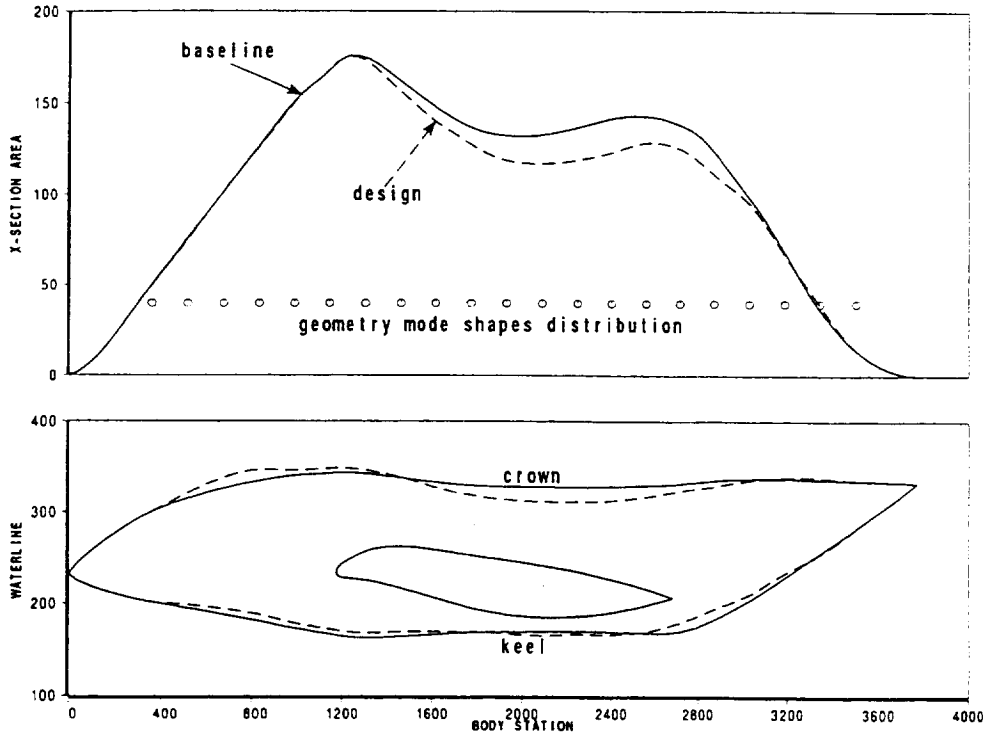
HSCT High Speed Aerodynamics



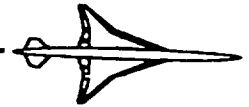
Finally, questions arose on the validity of the camber and camber and area point designs at off-design conditions. The new designs were therefore analyzed at a freestream Mach number of 1.1, and benefits were compared with standard cruise conditions. While the camber design was confirmed by an almost identical drag benefit (-1.3 count), the camber and area design yielded a much smaller benefit (-0.5 count). Neither designs came off worse than the baseline Reference H configuration. This conclusion, whether fortunate or not, should not detract us from attempting multi-point optimizations.



Reference H Camber & Area Body Optimization with Optimized Wing @ $M=2.4$ $CL=0.12$



Latest developments include camber and area-ruling of the baseline Reference H body in the presence of an optimized wing. The plot above shows the results of such an optimization. Once again the fore body is subject to re-cambering and the aft body to significant area-ruling changes. Airplane drag was reduced by 3.5 counts (a Navier-Stokes analysis also showed a 3 counts of drag reduction). This finding indicates that the effects of body and wing optimization are additive (although drag reduction mostly occurs on the wing).

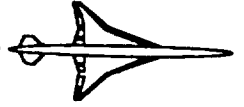


CONCLUSIONS

- **An Optimization Tool was Developed to Investigate Non-Linear Area-Ruling and Cambering Effects on the Reference H Configuration**
- **Optimizations Showed No Significant Improvements to Area-Ruling of Circular Cross-Section in Non-Lifting Conditions**
- **No Improvements Whether Nacelles Were Present or Not**
- **Improvements Due to Cambering of Body in Lifting Conditions**
- **Significant Improvements Due to Cambering and Area-Ruling of Body in Lifting Conditions**

A CFD optimization tool based on the TRANAIR code was developed and applied to the Reference H wing/body HSCT configuration. Constrained optimizations showed that no significant improvements could be made to the Reference H configuration in non-lifting conditions (uncambered flat wing/mid or low wing/axisymmetric body configurations could not be improved). This was also verified whether the engine nacelles were present or not.

Constrained optimizations were also run on the cambered Reference H configuration in lifting conditions. Both camber and camber and area optimizations showed significant reductions of the pressure drag (from 1 to 3 counts of drag). Since most improvements occurred in the wing region, it will be interesting to find out what happens when both body and wing optimizations are combined.



FOLLOW ON ACTIVITIES

- **Participate in 1996 Wind Tunnel TCA Model Definition**
- **Merge and Validate Wing and Body Subroutines**
- **Optimize Number of Variables in Body**
- **Multi-Point Optimization**

The principal activity for 1996 will be to support the design of a candidate optimization for wind tunnel testing. With that goal in mind, it will be necessary to merge the wing and body subroutines and apply it to the Technology Concept Airplane (TCA). A new definition of the cabin envelope (constraints) will be developed.

Given the current limitations on Cray C-90 usage (8 hour queue), it will be of prime interest to determine whether fewer variables (mode shapes) will yield equivalent optimization results. Finally, time permitting, attempts will be made at multi-point optimizations.

Fuselage Cross-Sectional Area and Camber Optimization Using Nonlinear Aerodynamic Tools

James O. Hager, Shreekant Agrawal
McDonnell Douglas Aerospace
Long Beach, California 90807-5309

Previous studies have shown that optimization using nonlinear aerodynamic tools can improve the aerodynamic performance of HSCT configurations designed using linear theory. These studies were restricted to wing camber and twist and fuselage camber changes. The current presentation examines the potential for improved aerodynamic performance by optimizing the fuselage cross-sectional area and camber using nonlinear aerodynamic tools.

The 1406 Opt1 configuration was used as the baseline geometry. This configuration was one of the geometries involved in the Technology Integration planform study. It has the same planform as the McDonnell Douglas Aerospace Arrow Wing HSCT configuration, M2.4-7A, and it includes a landing gear fairing in the wing geometry.

The results indicate that the fuselage waisting can be removed without incurring an L/D penalty at supersonic conditions (both $M_\infty=2.4$ and $M_\infty=1.1$). However, there is a small penalty (about three-quarters of a count of drag) at the transonic cruise condition ($M_\infty=0.95$).

Background and Objective

- Nonlinear optimization success
 - Wing camber and twist, and fuselage camber
 - Better design than linear theory
- Use nonlinear aerodynamics to optimize fuselage cross-sectional area

Nonlinear optimization has been used to produce HSCT designs with better aerodynamic performance than linear-theory designs. However, these studies were limited to changing wing camber and twist, and fuselage camber.

The objective of this presentation is to use nonlinear-aerodynamic optimization to improve the fuselage cross-sectional area and camber in order to improve the aerodynamic performance even further.

Outline

- Method
- Design results
 - Effect of design variables and design space
 - Evaluation of the best design
- Summary

The outline for the remainder of the presentation is as follows. First, a description of the design method will be presented. Then results will be presented; beginning with an evaluation of the effect of different design variables and the design space. Then a more substantial evaluation of the best design will be presented. Finally, the presentation will be summarized.

CFD-Based Optimization

- Geometry
 - Baseline + perturbation
- Flow solution
 - FLO67 (Euler) wing/body
 - Nacelle-effects modeled
 - ΔC_p on wing/body
 - $\Delta C_L, \Delta C_D$ due to nacelle/diverters
- Optimizer
 - ADS: method of feasible directions

The CFD-based optimization procedure models the geometry as a baseline that is modified by adding perturbations.

The flow solver for this work is FLO67, an Euler solver, and it is applied to the wing/body configuration. Nacelle effects are modeled in two parts. First, a ΔC_p field is applied to the wing/body surface to represent the influence of the nacelles and diverters on the wing and body. The ΔC_p 's are obtained by taking the difference between the fine grid wing/body/nacelle/diverter and wing/body solutions. The second part of the nacelle-effects modeling is a ΔC_L and ΔC_D increment that represents the forces acting on the nacelles and diverters themselves.

The ADS optimizer is used with the method of feasible directions. This allows constraints to be applied directly without penalty functions.

CFD-Based Optimization (Cont'd)

- Design variables
 - Deck placement and wing plunge
 - Fuselage camber and incidence
 - Fuselage cross-sectional area
- Constraints
 - Lift coefficient
 - Standard deck constraints
 - Fuselage cross-sectional area
 - Fuselage volume

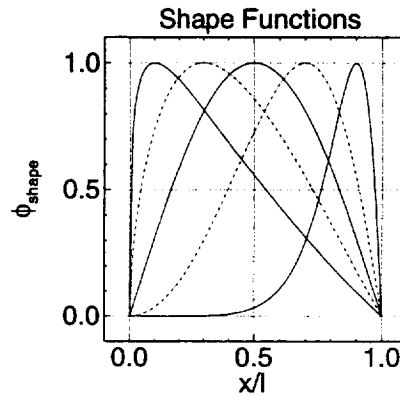
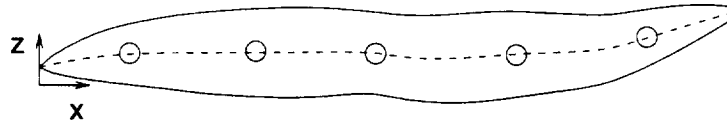
The design variables used in this study are: three for the deck placement and wing plunge, ten for the fuselage camber and incidence, and five or seven for the fuselage cross-sectional area. All of the designs use the deck-placement and wing-plunge design variables. If camber is used, incidence is also used.

The only aerodynamic constraint is applied to the lift coefficient: it is allowed to vary $\pm 2\%$ during the optimization. There are also several constraints on the deck placement: deck angle, cabin height, cargo height, and wing/deck clearance. There is also a constraint on the fuselage cross-sectional area near the cockpit to prevent the fuselage from becoming too pointy. And the final constraint is on the fuselage volume: the volume must not be smaller than the baseline.

Shape Function Fuselage Camber Perturbation

$$z = z_{\text{ref}} + \sum v \phi_{\text{shape}}$$

z = vertical position
 v = design variable



This slide shows how the fuselage camber is perturbed using Hicks-Henne shape functions. For this example, five shape functions are used to perturb the entire length, l , of the fuselage. The location of maximum displacement of each shape function is shown on the sketch of the fuselage by the circles. The vertical coordinate, z , of the reference fuselage, z_{ref} , is changed by adding the shape function multiplied by the design variable associated with that shape function.

Shape Function Fuselage Area Perturbation

$$A = A_{\text{ref}} + \phi_{\text{shape}}(v)$$

$$\Delta r = r - r_{\text{ref}} = (A/\pi)^{1/2} - (A_{\text{ref}}/\pi)^{1/2}$$

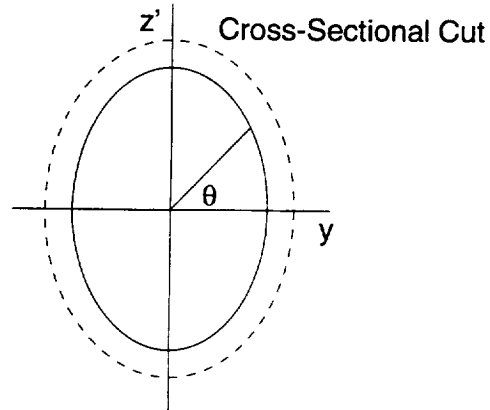
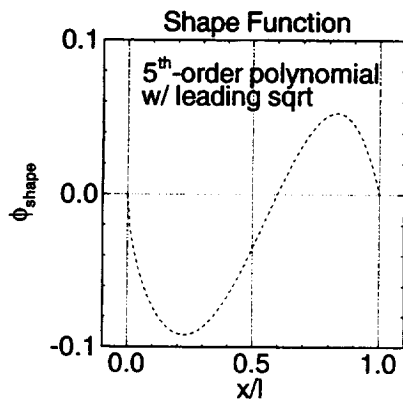
$$y = y_{\text{ref}} + \Delta r \cos\theta$$

$$z' = z'_{\text{ref}} + \Delta r \sin\theta$$

y = spanwise position

z = vertical position

v = design variables



This slide shows how the fuselage cross-sectional area is perturbed using a polynomial. The polynomial is defined using the design variables, v , as the coefficients of the polynomial. For an N^{th} -order polynomial with a leading square-root term ($v_0 \sqrt{x/l} + v_1 (x/l) + v_2 (x/l)^2 + \dots + v_N (x/l)^N$), N independent design variables are required to have zero displacement at $x/l=1$; v_N is the dependent coefficient to ensure closure. The shape function is used to change the cross-sectional area, A . The coordinates are changed by transforming the area change to an equivalent radius change.

Design Results

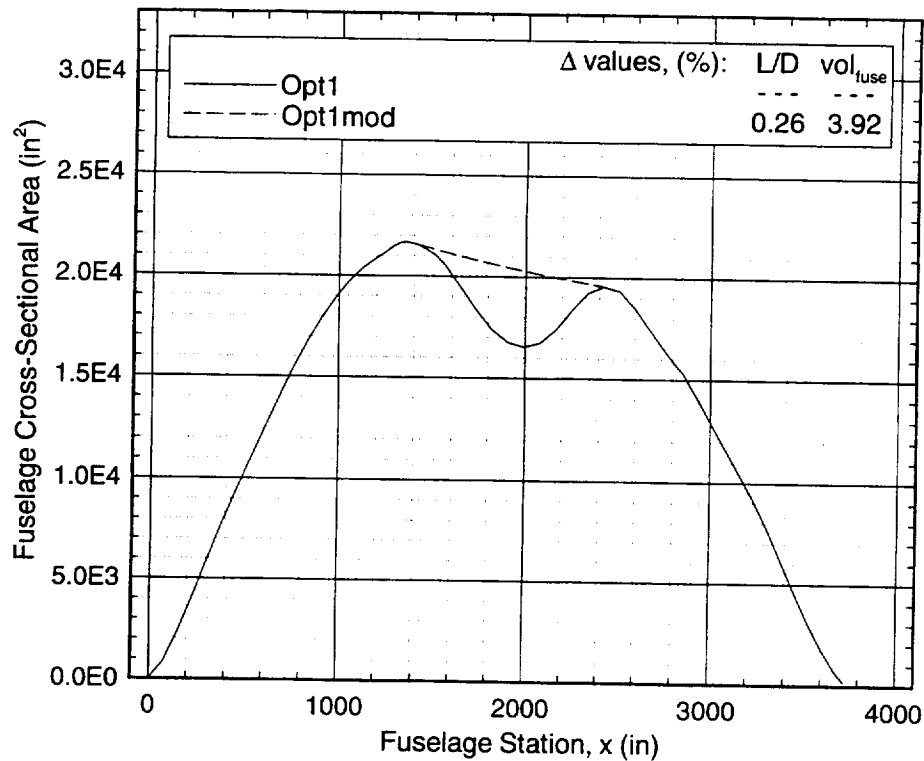
- 1406
 - Candidate geometry for Technology Integration planform study
 - Same planform as M2.4-7A
 - Wing geometry includes landing gear fairing
- 1406 Opt1
 - Optimized wing camber and twist, and fuselage camber

The baseline 1406 geometry, obtained using linear theory, was one of the geometries in the Technology Integration (TI) planform study. It has the same wing planform as the MDC M2.4-7A Arrow wing configuration. The main reason for selecting this geometry was that the wing geometry includes a landing gear fairing. Therefore, all of the significant geometric pieces that contribute to total cross-sectional area were included.

The 1406 Opt1 configuration was obtained during the TI planform study by applying nonlinear optimization to the wing camber and twist, and the fuselage camber.

The results in this presentation were obtained by using either the 1406 Opt1 geometry or a derivative of the 1406 Opt1 geometry.

1406 Fuselage Cross-Sectional Area

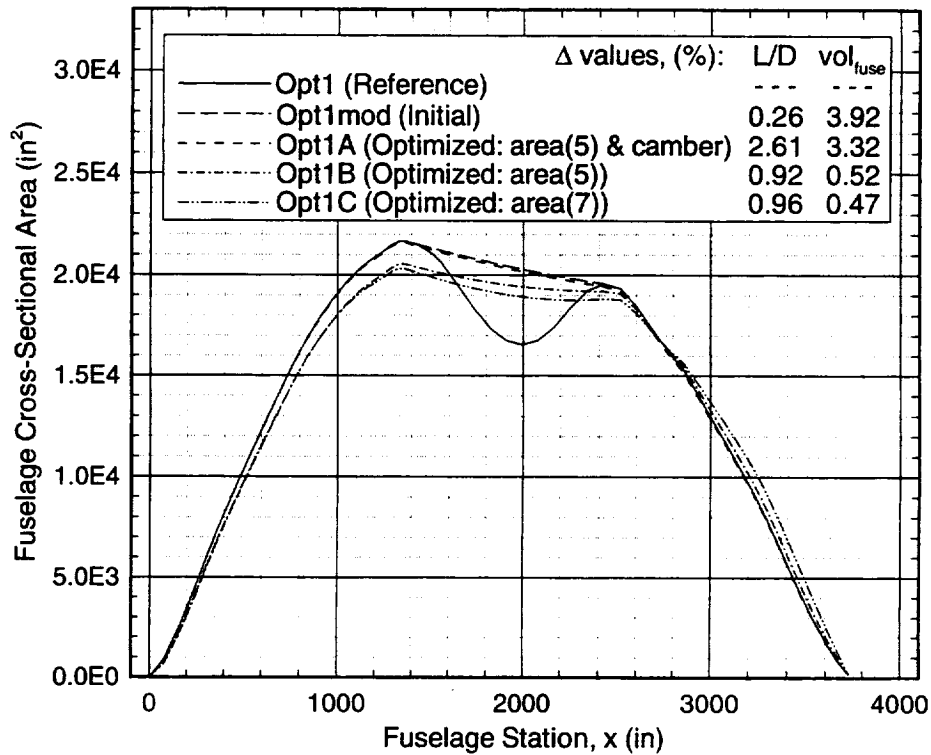


The first set of designs use a derivative of the 1406 Opt1 geometry. In a previous study, it was found that the fuselage waisting could not be removed using the shape functions. In order to evaluate the effect of removing the waist, a manual perturbation of the 1406 Opt1 was performed to remove the waisting. The cross-sections at the first hump (near $x=1400$ in.) and the second hump (near $x=2200$ in.) were used to linearly reconstruct the cross sections between them. Then, the camber line of the Opt1 geometry was imposed on the cross-sectional shape. This new geometry is called Opt1mod.

The right-hand side of the legend shows the L/D and fuselage volume change with respect to Opt1. L/D is from FLO67 predictions with nacelle effects at $M_\infty=2.4$ and $C_L=0.11$ (the design point).

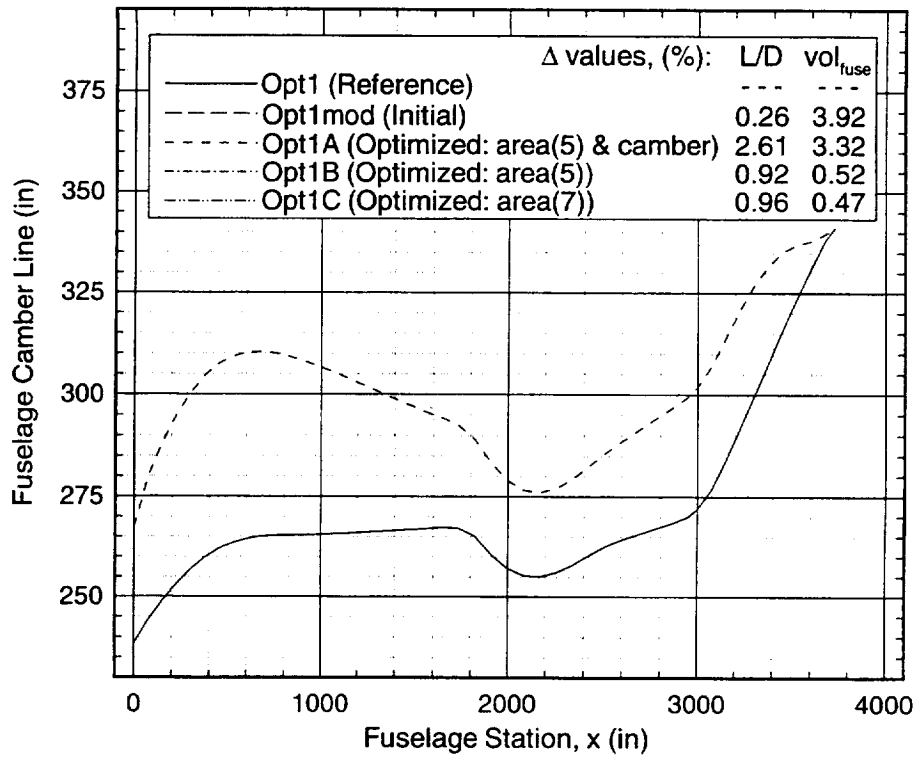
1406 Fuselage Cross-Sectional Area Optimization

Fuselage Cross-Sectional Area, 1406 Opt1mod Initial Geometry



This slide shows the fuselage cross-sectional area distribution for three designs obtained using Opt1mod as the initial geometry. (The Opt1 distribution is included for reference.) Opt1A included cross-sectional area (with a 5th-order polynomial) and camber. The volume of this design is slightly smaller than Opt1mod, but the shape of the area distribution is very similar. This design produced the highest L/D. Opt1B included only the cross-sectional area (with a 5th-order polynomial). The volume was reduced to be slightly larger than Opt1 by removing area from near the wing leading edge to aft of the trailing edge. Opt1C included only the cross-sectional area, but with a 7th-order polynomial. L/D is slightly higher than Opt1B with the 5th-order polynomial, and the trend to shift area from the wing region to aft of the wing is even more evident.

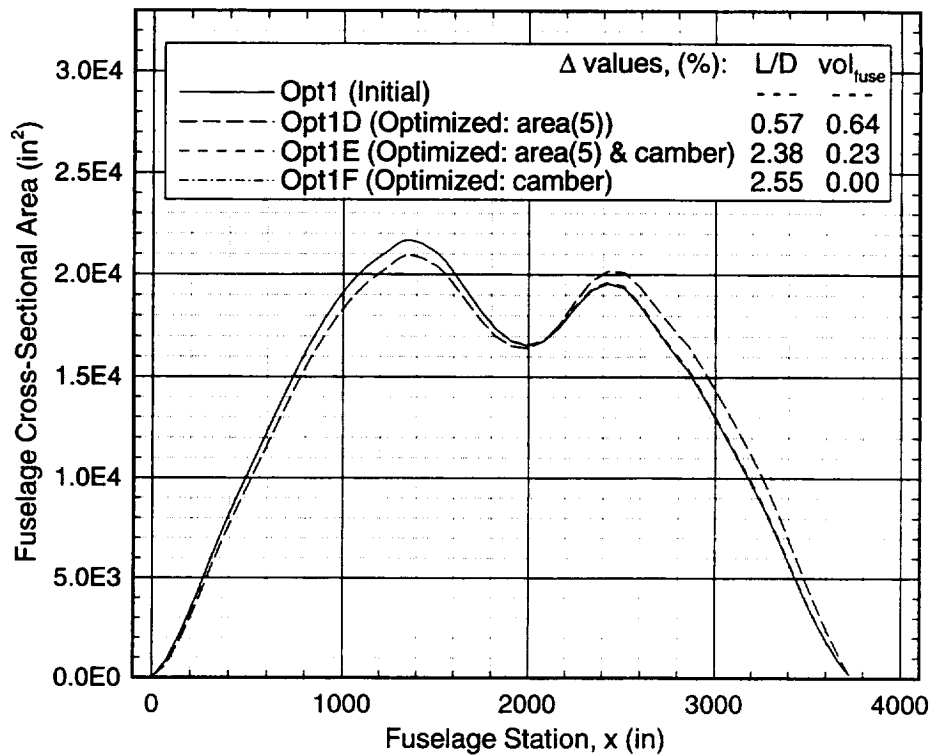
1406 Fuselage Cross-Sectional Area Optimization Camber-Line Distribution, 1406 Opt1 mod Initial Geometry



The camber line of the fuselage (the line mid-way between the crown and keel) is changed significantly with Opt1A: the incidence is increased and there is more curvature near $x=800$ in., and 3400 in., and less curvature near $x=1800$ in.

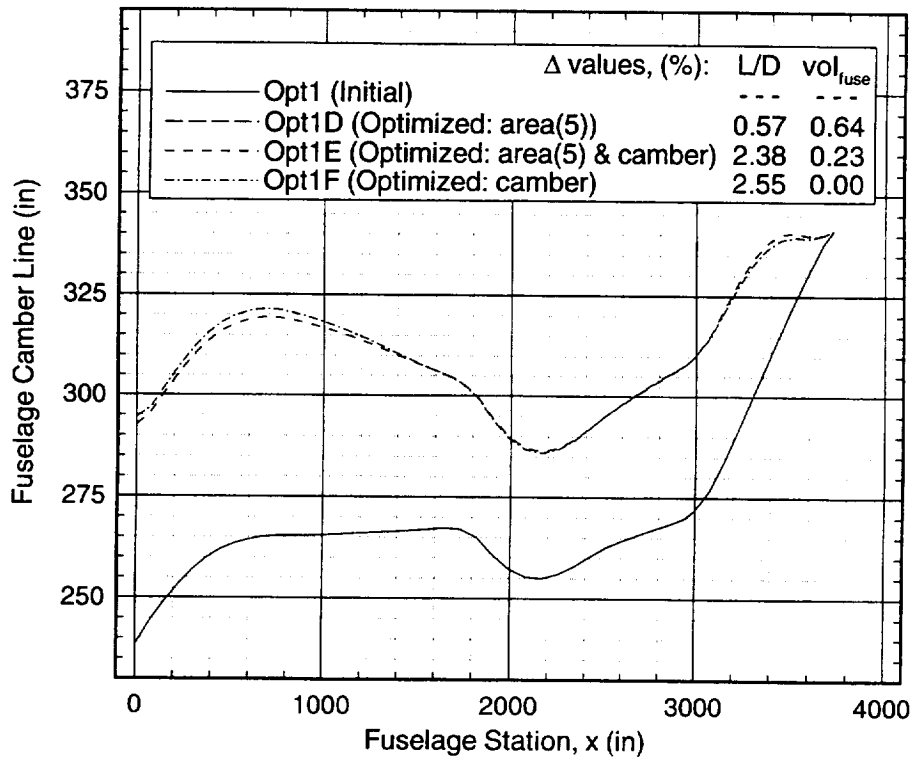
1406 Fuselage Cross-Sectional Area Optimization

Fuselage Cross-Sectional Area, 1406 Opt1 Initial Geometry



This slide shows the fuselage cross-sectional area distribution for three designs obtained using Opt1 as the initial geometry. Opt1D includes only area (with a 5th-order polynomial). The area distribution can be characterized by a shift of area from the front of the fuselage (in front of $x=2000$ in.) to the rear of the fuselage. The volume has increased slightly, and L/D is increased slightly. Opt1E includes both area (with a 5th-order polynomial) and camber. There is only a small change in the area distribution, once again an increase aft of the wing trailing edge, but there is a large increase in L/D. Opt1F includes camber only. There is no volume change, and the L/D is increased the most out of these three designs.

1406 Fuselage Cross-Sectional Area Optimization Camber-Line Distribution, 1406 Opt1 Initial Geometry



The fuselage camber-line distributions for Opt1E and Opt1F show the same trends as Opt1A shown earlier: the incidence is increased and there is more curvature near $x=800$ in., and 3400 in., and less curvature near $x=1800$ in. However, there is an additional increase in curvature near $x=100$ in.

1406 Area Optimization — Force and Volume Summary
FLO67 W/B Solution with Nacelle-Effects, $M_\infty=2.4$, $C_L=0.11$

Config.	Value			Δ			Δ (%)		
	C_D (cts)	L/D	vol _{fuse} (in. ³)	C_D (cts)	L/D	vol _{fuse} (in. ³)	C_D	L/D	vol _{fuse}
Opt1	133.80	8.221	5.159E+7	0.00	0.000	0.000E+0	0.000	0.000	0.000
Opt1mod	133.45	8.243	5.361E+7	-0.35	0.021	2.020E+6	-0.258	0.259	3.915
Opt1A	130.37	8.436	5.330E+7	-3.43	0.215	1.710E+6	-2.560	2.613	3.315
Opt1B	132.57	8.297	5.186E+7	-1.23	0.076	2.700E+5	-0.919	0.923	0.523
Opt1C	132.52	8.300	5.183E+7	-1.27	0.079	2.400E+5	-0.951	0.957	0.465
Opt1D	133.03	8.268	5.192E+7	-0.77	0.047	3.300E+5	-0.572	0.571	0.640
Opt1E	130.67	8.417	5.171E+7	-3.12	0.196	1.200E+5	-2.334	2.384	0.233
Opt1F	130.47	8.431	5.159E+7	-3.32	0.209	0.000E+0	-2.484	2.546	0.000

Opt1mod	remove waist
Opt1A	remove waist, area(5), fuselage camber and incidence
Opt1B	remove waist, area(5)
Opt1C	remove waist, area(7)
Opt1D	area(5)
Opt1E	area(5), fuselage camber and incidence
Opt1F	fuselage camber and incidence, relaxing camber bounds

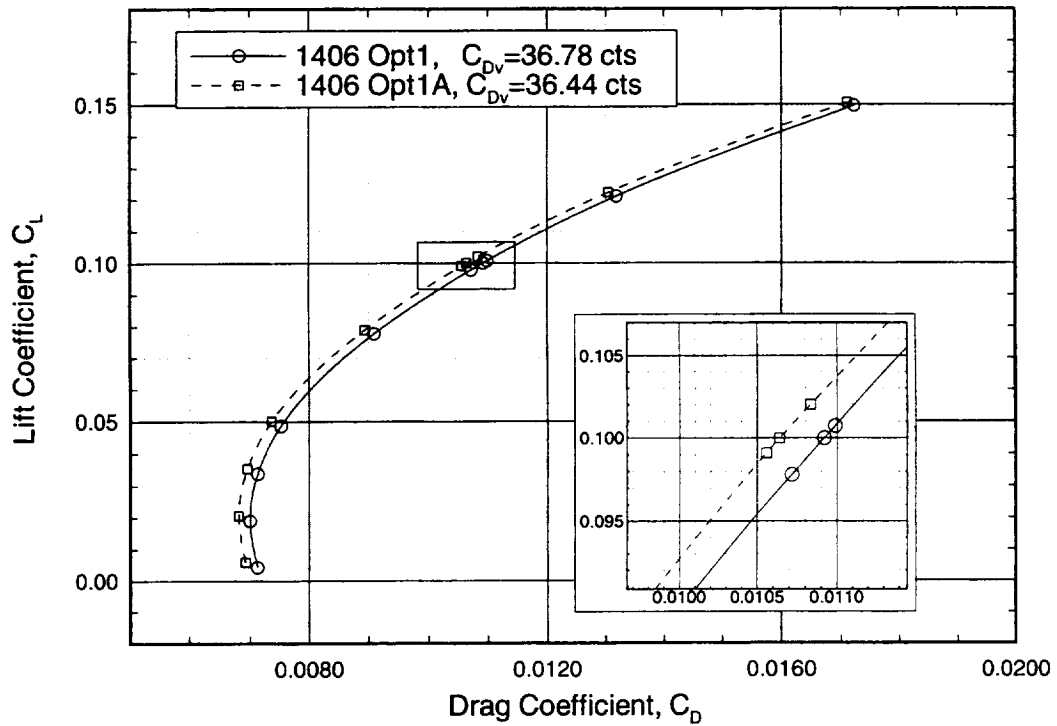
This table shows the change in drag, L/D, and fuselage volume for the various designs. The designs that include camber have the highest L/D. The Opt1A design (remove waist, area(5) & camber) has the highest L/D followed by the Opt1F design (camber). Note that Opt1A has 3.3% more fuselage volume than Opt1F.

Detailed Comparison

- 1406 Opt1
 - Optimized wing camber and twist, and fuselage camber
- 1406 Opt1A
 - Manual removal of fuselage waist
 - Optimized fuselage cross-sectional area, camber, and incidence

The remaining results will investigate the differences between Opt1 and Opt1A. This slide is to highlight the differences between the geometries. The Opt1 geometry was obtained by performing nonlinear optimization on a linear design to improve wing camber and twist and fuselage camber. Opt1A was obtained by first removing the waist of the Opt1 configuration. Then, nonlinear optimization was performed to obtain a better cross-sectional area distribution, fuselage camber, and fuselage incidence.

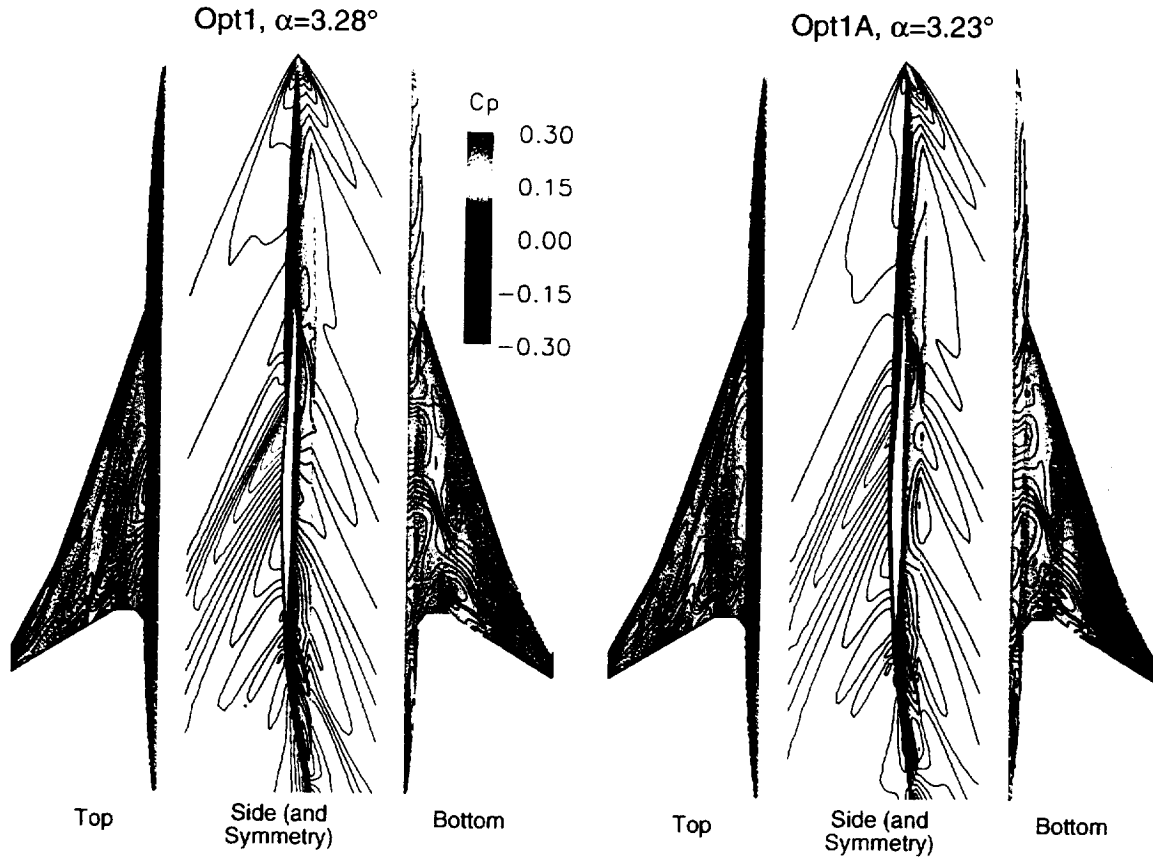
**Drag Polars for the 1406 Opt1 and Opt1A
Wing/Body Configurations**
CFL3D, Euler, $M_\infty=2.4$, $Re_c=177 \times 10^6$



A wing/body alpha-sweep was performed using CFL3D in the Euler mode at $M_\infty=2.4$. A skin-friction drag increment, obtained from a flat-plate estimate at the flight Reynolds number, was added to the Euler pressure-drag. At the cruise point ($C_L=0.1$), Opt1A has 2.8 counts less drag. This is comparable to the FLO67-predicted 3.4 cts. for the wing/body/nacelle/diverter. (Note that the FLO67 results include the same skin-friction increment for all configurations). The drag of Opt1A is less than Opt1 for the entire range of C_L evaluated.

1406 Wing/Body CFL3D Euler Solutions

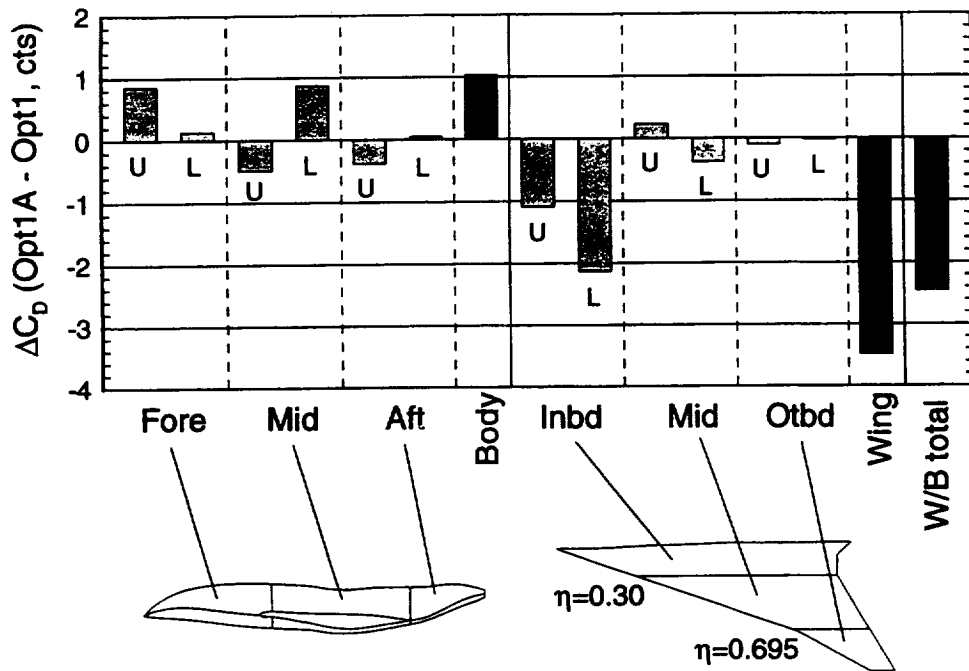
Pressure Coefficient Contours at $M_\infty=2.4$, $C_L=0.10$



This slide shows the CP distribution on the surface of the two configurations and the symmetry plane. The most-noticeable difference is the change in the compression pattern at the nose (as seen in the side views): the compression for Opt1A is asymmetric. The next feature to point out (as seen in the side views) is the reduced compression on the lower surface in the wing region. The final feature to be noted (as seen in the top views) is a change in the compression that parallels the leading edge: the compression on Opt1A is well-defined from the fuselage to the wing trailing edge, and the compression on Opt1 dissipates by mid-span.

1406 Delta-Drag Breakdown

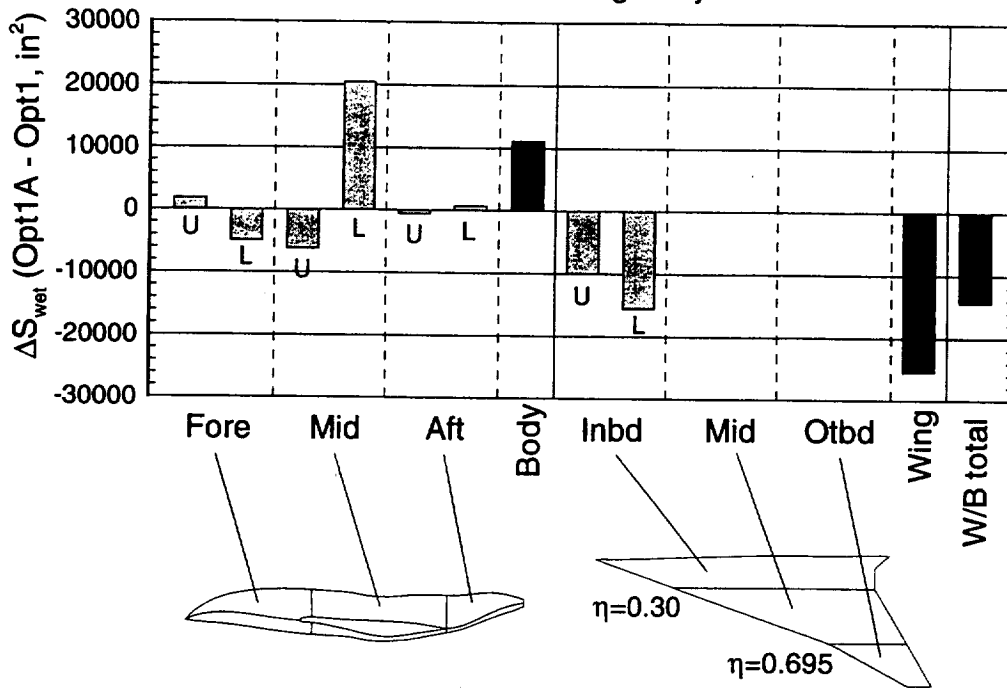
CFL3D Euler Wing/Body Solution at $M_\infty=2.4$, $C_L=0.1$



This slide shows how the pressure-drag changes from Opt1 to Opt1A in different regions of the geometry. “U” and “L” designate the Upper and Lower surfaces, respectively. It is interesting to see that the total drag of the fuselage increases. The drag increase on the upper surface of the forward section is expected from the CP distributions shown in the previous chart. However, the drag increase in the lower-mid section of the fuselage was not expected. This increase is due to the combination of the reduced compression and a reduction of the slope of the aft-facing fuselage surface (the combination on Opt1 produced thrust in the compression region).

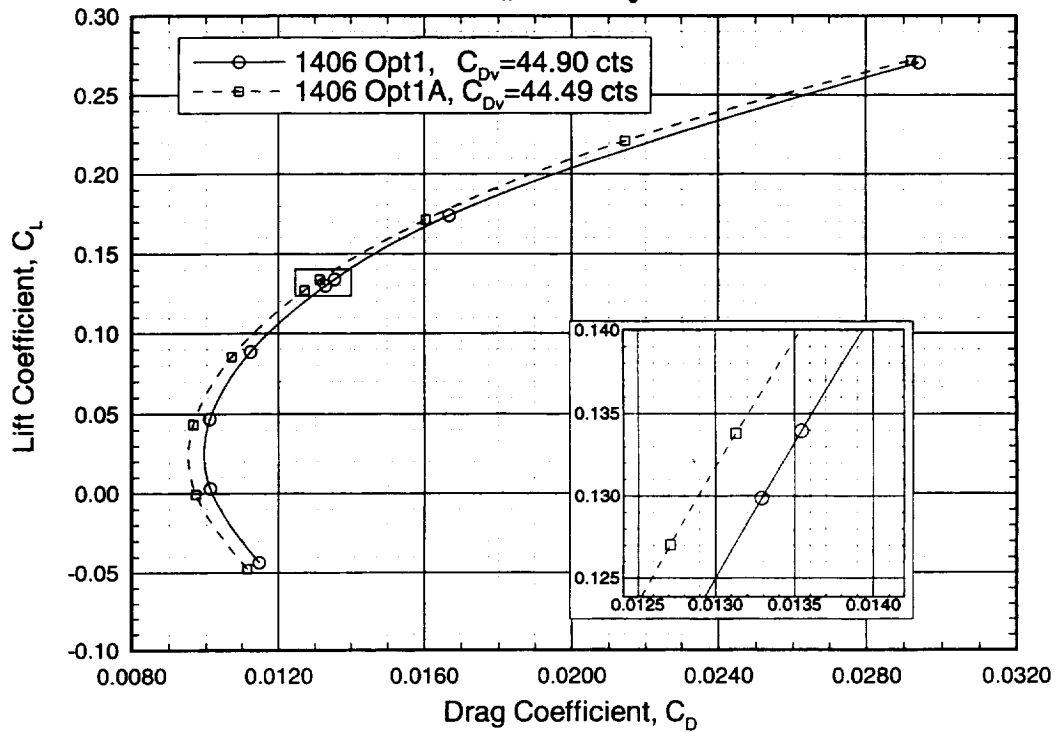
The total drag of the wing decreased, enough to provide the wing/body total drag reduction. The inboard wing provided the most drag reduction. The drag on upper-surface of the mid-wing was increased as might be expected from the stronger compression on the upper surface.

1406 Delta-Area Breakdown CFL3D Wing/Body



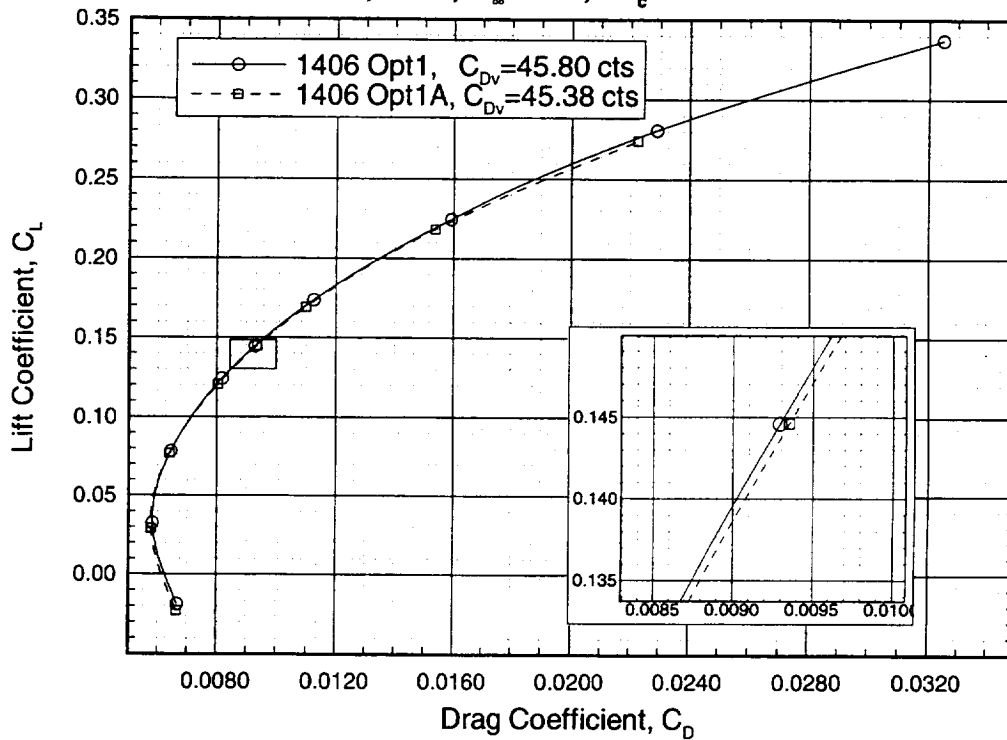
One must be careful when evaluating the change in drag because the wetted area also changed. This slide shows the change in wetted area (S_{wet}). Most of the difference in the fuselage forward upper and lower regions is due to a change in the vertical position of the upper/lower dividing line due to a wing leading-edge-position change. (The increased incidence of the Opt1A fuselage effectively drops the wing leading edge with respect to the crown line.) The large reduction in wing wetted area in the inboard region is due to the increased fuselage cross-sectional area. Note that the total wetted area of the wing/body configuration has been reduced.

**Drag Polars for the 1406 Opt1 and Opt1A
Wing/Body Configurations**
CFL3D, Euler, $M_\infty=1.1$, $Re_c=278 \times 10^6$



A wing/body alpha-sweep was performed at $M_\infty=1.1$ using CFL3D in the Euler mode. The thrust pinch-point (minimum excess thrust) occurs at this Mach number. A skin-friction drag increment, obtained from a flat-plate estimate at the flight Reynolds number, was added to the Euler pressure-drag. At the flight condition of interest ($C_L=0.134$), Opt1A has 4.2 counts less drag. It is very encouraging that the fuselage cross-sectional area optimization at the supersonic cruise point did not penalize the high-transonic performance. Once again, Opt1A has less drag throughout the C_L range evaluated.

**Drag Polars for the 1406 Opt1 and Opt1A
Wing/Body Configurations**
CFL3D, Euler, $M_\infty=0.95$, $Re_c=284 \times 10^6$



A wing/body alpha-sweep was also performed at $M_\infty=0.95$ using CFL3D in the Euler mode. A skin-friction drag increment, obtained from a flat-plate estimate at the flight Reynolds number, was added to the Euler pressure-drag. At the cruise condition, $C_L=0.145$, there is a 0.6 count drag penalty. This rather small penalty is offset by the significant increase in the high-transonic and supersonic performance.

Are These Really Optimum?

- Are nacelle-effects accurate?
 - ΔC_p not updated during design
- Can we model enough of the design space?
 - Could not remove waist using only design variables

It is still not certain that the designs presented are really optimum. First, the nacelle-effects modeling was less-accurate than usual because the ΔC_p field was obtained from the 1406 configuration before any nonlinear optimization was performed. Usually the ΔC_p field is updated as the design progresses.

The second cause of uncertainty is the representation of the potential design space. The results of this study show that the perturbations applied to the baseline cross-sectional area did not cover enough of the potential design space. The designs that began with the waisting removed retained a similar distribution to Opt1mod, and the designs that began with the waisting retained the waisting. Other work has shown that the change from Opt1 to Opt1mod cannot be accomplished even with a 10th-order polynomial or 9 Hicks-Henne functions with a large exponent (to localize the effect of the bump).

However, the designs do have better performance than the initial configurations.

Summary and Conclusions

- Waisting can be removed without L/D penalty
 - Supersonic cruise ($M_\infty=2.4$) and $M_\infty=1.1$
 - Small penalty at $M_\infty=0.95$
- Fuselage camber a bigger driver
- Smooth, global perturbations have limitations

These preliminary results show that the waisting can be removed without an L/D penalty at both the supersonic cruise point ($M_\infty=2.4$) and the high-transonic condition ($M_\infty=1.1$). However, there is a small penalty at the $M_\infty=0.95$ cruise point. A wing/body/nacelle/diverter solution and wind-tunnel tests are required to verify these results.

It was also shown that fuselage camber is a much bigger driver than cross-sectional area. All of the designs that included camber performed better than those that did not include camber. However, camber with cross-sectional area, when begun from a non-waisted fuselage, provided the highest L/D and a large fuselage volume.

Finally, smooth, global perturbations have limitations because they can limit the potential design space. More work needs to be performed in this area, as well as direct geometry representation, in order to find an efficient method to model the entire potential design space.

Wing Design and Suction/Cooling Requirements for an HSCT with Supersonic Laminar Flow Control

Bala Bharadvaj, Dino Roman, P. Sundaram, Art Powell & K. C. Chang

Advanced Transport Aircraft Systems
McDonnell Douglas Aerospace, Long Beach, CA

and

Lian Ng, Paul Vijgen & Pradip Parikh

Boeing Commercial Airplane Group
The Boeing Company, Seattle, WA

Background and Objectives

Previous studies on integrating Supersonic Laminar Flow Control (SLFC) on the High Speed Civil Transport (HSCT) have demonstrated significant potential benefits. However, these studies assumed that the aerodynamic design changes needed for laminar flow can be achieved with no adverse impact on the inviscid drag. Also, previous studies estimated suction requirements using conical analysis methods (which were the best tools available at that time). The objective of the present study was to develop an aerodynamic design for the wing of a realistic HSCT configuration, and make estimates of the suction needed using 3D boundary layer stability analysis methods. An additional objective was to explore ways to further reduce the suction needed using a Hybrid Laminar Flow Control (HLFC) scheme combined with surface cooling.

Aerodynamic Contour Design

The aerodynamic contour design was done to modify the pressure distribution over the inboard wing of the MDC 2.4-7A configuration to be compatible with SLFC while maintaining the angle of attack, overall lift ($C_L = 0.10$) and pitching moment ($C_M = -0.0050$) at supersonic cruise conditions. The aerodynamic surface was required to encompass the front and rear spars so that no adverse impacts on the structural design are introduced.

The Constrained Direct Iterative Surface Curvature (CDISC) design procedure integrated with the TLNS3D Euler CFD analysis was used. Starting from the 2.4-7A Opt 1 configuration, the pressure distribution over the inboard wing was modified to create a rapid acceleration near the leading edge and a favorable gradient over the rooftop region, along with no spanwise pressure gradient. Special attention was paid to the leading edge region during the design process. In general, the design process was very challenging not only because of the difficulties associated with the technical problem, but also because the computational tools had to be improved and refined as we went along.

The design was achieved in stages. The SLFC3A version of the design achieved a pressure distribution reasonably close to the target pressure distribution, meeting the geometric constraints at the front and rear spars. This design had a pressure drag that was higher than that for the Opt 1 baseline by 2.3 counts, however, the volume of the SLFC3A design was also quite a bit higher than that of the Opt 1 configuration. A further revision of the design (SLFC4) yielded a slightly lower pressure drag coefficient. A configuration with the same camber as SLFC3A and same volume as Opt 1 yielded pressure drag very comparable to that of Opt 1.

Suction Requirement

An estimate of the suction required to maintain laminar flow over the SLFC wing was made using 3D boundary layer analysis coupled with 3D boundary layer stability analysis. The boundary layer edge velocity distribution was based on the geometry of the SLFC3A configuration and the target SLFC pressure distribution. These analyses were done with the eMALIK code used in the maximum amplification mode of analysis. The suction at the attachment line region was estimated to maintain the momentum thickness Reynolds number below 210. Further downstream, the critical N-factor for transition was set at a nominal value of 15 and the suction requirement was adjusted to achieve an N-factor at the end of the laminar flow region between 14.5 and 15.5. The suction requirement was estimated both for the lower and upper surfaces using two types of distribution - SLFC with suction over the entire laminar flow region, and limited HLFC with suction applied only over the first 40% of the wing chord.

The results indicate that the suction requirement estimated in these studies are comparable to values computed in earlier studies using conical flow approximation. The integrated suction mass flow rate for the SLFC distribution and the limited HLFC distribution are comparable to each other. Computations indicate that decreasing or increasing the applied suction by 10% changes the N-factor at the end of the desired laminar flow region by about 3.

HLFC with Surface Cooling

A HLFC concept employing a combination of suction and surface cooling was also evaluated. In this case, active suction was applied only in a region very close to the leading edge up to 10% chord. The TS type instability was controlled by cooling the surface. It was assumed that the lowest surface temperature achievable was 100° F. Four HLFC/cooling schemes, with different combinations of applied HLFC suction and temperature distribution, were studied. Boundary layer stability analyses were made with the eMALIK code using the envelope method as well as the fixed wavelength integration strategy.

Results from this study indicate that laminar flow over 50% of wing chord should be achievable with suction only over the first 5 or 10% of the chord when combined with a tailored pressure distribution and a wing surface cooled to 100° F.

Conclusion:

These studies indicate that developing an aerodynamic design for the HSCT suitable for implementing SLFC is very feasible. The impact of the aerodynamic changes on the inviscid pressure drag is very small. The studies on the suction requirement indicate that the 3D methods predict a level of suction comparable to that estimated in earlier system studies, indicating that SLFC continues to be a technology with a significant potential benefit to the HSCT. The use of surface cooling could further reduce the suction needed and require active suction only over the first 5 to 10% of the chord.

Foreword

This paper summarizes the work performed by McDonnell Douglas Aerospace under Task 43 of the NASA High Speed System Studies Contract NAS1-19345, and The Boeing Company under Task 58 of the NASA Contract NAS1-19360. These tasks are part of the overall effort to develop technologies for an advanced supersonic transport aircraft, supported by NASA through the Langley Research Center. The work reported here is part of the strategy to develop technologies related to Supersonic Laminar Flow Control.

The NASA technical monitors for this task were Dr. Fayette Collier and Dr. Ajay Kumar, both from NASA Langley Research Center. Their support and encouragement during the course of this task is acknowledged.

Most of the wing contour design and estimation of suction flow rates based on the full chord suction was done at McDonnell Douglas. The studies on Hybrid Laminar Flow Control coupled with surface cooling were done at The Boeing Company.

In addition to the key personnel listed as authors of this work, the contributions of Feng Jiang and Chih Fang Shieh of McDonnell Douglas and Robert Ratcliff of Boeing are also acknowledged.



Wing Design and Suction/Cooling Requirements for an HSCT with Supersonic Laminar Flow Control

Bala Bharadvaj, Dino Roman, P. Sundaram,
Art Powell and K.C. Chang
McDonnell Douglas Aerospace, Long Beach, CA
&
Lian Ng, Paul Vijgen, and Pradip Parikh
Boeing Commercial Airplane Group, Seattle, WA

**First NASA/Industry High Speed Research
Configuration Aerodynamics Workshop
February 27-29, 1996, NASA LaRC**

This work addresses the Aerodynamic design of an HSCT configuration to make it suitable for laminar flow control. This paper is a summary of work done by a Team of researchers at McDonnell Douglas Aerospace (MDA) and The Boeing Company (Boeing).



Objectives

- Design HSCT wing contour conducive for Supersonic Laminar Flow Control (based on M2.4-7A), and evaluate the drag impact (MDA)
- Estimate suction requirements based on 3D BL stability analyses (MDA)
- Estimate HLFC suction/cooling requirements (BCAG)

The overall objectives of the effort are listed.

The goal of the wing contour design activity was to modify an existing HSCT configuration (the MDC 2.4-7A) to make the pressure distribution conducive for laminar flow control, and assess the impact of this change on the pressure drag. This work was done primarily at MDA.

A second objective was to make an estimate of suction requirements for the SLFC configuration using state-of-the-art 3D boundary layer stability analysis methods. This work was also done at MDA.

A further objective was to investigate if Hybrid Laminar Flow Control combined with surface cooling could further reduce the suction mass flow rates. This work was done at Boeing.



Wing Contour Design

The next several charts discuss the effort on the wing contour design.

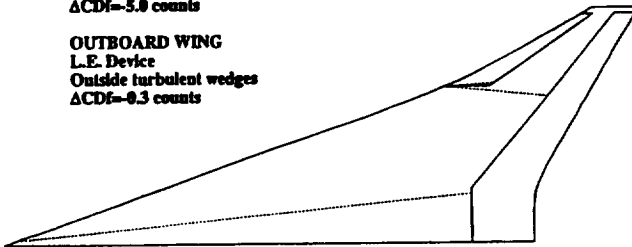


LAMINAR REGIONS AND POTENTIAL FRICTION DRAG REDUCTION

UPPER SURFACE LAMINAR REGION

INBOARD WING
L.E. to T.E. flap hinge line
Outside turbulent wedges
 $\Delta C_{Df} \approx 5.0$ counts

OUTBOARD WING
L.E. Device
Outside turbulent wedges
 $\Delta C_{Df} \approx 0.3$ counts



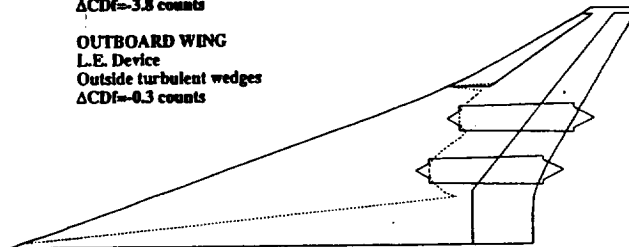
9.4 counts total friction drag reduction

8.8 counts (94%) from inboard wing panel

LOWER SURFACE LAMINAR REGION

INBOARD WING
L.E. to inlet spill shocks
Outside turbulent wedges
 $\Delta C_{Df} \approx 3.8$ counts

OUTBOARD WING
L.E. Device
Outside turbulent wedges
 $\Delta C_{Df} \approx 0.3$ counts



Upper surface and lower surface of the MDC 2.4-7A wing are shown. For the inboard wing, the goal was to laminarize the upper surface all the way to the flaps, and the lower surface up to the shock ahead of the engine inlets. It was assumed that there would be no flaps in the inboard wing - any improvement to subsonic L/D would come from boundary layer control. For the outboard wing, it was assumed that there would be a conventional flap in the leading edge and therefore, the region available for laminarization is limited to the flap segment. It was assumed that there would be a turbulent wedge growing from the wing-fuselage junction both on the upper and lower surfaces.

By laminarizing the areas indicated, it was estimated that the potential drag reduction would be about 9.4 counts. Of this, 8.8 counts is obtained from the inboard wing. Since this is a very large fraction of the total potential drag reduction, the wing design effort was focused on achieving laminar flow conducive pressure distribution only on the inboard wing in the regions shown above.



Wing Contour Design Objectives

- Design to specific chordwise pressure distribution
 - No chordwise adverse pressure gradients
 - Minimize cross-stream pressure gradient
 - Concentrate on laminarizable regions inboard of the L.E. break
 - No major contour changes within the inboard turbulent wedge
- Understand impact of leading edge region
 - Leading edge radius effects
 - Leading edge pressure gradient effects

The primary objective of wing contour design was to develop a contour to meet a specific pressure distribution that is conducive to laminar flow control. This pressure distribution is one that has no adverse pressure gradients in the streamwise (essentially chordwise) direction, and has no cross-stream gradients. Also, the acceleration near the leading edge is very steep to limit the region of cross-flow generation. The design goal was to achieve the desired pressure distribution only in the inboard laminarizable region shown in the previous figure.

Also, the impact of design changes at the leading edge were of interest. In particular, how the leading edge radius changes affect the leading edge pressure gradients and therefore the suction requirements were of interest.



Wing Design Constraints

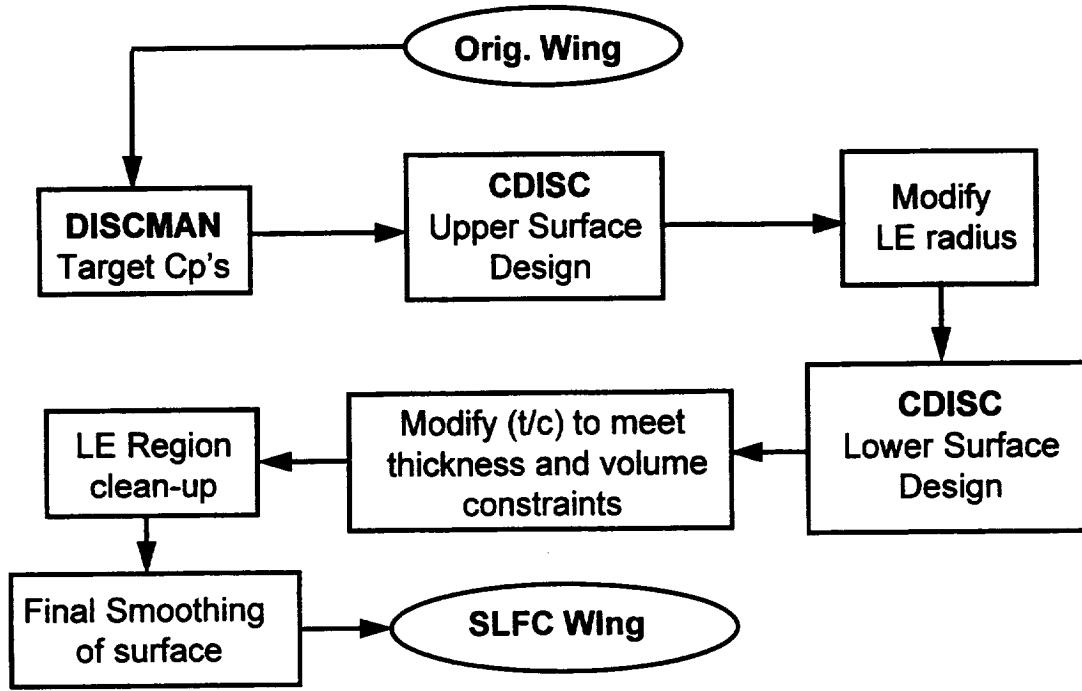
- Angle-of-attack $\leq 2^\circ$ (cabin floor angle limited)
- (t/c) between spars should be no less than for the baseline
 - maintain (t/c)max
 - maintain (t/c) at front and rear spar
- Maintain baseline fuel and main gear stowage volume
- Maintain nose down pitching moment same as baseline
- Spanwise C.P. location should not move outboard to avoid increase in wing bending moment

The wing design was to be achieved while satisfying several constraints listed above. These constraints were maintained to be the same as for the turbulent configuration that is used as the starting point for the SLFC design.

The constraints on angle of attack, spar thickness and volumes for fuel and gear stowage are dictated by the overall configuration requirements. The constraint on pitching moment was imposed to make sure that no additional trim drag was being introduced by the redesign for laminar flow control. Similarly, the spanwise center of pressure is maintained so that no additional structural weight issues are introduced.



CDISC Design Approach



Euler wing/body analysis using TLNS3D

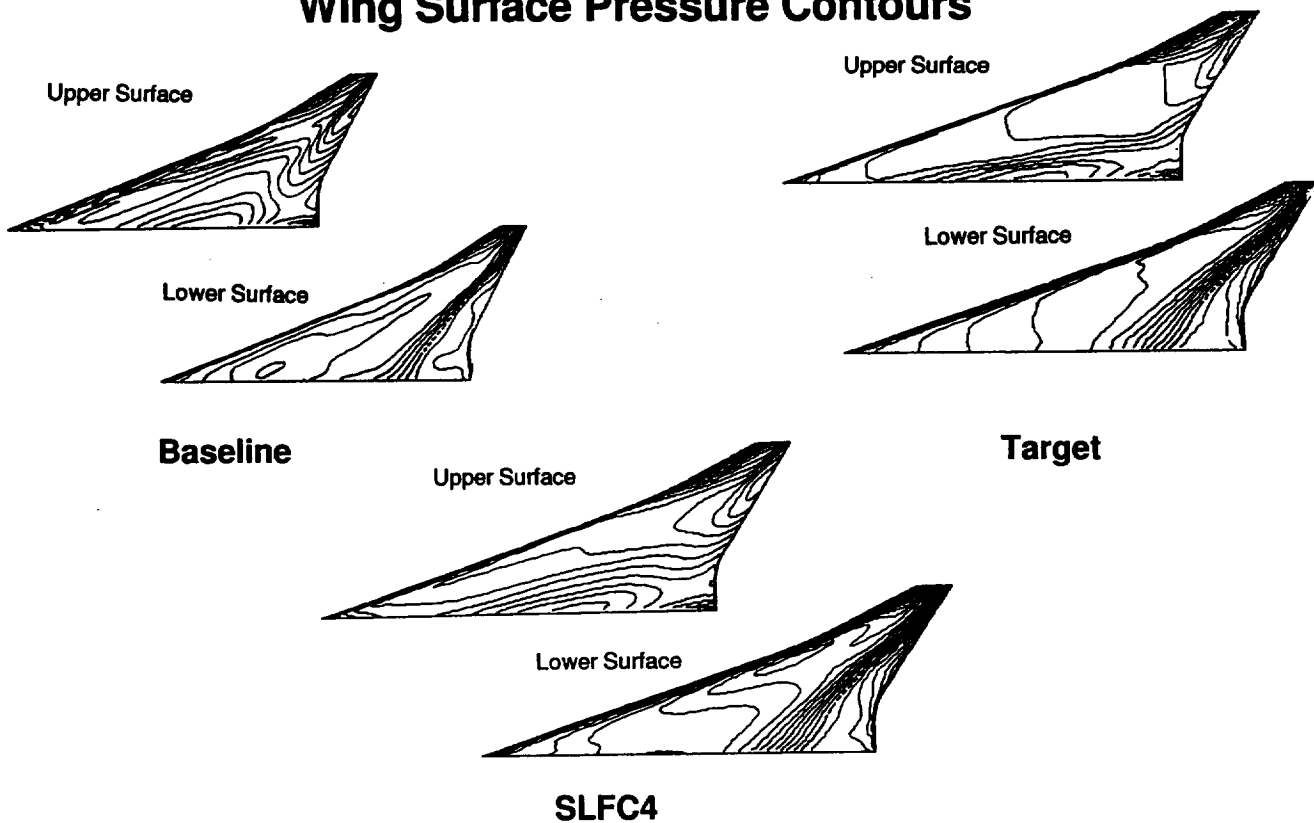
The overall approach to the design is indicated.

The CDISC (Constrained Direct Iterative Surface Curvature) method was coupled with the TLNS3D CFD analysis code and used for the design. The design studies were based on Euler solutions of the wing-body configuration.

It was possible to treat the wing upper surface and lower surfaces somewhat independently. The CDISC procedure was not able to get good control of the region very close to the leading edge and this had to be handled separately. The solutions from CDISC typically required smoothing, primarily in the spanwise direction, but also in the chordwise direction.



Wing Surface Pressure Contours

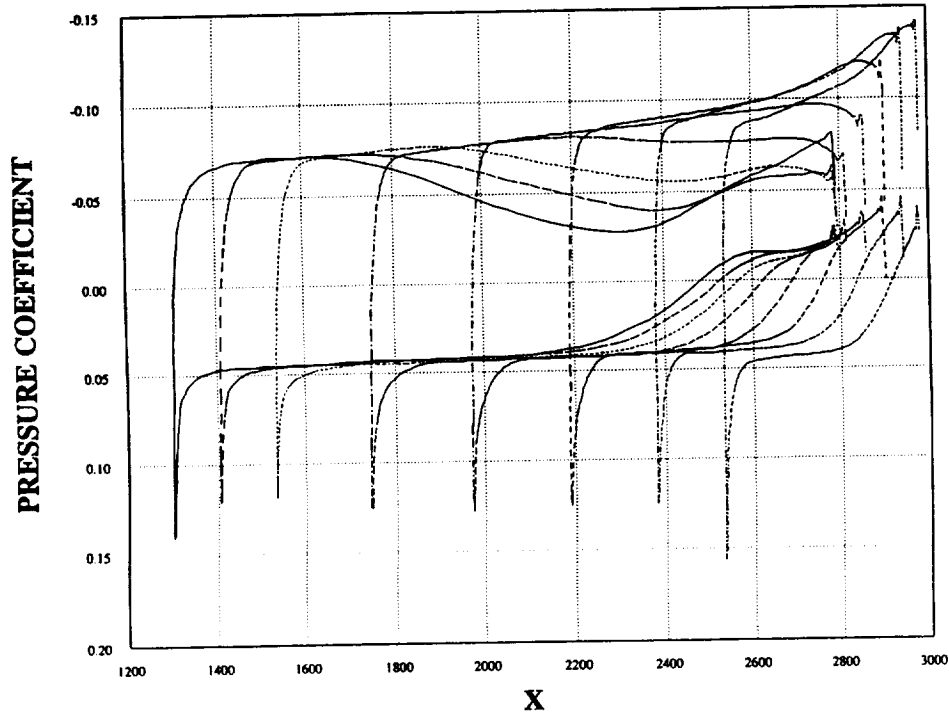


The pressure distributions on the upper and lower surfaces of the wing are shown. The "baseline" wing is the 2.4-7A Opt 1 configuration developed by Configuration Aerodynamics. The "target" corresponds to the desired laminar flow compatible pressure distribution that was provided as input to the CDISC/TLNS3D design process. "SLFC4" represents the pressure distribution that was achieved at the end of the design effort.

The target pressure distribution shows the laminar flow regions of the inboard wing having a nearly uniform pressure with a gradual favorable gradient in the chordwise direction (to meet the objectives of a laminar flow conducive pressure distribution). The pressure contours are drawn for every 0.01 change in pressure coefficient.



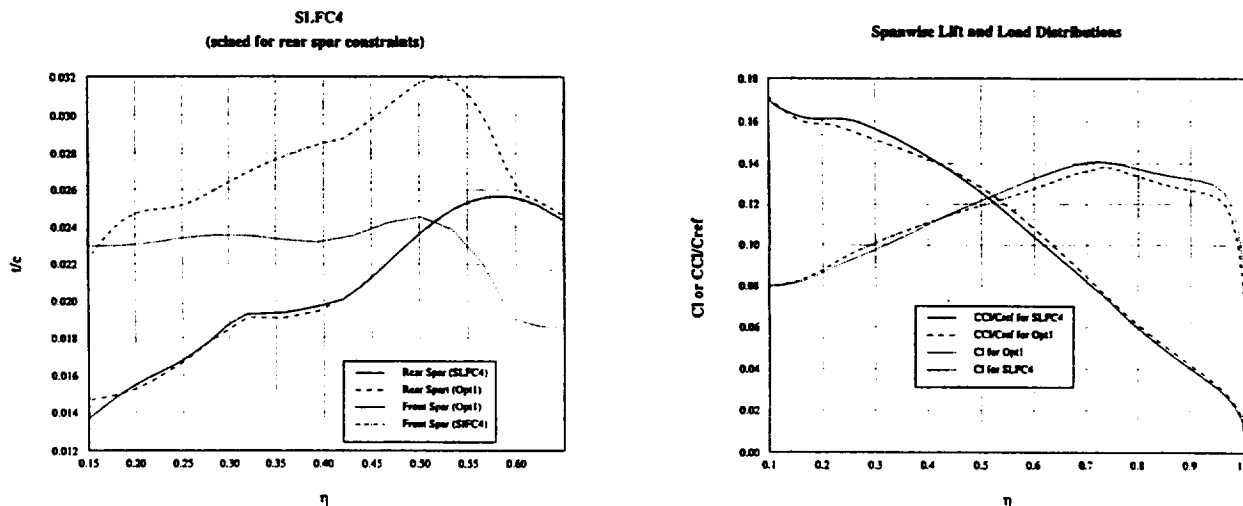
Stacked Pressure Distribution for SLFC4



Another view of the pressure distribution achieved at the end of the design process is shown. Here, the pressure coefficient is plotted against the actual axial coordinate (rather than x/c). The different curves represent the pressure distribution at the different span stations (most inboard station starting at the extreme left). This figure shows the rapid acceleration of the flow near the leading edge and a flattening of the pressures over the "roof-top" region where the pressure gradient is mildly favorable. It can be seen that the roof-top pressure levels at the different span stations tend to coalesce - this is consistent with the zero spanwise gradient. For the inboard stations, places where the pressure distribution deviates from the universal pressure level typically represents part of the wing outside the laminar flow region. It can be seen that the SLFC4 design nearly achieved the desired pressure distribution.



Constraints Comparison



This figure shows how the constraints were satisfied.

The thickness was matched at the rear spar (lower set of lines in the figure on the left). However, this made the thickness at the front spar to be much larger than required by the constraint. Consequently, this resulted in a much larger volume for the design that was achieved.

The span loading (figure on the right) achieved was very similar to that for the baseline configuration.



SUMMARY OF FORCE AND MOMENT RESULTS

M2.4-7A/OPT1 CONFIGURATION BASELINE TLNS3D-MZ EULER SOLUTIONS, M=2.4

Configuration	Angle-of-attack	Lift Coeff.	Pr. Drag (Counts)	Pitching Moment Coeff.
Baseline OPT1	1.900	0.100	64.0	-0.0500
SLFC3A	1.906	0.100	66.3	-0.0501
SLFC4	N/A	0.100	65.8	N/A
SLFC5	N/A	0.0962	60.0	N/A

A summary of lift, drag and pitching moment results are given in the table above.

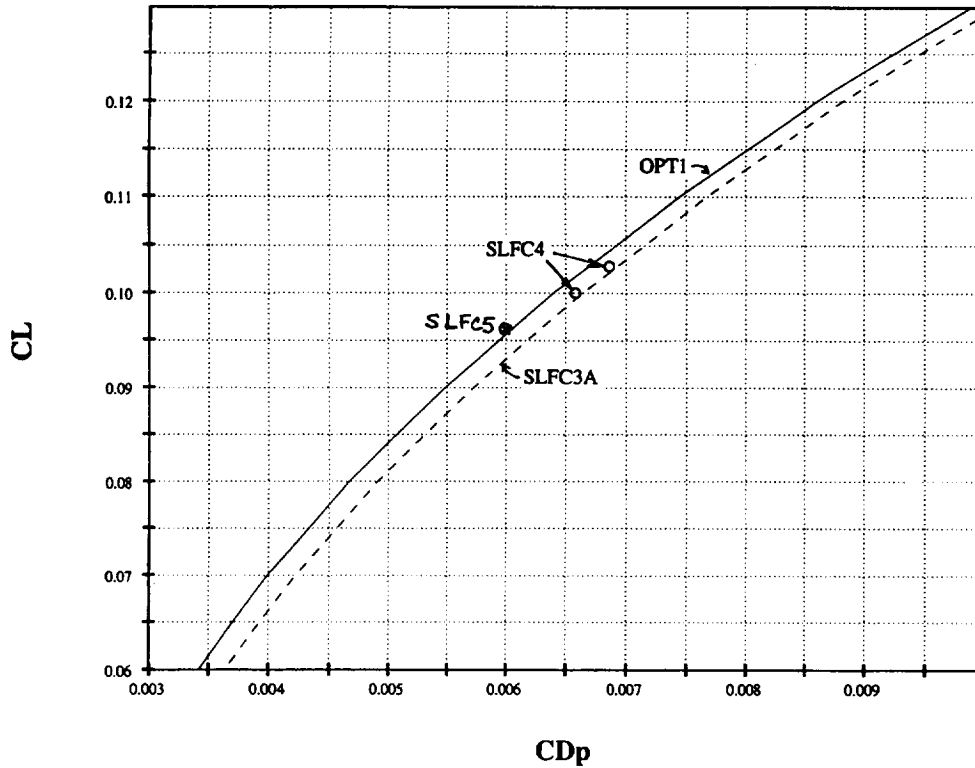
For the SLFC3A configuration, the angle of attack satisfied the constraint that was imposed (≤ 2 degrees). The pitching moment was also very close to that of the baseline configuration, as required. The pressure drag is higher than that for the baseline by 2.3 counts at a lift coefficient of 0.100.

SLFC4 was a refinement of the SLFC3A configuration based on a higher grid density in the analysis/design. The pressure drag has been reduced, and is now only 1.8 counts higher than the baseline. However, both SLFC3A and SLFC4 have higher volumes than the baseline and certainly some of the drag increase is attributable to the larger volume.

In order to eliminate the effect of the increased volume, a new wing (SLFC5) was synthesized, which used the camber of SLFC3A and thickness distribution of Opt1. This configuration resulted in a drag of only 60 counts, but at a reduced lift coefficient of 0.0962.



SUMMARY OF PRESSURE DRAG RESULTS



The drag polars for Opt1 and SLFC3A are shown, along with discrete data points for SLFC4 and SLFC5. It can be seen that the pressure drag for SLFC3A is consistently higher than that for Opt1. The two data points for SLFC4 show the same kind of trend. However, the data from SLFC5 (with the same volume as Opt1) clearly shows that the drag is comparable to that of Opt1. This indicates that the increased drag for SLFC3A and SLFC4 are due to the increased volume and the pressure distribution modification for laminar flow in itself does not increase the pressure drag.



Summary - Wing Design

- Developed an HSCT wing/body configuration for SLFC based on MDA's M2.4-7A Opt1 turbulent configuration
- Pressure drag is comparable to that of turbulent baseline
- Pitching moment and span loading are maintained - no additional trim drag
- CDISC approach is adequate for the wing contour design process in the roof-top region
- Design of LE is very challenging - need improvement in design tools

Starting from the MDC 2.4-7A Opt1 baseline configuration, a configuration suitable for laminar flow control has been developed.

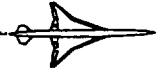
The design technique based on CDISC/TLNS3D is a reasonable approach to generate the laminar flow control configuration. The modification of the pressure distribution to be conducive for laminar flow control does not increase the pressure drag of the configuration. Also, there is no additional trim drag penalty since the pitching moment is same as for the baseline. This implies that the SLFC configuration does not introduce any additional pressure drag burden.

Even though no details are provided, the design of the leading edge region was challenging. CDISC alone was not able to generate the needed leading edge contours and substantial design work had to be done outside of the CDISC environment. This is a challenging design task for SLFC since it affects the total suction requirement significantly.

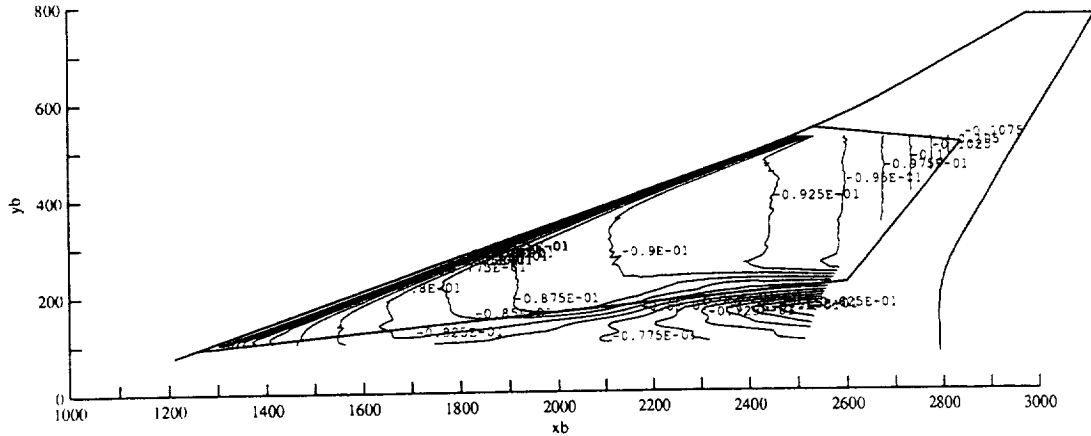


Suction & Cooling Estimates

The next several charts discuss the effort on estimating suction and cooling requirements.



Target Surface-Pressure Isobars for HLFC Wing Upper Surface (M = 2.4)



HSCT High-Speed Technology
SLFC

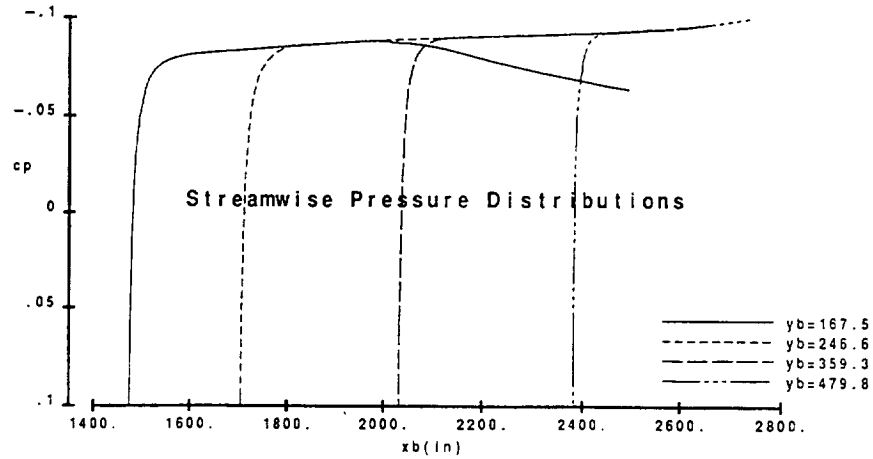
Target Surface-Pressure Isobars for HLFC Wing (Upper Surface)

The target isobars that were used by MDA to generate the inviscid edge conditions for input into the boundary-layer code are shown. A surface-Euler method was used to determine the edge conditions from these target pressures together with the SLFC3A geometry.

HSCT High-Speed Technology
SLFC



Target Streamwise Pressures for HLFC Wing Upper Surface (M = 2.4)



HSCT High-Speed Technology
SLFC

Target Streamwise-Pressures for HLFC Wing (Upper Surface)

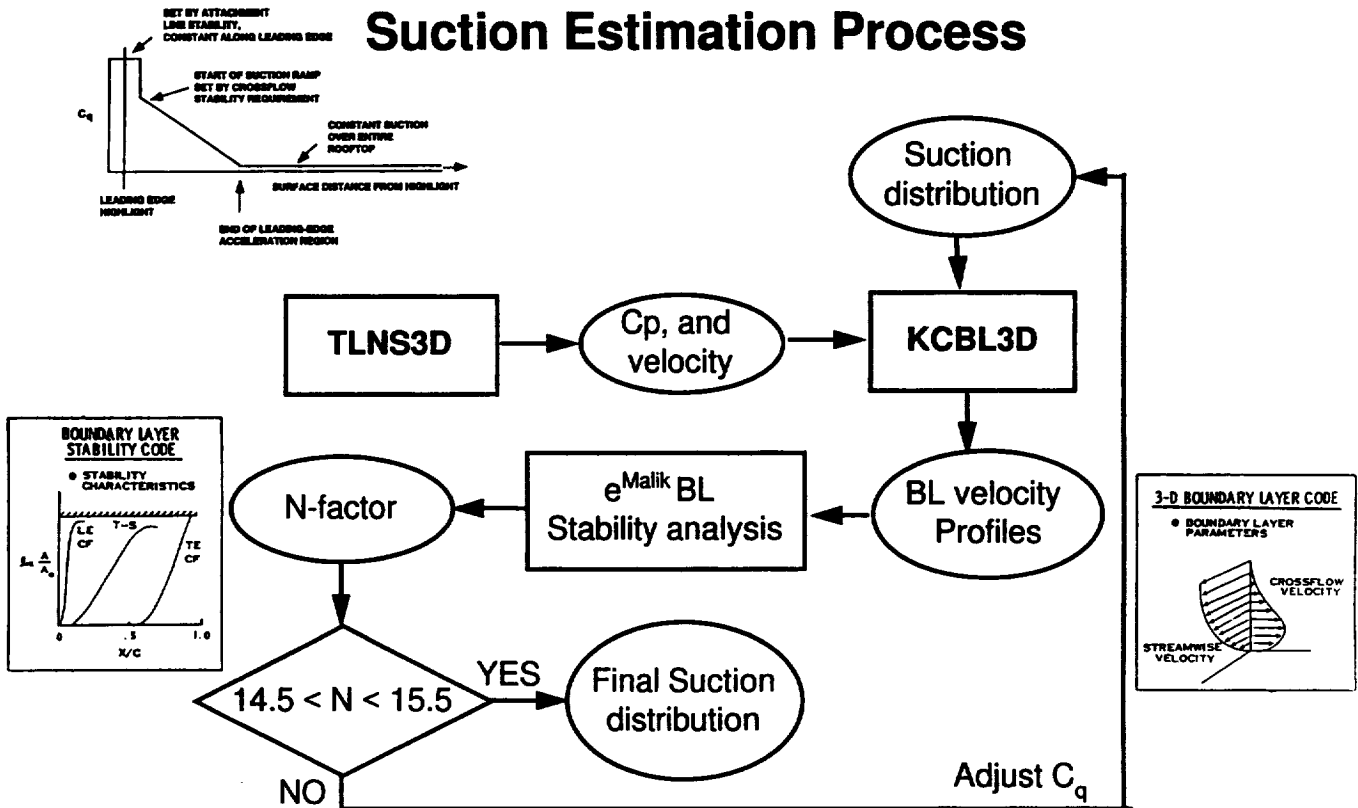
The streamwise pressure distributions that correspond to the target isobars shown in the previous figure are shown. The pressure gradient is favorable in the streamwise direction and no spanwise gradient exists in the roof-top region of interest.

The boundary-layer stability analyses presented here were conducted at a unit-Reynolds number of 1.76 million/ft (i.e., M = 2.4 at a cruising altitude of 60 Kft).

HSCT High-Speed Technology
SLFC



Suction Estimation Process

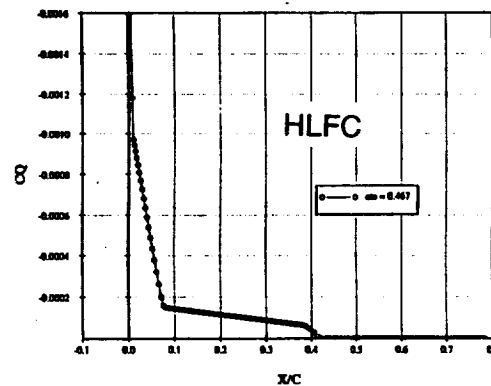
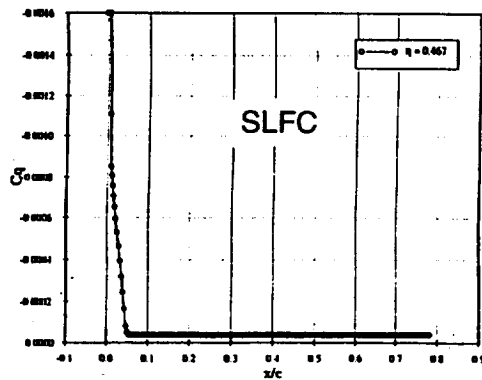
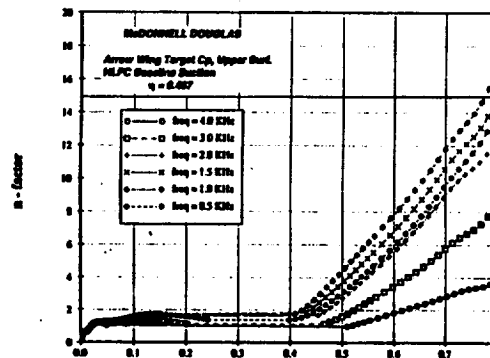
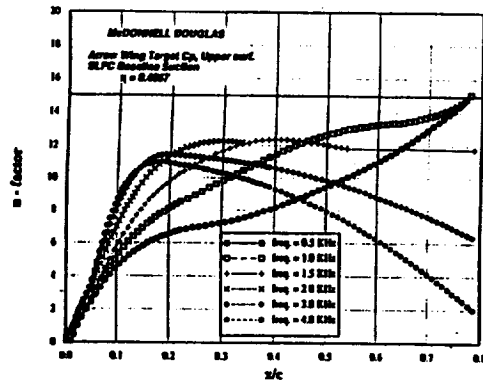


The above flow chart describes the suction estimation process.

The process begins with given distributions of pressure and boundary layer edge velocity distributions, typically generated by an Euler CFD solution. An initial estimate of the suction distribution (C_q) is made (a typical distribution is shown on the top left). Based on these, streamwise and crossflow profiles are computed by 3D boundary layer analysis. This data becomes the input for the 3D boundary layer stability analysis (done here with the e^{MALIK} code). This generates disturbance growth rates represented by N-factors. The goal of the suction estimation is to adjust the applied suction to achieve a specific N-factor for the disturbances. In this case, the disturbance N-factors were maintained between 14.5 and 15.5. If the computed N-factors did not fall within this range, the suction distribution was adjusted and the process repeated again until convergence was achieved in the N-factors. The design typically required three or four iterations on the assumed suction distribution.



N - factors for Suction Requirement

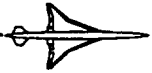


In the SLFC scheme, the suction was applied over the entire laminar flow region. As shown in the figure on the bottom left, the typical distribution had very large suction at and near the attachment line, a ramp of suction in the rapid acceleration region, and a low maintenance level of suction further downstream. The figure on the top left shows that the disturbance growth rate depends on the frequency of interest; however, in general, there is a tendency for gradual growth in the streamwise direction, with the N-factor reaching about 15 at the end of the laminar flow region.

In the limited HLFC suction scheme shown on the bottom right, the level of suction in the ramp region was increased to significantly suppress the disturbance growth in the acceleration region. The level of suction further downstream was kept high to keep the disturbances from growing. The suction was completely cut off around 40% chord and the TS waves allowed to grow such that the maximum N-factor did not exceed 15 (as shown at top right).

The levels of suction estimated from the current analysis for the SLFC scenario are comparable to estimates made previously using analysis methods based on conical flow approximations.

Also, interestingly enough, the integrated mass flows from both these cases were very comparable. However, since the limited HLFC does not require perforated skin downstream of 40% chord, this scheme would be preferable from a suction system point of view.



Hybrid Laminar-Flow Control Schemes for HSCT Wing

Approach

- HLFC concept relies on proper control of crossflow and streamwise (T-S) instabilities to prevent transition
- Subsonic HLFC concept successfully demonstrated during B-757 flight tests in 1990/1991
- Careful tailoring of pressure distribution required to minimize crossflow generation on highly swept wings
- Control crossflow generation in leading-edge region with strong suction
- Minimize T-S growth in roof-top region with streamwise favorable pressure-gradient tailoring and wall cooling

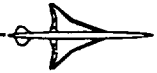
HSCT High-Speed Technology
SLFC

Hybrid Laminar-Flow Control Schemes for HSCT Wing

Approach

Hybrid Laminar-Flow Control (HLFC) implies that crossflow is controlled as much as possible with strong suction very close to the leading edge and T-S wave growth on the roof top is controlled with favorable pressure gradient and/or wall cooling. It is important to limit crossflow growth to the leading-edge region by imposing the types of pressure distributions discussed earlier.

HSCT High-Speed Technology
SLFC



Hybrid Laminar-Flow Control Schemes for HSCT Wing

Supersonic T-S Control with Wall Cooling

- Wall cooling has strong stabilizing effect on first-mode T-S waves (Mach numbers below 3)
- Transition length-Reynolds number of 90 million demonstrated at $M=2$ on nose cone of V2 rocket (1952)
- Wall-cooling ratios ($T_w/T_{adiabatic}$) of order 0.7 to 0.8 greatly damp T-S waves
- HSCT fuel heat-sink capacity could provide wall-cooling ratios of order 0.70 (at $M = 2.4$)

HSCT High-Speed Technology
SLFC

Hybrid Laminar-Flow Control Schemes for HSCT Wing

Supersonic T-S Control with Wall Cooling

From linear stability theory and from experimental wind-tunnel results it is known that the growth of unstable first-mode streamwise (T-S) instabilities can be largely reduced with wall cooling. Published results from a V2 flight test in the early 1950's indicates that a transition-length Reynolds number of about 90 million was achieved on the instrumented nose cone. It is presumed that the wall temperature was non-adiabatic during the experiment such that (large) wall cooling was achieved.

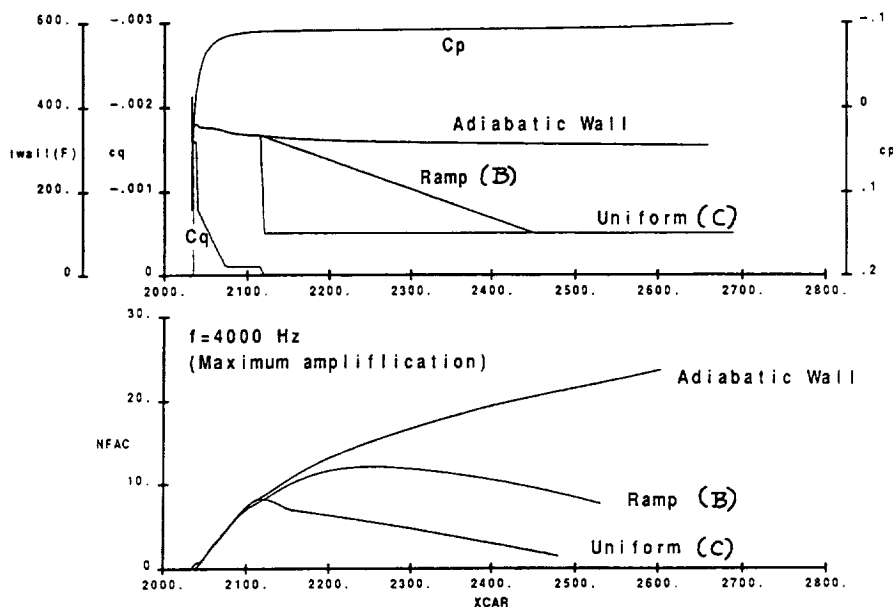
Boundary-layer stability analysis results indicate that wall-cooling ratios of about 0.7 to 0.8 are needed at $M = 2.4$ to greatly damp streamwise T-S waves for zero-pressure gradient flow.

The heat-sink capacity of the fuel aboard an HSCT could be used to provide certain levels of wall cooling. If the roof-top wall were cooled to about 100°F (using an active cooling scheme), wall-cooling ratios of order 0.7 could be achieved at $M = 2.4$.

HSCT High-Speed Technology
SLFC



Effect of Wall Cooling on Instability Growth
 SLFC3D Upper Surface; M= 2.4, Hp=60,000ft; WBL 360 (Envelope Method)

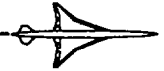


HSCT High-Speed Technology
 SLFC

Effect of Wall Cooling on Instability Growth

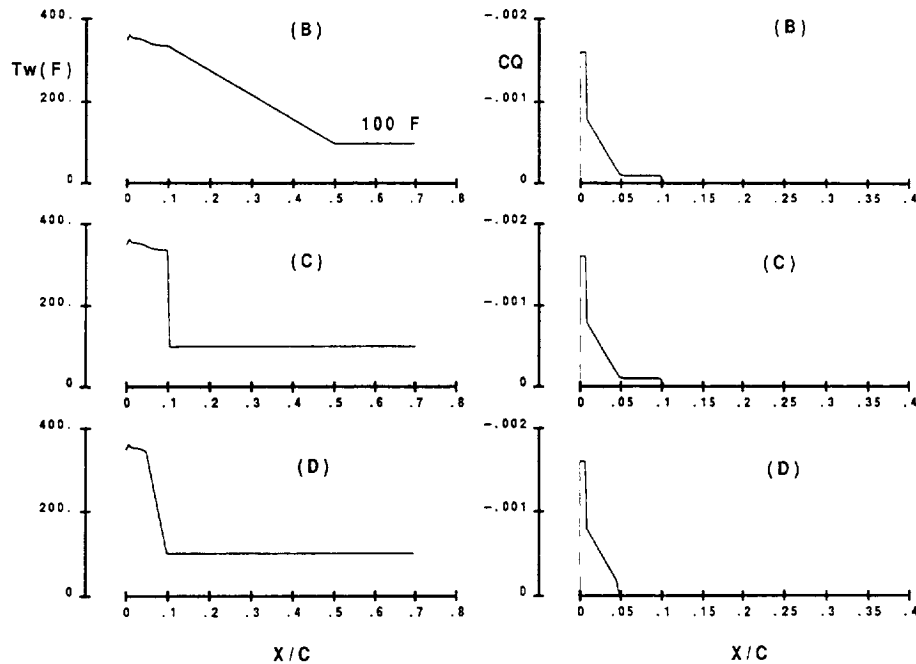
It was assumed that the lowest surface temperature achievable was 100°F using an active cooling scheme, and that suction should not extend beyond 10 percent of the chord. Three different HLFC roof-top cooling schemes were studied with cooling starting at 5 - 10 percent chord. This figure illustrates the strong damping effect on T-S waves for the cooling schemes with cooling starting at 10 percent chord. In comparison to the adiabatic-wall results, large reductions in n-factor are achievable. It is assumed in the present study that laminar flow is maintained if the maximum n-factor does not exceed 15 when using the "envelope approach" option in the *eMalik3d* stability-analysis method.

HSCT High-Speed Technology
 SLFC



HLFC Temperature and Suction Schemes Studied

WBL 360



HSCT High-Speed Technology
SLFC

HLFC Temperature and Suction Schemes Studied

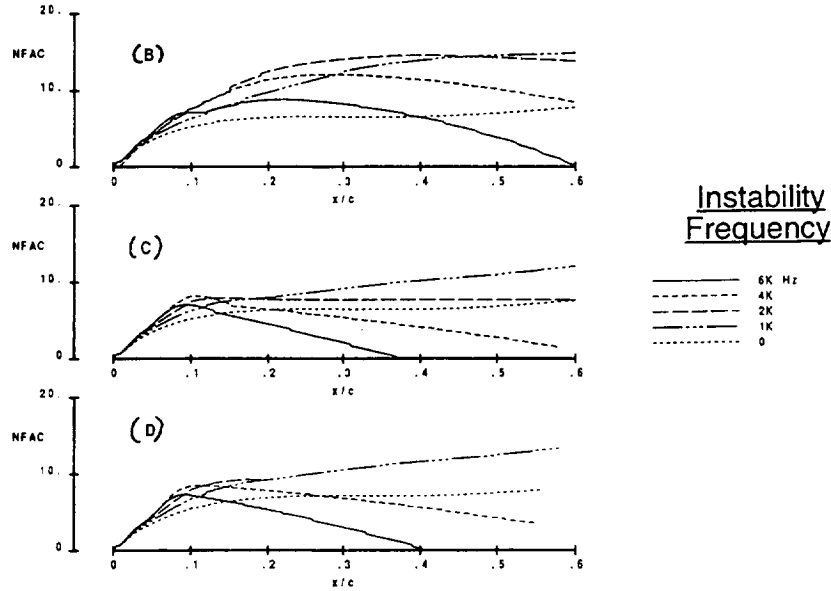
The figure presents the three HLFC wall-suction and wall-temperature profiles studied. In addition to the adiabatic case with suction up to 10 percent (see previous figure), the HLFC schemes are characterized as follows:

- Scheme B: Suction up to 10% chord. Surface temperature is assumed adiabatic up to 10% chord, and ramps down linearly to 100°F at the 50% chord location. The wall temperature is maintained at 100°F aft of 50% chord.
- Scheme C: Suction up to 10% chord. Surface temperature is assumed adiabatic up to 10% chord, then ramps down stepwise to 100°F. The temperature is maintained at 100°F aft of 10% chord.
- Scheme D: Suction up to 5% chord. Surface temperature is assumed adiabatic up to 5% chord, and ramps down linearly to 100°F at the 10% chord location. The wall temperature is maintained at 100°F aft of 10% chord.

HSCT High-Speed Technology
SLFC



Effect of Suction and Wall-Temperature Schemes
 M= 2.4, Hp=60,000ft; WBL 360 (Envelope Method)

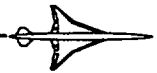


HSCT High-Speed Technology
 SLFC

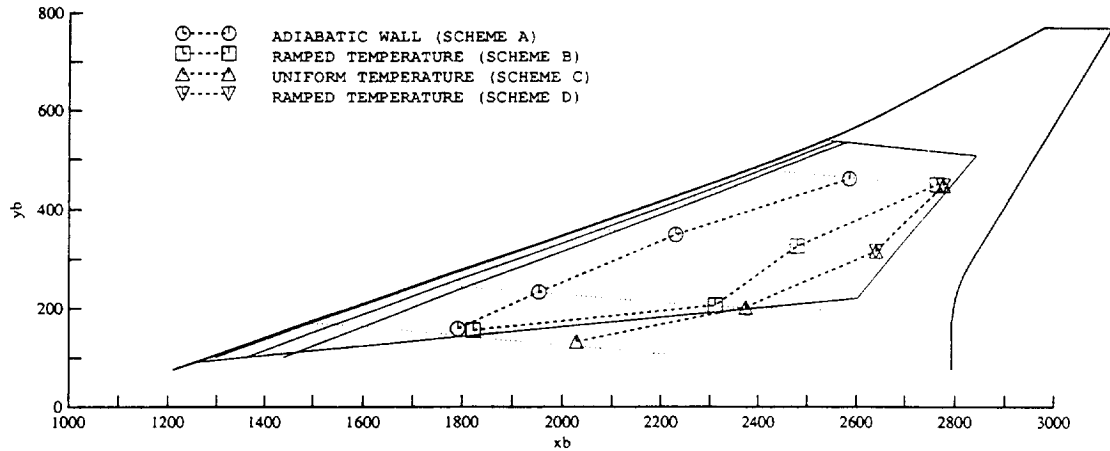
Effect of Suction and Wall-Temperature Schemes

The figure gives details of the resulting stability-analysis calculations at WBL 360 (other WBL's have similar results). It was found that the maximum n-factors remained (well) below 15 over most of the chord with Schemes B and C. In fact, n-factors do not exceed about 10 in the first 20% of the chord with these schemes. Reduction of suction from 10% to 5% chord in the leading edge region (combined with cooling starting at 5% chord - Scheme D) did not adversely affect the predicted n-factors.

HSCT High-Speed Technology
 SLFC



Effect of Wall-Cooling on HLFC Transition Location
 SLFC3D Upper Surface; M= 2.4, Hp=60,000ft; WBL 360 (Envelope Method)

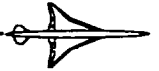


- Leading-edge suction specified to 10 percent chord (Schemes A, B, C) or to 5 percent (Scheme D)
- Specified maximum N-factor in envelope eN method is 15

HSCT High-Speed Technology
 SLFC

Effect of Wall Cooling on HLFC Transition Location

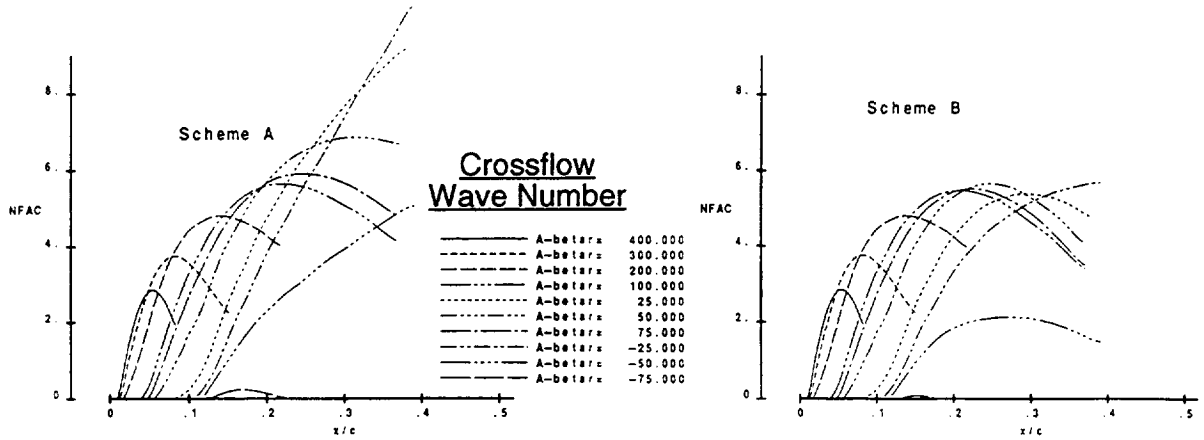
The figure summarizes the stability-analysis results across the span for the several schemes using the n-factor envelope method. These results indicate the potential for significant amounts of laminar flow with suction only in the leading-edge region and with wall cooling in the roof-top region.



Fixed-Wavelength Crossflow Analysis
 SLFC3D Upper Surface; M= 2.4, Hp=60,000ft; WBL 360 (f = 2,000 Hz)

Adiabatic Wall (Scheme A)

Ramped Cooling (Scheme B)



HSCT High-Speed Technology
SLFC

Fixed Wavelength Crossflow Analysis

The figure summarizes the crossflow stability-analysis results at WBL360 for the adiabatic and slow-ramped cooling scheme (scheme B) using the "constant wavelength" analysis option in the stability calculation. The predicted n-factors with scheme B are below 9 for the unstable wavelengths at a frequency of 2,000 Hz.

HSCT High-Speed Technology
SLFC

Summary - Suction / Cooling Requirements

- **Massflow estimates based on full-chord LFC are comparable to previous estimates (conical flow approximation)**
- **Laminar flow can be achieved with roof-top surface cooling and HLFC suction up to only 5% chord**

Summary - Suction / Cooling Requirements

Using a 3-D linear-theory transition-prediction method applied to the geometry with surface-pressure distributions tailored towards concentrating crossflow in the leading-edge region, it was determined that LFC can be achieved over the full extent of the designated region with suction mass-flow requirements that are comparable to earlier estimates (using conical boundary-layer analysis methods).

Moreover, wall cooling (wing-surface temperature down to 100°F) to control streamwise (T-S) instability on the roof-top region and leading-edge suction up to 5% chord to stabilize crossflow offers the potential of achieving substantial amounts of laminarization with HLFC, while further reducing massflow requirements and simplifying the suction-system design.



Follow-on Work Planned for 1996-97

Aero Tasks

- Wing contour design based on TCA
- Suction estimation based on analysis method calibrated against F-16XL database
- Effect of cooling on suction requirement

TI Task

- SLFC Integration including added weight of suction/cooling systems

During the PCD2 period, the wing design effort is planned to be continued.

Additional work is planned to be done in the area of wing contour design to develop an SLFC configuration starting from the Technology Concept Airplane.

The estimation of suction and cooling requirements is planned to be done using N-factor criteria guided by analysis of data from the F-16XL flight experiment.

Information obtained from the above studies will be provided as inputs to the SLFC Integration task under Technology Integration to assess the overall impact of implementing SLFC.

**Projecting and Tracking Advanced
Technology Improvements in L/D**

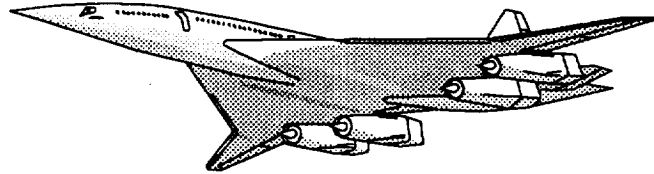
**Configuration Aerodynamics
Workshop**

**NASA Langley
February 26 - March 1, 1996**

**R.M. Kulfan
Boeing Commercial Airplane Group**

4/15/96 8:26 AM

Page 1



TOPICS

- **Importance of Accurate and Consistent L/D Projections**
- **Subsonic Aircraft Tops Down L/D Analyses**
- **Supersonic Drag Components**
- **“Tops Down” versus “Bottoms Up”**
- **Fundamental Aerodynamic Concepts**
- **Define “Acceptable” Aerodynamic Design Space**
- **Apply the process to the TCA Configuration**

4/8/96 11:07 AM

Page 2

We will discuss the importance of being able to make consistent and accurate of projections of the expected aerodynamic performance improvements that might be achieved by aggressive technology development programs.

“Tops Down” aerodynamic projection charts are often used to compare the aerodynamic efficiency of subsonic transports. The drag of a subsonic configuration is not highly dependent on the detailed geometric shape or on the streamwise distribution of lift. Hence, the Lift / Drag ratio can be related to a single parameter on a universal chart.

At supersonic speeds the cruise drag is very dependent on the volume, volume distribution as well as both the spanwise and streamwise distribution of lift.

Components of drag for a supersonic configuration will be reviewed. It will be shown that a single simple correlation parameter is not sufficient for supersonic aircraft.

Fundamental aerodynamic concepts based on linear theory will be reviewed. These concepts are valid for HSCT type configurations and are used to develop a “tops Down” process for defining “acceptable” aerodynamic design space.

This process will be applied to the TCA configuration to develop projections of the cruise L/D performance level.

Importance of Accurate and Consistent L/D Projections

- **Determine the Viability of an HSCT**
- **Define Meaningful Technology Development Goals**
- **Measure Technology Development Progress**
- **Proper focus of HSR Research Funds and Activities**
- **Support Correct Configuration Design Decisions**

4/20/06 11:07 AM

Page 3

Current HSCT configuration studies are focused on determining the technical, economic and environmental viability of an High Speed Civil Transport. These studies must by necessity include projections of anticipated technical improvements for all of the key disciplines (e.g. aerodynamic performance, structural materials and weights, propulsion system weights and performance, etc.).

The projections represent current assessments of what is expected to be achievable with aggressive technology development programs.

The emerging developments in aerodynamic non-linear design and analysis methods offer the potential of significant improvements in aerodynamic cruise lift/drag ratio. These improvements will have a major effect on the viability of an HSCT.

It is essential to identify realistic achievable goals and to be able to measure the progress to achieve these goals for cruise Lift/Drag ratio.. This is necessary to insure a properly focused technology developed program.

Technology Projection Approaches

1. Bottoms up "Guesstimates"

- Based on "experience" and / or previous successes
- Assume "We can do as good or better"
- Very dependent on initial baseline performance
- Requires similar geometry for direct application
- Not systematically adjustable for geometric differences
- No consistent process
- Can not be used to determine efficiency of initial design
- Lacks "Fundamental" basis
- Projection is an estimated increment to new baseline

4/9/96 11:07 AM

Page 4

There are two different approaches for making projections of potential improvements in aerodynamic performance lift to drag ratio, L/D.

The first approach is a "Bottoms Up Guesstimate" method. Based on previous experiences or successes we assume that we can do even better.

These estimates are very dependent on near similarity between the previous baseline configuration and the new configuration geometry for which projections are being made.

The projections are not absolute but related to the performance level of the new design or to some assumed achievable level.

This approach lacks a fundamental basis and is highly dependent on the prophetic wisdom of the individual. This certainly does not lead to consistent meaningful projections.

Technology Projection Approaches

2. Tops Down Estimates

- Based on aerodynamic “fundamentals”
- Independent of initial or current aerodynamic performance
- Can apply process to any configuration
- Process is rigorous and consistent
- Useful for determining efficiency of initial design
- Projection is a calculated “achievable upper bound”

4/2/96 11:07 AM

Page 5

The second approach is a “tops down Approach” based on fundamental aerodynamic principles.

The projections do not depend on the current aerodynamic performance of specific configurations are being made. They do, however, depend on the basic geometric features of the configuration.

This is the approach that will be presented in this presentation. The process is both rigorous and consistent. The projection is a calculated “achievable” upper bound.

This approach will first be illustrated for subsonic transport aircraft and then will be extended to supersonic configurations.

SUBSONIC DRAG

- **Not a Strong Function of Shape or Volume Distribution**
- **Depends on Spanwise Distribution of Lift**
- **Generally Thick Airfoils and High Cruise CL**
- **Cruise at Mach for $M(L/D)$ max**

4/8/96 11:07 AM

Page 6

The drag of subsonic transport configurations is not highly dependent on airfoil shapes or volume distributions at conditions below drag rise as long as the flow remains attached.

The lift dependent drag depends on the spanwise distribution of lift and not on the chordwise lift distribution.

The zero lift drag is primarily friction and profile drag and is very dependent on the overall wetted area of the configuration

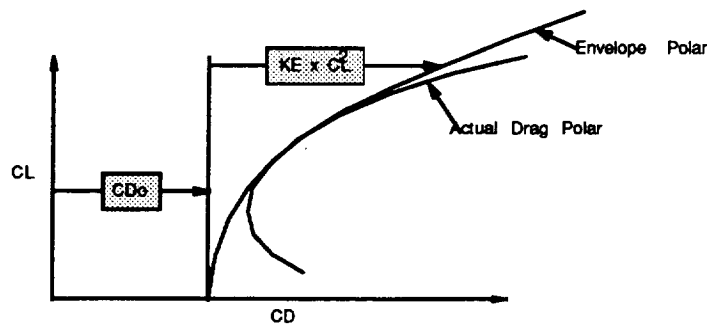
The aerodynamic efficiency for subsonic transports is usually specified at the Mach number for long range cruise. This Mach number is very dependent of the fundamental airfoils shapes of the wing.

Subsonic configurations tend to relatively thick wing sections and cruise at relatively high lift coefficients.

Subsonic Drag Polar Approximation

$$C_D = C_{D0} + K E \times C_L^2$$

$$L/D \text{ max} = \sqrt{\frac{0.5}{K E \times C_{D0}}}$$



na-pr21a 02108

4/8/86 11:07 AM

Page 7

We can approximate the subsonic drag polar by a simple parabolic equation.

$$C_D = C_{D0} + K E \times C_L^2$$

C_{D0} is called the zero lift drag.

KE is the drag due to lift factor.

Using this simple expression for drag, the L/D_{max} value is dependent on both KE and C_{D0} by a very simple expression.

$$L/D_{max} = \frac{0.5}{\sqrt{K E \times C_{D0}}}$$

Subsonic Drag Polar Approximation

$$L/D \text{ max} = \sqrt{\frac{0.5}{KE \times CDo}}$$

$$CD = CDo + KE \times CL^2$$

Lift Dependent Drag

- Induced Drag
- Profile Drag Due to Lift
- Drag Rise Due to Lift
- Trim Drag
- ??

Non Lift Dependent Drag

- Friction Drag
- Profile Drag Due to Volume
- Drag Rise
- Interference Drag
- Excrescence Drag
- Miscellaneous Drag

4/8/86 11:07 AM

Page 8

The Non-lift dependent drag consists of:

- Friction drag
- Profile drag due to thickness.
- Compressibility drag
- Interference drag
- Excrescence drag and miscellaneous drag

The lift-dependent drag items include

- Induced drag
- Profile drag due to lift
- Compressibility drag due to lift
- Trim Drag

Equations for Minimum Induced Drag

$$\frac{D_i}{q} = \frac{1}{2 * \pi} \int_{-\frac{b}{2}}^{\frac{b}{2}} \int_{-\frac{b}{2}}^{\frac{b}{2}} \frac{d\Gamma}{dy} \frac{d\Gamma}{d\eta} \ln |y - \eta| dy d\eta$$

Lift: $L = \rho V_{\infty} \Gamma$

Minimum Drag: Elliptic Load Distribution

$$\Gamma_{opt}(\eta) = \Gamma_0 \sqrt{1 - \eta^2}$$

4/9/86 11:07 AM

Page 9

The equation for induced drag at subsonic speeds is shown in the familiar integral form in terms of the wing circulation, Γ .

It will be shown there is a great similarity between this equation and the wave drag equations at supersonic speeds.

The wing lift distribution is elliptic for minimum induced drag.

Tops Down L/D Analysis

- (L/D)_{max} at (M L/d)_{max} Subsonic Aircraft

Lower Bound Drag:

- Fully Turbulent Flow Friction Drag
- Elliptic Load Induced Drag

$$C_D = C_{F_{ave}} \frac{A_{wet}}{S_{ref}} + \frac{C_L^2}{\pi AR}$$

$$A_{wet\ adj} = A_{wet} \frac{C_{F_{ave}}}{0.0021}$$

$$L/D\ max\ pct. = 19.34 \sqrt{\frac{b}{A_{wet\ adj}}}$$

4/8/96 11:07 AM

Page 10

For subsonic transport aircraft the lower bound drag components are usually considered to include:

- Minimum C_{D0} equal to fully turbulent flow flat plate skin friction drag.
- Minimum drag due to lift equal to the induced drag for planar wing configurations with elliptic load distributions .

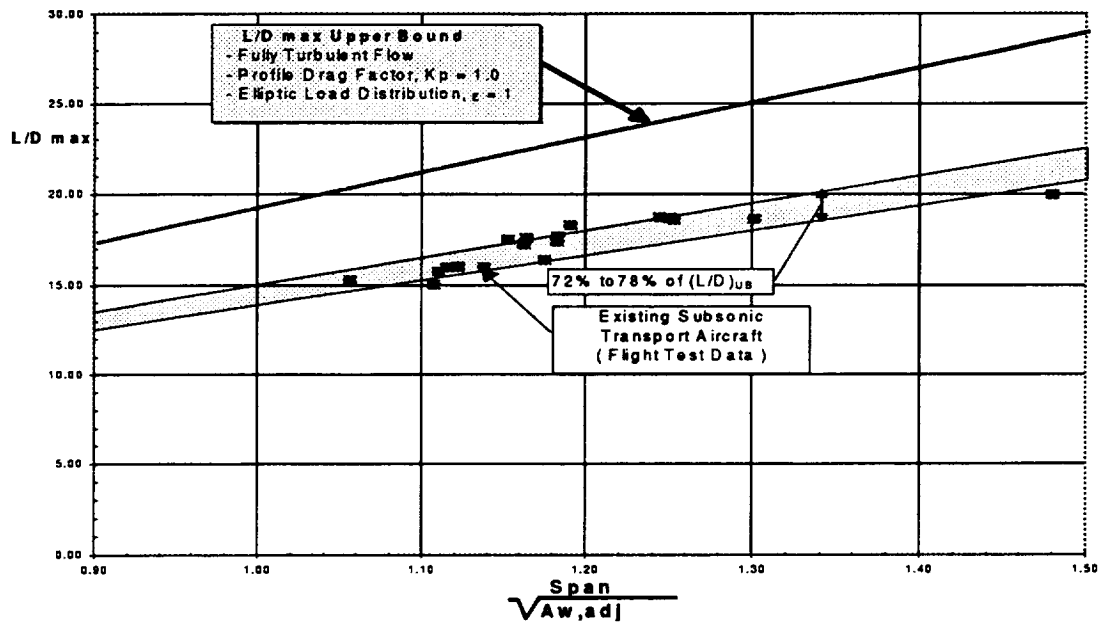
An adjusted wetted area is used to normalize out the effects of Reynolds number.

The adjusted wetted area is equal to the actual wetted area times the ratio of computed average skin friction coefficient to an average skin friction coefficient of 0.0021.

The "Tops Down" L/D max for subsonic transports is then equal to 19.34 times the wing span divided by the square root of the adjusted wetted area.

An "effective" span is used for aircraft having non-planar wing geometries such as tip fins. The "effective" span is the span of an equivalent planar wing that has the same induced drag as the non-planar wing.

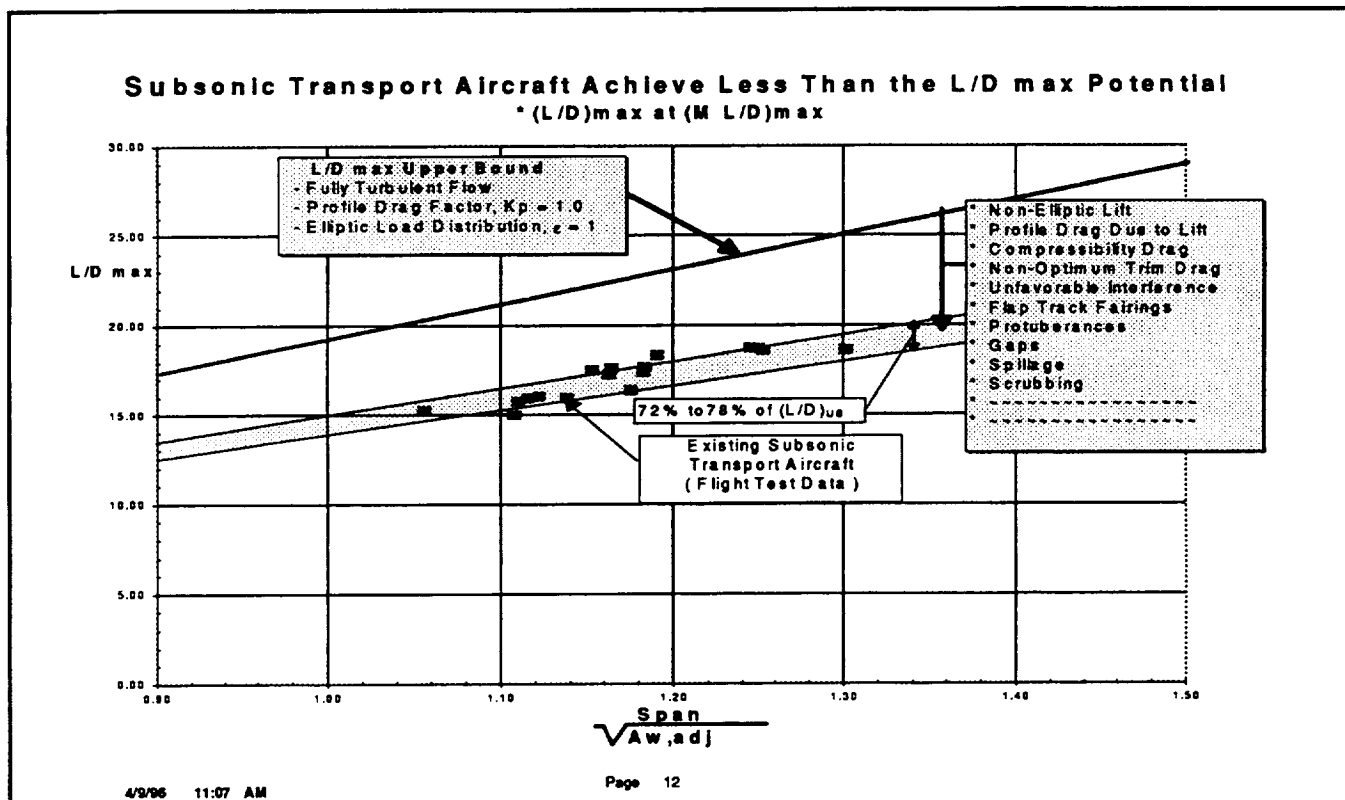
Subsonic Transport Aircraft L/D max Potential * (L/D)max at (M L/D)max



4/9/96 11:07 AM

Page 11

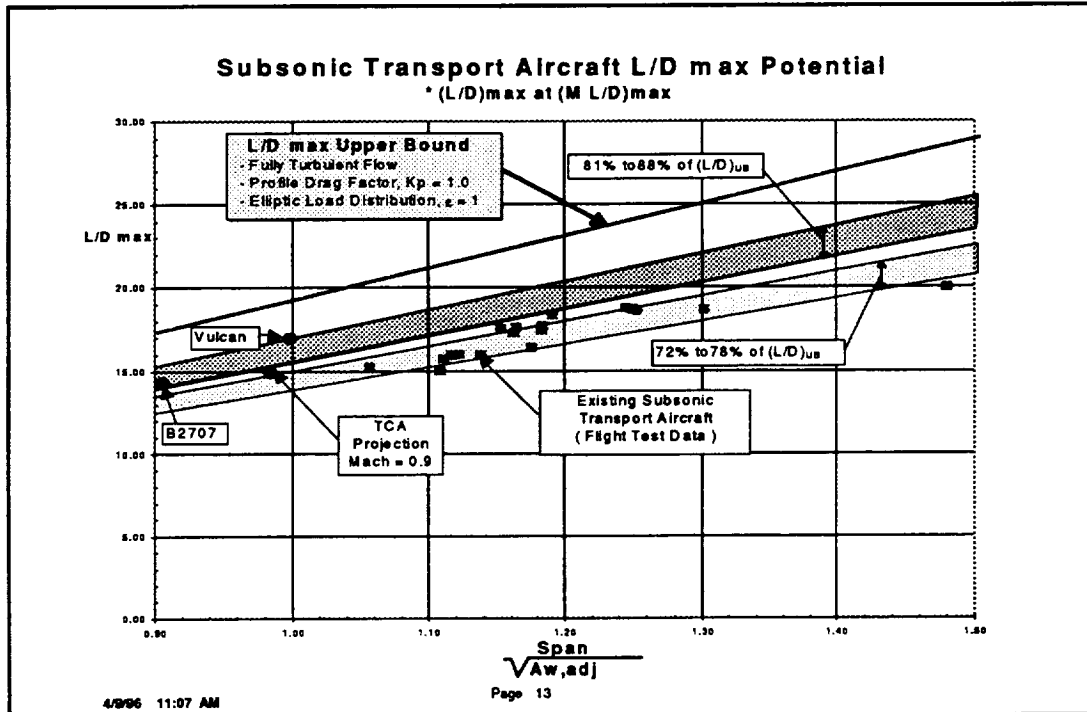
The values of L/Dmax at the Mach number corresponding to (M L/D)max are shown for existing subsonic transport aircraft based upon flight test data. The existing aircraft achieve about 72% to 78% of the “achievable upper limit”



The Subsonic Configurations fail to achieve this Upper Bound Lift / Drag level because of a number of additional drag items as shown in the figure. The most Significant of these additional drag items include:

- The relatively thick airfoils and wide fuselages result in a profile drag increase over the viscous friction drag by approximately 20% to 25 %.
- At the long range cruise Mach number, subsonic aircraft typically have 15 to 20 counts of drag rise ($\Delta CD = 0.0015$ to 0.0020).
- The spanwise load distributions based on structural design trades, tend to depart from the ideal load distribution. The typical spanwise load distributions are more heavily loaded near the wing root. This together with an increase in profile drag due to lift typically increases the induced drag approximately 10% to 12% above the ideal level.

These three drag items account for a 15% to 18% reduction in L/D from the Upper Limit L/D levels.



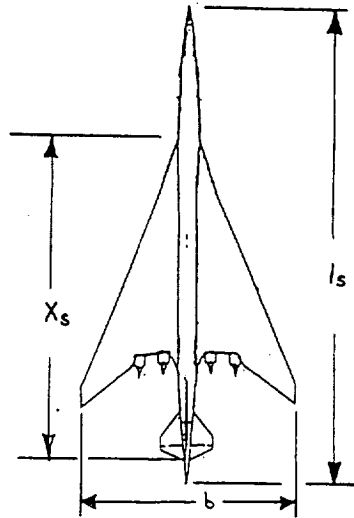
Supersonic type configurations tend to be long, thin and slender and cruise at relatively low lift coefficients. The subsonic viscous drag is essentially equal to flat plate skin friction drag.

The typical over land subsonic cruise Mach number for an HSCT of approximately 0.9. This is well below the drag rise Mach number.

Consequently, it is expected that an HSCT cruising with optimized flap settings should achieve well in excess of 80% of the corresponding upper limit for L/D_{max} at subsonic cruise conditions.

SUPER SONIC DRAG COMPONENTS

- $CD = CD_F + CD_{WV} + CD_{WL} + CDI + CD_{MISC}$
- $CD_F \approx \text{WETTED AREA} \implies \text{FRICTION DRAG}$
- $CD_{WV} \approx Vol^2 / L_s^4 \implies \text{VOLUME WAVE DRAG}$
- $CD_{WL} \approx (\text{LIFT} / X_s)^2 \implies \text{LIFT WAVE DRAG}$
- $CDI \approx (\text{LIFT} / b)^2 \implies \text{INDUCED DRAG}$



The drag components of an HSCT flying at supersonic speeds consists primarily of friction drag, wave drag due to volume, wave drag due to lift, induced drag and other miscellaneous drag items.

The friction drag is typically equal to flat plate skin friction drag on all of the component surfaces. The friction drag, therefore, depends primarily on the wetted area.

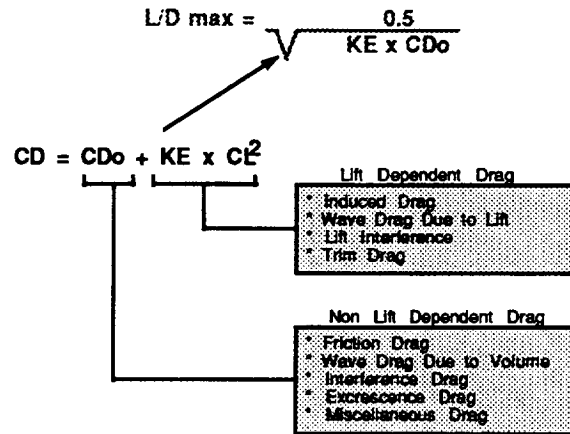
The volume wave drag primarily varies with the volume squared divided by the configuration length raised to the fourth power.

The induced drag varies with the ratio of lift over wing span squared.

The wave drag due to lift varies with lift over the streamwise length of the lifting surface squared. The wave drag due to lift vanishes as the supersonic Mach number approaches one.

It is evident that for low drag, supersonic configurations tend to be long, thin and slender.

Supersonic Drag Polar Approximation



4/8/96 11:07 AM

Page 15

Similar to the subsonic condition, we can represent the supersonic drag polar as a two term parabolic equation consisting of the non-lift dependent drag, C_{D0} , plus the lift dependent drag $KE \times C_L^2$.

The non-lift dependent drag includes:

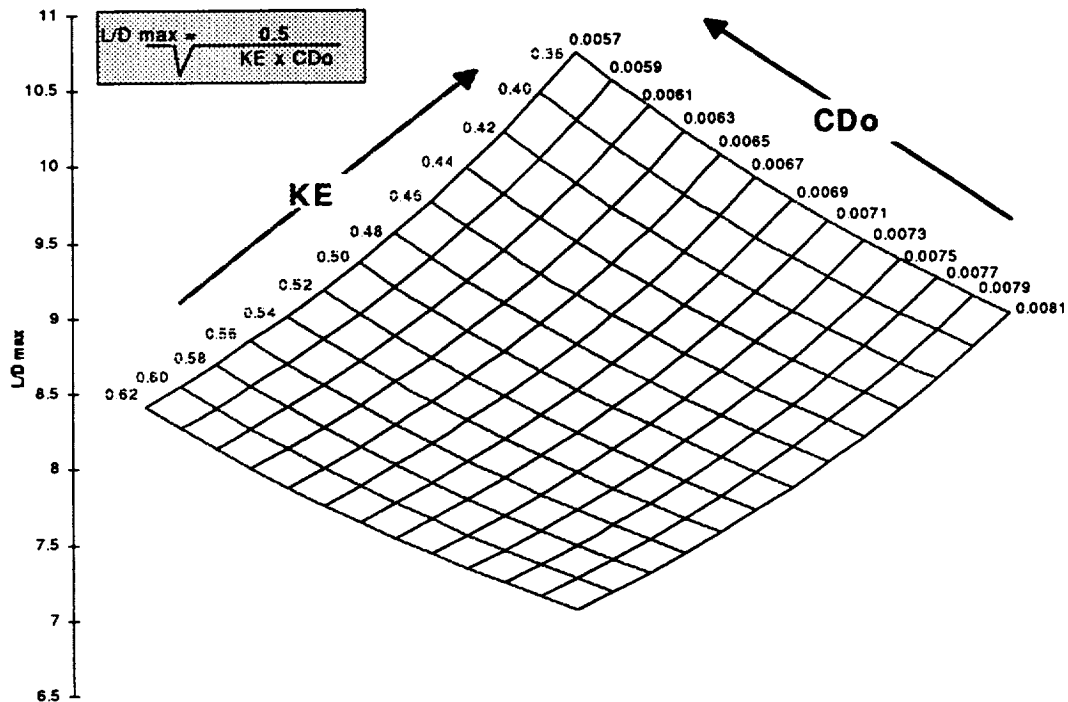
- Friction drag
- Wave drag due to volume
- Volume interference drag
- Excrescence and other miscellaneous drag items.

The lift dependent drag consists of :

- Induced drag
- Wave drag due to lift
- Lift interference effects
- Trim drag.

Based on the parabolic drag polar representation, it can be shown that L/D_{max} varies inversely with the square root of the product of C_{D0} and the drag due to lift factor KE .

HSCT Aerodynamic Performance Design



4/9/06 11:07 AM

Page 16

A way to view the dependency of L/D_{max} on C_{Do} and KE is in the form of a carpet plot. This is the form that we will use to develop the region for acceptable designs of a specific configuration. This is a two dimensional representation of the design space for supersonic configurations.

In the discussions that follow, it is assumed that the gross overall features of any configuration remain fixed. These include such things as wing area and location on the body, nacelle overall size and locations, planform shape and critical design constraints.

What we wish to determine is the region of acceptable designs that could be developed by different methods and techniques. We will then determine what is considered to be the overall upper limit of achievable L/D_{max} for that specific configuration.

To do this we will identify values of C_{Do} and KE that are considered too high for an acceptable design. We will then use fundamental aerodynamic concepts to determine lower bounds of achievable C_{Do} and KE .

CDo "TOO HIGH" LIMIT FOR ACCEPTABLE DESIGN

$$C_{D0} < C_{DF} + \sum C_{DW \text{ ISOL}} + C_{DMISC} + C_{DEXCRES}$$

- FULLY TURBULENT FRICTION DRAG
- SUM OF COMPONENT ISOLATED WAVE DRAG
[NO FAVORABLE INTERFERENCE]
- CURRENT TECHNOLOGY EXCRESCENCE AND MISCELLANEOUS DRAG
- *** DRAG CAN BE WORSE THAN THIS ***

4/9/86 11:07 AM

Page 17

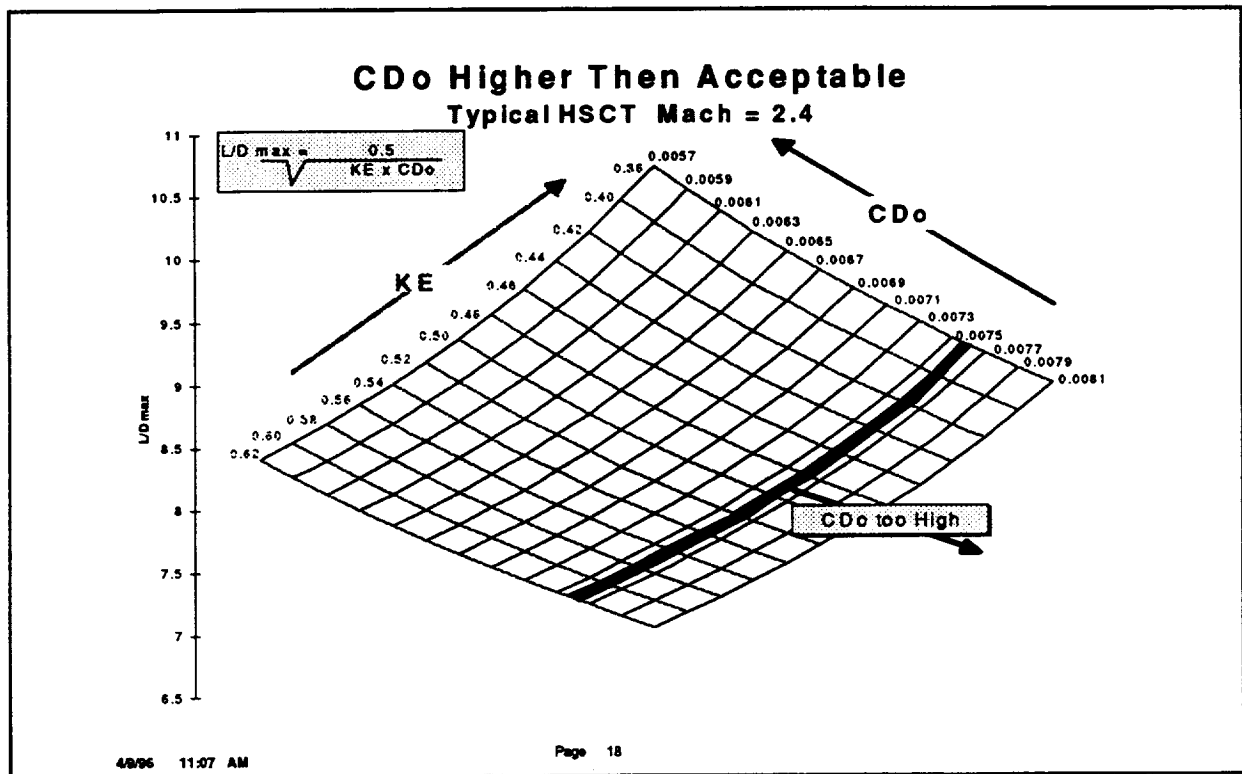
CDo is considered "too high" if the non-lift-dependent drag exceeds the sum of:

- CDF = Fully turbulent flow flat plate skin friction drag.
- CDW = The sum of the isolated wave drag of each of the configuration components. This corresponds to a design with no net favorable aerodynamic interference.
- CDmisc = Current technology miscellaneous drag including excrescence drag.

The most common causes of CDo being too high are:

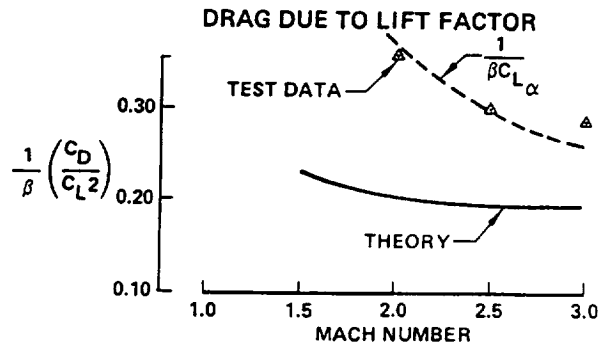
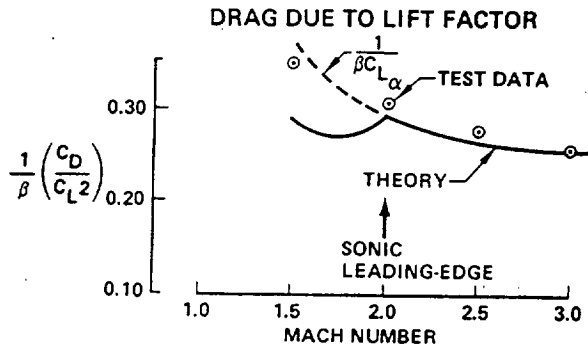
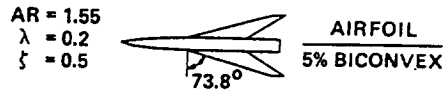
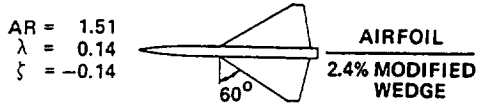
- Unfavorable wing / body interference drag for a non-area-ruled body.
- Nacelles designed and / or located to produce volume wave drag interference.
- Large out of contour bumps such as landing gear fairings
- Separated flow over the wing upper surface or in the vicinity of the nacelle / diverter intersection with the wing.

The zero lift drag can be worse than this acceptable upper limit for CDo.



By calculating the friction drag, the wave drag of the isolated components and the miscellaneous drag items, we can then locate on this chart a boundary beyond which CDo is considered to be "too high" for an acceptable design.

DRAG DUE TO LIFT OF FLAT SUPERSONIC WINGS



This figure compares the experimental drag due to for some flat supersonic configurations with the predicted theoretical drag due to lift. The test data matches the theoretical drag due to lift with zero suction ($s=0$). The drag due to lift for zero suction as shown in this figure is equal to one over the lift curve slope.

The "KE too high" limit corresponds to the drag due lift that could actually be achieved by a thin flat symmetric wing design.

KE " TOO HIGH" LIMIT FOR ACCEPTABLE DESIGN

$$KE < KE_{S=0}$$

- EQUIVALENT TO DRAG OF FLAT WING CONFIGURATION
- NO TRIM DRAG
- NO LIFT INTERFERENCE DRAG
- *** DRAG CAN ACTUALLY BE HIGHER ***

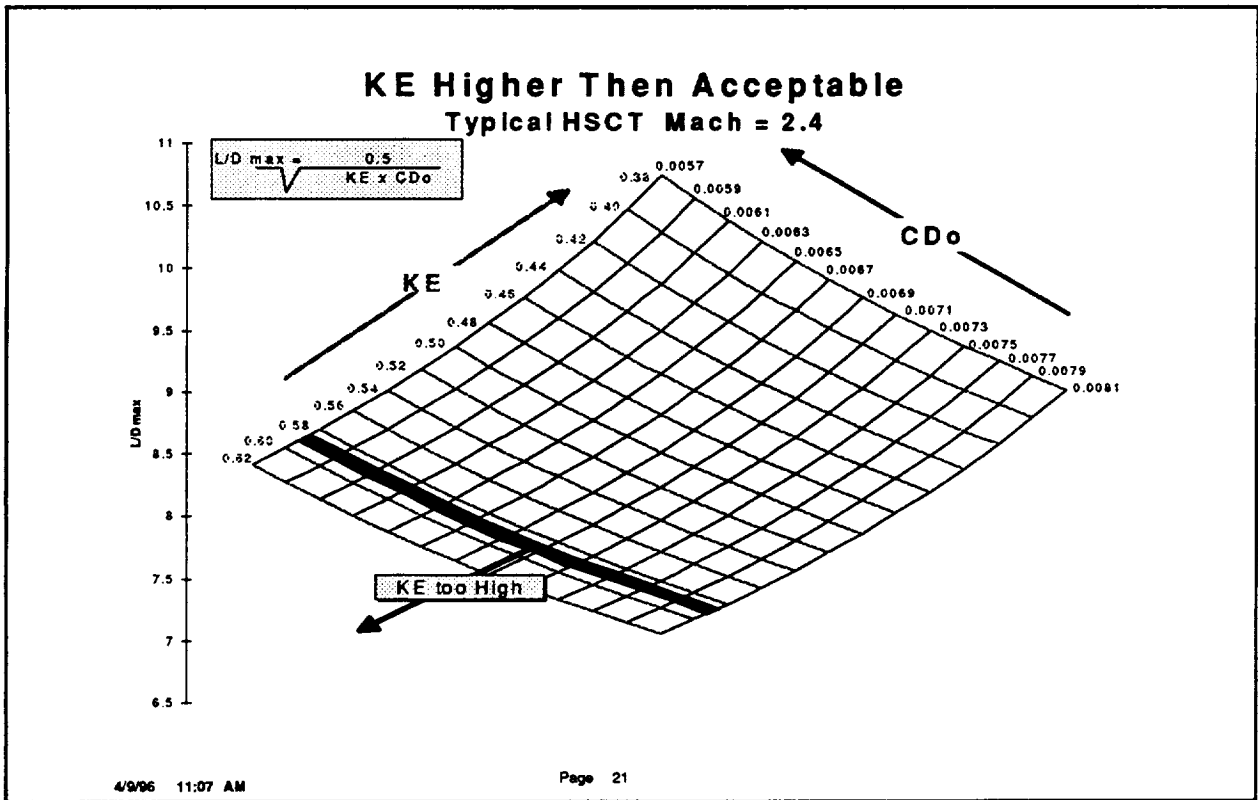
4/9/86 11:07 AM

Page 20

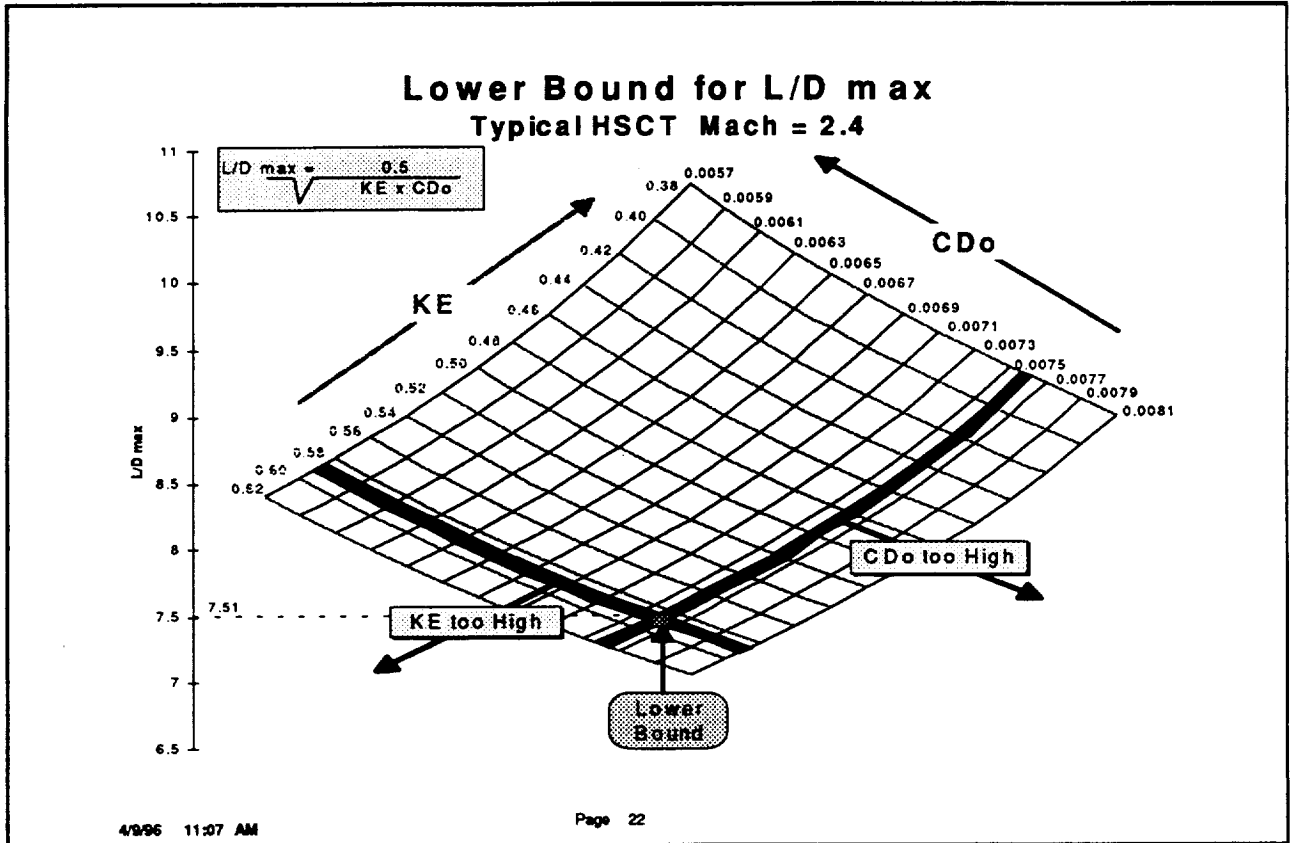
As an upper limit for KE we assume that the drag due to lift should be no worse the drag of a flat symmetric wing design with no leading edge suction.

We also assume no favorable interference lift or trim drag.

Again the drag for a very poor design can exceed this limit



This shows the “KE too high” boundary corresponding to the inverse of the lift curve slope.



The intersection of the “CDo too high” boundary and the “KE too high” boundary determines the lower bound for L/D max. This lower bound for L/Dmax essentially corresponds to the Concorde aerodynamic efficiency level.

LINEAR THEORY IS:

- LONG ON IDEAS
- SHORT ON ARITHMETIC

CFD IS:

- SHORT ON IDEAS
- LONG ON ARITHMETIC

R. T. Jones

4/9/96 11:07 AM

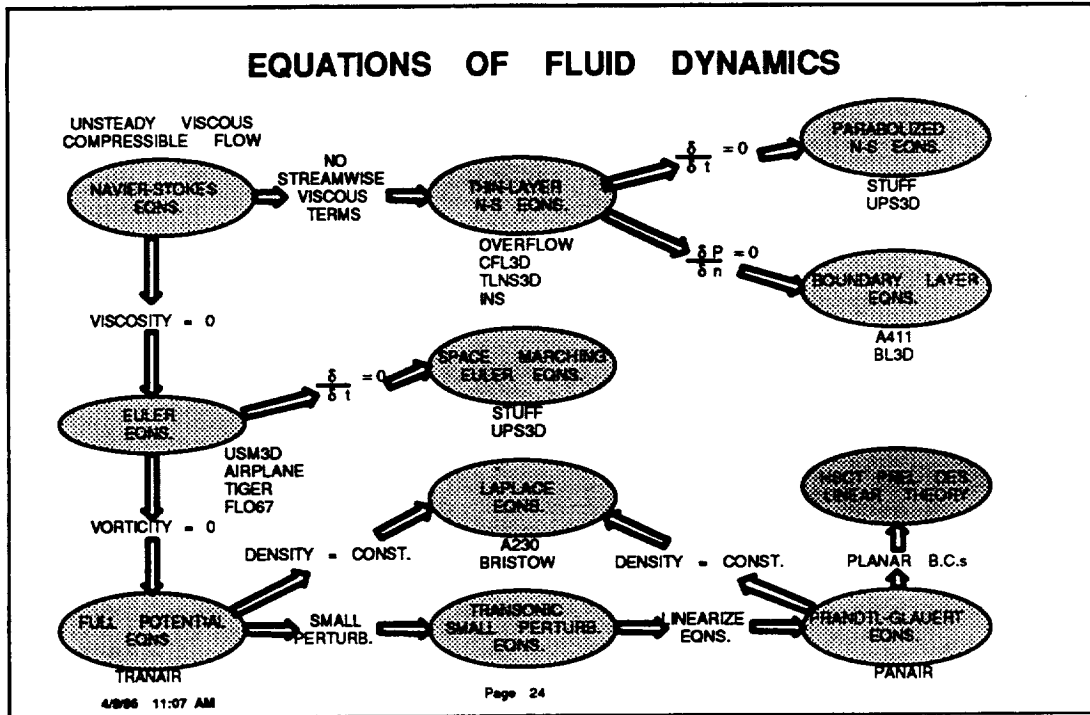
Page 23

In order to determine meaningful lower limits for both CDo and KE we will use fundamental aerodynamic concepts based on linear theory.

R. T. Jones has said: "Linear theory is long on ideas but short on arithmetic. CFD is short on ideas but long on arithmetic."

Linear theory formulations utilize elegant mathematical solutions of simplified flow equations. These solutions often provide insight into the nature of the flow fundamentals.

CFD utilizes powerful numerical solutions of complicated nonlinear flow equations. The solutions can provide details of the flow features for the analysis conditions.



This shows the hierarchy of fluid dynamic equations starting from the unsteady viscous compressible flow Navier-Stokes equations.

The key assumptions in reducing the complexity of the equations to move to the next lower level are also shown.

Some of the various CFD codes in use by NASA and industry are shown next to basic set of equations that are solved by the codes. The Navier-Stokes flow solvers also can be used to solve the Euler equations.

The The HSCT preliminary design linear theory methods reside at the bottom of the hierarchy.

Equations of Fluid Dynamics (continued)

There are a number of simplifying assumptions that are inherent even in the Navier-Stokes equations. The Navier-Stokes equations assume that the fluid medium is a single component perfect gas that can be treated as a continuum in which stress is proportional to strain, and pressure is proportional to density times temperature. Relative to the Navier-Stokes equations, the HSCT linear theory equations assume:

1. inviscid flow: The viscous effects are included in the skin friction drag. This requires care in applying the linear theory to avoid conditions leading to separated flow.
2. Irrotational Flow: The irrotational flow assumption greatly simplifies the numerics of a flow field solution since a single scalar equation is solved in terms of a velocity potential. The vector flow field can be obtained from the velocity potential scalar function. This limits the flow to moderate strength shocks, and non-rotational flow. However, these favorable flow conditions correspond to those on a low drag HSCT Configuration.
3. Small Perturbations. The Assumptions of small perturbations allows the velocity potential equations to be linearized. The solution process to becomes much easier. In addition, linearization allows the powerful concept of superposition to be used. This allows separation of the volume and the lifting effects and provides fundamental understanding of the flow phenomena. Again, the assumption of small perturbations is quite valid for HSCT low drag configurations which tend to be thin and slender, and operate at low lift coefficients.
4. Planar boundary conditions. The assumption of planar boundary conditions further simplifies the solution process. The sources / sinks and lifting elements that represent the geometry must lie on the axes of the fuselage, or the nacelles; and in the plane of the wing. These planar boundary conditions restrict the geometry to circular body and nacelle cross sections, and mid wing / body configurations. It is therefore easy to misapply the theory. In addition design details such as wing / body intersections or nacelle diverter geometry can not be analyzed directly.

Elegant numerical and analytic solutions are possible. These solutions can provide insight and a fundamental understanding of key design variables, design sensitivities and potential performance levels.

The major difficulty with the planar boundary conditions is that numerical singularities can occur in the solution processes. The numerical analyses methods must properly treat these localized numerical singularities.

Currently, the linear theory methods most commonly used for designing optimum wing camber and twist, result in singularities in the camber / twist definitions. The smoothing process significantly reduces the potential benefits of camber optimization. It is felt that non-linear optimization will be able to achieve drag benefits identified by the linear theory predictions but are unachievable by the linear designs.

TWO FUNDAMENTAL QUESTIONS

- 1. WHY CAN LINEAR THEORY DEFINE LIMITS ?**
- 2. WHY CAN'T LINEAR DESIGNS ACHIEVE LIMITS?**

4/9/06 11:07 AM

Page 26

We must answer two fundamental questions:

- Why can linear theory be used to define lower bounds for both CDO and KE that could be obtained using advanced non-linear CFD methods?
- Why can linear theory designs not achieve these lower limits ?

Linear Theory Analyses vs CFD Analyses

- Underestimates Compression Pressures
- Overestimates Expansion Pressures
- Disturbances Carried Along Free Stream Characteristics
- Easy to Incorrectly Apply Linear Theory
- Does not capture interference between lift and volume
- USES LINEAR PLANER BOUNDARY CONDITIONS
- ***** ARE THESE SIGNIFICANT ?? *****
- **FACT: Drag Predictions do Match Test Data for Good Designs**

4/8/06 11:07 AM

Page 27

Let us examine what the differences are in the results of linear theory analysis tools and results of corresponding non-linear CFD analysis. Not all linear theory methods are the same. The specific linear theory method used in the Boeing HSCT Preliminary design studies is the "Middleton / Carlson" program developed under a NASA contract in the mid 1907's time period. This methodology is a linear theory with planar boundary conditions. Consequently it is easy to incorrectly apply the theory by application to configurations for which planar boundary conditions are not adequate.

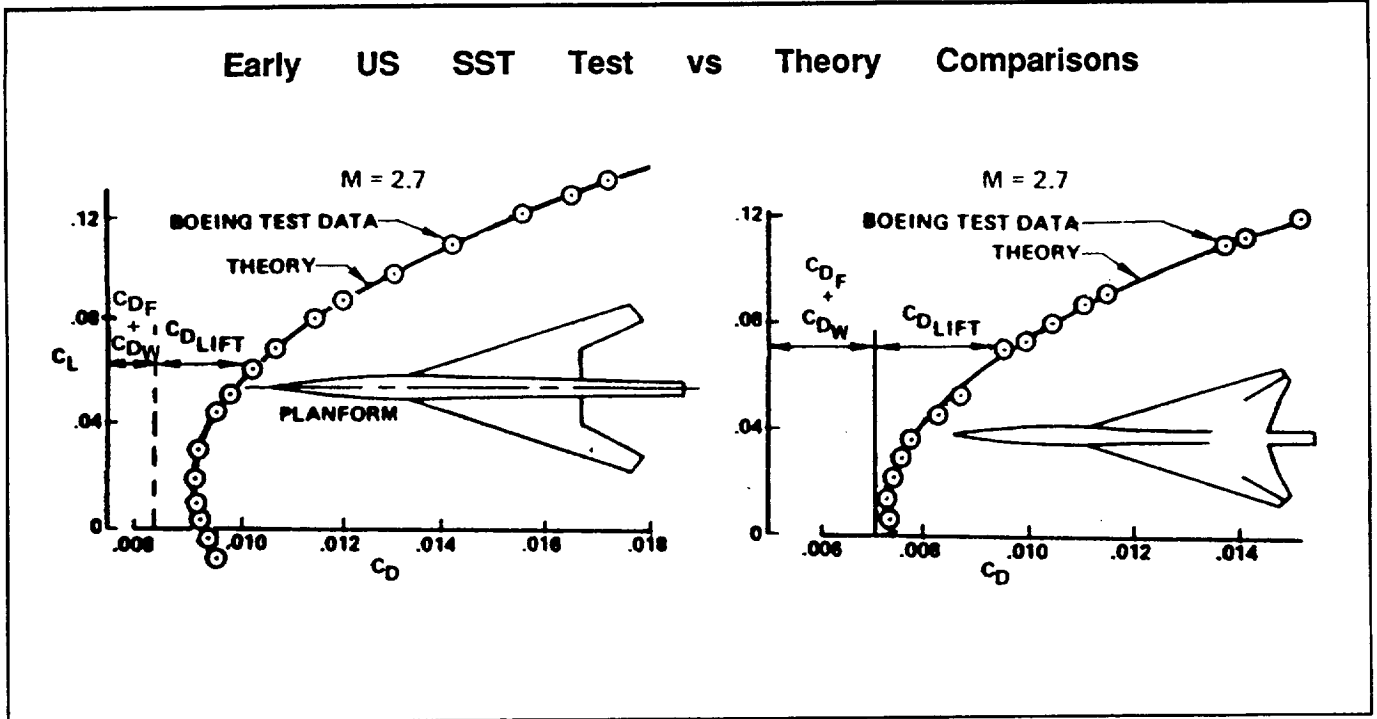
Linear theory under estimates compression pressures and over estimates expansion pressures. In addition, the linear theory disturbances are propagated along free stream Mach lines and therefore can not adequately predict shock formations. Linear theory does not predict interferences between lift and volume.

These are not significant effects for long slender , thin configurations at low lift coefficients. These are the conditions for low drag supersonic configurations.

The major restriction is in the use of planar boundary conditions. It is very easy to misuse the theory and produce significant errors. Properly used linear theory can predict the drag characteristics of well behaved configurations very accurately.

The following few charts show typical linear theory vs test data comparisons that have been made for a variety of supersonic configurations at or near the design conditions.

Early US SST Test vs Theory Comparisons



These wing / body configuration were two of the early Boeing SST baseline concepts. The configuration on the left is the Boeing variable sweep concept that was selected as the winner of the SST competition.

The configuration on the right is the Boeing variable sweep integrated wing / empennage concept. This was the last variable sweep design before the B2707-300 delta wing concept was developed as the final US SST design.

The theoretical drag predictions included friction drag, wave drag due to volume, and drag due to lift.

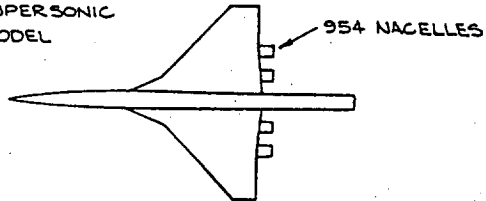
The skin friction drag was calculated as flat plate skin friction drag. The volume wave drag was calculated by the "Harris" far-field wave drag program. The drag due to lift was calculated by the Middleton /Carlson near field pressure integration method. These calculations were made in the early 1960's.

These are the same methods used today for the Boeing preliminary design studies.

The theoretical predictions agree very well with the test data.

Boeing B2707-300 US SST Configuration

B 2707 - 300
SUPERSONIC
MODEL

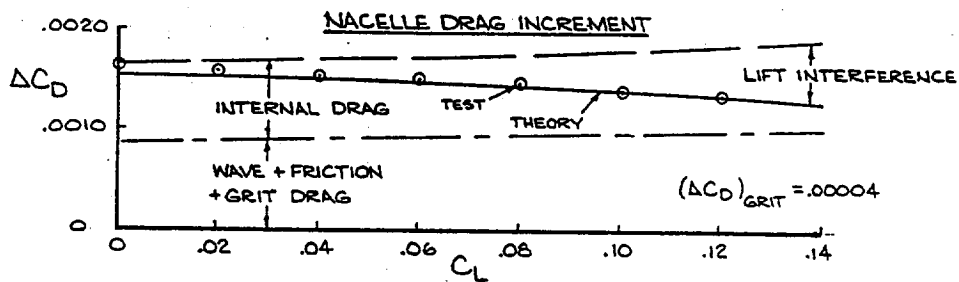


MACH 2.7

$R_e/FT. = 9.5 \times 10^6$

.01523 SCALE MODEL

SA - 1112 MODEL



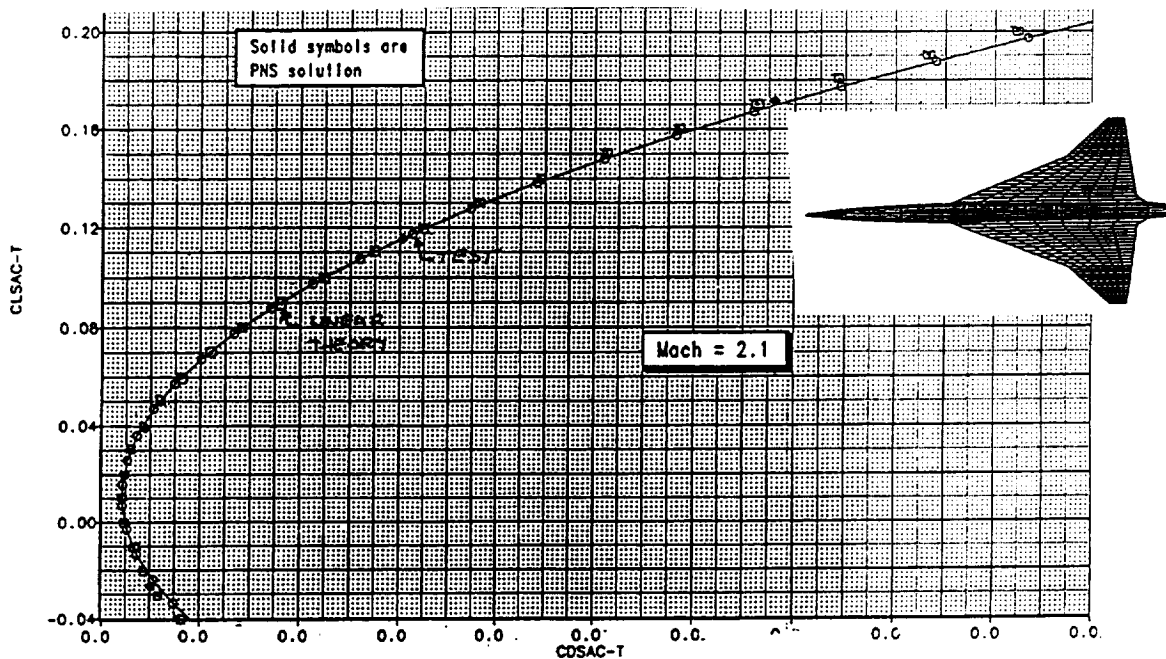
This compares measured and calculated nacelle installed drag increments for the US SST configuration.

Near field wave drag methods and drag due to lift methods were used together with flat plate skin friction calculations for the theoretical nacelle drag increments.

Linear theory was able to predict the significant amount of favorable interference drag that was actually achieved.

These calculations were made in the early time 1970 time period.

Boeing 1807 WT Configuration Mach = 2.1

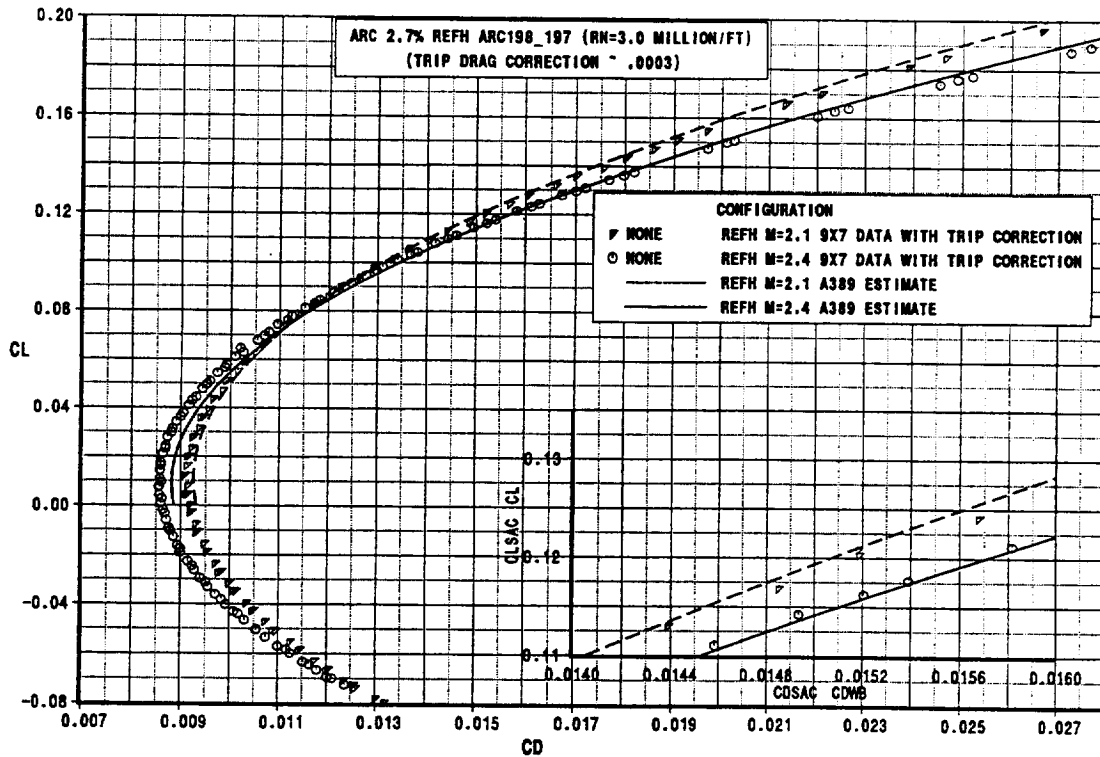


This was the first HSCT wind tunnel configuration that incorporated the unique Boeing developed blunt leading edge radius design. The design was developed by an iteration procedure of linear theory design and nonlinear theory analysis.

Linear theory drag predictions are compared with the test data at the original design Mach number of 2.1.

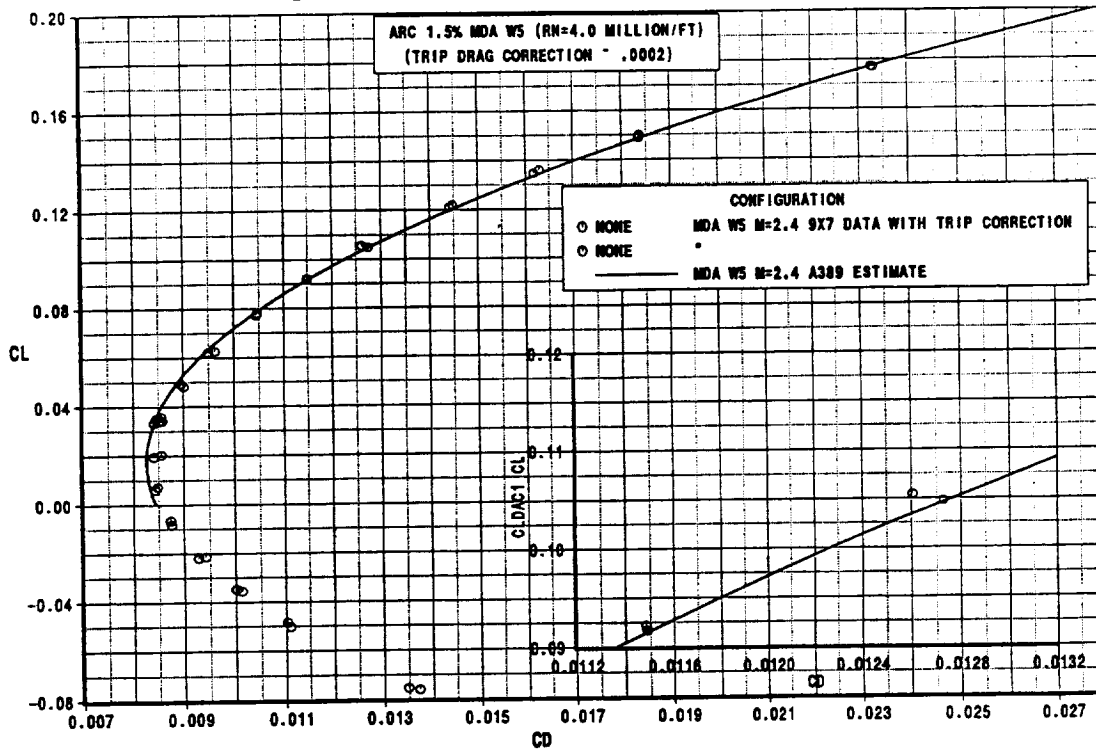
The test data are the circles with the curve drawn through them. The linear theory predictions are indicated by the squares. The predictions are in excellent agreement with the test data. This configuration was the predecessor to the Boeing developed Ref H geometry.

Comparison of Ref H Test Data With Predictions



The comparisons also indicate very good agreement with the linear theory predictions and the NASA Ames test data for the 2.7% Ref H wind tunnel model.

MDA Optimum W5 Arrow Wing Design



This figure shows a comparison of linear theory predictions with the test data for the NASA Ames / MDA non-linear arrow wing configuration, W5. This model was the result of a very successful NASA/ industry joint nonlinear design optimization activity involving NASA Ames and McDonnell-Douglas,

The test and theory agree very well. The comparisons in this figure and the previous figures were made at or near the design Mach number. The linear theory predictions typically do not agree as well with test data at off-design Mach numbers. The theory does not properly account for the leading edge forces that typically occur at the off design Mach numbers.

However for the purpose of establishing meaningful performance improvement projections, we are concerned about the usefulness of linear theory predictions at the design Mach number conditions.

Linear Theory Design

- **Near Field Design for Camber and Twist**
 - Develops leading edge singularities in pressures or slopes
 - Requires hand smoothing of camber surface
 - Fails to achieve drag due to lift potential
 - Very little applications to thickness optimization
- **Far Field Theory Design**
 - Not bothered by edge forces
 - Has been restricted to body optimization and area ruling
 - Verified by non-linear design applications
 - Very easy to misapply the theory
- **Planar boundary conditions limits design details**

4/9/96 11:07 AM

Page 33

“Near field” methods calculate the pressure distributions on the surface of a configuration. These pressure distributions are then are integrated to obtain the aerodynamic forces on the configuration.

Near field methods can be used develop optimized linear theory camber and twist distributions. Mathematical singularities in the solutions can produce localized infinite slopes or pressures. The designs that produce the pressure singularities are difficult to evaluate properly and can often lead to leading edge separated flow. The designs that result in singularities in the surface slopes require that the linear theory designs be hand modified in the regions where the singularities occur. These regions include the wing root and near any break in the leading edge sweep. This smoothing process has a rather significant adverse effect on the drag. Consequently the linear theory designs fail to achieve the theoretical low drag potential. Very little has been done in the area of wing thickness optimization using linear theory until very recently. A new far field approach has been developed and appears quite promising.

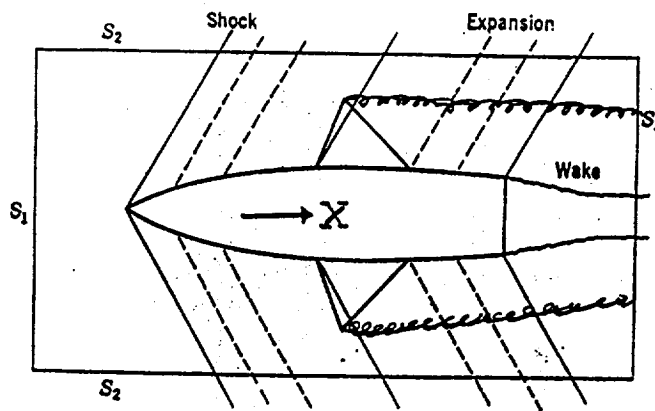
“Far field” theory has been used to optimize body area distribution and to develop area rule body shapes to minimize wing / body interference effects.

Linear theory concepts and methods have been very successful in developing low drag nacelle installations.

Because of the planar boundary conditions, linear theory cannot capture design details. This can also be a significant limitation.

The linear theory fundamentals are considered reasonable to identify meaningful lower bound drag levels, however, linear theory cannot produce the designs that achieve these levels.

FAR-FIELD THEORY DRAG CALCULATION



- MOMENTUM CHANGE THRU S_1 AND S_3 :
 - FRICTION DRAG
 - WAKE DRAG
 - VORTEX DRAG
- STREAMWISE MOMENTUM CHANGE THRU S_2
 - VOLUME WAVE DRAG
 - LIFT WAVE DRAG

Far field theory drag calculation methods are derived from a control volume approach. The configuration is enclosed in a large cylinder that extends both radially and downstream a great distance from the configuration. The streamwise momentum change through the ends of the cylinder is equal to the friction drag, any base or wake drag plus the induced drag. The induced drag equation for supersonic flow is exactly equal to the subsonic induced drag equation.

At supersonic speeds, the shock waves and expansion waves that are generated by the configuration pass through the cylindrical surface. The resulting streamwise loss of momentum through the cylindrical surface is equal to the volume wave drag plus the wave drag due to lift.

BODY WAVE DRAG

$$\frac{D_w}{q} = \frac{1}{2\pi} \int_0^L \int_0^L S''(x)S''(\xi) \ln|x - \xi| dx d\xi$$

This Similar to the Induced Drag Equation with: $\Gamma \approx \frac{dS}{dx}$

The Slope of the Optimum Body Area Distribution must be Elliptic

$$\left(\frac{dS}{dx}\right)_{Opt} \approx \sqrt{1 - \left(\frac{x}{L}\right)^2}$$

Therefore:
$$S_{Opt} = A \max \left[1 - \left(\frac{x}{L}\right)^2 \right]^{3/2}$$

MINIMUM DRAG FOR GIVEN VOLUME : SEARS-HAACK BODY

4/9/86 11:07 AM

Page 35

Von Karmen represented a body of revolution as line of sources and sinks. He obtained the above equation for the wave drag of a body of revolution.

This form of this equation is very similar to the induced drag equation shown earlier. The function in the induced drag equation is the spanwise derivative of the circulation or lift distribution, while the similar function in the wave drag equation is the second derivation of the area distribution.

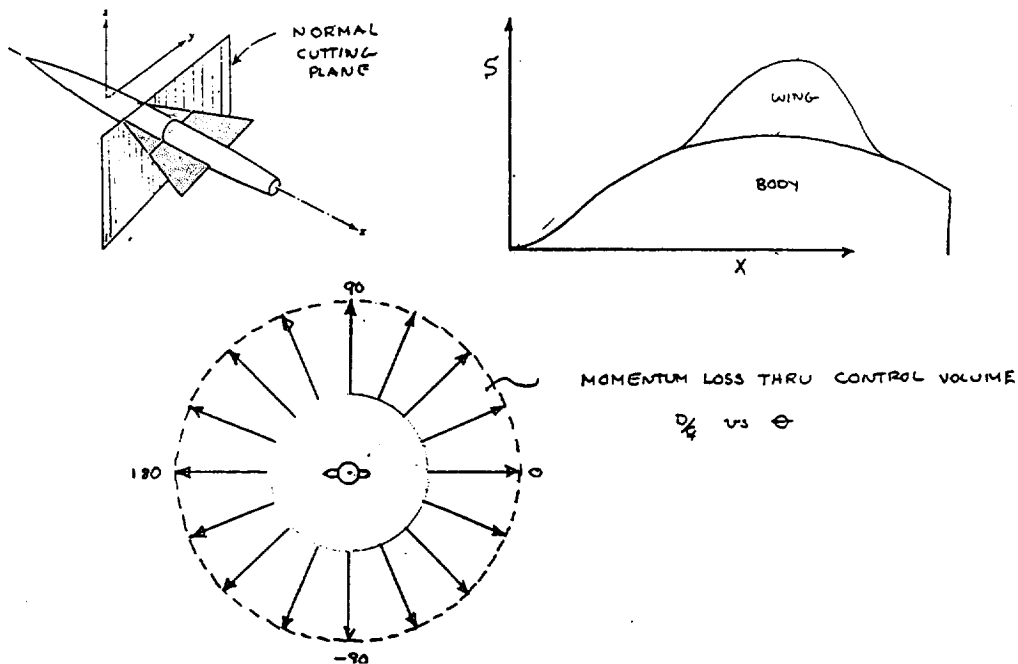
The optimum lift distribution for minimum drag is elliptic. Because of the mathematical similarity of the wave drag equation, we can immediately note that the slope of the optimum body shape must also be an elliptic distribution.

The optimum body area distribution for a given body is then obtained by integration of the elliptic slope distribution.

This resulting shape is called a Sears-Haack body, which is the minimum drag body shape for a given volume.

TRANSONIC AREA RULE

$M \approx 1.0$



- **MINIMUM DRAG: COMBINED NORMAL AREA DISTRIBUTION IS A SEARS-HAACK BODY**

A symmetric wing plus body, in linear theory, can be represented by line sources for the body and a planar sheet of sources for the wing.

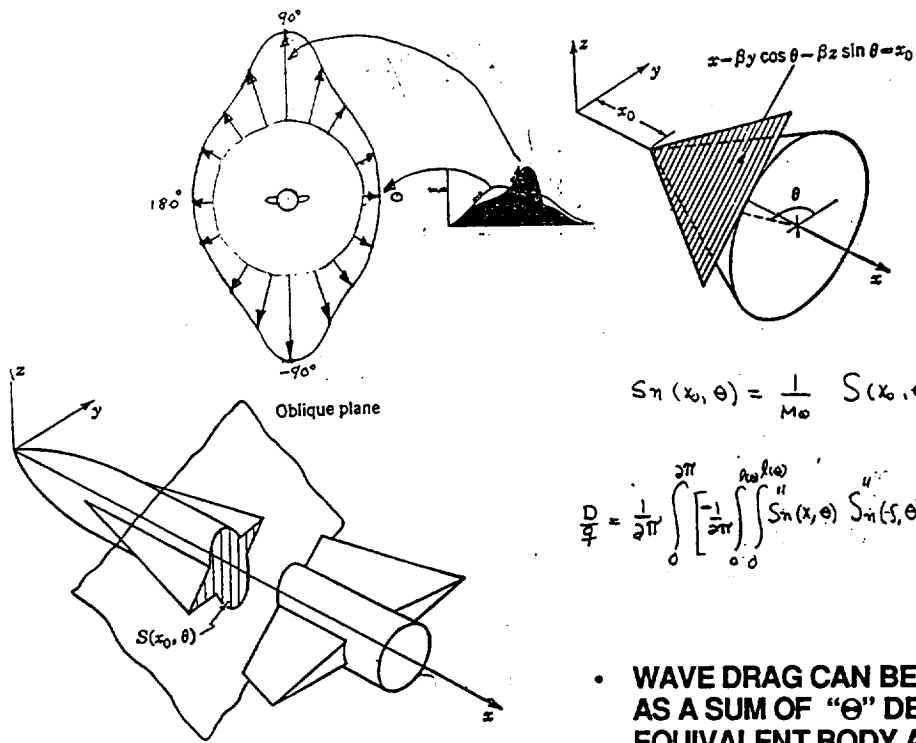
Whitcomb discovered experimentally and Hayes discovered analytically that near Mach one, the wave drag of the wing plus body is the same as that of an equivalent body which has an area distribution equal to the wing body cross sectional area distribution.

The physical interpretation of this result is as follows. Near Mach one the disturbances caused all of the sources radiate out in planes normal to the body axes. Linear theory allows superposition. Hence, all the sources in the same plane can be slide to the body axes without changing the drag. This results in the equivalent cross sectional area body.

Therefore, the wave drag at Mach one can be calculated by the isolated body wave drag equation with the area in the equation equal to the cross sectional area obtained by a cutting plane normal to the body axis.

Thus the minimum volume wave drag for a symmetric wing plus body near Mach one occurs if the combined area distribution is equal to a Sears-Haack body.

SUPERSONIC AREA RULE



$$S_n(x_0, \theta) = \frac{1}{M_\infty} S(x_0, \theta)$$

$$q_D = \frac{1}{2\pi} \int_0^{2\pi} \left[\int_0^{r_{max}(\theta)} S_n(x, \theta) S_n(s, \theta) \ln|x-s| dx ds \right] d\theta$$

- **WAVE DRAG CAN BE CALCULATED AS A SUM OF "θ" DEPENDENT EQUIVALENT BODY AREA DISTRIBUTIONS DRAGS**

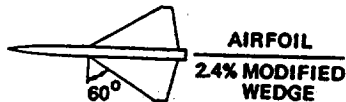
At supersonic speeds greater than Mach one, the disturbances from the sources and sinks that represent the wing / body propagate in the downstream Mach cones.

The momentum loss around the configuration is no longer symmetric. However the concept of sliding all sources / sinks in the same propagation plane still applies.

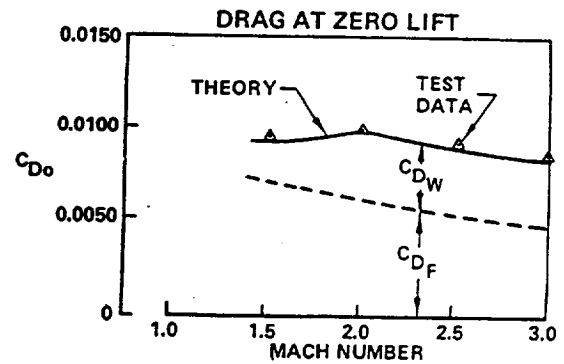
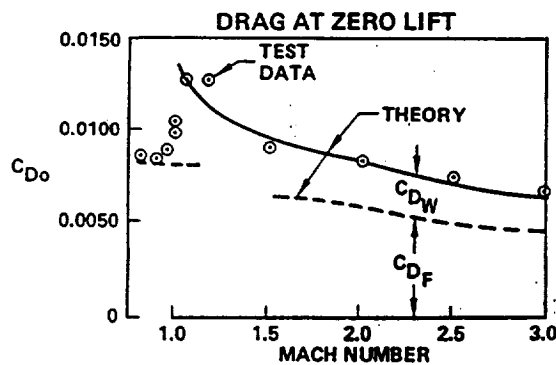
The propagation planes are tangent to Mach cones with vertices on the axes of the body. The propagation planes are identified by the angle theta. Theta zero represents momentum loss on the plane of the wing. Theta 90 represents momentum loss in the Z axes above the configuration. All the sources / sinks in the cut through the wing / body planar surface corresponding to the intersection of the propagation plane at a given angle theta are slid along the intersecting cut to the axes of the body. This creates a theta dependent equivalent body for each cutting plane angle from 0 to 360 degrees. The wave drag of the configuration is then calculated from the sum of the drags of the theta dependent bodies.

TYPICAL ZERO LIFT DRAG ASSESSMENTS - SYMMETRIC CONFIGURATIONS

AR = 1.51
 $\lambda = 0.14$
 $\zeta = -0.14$



AR = 1.55
 $\lambda = 0.2$
 $\zeta = 0.5$



This is a typical test versus theory comparison of drag at zero lift (C_{D0}) for two symmetric wing / body configurations.

The theoretical predictions include fully turbulent flow flat plate skin friction drag plus the volume wave drag calculated by the supersonic wave drag program.

The test versus theory agreement is very good and shows that the far field wave drag method can give valid drag predictions.

"LOWER BOUND" SUPERSONIC WING / BODY WAVE DRAG

$$\frac{D_{wv}}{q} = \frac{1}{2\pi} \int_0^{2\pi l(\theta)} \int_0^{l(\theta)} \int_0 S''(x, \theta) S''(\xi, \theta) \ln|x - \xi| dx d\xi d\theta$$

- "MINIMUM" DRAG: EACH "θ" EQUIVALENT BODY IS A SEARS-HAACK BODY
- USUALLY IMPOSSIBLE TO ACHIEVE

4/2/96 11:07 AM

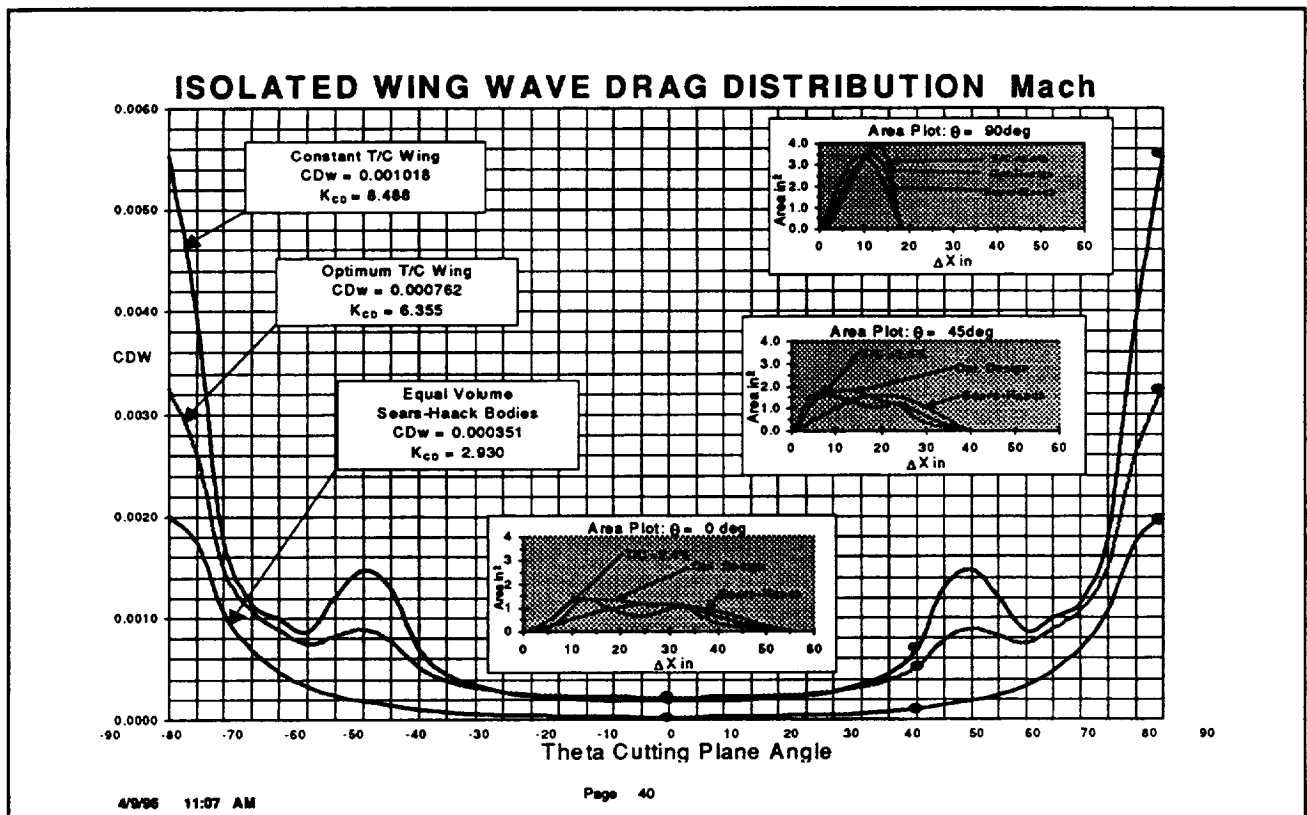
Page 39

This is the far field for a symmetric non-lifting configuration. The volume wave drag is the average of the theta dependent equivalent bodies.

Because of the similarity of this equation with the transonic wing / body equation, it follows that the lower bound zero lift wave drag for any symmetric configuration occurs if each of the theta dependent equivalent body is a Sears-Haack body for the same length and maximum area.

This lower bound is exact for a yawed elliptic wing with a circular arc wing section and constant spanwise curvature. However, it is generally impossible to define such a volume distribution for an arbitrary wing / body configuration.

Thus we need a more realistic lower bound for zero lift wave drag.



This figure shows the equivalent body wave drag as a function of the cutting plane angle. The angle is from -90 deg which is below the configuration around to the right of the configuration at 0 deg to the top of the configuration, theta = 90deg. The drag variation is symmetric around to the left of the configuration and is not shown in the figure.

This is the drag for an isolated cropped delta wing with a supersonic leading edge (60 deg sweep) at Mach 3.0. Three drag levels are shown and correspond to:

- Constant T/Cmax = 2.4% wing
- Optimized spanwise T/Cmax wing with the same wing volume.
- The drag at every theta angle if the body shape was a Sears-Haack body

The small insert figures compare the equivalent body shapes at theta angles of 0, 45 and 90 deg.

The wave drag for the constant T/C wing is approximately $CD_w = 0.00102$. The wave drag of the optimum wing is $CD_w = 0.00076$. The lower bound wing drag level is $CD_w = 0.00035$ which is half of the optimized wing drag.

The difference between the lower bound and optimum drag levels would be less than a factor of two for wing plus body.

Consequently a factor of 1.75 times the lower bound drag is used for our achievable lower bound limit on zero lift wave drag.

CD₀ "TOO LOW" LIMIT

$$CD_0 > CD_F + 1.75 CD_{W SH}$$

- FULLY TURBULENT FLAT PLATE SKIN FRICTION
- WING / BODY WAVE DRAG = 1.75 X EQUIVALENT SEARS-HAACK BODY
- ZERO INSTALLED NACELLE WAVE DRAG
- EMPENNAGE WAVE DRAG INCLUDED IN WING / BODY WAVE DRAG
- *** DRAG "CAN'T" BE LOWER THAN THIS ***

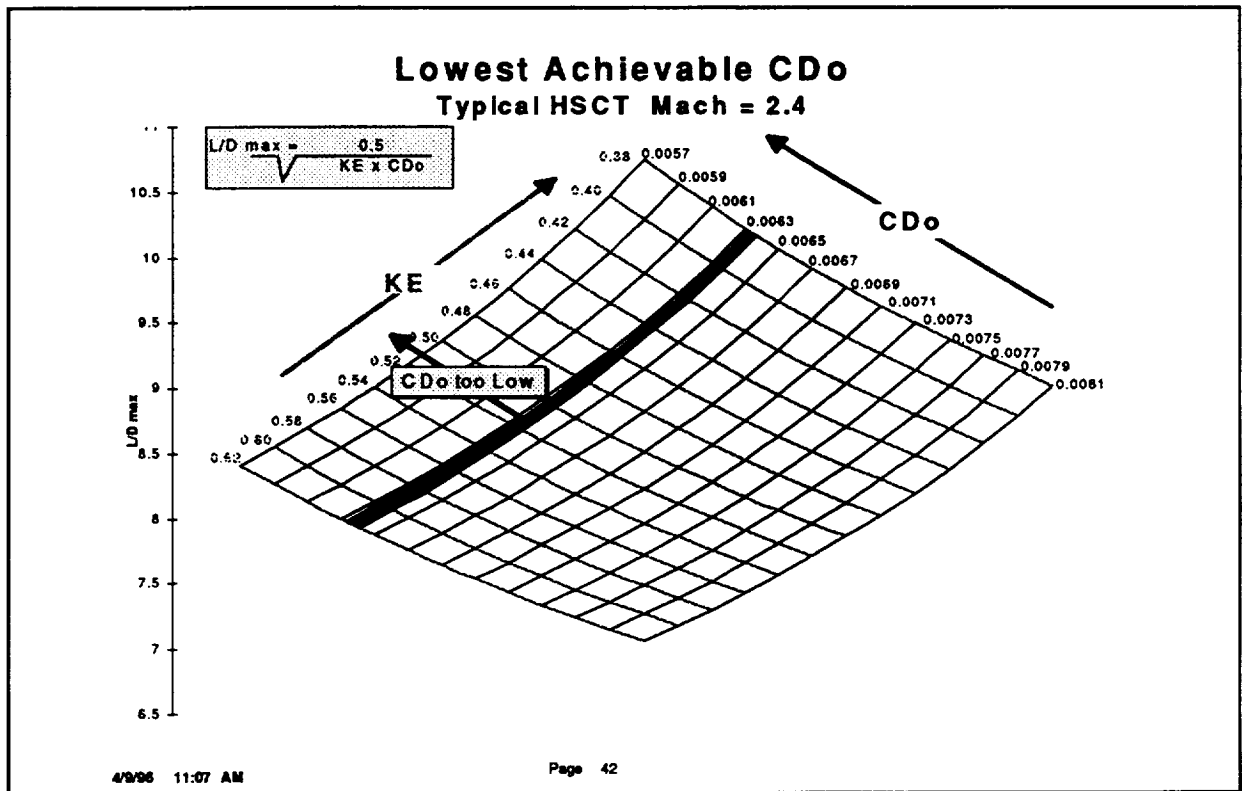
4/9/86 11:07 AM

Page 41

The "too low" limit for zero lift drag is equal to the sum of:

- Fully turbulent skin friction drag
- Wing / body volume wave drag equal to 1.75 times the drag of an equivalent Sears-Haack body having the same maximum area as the combined wing plus body area distribution and the length of the fuselage. The empennage drag is included as part of the wing / body drag.
- Zero installed nacelle wave drag

The zero lift "can't be lower" than this level for the given configuration.



This shows the CDo "too low" boundary for the example HSCT configuration.

Wave Drag Due to Lift

$$\frac{D_{wl}}{q} = \frac{\beta^2}{4\pi^2} \int_0^{2\pi} \sin^2(\theta) \int_0^{l(\theta)} \int_0^{l(\theta)} \frac{dl(x, \theta)}{dx} \frac{dl(\xi, \theta)}{d\xi} \ln|x - \xi| dx d\xi d\theta$$

$$\beta = \sqrt{M^2 - 1}$$

- **Lower Bound Drag:** Each “ θ ” Lift Distribution is Elliptic
- **Usually Mathematically Impossible** to Define such a overall lift distribution on the wing.

4/8/86 11:07 AM

Page 43

The far field theory drag equation can be extended to the calculation of wave drag due to lift by replacing the volume producing source elements by lift producing vortex elements. The resulting wave drag due to lift equation is shown in the figure.

Notice the $\sin^2\theta$ term in the equation. This indicates that the contribution to wave drag due to lift is zero in the $\theta = 0$ plane.

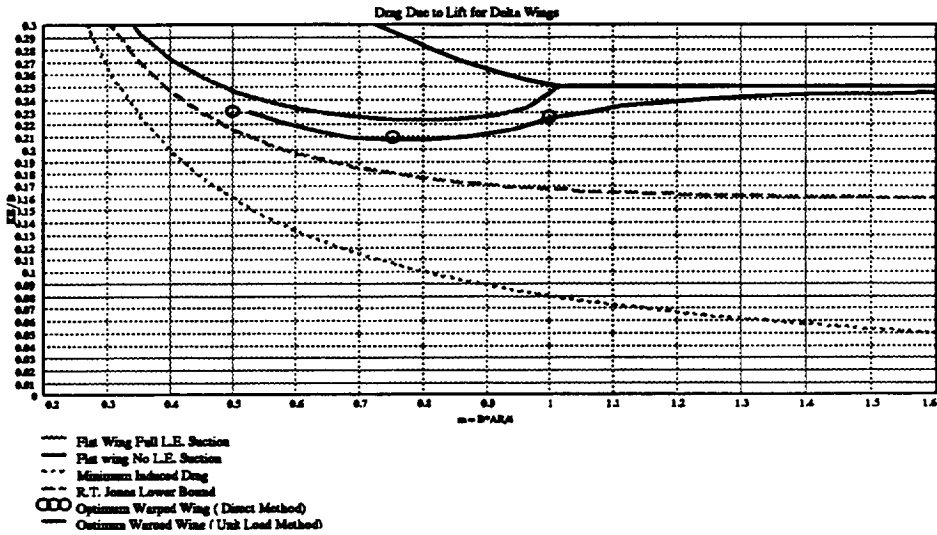
Because of the β^2 term, the wave drag due to lift is seem to equal zero at Mach =1 and increases rapidly with Mach number.

Since this equation is very similar to the previously shown induced drag equation and the supersonic wave drag equation, It is obvious that the lower bound for drag due to lift would occur if every “theta” lift distribution were elliptic.

This is exactly the case for a uniform load yawed elliptic wing. However it is usually impossible to prescribe a load distributions far any arbitrary planform that would be elliptic for all theta angles.

Hence this lower bound is in general not a realistic lower limit.

Delta Wing Supersonic Drag Due to Lift Potential



4/8/86 11:07 AM

Page 44

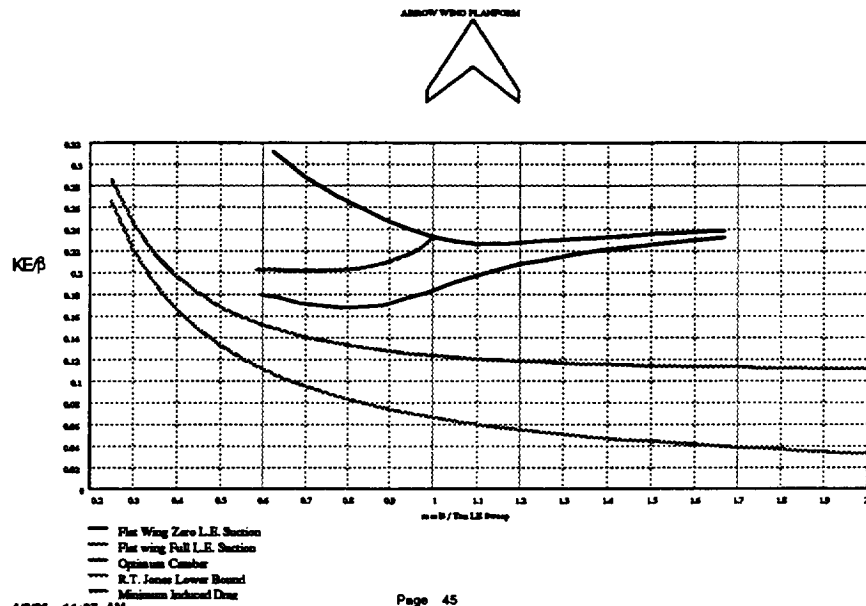
In order to arrive at a more meaningful achievable lower bound for supersonic drag due to lift let's look at various drag due to lift levels for a delta wing planform as shown in the above figure.

The horizontal axis variable m is the ratio of the tangent of the free stream Mach angle to the tangent of the wing leading edge sweep. A value of m less than one indicates that the leading edge is swept behind the Mach line (subsonic leading edge).

The lower "dotted line" is the minimum induced drag corresponding to an elliptic spanwise lift distribution. The "dash" line is the sum of the minimum induced drag plus the previously discussed lower bound wave drag due to lift. The upper curve is the upper bound for drag due to lift corresponding to a flat wing with zero leading suction. So the meaningful achievable drag due to lift must be somewhere between the "dash" curve and the upper curve.

The curve that starts at $m=1$ flat wing curve is the drag due to lift for a wing with full leading suction. The remaining drag due to lift curve is the minimum drag due to lift level calculated by near field linear theory. This drag level is about 95% of the flat wing with full leading edge suction. This is the simple criteria that is used for the achievable lower bound drag due to lift.

Arrow Wing Supersonic Drag Due to Lift Potential



This figure shows similar drag due to lift calculations for a classic swept arrow wing.

In this case, it is seen that the linear theory near field optimum drag due to lift potential is about 85% of the flat wing with full leading suction. As previously mentioned, the linear theory designs to achieve this drag level are physically impossible. However, it is felt that the drag level is achievable, but not by linear theory.

We will use for the achievable lower bound for wing body drag due to lift a level equal to 95% of the flat wing with full leading edge suction.

KE "TOO LOW" LIMIT

$$KE > KE_{S=1} \{ KE_{FAC} - 2 K_{NAC} (\Delta CL_W/CL) - K_{TRIM} (KE_{S=1}/K_{TAIL}) (S_{HT}/S_{REF}) \}$$

- WING / BODY KE 5% LOWER THAN "FULL SUCTION" DRAG LEVEL $\implies KE_{FAC} = 0.95$
- FAVORABLE LIFT INTERFERENCE : 65% OF "IDEAL" $\implies K_{NAC} = 0.65$
- FAVORABLE TRIM DRAG : 80% OF "IDEAL" $\implies K_{TRIM} = 0.80$

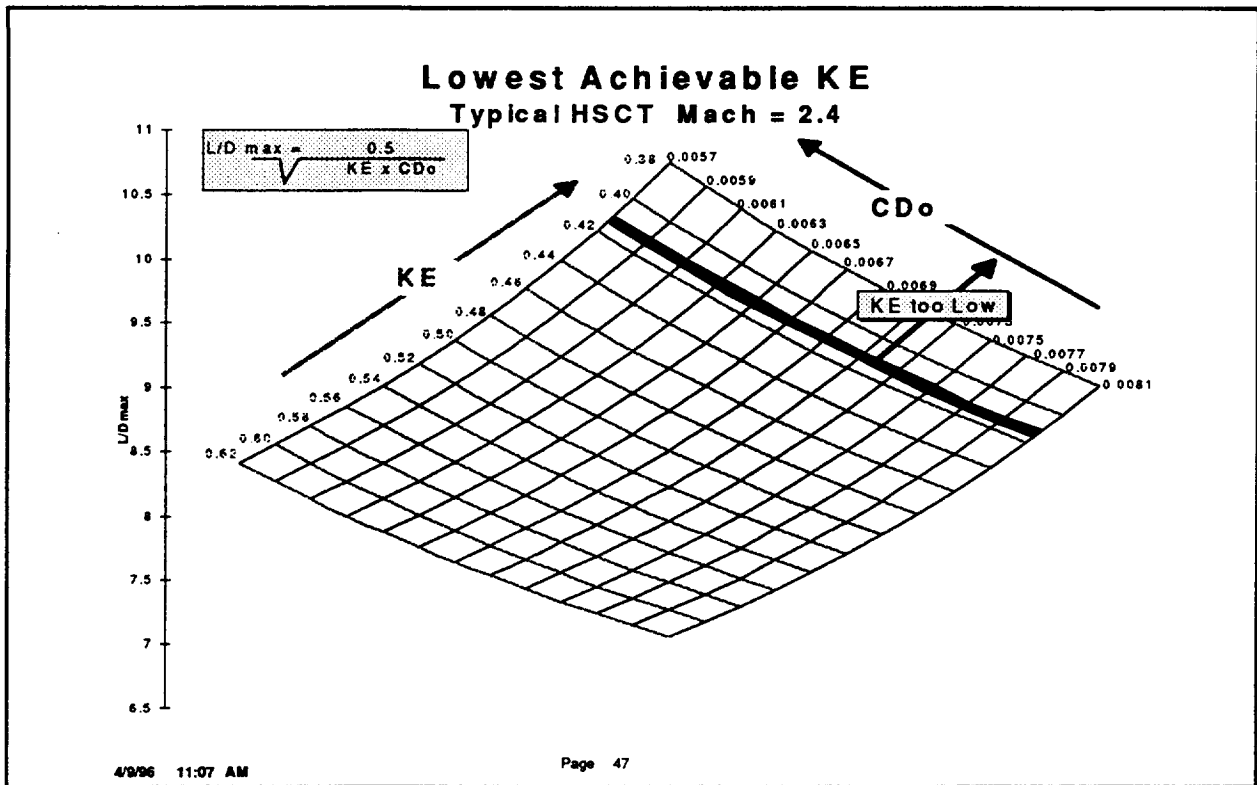
4/8/86 11:07 AM

Page 46

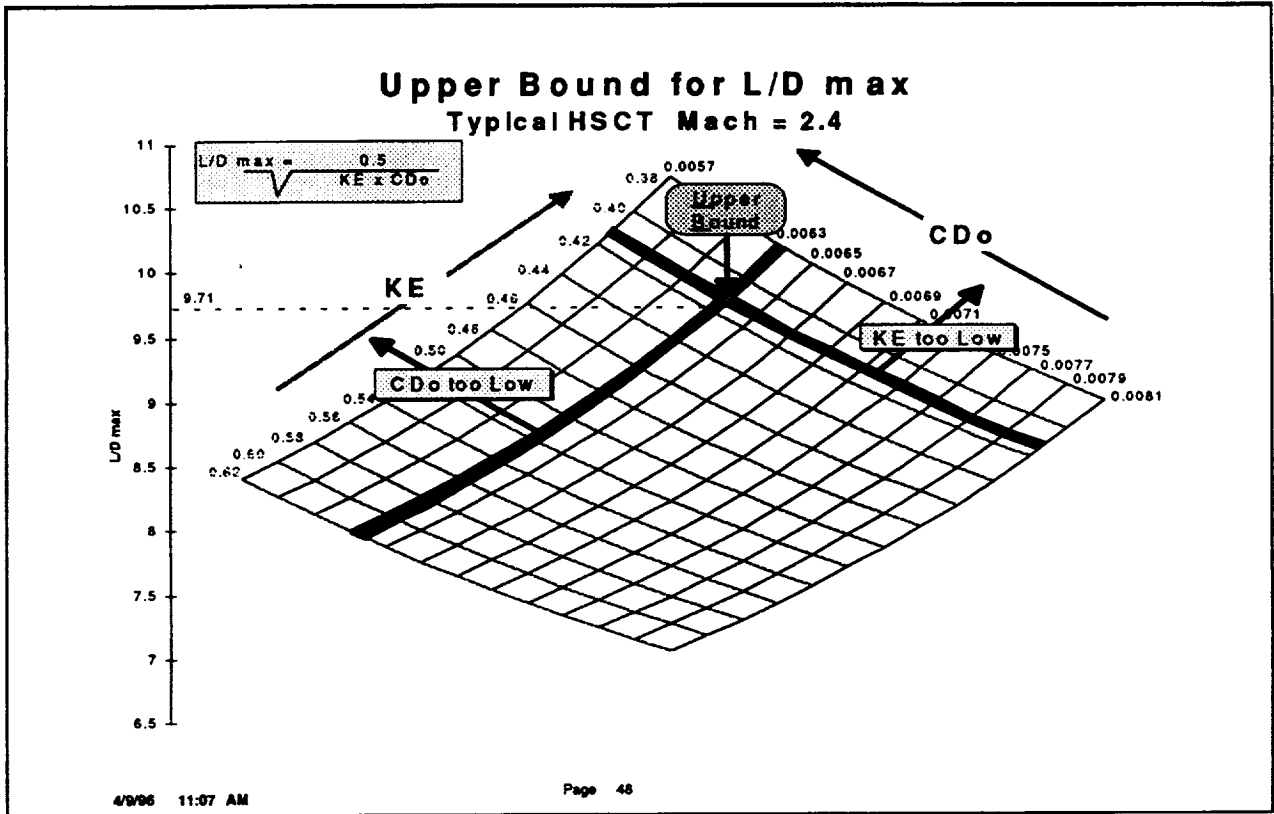
Nacelles designed properly to produce a positive pressure field on the lower surface of the wing can create a favorable interference lift that reduces the necessary wing / body lift for a given overall lift coefficient. This results in a reduction in wing / body drag due to lift. However, the nacelle pressure field acting on the wing camber surface produces a drag increment and the the wing lifting pressures acting on the nacelles produce an adverse buoyancy drag. On current nacelle installations about half of the ideal lift interference favorable interference is lost because of these two adverse effects. For the lower limit drag due to lift we assume that it is possible to achieve 65% of the ideal nacelle lift interference effects.

At supersonic speeds a horizontal tail upload will also result in a reduction in drag due to lift. The ideal level occurs when the tail upload is not reduced by any wing downwash effects. A favorable trim drag equal to 80% of the ideal level is considered to be achievable.

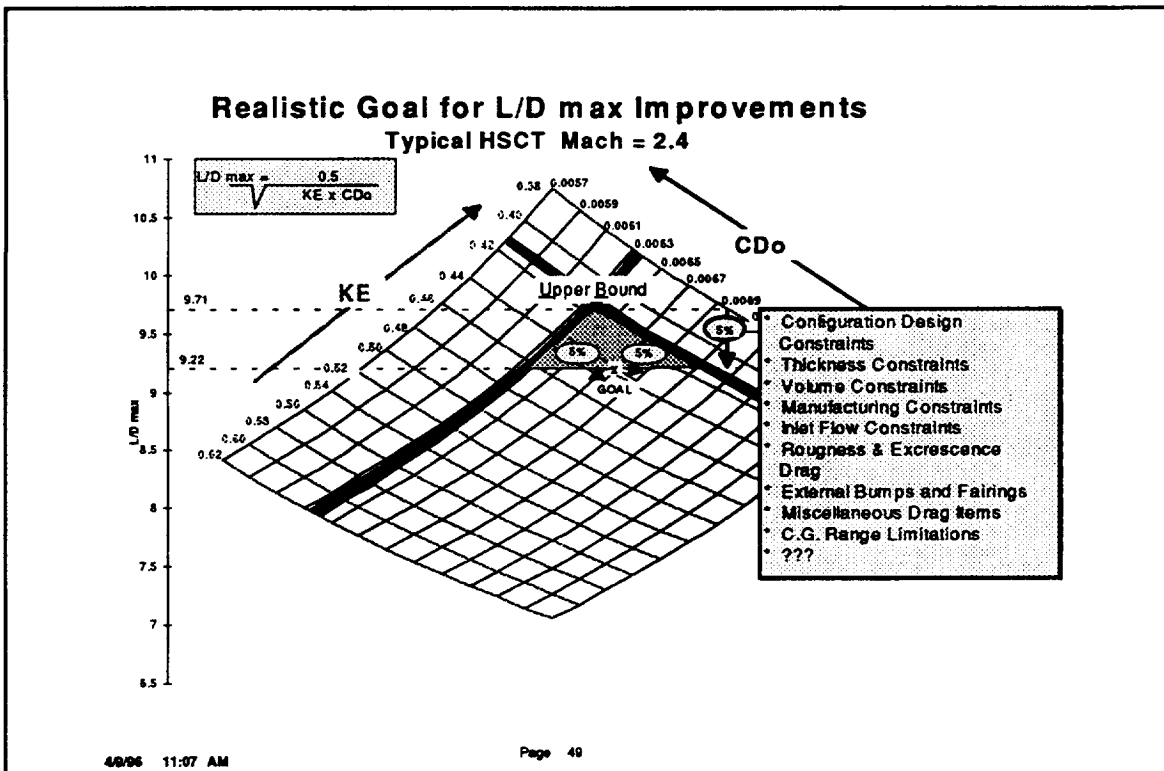
As previously mentioned, the achievable wing / body drag due to lift level that is used is equal to 95% of the flat wing with full leading suction.



This figure shows the "KE too Low" boundary for the example typical HSCT configuration.



The intersection of the CDo "too low" boundary with the KE "too low" boundary define the upper bound for L/Dmax

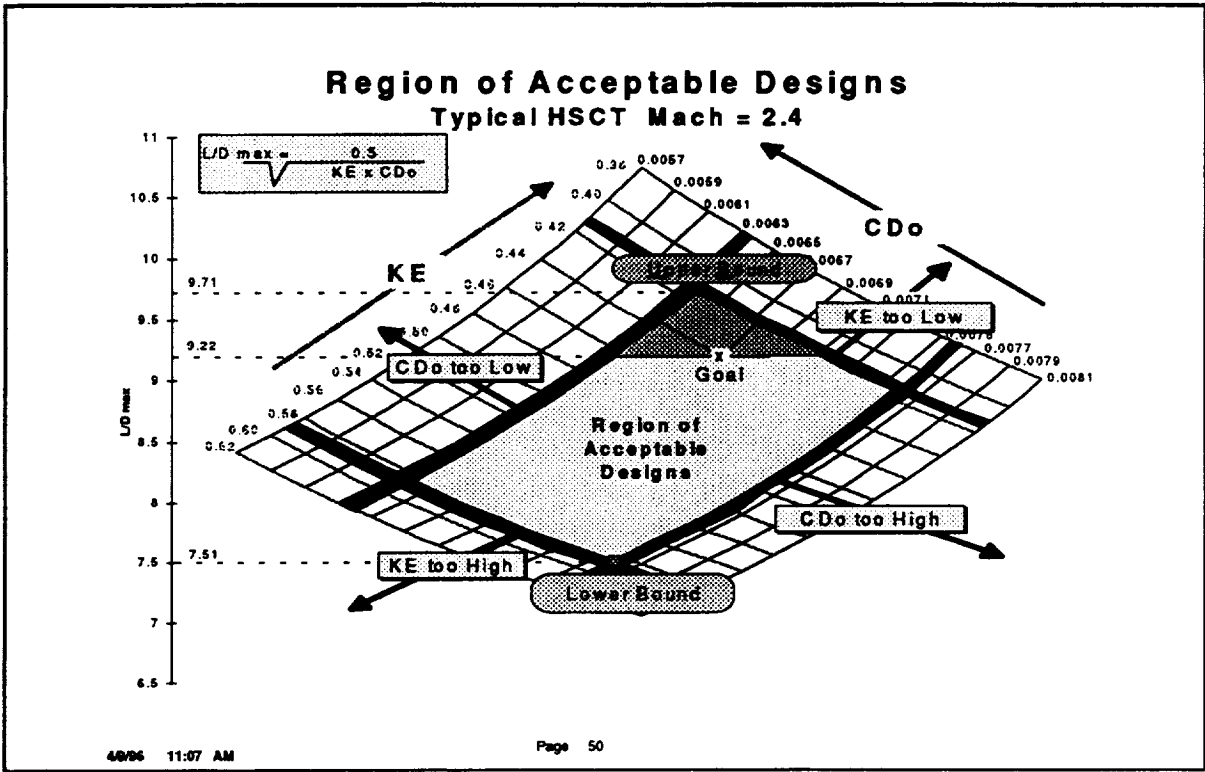


Similar to the subsonic aircraft “tops down”, the L/Dmax is practically not achievable because of other configuration design considerations.

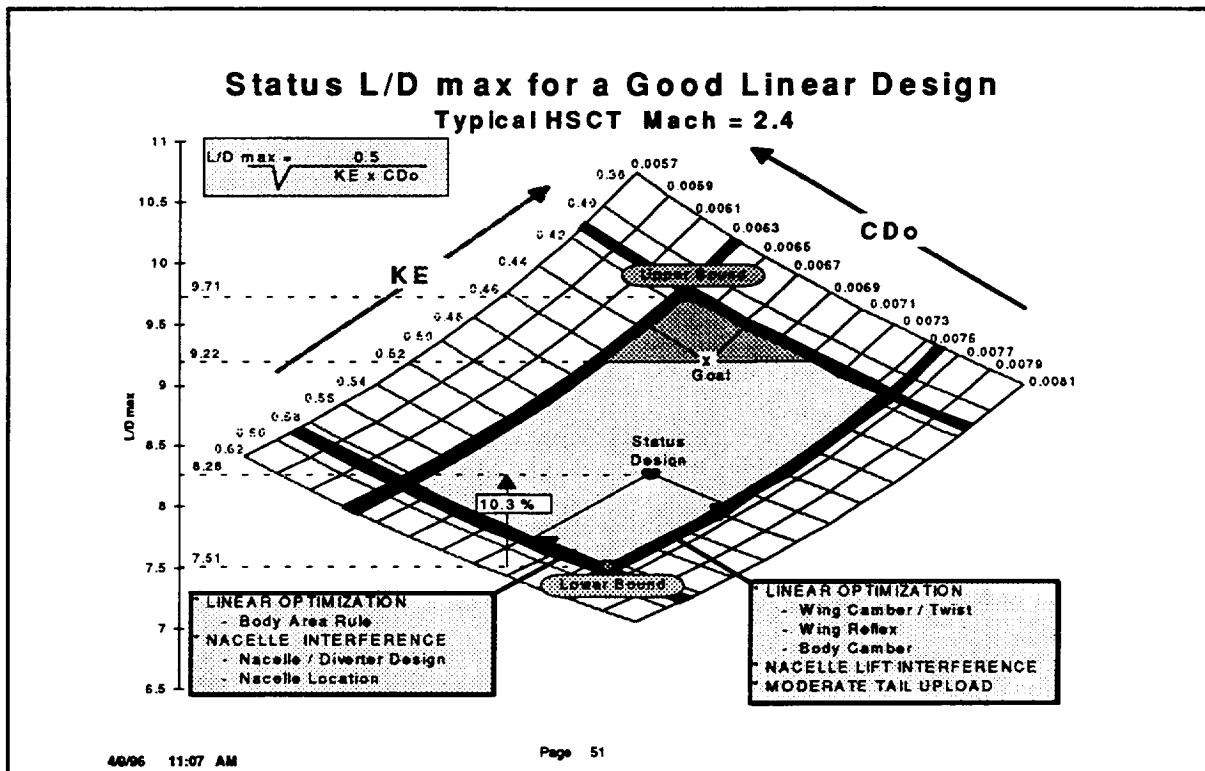
These factors for a supersonic transport aircraft include such factors as:

- Configuration thickness and volume constraints
- Manufacturing and surface curvature constraints
- Inlet flow constraints
- Ground clearance effects on aftbody upsweep
- External bumps and fairings
- Roughness and excrescence drag
- Cruise center cg gravity limitations
- Miscellaneous drag items

A “goal” L/Dmax equal to 95% of the achievable L/Dmax is used to account for these effects.



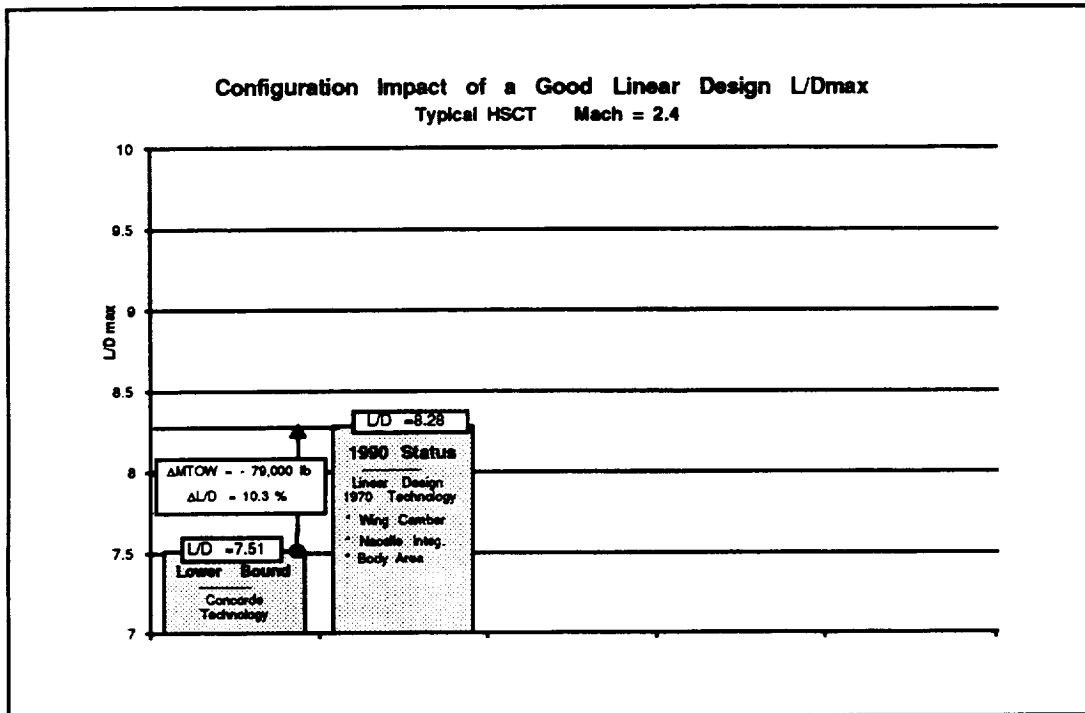
Combining the upper and lower boundaries for zero lift drag, CDo, and for drag due to lift factor, KE, defines the region of acceptable designs for a specific configuration. This acceptable design region is shown for the example HSCT in the figure above.



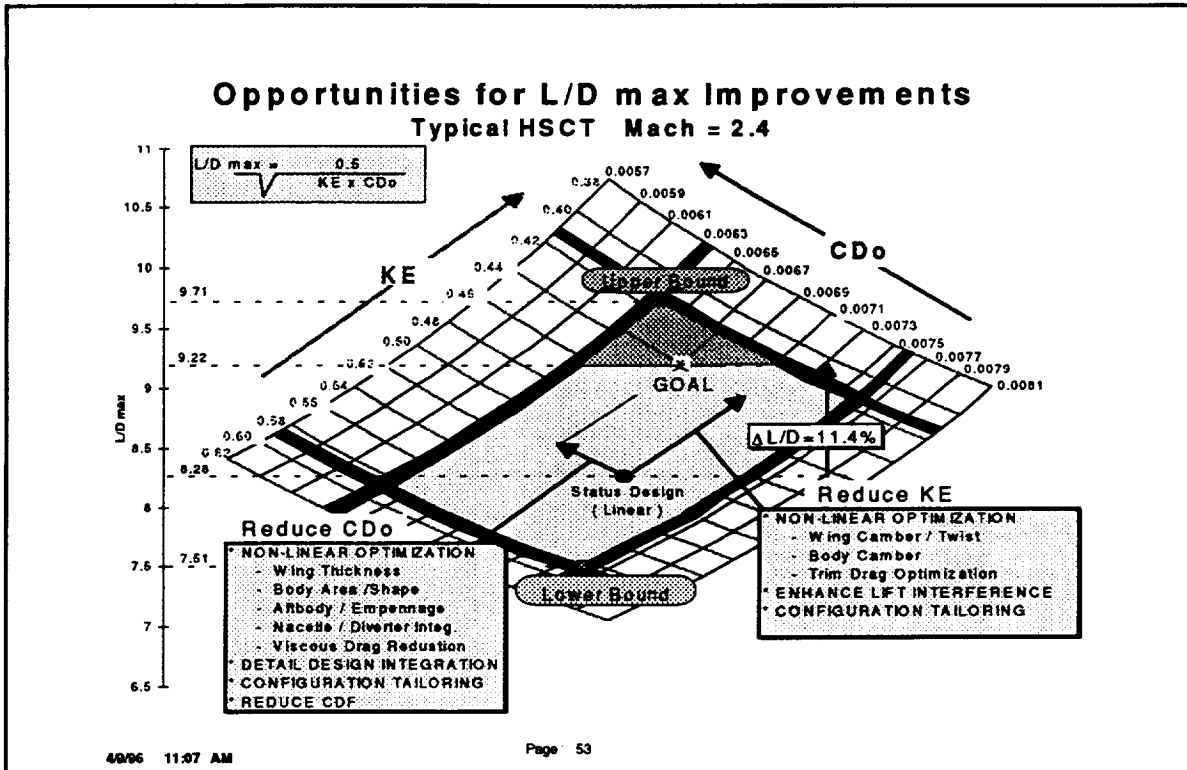
This figure can be used to identify the level of aerodynamic efficiency relative to the upper and lower L/D bounds.

In the above example, the linear theory status design has an L/Dmax that is 10.3% greater than the lower bound corresponding to the Concorde technology level. This configuration achieved favorable aerodynamics effects from a combination of:

- Reduced wing / body drag from body area ruling interference effects
- Favorable nacelle / airframe volume wave drag effects
- Reduced drag due to lift from the linear theory camber / twist design plus wing reflex to reduce the adverse nacelle on camber effects.
- Favorable nacelle lift interference effects.
- Favorable trim drag

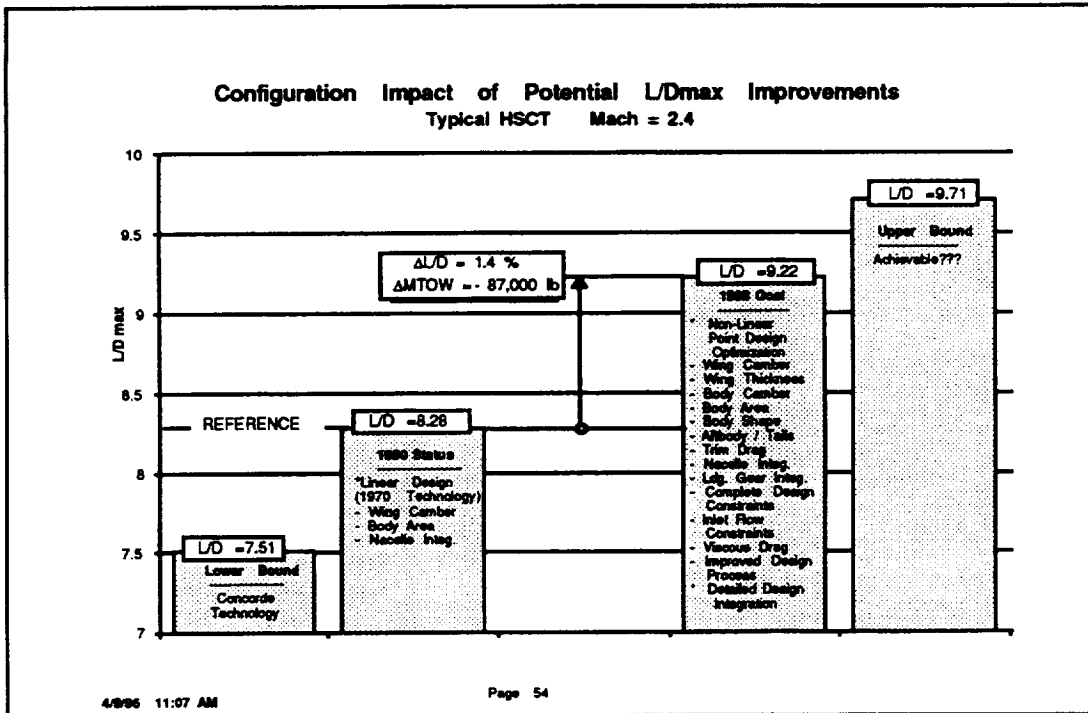


The net benefit of the status linear theory design relative to the lower bound L/D_{max} as shown in this figure results in a savings of 79,000 lbs in max take off weight, MTOW. This is representative of 1990 technology linear theory design capability.



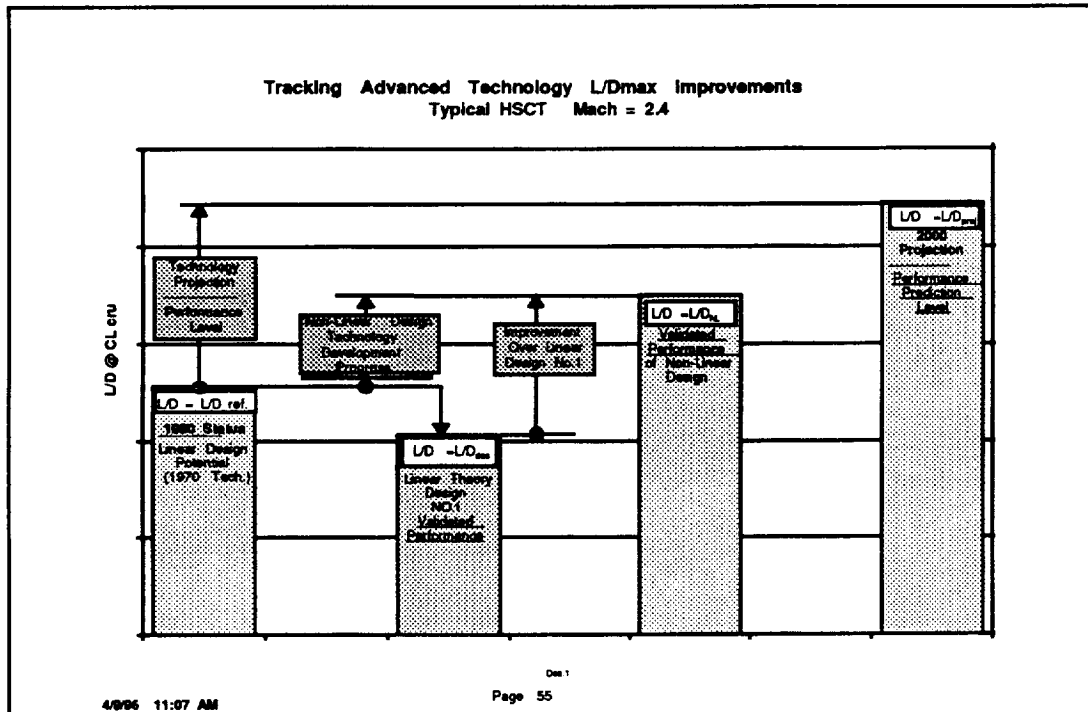
The difference between the goal L/Dmax level and the L/Dmax of the linear theory status design is the projected benefit of design optimization and design development using the emerging advanced nonlinear design and analysis methods.

The figure factors that are expected to contribute to reductions in both CDo and the drag due to lift factor, KE.



This figure shows the impacted of the projected improvements in cruise L/D_{max} on the MTOW of the mission sized HSCT configuration relative to the current linear design.

The 11.4% projected improvement in L/D_{max} will result in a reduction in the maximum takeoff weight of 87,000 lbs.

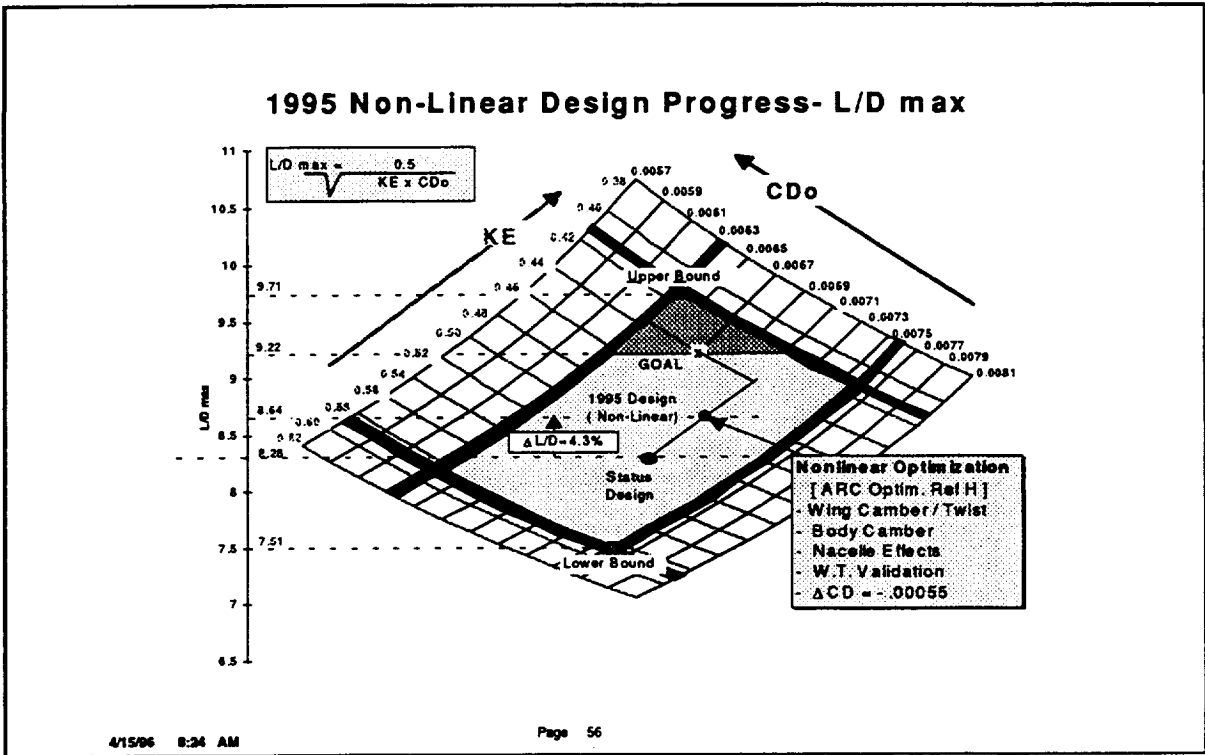


This chart shows the procedure that should be used to track the progress in improvements in cruise L/Dmax relative to a mission performance baseline.

Experience has shown that the preliminary theory design methods can identify a level of performance achievable by a linear theory design provided that a sufficient number of design iterations between linear design, nonlinear design analysis and modifications to the linear design are made. During this design iteration, the linear theory performance predictions do not vary very significantly. The linear theory design is considered validated if the nonlinear prediction or wind tunnel test data matches the linear theory design predicted performance.

The figure above illustrates the effect if the design process is not carried to convergence. A successful nonlinear design would show a greater improvement relative to the "poor" linear design. The technology gains must be measured relative to the performance levels of L/Dmax even though the actual performance improvement relative to a poor initial design is greater.

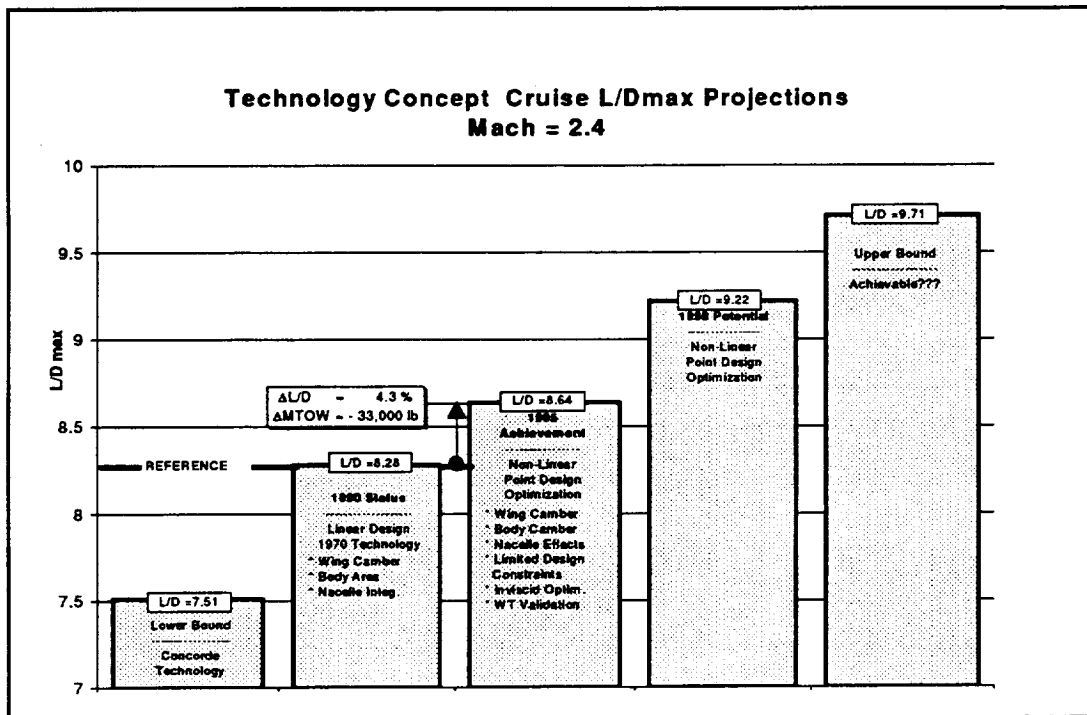
Of course, the ultimate level of success is how close a nonlinear design comes to the predicted target level of L/Dmax.



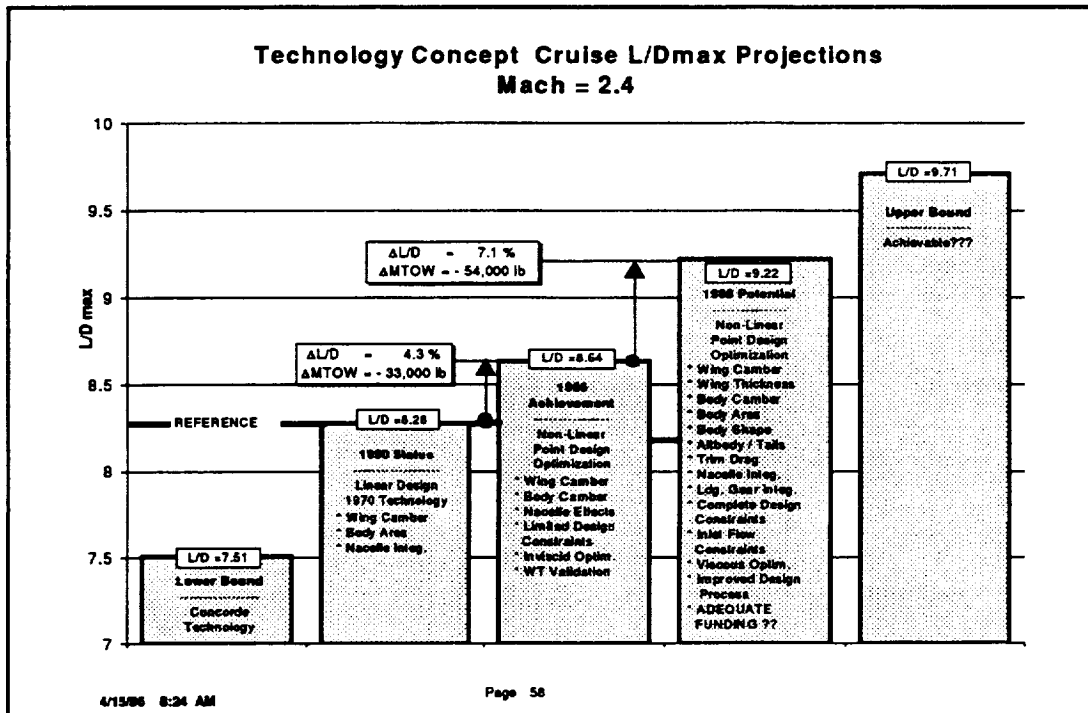
This demonstrates performance improvements achieved to date using nonlinear design optimization. The NASA Ames nonlinear design of the Ref H geometry, the Ames -704 design achieved a drag reduction at cruise of 5.5 drag counts ($\Delta CD = -0.00055$) for the wing / body / nacelle configuration.

The design variables included wing camber and twist, body camber, and some wing inboard leading edge thickness increases.

The performance is applicable to the example HSCT configuration which is similar to the Ref H configuration including the low drag nacelle installation. The increase on L/Dmax is 4.3%.

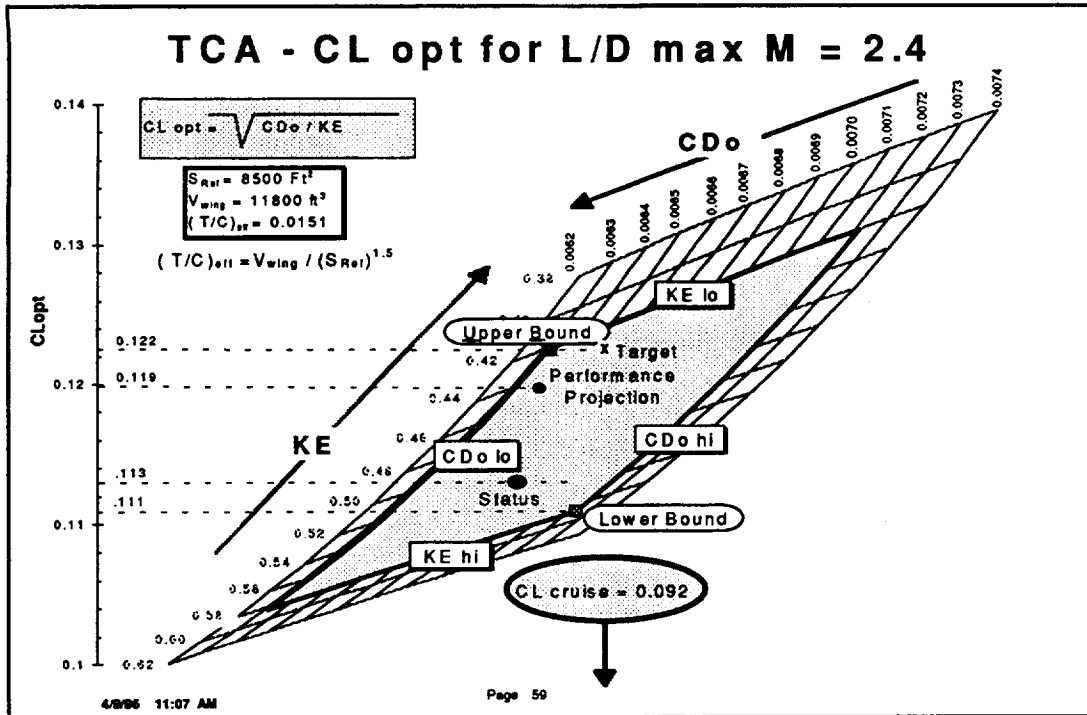


Achieving the 4.3% increase in L/D max, as demonstrated on the Ref H configuration, would result in approximately a 33,000 lb reduction in max takeoff weight for the resized airplane.



The projected further improvements in L/D_{max} will result further developments and enhancements in the emerging non-linear aerodynamic design optimization technology together with improvements in detailed design. Examples of anticipated improvements in the detailed design processes include:

- Nacelle / diverter design integration
- Landing gear design integration
- Wing / body junction design
- Viscous and excrescence drag reduction
- Multi-disciplinary design changes



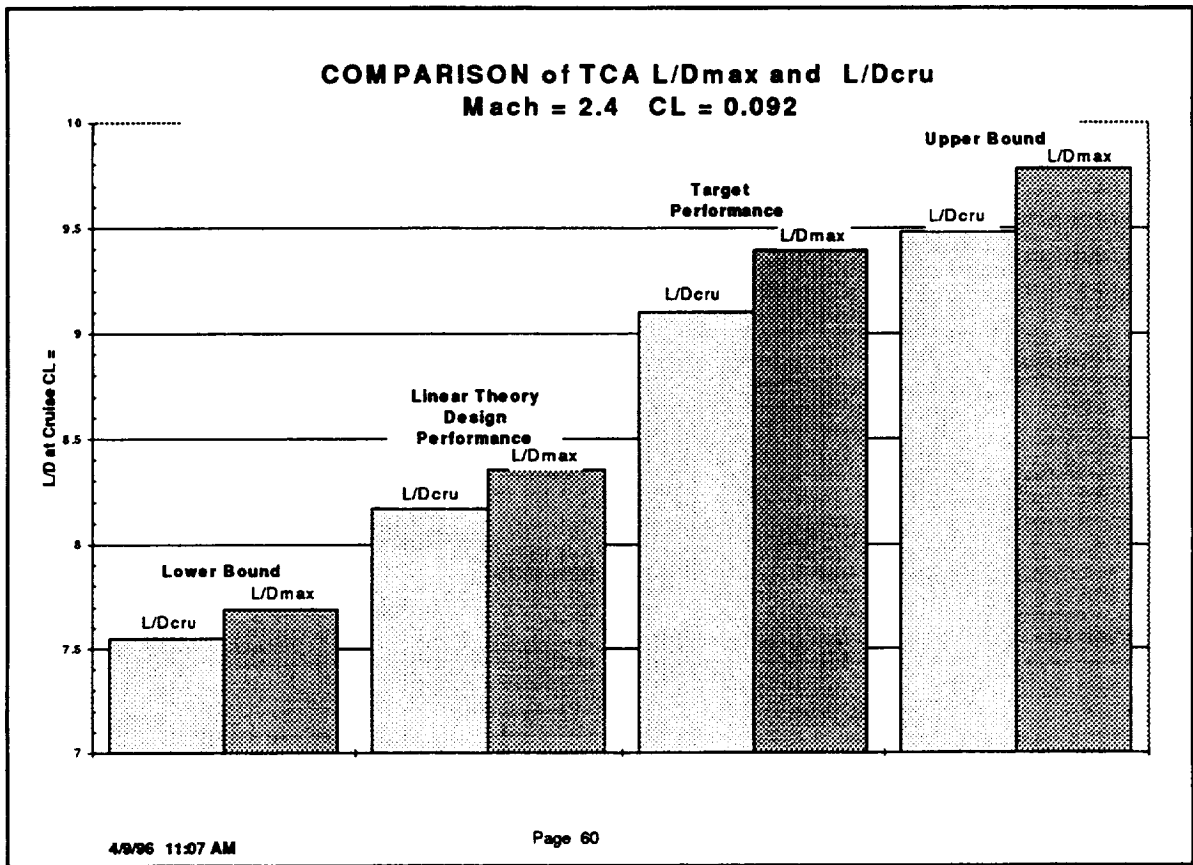
The CL for L/Dmax can be calculated from the zero lift drag coefficient, CDo, and the drag due to lift factor, KE as:

$$CL_{opt} = \sqrt{\frac{C_{Do}}{KE}}$$

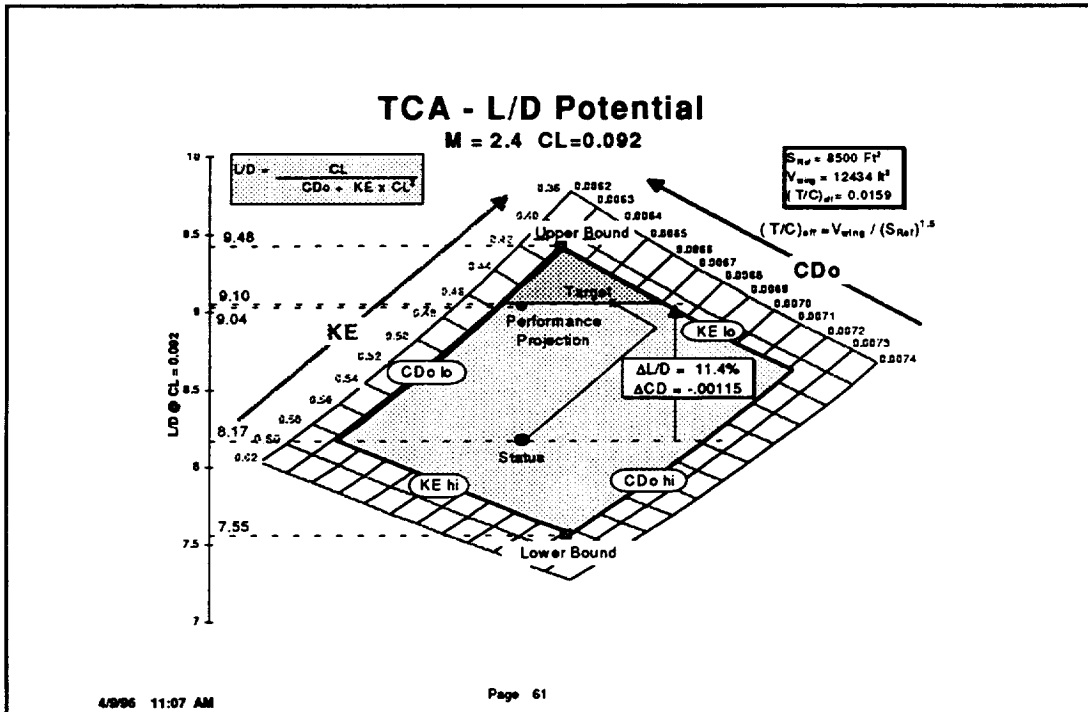
Reductions in CDo Reduce the optimum lift coefficient. Reductions in KE increase the optimum CL.

The current TCA configuration has a rather large wing area because of fuel volume requirements and takeoff noise constraints. Consequently, the cruise CL = 0.092 is substantially lower than the optimum design lift coefficient, CL = 0.120.

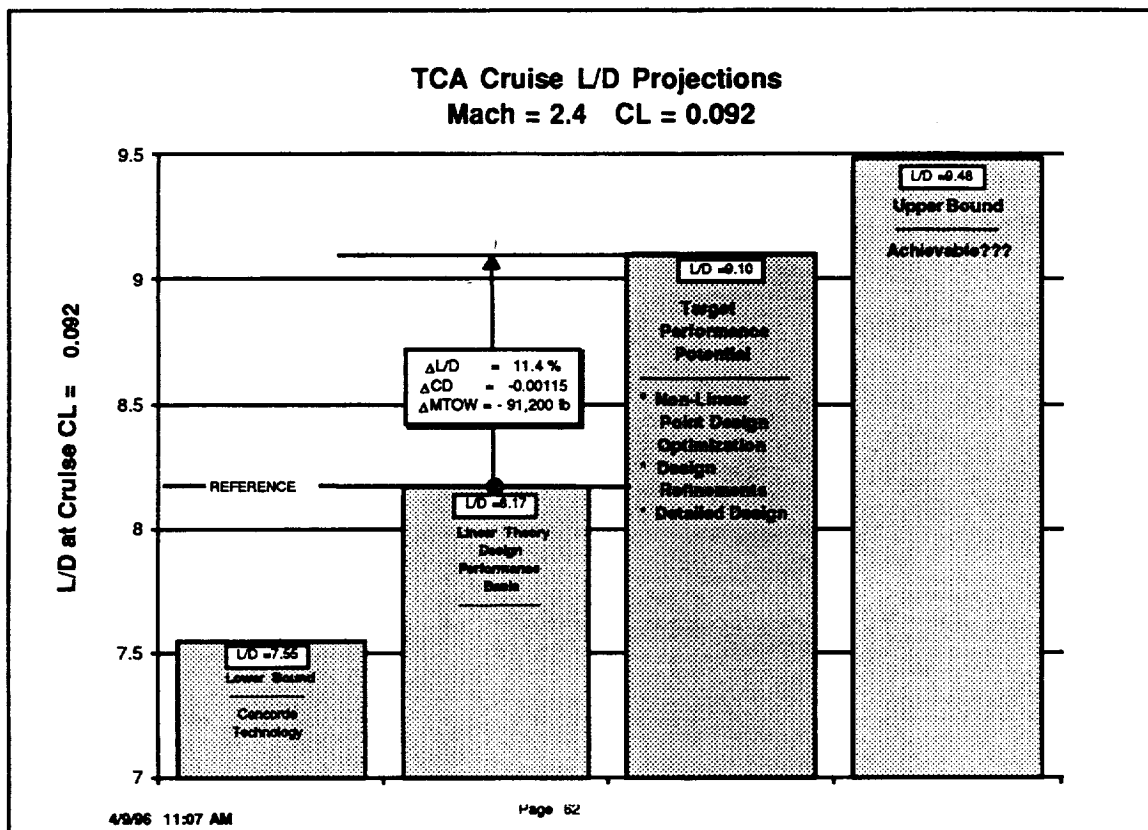
The performance projections should, therefore, be evaluated and tracked for the design CL.



The cruise and maximum values of L/D for the TCA are shown in this figure. The “target” cruise L/D of 9.1 is below the “target” maximum L/D of 9.35 performance limitations associated with the larger wing area.



This figure shows the aerodynamic design space for a cruise CL of 0.092. Relative to the linear design baseline performance level, nonlinear design optimization plus detailed design improvements using the nonlinear methods is projected to increase the cruise L/Dmax by 11.4%. This corresponds to a drag reduction of 11.5 counts, ($\Delta CD = -0.00115$).



The impact of the projected improvements in cruise L/D as shown in this figure are very significant.

The net benefit to the mission sized configuration is a reduction in the maximum takeoff weight of 91,200 lb.

Being able accurately and consistently predict and to achieve these benefits will have a major effect on developing a viable HSCT.

L/D PROJECTION PROCESS FEATURES

- **DEPENDENT ON OVERALL CONFIGURATION FEATURES**
- **NOT DEPENDENT ON INITIAL OR BASELINE DESIGN STATUS PERFORMANCE**
- **CONSISTENT PROCESS**
- **BASED ON FUNDAMENTAL AERODYNAMIC PRINCIPLES - AS WE KNOW THEM TODAY**
- **EASY TO APPLY THE PROCESS**
- **ADAPTABLE - GREATER INSIGHT OR KNOWLEDGE**

4/29/06 11:07 AM

Page 63

The features of the process presented in this paper for predicting potential performance improvements through the application of nonlinear design optimization and detailed design integration include:

- The projections are dependent on the overall features of the configurations as well as the relative component sizes such as the area of the wing or size of the nacelles.
- The projections are not dependent on the status performance of the baseline design.
- The process is consistent and robust in the sense that the projections are not dependent on the insight or experience of any individual. This process should, therefore, be useful in guiding correct early configuration decisions.
- The prediction process is based on fundamental aerodynamic principles as we know them today.
- The prediction can be readily adapted to include modifications that are identified from greater insight or knowledge into the achievable lower limits or the various drag elements.

FURTHER DEVELOPMENTS

- GET OTHER ITD MEMBERS TO AGREE WITH THIS PROCESS
- REPLACE C_{Dw} LOWER LIMIT CRITERIA BY NEW FAR FIELD VOLUME WAVE DRAG OPTIMIZATION PREDICTIONS
- REPLACE K_E LOWER LIMIT CRITERIA BY NEW FAR FIELD LIFT WAVE DRAG PLUS INDUCED DRAG OPTIMIZATION PREDICTIONS
- EXTEND CONVENTIONAL TOPS DOWN L/D max PREDICTION TO HSCT TYPE CONFIGURATIONS
- DEVELOP LOW SUPERSONIC MINIMUM K_E AND C_{D0} CRITERIA

4/15/96 8:28 AM

Page 64

We are currently working with the other members of the HSR Configuration Aerodynamics Integrated Technology Development Team members to get their concurrence with this projection process.

As previously mentioned, the process is adaptable to further enhancements. We have recently developed a new and unique method to use far field linear theory to calculate minimum wing / body volume wave drag, and minimum lift wave drag plus induced drag. These predictions will be incorporated in the projection process.

The aerodynamic performance at subsonic cruise Mach number has a significant on the overall fuel consumption. We will adapt the subsonic "Tops Down" L/D max prediction method to the HSCT configurations with optimized flap deflections.

The aerodynamic performance at low supersonic speeds may have a significant effect of the required engine size. Hence, this tends to be another critical design region. We will extend the supersonic two dimensional design space approach to establish target L/D levels achievable by off-design flap optimization.

REPORT DOCUMENTATION PAGE			Form Approved OMB No. 0704-0188	
Public reporting burden for this collection of information is estimated to average 1 hour per response, including the time for reviewing instructions, searching existing data sources, gathering and maintaining the data needed, and completing and reviewing the collection of information. Send comments regarding this burden estimate or any other aspect of this collection of information, including suggestions for reducing this burden, to Washington Headquarters Services, Directorate for Information Operations and Reports, 1215 Jefferson Davis Highway, Suite 1204, Arlington, VA 22202-4302, and to the Office of Management and Budget, Paperwork Reduction Project (0704-0188), Washington, DC 20503.				
1. AGENCY USE ONLY (Leave blank)	2. REPORT DATE December 1999	3. REPORT TYPE AND DATES COVERED Conference Publication		
4. TITLE AND SUBTITLE First NASA/Industry High-Speed Research Configuration Aerodynamics Workshop			5. FUNDING NUMBERS WU 537-07-20-20	
6. AUTHOR(S) Richard M. Wood, Editor				
7. PERFORMING ORGANIZATION NAME(S) AND ADDRESS(ES) NASA Langley Research Center Hampton, VA 23681-2199			8. PERFORMING ORGANIZATION REPORT NUMBER L-17574B	
9. SPONSORING/MONITORING AGENCY NAME(S) AND ADDRESS(ES) National Aeronautics and Space Administration Washington, DC 20546-0001			10. SPONSORING/MONITORING AGENCY REPORT NUMBER NASA/CP-1999-209690/PT2	
11. SUPPLEMENTARY NOTES				
12a. DISTRIBUTION/AVAILABILITY STATEMENT Unclassified-Unlimited Subject Category 02 Availability: NASA CASI (301) 621-0390			12b. DISTRIBUTION CODE Distribution: Nonstandard	
13. ABSTRACT (Maximum 200 words) This publication is a compilation of documents presented at the First NASA/Industry High Speed Research Configuration Aerodynamics Workshop held on February 27-29, 1996 at NASA Langley Research Center. The purpose of the workshop was to bring together the broad spectrum of aerodynamicists, engineers, and scientists working within the Configuration Aerodynamics element of the HSR Program to collectively evaluate the technology status and to define the needs within Computational Fluid Dynamics (CFD) Analysis Methodology, Aerodynamic Shape Design, Propulsion/Airframe Integration (PAI), Aerodynamic Performance, and Stability and Control (S&C) to support the development of an economically viable High Speed Civil Transport (HSCT) aircraft. To meet these objectives, papers were presented by representative from NASA Langley, Ames, and Lewis Research Centers; Boeing, McDonnell Douglas, Northrop-Grumman, Lockheed-Martin, Vigyan, Analytical Services, Dynacs, and RIACS.				
14. SUBJECT TERMS High speed research; Aerodynamic design; Computational fluid dynamics; Aerodynamics; Stability and control; Performance; Propulsion airframe integration			15. NUMBER OF PAGES 525	
			16. PRICE CODE A22	
17. SECURITY CLASSIFICATION OF REPORT Unclassified	18. SECURITY CLASSIFICATION OF THIS PAGE Unclassified	19. SECURITY CLASSIFICATION OF ABSTRACT Unclassified	20. LIMITATION OF ABSTRACT UL	



